Large eddy simulations of a dual-stream jet with shockcells and noise emission analysis

Carlos Pérez Arroyo

THÈSE

En vue de l'obtention du

DOCTORAT DE L'UNIVERSITÉ DE TOULOUSE

Délivré par :

Institut National Polytechnique de Toulouse (INP Toulouse)

Discipline ou spécialité :

Dynamique des fluides

Présentée et soutenue par :

M. CARLOS PEREZ ARROYO

le mercredi 2 novembre 2016

Titre :

LARGE EDDY SIMULATIONS OF A DUAL-STREAM JET WITH SHOCK-CELLS AND NOISE EMISSION ANALYSIS

Ecole doctorale :

Mécanique, Energétique, Génie civil, Procédés (MEGeP)

Unité de recherche :

Centre Européen de Recherche et Formation Avancées en Calcul Scientifique (CERFACS)

Directeur(s) de Thèse :

M. CHRISTOPHE AIRIAU

M. GUILLAUME PUIGT

Rapporteurs :

M. CHRISTOPHE BAILLY, ECOLE CENTRALE DE LYON

M. PAUL TUCKER, UNIVERSITE DE CAMBRIDGE

Membre(s) du jury :

M. YVES GERVAIS, UNIVERSITE DE POITIERS, Président

M. CHRISTOPHE AIRIAU, UNIVERSITE TOULOUSE 3, Membre

M. GUILLAUME PUIGT, CERFACS, Membre

M. XAVIER GLOERFELT, ENSAM - ARTS ET METIERS PARISTECH, Membre

a mamá y papá

Acknowledgements

I would like to thank my supervisors G. Puigt and C. Airiau for their supervision and support during this PhD thesis. I would like to express my gratitude to J-F. Boussuge for welcoming me to the CFD team at CERFACS. I am indebted to G. Daviller for the numerous discussions, invaluably constructive criticism, his support and guidance offered throughout this work.

I am thankful to the reviewers of this work C. Bailly and P. Tucker and to the members of the Jury for the PhD Defense Y. Gervais, X. Gloerfelt and A. Savarese, who accepted to evaluate the present study.

I would like to acknowledge C. Bailly, A. Savaresse and D. Guariglia for the experimental data that was shared which helped to the realization of this work.

I am sincerely thankful to L. Gefen and R. Camussi for welcoming several times to Università degli Studi Roma Tre during this thesis.

I express my warm thanks to my colleagues of the project: T. Ansaldi, S. Bidadi I. de Dominicis, C. Freitas, L. Gefen, F-J. Granados Ortiz, D. Guariglia, E. Hall, A. Mancini, E. Miguel, D. Di Stefano and M. Khalil. I am sincerely grateful to them for several collaborations, technical discussions related to the project and all the good moments that we shared together over this past three years. In addition, I would like to thank, my colleagues at CERFACS for their help. In particular, I would like to acknowledge R. Biolchini, S. Le Bras and M. Daroukh for the many exchanges of ideas and help offered in this thesis process. I would also like to thank the CSG team at CERFACS and M. Montagnac for their extraordinary technical support. In addition, I would like to acknowledge the work of the administration team. In particular, I would like to express my gratitude and appreciation to M. Campassens, M. Labadens and C. Nasri.

This research project would not have been possible without the economical support frrom the Marie Curie Initial Training Networks (ITN) AeroTraNet 2 of the European Community's Seventh Framework Programme, under contract number PITN-GA-2012-317142. This work was performed using HPC resources from CERFACS and GENCI - [CCRT/CINES/IDRIS] (Grant 2016-[x20162a6074]). The author acknowledges Onera for licensing CERFACS to use the code ***elsA***.

Finally, I would like to thank my family and all my friends, old and new. Thank you for sharing many memorable moments.

Contents

Nomenclature

Subscript and superscript symbols

a	Acoustic component
c	Convective value
cr	Critical value
e	Values at the exit of the nozzle
h	Hydrodynamic component
j	Design or perfectly expanded conditions
L	Referenced to the left side
p	Referenced to the primary nozzle
R	Referenced to the right side
s	Referenced to the secondary nozzle
t	Total values
th	Values at the throat of the nozzle
x'	Fluctuations of x with respect to the mean value
∞	Value defined at quiescent conditions

Greek symbols

β	Shock parameter
γ	Polytropic coefficient
$\delta(x)$	Dirac delta defined at x
δ_{ij}	Kronecker delta defined as 1 if $i = j$ or 0 otherwise
Δt	Time-step
θ	Measured angle with respect to the jet direction
κ	thermal conductivity
λ	Wavelength
λ	Laminar thermal conductivity
μ	Molecular dynamic viscosity
μ_{ref}	Reference molecular dynamic viscosity for Sutherland's Law
ρ	Density
τ	Translation parameter
τ_r	Retarded time
τ_{ij}	Reynolds stress tensor in Einstein notation
$\psi_0(\eta)$	Mother wavelet
ω	Angular frequency

Roman symbols

a	Speed of sound
A	Area
C_p	Specific heat at constant pressure
C_v	Specific heat at constant volume
D	Diameter
e_c	Specific kinetic energy
e_i	Specific internal energy
e_t	Specific total energy
$\mathbf{E}$	Vector of convective fluxes in the x direction
$\mathbf{E}^v$	Vector of viscous fluxes in the x direction
f	Frequency
$f(s)$	Equivalent Frequency with respect to a scale
$\mathbf{F}$	Vector of convective fluxes in the y direction
$\mathbf{F}^v$	Vector of viscous fluxes in the y direction
$\mathbf{G}$	Vector of convective fluxes in the z direction
$\mathbf{G}^v$	Vector of viscous fluxes in the z direction
He	Helmholtz number
$\mathbf{I}$	Identity matrix
k	wavenumber
L	Typical length-scale
L_{sh}	Shock-cell length
$\dot{m}$	mass flow rate
M	Mach number
p	pressure
Pr	Prandtl number
$\mathbf{q}$	heat conduction vector
R	Gas constant
R_{ab}	Cross-correlation of the variable a with b
Re	Reynolds number
s	Scale
St	Strouhal number
$St(s)$	Equivalent Strouhal number with respect to a scale
T	Temperature
T_{ij}	Lighthill tensor
T_{ref}	Reference temperature for Sutherland's Law
$\mathbf{u}$	velocity vector composed by (u_1, u_2, u_3) or (u, v, w)
$\mathbf{U}$	Vector of conservative variables
$\overline{\mathbf{U}}$	Vector of cell-averaged conservative variables
$\overline{U}$	Cell-averaged component of the conservative variables
$\hat{U}$	Filtered component of the conservative variables
V	Volume
$w(s, \eta)$	Wavelet transform
$\mathbf{W}$	Vector of primitive variables
$\overline{\mathbf{W}}$	Vector of cell-averaged primitive variables
$\widehat{\mathbf{W}}$	Filtered vector of primitive variables
$\mathbf{x}$	Space vector composed by (x_1, x_2, x_3) or (x, y, z)

Acronyms

BBSAN	BroadBand Shock-Associated Noise
CAA	Computational AeroAcoustics
CFD	Computational Fluid Dynamics
CNPR	Core Nozzle to Pressure Ratio
DCS	Direct Computation of Sound
DNS	Direct Numerical Simulation
DOG	Derivative of a Gaussian
DRP	Dispersion-Relation-Preserving
FNPR	Fan Nozzle to Pressure Ratio
FWH	Ffowcs-Williams and Hawkings
LES	Large Eddy Simulation
LIM	Local Intermittency Measure
NPR	Nozzle to Pressure Ratio
NLDE	Non-Linear Disturbance Equations
OASPL	Overall Sound Pressure Level
PSD	Power Spectral Density
PSE	Parabolized Stability Equations
RANS	Reynolds Averaged Navier-Stokes
SCN	Shock-Cell Noise
SPL	Sound Pressure Level
URANS	Unsteady Reynolds Averaged Navier-Stokes

Preamble

Background

Noise is defined as a loud or unpleasant sound. In aviation, even though a small fraction of the energy required by the propulsion systems of an aircraft is transformed into sound, that fraction represents a large power source. Over the last decades, aircraft noise has been an increasing annoying phenomena that affects our health and environment. The noise encountered in the surroundings of an airport affects our quality of life and generally disturbs activities related to speech communication and sleep. Moreover, it might have adverse effects on the heart rate and blood pressure. Several studies reported in [1] suggest that aircraft noise alters children development in reading comprehension. Noise also affects our ecosystem giving prevalence to species adapted to urban environments [2]. All the projections show that the growth of passengers at the airports and the number of operations per day will continue to increase. Furthermore, changes in regulations make it possible for new accommodations to be built in the vicinity of the airports. Overall, the noise perceived by the population will grow unless the technology is improved and the laws are prepared for the future.

For this purpose, in 2001, the Advisory Council for Aeronautics Research in Europe (ACARE) developed a path to guide the development goals for 2020 [3] with the support of several aeronautic stakeholders and governments. Among all the objectives of this agreement, the main goals regarding the environment were: the reduction of perceived noise by one half of current average levels, and a 50% and 80% cut per passenger kilometer in CO_2 and nitrogen oxide emissions respectively. These objectives were revisited in 2012 with the publication of the FlightPath 2050 [4]. A new goal was established for 2050 for a reduction of 65% in perceived noise relative to the year 2000. For this matter, investigations about noise have been a case of intensive study for the past 15 years.

The studies carried out in order to reduce aircraft noise are not only focused on the noise radiated to the surroundings of the airports (ground noise) but also on the noise that is propagated to the interior of the cabin. Crew and passengers are affected by cabin noise in a daily basis. The repercussions are of course linked to the flight time, having a lesser impact for short flights. The noise that is transmitted into the cabin can be classified in three groups. The first group is the noise that is generated aerodynamically on the exterior of the aircraft and then propagated into the cabin throughout all the flight time. This noise named airborne noise, usually comes from the boundary layer formed around the aircraft and also from the exhaust jet of the engines. The second group called structure-borne noise categorizes the noise that is transmitted via direct vibrations from the propellers, turbines, compressors and other systems. The third group gathers all the noise sources that appear only during a short period

of time like the noise generated by the landing gear, the gearboxes or the hydraulic systems. Nonetheless, the noise as a nuisance is not the only factor to be taken into account to seek for a reduction in aircraft noise. From a structural point of view, sonic fatigue can appear in the thin surfaces of the aircraft produced by the high frequency noise radiated from the engines, specially in military applications [5].

Framework

This PhD thesis is enclosed in the AeroTraNet2 Project, a Marie Curie Action of the European Commission's 7th Framework Programme (FP7) between several laboratories and researchers around Europe. The project aims at generating a ready to use model for shock-cell noise characterization. Shock-cell noise is a distinctive noise that appears in industrial turbofans at off-cruise design flight conditions. Six academic partners collaborate to address the common objective of modeling shock-cell noise in a wide-body aircraft engine configuration from private sector partner Airbus France, by shock-tolerant numerical modeling for under-expanded jets (University of Leicester), large eddy simulations for turbulent jets with weak shocks (CERFACS), advanced flow-noise correlations (Università degli Studi Roma Tre), jet and near-field noise experiments (von Karman Institute for Fluid Dynamics), reduced-order modeling and flow control (Institut de Méchanique des Fluides de Toulouse, IMFT-INP), and advanced laser-based measurement techniques (the Italian Ship Model Basin, CNR-INSEAN). Knowledge output is synthesized through a dedicated knowledge capturing program by the University of Greenwich, which is used by private sector partner General Electric. In AeroTraNet2, the research output becomes itself object of knowledge management research, which is a novel supra-disciplinary element. AeroTraNet2 is the successor of AeroTraNet project which studied the unsteady flow in airframe fuel vents.

This project is part of the actual effort of the community to study aircraft noise. For this purpose, AeroTraNet2 investigates three complementary approaches in a collaborative environment. The first one is a pure mathematical view of the problem. However, due to the large non-linearities of the flow, it is not always possible to reduce a physical model to an analytical one. The second option is based on experimental studies carried out in the laboratory. They are costly and even though the acquisition time is large, the measured locations are restricted to the investments in the facility. On the other hand, numerical simulations are able to capture the flow at any point of space assuming available data storage capacity. In contrast to experimental studies, due to simulation time restrictions, the numerical computations have a small acquisition time.

Objectives

The global objective of the thesis is to study numerically the physics behind shock-cell noise generation as a first step to design new noise attenuation devices for jet noise in aviation. To that end, aeroacoustic Large Eddy Simulations (LES) of supersonic under-expanded axisymmetric jets are carried out with a high-order solver based on a compact scheme.

Under-expanded jets are characteristic for the formation of a shock-cell structure. Due to a mismatch in pressure at the exit of the nozzle, a system of expansion and compression waves, known as shock-cells, are generated inside the jet which are responsible for shock-associated

noise. The high-order compact schemes used in this work, have been validated for subsonic jets [6]. However, the behavior of such schemes in supersonic jets is an open question. On one hand, high-order compact schemes suffer from high-frequency oscillations in shock-free turbulent regions which are dissipated by the addition of a spatial filter. On the other hand, this dissipation is insufficient to capture strong discontinuities in the flow-field such as shocks. As a result, unphysical oscillations referred to as Gibbs' phenomena are generated that increase numerical instabilities and contaminate the solution [7]. The first objective of this thesis is to validate the numerical schemes for the aeroacoustic simulation of a supersonic under-expanded single jet.

Following the validation, the complexity of the case of study is increased with the computation of a configuration representative of a modern industrial turbofan. In cruise flight conditions, the exhaust of the turbofan engine can be under-expanded and present a similar system of shock-cells than the one obtained for a single jet. Due to the fact that the gases of the primary stream go through the combustion chamber, its temperature is higher than the one encountered in the secondary stream. For this reason, it is most likely to find the shock-cell structure in the secondary stream. The second objective is to carry out an LES of a dual stream configuration with the secondary stream under-expanded.

The aerodynamic and acoustic fields obtained from an LES of a jet have to be analyzed in detail in order to study the physics concerning the generation of noise. Common analysis techniques can be used to extract the characteristic length-scales of the aerodynamics and the spectra of the acoustics. As a third objective, the results employing advanced post-treatment techniques are analyzed to gain a new insight into shock-cell noise. The objectives of the thesis are summarized in three key points:

- Validation of the current high-order schemes for a supersonic under-expanded single jet.
- Large eddy simulation of a dual stream jet representative of an industrial turbofan.
- Analysis of the physics of shock-cell noise with advanced post-treatments.

Outline

The manuscript is structured as follows. Chapter 1 introduces the reader to the history of aeroacoustics, the dynamics of jets and the physics behind supersonic jet noise. At the end of this chapter, a bibliographical research about computational aeroacoustics and jet noise reduction techniques are presented. Chapter 2 explains the numerical schemes implemented in the solver for aeroacoustic simulations. Chapter 3 familiarizes the reader with the methodology followed in this work for aeroacoustic large eddy simulations of supersonic jets. This chapter includes a description of the mesh generation, the computation and standard post-treatment techniques. Chapter 4 describes a wavelet-based analysis that is used to investigate the main characteristic features of a jet and its acoustics. Chapter 5 and Ch. 6 detail the large eddy simulation of an under-expanded single and dual stream jet respectively with a focus on the physical analysis of shock-cell noise. Some numerical concerns exposed in Ch. 6 are treated in Ch. 7 with the development of a new shock-capturing technique adapted to high-order compact schemes. Last, the conclusions and perspectives of this work are presented.

Publications

Some specific elements of the work performed during this thesis were presented in various conferences and submitted to reffered journals and are listed here:

(a) C. Pérez Arroyo, G. Daviller, G. Puigt, and C. Airiau, "Shock-cell noise of supersonic under expanded jets," in *50th 3AF International Conference on Applied Aerodynamics, 29 - 30 March, 01 April, Toulouse, France*, 2015.

(b) C. Pérez Arroyo, G. Daviller, G. Puigt, and C. Airiau, "Hydrodynamic – acoustic filtering of a supersonic under-expanded jet," in *ERCOFTAC WORKSHOP Direct and Large-Eddy Simulation 10, 27 - 29 May, Limassol, Cyprus*, 2015.

(c) C. Pérez Arroyo, G. Daviller, G. Puigt, and C. Airiau, "Modal structure of a supersonic under-expanded jet," in *22èeme Congrès Français de Mécanique, 24 - 28 August, Lyon, France*, 2015.

(d) C. Pérez Arroyo, G. Puigt, and C. Airiau, "Large eddy simulation of shock-cell noise from a dual stream jet," in *22nd AIAA/CEAS Aeroacoustics Conference, 30 May - 1 June, Lyon, France, AIAA Paper 2016–2798*, 2016.

(e) S. Bidadi, C. Pérez Arroyo, G. Puigt, and J.-F. Boussuge, "A high-order adaptive finite volume methodology for shock-turbulence interaction," *submitted to J. Comput. Phys.*, 2016.

Other publications related to several collaboration within this project are detailed in Appx. C and listed in the following:

(f) T. Ansaldi, C. Airiau, C. Pérez Arroyo, and G. Puigt, "PSE-based sensitivity analysis of turbulent and supersonic single stream jet," in *22nd AIAA/CEAS Aeroacoustics Conference, 30 May - 1 June, Lyon, France, AIAA Paper 2016–3052*, 2016.

(g) L. Gefen, C. Pérez Arroyo, R. Camussi, G. Puigt, and C. Airiau, "Broadband shock-cell noise signature identification using a wavelet-based method," in *22nd AIAA/CEAS Aeroacoustics Conference, 30 May - 1 June, Lyon, France, AIAA Paper 2016–2732*, 2016.

(h) F. J. Granados-Ortiz, C. Pérez Arroyo, C.-H. L. G. Puigt, and C. Airiau, "Uncertainty quantification and sensitivity analysis applied to an under-expanded single jet," in *AIAA/AVIATION Conference, 13 - 17 June, Washington, Washington D.C, AIAA Paper 2016–4091*, 2016.

(i) F. J. Granados-Ortiz, C. Pérez Arroyo, C.-H. L. G. Puigt, and C. Airiau, "Uncertainty quantification and sensitivity analysis applied to an under-expanded single jet," *submitted to AIAA J.*, 2016.

Chapter 1

Aerodynamics and aeroacoustics of subsonic and supersonic jets

Aeroacoustics is the branch of the acoustics that is concerned with the sound generated by aerodynamic forces or motions originated in a flow. The sound generated by externally applied forces or classical acoustics such as the sound generated by the vibrating string of a guitar does not fall into this category. The study of the aerodynamics of jets is essential for a better understanding of the underlying phenomena responsible for the generation of aerodynamic sound. The study of aeroacoustics is closely related to the aerodynamics not only because the generation of sound is made by the turbulent motion of the flow but also because the sound perturbations interact with the flow itself. Therefore, the study of aerodynamic sound generated by jets has to be linked with the aerodynamics.

This introductory chapter presents the history of the dawn of modern aeroacoustics and its relation to jets. First, an overview of the acoustic analogies is given in Sec. 1.1. Second, Sec. 1.2 explains the dynamics of supersonic under-expanded jets. Third, in Sec. 1.3, the aeroacoustics of the jets is presented in a chronological way. A bibliographical survey of computational aeroacoustics for jets is summarized in Sec. 1.4. Then, some insight is given to the actual under-development technologies for reduction of jet noise in Sec. 1.5. Last, the chapter ends with a summary and perspectives.

1.1 Acoustic analogy: a look into the past

The history of modern acoustics started with the compendium about the theory of sound written by Lord Rayleigh [8, 9] at the end of the 19th century. Even though the compendium is based on the work of many authors, it helped in the unification of the knowledge related to sound phenomena and set the basis for further studies. In fact, it is only the chapter *XXI*, with the study of a vortex sheet and sensitive jets that is closely related to jet noise. However, Lord Rayleigh already highlighted the importance of such topic as seen in the following quote that corresponds to the beginning of the chapter:

> "A large and important group of acoustical phenomena have their origin in the instability of certain fluid motions of the kind classified in hydrodynamics as steady

[...] These phenomena are still very imperfectly understood; but their importance is such as to demand all the consideration that we can give them."

Despite the fact of this early document, the publication of Lighthill in the fifties [10, 11] and later on in 1962 [12] gives the first theoretical approach to the sound generated aerodynamically. The aerodynamic noise is the noise generated by the flow itself without the help of vibrating solid boundaries. Lighthill based his studies on the fact that the theory of sound should be based in terms of mass density, ρ, and momentum density, $\rho\mathbf{u}$, where $\mathbf{u}$ stands for the flow velocity vector, $\mathbf{u} = (u_1, u_2, u_3) = (u, v, w)$, in the Cartesian coordinates $\mathbf{x}$ (where $\mathbf{x} = (x_1, x_2, x_3) = (x, y, z)$). The equations relate the change of mass or momentum in a small volume to the total mass transport or momentum transport out of the volume as

$$\frac{\partial \rho}{\partial t} + \frac{\partial (\rho u_i)}{\partial x_i} = 0, \quad \frac{\partial (\rho u_i)}{\partial t} + \frac{\partial (\rho u_i u_j + p\delta_{ij})}{\partial x_j} = 0, \tag{1.1}$$

where p is the pressure, and $\frac{\partial}{\partial t}$ is the partial derivative with respect to time t. Here, the subscripts $\{\bullet\}_i$, $\{\bullet\}_j$ and $\{\bullet\}_k$, follow the Einstein notation and δ_{ij} is 1 when $i = j$ and zero otherwise. In the previous equation (1.1), $\rho u_i u_j$ represents direct convection of the momentum component ρu_i by the velocity component u_j, while p is the stress between adjacent elements of fluid, which equally transfer momentum. Equation (1.1) yields the standard equations of acoustics when an isotropic pressure is considered, *i.e.*, the pressure variations are linked to the density variations by the square of the velocity of sound a as

$$\left.\frac{dp}{\partial \rho}\right|_s = a^2, \tag{1.2}$$

which is approximated to a_∞^2 for a uniform flow and small perturbations characteristic of the undisturbed fluid noted by the subscript $\{\bullet\}_\infty$. Starting from Eq. (1.1), using an isotropic pressure and assuming small perturbations, the transformed equations read as

$$\frac{\partial \rho}{\partial t} + \frac{\partial (\rho u_i)}{\partial x_i} = 0, \quad \frac{\partial (\rho u_i)}{\partial t} + a_\infty^2 \frac{\partial \rho}{\partial x_i} = 0, \tag{1.3}$$

so that the density ρ satisfies the standard wave equation

$$\frac{\partial^2 \rho}{\partial t^2} + a_\infty^2 \frac{\partial^2 \rho}{\partial x_i^2} = 0. \tag{1.4}$$

However, without making any approximation, the equations can be divided into two parts: first, the acoustic term, $a_\infty^2 \rho \delta_{ij}$, and second, the remainder, which can be written as

$$T_{ij} = \rho u_i v_j + (p - \rho a_\infty^2)\delta_{ij}. \tag{1.5}$$

This term appears in the right hand side of the momentum equation as

$$\frac{\partial \rho}{\partial t} + \frac{\partial (\rho u_i)}{\partial x_i} = 0, \quad \frac{\partial (\rho u_i)}{\partial t} + a_\infty^2 \frac{\partial \rho}{\partial x_i} = \frac{\partial T_{ij}}{\partial x_j}. \tag{1.6}$$

Equation (1.6) can be reformulated as an inhomogeneous wave equation as

$$\frac{\partial^2 \rho}{\partial t^2} + a_\infty^2 \frac{\partial^2 \rho}{\partial x_i^2} = \frac{\partial T_{ij}}{\partial x_j}, \tag{1.7}$$

where the term on the right hand side represents noise sources as an external forcing to the wave equation Eq. (1.4).

If the same derivation is carried out in the Navier-Stokes equations (full formulation shown in Ch. 2), the stress tensor T_{ij} will account as well for the viscous terms as

$$T_{ij} = \rho u_i u_j + (p - \rho a_\infty^2)\delta_{ij} - \tau_{ij}, \tag{1.8}$$

where viscous stresses are defined as

$$\tau_{ij} = \mu\left(\frac{\partial u_i}{\partial x_j} + \frac{\partial u_j}{\partial x_i}\right) - \frac{2}{3}\mu\frac{\partial u_k}{\partial x_k}\delta_{ij} \tag{1.9}$$

and μ is the molecular viscosity.

The impact of the work of Lighthill made the term T_{ij} to be known as the Lighthill tensor. The term $\rho u_i u_j$ of the Lighthill tensor corresponds to the noise generated by the fluctuations of turbulence. The second term $(p - \rho a_\infty^2)\delta_{ij}$ identifies the noise associated to temperature fluctuations. Finally, the last term τ_{ij} characterizes the noise from viscous dissipation. For low Mach number high Reynolds number unheated flows, the viscous stresses can be ignored and the density can be set to $\rho = \rho_\infty$, simplifying the Lighthill tensor to $T_{ij} = \rho_\infty u_i u_j$ with a proportional error of the order of the square of the Mach number. This publication meant the beginning of the Acoustic Analogy Theory, extensively used nowadays to propagate sound to the far-field.

The source term $\frac{\partial^2 T_{ij}}{\partial x_i \partial x_j}$ of Eq. 1.7 involves second spatial derivatives that behave in noise emission as quadrupoles. Noise sources can be usually decomposed in three types, monopole, dipole and quadrupole sources, which corresponds to three ways to generate acoustic radiation. The monopole sources are the simplest and more effective way of producing sound. They represent a volumetric variation of the flow from a pulsating compact sphere. The dipole, is seen as a vibrating compact sphere of constant volume or by two monopoles of opposite phase. Either way, this source does not generate sound by feeding new fluid into the flow but by its vibration, which makes it a less efficient sound source than the monopole. Finally, the most well-known multipole, the quadrupole, consists in 2 dipoles usually positioned in an array of 2 by 2 with asymmetric phase.

Equation 1.7 can be solved analytically by means of applying the free-space Green function

$$G(x,t) = \frac{1}{4\pi a_\infty^2 r}\delta(\tau_r), \tag{1.10}$$

where δ is the Dirac delta and τ_r is the retarded time defined as

$$\tau_r = t - \frac{r}{a_\infty}, \tag{1.11}$$

and r is the distance between the emission $\mathbf{x}$ and the observation points $\mathbf{y}$ such that $r = |\mathbf{x} - \mathbf{y}|$. The density fluctuations ρ' of the field can then be expressed as

$$\rho'(\mathbf{x},t) = \rho - \rho_\infty = \frac{1}{4\pi a_\infty^2 r}\frac{\partial^2}{\partial x_i \partial x_j}\int_V T_{ij}\left(\mathbf{y}, \tau_r\right)\frac{d\mathbf{y}}{r}. \tag{1.12}$$

Equation (1.12) can be simplified for a point far enough from the flow compared to a typical wave-length. In that case, the differentiation $\frac{\partial^2}{\partial x_i \partial x_j}$ can be directly applied to T_{ij}, giving

$$\rho'(\mathbf{x},t) = \rho - \rho_\infty \approx \frac{1}{4\pi a_\infty^2} \int_V \frac{(x_i - y_i)(x_j - y_j)}{|\mathbf{x}-\mathbf{y}|^3} \frac{1}{a_\infty^2} \frac{\partial^2}{\partial t^2} T_{ij}\left(\mathbf{y}, \tau_r\right) dy. \tag{1.13}$$

One of the most known results from Lighthill [10] is the dimensional analysis to estimate the aerodynamic sound production. By considering low Mach number high Reynolds number similar flows with a typical velocity U, a typical length ℓ and the other constants of the gas, the Lighthill tensor T_{ij} is proportional to $\rho_\infty U^2$. If the fluctuations are generated by instabilities rather than by any direct external perturbations, the dominant frequency of the problem will be proportional to ℓ/U. Therefore, the density variations at a far distance x from the origin of the perturbations (Eq. (1.13)) are proportional to

$$\rho' \propto \frac{1}{a_\infty^2} \frac{1}{x} \frac{1}{a_\infty^2} \left(\frac{U}{\ell}\right)^2 \rho_\infty U^2 \ell^3 = \rho_\infty \left(\frac{U}{a_\infty}\right)^4 \frac{\ell}{x}. \tag{1.14}$$

The intensity of sound is proportional to a_∞^3/ρ_∞ and can be expressed as

$$I(x) = \frac{a_\infty^3}{\rho_\infty} \sigma^2(\rho(x,t)), \tag{1.15}$$

where $\sigma^2(\rho)$ is the variance of the density ρ also expressed as $\overline{(\rho - \overline{\rho})^2}$ and known as the mean square fluctuation. If the dimensional analysis of Eq. (1.14) is applied to the intensity of sound shown in Eq. (1.15), one concludes that the intensity of sound is proportional to

$$\rho_\infty \frac{U^8}{a_\infty^5} \left(\frac{\ell}{x}\right)^2, \tag{1.16}$$

and consequently, the acoustic power is proportional to $\rho_\infty U^8 a_\infty^{-5} \ell^2$. This proportionality relation is known as the U^8 power law. This dimensional analysis establishes that the acoustic power radiated by a jet increases as the eighth power of the jet characteristic velocity, *i.e.* the jet exit velocity.

The quadrupoles (noise sources) are transported downstream with the flow which has an impact on the directivity of the jet noise. Taking into consideration a limited source volume, and a Doppler factor for a moving observation point, the proportionality relation for the intensity of Eq. (1.16) is modified by a factor $|1 - M\cos\theta|^{-5}$, where θ is the angle measured with respect to the direction of motion. *Per contra*, at supersonic speeds, this factor becomes singular when $M\cos\theta = 1$. At this condition, the quadrupoles are heard independently [13].

The Lighthill analogy was improved by Ffowcs-Williams and Hawkings [14] to account for this effect specially important for very high speed jets. His work led to a modification of the exponent in the acoustic power law. For high speed flows (Mach number higher than 3), the acoustic intensity becomes proportional to

$$\rho_\infty U^3 \left(\frac{\ell}{x}\right)^2. \tag{1.17}$$

Moreover, due to the non-uniformity of the jet, the waves undergo refraction. This deviation impacts the directivity by the generation of a relative quiet zone downstream, known as the 'cone of silence'. Lighthill's analogy was later modified by Lilley [15], using the Euler equations as a wave operator to take into account the refraction effects. The acoustic analogies are globally used nowadays to propagate the noise to the far-field. In this work the analogy of Ffowcs-Williams and Hawkings [14] is applied in order to propagate the noise generated by supersonic under-expanded jets to the far-field (see Sec. 3.3.1). The next section presents the dynamics of the jets and its associated noise.

1.2 Dynamics of jets

Jets consist in a flux of flow caused by a difference in pressure. This section explains the different jet topologies according to the Δp between the reservoir or the stage before the nozzle, and the ambient pressure encountered where the jet is issued as shown in the sketch of Fig. 1.1.

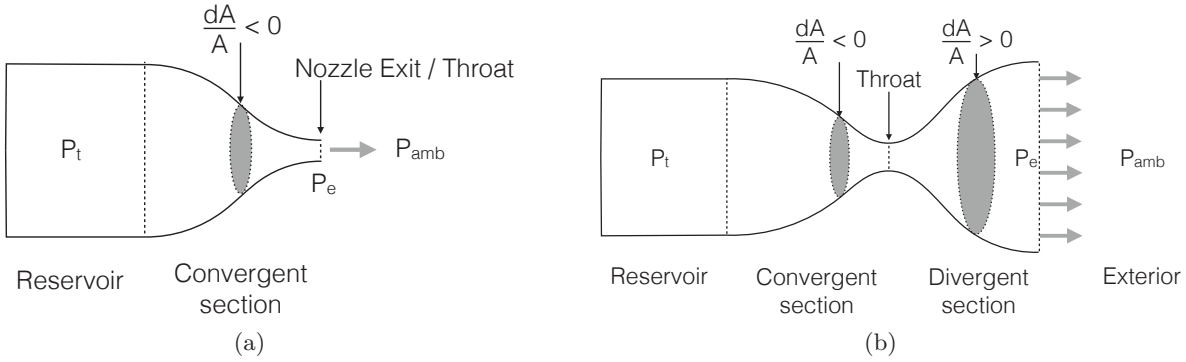

Figure 1.1: *Sketch of a jet issued from a* ***(a)*** *convergent nozzle and a* ***(b)*** *convergent-divergent nozzle*

The topology itself depends on the difference in pressure and also on the shape of the nozzle. The nozzles are divided in three categories, convergent nozzles, divergent nozzles and convergent-divergent nozzles. Combining the equation of conservation of mass and momentum, the isentropic relations and the cross-sectional area A, one obtains

$$(1 - M^2)\frac{du}{u} = \frac{dA}{A}, \tag{1.18}$$

where u is the cross-sectional average velocity and M the Mach number. This equation tells that convergent nozzles ($\frac{dA}{A} < 0$) are able to accelerate a subsonic flow ($M < 1$) up to maximum, the sonic velocity at the throat or the most convergent section of the nozzle ($\frac{dA}{A} = 0$). A supersonic flow ($M > 1$) would decelerate with the same shape. The contrary effect occurs for divergent nozzles where $\frac{dA}{A} > 0$, the subsonic flow decelerates, and the supersonic flow accelerates. Taking these behaviors into account, the convergent-divergent nozzle known as *de Laval* nozzle, can accelerate a flow from rest at subsonic conditions up to the throat of the nozzle, where it reaches the sonic Mach number of one, and then continues to accelerate in the divergent region to a supersonic Mach number. This opposite physical behavior appears

due to the fact that in a subsonic flow, the density remains moderately constant so that the decrease in area in a convergent nozzle produces an increase in velocity in order to conserve the mass flow. On the contrary, in a supersonic flow, both the density and velocity change. In a divergent nozzle, the velocity increases and the density decreases as the area is increased for a supersonic jet. This section focuses on jets issued only from convergent nozzles, more information about the other topologies can be found in [16].

As mentioned above, the difference in pressure has an impact on the development of the jet. The nozzle pressure ratio (NPR) is defined as

$$NPR = p_t/p_\infty, \tag{1.19}$$

that is the ratio between the reservoir or total pressure p_t and the ambient pressure p_∞. Four different topologies can be found depending on this parameter and on the exit pressure at the nozzle exit p_e:

- Perfectly expanded $p_e = p_\infty$ with subsonic exit;
- Perfectly expanded $p_e = p_\infty$ with sonic exit;
- Under-expanded $p_e > p_\infty$ with sonic exit and shock-cell formation;
- Under-expanded $p_e \gg p_\infty$ with sonic exit, shock-cell formation and the appearance of a shock-disk.

The first case is the one of a subsonic jet (the exit Mach number is lower than 1). Under these conditions, the exit pressure is equal to the ambient pressure and thus it is perfectly expanded. If the reservoir pressure is increased, the exit Mach number M_e will increase as well following the isentropic relation

$$\frac{p_t}{p_e} = \frac{p_t}{p_\infty} = \left(1 + \frac{\gamma - 1}{2} M_e^2\right)^{\frac{\gamma}{\gamma-1}}, \tag{1.20}$$

if the energy losses are not taken into account. The symbol γ stands for the specific heat ratio. In a convergent nozzle, the Mach number will continue to increase until $M_e = 1$ is reached at the exit. At this point, a sonic exit with the exit pressure equal to the ambient pressure. At these conditions, and assuming $\gamma = 1.4$, the NPR reaches the critical value

$$NPR_{cr} = \frac{p_t}{p_\infty} = \left(1 + \frac{\gamma - 1}{2} M_{cr}^2\right)^{\frac{\gamma}{\gamma-1}} = \left(\frac{\gamma + 1}{2}\right)^{\frac{\gamma}{\gamma-1}} \approx 1.8929, \tag{1.21}$$

and the Mach number M inside the nozzle is entirely defined by the geometry as

$$\frac{A}{A_e} = \frac{1}{M}\left(\frac{2}{\gamma + 1}\left(1 + \frac{\gamma - 1}{2} M_e^2\right)\right)^{\frac{\gamma}{2(\gamma-1)}}, \tag{1.22}$$

where A_e is the area at the nozzle exit plane. Similarly, the mass flow rate $\dot{m}$ is deduced from the isentropic relations as

$$\dot{m} = \rho u A = \frac{p_t A}{a_t} \gamma^2 M \left(1 + \frac{\gamma - 1}{2} M^2\right)^{-\frac{\gamma+1}{2(\gamma-1)}}, \tag{1.23}$$

where a_t is the sound speed computed with the total temperature T_t. The maximum mass flow rate is achieved for a choked nozzle where $M = 1$. The expression reduces to

$$\dot{m} = \frac{p_t A_e}{a_t}\gamma^2 \left(1 + \frac{\gamma - 1}{2}\right)^{-\frac{\gamma+1}{2(\gamma-1)}} = \frac{p_t A_e}{a_t} 0.8102 \,, \tag{1.24}$$

where A was substituted by A_e because for a convergent nozzle, $M = 1$ can only be reached at the nozzle exit.

Up to this point, the flow was expanding and accelerating in order to reach the ambient pressure. On the third case, as the Mach number cannot increase above 1 (due to the flow behavior in convergent nozzles), and therefore, cannot expand up to p_∞, a further increase in the reservoir pressure will imply a mismatch in the exit pressure with $p_e > p_\infty$. The jet is then said to be under-expanded. Under these conditions, the only physical way that the flow expands to the ambient pressure is via an expansion fan which appears at the exit plane. The expansion waves of the expansion fan bounce in the symmetry plane and are reflected as compression waves. The compression waves are reflected again in the shear-layer of the jet as expansion waves, creating a system of shock-cells as shown in Fig.1.2 (a). These quasi-periodical structures are repeated inside the potential core that is being absorbed by the shear-layer developed around the jet.

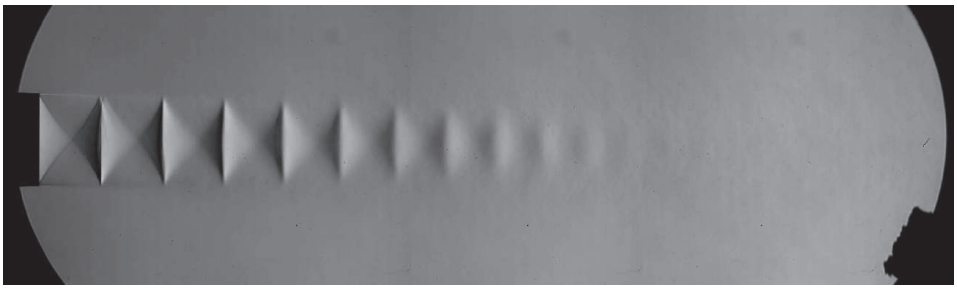

(a)

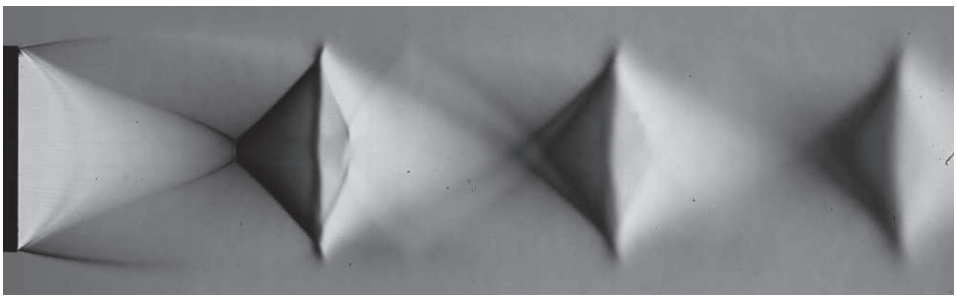

(b)

Figure 1.2: ***(a)*** *Experimental shock-cell pattern generated by a $M_j = 1.15$ from André [17].* ***(b)*** *Shock-cell pattern and shock-disk generated by a $M_j = 1.5$ from André [17].*

Despite this fact, a design Mach number M_j or, the Mach number that would be achieved if the flow could perfectly expand to ambient conditions can be defined with the NPR as

$$NPR = \frac{p_t}{p_\infty} = \left(1 + \frac{\gamma - 1}{2} M_j^2\right)^{\frac{\gamma}{\gamma-1}} \,, \tag{1.25}$$

where the subscript $\{\bullet\}_j$ denotes the conditions of a perfectly expanded jet also referred to as design conditions. In a similar fashion, the other flow variables can be defined. The perfectly expanded temperature T_j is determined as

$$\frac{T_j}{T_t} = \left(1 + \frac{\gamma - 1}{2} M_j^2\right)^{-1}, \tag{1.26}$$

where T_t is the total temperature or reservoir temperature which is kept constant up to the end of the potential core of the jet. The perfectly expanded velocity U_j is defined with M_j as

$$U_j = M_j \sqrt{\gamma R T_j}, \tag{1.27}$$

where R is the gas constant and the density ρ_j is computed using the perfect gas law $p = \rho RT$ as

$$\rho_j = \frac{p_\infty}{R T_j}. \tag{1.28}$$

One needs to remember that the perfectly expanded conditions can be only reached if a convergent-divergent nozzle is employed because the flow cannot go over $M_e > 1$. The diameter D_j at the exit of the perfectly expanded divergent nozzle can be computed as

$$\frac{D_j}{D_{th}} = \left(\frac{1 + \frac{\gamma - 1}{2} M_j^2}{1 + \frac{\gamma - 1}{2}}\right)^{\frac{\gamma+1}{4(\gamma-1)}} \left(\frac{1}{M_j}\right)^{\frac{1}{2}}, \tag{1.29}$$

where D_{th} is the diameter at the throat of the convergent-divergent nozzle. If the total pressure is further increased, a normal shock appears at the end of the first shock-cell as shown in Fig. 1.2 (b). This work focuses on the noise generated by weakly under-expanded jets with the formation of a shock-cell structure. The noise generated by the different topologies is explained in detail in the next section.

1.3 Aeroacoustics of supersonic jets

Aeroacoustics of jets have been extensively studied for many years. The physics behind the noise radiated by subsonic and supersonic jets, the effect of Reynolds number, the influence of temperature and co-flow have been investigated in order to develop new technologies able to attenuate the noise in the aeronautical and aerospace fields. This section explains the physics of supersonic jet noise. The sources of aerodynamic supersonic jet noise can be grouped into two categories: jet mixing noise and Shock-Cell Noise (SCN). The first one can be found in all jet topologies illustrated in Sec. 1.2, however, shock-cell noise can only appear when shocks are developed. The difference in the nozzle exit pressure and the ambient pressure drastically changes the generation of sound of a jet. The typical spectrum at the upstream direction for a supersonic under-expanded jet is shown in Fig. 1.3. The mixing noise, also found in subsonic jets, can be easily distinguished from the shock-associated noise having an amplitude about 10 dB lower and a dominant frequency of one order of magnitude inferior with respect to the SCN.

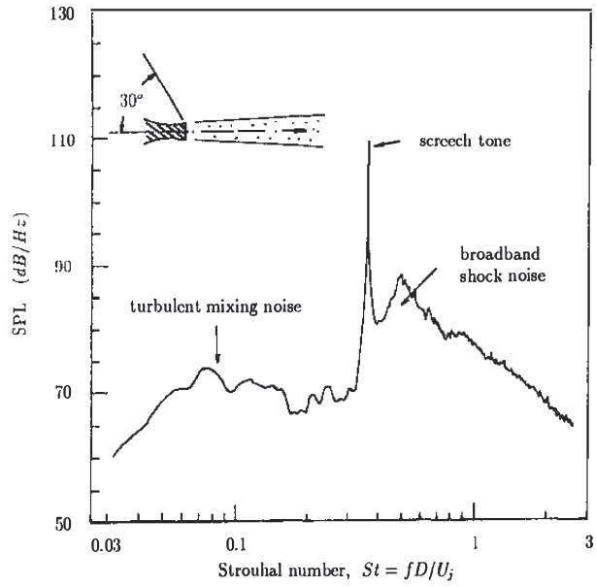

Figure 1.3: *Typical far-field supersonic jet noise spectrum at* 150° *from the downstream direction, from Seiner et al. [18].*

1.3.1 Mixing noise

Turbulence and free shear flows were intensively investigated in the seventies [19, 20, 21]. The researchers found that turbulence of free jets was composed by two different scales, the fine-scale turbulence and the large turbulence structures. Later on, it was deduced that the large structures were important jet noise sources in supersonic jets. In order to study the jet mixing noise, a mathematical description of the fine-scale and large turbulence structures was necessary. Tam *et al.* [22] developed the stochastic instability wave model. According to this theory, the large turbulence structures can be composed of a linear combination of the hydrodynamic stability modes of the flow. The eddies generated near the nozzle exit are convected downstream, growing, but keeping a coherent form over a typical size of the jet diameter. This is equivalent to a pressure instability wave expressed for simplicity as

$$p = A\mathrm{e}^{i(kx-\omega t)}, \tag{1.30}$$

where ω is the angular frequency of the jet, k the wavenumber and A the amplitude. The instability acts as a wavy wall with the same wavenumber and frequency [23]. The wavy wall analogy represents a wall with a small sinusoidal oscillation in height moving parallel to its surface. If the speed of the surface is less than the ambient speed of sound a_∞ in the fluid above, the pressure fluctuations will decay exponentially with the distance from the wall. However, if the phase velocity or propagation speed of the wavy wall ω/k is supersonic with respect to the ambient sound speed, noise will be radiated as Mach waves at an angle

$$\theta = \arccos\left(\frac{1}{M_c}\right), \tag{1.31}$$

where M_c is the convective Mach number of the eddies as depicted in Fig. 1.4. On the other hand, when the phase speed is subsonic and the wavenumber is discrete, no acoustic radiation

appears. Nonetheless, Tam and Burton showed [24, 25] that this sound generation phenomena is also encountered in subsonic jets even though the convection speed is subsonic. This is possible, due to the growth and decay of the instability waves in the jet. This phenomena is easily explained if the amplitude overcomes growth and decay. Under these conditions, the wave number is no longer discrete but a set of broadband wave numbers. Therefore, part of the broadband wave number spectrum could reach a supersonic phase velocity, thus generating the Mach waves.

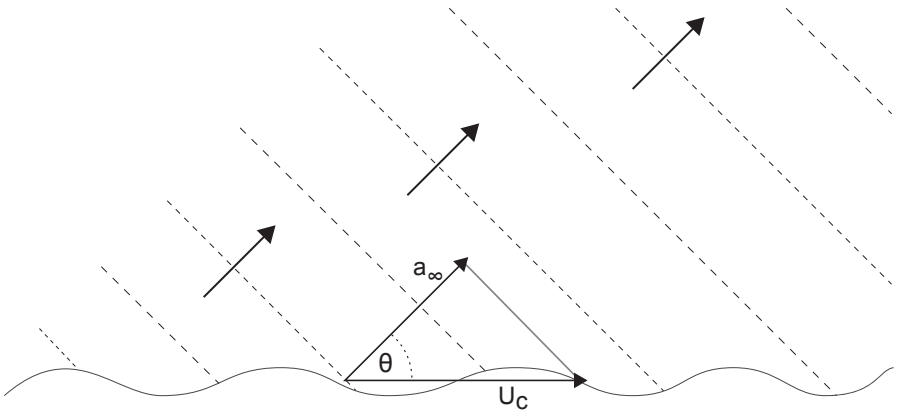

Figure 1.4: *Sketch of a supersonic wavy wall with Mach wave radiation at angle θ.*

The large turbulence structures are considered as a non-compact source. This means that the dimension of the structure is much larger than the wavelength of radiation. They appear as a broad peak in the spectrum. This noise is mainly radiated in the downstream direction due to the downstream convection of the eddies that develop when the shear-layer becomes unstable. On the other hand, the fine-scale turbulence is a compact source, *i.e.*, the characteristic dimension of the structures is much smaller than their wavelength of radiation. It produces broadband noise due to the inherent unsteadiness of the turbulence and it is nearly omni-directional with a downstream preponderance with the exception of the cone of silence.

This identification of the jet mixing noise into two different sources was confirmed by Tam and Golebiowski [26] when they found a similarity spectra for both components. Tam *et al.* were able to collapse a large database of spectra into an empirical similarity spectrum regardless of the jet Mach number (subsonic or supersonic), the jet temperature ratio, the directivity and whether or not the jet was perfectly expanded. The similarity spectrum is

$$S = \left[A \cdot F\left(\frac{f}{f_L}\right) + B \cdot G\left(\frac{f}{f_F}\right)\right]\left(\frac{D_j}{r}\right)^2, \tag{1.32}$$

where A and B are the amplitudes of the independent spectra, f_L and f_F are the peak frequencies, function of the jet operating parameters, and $F\left(\frac{f}{f_L}\right)$ and $G\left(\frac{f}{f_F}\right)$ are the similarity spectra that correspond to the large and fine turbulence scales respectively [26]. The shape of the similarity spectra is shown in 1.5.

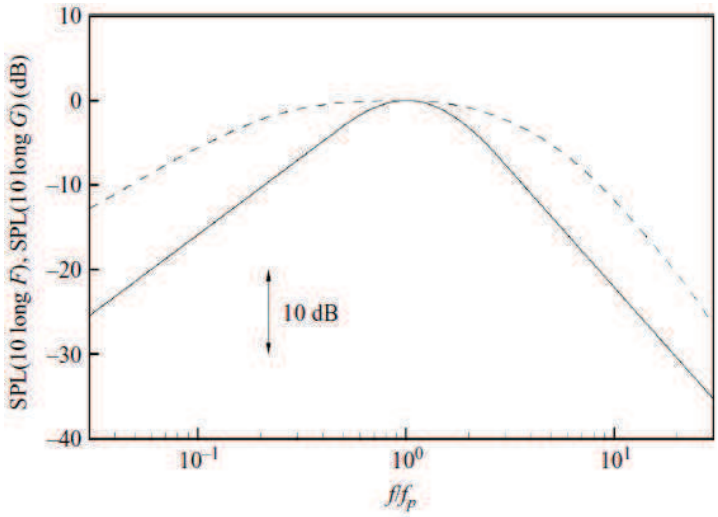

Figure 1.5: *Similarity spectra for the two components of turbulent mixing noise (Solid line for the large turbulent structures and dashed line for the fine-scales of turbulence), from Tam [27].*

1.3.2 Shock-associated noise

Shock-associated noise is found for imperfectly expanded supersonic jets. As explained above, a shock-cell pattern appears due to the expansion that occurs at the nozzle exit plane. Shock-associated noise can be divided into a tonal noise, called screech, and a broadband component known as BroadBand Shock-Associated Noise or $BBSAN$.

Broadband shock-associated noise

In a simple way, Tam explains the generation of BBSAN [23] by the weak interaction between the downstream propagating large turbulence structures of the jet flow and the quasi-periodic shock-cell structure during the passage of the former through the latter. Large turbulence structures are being generated at the nozzle lip due to the inherent instabilities of the flow. These structures are shed and convected downstream by the main flow. The broadband noise is generated by the interaction between these structures and the shocks that appear in the shock-cell pattern. The shock-cell pattern is defined as a quasi-periodic pattern because, first, due to viscosity effects, the strength of the shocks decreases and eventually disappears, second, due to the unsteadiness of the flow, the shocks oscillate, and third, the shear-layer that is being generated around the jet ends up swallowing the potential core of the jet.

Through the stochastic model theory [28], Tam showed the interaction between the large turbulence structures and the shock-cells. The stochastic model is based on solving a non-homogeneous boundary value problem. However, at the time, it was too complex and slow to solve, and so, it was better to use the so-called similarity spectrum based on the assumption that the noise source spectra had no intrinsic length or time scale. Tam managed to obtain good agreement against experimental data in terms of directivity and amplitude using the instability wave theory with some parameters determined empirically.

This model is based on considering the shock-cell structure as disturbances trapped inside the

jet by the mixing layer around the jet. The jet behaves like a waveguide for the disturbances that form the shock-cells. The sound generated can be explained with a one-dimensional model. The velocity fluctuation u_t associated with the large turbulence structures can be represented by the real part of a traveling wave of the form

$$u_t = \mathcal{R}e[A\mathrm{e}^{i(kx-\omega t)}], \tag{1.33}$$

where A is the amplitude, k is the wavenumber and ω is the frequency of the disturbance. The waveguide mode of the shock-cells $k = \omega/U_c$ can be defined by a periodic function

$$u_s = \frac{B}{2}(\mathrm{e}^{tk_n x} + \mathrm{e}^{-ik_n x}), \tag{1.34}$$

where U_c is the convection velocity of the structures, k_n is the nth shock-cell wavenumber and B is the amplitude. The interaction between the convected structures and the shock-cells can be represented by the product of Eqs. 1.33 and 1.34 as

$$\mathcal{R}\left[\frac{AB}{2}\mathrm{e}^{i[(k-k_n)x-\omega t]}\right], \tag{1.35}$$

that represents a traveling wave with wavenumber $(k - k_n)$. If k_n is larger than k, the phase speed $C = \omega/(k - k_n)$ will be negative and supersonic. According to the wavy wall analogy, it would radiate towards the upstream direction at an angle θ defined by $\cos\theta = a_\infty/C$. The spectral peak frequency can be defined for different angles of radiation as

$$f = \frac{U_c}{L^i_{sh}(1 + U_c\cos\theta/a_\infty)} \tag{1.36}$$

where L^i_{sh} is the shock-cell spacing at the shock-cell i that can be approximated with the formulation of Prandtl [29] and Pack [30] as

$$L^i_{sh} \approx \frac{2\pi}{k_i} = \pi(M_j^2 - 1)^{1/2}\frac{D_j}{\sigma_i}, \tag{1.37}$$

where M_j and D_j are the perfectly expanded Mach number and diameter respectively and σ_i are the zeros of the Bessel function of order 0.

Fifty years later from the study of the shock-cell structure [29] using a linear vortex sheet model by Prandtl, Pack expanded it for slightly imperfectly expanded jets [30]. Let p' be the pressure disturbance of the shock-cells:

$$p' = \sum_{i=1}^{\infty} A_i\Phi_i(r)\cos(k_i x), \tag{1.38}$$

where $A_i = 2\Delta p/\sigma_i$, is the amplitude, $\Phi_i(r) = J_0(2\sigma_i r)/J_1(\sigma_i)$ and $k_i = 2\sigma_i/[D_j(M_j^2 - 1)^{1/2}]$; $i = 1, 2, 3\ldots$, the wave-number of the ith waveguide mode. Δp is the static pressure difference at the nozzle exit plane and J_0 and J_1 are the Bessel functions of order 0 and 1 where $J_0(\sigma_i) = 0$. The general approximated shock-cell spacing using Eq. (1.37) would be the one given by the longest wavelength (*i.e.* when $i = 1$).

Screech tonal noise

The appearance of the shock-cell pattern induces a broadband shock-associated noise, however, the conditions to obtain the tonal noise, named screech, are not so easy to accomplish. Depending on the flow conditions, and the surroundings of the jet, specially the surfaces around the nozzle exit plane, including the nozzle lip, screech could or could not appear, with or without the presence of some harmonics. The BBSAN is a well known phenomena that can be predicted both in frequency and amplitude. Screech on the other hand, is still difficult to predict in terms of the amplitude.

The generation of screech is similar to that of the broadband shock-associated noise. The turbulent structures that are convected downstream and interact with the shock-cells, generate new acoustic perturbations that are radiated upstream. This collateral perturbations reach the nozzle lip, inducing new perturbations that are convected downstream. Eventually, these new perturbations reach the shock-cells, closing a feedback loop as sketched in Fig. 1.6.

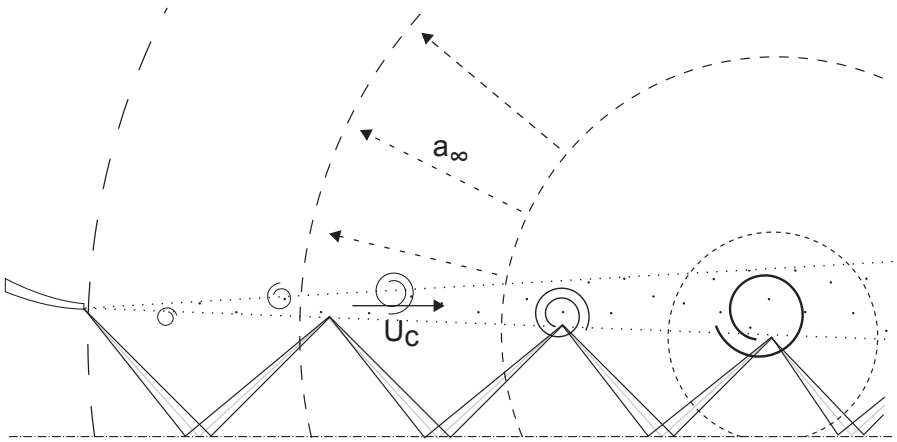

Figure 1.6: *Sketch of the generation of the screech. U_c is the convective speed of the eddies, and a_∞ the speed of the acoustic perturbations generated by the interaction of the eddies with the shock-cells.*

Screech has been studied from the fifties by Powell [31] due to its inherent capability to enhance the mixing of the flow. Powell was the first to detect the upstream directivity of the shock noise when examining some Schlieren pictures of supersonic jets. He tried to explain this phenomena with a phased array of monopoles localized at the edge of the jet. In order to generate noise, first, the phase needed to be such that the travel time of the hydrodynamic disturbances that are convected downstream and the upstream acoustic perturbations would sum up to an integral number of screech cycles or periods. And second, the amplitude needed to be maximum in the upstream direction. The directivity pattern of the screech is given by Powell [31] as

$$D_f = \frac{1}{3} + \frac{2}{3}\cos\left(2\pi\frac{L}{\lambda}(1 - M_c\cos\theta)\right) \tag{1.39}$$

and

$$D_h = \frac{1}{3} + \frac{2}{3}\cos\left(4\pi\frac{L}{\lambda}(1 - M_c\cos\theta)\right) \tag{1.40}$$

for the fundamental and the harmonic tones respectively. In Eq. (1.39) and Eq. (1.40), L is the shock-cell spacing, θ the angle measured with respect to the downstream direction. M_c and λ_c are the convective Mach number and the wavelength of the disturbance respectively. The maximum directivity of the fundamental tone is obtained for the upstream direction ($\theta = 180°$) whereas for the harmonics it is at 90°. The frequency of the fundamental tone can be approximated by

$$f = \frac{U_c}{L(1 + M_c)}, \tag{1.41}$$

where U_c, *i.e.* the velocity of the convected structures, is usually taken as a first approximation as 0.7 U_j where U_j is the fully expanded jet velocity. The screech period or cycle is defined as the time that takes for an acoustic perturbation to cross a shock-cell, plus the time of the convected structure to cross the same space. It can be defined as

$$T_s = \frac{L}{U_c} + \frac{L}{a_\infty}, \tag{1.42}$$

where a_∞ is the ambient speed of sound. Eq. (1.42) clearly depends on the convective velocity, and how the spacing is defined, particularly if one takes into account all the unsteadiness of the process. Tam, Seiner and Yu [32] improved the equation to predict the screech frequency of Prandtl (Eq. (1.41)) by taking into account temperature effects. The frequency can now be expressed as

$$f = \frac{U_c}{L_{sh}}\left[1 + M_c\left(1 + \frac{\gamma - 1}{2}M_j^2\right)^{-1/2}\left(\frac{T_t}{T_\infty}\right)^{1/2}\right]^{-1}, \tag{1.43}$$

where T_t is the total temperature of the jet, T_∞ is the ambient temperature and L_{sh} is defined as in Eq. (1.37) for σ_1. A simplified formula can be used by adopting the empirical result of $U_c \approx 0.7U_j$, a shock-cell spacing 20% smaller and rearranging the terms to express it as the Strouhal number as

$$\frac{f_s D_j}{U_j} = 0.67(M_j^2 - 1)^{-1/2}\left[1 + 0.7M_j\left(1 + \frac{\gamma - 1}{2}M_j^2\right)^{-1/2}\left(\frac{T_t}{T_\infty}\right)^{1/2}\right]^{-1}. \tag{1.44}$$

This formulation was later modified by Panda [33] to account for standing waves outside the shear-layer of the supersonic screeching jets. The standing waves have a resultant wavenumber $k_{sw} = k_h + k_a$, and are formed due to the interference between downstream propagating hydrodynamic fluctuations k_h and upstream propagating acoustic waves k_s. In terms of the wavelength, the previous expression can be defined as $1/\lambda_{sw} = 1/\lambda_a + 1/\lambda_h$, where λ_s and λ_h are the wavelength of the acoustic wave and hydrodynamic fluctuations respectively. This shock-cell spacing can be substituted into Eqs. 1.41 or 1.43 to obtain the screech frequency based on the standing waves.

The first formulations were based on the resonator behavior of screech and were proposed as a tool that was able to compute the frequencies at which, if screech was present, it would

resonate. However, the physics behind the screech phenomena were still unknown. In the last decades, they have been extensively studied. Following the description of Raman [34] and Tam [23], screech can be defined with four key mechanisms: the instability wave growth, the instability-shock interaction, the acoustic feedback and the receptivity process.

The key mechanism for the generation of screech is the perturbation of an instability wave that grows by the shock-cell pattern. The mean flow accelerates between the shocks and decelerates when approaching them. It can then be supposed that the disturbances are perturbed in the same way. The exponential growth of the instabilities is modulated by the shocks and the amplitude by the fluctuations of velocity.

Even though the growth is partially modified by the shock-cells, the instability needs to grow up to a certain amplitude in order to interact with the shocks (*i.e.* usually between the 3rd and the 5th shock-cell). One of the key aspects of screech is the prediction of the spacing of the shock-cells. The frequency of the screech for instance, is proportional to the inverse of the shock-cell length as seen in Eq. (1.41). For this matter, models formulated to predict the shock-cell spacing are needed. Some examples are the Prandtl model explained in Sec. 1.3.2 or the one developed by Tam *et al.* [35] that solves an eigenfunction expansion of a modeled shock-cell system inside a jet surrounded by a vortex sheet. Another example is the work of Tam [36] that accurately calculates the structures and screech tone frequencies of rectangular and non-axisymmetric supersonic jets.

However, better modeling to characterize the shock-cell spacing is required to take into account non-uniformities in the shock-cells of the unsteady flows. Panda showed [37] how the shock moves inside the shock-cell pattern due to the turbulent structures that are convected downstream from the nozzle lip. These structures shape the potential core of the jet. The shock center moves downstream, loosing strength and a weaker shock appears upstream, which in the process will become stronger but it will start from the opposite side of the shear-layer. This process is illustrated in the sketch in Fig. 1.7 by Suda *et al.* [38]. The anchor point A, moves forward to the point A' and then point B moves backward until the starting position is reached.

Later on, Suzuki and Lele [39] introduced the concept of shock leakage. The phenomenon of shock leakage occurs near the saddle points of the vortices convected downstream in the mixing layer surrounding the jet (see Fig. 1.8). The noise radiated from usually the third shock-cell happens because the shock waves leak through the mixing layer. The location is not arbitrary, near the third shock-cell, the vortices are developed enough to have a clear saddle point. Downstream of the third shock-cell, no saddle points are clearly identified due to the turbulence. This leakage, is considered as the acoustic perturbations that are convected upstream. The turbulence reduces the intensity of the shock noise by scattering the fronts. Lui and Lele [40] studied the test-case of an impinging shock into a shear-layer which bounces back as a compression shock. Lui *et al.* determined wih Direct Numerical Simulation (DNS) that the pressure fluctuation scales with the peak strength of the shock tip of the compression-expansion wave. They concluded that the shock-associated noise is generated by the scattering of the shock wave of the energetic streamwise velocity fluctuations in the shear-layer.

When the acoustic perturbations reach the nozzle lip, a coupling of aerodynamic and acoustic disturbances occurs called receptivity. Receptivity is the phenomenon from which perturbations alter the instabilities of the flow. This process is most known in the transition of the boundary layer where outer perturbations enter the boundary layer and amplify the instabili-

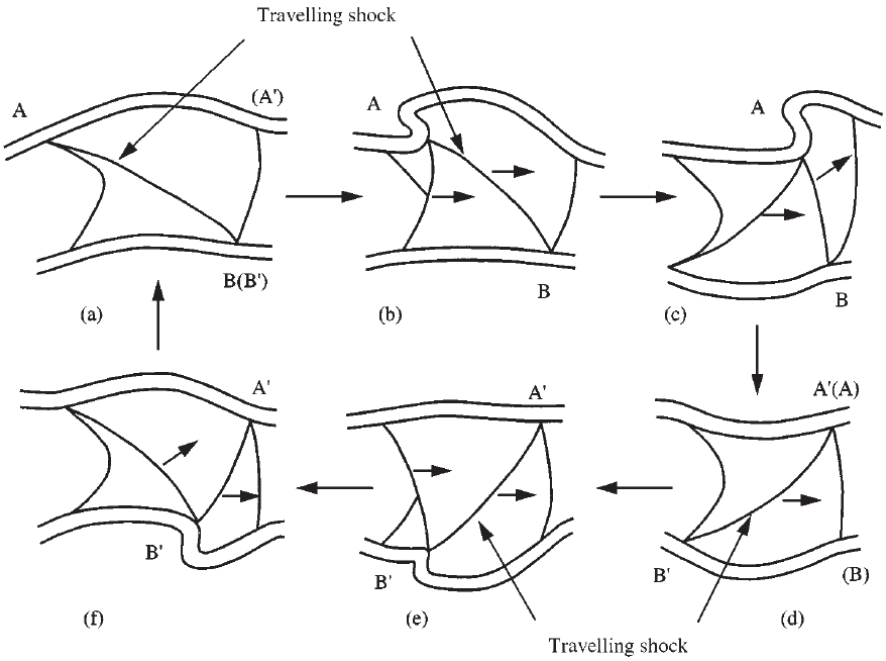

Figure 1.7: *Dynamic motion of the traveling shock in the third shock-cell from Suda et al. [38].*

ties that lead to transition to turbulence. The acoustic disturbances act like a forcing term in the starting location of the shear-layer in the nozzle lip by generating hydrodynamic structures that are convected downstream. In fact, it was shown by Norum [41], that the thickening of the nozzle lip could increase screech up to 10 dB. This newly generated structures eventually interact with the shock-cells, closing the feedback loop.

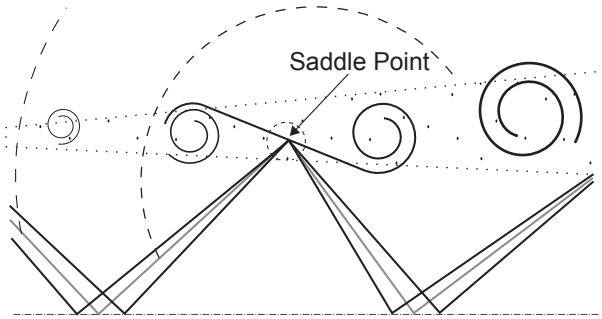

Figure 1.8: *Sketch of the saddle point between two vortices where the shock leakage occurs.*

Screech does not only appear as a tonal noise, but also as a modal behavior of the flow. The jet undergoes different modes depending on the geometry of the nozzle and the jet flow conditions, oscillating at the screech frequency. Powell [31] isolated 4 modes for the rounded jets that he named A, B, C and D with toroidal or helical oscillations. The change between modes can be seen as jumps in frequency and amplitude. The first mode A, can be actually split into two, A1 and A2, both toroidal modes. The modes B and C are flapping modes with a non-stationary flapping plane. Mode D is defined as an antisymmetric mode made of two

contra-rotative helicoidal modes with the same frequency and amplitude. Hysteresis is found when coming from mode C to mode D. Another mode E at the end of the curve was shown by Panda, Raman and Zaman [42] for high Mach numbers.

The screech staging process was demonstrated by André *et al.* [43] to have enough influence on the jet dynamics to actually affect the BBSAN. Depending on the intensity of the screech, the shock-cells may collapse and disappear after the screech emitting shock-cell. Both the broadband shock-associated noise (BBSAN) and the Overall Sound Pressure Level (OASPL) increase in frequency when screech is eliminated. André *et al.* assumed that this is due to the excess high frequency content produced by the additional shock-cells downstream of the most critical shock-cell for the screech. Among their studies, they found first, that the screech amplitude and oscillations increase with flight velocity (*i.e.* the velocity of the flow outside the jet). Second, the amplitude of the screech decreases with temperature but for a constant temperature, it is independent of the shock strength. And third, a minimum strength is needed to originate screech, but the amplitude does not vary once screech appears. This supposition may not apply to high Mach numbers where one could not get screech at all, for whichever shock strength one had.

Even though many advances have been done when dealing with screech phenomena, complex or just non-axisymmetrical configurations do not show this tonal noise. Furthermore, the different subtleties for the appearance, makes it difficult to predict analytically, leaving as only option, numerical costly computations.

1.3.3 Dual stream jets

The noise generated by dual stream jets is mostly the same as the one generated by single jets. Even though the topology of the jet is different, the mechanism for noise generation does not change. The interest for dual stream jets comes from the development of turbofan engines. Turbofan engines were initially used in the fifties with the design of the engine Rolls-Royce RB.80 Conway and they have been evolving ever since, increasing in performance and by-pass ratio. The first studies on shock-cell noise for dual stream jets was carried out by Tanna *et al.* [44] in the seventies. It was found that the shock-cell structure and its produced noise were closely linked to the relation between the total to ambient pressure ratio of the core and the fan jets. In particular, Tanna *et al.* [45, 46] and Tam *et al.* [47, 48] showed that having a slightly supercritical primary jet would yield an almost complete destruction of the shock-cell system of the secondary stream, reducing the overall shock-cell noise. Dahl *et al.* [49, 50] applied the instability wave noise generation model of Tam *et al.* [24, 25] to supersonic dual jets having good agreement with experiments. The structure of the shock-cell system and the appearance and location of a shock-disk on the primary jet was studied by Rao [51]. The appearance of screech on dual stream jets was studied experimentally by Bent *et al.* [52]. It was found that the 'tonal' shock-cell noise disappeared when the nozzle had bifurcations inside the secondary stream. This illustrates how the effect of a pylon and the internal struts of commercial turbofans would disengage screech from being present in commercial aviation. Murakami *et al.* [53, 54] studied the lengths of the potential cores as well as the spreading angle of both the primary and the secondary jets obtaining good agreement with the theory. Their case of study was the one where the primary jet is supersonic and the secondary is subsonic. Dahl *et al.* [55] studied a perfectly expanded dual stream jet where they

showed that the mixing noise can be also adapted by the similarity spectra used for single jets. Different configurations can be studied in coaxial jets, depending on the flow conditions of the primary and the secondary jet. The primary jet is the one in the center, and the secondary jet, the one surrounding the primary jet.

The constant increase in by-pass ratio and the new regulatory terms that were agreed by the community on noise reduction led the industry to focus again on the noise generated by the turbofans. An extensive experimental campaign on subsonic and supersonic dual stream jets was initiated by Viswanathan [56, 57] and Viswanathan *et al.* [58] in order to carry out a parametric study on the effect of the primary and secondary nozzle pressure ratio, the secondary-to-primary jet velocity ratio and the secondary-to-primary nozzle area ratio. The main conclusions are summarized in the following. First, the shock-associated noise strongly depends on the geometrical shape of the nozzle and to whether or not the shocks are found in the primary or in the secondary jets. When the shock-cell structure appears in the secondary stream, there is a strong radiation to the aft angles. Second, the velocity ratio is relevant for mixing noise but insignificant for shock-cell noise, hence obtaining the noise characteristics similar of those from a single stream jet when it is less than 0.5. On the other hand, when this parameter is high enough, the contribution from the secondary jet is dominant at high frequencies and upstream angles. Last, the noise propagated at downstream angles remains invariant for all geometric and jet conditions. Another experimental campaign was carried out by Bhat *et al.* [59] who concluded that even though shock-cell noise does not increase monotonically with increasing power settings [56], the overall power level does. Viswanathan [56] found different behaviors when studying different topologies for dual stream jets. The shock-associated noise is dominant for all angles, similar to a single jet, when the primary jet is supersonic. In this case, the effect of the secondary shear-layer can be omitted. Additionally, if the topology is inversed, *i.e.* the supersonic jet is the secondary stream, the shock-associated noise will become apparent in the forward angles. Increasing the temperature in the primary stream only, slightly affects the lower frequencies at lower angles.

The dual stream topology of interest in this work is the one where the primary jet is high subsonic, and the secondary jet is supersonic and under-expanded as displayed in Fig. 1.9. These flow conditions allow the appearance of the system of shock-cells in the surrounding stream, *i.e.*the secondary jet, in a circular pattern. The two jets at different flow conditions generate two shear-layers. Dahl *et al.* [55] identified the location of the noise sources for the mixing noise downstream of the outer potential core when both shear-layers merge. Using instability wave analysis, they showed that the instability waves generated in the inner shear-layer reached the maximum amplitude at the same location.

Shock-associated noise is originated from the interaction between the vortical structures that develop in the shear-layer and the shock-cell system. When the secondary stream is imperfectly expanded, the shock-cell system is contoured by the inner and the outer shear-layers. Therefore, two possible shock-associated noise sources from the interaction with both shear-layers take place. New factors need to be taken into account for the propagation of the noise from the noise sources to the far-field because it has to cross the jet itself, now, with a different topology than for the single jet. The acoustic perturbations generated inside the primary jet have to cross the surrounding shocked stream, modifying both directivity and amplitude in the process. The generation of screech and BBSAN have the same key mechanisms, but in a dual stream jet, where the under-expanded jet is the secondary stream, the turbulence structures

that are being convected downstream from the nozzle lip double because of the dual nozzle, and shear-layer.

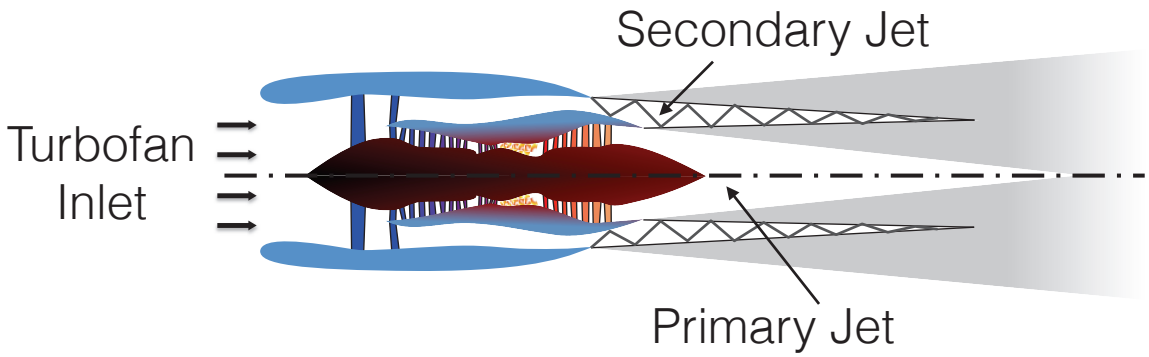

Figure 1.9: *Skecth of a turbofan engine with the secondary stream under-expanded.*

Moreover, Abdelhamid *et al.* [60] found that the high frequency components developed in the primary shear-layer whereas the low frequency components originated on the secondary shear-layer. This phenomena was further studied by Tam *et al.* [61] who identified two different components for the broadband shock-associated noise as seen in Fig. 1.10.

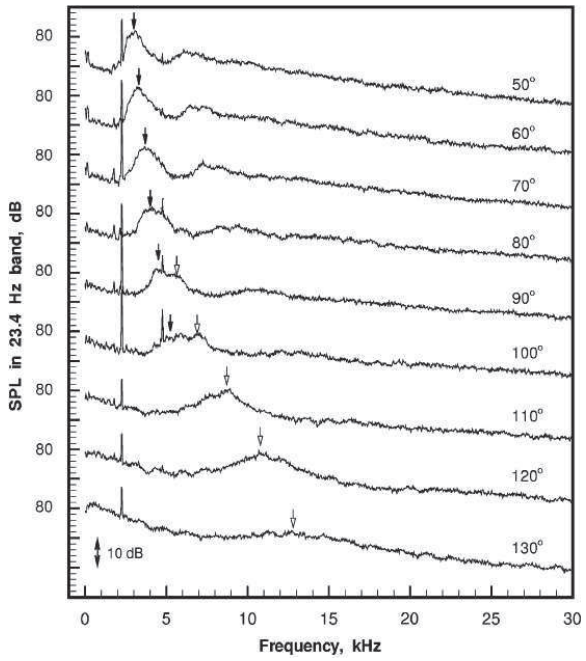

Figure 1.10: *Noise spectra of a dual stream jet with subsonic primary jet* $M_p = 0.76$ *and supersonic under-expanded secondary jet* $M_s = 1.36$ *from Tam et al. [61]. Black arrows indicate the first component of broadband shock-associated noise and open arrows indicate the second component.*

The first component is the equivalent to the one of the single jet, generated due to the interaction of the turbulent structures with the outer shear-layer. The behavior of this component does not change, the maximum amplitude is encountered in the upstream direction. However

the second component generated by the interaction with the inner shear-layer was found to radiate mostly downstream, reducing the amplitude at 90°. The physical explanation for this roll-off is that the source responsible for generation of noise at large angles is moving at a subsonic speed relative to the supersonic secondary jet. The disturbances generated decay when they are transmitted through the secondary jet, which results in a reduction of the noise at high inlet angles. Good agreement was found against the experimental data by applying a dual sheet vortex model. Tam *et al.* developed a model [61] able to predict the shock-associated noise frequency peaks from both primary and secondary shear-layers using a Fourier decomposition of the shock-cell system [62]. The advances in high performance computing (HPC), have provided with the possibility of running high Reynolds number large eddy simulations of dual stream jets [63, 64, 65, 66, 67, 68]. Some of the main methodologies for computational fluid dynamics in aeroacoustics are presented in the next section.

1.4 Computational aeroacoustics

The branch of Computational Fluid Dynamics (CFD) where the main focus is drawn to the generation and propagation of the acoustic phenomena generated by the aerodynamics is called Computational AeroAcoustics (CAA). Acoustics perturbations are by definition an unsteady process. Therefore, in order to be able to compute acoustic waves and sound phenomena computationally, an unsteady calculation or acoustic models are needed. Moreover, the errors committed by the numerical model and machine related errors must be lower than the acoustic perturbations itself. Numerical errors can lead to the underestimation of noise because the acoustic efficiency is very low even for loud flows. Moreover, the propagation of acoustic waves over long distances occurs with a very low attenuation. In order to perturb as less as possible the low amplitude acoustic waves (*i.e.*, decay in amplitude and a shift in phase), the dissipation and dispersion effects of the numerical schemes need to be kept as low as possible. As exposed by Colonius [69], two methodologies can be followed to compute the sound field: direct computation of sound, and hybrid methods.

1.4.1 Direct computation of sound

The Direct Computation of Sound (DCS) aims to compute both the unsteady flow of the problem, and the sound generated by itself. For this matter, the computational domain must contain the noise producing region of the flow, and part of the near-field where the noise is measured. The computational mesh needs to be selected to represent well both the flow and the sound waves. At the beginning of computational aeroacoustics, DCS was usually used to obtain underlying sound generation processes. This was in part, due to memory and time restrictions originated by the meshes that were needed for actual industrial problems. The above-mentioned shock leakage phenomena studied by Suzuki and Lele [39] or the work of Lui *et al.* [40] are some examples. Thanks to the computer development of the last decade, not only underlying phenomena has been studied but also real small contained problems.

The direct computation of sound can be done using Direct Numerical Simulation (DNS), Large Eddy Simulation (LES) or Unsteady Reynolds Averaged Navier-Stokes simulation. The objective of the DNS is to compute all the scales characteristic of the turbulent kinetic energy without any modeling. This implies solving the Navier-Stokes equations, and thus, having

a mesh able to resolve the Kolmogorov scale l_η characteristic of the dissipative scales. The integral length-scale L representative of the flow structures can be related to the Kolgomorov scale by the dimensional relation obtained for isotropic turbulence $L/l_\eta = Re_L^{3/4}$, where Re_L is the Reynolds number of the flow characterized by the integral length-scale and the velocity perturbation. The number of points needed to describe all the significant turbulence scales varies in function of $N \approx Re_L^{9/4}$ which makes DNS quite restrictive in terms of memory cost for cases with a high Reynolds number. A way to reduce the computational cost, yet resolving most of the turbulence scales is to use LES. Large eddy simulations consist in computing the biggest turbulence scales and modeling the smallest ones by using a spatial filtering. The flow is resolved up to the Taylor microscale λ_g. In general, a subgrid scale model is introduced to model the dissipative scales. One of the first subgrid scale model is the Smagorinsky model [70] where an algebraic relation models the turbulent viscosity of the dissipative scales. Linking the Taylor microscale with the characteristic length-scale of the flow one recovers the relation with the Reynolds number of $L/\lambda_g \approx Re_L^{1/2}$. This new relation gives an approximative number of nodes of $N \approx Re_L^{3/2}$ which is considerably smaller than the one needed using DNS. Obviously, the decrease in accuracy by modeling the smaller scales and decrease in computational cost, comes at the price of a worse representation of the flow features and the acoustics. At the lower end, there is the URANS or unsteady RANS. The unsteady RANS is derived from the Reynolds Averaged Navier-Stokes equations where the flow is decomposed in the mean component and the perturbations. The conservative equations are solved for the mean quantities and different transport equations (depending on the model) are used to model the turbulent quantities.

From the three above-mentioned methodologies, LES is the one that offers the best trade-off between accuracy of the modeled physics and computational cost. Many studies of subsonic jet noise has been already done using large eddy simulations ([71, 72, 73, 74, 75, 76, 77] among others). In particular, Bogey *et al.* [71] found for a subsonic LES of a jet at $M = 0.9$ and $Re = 65\,000$ that the generation of sound was related to the breakdown of the shear-layer in the central zone of the jet at the end of the potential core. Bodony and Lele [72] studied the temperature effect of the jet, finding good agreement with the published experimental data. Bogey and Bailly [73] studied the impact of different inflow forcing conditions on the flow development and the sound field. If a forced ring vortex is used, involving several azimuthal modes, the first four modes will have the biggest impact; removing them, will reduce the turbulence intensity, giving a quieter flow. Direct numerical simulations of subsonic jets at Reynolds number based on the diameter of $18,100$ were carried out by Buhler *et al.* [78], obtaining good agreement with the experiments. Sanjosé *et al.* [68] used LES to compute the acoustic field of a dual stream subsonic jet, showing good agreement with experimental results for the downward angles.

Supersonic jets have been studied numerically as well. Schulze and Sesterhenn [79], Schulze *et al.* [80] and Berland [81] simulated a 3D supersonic under-expanded planar jet. Berland *et al.* put in evidence the shock-leakage theory studied by Suzuki and Lele [39] for a real jet that exhibited shock-vortex interactions in the third shock-cell. Mendez *et al.* [82] studied supersonic perfectly expanded axisymmetric jets at $M_j = 1.4$ using LES and Bodony *et al.* [83] studied supersonic under-expanded and perfectly expanded jets at $M_j = 1.95$. The same jet was studied by Lo *et al.* [84], obtaining good agreement with the numerical results from Bodony *et al.* [83]. The noise emitted from supersonic under-expanded rectangular nozzles at $M_j = 1.4$ and the effect of chevrons was studied by Nichols *et al.* [85, 86].

Numerical simulations will be able to capture the sound of the respective resolved scales if the mesh at the target location is sufficiently fine. The maximum sound frequency f captured by the mesh can be expressed as $f = a_\infty/\lambda$ where a_∞ is the ambient speed of sound and $\lambda = n\Delta s$, the wavelength that can be resolved by a specific number of cells n with spacing Δs. The number of cells n needed to represent a wavelength depends on the numerical scheme used. Mesh design for DCS is not a trivial task. Moreover, mesh stretching can introduce numerical artifacts in the solution. More information about the mesh is given in Sec. 3.1. Nonetheless, the propagation of acoustic perturbations is costly for high frequency ranges. The solution should be extrapolated to the far-field without being concerned by meshing constrains. For this purpose, analytical methods or integral formulations of the wave equation using a Kirchoff or Ffowcs-Williams and Hawkings surface enclosing the flow can be used as Anderson [87] for a subsonic jet. If the computation of the acoustic waves at the far-field is needed, a domain extension with a simplified Cartesian mesh can be used where the Euler equations are solved. An accurate result strongly depends on the interpolation zone at the grid interface between the DCS domain and the extrapolation region. The methodology was carried out solving the linear wave equation by Bogey [88] for a dual stream jet and Freund *et al.* for a subsonic and supersonic jet [89, 90] respectively among other studies.

1.4.2 Hybrid methods

The second procedure to compute the noise is by means of hybrid methods. The hybrid methods rely on the main computation to solve the general dynamics of the flow and a second calculation to predict the noise. This second computation can be done *a posteriori* or at the same time as the main computation. DNS and LES as well as RANS simulations are adopted to compute the sound sources that will feed the computation of an acoustic analogy. As mentioned in Sec. 1.1.3.2, Tam and Tanna [91] implemented a model where the intensity of the broadband shock-associated noise was scaled as a factor of $\left(M_j^2 - M_e^2\right)^2$, where M_j is the perfectly expanded Mach number, and M_e the actual exit Mach number. Tam [28] used this work to develop a stochastic model wherein the large scale turbulence structures are modeled by a superposition of the instability waves of the mean-flow of the jet. Bailly [92] computed the noise of a subsonic and a supersonic jet from statistical source models by combining a $k-\varepsilon$ RANS model with an acoustic analogy. Colonius [93] compared the sound generated by a vortex pairing in a two dimensional compressible mixing layer using DNS itself and Lilley's analogy based on the flow computed by the DNS simulation. Vortex methods [94] can also be applied in conjunction with the acoustic analogies in order to reduce the computational time. Vortex methods provide a quick assessment of the impact of the main variables on the radiated noise. A different hybrid method mixes the solution of the incompressible equations for the flow, and a simplified set of compressible equations to predict the radiated noise. This methodology known as Non-Linear Disturbance Equations (NLDE) [95] allows to compute the acoustic field from the near-field density variations. The near-field density variations, also known as hydrodynamic density correction, appear when solving the incompressible equations due to the inherent pressure variations. These variations define a set of non-linear disturbance equations that are used to compute the acoustic field. Last, Henry *et al.* [96] extended the near-field compressible flow data to the radiated acoustic field with specific source-terms of the numerical solution of the Linearized Euler Equations (LEE). Morris and Miller [97, 98] used the solution of a RANS simulation together with the LEE to compute the acoustics of

an under-expanded jet. The source terms are obtained with the product of the fluctuations associated with the jet's shock-cell structure and the turbulent velocity fluctuations of the jet shear-layer. The model has been recently revisited by Kalyan and Karabasov [99] to improve the predictions at higher frequencies. The new model includes an axial mean-flow velocity gradient in the definition of the correlated scale of the acoustic source.

1.5 Reduction of jet noise

Any study of the underlying physics of jet noise normally has one main ulterior goal: the reduction of jet noise. Even if the main goal of a study is not the development of technologies for noise reduction, all the advances made by the whole scientific community will contribute in one way or another to the reduction of jet noise. If progress is made in the private sector that can be beneficial to ordinary people, it should be shared with the community. Noise generated by aviation can be propagated from the aircrafts to the ground and also to the interior of the cabin. The reduction of noise in the cabin can either be achieved by controlling the noise generated by the external aeroacoustic sources, or by controlling the transmission of loss through the fuselage sidewall. Main external aeroacoustic sources that affect cabin noise are boundary layer noise and engine noise, composed of fan noise and jet noise. This section reviews the most common technologies being developed for the purpose of reduction of jet noise in aviation.

Most of the technologies used for jet noise reduction are based on enhancing the mixing in the shear-layer of the jet. Enhancing the mixing lowers the effective velocity in the main noise-producing region of the jet reducing the turbulence in that region but increasing it at the exit of the nozzle. This reduces the low frequency noise generated by the large turbulence structures. However, it also increases the high frequency noise generated from the enhanced mixing. This trade-off between low and high frequency noise may imply an additional penalty for the aviation industry. The technologies developed for jet noise reduction should not conflict with the efficiency of the aircraft, *i.e.* the net thrust and the total weight. Here, these technologies are grouped into three different categories: fluidic injection, nozzle alteration and noise shielding.

1.5.1 Fluidic injection

The injection of mass to the jet has been extensively studied over the past fifty years. Fluidic injection is usually done via microjets inserted at the exit of the nozzle. Both aqueous and gaseous injection concepts for supersonic and subsonic jet exhausts have been developed.

Aqueous injection reduces jet noise by reducing the jet temperature through evaporation and the jet velocity through momentum exchange between the water droplets and the main jet. Of course, aqueous injection is prohibited for in-flight use due to the large quantities of water needed for an effective reduction of jet noise. Moreover, water pressures above 2000 kPa and water-to-main-jet mass flow rates above 10% are required to achieve an overall sound pressure level reduction of roughly 6 dB. On the other hand, this is a common operation at lift-off for aerospace launch vehicles as the water can be stored and injected from the ground. The reader is referred to the review of Henderson [100] for more information.

Differently, gaseous injection reduces noise through the introduction of streamwise vorticity

in the jet. A reduction of 2 dB can be accomplished for subsonic single jets and of about 1 dB for subsonic dual stream jets. Henderson *et al.* [101] studied the application of microjets to real configurations with pylon and central plug of supersonic single jets and dual stream jets where the supersonic stream is the secondary. The setup is shown in Fig. 1.11. On their experiments, they installed the microjets at the exit of the primary nozzle. Fluidic injection eliminates the shock-cell pattern and its associated broadband shock-associated noise only if the micro jets are installed in the outer shear-layer of the under-expanded stream. The turbulent kinetic energy is also reduced at the end of the potential core as expected. Morris *et al.* [102] achieved a reduction of 4 dB for mixing noise and 2 dB for broadband shock-associated (BBSAN) noise in low by-pass ratio turbofan engines with the microjets installed at the walls of the convergent-divergent nozzle. In general, turbulent mixing noise and BBSAN correlates with the ratio of microjet to primary jet driving pressures normalized by the ratio of corresponding diameters [103]. Depending on the driving pressure of the microjets, they could reach under-expanded conditions and generate a shock-associated noise by themselves. Gaseous injection has been also studied numerically with LES [104, 105, 106] and Lattice-Boltzmann Methods [107] (LBM) obtaining the same conclusions. In addition, Huet *et al.* [104] studied numerically an effective mixing noise reduction with minimum thrust loss using a pulsed fluidic injection.

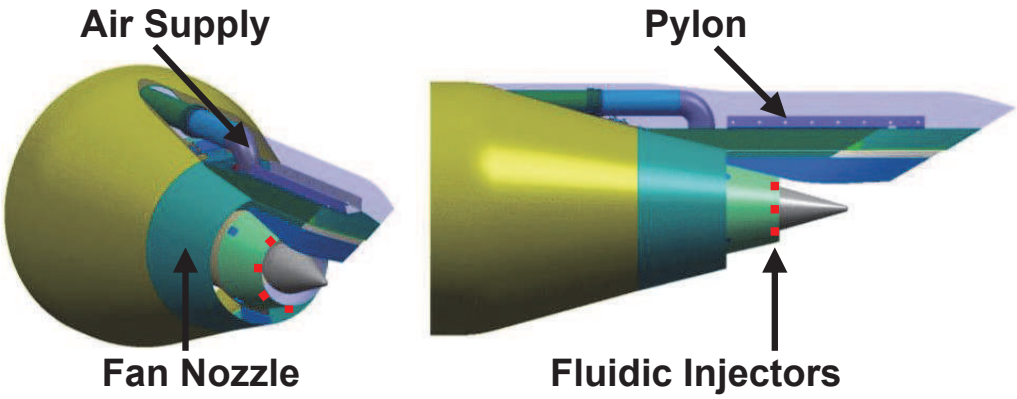

Figure 1.11: *Sketch of the fluidic injection applied to the core nozzle of a turbofan from Henderson et al. [101].*

Overall, fluidic injections seem as a promising technology to apply in real turbofans. Nonetheless, the installation of microjets in real engines is not as straightforward as in the experimental model and thus, a major revisit of the engine, pylon, and wing should be carried out.

1.5.2 Geometrical nozzle alteration

The study of the effect on noise emission by modifying the shape of the exhaust nozzle started in the fifties. Westley *et al.* [108] investigated different nozzles and not much later, realizing the great impact for jet noise, published a patent [109] with some of the basis of the nowadays noise suppression techniques used in aviation. Many other patents were submitted in the following years by Rolls Royce [110] and others. The alteration of the exhaust nozzle can be grouped into two categories: addition of Vortex Generators (VG) and modification of the contour of the nozzle. In this section, only the most recent studies are commented.

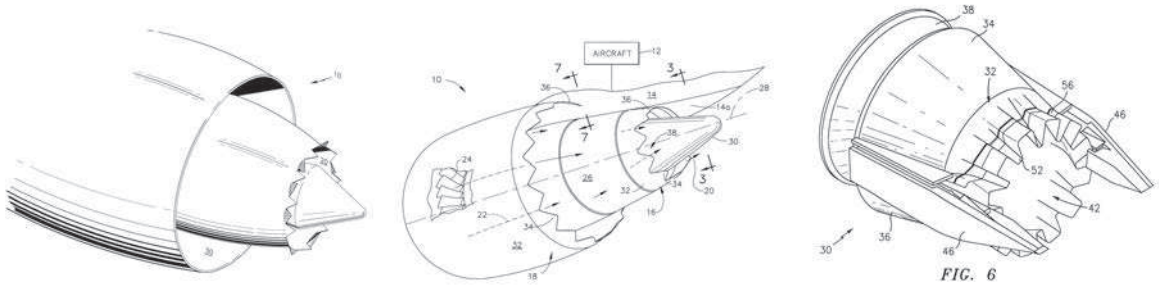

(a) (b) (c)

Figure 1.12: ***(a)*** *Tabbed nozzle sketch from [111].* ***(b)*** *Chevron Nozzle sketch from [112].* ***(c)*** *Lobbed nozzle from [113]*

Vortex generators (VG) are small protuberances added to a surface and are usually used on the different airplane surfaces in order to assure the development of a turbulent attached boundary layer. Samimy *et al.* [114] studied experimentally the effect of vortex generators for jets with Mach numbers ranging from 0.3 to 1.81. The vortex generators that were normally projected into the flow at the nozzle exit, introduced the same level of distortion in the flow for the subsonic and supersonic cases. The VG or tabs, introduce an indentation into the high speed side of the shear-layer via the action of streamwise vortices called trailing vortices. The implementation of these vortex generators was shown to suppress screech and greatly alter the shock-cell structure. A similar concept was studied later by Papamoschou *et al.* [115, 116, 117] with the installation of turning vanes in the by-pass exhaust of a turbofan engine with by-pass ratio of 3. The vanes produce locally-skewed mixing layers that reduce the length of the core noise source region and thickens the by-pass stream on the underside of the jet. The overall sound pressure level was reduced about 8 dB with only 2% of thrust losses. More recently, Papamoschou [118] investigated pylon-based deployable flaps in turbofan engines with by-pass ratio of 8. Using a fine perforation in the flaps, yielded a noise reduction of 2.1 dB in the downward direction and 1.0 dB in the sideline direction. The thrust was impacted by a loss of 0.7%.

The modification of the shape of the nozzle for jet noise reduction can be classified into different categories depending on the actual modification. In the literature, they are all sometimes generalized and referred to as chevrons. The so-called chevrons are a set of indentations or serrations on the edge of the circumferential nozzle exit. Three types of indentations are shown in Fig. 1.12. If the indentations are perpendicular, or with a high angle of penetration into the flow, they are referred to as tabs. The tabs act similarly to the vortex generators explained above. If the circumferential shape of the nozzle exit is modified with a series of contoured lobes then one is dealing with lobed nozzles. Lobed nozzles were studied by Zaman *et al.* [119]. They determined that increasing the number of lobes reduces the turbulence intensity, the radiated noise, but also reduces the thrust coefficient, and increases the high frequency noise. Despite the known thrust losses, some patents were submitted at the beginning of the 21st century [120, 113, 111]. Next, the actual chevrons are discussed in detail.

The geometry of the chevrons and their effect on noise reduction was investigated by Bridges *et al.* [121]. In their parametric study, they changed the number of chevrons (or serrations), the penetration in the flow and their length. They concluded that the chevron length had no

major impact on either the flow or noise. The chevron penetration, *i.e.* the angle that is being deflected inside the nozzle with respect to the base profile, increases noise at high frequency and lowers it at low frequency. This is especially aggravated for a small chevron count. On the other hand, a good compromise in the frequency range is found for a higher number of chevrons. The trends are similar for a cold and a hot jet. The impact of the chevrons with co-flow on under-expanded jets was studied by Rask *et al.* [122] and Gutmark *et al.* [123]. A higher noise was achieved when a low subsonic co-flow was applied. The flow presented higher turbulence levels while keeping a similar shock-cell strength. Furthermore, the increase in velocity of the co-flow reduced the strength of the shocks which led to a reduction of the overall perceived noise. Schlinker *et al.* [124] investigated chevrons on supersonic jets at perfectly expanded, over-expanded and under-expanded conditions for a range of stagnation temperature ratios between 0.75 and 2. They found that chevrons reduced the screech amplitude for all temperature ratios. In-flight tests were done by Mengle *et al.* [125, 126] and Bultemeier *et al.* [127] with chevrons located in the secondary fan of the engines. They showed a consistent reduction of 5 dB in the low frequencies on the external fuselage skin of the airplane and an increase in the high frequencies. A slight reduction of efficiency of the engines was observed when the flight test were done with the engines with chevrons. Some researchers suggest that chevrons are used merely as propaganda. Either way, Huber *et al.* [128] demonstrated that the effect of chevrons was nozzle-dependent. They obtained contradictory results using the same type of chevrons but different nozzles. On one case, the low and high frequencies were reduced, on the other model, the chevrons tended to either leave unchanged or increase the peak levels of the broadband shock-associated noise. From their work, they concluded that the BBSAN reduction does not originate solely from the increased mixing produced by the chevrons but it depends as well from the quality of the expansion of the jet in the near-nozzle region. The underlying nozzle aerodynamic characteristics drive the development of the compression-expansion system further downstream where the shock-associated noise is originated. Nonetheless, several large eddy simulations were carried out, showing good agreement with experimental results [129, 63, 130, 131, 85, 132, 86, 133, 134] when the same geometries were used.

Many studies are still needed in order to understand all the underlying phenomena behind the origin and the suppression of jet noise. Additionally, studies such as those by Alkislar [135] where he combines chevrons and microjets could help to increase the knowledge in the field.

1.5.3 Shielding of noise

In axisymmetric configurations, jet noise is emitted with the same levels at each azimuthal position, regardless of the fact that non-axisymmetric modes could appear. If one wants to reduce the noise propagated to the ground it will be reasonable to try to reduce the noise only on the down-facing directions. A sketch from a patent for the application in turbofans by Viswanathan [136] is shown in Fig. 1.13. This has been specially investigated for military applications by Viswanathan *et al.* [137, 138, 139] with the introduction of beveled nozzles. With the same plenum conditions, and an increase in thrust between 1% and 2% a reduction of 4 dB is achieved with a bevel of 35 degrees. Advantage is taken from the asymmetry of the exhaust jet. In turbofan engines, the asymmetry is assured by the supporting pylon, however, while the intake of the turbofan has a rounded, but not axisymmetrical intake, the exhaust is cylindrical. Moreover, the secondary stream of the turbofan, besides increasing the efficiency of the engines, also provides with an acoustic shielding effect for the primary jet. On the same

basis, Henderson [140] studied the impact of three stream jets operated at subsonic conditions. She found that the third stream provided a reduction in the high frequency range at broadside and peak jet noise angles. Additionally, Henderson *et al.* [141] investigated the effect of an offset on the tertiary nozzle. A reduction of up to 8 dB was achieved on the thick side of the offset. Papamoschou *et al.* [142] obtained good agreement with the experiments using RANS hybrid computations. Nonetheless, the addition of a third stream seems to be in contradiction with the trend of bigger by-pass ratios that at the moment, are constrained by the available space for the turbofan between the wing, and the ground.

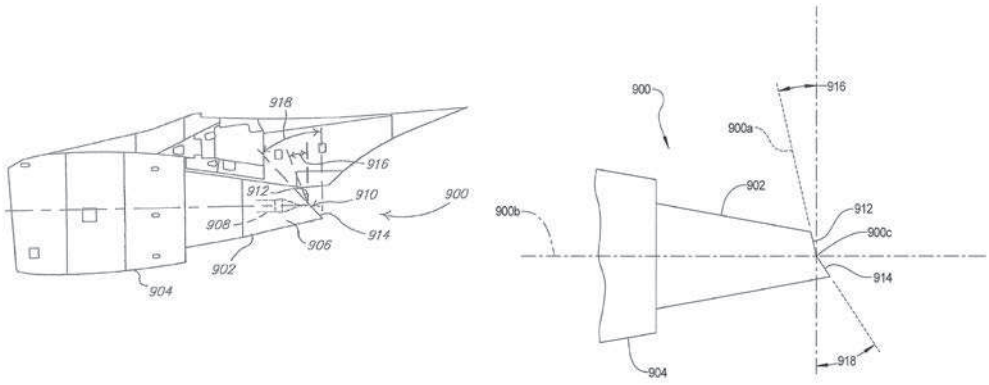

Figure 1.13: *Sketch of the beveled nozzle applied to the core nozzle of a turbofan from Viswanathan et al. [136].*

1.6 Summary and perspectives

The aerodynamics and aeroacoustics of jets have interested researchers from the dawn of the modern era of aviation. The study of the aerodynamics of jets does not only come from an efficiency point of view, but also from the noise generated. The first theories and analogies studied by Lighthill and the successfully applied technologies for noise reduction by Westley increased the interest of this field to the scientific community. Obtaining different noise emissions by different topologies of jets gave raise to different models. Nonetheless, Tam *et al.* found some intrinsic noise generation mechanisms that could be applied to any jet topology. In subsonic jets, the noise is driven by the mixing noise from small-scale turbulence and the large-scale turbulence structures. In supersonic imperfectly expanded jets, shock-cell noise is the most important noise component. Shock-cell noise is the noise generated from the interaction between the convected vortical structures generated in the shear-layer of the jet, and the shock-cell structure that appears from the imperfectly expansion of the jet to ambient conditions. A particular shock-cell noise is the screech, which is a tonal noise generated by a closed feedback loop between the vortical structures convected downstream and the acoustic perturbations propagated upstream. The underlying physics behind jet noise has been deeply studied experimentally. The advances in computational fluid dynamics have made possible to study in more detail subsonic jets, its turbulence and its associated mixing noise. Recently, supersonic jets and shock-cell noise have been numerically studied as well.

The theoretical, experimental, and numerical studies of jet noise are encouraged by the techno-

logical need. The evolution of new technologies in aircraft propulsion has obliged the scientific community to give an insight to new noise generating mechanisms encountered. Fluidic injection and chevrons are some of the noise suppression techniques that are being developed nowadays. The sole apparition of the turbofan engine already reduced drastically the noise emissions while increasing the performances. Nevertheless, the technological evolution does not stop, nor the search for knowledge. The technological evolutions came hand to hand with new noise models and theories as well as new noise suppression technologies over the past fifty years. Nowadays, the society is aware of the medical problems associated with noise and the general annoyance of it. Furthermore, the cities are expanding closer and closer to the vicinity of the airports and the number of flights does not stop increasing. New noise suppression technologies as well as new numerical methodologies are to come if the noise objectives set by the aeronautical community have to be achieved. In order to accomplish this, not only the models and equations that represent the flow around an airplane or at the exhaust jet of the engines must increase in accuracy but also the numerical schemes must become more efficient and accurate.

Chapter 2

Numerical schemes for the Navier-Stokes equations

In physics, the Navier-Stokes equations describe the motion of viscous fluids. They govern the atmosphere, the oceanic currents and the flow around cars, airplanes and rockets. These equations are obtained from applying Newton's second law of fluid motion to a fluid volume, together with the assumption that the stress in the fluid is the sum of a diffusing viscous term and a pressure term. The Navier-Stokes equations form a system of non-linear equations with no general analytical solution. For this reason, they are discretized and solved numerically in what it is known as Computational Fluid Dynamics.

In this PhD thesis, the Navier-Stokes equations are solved using the solver ***elsA*** [143] from ONERA and co-developed by CERFACS. The code is a multidisciplinary tool that can be used to study internal or external flows for different applications. The code ***elsA*** is a Finite Volume multi-block structured solver optimized for parallel computations. The code is object oriented and it is based on an interface coded in Python, the core in C++ and specific subroutines in Fortran.

In this chapter, the discretization of the Navier-Stokes equations is presented in Sec. 2.1. Then the numerical discretization of the convective and diffusive fluxes is given in Sec. 2.2 and Sec. 2.4 respectively. The discretization of the spatial schemes is reformulated at the walls in Sec. 2.5 and at the interfaces in Sec. 2.6. Then, the boundary conditions suitable for aeroacoustic computations are introduced in Sec 2.7. Moreover, a shock-limiting technique used for the case study of Ch. 6 is presented in Sec. 2.3. The chapter ends with a summary and perspectives.

2.1 Governing equations and finite volume discretization

The governing equations considered in this chapter are the conservative form of the Navier-Stokes equations. In three-dimensional space, the equations in Cartesian coordinates can be written as

$$\frac{\partial \mathbf{U}}{\partial t} + \frac{\partial \mathbf{E}}{\partial x} + \frac{\partial \mathbf{F}}{\partial y} + \frac{\partial \mathbf{G}}{\partial z} = \frac{\partial \mathbf{E}^v}{\partial x} + \frac{\partial \mathbf{F}^v}{\partial y} + \frac{\partial \mathbf{G}^v}{\partial z}, \tag{2.1}$$

where the vector of conserved variables $\mathbf{U}$, convective fluxes $\mathbf{E}$, $\mathbf{F}$ and $\mathbf{G}$, and viscous fluxes $\mathbf{E}^v$, $\mathbf{F}^v$ and $\mathbf{G}^v$ in the x, y and z directions are

$$\mathbf{U} = \begin{bmatrix} \rho \\ \rho u \\ \rho v \\ \rho w \\ \rho e_t \end{bmatrix}, \quad \mathbf{E} = \begin{bmatrix} \rho u \\ \rho u^2 + p \\ \rho uv \\ \rho uw \\ \rho u e_t + pu \end{bmatrix}, \quad \mathbf{F} = \begin{bmatrix} \rho v \\ \rho vu \\ \rho v^2 + p \\ \rho vw \\ \rho v e_t + pv \end{bmatrix}, \quad \mathbf{G} = \begin{bmatrix} \rho w \\ \rho wu \\ \rho wv \\ \rho w^2 + p \\ \rho w e_t + pw \end{bmatrix}, \tag{2.2}$$

$$\mathbf{E}^v = \begin{bmatrix} 0 \\ \tau_{xx} \\ \tau_{xy} \\ \tau_{xz} \\ u\tau_{xx} + v\tau_{xy} + w\tau_{xz} - q_x \end{bmatrix}, \quad \mathbf{F}^v = \begin{bmatrix} 0 \\ \tau_{yx} \\ \tau_{yy} \\ \tau_{yz} \\ u\tau_{yx} + v\tau_{yy} + w\tau_{yz} - q_y \end{bmatrix}, \quad \mathbf{G}^v = \begin{bmatrix} 0 \\ \tau_{zx} \\ \tau_{zy} \\ \tau_{zz} \\ u\tau_{zx} + v\tau_{zy} + w\tau_{zz} - q_z \end{bmatrix}. \tag{2.3}$$

The state quantities, ρ, $\mathbf{u} = (u, v, w)$, p and e_t are the density, velocity components in the x, y and z directions, pressure and total energy, respectively. Assuming a newtonian fluid and the Stokes hypothesis [144], the viscous stress tensor, τ_{ij} can be modeled as

$$\tau = \mu \left(\nabla \mathbf{u} + \nabla \mathbf{u}^T \right) - \frac{2}{3} \mu \nabla \cdot \mathbf{u} \times \mathbf{I}, \tag{2.4}$$

where μ is the molecular viscosity, $\mathbf{I}$ is the identity matrix, and the supercript $\{\bullet\}^T$ stands for the transposed matrix. The heat conduction vector, $\mathbf{q}$ can be expressed with Fourier's Law as

$$\mathbf{q} = \kappa \nabla \cdot T, \tag{2.5}$$

where κ are is thermal conductivity and T the temperature. The molecular viscosity μ and the thermal conductivity κ are related by a constant Prandtl number,

$$Pr = \mu C_p / \kappa. \tag{2.6}$$

Here, C_p is the specific heat at constant pressure. The molecular viscosity is obtained from Sutherland's law,

$$\mu(T) = \mu_{ref} \left(\frac{T}{T_{ref}} \right)^{3/2} \frac{T_{ref} + S}{T + S}, \tag{2.7}$$

where S, μ_{ref} and T_{ref} are constants that depend on the gas of consideration. For air $S = 110.4$ K, $\mu_{ref} = 1.716\ 10^{-5}$ kg m^{-1} s^{-1} and $T_{ref} = 273.10$ K. The system is closed by assuming a polytropic perfect gas which is characterized by constant C_p and constant specific heat at constant volume C_v defined with the specific heat ratio γ as

$$\gamma = \frac{C_p}{C_v}, \tag{2.8}$$

giving the ideal gas law relation

$$p = \rho RT, \tag{2.9}$$

where R is the gas constant. Last, the specific total energy e_t can be given by

$$e_t = e_i + e_c = \frac{p}{\rho(\gamma - 1)} + \frac{1}{2}(u^2 + v^2 + w^2) \tag{2.10}$$

where e_i and e_c are the specific internal energy and the specific kinetic energy respectively.

The governing equations (2.1) can be expressed in compact form as

$$\frac{\partial \mathbf{U}}{\partial t} + \nabla \cdot \mathbf{F}_U^{net} = 0, \tag{2.11}$$

where $\mathbf{F}_U^{net} = (\mathbf{E} - \mathbf{E}^v)\,\hat{\mathbf{e}}_x + (\mathbf{F} - \mathbf{F}^v)\,\hat{\mathbf{e}}_y + (\mathbf{G} - \mathbf{G}^v)\,\hat{\mathbf{e}}_z$. Here, $\hat{\mathbf{e}}_x$, $\hat{\mathbf{e}}_y$,$\hat{\mathbf{e}}_z$ are the components of the unit vector for the x, y and z directions.

The finite volume method is employed to discretize the system, where the equations are integrated over a cell C of volume V. This is followed by an application of the Gauss divergence theorem to yield

$$\frac{d}{dt}\int_C \mathbf{U}(\mathbf{x}, t)\, dV + \int_S \mathbf{F}_U^{net} \cdot \mathbf{n}\; dS = 0, \tag{2.12}$$

where $\mathbf{n}$ is the unit-normal vector of the cell's surface of area S. Introducing the vector of averaged quantities over the cell $\overline{\mathbf{U}}$ and the vector of mean flux over the interface $\overline{\mathbf{F}_U^{net}}$ results in the following semi-discretized equation

$$\frac{d\overline{\mathbf{U}}(t)}{dt}\, V + \sum_{f \in \{\text{faces of } C\}} (\overline{\mathbf{F}_U^{net}} \cdot \mathbf{n})_f \; S_f = 0. \tag{2.13}$$

The face normal flux in the expression is

$$\left(\overline{\mathbf{F}_U^{net}} \cdot \mathbf{n}\right)_f = \left(\left(\overline{\mathbf{E}} - \overline{\mathbf{E}^v}\right) n_x + \left(\overline{\mathbf{F}} - \overline{\mathbf{F}^v}\right) n_y + \left(\overline{\mathbf{G}} - \overline{\mathbf{G}^v}\right) n_z \right)_f . \tag{2.14}$$

The time derivative in Eq. (2.13) is discretized using the six-step low-storage optimized Dispersion-Relation-Preserving (DRP) Runge-Kutta scheme of Bogey and Bailly [145]. It is of the form

$$\overline{U}^{n+1} = \overline{U}^n + \sum_{j=1}^{p} \gamma_j \Delta t^j \frac{\partial^j \overline{U}^n}{\partial t^j}, \tag{2.15}$$

where $\overline{U}$ denotes the cell-averaged component of the conserved variable vector in Eq. (2.2), n is the physical time step, p is the number of stages and Δt is the time step. The optimized parameters γ_j for the six-stage (*i.e.*, $p = 6$) Runge-Kutta scheme are provided in Table 1. Optimization is performed by minimizing the dispersion and dissipation errors up to the angular frequency $\omega = \frac{\pi}{2\Delta t}$.

Table 2.1: Coefficients of the six-stage optimized Runge-Kutta algorithm of Bogey and Bailly [145]

γ_1	1
γ_2	1/2
γ_3	0.165919771368
γ_4	0.040919732041
γ_5	0.007555704391
γ_6	0.000891421261

2.2 Numerical discretization of the convective fluxes

2.2.1 Base scheme

The base scheme employed is the compact sixth-order accurate finite volume formulation of Fosso *et al.* [146]. The method evaluates the (averaged) conservative quantities $\overline{U}$ at the cell interfaces based on an implicit formulation which is similar to the finite difference scheme of Lele [147]. While the Padé schemes were developed to compute the derivatives at the grid points, the method of Fosso *et al.* [146] determines the interface quantities from which the corresponding numerical fluxes are derived. The interpolation formula is of the form

$$\alpha\overline{U}_{i-1/2} + \overline{U}_{i+1/2} + \beta\overline{U}_{i+3/2} = a\overline{U}_{i-1} + b\overline{U}_i + c\overline{U}_{i+1} + d\overline{U}_{i+2}, \tag{2.16}$$

where the coefficients on a uniform Cartesian mesh are $\alpha = \beta = 1/3$, $a = d = 1/36$ and $b = c = 29/36$. These sixth-order coefficients are obtained by performing Taylor-Series expansion of each term about the interface $i + 1/2$ and matching the left- and right-hand side coefficients up to fifth-order. The form of the expression is similar to the upwinding compact scheme of Pirozzoli [7]. However, the present scheme is centered and therefore non-dissipative. The coefficients on non-uniform and curvilinear meshes can be obtained in a similar manner. The compact formulation generates a tridiagonal system of equations that is solved using Thomas algorithm.

2.2.2 Spatial filtering

The non-dissipative compact interpolation scheme shown in Eq. (2.16) is susceptible to grid-to-grid oscillations. In general, unphysical oscillations with compact schemes arise due to mesh non-uniformities, approximate boundary conditions and jump discontinuities such as shock waves [148]. In the case of turbulent flows, the methods are also responsible for generating aliasing errors [149]. In order to mitigate the high-frequency oscillations without compromising on the accuracy of the base scheme, a low-pass filter is typically utilized. Here, either the sixth- or eighth-order symmetric compact filter of Visbal and Gaitonde [150] is employed. The filtering algorithm supplies dissipation to damp the high-wavenumber modes responsible for the instabilities. In the large eddy simulation approach used in this PhD thesis, the spatial filtering is also used as sub-grid scale model. It is expressed as

$$\alpha_f\hat{U}_{i-1} + \hat{U}_i + \alpha_f\hat{U}_{i+1} = \sum_{n=0}^{N} \frac{a_n}{2}\left(\overline{U}_{i+n} + \overline{U}_{i-n}\right), \tag{2.17}$$

where $\hat{U}$ denotes a filtered quantity, a_n are the filter coefficients and α_f is an adjustable parameter between -0.5 and 0.5. The $N+1$ coefficients for the sixth- and eighth-order spatial filter are provided in Table 2.2. The coefficients are functions of the free parameter α_f which controls the width of the low-pass filter. Increasing α_f reduces the overall dissipation supplied by the filter. Furthermore, the dissipation is confined to a narrow band of high wavenumbers. To prevent excess diffusion of turbulent quantities and acoustic waves, α_f is set to 0.47 in the current study [151].

Moreover, the filtering operation in Eq. (2.17) is performed once at the end of the Runge-Kutta time stepping. In studies [148, 152] involving shock-turbulence interaction, the spatial filter is restricted to smooth turbulent regions of the flow.

Table 2.2: Coefficients for the sixth- and eighth-order compact filter in Eq. (2.17)

	a_0	a_1	a_2	a_3	a_4
6th order	$\frac{11+10\alpha_f}{16}$	$\frac{15+34\alpha_f}{32}$	$\frac{-3+6\alpha_f}{16}$	$\frac{1-2\alpha_f}{32}$	0
8th order	$\frac{93+70\alpha_f}{128}$	$\frac{7+18\alpha_f}{16}$	$\frac{-7+14\alpha_f}{32}$	$\frac{1-2\alpha_f}{16}$	$\frac{-1+2\alpha_f}{128}$

In this work, however, the filtering algorithm is applied throughout the domain, including regions where shocks and contact discontinuities exist. The following section explains a limiting procedure applied to the convective fluxes when shocks develop in the flow.

2.3 Shock-limiting technique

In the case of high-speed turbulent flows, numerical schemes must be capable of not only handling the unsteady multi-scale flow features but also resolving strong non-linearities such as shock-waves. Although the high-frequency oscillations in shock-free turbulent regions is dissipated by the spatial filter introduced in Sec. 2.2.2, it is insufficient to capture discontinuities in the flow-field. As a result, unphysical oscillations referred to as Gibbs' phenomena are generated that increase instabilities and contaminate the solution [7]. To address this issue, Visbal and Gaitonde [148] developed an adaptive filter algorithm that retained the baseline compact scheme [147] throughout the domain and gradually reduce the order of an eight-order spatial filter to two near shocks. In practice, the algorithm to modify the spatial filter is expensive and results in loss of accuracy due to its implicit formulation. In this work, an in-house solution [153] is used that limits the jump between two adjacent cells based on the limiters of the piece-wise parabolic method from Colella and Woodward [154].

The procedure can be described in three steps. First, the compact scheme from Eq. (2.16) is used to compute the primitive values $\overline{W}_{i+1/2}$ at the cell interface $I_{1/2}$. Second, a limiting procedure is applied to the interface where two values are obtained, from the left side of the interface of a cell $\overline{\mathbf{W}}^L_{i+1/2}$ and from the right side $\overline{\mathbf{W}}^R_{i+1/2}$ as sketched in Fig. 2.1. Last, the actual flux of the interface is computed using a Riemann solver [155] from the two states $\overline{\mathbf{W}}^L_{i+1/2}$ and $\overline{\mathbf{W}}^R_{i+1/2}$.

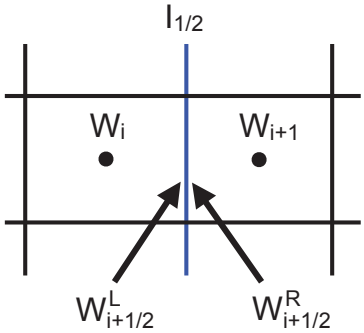

Figure 2.1: Discretization at the block interface for the compact scheme.

The limiting procedure is based on the condition that the values from three consecutive points $\{P_{i-1/2}, P_i, P_{i+1}\}$, $\{P_{i-1}, P_i, P_{i+1/2}\}$ or $\{P_{i-1/2}, P_i, P_{i+1/2}\}$ define a parabola without an extrema. This condition can be expressed as.

$$\begin{aligned}
\overline{\mathbf{W}}^R_{i-1/2} = \overline{\mathbf{W}}_i,\ \overline{\mathbf{W}}^L_{i+1/2} = \overline{\mathbf{W}} \quad & if \quad (\overline{\mathbf{W}}^L_{i+1/2} - \overline{\mathbf{W}}_i)(\overline{\mathbf{W}}_i - \overline{\mathbf{W}}^R_{i-1/2}) \leq 0, \\
\overline{\mathbf{W}}^R_{i-1/2} = 3\overline{\mathbf{W}}_i - 2\overline{\mathbf{W}}^L_{i+1/2} \quad & if \quad (\overline{\mathbf{W}}^L_{i+1/2} - \overline{\mathbf{W}}^R_{i-1/2}) \left(\overline{\mathbf{W}}_i - \frac{1}{2}(\overline{\mathbf{W}}^R_{i-1/2} + \overline{\mathbf{W}}^L_{i+1/2})\right) \\
& \qquad > \frac{(\overline{\mathbf{W}}^L_{i+1/2} - \overline{\mathbf{W}}^R_{i-1/2})^2}{6}, \\
\overline{\mathbf{W}}^L_{i+1/2} = 3\overline{\mathbf{W}}_i - 2\overline{\mathbf{W}}^R_{i-1/2} \quad & if \quad (\overline{\mathbf{W}}^L_{i+1/2} - \overline{\mathbf{W}}^R_{i-1/2}) \left(\overline{\mathbf{W}}_i - \frac{1}{2}(\overline{\mathbf{W}}^R_{i-1/2} + \overline{\mathbf{W}}^L_{i+1/2})\right) \\
& \qquad < -\frac{(\overline{\mathbf{W}}^L_{i+1/2} - \overline{\mathbf{W}}^R_{i-1/2})^2}{6}.
\end{aligned} \tag{2.18}$$

2.4 Numerical discretization of the diffusive fluxes

Aeroacoustic simulations of industrial jets are associated with high Reynolds numbers and thus, dominated by the convective effects rather than by the diffusive ones. In this context, the diffusive terms can be discretized by a second order scheme instead of a high order scheme.

The finite volume discretization of the diffusive term involves an integral on any mesh interface. The integrand combines both the solution gradients and its value on the interface. The value on the interface is taken from the compact finite volume formulation used for the convective term. As a consequence, the definition of the discretized diffusive term needs the computation of the gradient on the interface.

For structured grids, the standard way to compute interface gradients follows a two-steps procedure. First, the computation of the cell-centered gradient is carried out by applying the Gauss divergence theorem and second, the interface gradient is defined from the cell-centered quantities.

Step 1: computation of the cell-centered gradient

For a cell C of volume V, the Gauss divergence theorem gives

$$V\nabla\overline{\mathbf{U}} = \sum_{f\in\text{faces of } C} (\overline{U}_f \cdot \mathbf{n})_f \; S_f, \tag{2.19}$$

where $\overline{U}_f$ is the interface quantity. The interface f is shared by two adjacent control volumes and the interface quantity can be the average of left and right contributions, with the constant weight coefficient of 1/2 or the extrapolated quantity from the compact scheme.

Step 2: computation of the interface gradient

Taking the interface gradient as an average of left and right gradients (with a constant weight coefficient of 1/2) is the simplest scheme but such a scheme is known to lead to odd/even decoupling and does not damp high frequency modes. The *5p-cor* scheme can be seen as a correction of the simplest centered diffusion scheme.

In this section, explanations on the scheme follow the notations introduced in Fig. 2.2 and the goal is to define the gradient on the interface labeled $(i-1/2, j)$ located between cells $(i-1, j)$ and (i, j). The scheme defines the gradient on the dual (blue) volume that is directly used in the flux computation. The formulation of this interface gradient from the dual volume explains why it can be seen as a correction of the standard centered scheme.

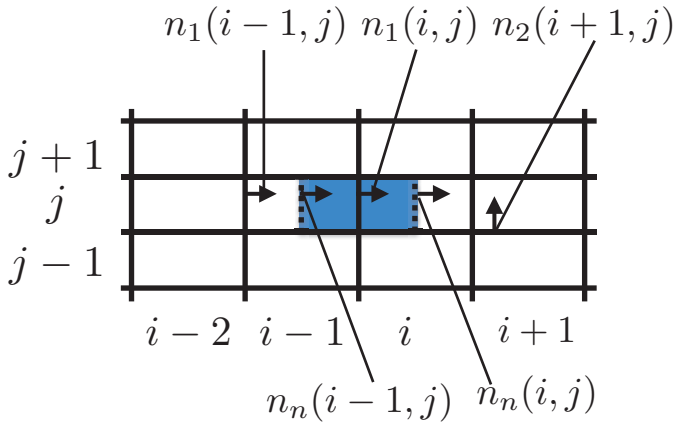

Figure 2.2: Sketch of a mesh for explanations regarding the diffusive scheme.

First, following the Gauss divergence formulation on the dual cell, the averaged gradient on the dual cell is linked with interface quantities. The shape of the elements are not accounted for and introducing interface quantities with non integer indices, the formulation can be expressed

as

$$\frac{V_{(i-1,j)}+V_{(i,j)}}{2}\nabla\overline{U}_{(i+1/2,j)} = -\overline{U}_{(i-1,j)}n_n(i-1,j)S_n(i-1,j)+\overline{U}_{(i,j)}n_n(i,j)S_n(i,j)$$
$$+\frac{1}{2}\Big(\overline{U}_{(i-1,j+1/2)}n_2(i-1,j+1)S_2(i-1,j+1)$$
$$+\overline{U}_{(i,j+1/2)}n_2(i,j+1)S_2(i,j+1)\Big)$$
$$-\frac{1}{2}\Big(\overline{U}_{(i-1,j-1/2)}n_2(i-1,j-1)S_2(i-1,j-1)$$
$$+\overline{U}_{(i,j-1/2)}n_2(i,j-1)S_2(i,j-1)\Big). \tag{2.20}$$

Then, it should be noted that the contributions following n_2 direction also found for the computation of the cell centered gradients on cells indices $(i-1,j)$ and (i,j) as

$$\begin{aligned}\overline{U}_{(i-1,j+1/2)}n_2(i-1,j+1)S_2(i-1,j+1)+&\\ \overline{U}_{(i,j+1/2)}n_2(i,j+1)S_2(i,j+1)-&\\ \overline{U}_{(i-1,j-1/2)}n_2(i-1,j-1)S_2(i-1,j-1)-&\\ \overline{U}_{(i,j-1/2)}n_2(i,j-1)S_2(i,j-1)&\\ = V_{(i-1,j)}\nabla U_{(i-1,j)}+V_{(i,j)}\nabla U_{(i,j)}&\\ +\overline{U}_{(i+1/2,j)}n_1(i+1,j)S_1(i+1,j)&\\ -\overline{U}_{(i-1/2,j)}n_1(i-1,j)S_1(i-1,j).&\end{aligned} \tag{2.21}$$

On the dashed lines, the normal vector $n_n(i,j)$ is defined as the averaged of left and right interface normals as

$$n_n(i,j)S_n(i,j) = \frac{n_1(i-1,j)S_1(i-1,j)+n_1(i,j)S_1(i,j)}{2}$$

The final formulation is obtained by injecting Eq. 2.21 in Eq. 2.20. This diffusive scheme was successfully applied to aeroacoustics computations in the past [156].

2.5 Spatial discretization at the walls

The high-order numerical schemes considered in our approach for the computation of the convective fluxes are based on implicit formulations using a relative high number of points. Close to the boundaries of the computational domain, the number of points available is reduced and the numerical schemes used in the interior of the domain can not be longer used to compute the primitive variables $\mathbf{W}$=(u, v, w, p, T). In a similar way, the high-order spatial filter given by Eq. (2.17) can not be used close to the boundaries.

The numerical discretization adapted to finite volume is used to reconstruct the velocity components, the temperature and the pressure. At the wall, the velocity satisfies the Dirichlet

condition, *i.e.* a null velocity. The pressure, follows a Neumann condition with a null perpendicular gradient

$$\left.\frac{\partial p}{\partial \mathbf{n}}\right|_{wall}. \tag{2.22}$$

An isothermal wall is characterized by a Dirichlet condition for the temperature with $T = T_w$, whereas for an adiabatic condition, the Neumann condition is applied as

$$\left.\frac{\partial T}{\partial \mathbf{n}}\right|_{wall}. \tag{2.23}$$

The numerical discretizations at the wall for the compact scheme and the filter of order 6 are described in the following.

Discretization at the wall for the compact scheme

In this work, the components of **W** are not directly imposed at the wall but computed from the compact scheme from Eq. (2.16). The implicit scheme can be applied over 4 points up to the wall if the numerical domain is extended by adding two additional ghost cells and a ghost interface as shown in Fig. 2.3. The ghost cells and the interface are situated symmetrically from the wall. The variables are then computed at these ghost cells by adding some constraints. In order to obtain a null velocity at the wall, the velocity is considered as an odd function following the normal direction to the wall. This implies computing the velocity at the points P_0 and P_{-1} and at the interface $I_{1/2}$ as

$$\begin{cases} \bar{u}_i = -\bar{u}_{1-i} \\ \bar{v}_i = -\bar{v}_{1-i} \\ \bar{w}_i = -\bar{w}_{1-i} \end{cases} \quad \text{for i=0, -1, and -1/2} \tag{2.24}$$

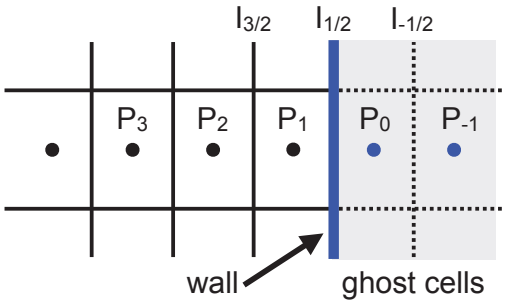

Figure 2.3: Discretization at the wall for the compact scheme.

Applying the compact scheme from Eq. (2.16) to Eq. (2.24) gives a null velocity at the wall. For an isothermal wall, the fictitious values are defined to obtain a temperature T_w at the wall as

$$\overline{T}_i = 2T_w - \overline{T}_{1-i} \quad \text{for i=0, -1 and -1/2,} \tag{2.25}$$

Last, the temperature in an adiabatic wall and the pressure are characterized from a Neumann condition with a null gradient normal to the wall. One simple way to take this into consideration is by considering the temperature and the pressure as even functions with respect to the

normal direction to the wall. In this case, the temperature is computed as

$$\overline{T}_i = \overline{T}_{1-i} \quad \text{for i=0, -1 and -1/2,} \tag{2.26}$$

and the pressure as

$$\bar{p}_i = \bar{p}_{1-i} \quad \text{for i=0, -1 and -1/2.} \tag{2.27}$$

Discretization at the wall for the filter

The spatial discretization for the filter of order 6 from Eq. (2.17) is similar to the one of the compact scheme. The formulation of 7 points can be applied up to the first point on the wall by adding 3 additional ghost cells as shown in Fig. 2.4. The values of the velocity components, the pressure and the temperature can be computed on P_0 and P_{-1} using the regular scheme. The point P_3 is used to compute the variables on the point P_{-2}. In order to use the implicit filter from Eq. (2.17), the values at P_0 must be known. These values are computed from the filtered variables at P_1. For example, the velocity components are

$$\begin{cases} \hat{u}_0 = -\hat{u}_1 \\ \hat{v}_0 = -\hat{v}_1 \\ \hat{w}_0 = -\hat{w}_1 \end{cases} \tag{2.28}$$

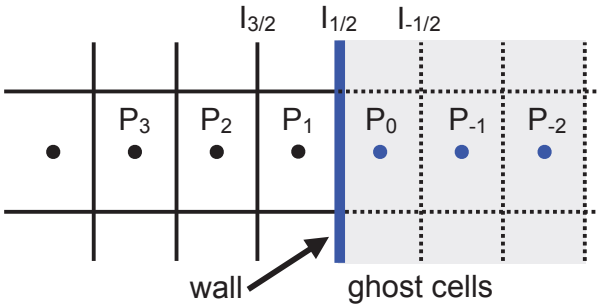

Figure 2.4: Discretization at the wall for the filter.

2.6 Spatial discretization at the block interfaces

The solver ***elsA*** allows to carry out simulations based on parallel computer architectures. To this end, the numerical domains are split into different sub-domains named blocks. The blocks are then balanced over different processors to reduce the time of the simulations. In the computation, a system of equations is solved for each block of the domain as

$$\alpha_{1/2}\widetilde{\mathbf{W}}_{-1/2} + \widetilde{\mathbf{W}}_{1/2} + \beta_{1/2}\widetilde{\mathbf{W}}_{3/2} = \sum_{j=-1}^{2} a_j \overline{\mathbf{W}}_j. \tag{2.29}$$

An interchange of information is then needed between each adjacent block. The representation of a mono-dimensional domain split in two blocks A and B by the interface $I_{1/2}$ is sketched

in Fig. 2.5. The interchange of information between the blocks allows to artificially extend the blocks with ghost cells. For example, block A is extended by the cells P_{-1} and P_0 that correspond to the cells of block B.

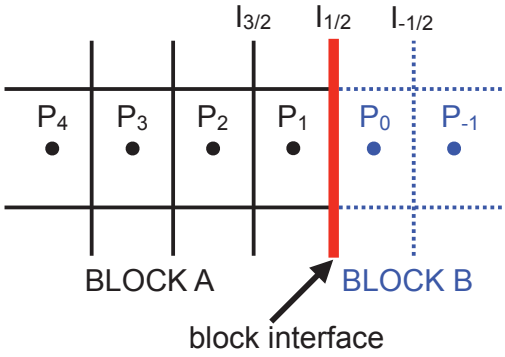

Figure 2.5: Discretization at the block interface for the compact scheme.

Discretization at the block interface for the compact scheme

From Fig. 2.5, inside block A it is possible to apply the implicit scheme from Eq. (2.16) up to the interface $I_{3/2}$. At the interface $I_{1/2}$, Fosso proposes to use a decentered scheme of order 5 to compute the state $\widetilde{\mathbf{W}}_{1/2}$ as

$$\widetilde{\mathbf{W}}_{1/2} + \beta''_{1/2}\widetilde{\mathbf{W}}_{3/2} = \sum_{j=-1}^{2} a''_j \overline{\mathbf{W}}_j \tag{2.30}$$

where $\beta''_{1/2}$ and a''_j are interpolation coefficients determined from Taylor expansions of order 5. Using a decentered scheme on the block interface $I_{1/2}$ implies that the value computed for the block A $\mathbf{W}^A_{1/2}$ and the value computed for the block B $\mathbf{W}^B_{1/2}$ are different. In order to conserve the fluxes at the interface, a Riemann solver is applied [155]. It defines a single flux at the interface computed from the values $\mathbf{W}^A_{1/2}$ and $\mathbf{W}^B_{1/2}$.

Discretization at the block interface for the filter

The original formulation from Visbal and Gaitonde [150] is based on a decentered scheme of the filter. However, Fosso [146] observed that this formulation introduced an important dispersion, responsible for parasitic oscillations at the interfaces. For this reason, he proposed to conserve the implicit formulation from Eq. (2.17) that reads as

$$\begin{cases} \alpha_f \widehat{\mathbf{W}}_{i-1} + \widehat{\mathbf{W}}_i + \alpha_f \widehat{\mathbf{W}}_{i+1} = \displaystyle\sum_{j=0}^{3} \frac{\beta_j}{2} \left(\overline{\mathbf{W}}_{i+j} + \overline{\mathbf{W}}_{i-j} \right) \text{ pour } i \geq -1 \\ \widehat{\mathbf{W}}_{-2} = \overline{\mathbf{W}}_{-2} \end{cases} \tag{2.31}$$

2.7 Aeroacoustic treatments at the inflow and outflow boundaries

In Computational Fluid Dynamics, the Navier-Stokes equations are solved within a finite domain. The boundary conditions are the numerical conditions that are imposed at the boundaries of the domain. The definition of boundary conditions plays an even more important role in aeroacoustic simulations that are based on non-dissipative algorithms because of the possibility of numerical instabilities and spurious wave reflections at the boundaries. Therefore, in order to achieve clean and accurate solutions, the boundaries must allow the free passage of incoming and outgoing waves without introducing parasitic perturbations. In this work, the boundary conditions based on characteristic and radiative conditions are used and presented in the following. Moreover, an accurate and realistic definition of the turbulent boundary layers that develop inside the nozzles is a must to obtain the same mixing conditions in the shear-layer of the jet. This turbulent boundary layer can be achieved by using a long enough duct inside the nozzle that allows for the growth of instabilities and transition of the boundary layer to turbulent regime. The modeling of the duct implies that the mesh is able to capture the instabilities that lead to transition which increases the cost of the simulation. An external forcing can be used as a less expensive workaround in order to help the transition to turbulent regime. In this work, a forcing based on divergence free disturbances is explained in Sec. 2.7.4.

2.7.1 Characteristic boundary conditions

The first kind of boundary conditions is based on a decomposition of the Navier-Stokes equations in characteristic variables. They were initially introduced by Thompson [157] for hyperbolic equations, this approach was extended to the Navier-Stokes equations by Poinsot and Lele [158]. For the sake of clarity, the approach considers only the two-dimensional Euler equations in Cartesian coordinates. The equations are written in non-conservative form and primitive variables as

$$\frac{\partial \mathbf{W}}{\partial t} + A\frac{\partial \mathbf{W}}{\partial x} + B\frac{\partial \mathbf{W}}{\partial y} = \mathbf{0}, \tag{2.32}$$

where $\mathbf{W} = [\rho, u, v, p]^t$ is the vector of primitive variables, and A and B are the matrices

$$A = \begin{bmatrix} u & \rho & 0 & 0 \\ 0 & u & 0 & 1/\rho \\ 0 & 0 & u & 0 \\ 0 & p\gamma & 0 & u \end{bmatrix} \text{ et } \; B = \begin{bmatrix} v & 0 & \rho & 0 \\ 0 & v & 0 & 0 \\ 0 & 0 & v & 1/\rho \\ 0 & 0 & p\gamma & v \end{bmatrix}. \tag{2.33}$$

Considering a boundary with normal direction x and assuming that the term $B\frac{\partial \mathbf{W}}{\partial y}$ is constant in the x direction, the system of equations (2.32) reduces to

$$\frac{\partial \mathbf{W}}{\partial t} + A\frac{\partial \mathbf{W}}{\partial x} + \mathbf{K} = \mathbf{0}. \tag{2.34}$$

According to the approach detailed by Thompson [157], the matrix A is diagonalized and can be expressed as a function of the matrix of eigenvalues S as

$$D = S^{-1}AS, \tag{2.35}$$

where D is the diagonal matrix of eigenvalues of A as

$$D = \begin{bmatrix} u-c & 0 & 0 & 0 \\ 0 & u & 0 & 0 \\ 0 & 0 & u & 0 \\ 0 & 0 & 0 & u+c \end{bmatrix}. \tag{2.36}$$

The equation (2.32) then can be written as

$$\frac{\partial \mathbf{W}}{\partial t} + SL + \mathbf{K} = \mathbf{0}, \tag{2.37}$$

where $L_i = \lambda_i l_i^t \dfrac{\partial \mathbf{W}}{\partial x}$ with

$$\begin{cases} l_1^t = \begin{bmatrix} 0 & -\rho a & 0 & 1 \end{bmatrix}, \\ l_2^t = \begin{bmatrix} a^2 & 0 & 0 & -1 \end{bmatrix}, \\ l_3^t = \begin{bmatrix} 0 & 0 & 1 & 0 \end{bmatrix}, \\ l_4^t = \begin{bmatrix} 0 & \rho a & 0 & 1 \end{bmatrix}. \end{cases} \tag{2.38}$$

The equation (2.37) is then expressed as

$$\begin{cases} \dfrac{\partial p}{\partial t} - \rho a \dfrac{\partial u}{\partial t} = -L_1 - K_4 + \rho a K_2, \\ \dfrac{\partial \rho}{\partial t} - \dfrac{\partial p}{\partial t} = -L_2 - a^2 K_1 + K_4, \\ \dfrac{\partial v}{\partial t} = -L_3 - K_2, \\ \dfrac{\partial p}{\partial t} + \rho a \dfrac{\partial u}{\partial t} = -L_4 - K_4 - \rho a K_2. \end{cases} \tag{2.39}$$

In order to apply this set of non-reflective boundary conditions, the waves L_1, L_2, L_3 et L_4 must be discerned among incoming or outgoing waves. For example, in the case where the boundary considered is located downstream of the flow of a subsonic jet directed along x, only the wave L_1 is incoming ($U - a < 0$) and the three waves L_2, L_3 and L_4 are outgoing. The amplitude of the wave L_1 is then imposed null, which allows to write the following boundary conditions as

$$\begin{cases} L_1 = 0 \\ L_2 = u \left(a^2 \dfrac{\partial \rho}{\partial x} - \dfrac{\partial p}{\partial x} \right) \\ L_3 = u \left(\dfrac{\partial v}{\partial x} \right) \\ L_4 = (u+a) \left(\dfrac{\partial p}{\partial x} + \rho a \dfrac{\partial u}{\partial x} \right). \end{cases} \tag{2.40}$$

The spatial derivatives in expressions L_2, L_3 and L_4 are obtained from the decentered discretized schemes. The temporal derivatives for the points in the borders are computed using the system of equations (2.39). A similar procedure is carried out in order to obtain the boundary conditions in the transverse y direction. For aeroacoustic computations of jets with ***elsA***, the characteristic conditions are used at the exit of the domain.

2.7.2 Radiative boundary conditions

The second category of boundary conditions was elaborated from the linearized form of the Euler equations valid in the acoustic far-field. Tam and Webb [159] proposed a formulation for the linearized Euler Equations in two dimensions. The radiative condition was established assuming that the pressure perturbations are purely acoustic and they behave as spherical waves that come from a punctual source inside the computational domain. The approach was extended to the Euler equations with the presence of a flow by Tam and Dong [160] and generalized to three-dimensional flows by Bogey and Bailly [161]. The three-dimensional formulation is written in spherical coordinates (r, θ, Φ), with the source of the emission at the origin. The three-dimensional radiative conditions [161] are written as

$$\left\{ \frac{\partial}{\partial t}\begin{pmatrix}\rho'\\ \mathbf{v}'\\ p'\end{pmatrix} + v_g\left(\frac{\partial}{\partial r}+\frac{1}{\alpha r}\right)\begin{pmatrix}\rho'\\ \mathbf{v}'\\ p'\end{pmatrix} = 0, \right. \tag{2.41}$$

where $\mathbf{u}'$ is the vector of fluctuating velocities (u', v', w'), α is a constant equal to 2 in two dimensions and 3 in three dimensions, and v_g is the group velocity of the acoustic waves defined by

$$v_g = \mathbf{u}\cdot\hat{\mathbf{e}}_r + \sqrt{\overline{a}^2 - (\mathbf{u}\cdot\hat{\mathbf{e}}_\theta)^2 - (\mathbf{u}\cdot\hat{\mathbf{e}}_\Phi)^2}, \tag{2.42}$$

where ($\hat{\mathbf{e}}_r$, $\hat{\mathbf{e}}_\theta$, $\hat{\mathbf{e}}_\Phi$) are the three unit vectors in the directions r, θ, Φ .

For an exit condition, the boundary not only encounters acoustic perturbations but also aerodynamic perturbations that usually are several orders of magnitude higher in amplitude. These entropic and vortical modes are taken into account in the equations as

$$\left\{ \begin{array}{l} \dfrac{\partial \rho'}{\partial t} + \overline{\mathbf{u}}\cdot\nabla\rho' = \dfrac{1}{\overline{a}^2}\left(\dfrac{\partial p'}{\partial t} + \overline{\mathbf{u}}\cdot\nabla p'\right) \\ \dfrac{\partial u'}{\partial t} + \overline{\mathbf{u}}\cdot\nabla u' = -\dfrac{1}{\overline{\rho}}\left(\nabla p'\right) \\ \dfrac{\partial v'}{\partial t} + \overline{\mathbf{u}}\cdot\nabla v' = -\dfrac{1}{\overline{\rho}}\left(\nabla p'\right) \\ \dfrac{\partial w'}{\partial t} + \overline{\mathbf{u}}\cdot\nabla w' = -\dfrac{1}{\overline{\rho}}\left(\nabla p'\right) \\ \dfrac{\partial p'}{\partial t} + v_g\left(\dfrac{\partial}{\partial r}+\dfrac{1}{\alpha r}\right)p' = 0. \end{array} \right. \tag{2.43}$$

One of the main difficulties of the approach is to have a mean flow from which to compute the perturbations $(\rho', \mathbf{u}', p')$. In practice, this mean flow can be obtained from a preliminary RANS computation or by using an average of the flow during the computation.

Some comparisons between the radiative conditions and the characteristic conditions are found in the literature [162, 163] showing that the radiative conditions give good results for acoustic propagation cases [162]. For aeroacoustic computations of jets with ***elsA***, the radiative conditions are applied to the lateral boundaries of the domain.

2.7.3 Sponge zones

The non-reflective boundary conditions do not guarantee the complete absence of reflexions of significant waves into the interior of the domain when the amplitude of the aerodynamic fluctuations is too important. It is then necessary to define some regions where the fluctuations of the flow are damped before the boundaries. These regions are known as sponge zones. There exist two main techniques for the generation of a sponge zone. The first technique consists in stretching the mesh. This methodology presents also the interest of decreasing the number of points in the mesh. On the other hand, the stretching can cause the generation of parasitic waves that could be propagated inside the domain. For this reason, inside a sponge zone a second technique is used with the first one. It consists in introducing an artificial dissipation with the bias of a stabilizing operators. For this purpose, inside the code ***elsA***, a filter of second order or a source term can be used in a non-exclusive way.

Second order filter

The filter of second order is given by the following explicit relation

$$u^f_{i,j,k} = u_{i,j,k} - \sigma_f \left(\frac{x_f - x}{x_f - x_d} \right)^p \left(\frac{1}{4} u_{i-1,j,k} - \frac{1}{2} u_{i,j,k} + \frac{1}{4} u_{i+1,j,k} \right), \tag{2.44}$$

where u is the field before the filtering, u^f is the variable filtered, σ_f is the filtering constant, x_d and x_f are the coordinates of the beginning and end of the sponge zone, and p is an index set to 2.

Source term

The utilization of a stabilizing operator under the shape of a source term is carried out by adding a callback function in the equations as

$$\frac{\partial u}{\partial t} + ... = \sigma_r \frac{a}{\Delta x} \left(\frac{x_f - x}{x_f - x_d} \right)^p (u - U_{tar}) \tag{2.45}$$

where U_{tar} is the target value for the field u, σ_r is the callback amplitude, Δx is the size of the considered cell, and p is an exponent set to 2.

2.7.4 Turbulence forcing

The transition of a jet to a turbulence regime can be established over a long distance. In this case, the phenomena related to vortex pairing shows a similar transition that the one of a laminar shear-layer. In order to have a fair comparison with the reality and the experimental data, the jet must be already turbulent at the exit of the nozzle. It is therefore compulsory to help the transition to turbulence inside the nozzle by injecting some kind of synthetic turbulence perturbations. When dealing with aeroacoustic simulations, one of the main constraints is the parasitic noise associated to the synthetic perturbations. To an extent, this is avoided using velocity perturbations with null divergence. However, numerical errors caused by the

discretization generate small perturbations that are propagated throughout the computational domain. The formulation of Bogey and Bailly [73] used in this work is detailed in the following.

The divergence free disturbances added to the velocity profiles in the shear-layer zone are based on a combination of the jet azimuthal modes m, and they modify the axial and radial velocities every time step in the following way

$$\begin{bmatrix} u \\ v \end{bmatrix} = \begin{bmatrix} u \\ v \end{bmatrix} + \alpha u_j \sum_{i=n}^{m} \epsilon_i \cos(i\phi + \phi_i) \begin{bmatrix} u^{ring} \\ v^{ring} \end{bmatrix}, \tag{2.46}$$

where the amplitudes $-1 \leq \epsilon_i \leq 1$ and the phases $0 \leq \phi_i \leq 2\pi$ of each mode are randomly updated every iteration. The unit vortex ring velocities are expressed, for $r = \sqrt{y^2 + z^2} \neq 0$, as

$$\begin{bmatrix} u^{ring} \\ v^{ring} \end{bmatrix} = \frac{2r_0}{r\Delta y} \exp\left(-\ln(2)\frac{\Delta(x,r)^2}{\Delta y^2}\right) \begin{bmatrix} r - r_0 \\ x_0 - x \end{bmatrix}, \tag{2.47}$$

where $\Delta(x,r)^2 = (x-x_0)^2 + (r-r_0)^2$, Δy is the transverse grid spacing, and the axial location is $x_0 \simeq r_0$.

2.8 Summary and perspectives

In this chapter, the numerical schemes of the solver ***elsA*** used for aeroacoustic simulations in the presence of shocks were presented. The Navier-Stokes equations were as well introduced with all the assumptions and hypotheses used for its simplification. The resulting equations are discretized in time and in space. The temporal discretization is based on the six-step low-storage optimized Dispersion-Relation-Preserving (DRP) Runge-Kutta scheme of Bogey and Bailly [145]. The spatial discretization can be divided into the discretization of the convective fluxes and the diffusive fluxes. The convective fluxes are discretized with the implicit sixth-order compact scheme from Fosso *et al.* [146]. The low-dissipative low-dispersive high-order scheme allows for a good discretization of the acoustic pressure waves that have several orders of magnitude less than the mean pressure of the flow. In order to avoid the high-frequency oscillations generated by the compact-scheme, a sixth- or eight-order spatial filter from Visbal and Gaitonde is applied. The filtering algorithm supplies dissipation to damp the high-wavenumber modes and it is also used as sub-grid scale model in the large eddy simulations. On the other hand, the discretization of the diffusive fluxes is done by a second order scheme due to the fact that the aeroacoustic simulations of industrial jets are mainly dominated by convective effects rather than by the diffusive ones. In addition, the spatial discretization of the convective fluxes and the spatial filter are modified at the boundaries to take into account the stencil of the compact scheme. Then, an in-house shock-limiting technique was presented. This technique is based on the limiters from the piece-wise parabolic method from Colella and Woodward [154]. Last, the treatments specified for aeroacoustic simulations were introduced. In particular, the characteristic boundary conditions from Poinsot and Lele [158] and the radiative conditions Tam and Dong [160] and generalized to three-dimensional flows by Bogey and Bailly [161] were introduced. The formulation of the sponge zones used on the boundaries of the computational domain and the turbulence forcing used to generate synthetic turbulence were explained.

The numerical base schemes presented in this chapter have been widely validated. On the other hand, as it is shown in Ch. 6, the actual shock-limiting schemes lack from consistency. A new

shock-capturing technique was developed and it is detailed in the latest chapter. Moreover, new formulations for wall-models adapted to high-order schemes have been developed by Le Bras *et al.* [164] which could reduce the cost of the aeroacoustic large eddy simulations of jets.

Chapter 3

Large eddy simulation methodology for jet noise computations

In the present study, the flow and its associated acoustic field are computed with LES for different topologies of supersonic under-expanded jets. A good knowhow and methodology could determine a successful computation against one that has a higher degree of uncertainty. Once some initial problems are solved, computational fluid dynamics allow to investigate the evolution of a flow. It is up to the user to decide the level of accuracy of the simulation. Questions such as, is the mesh refined enough? is the time-step appropriate? or, are enough flow snapshots saved? could determine if a computation was worth doing, or if it will remain simply as part of a process of trial and error.

This chapter explains the general methodology carried out for aeroacoustic jet simulations focusing on: the pre-processing, the computation and the post-processing techniques. First, the mesh generation procedure is explained in Sec. 3.1. Second, in Sec. 3.2 the setup of the simulations is explained. Then, an overview about some standard post-processing techniques is given in Sec. 3.3. In particular, this section focuses on the method for far-field noise propagation, a hydrodynamic-acoustic filtering, and the azimuthal decomposition. Last, a summary and some perspectives are presented.

3.1 Mesh generation

This section explains the procedure for the generation of the mesh adapted for jet noise aeroacoustic computations. The CFD solver (***elsA***[143]) used during this work is a multi-block structured solver. A structured solver implies that the mesh must be constructed with a structured approach where different blocks are defined to accommodate the model geometry. The type of elements encountered in the mesh are quadrilaterally-faced hexahedra. The connectivity between blocks can be conformal, where the grid lines are continuous in the interface of the blocks, or non-conformal. In the latest, each block can have a different number of elements in the connected faces which leaves the interface with hanging nodes. The meshes in this work are conformal and they were generated with the commercial software IGG (AutoGrid v10.1rc) from Numeca. The mesh generation was carried out mostly in batch mode. The scripts implemented to generate the mesh account for the generation of the model geometry

and the domain geometry, the generation of the blocks and its different discretization laws and the definition of the boundary patches.

The mesh topology is of the type butterfly [87, 63]. The use of a solver developed in Cartesian coordinates and its application to axisymmetric cases such as cylindrical jets is not straightforward. A cylindrical mesh shows a singularity at the axis where one of the faces of the hexahedral elements is null as shown in Fig. 3.1 (a). This is avoided with the implementation of a butterfly mesh. This topology replaces the area surrounding the axis by a square-like block as shown in Fig. 3.1 (b). This kind of mesh topology avoids the over discretization at the axis. In a cylindrical structured conformal mesh, the azimuthal discretization is fixed and dimensioned according to the vortical structures that develop in the shear-layer. This implies that the number of azimuthally distributed cells near the axis directly depends on a predefined value. Overall, a butterfly topology allows for a more uniform mesh in the central region.

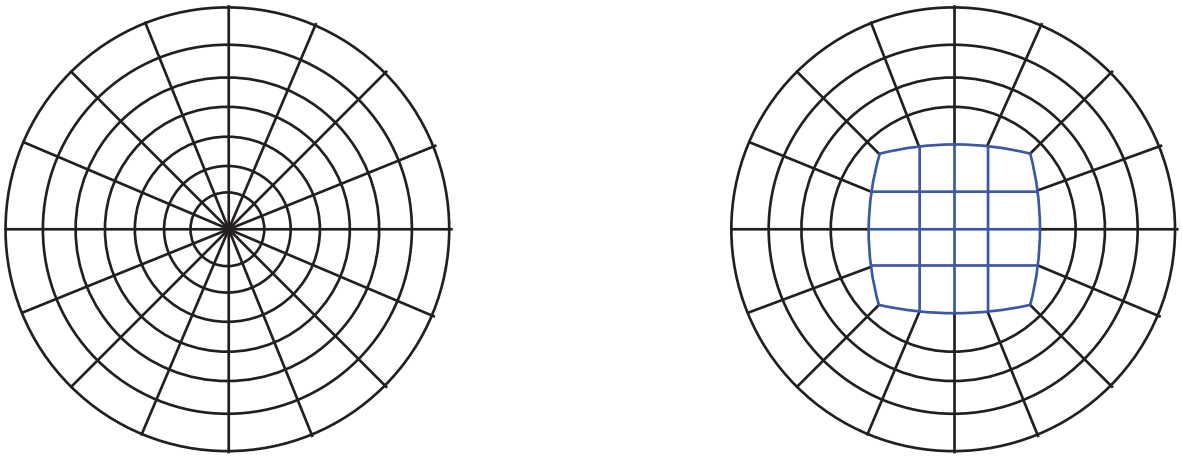

Figure 3.1: *Sketch of* ***(a)*** *a cylindrical mesh and* ***(b)*** *a butterfly mesh.*

A general multi-block structured butterfly mesh of an isolated single jet can be defined by 18 blocks if no merging of different compatible topological blocks is done. Figure 3.2 shows in solid line the contour of the different blocks needed for a general mesh of a single jet. The inner region groups the central block and the adjacent blocks inside and outside the nozzle. The outer blocks group the lip region, the near-field physical domain and the sponge regions that encloses the whole domain of interest. The domain, and therefore the blocks, grow radially with the axial position. This expansion of the domain has to be taken into account to avoid a denser outflow boundary. When dealing with conformal structured meshes, the number of cells is propagated through the connected blocks, *e.g.* the radial discretization of the central block inside the nozzle determines the radial discretization of the central block outside the nozzle as this discretization is propagated by the connected joined face at the nozzle exit plane. The size of the outflow boundary must be increased in order to have a uniformly distributed boundary that contains the same number of cells in the radial direction as the blocks inside the nozzle. This expansion also helps in having a better isotropy of the mesh following the expansion of the jet. The axial discretization shared between connected blocks, is changed from the regions noted with the letters A, B, C. In region A and C, an expansion ratio of less than 4% is considered. On the other hand, in region B, the mesh is uniformly distributed. The choice

of the size of the three regions depends on the case of consideration and has a big impact on the total number of cells of the mesh, and thus, on the cost of the simulation. The maximum expansion ratio in the physical domain was restricted to 4% and the skewness of the cells to a minimum of 54 degrees to avoid spurious noise [151]. In the sponge layer, an expansion ratio of 10% was used. An example of the mesh is shown in Ch. 5 and Ch. 6 for particular jets.

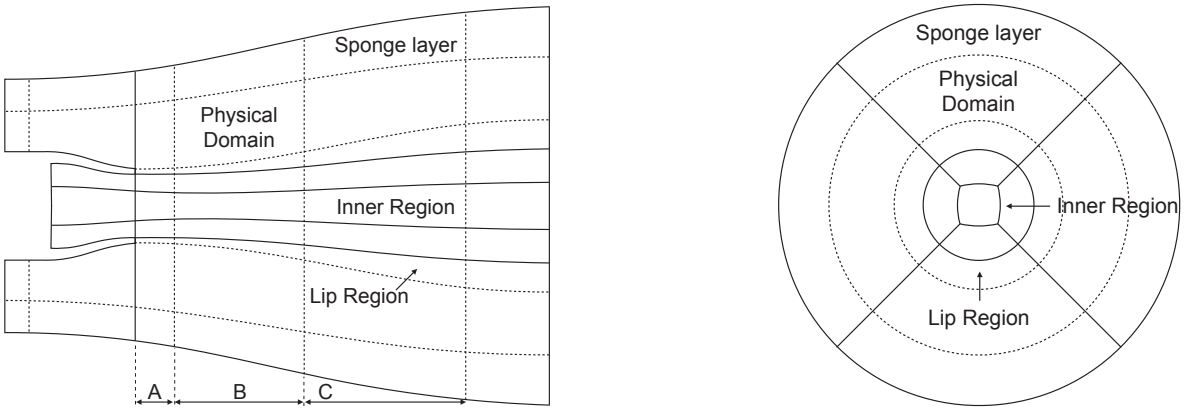

Figure 3.2: *Sketch of a domain for a jet. In solid lines are represented the block boundaries and in dashed lines the different regions inside each block.* ***(a)*** *axial representation.* ***(b)*** *radial representation.*

The three dimensional mesh generated for an aeroacoustic computation of a jet has to be adapted based on the numerical schemes used, the type of boundary conditions, the flow conditions and the level of discretization of the pressure perturbations. Capturing the noise source mechanism in a jet is related to the level of discretization of the mesh according to the different turbulence scales [165]. For a large eddy simulation, the mesh should be able to resolve down to the order of the Taylor microscale [166]. The Taylor microscale is the intermediate length-scale at which fluid viscosity significantly affects the dynamics of turbulent eddies in the flow. These microscales are found in the dissipation range and are modeled by the subgrid scale equivalent model of the LES (see Ch. 2). The noise source mechanism can be related to the turbulence interaction on the mean flow known as mean noise and the noise generated by the turbulence itself known as self-noise [167]. On the other hand, the propagation of noise disturbances in the near-field is linked with the spatial numerical schemes and the resolvable frequencies. The high-order compact schemes explained in Ch. 2, allow for the discretization of a wave with a negligible dispersion and dissipation using only 6 points per wavelength. The mesh size is then defined by

$$\Delta s = \frac{a_\infty}{6f}, \tag{3.1}$$

where a_∞ is the ambient speed of sound and f is the resolvable frequency of interest which is defined according to the physics of the case of study.

Once the mesh is generated, it is split for parallel computations. The split is done to distribute the new blocks among the processors. The splitting of the mesh was done internally with ***elsA***[143] which is based on the Greedy algorithm [168]. The Greedy algorithm does not give the best optimal load balance between each processor, instead, it yields locally optimal

splits that approximate the global optimal distribution after some iterations. A maximum load balance error of 10% was obtained throughout all the parallel computations to assure a good efficiency of the computation.

3.2 Large eddy simulation procedure

3.2.1 Two-step procedure

The definition of the boundary conditions and the initial conditions are necessary for a computation. In this work, a two-step procedure using a Reynolds Average Navier-Stokes simulation (RANS) is used as boundary and initial conditions as in [63]. The LES is initialized with the RANS in a coarse mesh before using the refined and case adapted mesh to accelerate the transient phase. The diagram of the procedure is summarized in Fig. 3.3.

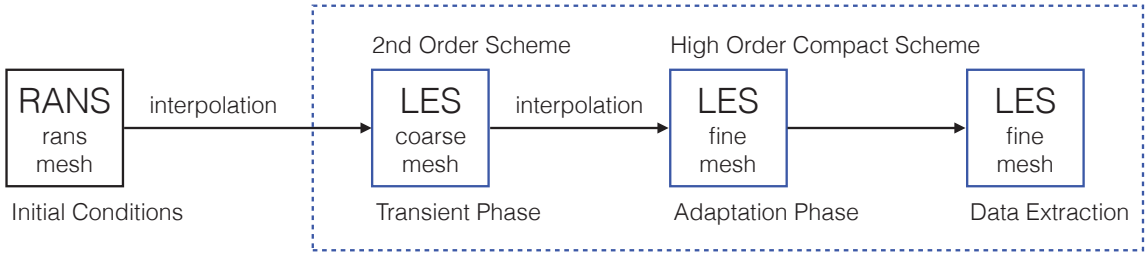

Figure 3.3: *Simulation procedure scheme.*

The RANS simulations are carried out as well with the solver ***elsA***[143]. Some details about the RANS simulations are explained in the following. The turbulence model used in the computations is the one-equation Spalart-Allmaras standard model [169]. The convective flux is computed using an upwind approach based on the Roe's approximate Riemann solver [155]. The scheme's accuracy is increased by either a second order MUSCL extrapolation [170] coupled with the *minmod* limiter or a third order extrapolation technique [171]. The last technique does not include any limiter but the convergence to the steady state does not suffer from this numerical parameter. Finally, Harten's correction [172] is included to avoid non-entropic solutions. The convection term of the Spalart-Allmaras turbulence model is discretized following the formalism of Larrouturou [173]. In order to efficiently attain the steady state, the backward Euler time integration is coupled with a V-type multigrid technique with three levels of coarsening. The implicit system is solved at $CFL = 100$ with a $LU - SSOR$ algorithm with four sweeps [174]. A minimum of 4-6 drops of order of magnitude in the residuals is obtained for the all RANS simulations after $10,000$ multigrid cycles.

The full three-dimensional mesh used for the RANS simulations has the same topology as the LES mesh explained in Sec. 3.1. However, the domain is bigger reaching up to 100 diameters in the axial and in the radial direction for the single jet presented in Ch. 5. Moreover, as it is expected, the mesh expansion ratios are not as limited as those for LES. The flow has been interpolated from the RANS mesh into the LES mesh with the interpolation treatment of Antares [175]. The interpolation is done with 8 neighboring points weighted with the inverse distance to a predefined power. The source terms of the non-reflective boundary conditions

detailed in Ch. 2 are obtained as well, directly from the RANS. Because the domain is smaller for the LES than for the RANS simulation, ambient pressure conditions are not fully reached at the exit of the domain (when this one was interpolated into the LES mesh). Therefore, the RANS solution gives a better approximation of the conservative variables at the boundary than imposed ambient values.

When the LES is initialized from a RANS solution, the flow needs to adapt from time-averaged variables, to the instantaneous time-resolved solution. Due to the fact that the RANS is not a solution of the Navier-Stokes equations, because they are not averaged in time, an unphysical behavior of the flow may appear. Moreover, the simulation overcomes a transient phase from the RANS to the LES, where the vortices in the shear-layer and all the transient phenomena start to develop. In order to accelerate this transient phase, a coarse mesh could be used in-between. The coarse mesh and the utilization of a second order upwinding convection scheme kills the unphysical phenomena when switching from RANS to LES faster than directly computing with the refined mesh and the high-order schemes presented in Ch. 2. Afterwards, the computation can be continued with the refined mesh. The use of RANS has the advantage of applying a fully developed jet as initial conditions. The velocity entrained by the jet helps to evacuate the transient phenomena at a faster pace than when quiescent conditions are used as initial conditions. An alternative procedure would have been to impose an analytical solution as initial conditions. This approach is beneficial when the resources are not available to compute an initial RANS. An example of the transient phase of the dual stream from Ch. 6 is shown in Fig. 3.4.

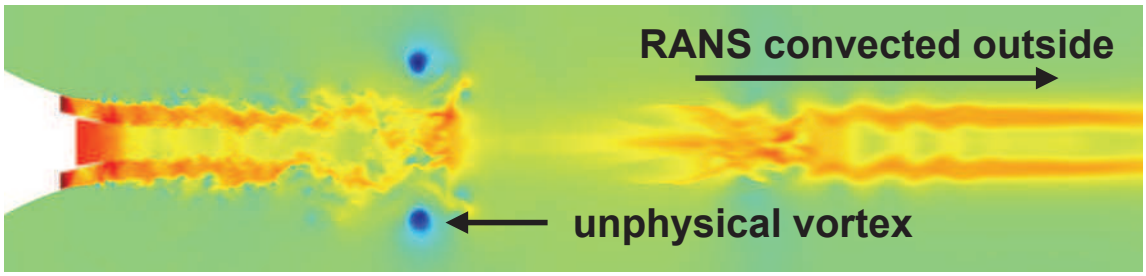

Figure 3.4: *Pressure contours of a dual stream jet at the transient phase between RANS and LES.*

In this step, unphysical vortices appear due to the initialization with RANS and must be convected outside the physical domain. Additionally, the Courant-Friedrich-Levy (CFL) condition is less impacted when the RANS is used as initial conditions with respect to quiescent initial conditions. Our experience shows that the full development of a jet from quiescent conditions could produce a different phenomena, that could be more detrimental to the time-step defined by the CFL condition than when using RANS as initial conditions. The impact on the time-step of the simulation would eventually affect the computational time of the simulation. Because the time integration is done explicitly, the time-step of the whole mesh is determined by the cell with the most restrictive CFL. The time-step is defined based on the initialization of the simulation. In this step, the CFL is set to 0.95 which allows for a variable time-step. The time-steps achieved during this phase define the final constant time-step of the LES.

3.2.2 Data extraction

Once the LES has overcome the transient phase, the data extraction phase can be started. Experiments and Computational Fluid Dynamics are complementary results. Normally, an experience is used to validate the CFD. After this first step is validated, the rest of the CFD flow can be studied with a higher degree of confidence. The experiments can usually be run for a longer period of time, *i.e.* obtain more samples, but the location, number of probes or variables is restricted by the cost, the positioning of the measurement tools and the type of experimental apparatus. In a CFD simulation, the positioning of the numerical probes depends only on the discretization of the mesh due to the fact that one can measure any computed quantity at each cell in the domain. Several variables can be computed at the same time in the same location and different numerical measurements can be done at the same time. Moreover, the extracted data is not perturbed by the extraction tool as it can happen in some experimental procedures. On the other hand, the physical time of the simulation is usually less than 1% the measured time in the experiments. Experiments and CFD are therefore complementary.

A large eddy simulation of a jet can supply the researcher with enormous quantities of data to analyze. Before launching a simulation and extracting all the data of each cell of the mesh at each iteration, one needs to keep in mind three factors. First, the researcher needs to think about the interest of the data being saved. For example, if the time-step of a simulation is of the order of 10^{-8} seconds, the equivalent frequency sampling would be of 100 MHz. If the frequency of the physical phenomena occurring in the simulation is of several orders of magnitude lower, as it would be in most jet simulations, the data could be saved every 100 iterations, instead of at each iteration. Also, maybe the data near the boundaries or in other regions are not relevant for the physics of interest and they could be spared. Second, the computational cost in terms of time and memory space needs to be foreseen. Depending on the solver, it may occur that extracting the data in the whole domain, slows down the simulation due to Input/Output performances based on the software or the hardware architecture. Certainly, the quantity of data extracted needs to be predicted in order to avoid filling all the memory space of the storage systems. Last, the data extracted has to be analyzed. Depending on the post-processing techniques used, it could involve loading in memory the whole dataset. This could be impractical if the memory required is higher than the one installed on the post-processing stations.

For the reasons mentioned above, the data extracted in the jet simulations of Ch. 5 and Ch. 6 is only composed of numerical probes, topological surfaces, plane-cuts and the mean in the complete three-dimensional domain. The full instantaneous three-dimensional flow was not saved due to memory constraints. More details about the positioning are given in each respective chapter. The numerical probes extract the conservative cell-variables and other computed quantities such as the vorticity in some locations of the domain that are specified in a list. The probes are located in the shear-layer at different radial locations and distributed axially and azimuthally over the domain. The topological surfaces are obtained following a gridplane of the structured mesh. The extracted topological surfaces contain the conservative variables of each cell-face. Plane cuts are also extracted using the cut treatment of Antares [175] that is based on VTK libraries [176]. Always in the interest of saving computational memory, only some axial cuts are saved. Some of these surfaces are used to propagate the noise to the far-field with the formulation presented in Sec. 3.3.1.

3.3 Standard post-processing techniques

3.3.1 Acoustic far-field characterization

For a direct computation of sound approach such as the one used in this study, the aerodynamic field contains the hydrodynamic disturbances as well as the acoustic perturbations (see Sec. 1.4.1). The hydrodynamic disturbances act as noise sources and are indiscernible from the acoustics due to the inherent non-linearities of the flow. Pressure perturbations can always be measured inside the flow, however, the separation from hydrodynamics and acoustics, is not clear, if the measure is done in the non-linear region of the flow. In the near-field region where the non-linearities are small compared to the linear terms, a proper acoustic measurement can be done. For a jet, this is the region outside the shear-layer. Nonetheless, the near-field region also contains hydrodynamic perturbations known as pseudo-sound perturbations. They are pressure perturbations originated from the convection of vortical structures but that do not travel at the ambient speed of sound. The hydrodynamic-acoustic filtering is explained in Sec. 3.3.2. The far-field condition is reached when the noise sources can be considered punctual, *i.e.* the noise is emitted from one single punctual location. In the far-field, the amplitude of the acoustic perturbations are attenuated with the inverse square distance and the shape remains constant. The acoustic field in the far-field can be computed numerically or with an acoustic analogy. If the acoustic field is computed numerically, for example with the acoustic wave equation, the region between the near-field and the far-field must be discretized. In order to reduce the computational cost, acoustic analogies are available to analytically propagate the noise to the far-field using Green functions. The Lighthill acoustic analogy presented in Sec. 1.1 is an example of it, however, it is not consistent since all the sources are modeled as quadrupoles. Curle [177] and then Powell [178] extended the Lighthill analogy to take into account boundary conditions without the need of a modified Green function. Later, Ffowcs-Williams and Hawkings [179] proposed a surfacic formulation. In this work, the formulation of Farassat [180] is implemented and presented in the following.

Formulation

A surface Σ defined by $f(x,t)=0$ is considered. Inside the surface Σ the function f is defined negative as $f(x,t)<0$. The velocity of the surface Σ is denoted as $\mathbf{v}$. Multiplying the mass and momentum conservation equations by the Heaviside function $H(f)$ and combining them together results in

$$\begin{aligned}\frac{\partial^2}{\partial t^2}\left(\left(\rho-\rho_0\right)H(f)\right)+a_\infty^2\nabla^2\left(\left(\rho-\rho_0\right)H(f)\right)\\ =\frac{\partial^2}{\partial x_i\partial x_j}\left(T_{ij}H(f)\right)+\frac{\partial}{\partial x_i}\left(L_i\delta(f)\right)+\frac{\partial}{\partial t}\left(Q\delta(f)\right),\end{aligned}\tag{3.2}$$

where T_{ij} is the Lightill tensor defined as $T_{ij}=\rho v_i v_j+(p-\rho a_\infty^2)\delta_{ij}-\tau_{ij}$ and the components L_i and Q are defined as

$$L_i=-(\rho u_i(u_j-v_j)+(p-p_0)\delta ij-\tau_{ij})n_j,\tag{3.3}$$

$$Q=(\rho(u_i-v_i)+\rho_0 v_i)n_i,\tag{3.4}$$

where $\mathbf{n}$ is the exiting normal vector to Σ. Using the free Green function it is found

$$\begin{aligned} a_\infty^2 \left(\rho - \rho_0\right) H(f) =& \frac{1}{4\pi a_\infty^2} \Bigg(\frac{\partial^2}{\partial x_i \partial x_j} \int\int\int_{f>0} \frac{1}{r \mid 1 - M_r \mid} T_{ij} \left(\mathbf{y}, t - \frac{r}{a_\infty} \right) d\mathbf{y} \\ &+ \frac{\partial}{\partial x_i} \int\int_{f=0} \frac{1}{r \mid 1 - M_r \mid} L_{ij} \left(\mathbf{y}, t - \frac{r}{a_\infty} \right) d\Sigma \\ &+ \frac{\partial}{\partial x_i} \int\int_{f=0} \frac{1}{r \mid 1 - M_r \mid} Q_{ij} \left(\mathbf{y}, t - \frac{r}{a_\infty} \right) d\Sigma \Bigg), \end{aligned} \tag{3.5}$$

where $r = \mid \mathbf{x} - \mathbf{y} \mid$ and $M_r = (\mathbf{u} \cdot \mathbf{r})/(r a_\infty)$. The density fluctuation corresponds to the superposition of three components: a quadrupole source, a dipole source and a monopole source. The quadrupole source is represented by the Lighthill tensor T_{ij} and encloses all the quadrupole sources found inside the surface Σ. The dipole source, known as loading source term noted by L_i represents the constraints exerted on the surface. The monopole source, also known as the thickness source term noted by Q accounts for the displacement of fluid produced by the body. The loading and thickness source terms are surface distributions of sources and represent all the fluctuations generated by the flow in the interior of the surface.

Setup

The computation of the FWH analogy is done directly on-the-fly with an in-house implementation in ***elsA***. The propagation of sound to the far-field is done at each iteration. In addition, the topological surfaces used for the analogy are saved at a specified frequency. Computing the propagated sound on-the-fly implies that the observers must be defined before the data extraction step starts. The surfaces are saved in order to be able to do *a posteriori* computation of the far-field sound specifying new observers. The surfaces saved are topological surfaces that follow one gridplane of the mesh in the cylindrical direction. The values at the interface are directly obtained from the compact scheme. Moreover, a topological surface has the advantage of avoiding interpolations with respect to a simple conical cut. In addition, the surface follows the mesh. This means that the construction of the mesh must take into account the expansion of the jet to avoid extracting a topological surface that crosses the jet plume. An example of such a surface is illustrated in Fig. 3.5.

In the present work, the FWH surfaces are open at the outflow boundary where the jet exits the domain. A spatial average can be done for a set of surfaces located at the exit of the domain to account for the noise produced by the exiting vortices without adding the hydrodynamic pseudo-sound. This procedure improves the accuracy in the low-frequency range [129]. However, this methodology was not implemented as the shock-cell noise is radiated mainly in the upstream direction where the surface is closed and the frequency range is higher than the one affected by the closing surfaces.

3.3.2 Hydrodynamic-acoustic filtering

As it was mentioned in Sec. 3.3.1, the near-field flow is composed of hydrodynamic and acoustic perturbations. The pressure perturbations obtained in the irrotational near-field of a turbulent jet are composed of both components in an *a priori* unknown fashion. In order to focus the study on either the hydrodynamic or the acoustic component, the acoustic-hydrodynamic

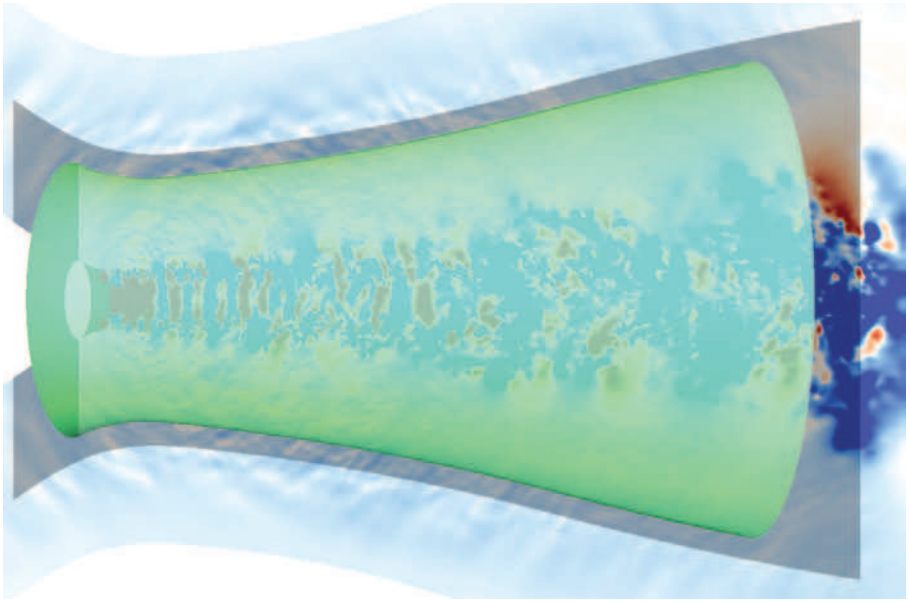

Figure 3.5: *FWH extraction surface of a dual stream jet in green. The contours of the pressure perturbation are shown in the background image. The shaded region represents the physical domain.*

filtering of Tinney and Jordan [181] was implemented. This filtering allows for a more rigorous study of the underlying source mechanism related to the measured pressures in the near-field. The decomposition into hydrodynamic and an acoustic components is not possible for Mach numbers of order unity, as the modes from both components are coupled together [182]. Nonetheless, the near irrotational pressure field gives a meaningful differentiation between the pressure fluctuations associated with the passage of the vortex cores [183]. This hydrodynamic footprint, even if it consists of pressure perturbations that do not travel at the speed of sound, they are responsible for sound generation [167]. The pressure near-field of a subsonic jet was filtered in hydrodynamic and acoustic perturbations in [184], showing all the above-mentioned features.

For the case of interest, *i.e.* a supersonic jet, the filtering can be performed outside the jet where the flow is mostly irrotational. The idea behind the filtering is to separate the two components using geometrical relations of the acoustics waves with respect to a linear array of probes. In order to filter a signal, an array of probes following a straight line is needed. The quality of the hydrodynamic filtering is affected by the number of probes used and by its distribution. An array of probes that follows the expansion of the jet is best suited for this filtering in comparison with a horizontal one. A horizontal array of probes should be placed farther away from the jet to avoid a crossing with the jet plume. At this location, the field would most likely be composed of only the acoustic component making probably pointless the filtering. The separation is carried out taking advantage of the transformation into the wavelength-frequency domain. The pressure signal of the probe array $p(x', t)$ is expressed in the wavelength-frequency domain as

$$p(k, \omega) = \int \int p(x', t) W(x') \mathrm{e}^{-i(kx' + \omega t)} dx' dt, \tag{3.6}$$

where the reference coordinate x' is set parallel to the array. $W(x')$ is a weight function that smooths the signal at the axial ends of the array. In this work, the smoothing window is applied over one diameter. An acoustic fluctuation generated by a noise source inside the jet is propagated outside the jet at the ambient sound speed a_∞. However, the acoustic perturbation is propagated at a relative supersonic speed obtained with the geometrical relation

$$a'^2 = a_\infty(2rf + a_\infty), \tag{3.7}$$

in the x' coordinate system, where r is the perpendicular distance from the axis situated on the array to the noise source and f is its frequency. Alternatively, the propagation speed seen by the axis x' can be geometrically linked to the perpendicular and parallel wavelengths of the noise source that emits at a frequency $f = a_\infty/\lambda$. The different wavelengths and distances are sketched in Fig. 3.6. The propagation speed is then

$$\frac{a'}{a_\infty} = \frac{\lambda'}{\sqrt{r^2 + \lambda'^2} - r} = \sqrt{\frac{2\lambda}{r} + 1}, \tag{3.8}$$

where λ' is a pseudo-wavelength parallel to the axis x' and λ is the actual wavelength perpendicular to the axis x'.

In order to clarify the previous relations easily, two extrema can be studied. When the distance from the source to the array r tends to infinity, a plane wave is sensed by the array. Therefore, the plane wave has an infinite wavelength δ' in the x' axis or the sound speed a' goes to infinity (see Eq. (3.7)). If the noise source is located in the same axis as the linear array, the perpendicular distance r will be equal to zero. At this point, the acoustic perturbations are convected at the sound speed a_∞ and the hydrodynamic perturbations at a lower speed. In the general case, when the distance r is finite and not zero, the acoustic perturbations travel in the x' axis at a velocity higher than the speed of sound having the limit at the ambient speed of sound a_∞. This component is referred to as the supersonic or acoustic component. In the same fashion, the hydrodynamic perturbations developed by the convected vortices travel at a velocity smaller than the speed of sound a_∞. This component is referred to as the subsonic or hydrodynamic component.

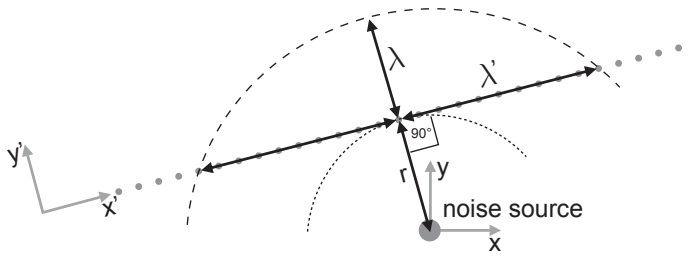

Figure 3.6: *Sketch of the different wavelengths with respect to different axes from a noise source situated at a distance r from the array.*

Then, the subsonic and supersonic components can be recovered from the transformed signal obtained by Eq. (3.6) using only the ranges $p(k > \omega/a_\infty, \omega < ka_\infty)$ and $p(k < \omega/a_\infty, \omega > ka_\infty)$

respectively as

$$p_h(x',t) = \int\int p(k > \omega/a_\infty, \omega < ka_\infty) \mathrm{e}^{-i(kx'+\omega t)} dk d\omega, \tag{3.9}$$

$$p_a(x',t) = \int\int p(k < \omega/a_\infty, \omega > ka_\infty) \mathrm{e}^{-i(kx'+\omega t)} dk d\omega, \tag{3.10}$$

where the subscript $\{\bullet\}_h$ represents the hydrodynamic perturbations characterized by subsonic phase velocities and the subscript $\{\bullet\}_a$ the acoustic perturbations characterized by supersonic phase velocities. An example of this decomposition is shown in Fig. 3.7.

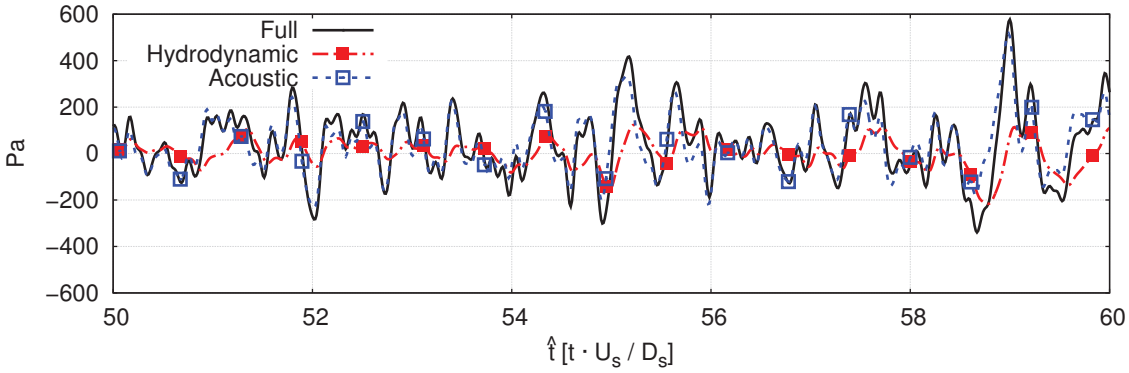

Figure 3.7: *Near-field pressure signal decomposed into the hydrodynamic and the acoustic components. Signal extracted from the supersonic under-expanded single jet from Ch. 5 at* 3 *D from the nozzle exit and an expansion angle of* 5 *degrees.*

3.3.3 Azimuthal decomposition

The azimuthal decomposition decomposes a signal recorded in an azimuthally distributed array of probes into the azimuthal modes based on Fourier coefficients. The azimuthal decomposition has been widely applied to the study of supersonic jets. In particular, in the study of supersonic screeching jets. These kinds of jets follow different azimuthal behaviors depending on the exit Mach number of the jet. As it was shown by Powell [31], screech sound can affect the azimuthal modal behavior and development of the flow. The azimuthal decomposition gives information about the energy of each mode, and can be used to study each mode separately to gain more insight of the physics that lay behind the generation of shock-cell noise.

Two similar methodologies based on the Fourier decomposition were found in the literature [185, 186]. However, being based on the same basis, the results are equivalent. Both methodologies imply that the actual signal is based on a linear superposition of different azimuthal modes. If the flow contains a high order of non-linearities, the azimuthal decomposition will give less accurate results as it tries to model a non-linear flow as linear (see Appx. B). The energy of the non-linear terms would be hidden inside the linear terms.

The first methodology [186], decomposes the real signal directly into the different modes by

expressing it as a Fourier series such that

$$p\left(\phi,t\right)=\frac{a_0\left(t\right)}{2}+\sum_{m=1}^{M}\left(a_m\left(t\right)\cos\left(m\phi\right)+b_m\left(t\right)\sin\left(m\phi\right)\right), \tag{3.11}$$

where ϕ is the azimuthal coordinate, M the number of azimuthal modes solved, and the set $\{a_o, a_m, b_m\}$, with $m = 1...M$, are the Fourier coefficients corresponding to the different modes. In order to recover the different Fourier coefficients and retrieve the azimuthal modes, it is necessary to solve a linear problem obtained from equation 3.11. The linear problem to solve with $2M + 1 = N$ is $F = T^{-1}P$ where P is a vector containing the different signals on the azimuthal array as

$$P=\begin{pmatrix} p\left(\phi_1,t\right)\\ \vdots\\ p\left(\phi_N,t\right)\end{pmatrix}. \tag{3.12}$$

F is a vector containing the Fourier coefficients of the series as

$$F=\begin{pmatrix} a_0(t)\\ a_1(t)\\ b_1(t)\\ \vdots\\ a_N(t)\\ b_N(t)\end{pmatrix}. \tag{3.13}$$

And T is a matrix of trigonometrical functions:

$$T=\begin{pmatrix} 1 & \cos(\phi_1) & \sin(\phi_1) & \cdots & \cos(M\phi) & \sin(M\phi)\\ \vdots & \vdots & \vdots & \ddots & \vdots & \vdots\\ 1 & \cos(\phi_N) & \sin(\phi_N) & \cdots & \cos(M\phi_N) & \sin(M\phi_N)\end{pmatrix}. \tag{3.14}$$

The second, but equivalent methodology, expresses instead, the spectrum of the signal as Fourier series as in [185]. The cross-spectra is computed between the different azimuthal probes with respect to a reference probe. The complex amplitudes of the cross-spectra are used to solve for the modal composition by solving the system of equations

$$F_k(\phi_k)=c_0+\sum_{m=1}^{M/2-1}c_m^{-}\mathrm{e}^{im\phi_k}+\sum_{m=1}^{M/2-1}c_m^{+}\mathrm{e}^{-im\phi_k}, \tag{3.15}$$

where F_k is the cross-spectra between one probe and the reference probe. In a similar way as explained for the first methodology, the system of equations can be resolved and the complex Fourier coefficients retrieved. Using the cross-spectra with respect to a reference probe means that the phase and the amplitude of the complex coefficients are referenced to the ones of the reference probe. In the current work, no reference probe was used, always leaving the reference phase with respect to the plane $z = 0$ with positive y and the amplitude untouched. The Fourier coefficients of the Fourier series are the same for the Fourier transform for discrete signals.

3.4 Summary and perspectives

In this chapter, three aspects of the simulations carried out were explained. First, the generation of the mesh for aeroacoustic simulations of jets was explained. The type of solver determines the topology of the mesh. In the present study, the use of a structured solver influenced the author to adopt a butterfly topology. The details of the mesh that are needed with the constraints of the numerical schemes were also described. In particular, the stretching ratio of the cells must not be higher than 4% to avoid spurious noise. Additionally, a general definition of the blocking system was described. The methodology for the LES was split in a two-step procedure where the initial conditions are computed *via* a RANS simulation. The Reynolds-averaged Navier-Stokes simulation was carried out using a mesh with the same topology as the LES but with lighter mesh constraints. The RANS solution is interpolated into a coarse LES mesh to evacuate the transient phase out of the domain. Then it is again interpolated into the final refined LES mesh. After the transient phase is done, the data extraction phase can start. In this work, the amount of data extracted was kept low due to memory constraints while trying to get a good picture of the physics of the problem. In order to analyze the acoustics of supersonic under-expanded jets, several post-processing techniques were implemented. This chapter presented the procedure followed for the propagation of the noise to the far-field, the hydrodynamic-acoustic filtering and the azimuthal decomposition. The pressure perturbations are propagated to the far-field with the Ffowcs-Williams and Hawkings analogy and the information saved on topological open surfaces inside the domain. The hydrodynamic-acoustic filtering allows for a separation of hydrodynamic disturbances and acoustic waves in the near-field region of the jet. This is done by transforming the data of a linear array of numerical probes into the frequency-wavenumber domain and then discriminating the relative phase velocities of each component.

The methodology developed for this work has a good efficiency in terms of time needed to carry out a complete simulation, however, the procedure could become too cumbersome if data exchanges must be done between different computing stations, storage systems etc. On the other hand, this methodology is easier to implement if all the steps can be done on the same computing station (such as a supercomputer). Due to memory constraints, some of the steps such as interpolations, or the generation of the mesh were carried out in a different computing station which meant a transfer of bulky files.

Chapter 4

Wavelet-based signature identification procedure

This chapter explains the wavelet-based post-processing procedure implemented in order to extract the most characteristic events of the flow. This tool was studied because it allows for a decomposition of the signal in different scales or frequencies in order to identify different events while keeping the discretization in time and is shown to be a powerful tool even for short time signals. The signal is decomposed into the wavelet domain where some energetic requisites are checked to select the most representative events of the signal. A window is centered at each detected event and then all the windows associated to each event are averaged. The result is a signature characteristic of a true feature of the signal.

The signal used in this chapter comes from the dual stream jet investigated in Ch. 6. In particular, in the first part of this chapter, the temporal signal is a pressure signal representative of shock-cell noise obtained in the far-field at 160° from the jet axis. For the selection of the scale of Sec. 4.5, a signal located in the near-field is analyzed at $r/D_s = 1.5$, which extends from $0 < x/D_s \leq 10$.

The chapter is split as follows. First, an overview of the continuous wavelet transform is given in Sec. 4.1. Second, two different methodologies are explained in Sec. 4.2 in order to detect the events and the conditional average is explained in Sec. 4.3. Third, a parametrization study of the procedure is given in Sec. 4.4 in terms of the mother wavelet, the methodology applied to detect the events, the filtering of the events and the size of the filtering window. Then, the effect of the scale chosen is explained in Sec. 4.5. Finally, some conclusions are drawn.

Some of the procedures detailed in this chapter were developed in collaboration with L. Gefen from Università degli Studi Roma Tre in Rome, partner of the AeroTraNet2 project. More details about the collaboration are given in Appx. C.

4.1 Continuous wavelet transform

The wavelet transform originated in the eighties with Morlet [187] and is nowadays one of the most popular time-frequency transforms. The regular wavelet transform decomposes a one dimensional signal into a two-dimensional representation of the signal. For a temporal signal,

the wavelet transform represents the signal in time and scale. The Fourier transform has been the choice by default of many researchers due to its well known characteristics, and easy to access functionalities. However the main disadvantage of the Fourier transform is that it looses the time-information. In order to overcome this issue, the windowed Fourier transform (WFT) allows for a transformation of the signal in time and frequency. This is a Fourier transform applied on a sliding window over the signal, instead of applying it to the entire signal. One of the main drawbacks of the WFT, is that the length of the sliding window has to be kept constant over the whole signal. The length of the window influences the time resolution of the transformation: a larger window would give a better decomposition at lower frequencies but a worse one for the higher frequencies and vice-versa. This is where the wavelet transform surpasses the Fourier transform. Using the analogy of the Fourier transform, the wavelet transform allows for a decomposition in time and frequency for a set of different scales where each of them was transformed with a scaled window, thus avoiding the use of a constant length window that would benefit only one region of the spectrum.

The continuous wavelet transform can be expressed as

$$w\left(s,\tau\right)=\frac{1}{\sqrt{|s|}}\int_{-\infty}^{+\infty}f\left(t\right)\psi^{*}\left(\frac{t-\tau}{s}\right)dt, \tag{4.1}$$

where $f\left(t\right)$ is the temporal signal, $\{w\left(s,\tau\right)\}$ is the set of wavelet coefficients, τ is the translation parameter, s is the dilatation or scale parameter and $\psi^{*}\left(\frac{t-\tau}{s}\right)$ is the complex conjugate of the daughter wavelet $\psi\left(\frac{t-\tau}{s}\right)$ obtained by the translation and dilatation of the so-called mother wavelet $\psi_{0}\left(t\right)$. Mathematically, the wavelet transform is a convolution of a temporal signal with a dilated function with different scales of dilatation. Each scale represents a different window size in the windowed Fourier transform.

The discrete form of the continuous wavelet transform of a discrete signal f_n is defined as the convolution of f_n with the daughter wavelet $\psi^{*}\left(t\right)$ as

$$w_{n}\left(s\right)=\sum_{n'=0}^{N-1}f_{n'}\psi^{*}\left[\frac{(n'-n)\delta t}{s}\right], \tag{4.2}$$

where n is the localized time index, N is the number of points in the time signal and δt the time step. If the convolution of Eq. (4.2) is done N times, the calculation can be conducted in Fourier space simultaneously for all N times. The discrete Fourier transform (DFT) of the time series f_n is

$$\hat{x}_{k}=\frac{1}{N}\sum_{n=0}^{N-1}f_{n}\mathrm{e}^{-2\pi ikn/N}, \tag{4.3}$$

where k is the frequency index. The Fourier transform of the wavelet $\psi\left(t/s\right)$ is given by $\hat{\psi}\left(s\omega\right)$. The convolution theorem states that the wavelet transform is the inverse Fourier transform of the product of the Fourier coefficients obtained with Eq. (4.3) and the wavelet in Fourier space as

$$w_{n}\left(s\right)=\sum_{k=0}^{N-1}\hat{x}_{k}\hat{\psi}^{*}\left(s\omega_{k}\right)\mathrm{e}^{i\omega_{k}n\delta t}, \tag{4.4}$$

where ω_k is the angular frequency defined as $\pm\frac{2\pi k}{N\delta t}$, positive when $k\leq N/2$ and negative otherwise. Here, the mother wavelet is normalized at each scale to have unit energy. This allows for a fair comparison between each scale.

The mother wavelet used in the wavelet transform needs to have zero mean and be represented both in time and frequency space to fulfill the admissibility condition [188]. The main factors that define a mother wavelet are the orthogonality, the set of numbers to which they belong, the width and the shape. The wavelet transform can be orthogonal or nonorthogonal. In the orthogonal wavelet transform, the time is depicted by discrete blocks proportional to the width of the wavelet basis at each scale, allowing a compact representation of the signal. The nonorthogonal wavelet transform gives a continuous convolution for each scale producing smooth and high correlated wavelet spectrum at adjacent times. In this methodology, only the nonorthogonal continuous wavelet transform is used. A mother wavelet can be complex, or real. The complex mother wavelet decomposes the signal in a real and imaginary part that defines the amplitude (modulus), and phase (angle) and it is better suited for capturing an oscillatory behavior. On the other hand, a real mother wavelet decomposes the signal only in a real component which gives a better discretization of peaks or discontinuities. The width of the mother wavelet determines the resolution in frequency. A narrow mother wavelet has a good time resolution but a poor frequency resolution and vice-versa. Because the wavelet transformation acts like a convolution, a mother wavelet whose shape is similar to the phenomena that one wants to capture would give a better resolution in amplitude. For further information about the wavelet transform, the reader can refer to [188, 189, 190].

In the current study, three mother wavelets are investigated: Morlet, Paul ($m = 4$) and the second derivative of a Gaussian (DOG with $m = 2$) known also as Marr or Mexican Hat. The Morlet mother wavelet is a complex function adapted for analysis of local periodicity of the signal. A good discretization is achieved in the frequency (scale) domain. The Morlet mother wavelet is defined as

$$\psi_0(\eta) = \pi^{-1/4} \mathrm{e}^{i\omega_0\eta} \mathrm{e}^{-\eta^2/2}, \tag{4.5}$$

where $\omega = 6$ to fulfill the admissibility condition. The DOG ($m = 2$) mother wavelet is a real function and is good for a search of localized structures due to a better discretization in time. The function is defined as

$$\psi_0(\eta) = \frac{d^m}{d\eta^m} \mathrm{e}^{-\eta^2/2}, \tag{4.6}$$

where $m = 2$. Half-way through between both above-mentioned mother wavelets, there is the mother wavelet Paul defined as

$$\psi_0(\eta) = \frac{2^m i^m m!}{\sqrt{\pi(2m)!}} \frac{1}{(1 - i\eta)^{m+1}}, \tag{4.7}$$

with $m = 4$ in this work. The representation in time of the three mother wavelets is shown in Fig. 4.1.

The scale s in the wavelet transform can be expressed as a frequency with different factors depending on the mother wavelet. From here on, the wavelet scale s is represented with $f(s)$ where the scales of the three mother wavelets vary from each other to have the same $f(s)$ bounds. In order to avoid confusion, the frequency obtained from a Fourier analysis of any temporal signal is represented simply as f. The relations between the frequency and the scales

for all three mother wavelets are

$$\begin{aligned} Morlet: \quad & f(s) = \frac{\omega_0 + \sqrt{2 + \omega_0}}{4\pi s} \\ Paul: \quad & f(s) = \frac{2m+1}{4\pi s} \\ Dog: \quad & f(s) = \frac{\sqrt{m+\frac{1}{2}}}{2\pi s} \end{aligned} \tag{4.8}$$

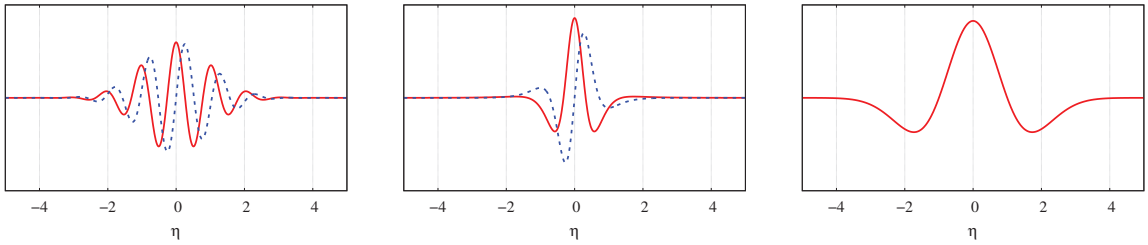

(a) (b) (c)

Figure 4.1: *Representation in time η of the mother wavelet* ***(a)*** *Morlet,* ***(b)*** *Paul ($m = 2$) and* ***(c)*** *DOG ($m = 2$). The solid line represents the real part and the dashed line the imaginary part.*

The signal that is analyzed in this part of the chapter is the pressure at the far-field of the supersonic dual stream jet from Ch. 6. The signal, shown in Fig. 4.2 (a), is computed at 160° from the jet axis at a distance of $30D_s$. This signal was chosen as the most characteristic of shock-cell noise for the dual stream jet. The signal has a length of 10 ms with a time-step of 7.5 μs which gives a frequency sampling of 130 kHz or a $St_s = 20$. In this chapter, the results are averaged by 16 azimuthal positions unless otherwise stated. The averaged Sound Pressure Level (SPL) is displayed in Fig. 4.2 (b). The peak of the broadband shock-associated noise (BBSAN) is located just below $St_s = 1$ and it extends up to $St_s = 1.5$.

Figure 4.3 shows the wavelet power transform of the signal of one azimuthal position for the three mother wavelets. The difference between the three mother wavelets is clear. The wavelet power with Morlet mother wavelet (see Fig. 4.3 (a)) displays a good discretization in $f(s)$, enhancing the intervals where the signal is important at a specific $f(s)$. However, the time discretization is limited. On the other hand, DOG has a poor discretization in $f(s)$, but a better one in time (see Fig. 4.3 (c)). The wavelet power transform obtained with Paul shown in Fig. 4.3 (b) is a compromise between both of them. In the three cases, the BBSAN is visible in the range of $0.8 < St_s < 1.5$ as for the SPL in Fig. 4.2 (b).

The small cross-hatched region in Fig. 4.3 is known as the Cone Of Influence (COI). Because the formulation of the discrete wavelet transform (Eq. (4.4)) makes use of the Fourier transform, errors will occur at the extremes of the signal. In order to reduce this effect, the signal was padded with zeros up to the next power of two and then removed after the wavelet transform was done. The cone of influence is the region of the transform where the edge effects are important. Inside the COI, the amplitude of the power wavelet is reduced due to the zero-padding. The cone of influence is defined as the e-folding time for the auto-correlation of wavelet power at each scale.

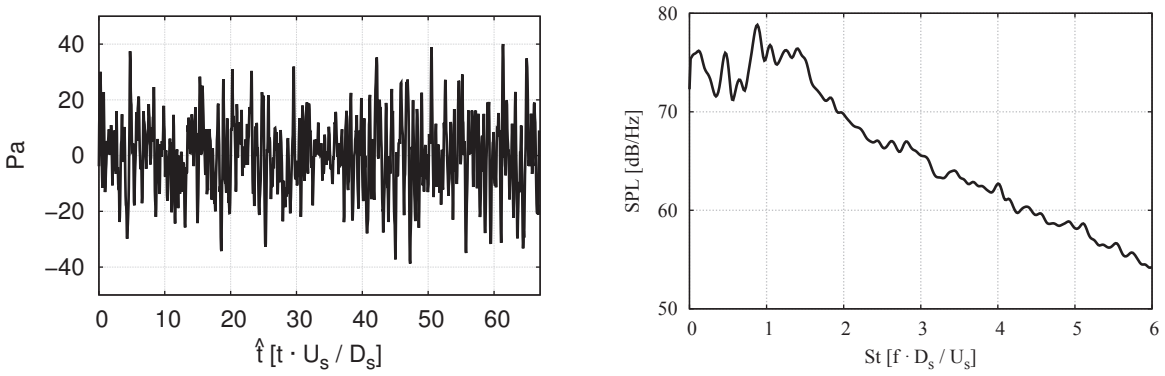

(a) (b)

Figure 4.2: ***(a)*** *Temporal signal of one azimuthal position at* 160° *in the far-field,* ***(b)*** *Sound Pressure Level in* dB/Hz *averaged by all the azimuthal signals at* 160°.

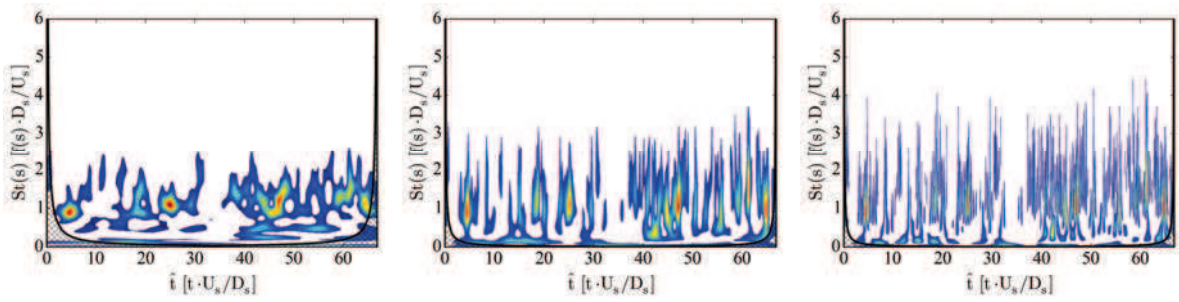

(a) (b) (c)

Figure 4.3: *Wavelet Power using the mother wavelets:* ***(a)*** *Morlet,* ***(b)*** *Paul* ($m = 4$)*and* ***(c)*** *DOG* ($m = 2$)

4.2 Event detection

Once the power wavelet is computed at each scale $f(s)$, the characteristic events have to be discerned from the signal. Two techniques are presented in this section. The first one is the so-called Local Intermittency Measure (LIM) introduced by Farge[188] which gives a local measure of the ratio between the local energy and the time-averaged mean for a specific scale. The second technique compares the local energy with a defined background spectrum energy at all scales, then the events detected can be assumed a true feature of the flow with a certain significance level [189].

4.2.1 Local intermittency measure

The LIM gives a measure of the local energy with respect to the time averaged mean energy at all the scales. The LIM's mathematical formulation, noted $L\,(s,\tau)$, is written as

$$L(s,\tau) = \frac{w^2(s,\tau)}{\langle w(^2s,\tau)\rangle_\tau}, \tag{4.9}$$

where $w^2(s,\tau)$ is the local energy for a specific time and scale, and $\langle \bullet \rangle_\tau$ represents the time average.

The value of the LIM gives an indication about the fluctuation of the energy. It is possible to select the most energetic events in a signal $f\,(t)$ by selecting a proper threshold T. The events are found where $L(s,\tau) > T$ and there is a local maxima in the power wavelet. In this study, the value of the threshold is chosen to be 1 in order to increase the number of events detected as the time-length of the signal on which the analysis is performed is short.

4.2.2 Significance levels

This procedure noted as SIG95 compares the local energy with a defined background spectrum energy at all scales. The null hypothesis states that the events detected can be assumed a true feature of the flow with a certain significance level if their wavelet power spectrum is significantly above this background spectrum.

The discrete wavelet transform of Eq. (4.4) links the Fourier coefficients, with the wavelet coefficients, therefore, if the Fourier coefficients are normally distributed, then the wavelet coefficients should be also normally distributed. The normalized Fourier power spectrum is given by $N|\hat{x_k}|^2/2\sigma^2$, where σ^2 is the variance of the signal. If x_n is normally distributed, then the power will be χ^2 distributed with two degrees of freedom denoted by χ^2_2. The distribution for the Fourier power spectrum is expressed as

$$\frac{N|\hat{x_k}|^2}{2\sigma^2} \Rightarrow \frac{1}{2} P_k \chi^2_2, \tag{4.10}$$

where P_k is the normalized Fourier power spectrum and k is the frequency index. The symbol $\Rightarrow$ indicates "distributed as". The corresponding distribution for the local wavelet power spectrum is then

$$\frac{N|w_n(s)|^2}{\sigma^2} \Rightarrow \frac{1}{2} P_k \chi^2_2, \tag{4.11}$$

for each scale s and time n. Once an appropriate background spectrum is chosen and a particular threshold for the confidence for the χ^2 is selected, the distribution can be calculated at each scale following Eq. (4.11) and the events selected if they are superior to the threshold value. In this study, a white noise background spectrum was selected with a confidence level of 95%, however, other background noises such as red noise (increasing power with decreasing frequency) can be used. For more information, the reader is referred to [189].

4.3 Conditional average

The event detection gives as output a set of times when the energetic events occur in the time series. At each time location corresponding to a peak of energy it is possible to extract a window W, of fixed time-length t_W, from the original signal $f(t)$. The conditional-average, $\tilde{f}$ can be calculated from this set of windows as the average of all the windows ξ_i centered at the times t_i as

$$\tilde{f}_m^n(t) = \langle p_m | P_k \rangle_{\tilde{\tau}_s^n} = \frac{1}{N^n} \sum_{i=1}^{N^n} f_m(\xi_i), \tag{4.12}$$

where the superscript n and subscript $\{\bullet\}_m$ stand for the position of the reference signal and of any other signal respectively, the subscript $\{\bullet\}_s$ stands for the scale, N^n is the number of detected events, $\tilde{\tau}_s^n$ is the set of corresponding times for a specific scale s at which these events are occurring and $\{\xi_i\}$ is the interval surrounding each peak, $\xi_i \in \left[\tilde{t}_i - \frac{t_W}{2}, \tilde{t}_i + \frac{t_W}{2}\right]$, $\tilde{t}_i \in \tilde{\tau}_s^n$. The averaged signal is known as the signature. An example of a signature is shown in Fig. 4.5.

The conditional average can be split into auto-conditioning and cross-conditioning as the regular auto- and cross-correlation of a signal. The events are located in a reference signal (denoted with the superscript n), for a reference variable (*e.g.* pressure in the far-field) and then, the window average can be applied to the same signal with the same variable, or to a different signal, with the same, or another variable (denoted with the subscript $\{\bullet\}_m$). In the first case, it is referred as auto-conditioning, while in the second case, it is referred as cross-conditioning.

Before the averaging of the windows, the events can be differentiated by sign, and filtered by a window. The sign discrimination is carried out into positive and negative events depending on the sign of the time series at the instants where the events were located. Moreover, the events can be filtered by a window size. If the events are too close between each other, the window average could be biased by the surrounding events. This window filtering can be done before or after the sign discrimination. The effect of the filtering and the discrimination of the sign are further discussed in the following section.

4.4 Parametrization of the procedure

This section studies the effect of the different parameters on the final signature obtained with the conditional average. The parameters of study are: the mother wavelet, the event detection procedure, the sign discrimination and the filtering. All these parameters have an impact on the scale chosen and on the final number of events used on the conditional average. One needs to keep in mind that some parameters need to be set constant to allow for an automation of

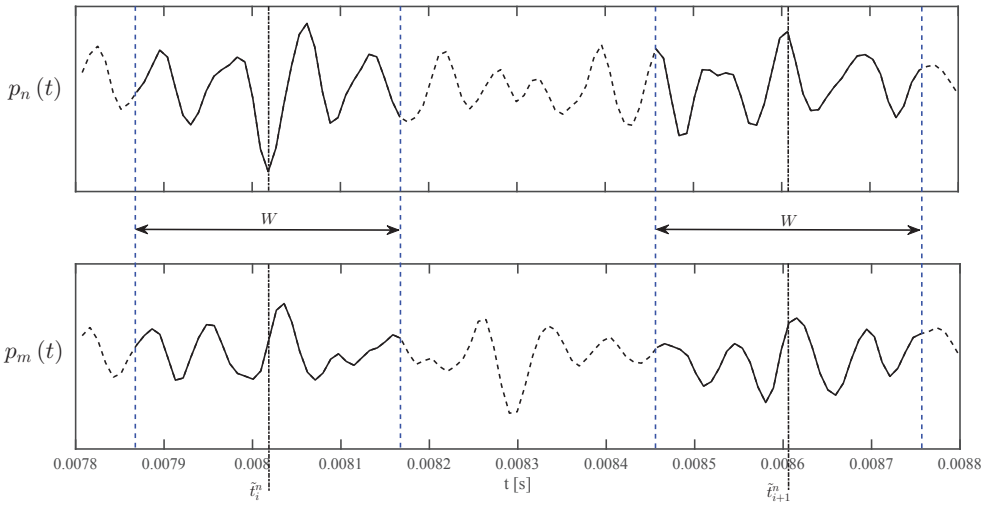

Figure 4.4: *Auto-conditioning of a signal $f_n(t)$ and cross-conditioning of a signal $f_n(t)$*

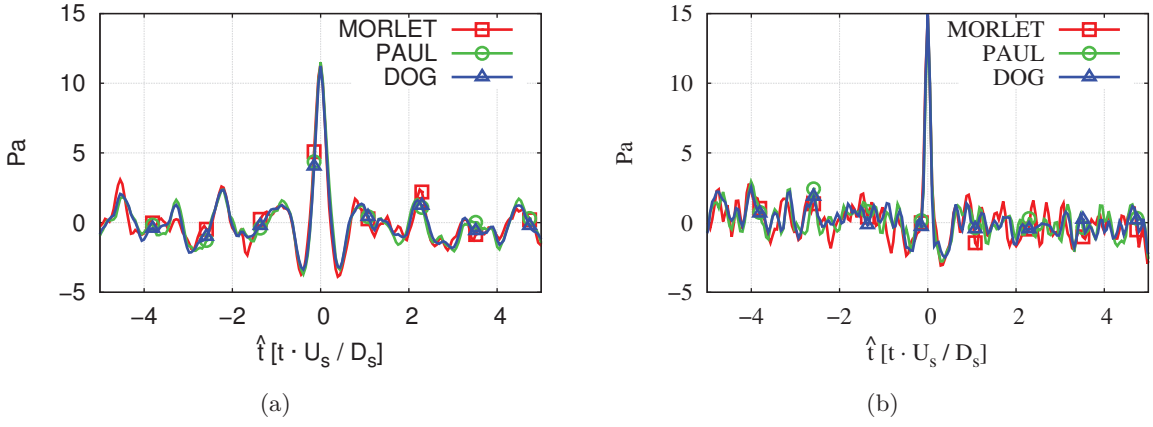

Figure 4.5: *Signature in the far-field* ***(a)****, at* 160° *and* ***(b)*** *at* 60°.

the procedure at all the different positions of the probes of study. It may happen that some of the conclusions reached on this section do not apply to other signals, specially if they have a different order of magnitude in terms of the number of temporal instants, harmonics and phase between them. This analysis is carried on a short signal where there is only a dominant peak in the spectrum.

4.4.1 Effect of the mother wavelet and the event detection procedure

Because each mother wavelet has a different representation in time and scale of the events when the signal is decomposed into the wavelet power, each mother wavelet modifies the number of events detected per scale. Figure 4.6 shows the total number of events detected without filtering with (a) LIM and (b) SIG95 for the three mother wavelets. The mother wavelet DOG allows to detect the highest number of events, on the other hand, Morlet detects the smallest number of events. As it was discussed in Sec. 4.1, the Morlet mother wavelet tends to group the events in periodic signals throughout time. The number of events detected with Paul lays in between. Depending on the detection procedure, the number of events either grows with $f(s)$ or a peak shows. Figure 4.6 (a) illustrates that for LIM, more events are detected for higher $f(s)$ or smaller scales s. A change in the slope is discernible between $1 < St_s < 2$, that is where the SPL is higher (Fig. 4.2 (b)). In addition, SIG95 detects a peak in number of events in the same range for SIG95. Nonetheless, in this range, the number of events detected with LIM is of the same order of magnitude than with SIG95.

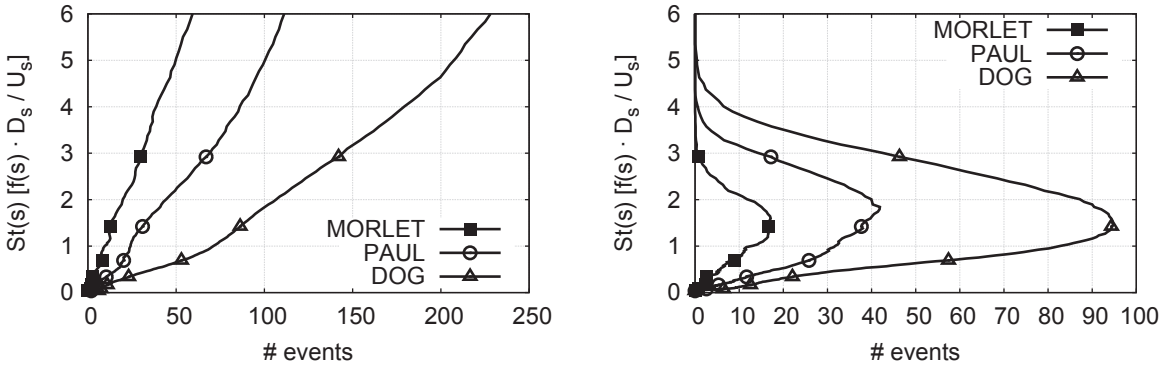

Figure 4.6: *Number of events detected according to the mother wavelet using* ***(a)****, LIM and* ***(b)*** *SIG95. No filtering is used.*

The signatures computed from the auto-conditioning are shown in Fig. 4.7 and Fig. 4.8 for LIM and SIG95 respectively. When LIM is used, the signature does not vary with the scale. This is mainly true, because in our signal, there is no other higher frequency component of similar or higher amplitude. As a consequence, the average of the windows falls into the same signature above $St_s = 1$. This averaging is more obvious with DOG because of the higher number of events detected. On the other hand, the signature is noisier at lower $f(s)$ when using Morlet. Of course, SIG95 gives a null signature above the $f(s)$ where there are no events detected.

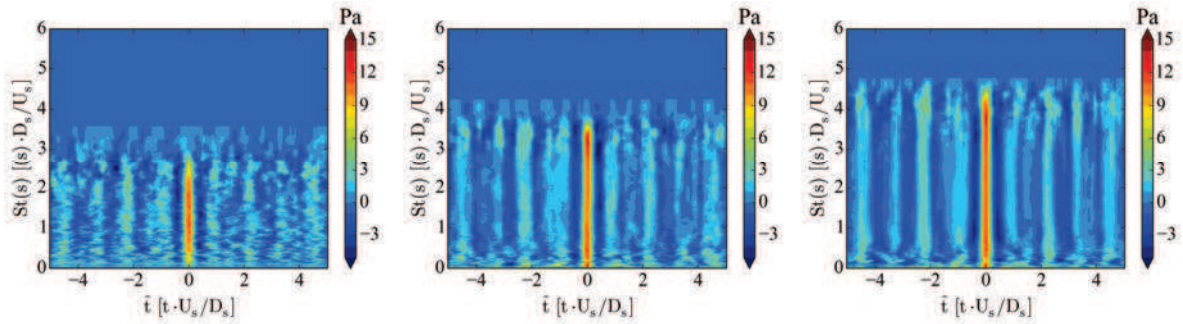

Figure 4.7: *Difference signature obtained at all scales $f(s)$ using LIM and the mother wavelet* ***(a)*** *Morlet,* ***(b)*** *Paul ($m = 4$) and* ***(c)*** *DOG ($m = 2$). No filtering is used.*

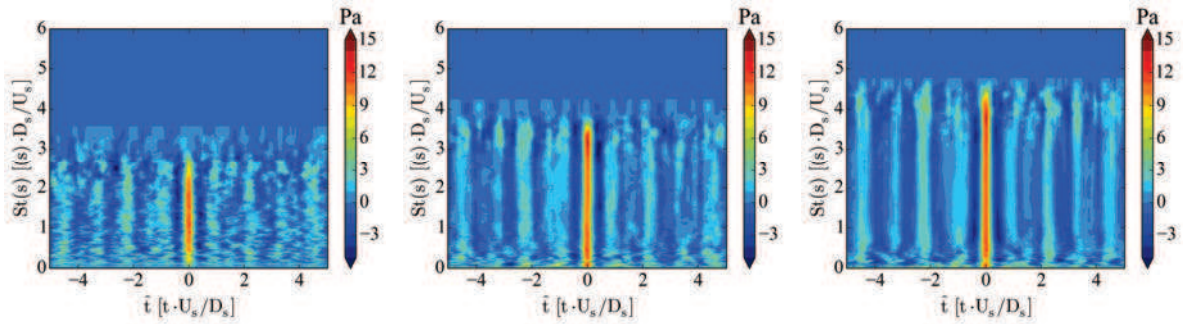

Figure 4.8: *Difference signature obtained at all scales $f(s)$ using SIG95 and the mother wavelet* ***(a)*** *Morlet,* ***(b)*** *Paul ($m = 4$) and* ***(c)*** *DOG ($m = 2$)*

4.4.2 Effect of the sign discrimination and the filtering

When the events are detected they can be discriminated according to the corresponding sign in the time series. The total number of events is the sum of the positive and negative events with respect to the mean value of the signal. Figures 4.9 and 4.10 show the number of events using LIM and SIG95 respectively. Overall, the number of positive events is slightly higher than the negative events. However, this is not the case for Morlet due to the small number of events detected.

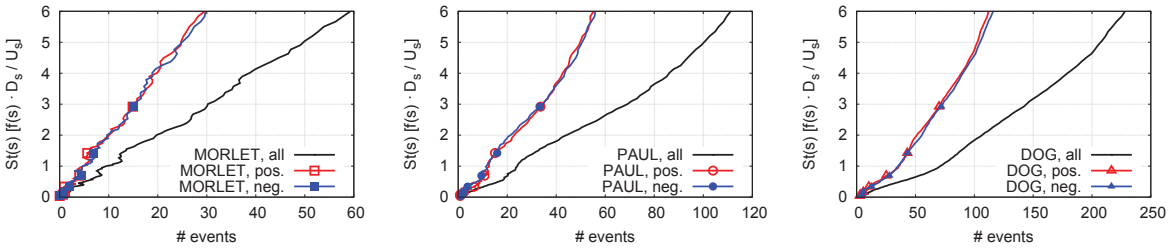

(a) (b) (c)

Figure 4.9: *Number of events detected according to the sign of the event selected using LIM and the mother wavelet* ***(a)*** *Morlet,* ***(b)*** *Paul ($m = 4$) and* ***(c)*** *DOG ($m = 2$). No filtering is used.*

The signature can be computed doing the conditional average on the positive events, the negative events, the difference average or the mean average. Usually, the complete signature is computed from the average of all the events. However, when dealing with short time series with an overall small number of events, it is better to treat them independently. Figure 4.11 shows the signatures calculated at all scales with different types of the average. Figure 4.11 (a) presents the signature obtained only with positive events. In addition, Fig. 4.11 (c) shows the signature that corresponds to the negative events. Here, the color palette was inverted in order to keep the same color scheme. Figure 4.11 (d) is the difference average, that is, $(sgn.^{+} - sgn^{-})/2$, and Fig. 4.11 (d) is the mean of the positive and negative signatures, without the sign swap. Here, *sgn* defines the sign of the temporal signal. In a fully acoustic field, the difference between a negative and a positive event is minimal, they are just dephased by π rad. This is why the positive, negative and difference signatures have a similar shape. However, if the regular average is done, the signature is completely lost (see Fig.4.11 (d)).

4.4.3 Effect of the filtering

The detected events can be filtered according to a filtering window size. The selection of the events is done starting with the events with a higher energy and clearing the surrounding events that lay within a window length around it. Next, the event with the second highest wavelet power is selected and the events around it filtered. This process is repeated until no more events are left. The application of this filtering window eliminates the events that could bias the signature. The filtering window length should be of the order of the true feature of the signature, *a priori* unknown. This filtering process can be applied before, or after the sign discrimination. When it is applied before the sign discrimination, the events are filtered regardless of the sign of the event, thus obtaining a lesser number of events for the

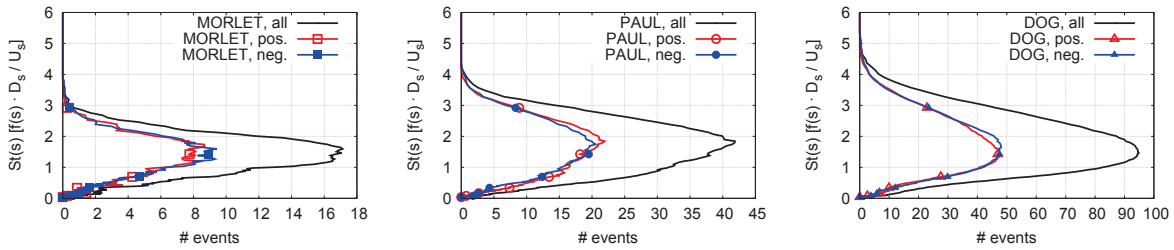

(a) (b) (c)

Figure 4.10: *Number of events detected according to the sign of the event selected using SIG95 and the mother wavelet* ***(a)*** *Morlet,* ***(b)*** *Paul ($m = 4$) and* ***(c)*** *DOG ($m = 2$). No filtering is used.*

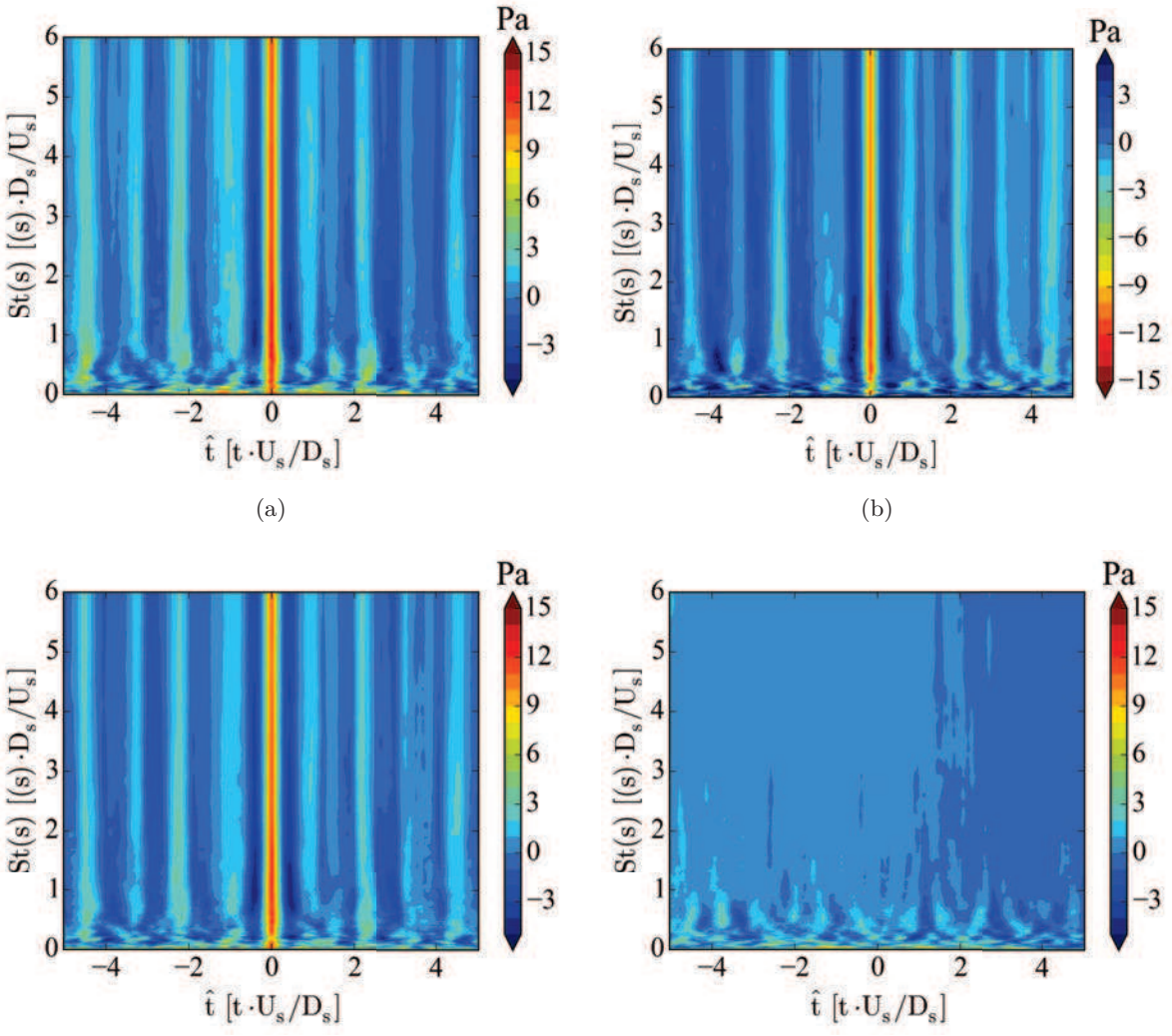

(a) (b) (c) (d)

Figure 4.11: *Signature obtained at all scales $f(s)$ using LIM and the mother wavelet DOG.* ***(a)*** *Positive signature,* ***(b)*** *negative signature,* ***(c)*** *difference signature and* ***(d)*** *average signature. No filtering is used.*

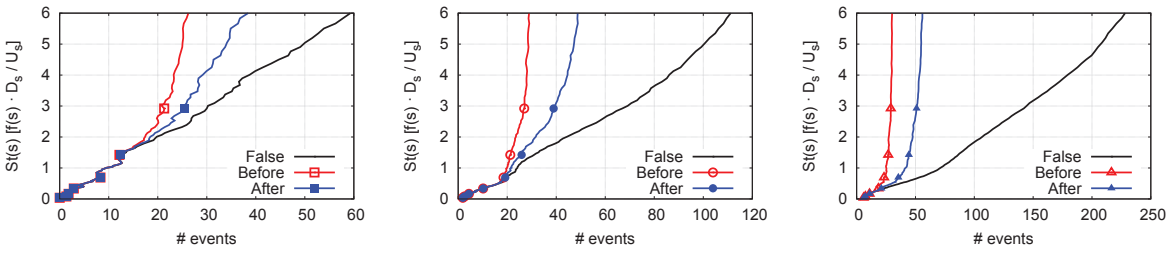

(a) (b) (c)

Figure 4.12: *Number of events detected according to the filtering of the events using LIM and the mother wavelet* ***(a)*** *Morlet,* ***(b)*** *Paul* ($m = 4$) *and* ***(c)*** *DOG* ($m = 2$)

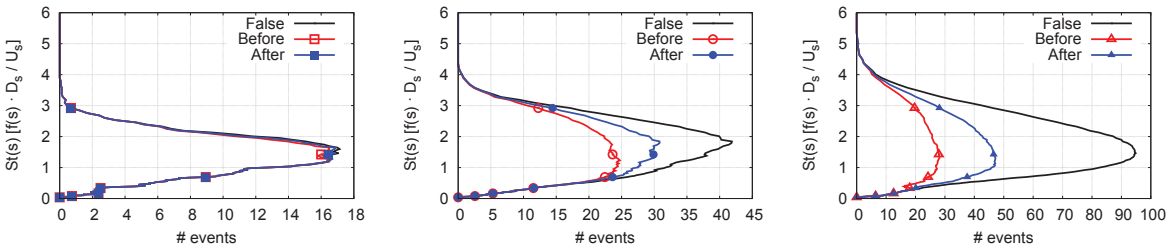

(a) (b) (c)

Figure 4.13: *Number of events detected according to the filtering of the events using SIG95 and the mother wavelet* ***(a)*** *Morlet,* ***(b)*** *Paul* ($m = 4$) *and* ***(c)*** *DOG* ($m = 2$)

conditional average. On the other hand, if the filtering is done after the sign discrimination, a higher number of events remains because the positive and negative events are taken into account separately. Figure 4.12 and 4.13 show the filtering of the events with a windows of 2.5 non-dimensional time units with LIM and SIG95 respectively. Whether the events are detected with LIM or the significance levels, the filtering has a bigger impact on the number of remaining events with the DOG mother wavelet. This is due to the fact that the events are more frequent and closer one to each other than the filtering window length chosen. When using the Morlet mother wavelet, the filtering does not affect the results because the events are farther apart than the size of the windows length.

The signature obtained with the filtered events is noisier because less events are taken into account for the average. Figure 4.14 shows the difference signature using the mother wavelet DOG and the event detection based on the significance levels. Figure 4.14 (a), where no filtering is done depicts a clearer image than Fig. 4.14 (b) or (c) because of the higher number of events used in the conditional average.

4.5 Scale selection procedure

The wavelet transform decomposes the signal into a set of scales. The conditional average is a process that requires the selection of a particular scale. As it is shown in Sec. 4.4, the number of events detected at each scale varies with the scale $f(s)$. In particular, the number of events

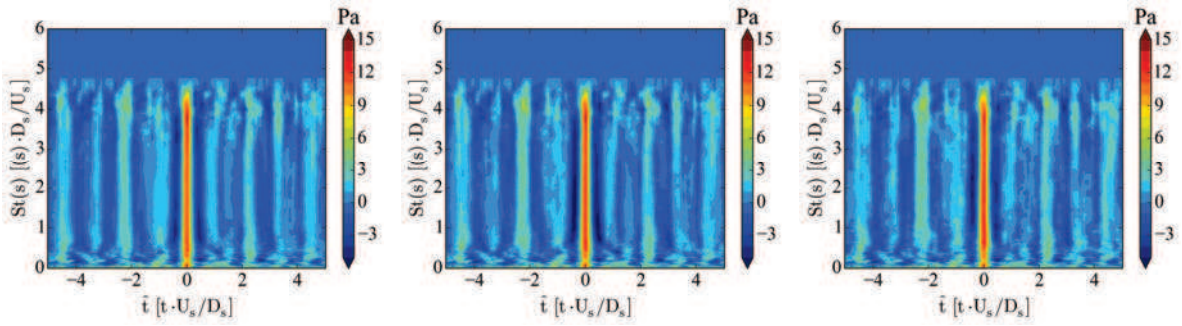

Figure 4.14: *Difference signature obtained at all scales $f(s)$ using SIG95 and the mother wavelet DOG.* ***(a)*** *No filtering,* ***(b)*** *filtering after sign discrimination and* ***(c)*** *filtering before sign discrimination.*

tends to increase with $f(s)$ for LIM. The conditional average will select these events, filtered or not, and it will carry out the conditional window average of all of them, giving in theory a different signature for each scale. As it was mentioned before, the signal post-processed so far, only contains one peak in the spectrum. The signature obtained has a peculiar independence to the scale selected, if a minimum number of events is used in the conditional average. Furthermore, because the conditional average is carried out in the complete signal, it could happen that the events of completely different scales are in phase with each other, acquiring a signature that is the net combined effect of both features. Depending on the objective of the signature extraction, a reconstruction by scales could be done with only the set of scales required like a band pass filter as

$$f_n = \frac{\delta j \delta t^{1/2}}{C_\delta \psi_0(0)} \sum_{j=0}^{J} \frac{\mathcal{R}e\left\{w_n\left(s_j\right)\right\}}{s_j^{1/2}}, \tag{4.13}$$

where δj is the spacing between the discrete scales, δt is the time-step of the time series and C_δ is a constant that depends on the mother wavelet. The factor $\psi_0(0)$ removes the energy scaling and the factor $s_j^{1/2}$ converts the wavelet transform to an energy density. The reconstruction of the signal of Eq. (4.13) uses the real part of the wavelet transform. If only one complete signature is to be obtained, the conditional average can be applied directly to the original time series.

The generation of a signature at each scale as it is discussed in Sec. 4.4, can be a costly task, specially if the number of scales is high, and the time series are long. This computation can not be always done, thus requiring the selection of a unique scale to represent the true feature of the signal, or the feature one is interested in study, which may differ. Different approaches can be discussed to select the scale. First, the scale can be chosen depending upon the number of events, selecting the scale where there is a maximum. This can be useful if the events are detected with a procedure like the significance levels that display a maximum in the region where the energy is also maximum (Sec. 4.4.1). Regardless on whether or not, the signature is independent on the scale for LIM, the smallest scale s (or highest $f(s)$) would systematically be chosen as the one with the highest number of events if the threshold was kept at one. If LIM is applied, a different method should be probably used in order to select the scale or the

threshold. In this study, the results of four different automatically selected scales are analyzed. First, the scale chosen can be the one where there are more events detected. Second, the scale can be selected where there is the maximum of energy based on either the global wavelet spectrum, the global wavelet spectrum scaled by the global significance levels or the global wavelet spectrum transformed into an energy density.

The global wavelet spectrum is computed when the wavelet spectra is averaged in time as

$$\overline{w}^2(s) = \frac{1}{N}\sum_{n=0}^{N-1}|w_n(s)|^2. \tag{4.14}$$

This global wavelet spectrum can be scaled by the significance levels calculated globally. By doing so, the scales that have most of the energy above the confidence level have more importance than the others. However, it dependents on the background noise. Finally, the global wavelet spectrum can be scaled by the scales in order to transform the wavelet spectrum into an energy density. Figure 4.15 shows the different global wavelet spectrum and the Fourier power scaled by the maximum values as it is the maximum of each curve that will be used to select the scale. As a reference, the maximum of the Fourier power is set for the selection of the scale. In this case, it peaks near $St_s = 1$. For the global wavelet spectrum, noted as *mean* in Fig. 4.15, the maximum is found at the same positions for all the mother wavelets except Morlet where it is at a lower frequency $f(s)$. If the global wavelet spectrum is scaled by the global significance levels, the maximum is recovered near $St_s(s) = 1$ for all the mother wavelets used. Using the energy density deviates the peak to higher scales $f(s)$ between $1 < St_s(s) \leq 2$.

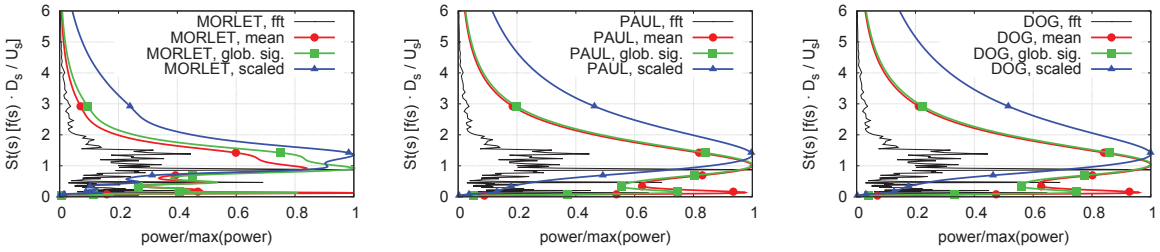

(a) (b) (c)

Figure 4.15: *Time averaged mean wavelet power using the complete signal and the mother wavelet* ***(a)*** *Morlet,* ***(b)*** *Paul ($m = 4$) and* ***(c)*** *DOG ($m = 2$).*

As it was shown in the previous sections, the selection of the scale does not have a great influence on the computed signature. In order to have a better view of the effect of the scale selection on the signature, an extended set of signals is chosen. The data are located in the near-field at $r/D_s = 1.5$, they extend from $0 < x/D_s \leq 10$ and are azimuthally distributed with 16 positions. First, the signatures obtained when selecting the scales by the number of events are discussed. Second, the scale selection is based on an energy criteria.

As it was shown in Sec. 4.4.1, the selection of events based on the significance levels or the local intermittency measure (LIM), is radically different. This is illustrated in Fig. 4.16 and Fig. 4.17 with LIM and SIG95 respectively, where the number of events detected is depicted at each axial position. The black dots represent the maximum number of events at each axial position. The signature computed with the scales at the maxima is shown in Fig. 4.18 and Fig. 4.19

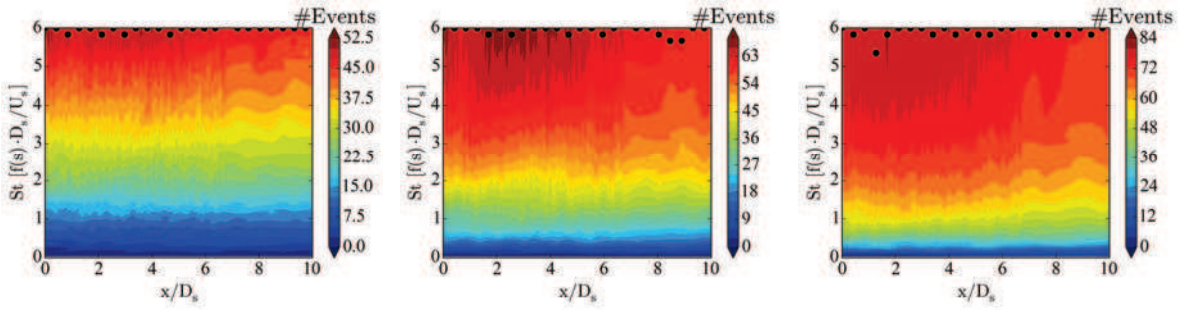

Figure 4.16: *Number of events at each axial position using LIM and the mother wavelet* ***(a)*** *Morlet,* ***(b)*** *Paul ($m = 4$) and* ***(c)*** *DOG ($m = 2$). The black dots represent the maximum at each axial position.*

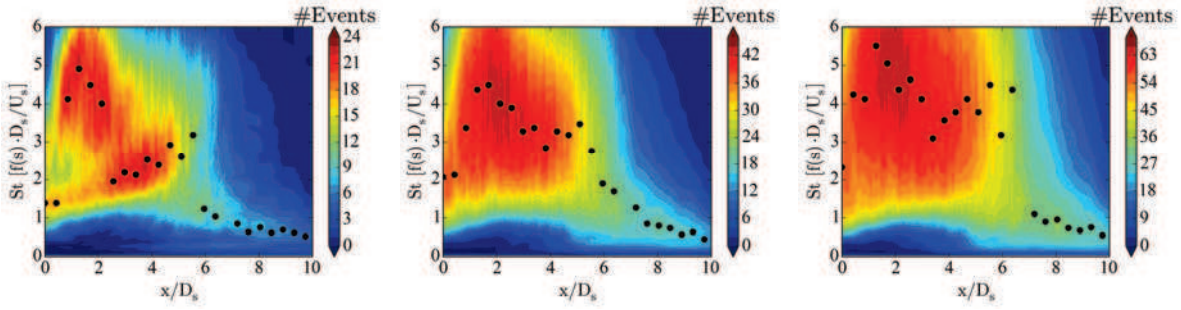

Figure 4.17: *Number of events at each axial position using SIG95 and the mother wavelet* ***(a)*** *Morlet,* ***(b)*** *Paul ($m = 4$) and* ***(c)*** *DOG ($m = 2$). The black dots represent the maximum at each axial position.*

with LIM and SIG95 respectively. The signature corresponds to the positive filtered events after the sign discrimination. Figure 4.16 shows that when LIM is applied, the location of the maximum number of events (black dots), which determines the scale selected, does not vary with the different mother wavelet used. This translates into a similar signature (Fig. 4.18) for the different mother wavelets. Evidently, the number of events detected vary with the mother wavelet which gives a cleaner signature when more events are detected. On the other hand, when the events are detected with the significance levels as shown in Fig. 4.17, the maxima are found at similar, but different scales $f(s)$ for the different mother wavelets. Nonetheless, the respective signatures displayed in Fig. 4.19 do not exhibit a clear difference between them or the ones obtained using LIM. If the scale is selected with the maximum number of events, and the events are filtered, the resulting signature will not depend on the method of event detection, nor the mother wavelet.

The same analysis can be carried out selecting the scales with respect to the maximum in energy of the global wavelet spectrum as illustrated in Fig. 4.15. Figures 4.20, 4.21 and 4.22 show the global wavelet spectra for each mother wavelet, and each normalization of the global wavelet spectra respectively. The maxima is located at the same scales $f(s)$ regardless of the

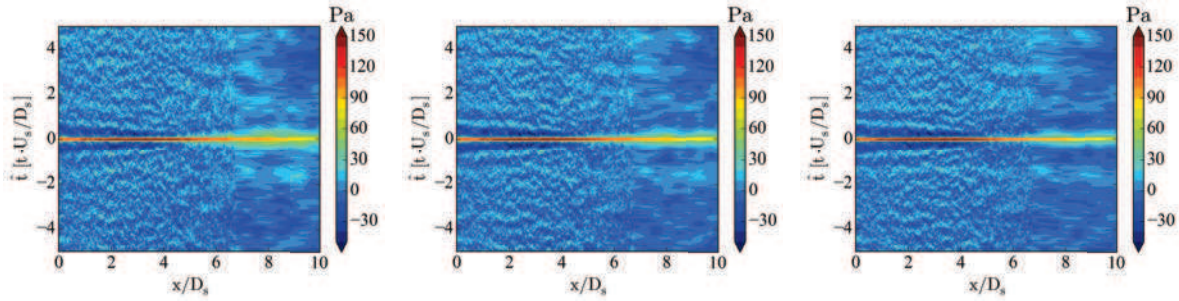

(a) (b) (c)

Figure 4.18: *Signature selecting the scales where the maximum of the number of events is found using LIM and the mother wavelet* ***(a)*** *Morlet,* ***(b)*** *Paul* ($m = 4$) *and* ***(c)*** *DOG* ($m = 2$). *The black dots represent the maximum at each axial position.*

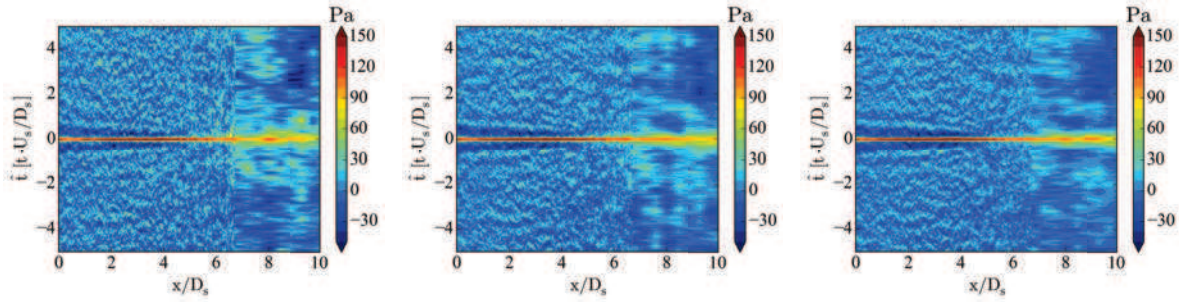

(a) (b) (c)

Figure 4.19: *Signature selecting the scales where the maximum of the number of events is found using SIG95 and the mother wavelet* ***(a)*** *Morlet,* ***(b)*** *Paul* ($m = 4$) *and* ***(c)*** *DOG* ($m = 2$). *The black dots represent the maximum at each axial position.*

mother wavelet and if the global wavelet spectrum is normalized by the significance levels or not. If the global wavelet spectrum is normalized by the scales s (Fig. 4.22), the maxima is found at different scales $f(s)$. The position of the maxima clearly differs with the mother wavelet Morlet. Finally, the signature of the different cases is displayed in Fig. 4.23, Fig. 4.24 and Fig. 4.25 for each normalization respectively. When the first two methods are used, there is a clear distinction between the ranges from $0 < x/D_s \leq 4$ and $4 < x/D_s \leq 10$, however, when using the global wavelet spectrum scaled by the scales, the transition is smoother. Moreover, the signatures in the range $4 < x/D_s \leq 10$ are considerably different between the different mother wavelets. This occurs, mainly because of the discrepancy in number of events detected at those scales. Even if the global wavelet spectrum showed a maximum at one particular scale, the fact that not many events are detected at those scales (Fig. 4.17) gives a noisier not well averaged signature. This is probably a particular case when dealing with short signals as those obtained in costly simulations.

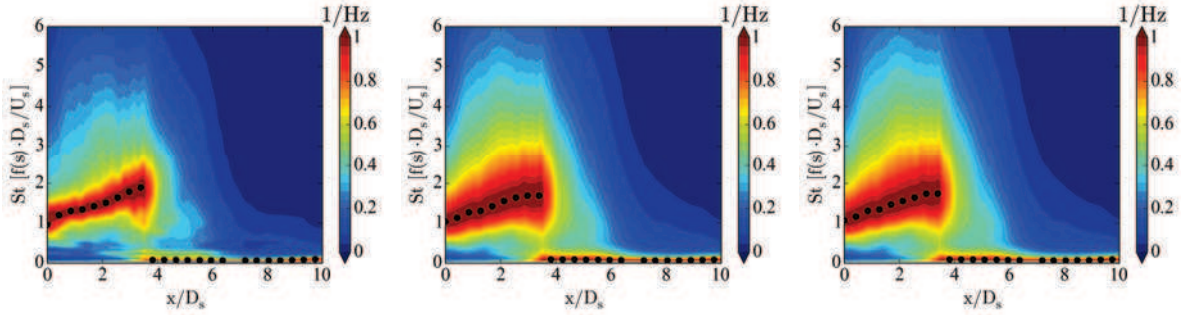

(a) (b) (c)

Figure 4.20: *Normalized energy spectrum at each axial position using the global wavelet spectrum and the mother wavelet* ***(a)*** *Morlet,* ***(b)*** *Paul ($m = 4$) and* ***(c)*** *DOG ($m = 2$). The black dots represent the maximum at each axial position.*

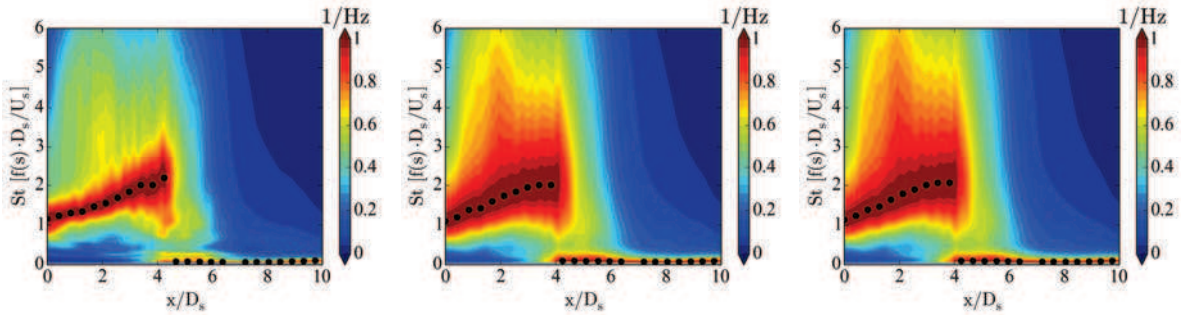

(a) (b) (c)

Figure 4.21: *Normalized energy spectrum at each axial position using the global wavelet spectrum normalized by the global significance levels and the mother wavelet* ***(a)*** *Morlet,* ***(b)*** *Paul ($m = 4$) and* ***(c)*** *DOG ($m = 2$). The black dots represent the maximum at each axial position.*

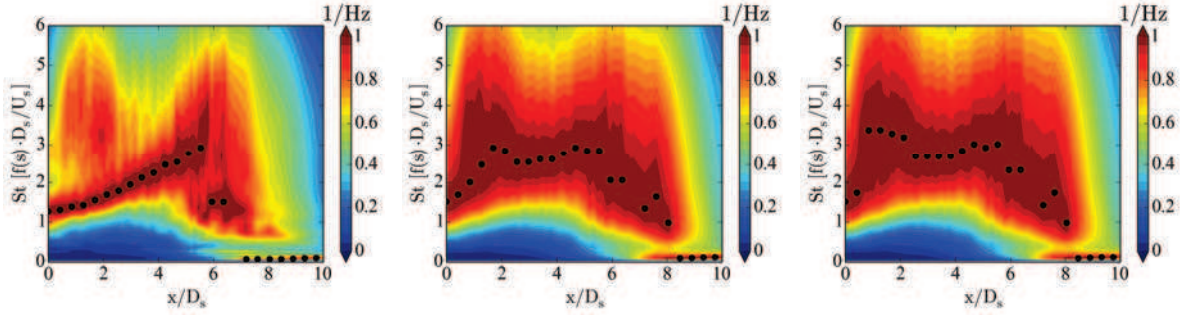

(a) (b) (c)

Figure 4.22: *Normalized energy spectrum at each axial position using global wavelet spectrum normalized by the scales and the mother wavelet* ***(a)*** *Morlet,* ***(b)*** *Paul ($m = 4$) and* ***(c)*** *DOG ($m = 2$). The black dots represent the maximum at each axial position.*

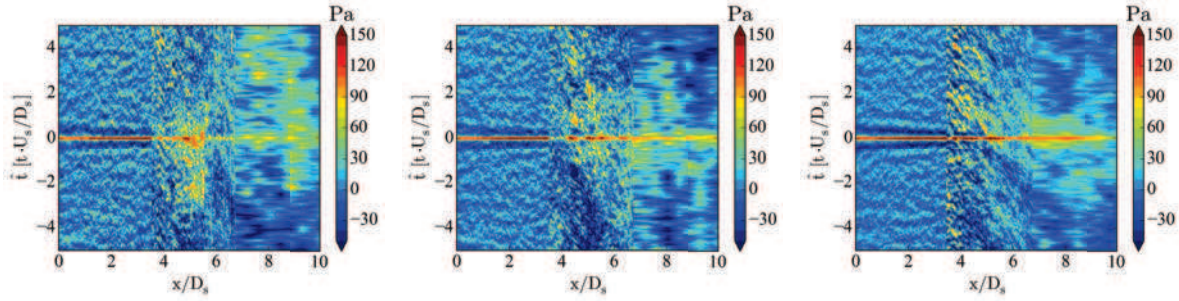

(a) (b) (c)

Figure 4.23: *Signature selecting the scales where the maximum of the normalized energy spectrum is found using the global wavelet spectrum and the mother wavelet* ***(a)*** *Morlet,* ***(b)*** *Paul ($m = 4$) and* ***(c)*** *DOG ($m = 2$). The events are extracted using the significance levels.*

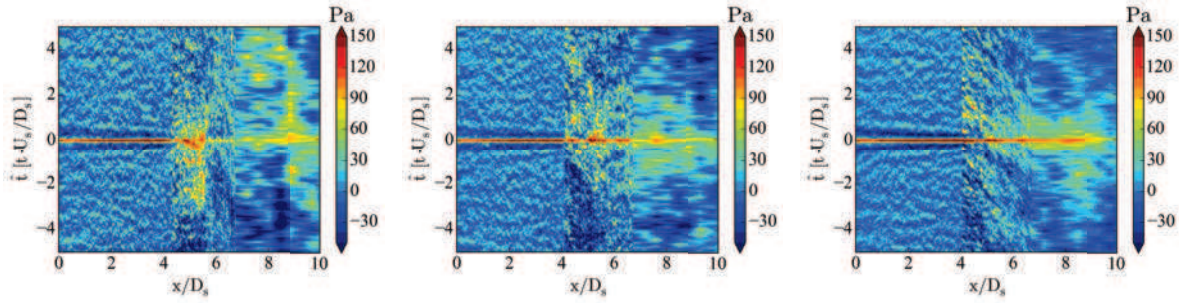

(a) (b) (c)

Figure 4.24: *Signature selecting the scales where the maximum of the normalized energy spectrum is found using the global wavelet spectrum normalized by the global significance levels and the mother wavelet* ***(a)*** *Morlet,* ***(b)*** *Paul ($m = 4$) and* ***(c)*** *DOG ($m = 2$). The events are extracted using the significance levels.*

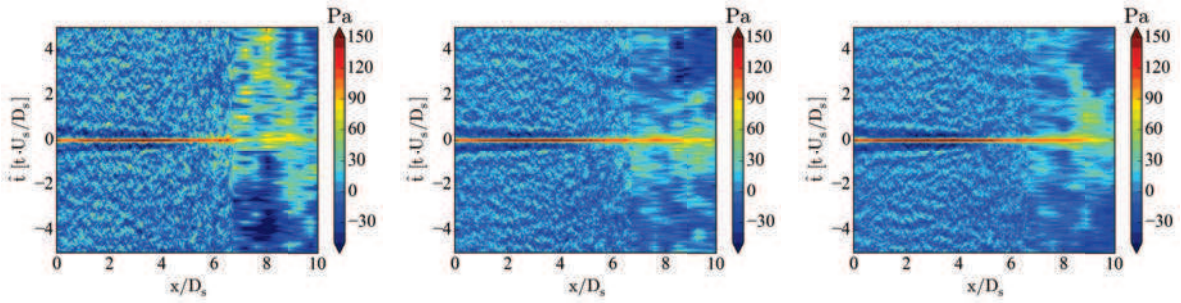

(a) (b) (c)

Figure 4.25: *Signature selecting the scales where the maximum of the normalized energy spectrum is found using the global wavelet spectrum normalized by the scales and the mother wavelet* ***(a)*** *Morlet,* ***(b)*** *Paul ($m = 4$) and* ***(c)*** *DOG ($m = 2$). The events are extracted using the significance levels.*

4.6 Summary and perspectives

In this chapter, a wavelet-based signature identification procedure was presented and analyzed with respect to different parameters and methodologies. The signature corresponds to a characteristic feature of the flow. The signature was obtained by averaging several temporal windows centered in time at the instants where some energy requisites are accomplished in a signal. The resulting signature conserves the same units as the original signal. The selection of the instants where the windows are centered is done *via* a continuous wavelet transformation of the signal. The power wavelet was computed, and compared against a specific threshold in order to detect the events in time. This chapter explains the basics of the continuous wavelet transform, the methodology followed and the impact of different parameters in the resulting signature. First, the choice of mother wavelet and the event detection methodology was discussed. Second, the effect of the sign discrimination and filtering was explained. Last, the selection of the scale used in the event detection was examined.

When using wavelet transforms, the choice of the mother wavelet should be based on what is investigated. However, if one is only dealing with event detection, the most significant impact on the choice of the mother wavelet, is the number of events detected. Here, three mother wavelets were discussed. The mother wavelet Morlet, gives a better discretization in scale $f(s)$, but also gives the smallest number of events detected, as it tends to group the intermittent phenomena in time. The derivative of a Gaussian (DOG, $m = 2$), has a weak scale discretization but it accurately represents the events in time, obtaining the larger number of events detected. The third mother wavelet studied named Paul, lays in between the other two mother wavelets giving a fairly good discretization in scale, and a number of events higher than with Morlet.

The detection of the events can be done comparing the signal to some background noise like white noise or red noise, or by checking the local intermittency measure (LIM). Both methods depend on a single parameter. On the first case, the typical background noise has to be defined, which may not be known *a priori*. The second method, needs to be compared against a threshold level. In this study, the background noise was defined as white noise, and the threshold in LIM to 1. When the significance levels method was used, the number

of events detected presented a maximum mostly where the events were more energetic, hence demonstrating a better localization in scale $f(s)$. On the other hand, a higher number of events was detected when using LIM, but it was systematically found for the highest scales $f(s)$.

The signature can be computed with positive or negative events depending on the sign of the signal at the instants when the events are detected. The events are detected with the wavelet power, and thus, there is no sign discrimination. The resulting positive and negative signatures are representative of the positive and negative events. When dealing with acoustics normally distributed, the positive and negative signature could have the same shape and only change in sign. Then, a difference average could be applied in order to increase the smoothness of the signature. This average could have no meaning inside a jet where positive and negative events do not correspond to the same features of the flow. Moreover, the events detected can be filtered by a window to avoid a biased signature by different energetic events that lay within the same averaging window. If the filter is applied before the sign discrimination, more events will be filtered, obtaining a remaining number of events inferior to those obtained if the events are filtered after the sign discrimination. Filtering the events before the sign discrimination implies that the positive and negative events are treated equally and no bias is appreciated between them. However, the filtering can not be carried out always before if a small number of events remains.

Finally, the scale where the events are considered has to be chosen. The selection of the scale can be done with respect to the number of events detected or with respect to the energy of the global wavelet spectrum. The signature is cleaner when it is computed using the scales where the maximum number of events is detected. When the number of events is small due to the fact that the signal is short in time, this should be the method to apply. If the scale is selected with respect to the global wavelet energy, and the signal is short, it may occur that the number of events is too small to have a proper converged conditional average.

The wavelet-based signature identification is shown to be a good method to identify the true features of a signal. However, the choice of the optimal mother wavelet, event detection procedure, filtering windows, and scale depend on the case of consideration and the physics of interest. In this chapter, only the signatures that correspond to the auto-conditioning were investigated, however, the interest of this procedure increases when dealing with cross-conditionings between pressure and velocity. This analysis is carried out for the single jet in Ch. 5 and the dual stream jet in Ch. 6.

Chapter 5

Supersonic under-expanded single jet

In the aeronautic field, shock-cell noise is encountered in military aircrafts, space launch systems and commercial aviation. The engines of military aircrafts and the exhaust nozzles of space launch systems can be modeled as a supersonic single jet. Depending on the thrust required, and the ambient pressure (which is function of the altitude), the jet that is formed at the exit of the nozzle can be under-expanded, perfectly expanded or over-expanded.

This chapter discusses the results obtained with LES of an under-expanded single jet. This case of study allows to validate the numerical schemes applied to a jet encountering shock-cells, the general LES methodology, and the post-treatment tools developed to analyze the data. First, the definition of the case of study, the characteristics of the mesh and the simulation parameters are described in Sec. 5.1. Some details are given in Sec. 5.2 about the experimental results used for comparison. Then, the results are analyzed in Sec. 5.3. Last, a summary and some perspectives are introduced.

Some of the results discussed in this chapter were presented in several conferences such as 3AF [191], DLES10 [192] and CFM [193]. Some of the data produced with this case of study was shared among other partners of the project AeroTraNet2. More information about the collaborations is explained in Appx. C.

5.1 LES configuration

This section describes the main characteristics of the large eddy simulation of a single jet. The characteristics of the code used for the LES are explained in Ch. 2. For additional information on the LES procedure and mesh generation, the reader is referred to Ch. 3.

5.1.1 Case conditions

The case of study is a cold under-expanded single jet with a perfectly expanded exit Mach number of $M_j = 1.15$ ($NPR = 2.27$). Here, NPR stands for Nozzle to Pressure Ratio (see Ch. 1 for a wider explanation). The jet is established from an axisymmetric convergent nozzle

with diameter D of 38.0 mm. The lip of the nozzle at the exit has a thickness of 0.5 mm. The Reynolds number based on the exit diameter and the perfectly expanded conditions is

$$Re_j = \frac{\rho_j U_j D}{\mu_j} = 1.25 \times 10^6. \tag{5.1}$$

The ambient conditions used for this case are an ambient pressure p_∞ of 98,000 Pa and an ambient temperature T_∞ of 288.15 K. The generating pressure or total pressure is set to $p_t = 2.225 \times 10^5$ Pa. The total temperature is defined equal to $T_t = 303.15$ K. A small external flow of 0.5 m/s is added to help with the convergence of the simulation.

The main conditions are summarized in table 5.1.

D [mm]	M_j	NPR	p_t [Pa]	T_t [K]	Re_j
38	1.15	2.27	2.225×10^5	303.15	1.25×10^6

Table 5.1: *Conditions for the supersonic under-expanded single jet.*

5.1.2 Mesh definition

The structured multi-block mesh used for the LES is defined in this section. The mesh contains 75×10^6 cells with about $(1052 \times 270 \times 256)$ cells in the axial, radial and azimuthal directions respectively. Figure 5.1 (a) displays a gridplane of the mesh at $z/D = 0$ where the pink lines represent the edge of the physical domain. The sponge zone is located outside the pink region. As explained in Ch. 3, the mesh has a butterfly shape in order to avoid the singularity at the axis. The lip of the nozzle is discretized with 8 cells. A zoomed view is shown in Fig. 5.1 (b) and Fig. 5.1 (c) displays the axial gridplane located at the exit of the nozzles.

The maximum expansion ratio between adjacent cells achieved in the mesh is not greater than 4%. The radial discretization at different axial positions is depicted in Fig. 5.2 (a). The maximum Helmholtz number ($He = fD/a_\infty$) that the mesh is able to capture at the end of the physical domain is about 2. The radial domain size grows with the axial position in order to take into account the expansion of the jet (from $r/D = 3.5$ at the exit of the nozzle to $r/D = 8$ at $x/D = 30$), nonetheless, the maximum He number is kept constant at the boundary with the sponge layer. The axial discretization shown in Fig. 5.2 (b) is composed of 4 sections defined by the numbers 1 to 3. At the nozzle exit ($x/D = 0$), the mesh has an aspect ratio of 2.5; this ensures an appropriate definition of the first expansion fan of the shock-cell system. Then, up to point 1, the mesh elongates at a rate of 3%. This stretching allows for a drastic reduction of the total amount of cells in the axial direction. The segment $\overline{1\ 2}$ consists in a uniform discretization. Then, in segment $\overline{2\ 3}$, the mesh is slowly elongated up to a mesh size able to capture a Helmholtz number of 2. The last section, starting at point 3, is the one corresponding to the sponge layer where the mesh has a stretching ratio of 10%.

The nozzle geometry can be divided into the internal and the external part. In this work, the internal part of the nozzle is not modeled and no wall turbulence models are used. In order to have a good approximation of the boundary layer, either the mesh at the wall is fully resolved, or wall models are applied. Unfortunately, the wall models were not yet implemented nor tested for high-order compact schemes at the time of the computation. Moreover, using a fully

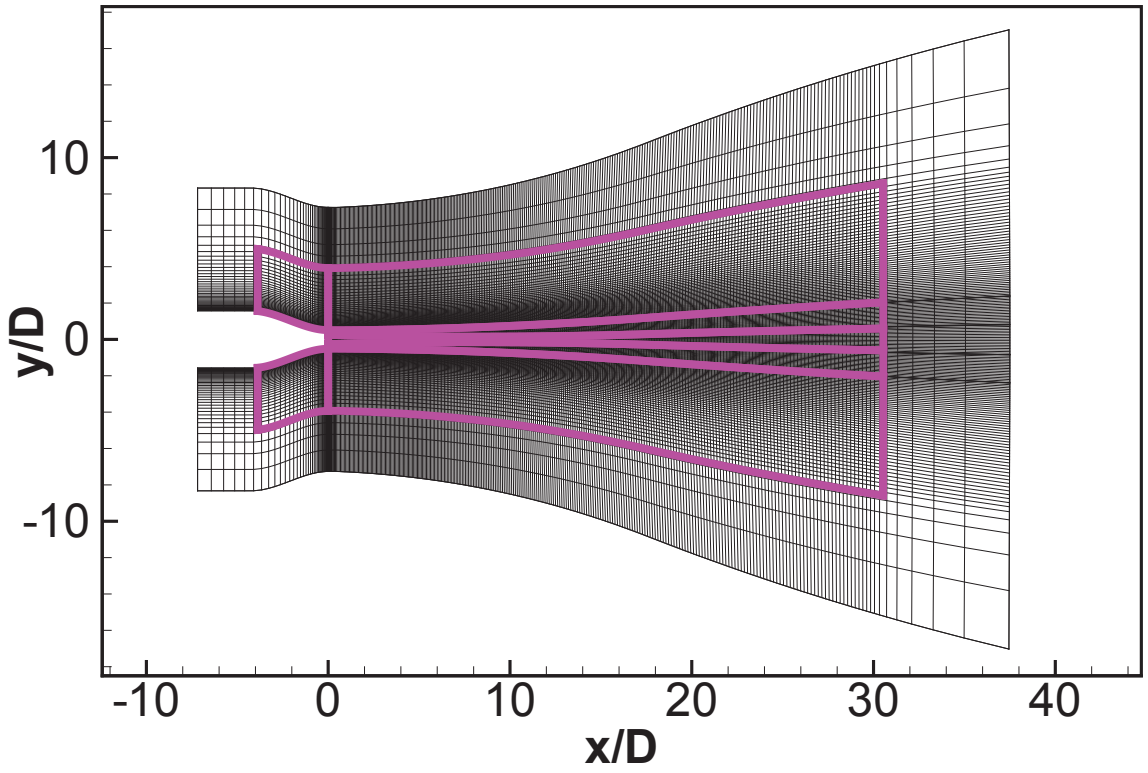

(a)

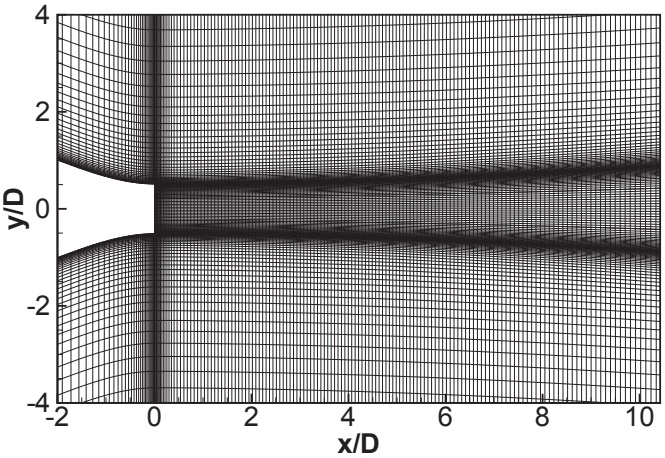

(b)

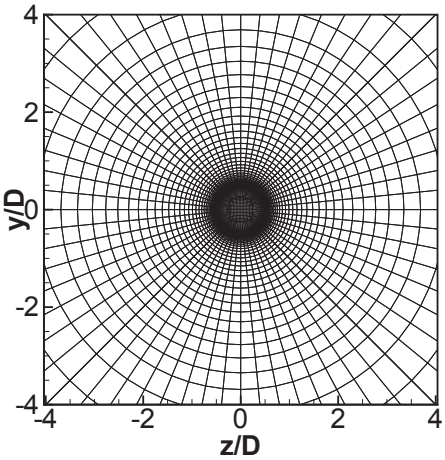

(c)

Figure 5.1: *Mesh grid planes representing every fourth nodes in the plane $z/D = 0$ for* ***(a)*** *a general view and* ***(b)*** *a closer look at the nozzle exit.* ***(c)*** *shows the exit plane of the nozzle.*

resolved grid at the interior of the nozzle with conformed structured meshes would multiply the number of cells by about 5. The boundary layer at the exit of the nozzle could drastically change inside the nozzle without wall models or a fully resolved mesh. The boundary layer would therefore be modified with respect to the one obtained with the fully resolved RANS simulation. Therefore, not being able to assure a good definition of the boundary layer, it was decided to completely remove the internal part of the nozzle. In the following sections it is shown that the shear-layer transitions to turbulence in less than 1 diameter. An alternative solution could have been to model the interior of the nozzle with an unresolved mesh, but apply the correct level of synthetic turbulence (Sec. 2.7.4) to match the experimental boundary layer. On the other hand, the walls of the external sections of the nozzle attain a resolution at the wall of $y^+ \approx 25$ with 20 points in the boundary layer that is generated by the suction of the jet and the small co-flow used.

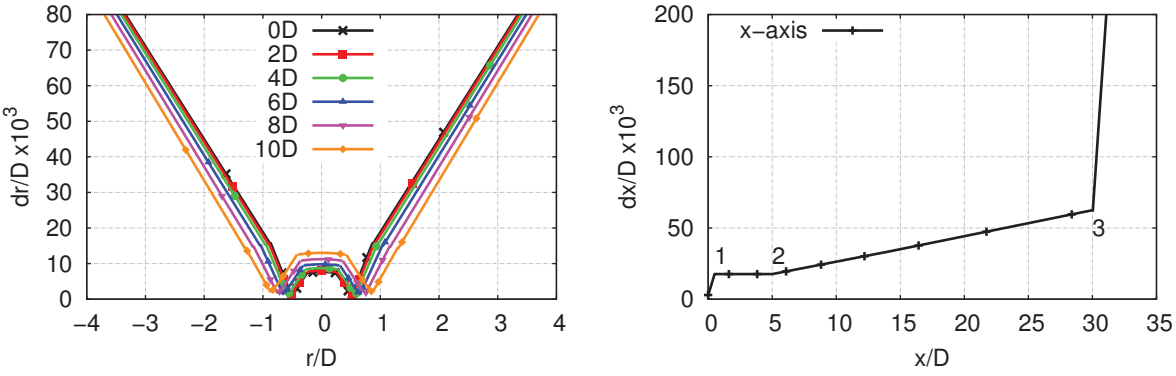

(a) (b)

Figure 5.2: *Discretization of the mesh along* ***(a)*** *the radial distribution for different x/D and* ***(b)*** *the axial distribution along the axis, where dr is the radial step and dx the streamwise one.*

During this thesis, an exchange of data and knowledge was done with Leicester, partner of the AeroTraNet2 project. Their in-house code, COSMIC, is a second-order multi-block finite volume explicit time-resolved LES and Detached Eddy Simulation (DES) solver developed at the University of Leicester [194, 195]. Moreover, the mesh used for the COSMIC simulations was generated at CERFACS because they lacked of a structured meshing software. A special care was taken when designing the mesh for COSMIC in order to have a higher maximum resolvable Strouhal number of 3. Due to the fact that the solver is second-order, the mesh was generated with a finer radial and axial discretization. Nonetheless, the mesh generated for COSMIC has the same number of cells than the one used in ***elsA***. This has been achieved by reducing the number of azimuthal cells from 256 to 64.

Remark: The far-field SPL obtained by Leicester with DES using COSMIC are included in Sec. 5.3.3 for completeness. Further details about the computation parameters and an exhaustive examination of the results will be given in the PhD thesis of A. Mancini.

5.1.3 Simulation parameters

The computation is initialized by a Reynolds-Averaged Navier-Stokes (RANS) simulation using the Spalart-Allmaras turbulence model [169]. Contrary to the LES mesh shown in the previous

Sec. 5.1.2, the internal nozzle is modeled for the RANS computation which is fully wall-resolved in the internal and external sections of the nozzles with a maximum wall unit (y^+) of unity and 25 points in the boundary layer. The nozzle is modeled in the interior up to 10 diameters and the RANS domains extends to 100 diameters in the radial and axial directions. The effect of the mesh on the RANS simulations was studied together with an uncertainty quantification for the under-expanded single jet as part of a collaboration with Greenwich University (see Appx. C). The LES is then initialized from the RANS keeping the exit profile. The flow is initialized over 120 dimensionless convective times ($\hat{t} = ta_\infty/D$). The final computation is then run for 140 dimensionless convective times in order to obtain the statistics. A non-dimensional time step Δt of 0.0004 equivalent to a CFL about 0.9 is selected for the data extraction phase. In dimensional quantities, the time step is equivalent to 0.045 μs.

The boundary conditions applied in the simulation are sketched in Fig. 5.3. Non-reflective boundary conditions of Tam and Dong [160] extended to three dimensions by Bogey and Bailly [161] are used at the lateral boundaries. The exit boundary condition is based on the characteristic formulation of Poinsot and Lele [158]. Additionally, sponge layers are set around the domain to attenuate exiting vorticity waves. No inflow forcing is applied as the interior of the nozzle is not modeled. Last, no-slip adiabatic wall conditions are defined at all the external wall boundaries of the nozzle.

This simulation was run without the shock-limiting schemes explained in Sec. 2.3 as the maximum Mach number is relatively low and no strong discontinuities are encountered throughout the shock-cells. Moreover, avoiding the use of the shock-limiting scheme allowed for a longer computational time. The spatial filter of order 6 (Sec. 2.2.2) was applied to this case of study.

The simulation was run on 128 processors on the internal supercomputer Bullx B510 at CERFACS. The total computational time was about 420,000 CPU h, which includes the RANS computation used to initialize the LES, the LES on the coarse mesh, the adaptation phase from the coarse mesh to the fine mesh, and the actual large eddy simulation of 140 non-dimensional convective times.

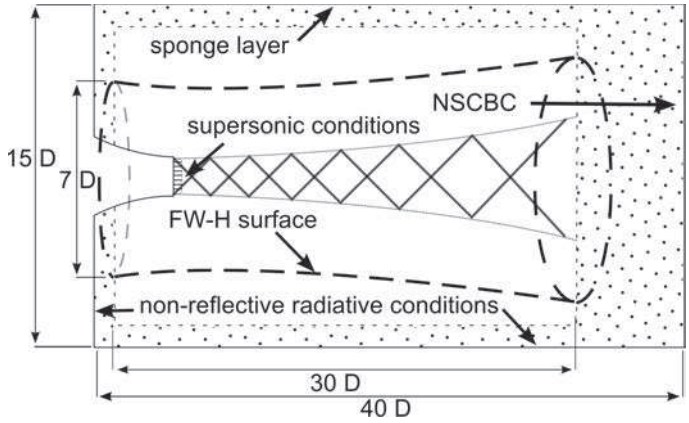

Figure 5.3: *Sketch of the domain representing the different boundary conditions and dimensions.*

5.1.4 Data extraction

The data extracted in this simulation was mainly limited due to memory storage constraints as explained in Ch. 3. The data extracted is divided in the mean, cuts, numerical probes and topological surfaces. The cuts, numerical probes and topological surfaces were extracted every 200 iterations which is equivalent to a frequency of 112.37 kHz.

Plane cuts were extracted at $z/D = 0$ and $y/D = 0$, and at the axial locations $x/D \in \{0, 1, 2, 3, 4, 5, 6, 7, 8, 9, 10\}$. These cuts were used to extract several linear arrays of probes at different locations with an axial discretization of $\Delta x = 0.05$ D, or for azimuthal arrays with 20 probes.

Numerical probes were extracted at the axis every 0.1 D (noted as AXIS), at the lip-line (noted as LIP_LINE) and in the near-field at 1 D, 2 D and 3 D from the nozzle exit and an expansion angle of 5 degrees (noted as NF1D, NF2D and NF3D respectively).

The far-field sound is obtained by means of the Ffowcs-Williams and Hawkings analogy (FWH) [196]. The surface used to extrapolate the variables to the far-field is located in a topological surface starting at $r/D = 3.5$ from the axis and growing with the mesh. The cut-off mesh Strouhal number is $St = fD/U_j \approx 1.8$. The sampling frequency was set to 112.37 kHz which gives a sampling Strouhal number higher than the mesh cut-off limit. The noise was propagated up to a distance of 53 D as in the experiments.

5.2 Experimental setups

The numerical results from the LES are compared against different experimental results in order to validate the numerical schemes and the overall methodology. The simulation is based on the experimental campaign performed at LMFA in Lyon [17] but two other experiments are used for completeness of the comparison. The additional experimental results come from the Institut Pprime at Poitiers [197] (France), and the VKI at Rhode-St-Genèse (Belgium) [198].

The NPR of the computation is based on the same NPR set at the LMFA of 2.27. On the other hand the closest NPR to the reference one for Pprime and the VKI is 2.30. Moreover, the nozzles differ in the interior shape and the diameters from the one used at LMFA of 38 mm to 40 mm at Pprime and 24 mm at VKI. The facility at VKI is explained in detail in Sec. 6.2.

The experiments from LMFA are considered in order to compare the Mach number profiles at the axis, the shear-layer development for the RANS and the LES, the turbulence values in the lip-line, the velocity length-scales, the Schlieren images and the far-field noise. The experiments from Pprime are used for comparisons with the near-field pressure spectra. Last, the results from VKI are examined in order to compare the PIV contour plots and the far-field spectra.

5.3 Analysis of results

5.3.1 Aerodynamic field

As explained in the introduction, shock-cell noise is generated from the interaction between the vortices developed in the mixing layer that are convected downstream, and the shock-cell system that appears from the mismatch in pressure at the exit of the nozzle. The frequency of the main peak of the broadband shock-associated noise (BBSAN) [199] can be easily calculated with the convection velocity of the vortices and the spacing of the shock-cells as

$$f_p = \frac{U_c}{\overline{L}_{sh}} \frac{1}{1 - M_c \cos(\theta)}, \tag{5.2}$$

where U_c is the convection velocity, $\overline{L}_{sh}$ is the averaged shock-cell spacing, θ is the angle with respect to the jet direction and M_c is the convective Mach number defined as $\frac{U_c}{a_\infty}$ where a_∞ is the ambient speed of sound. The fundamental frequency $\frac{U_c}{\overline{L}_{sh}}$ of the interaction of the vortices and the shock-cell system is shifted due to the Doppler effect by the factor $\frac{1}{1-M_c \cos(\theta)}$. The Doppler effect can be seen as the noise produced by an array of phased monopoles situated on the shock-cells that radiate noise only when the vortices interact with them. Hence obtaining a lower frequency at the upstream angles and a higher frequency at the downstream angles.

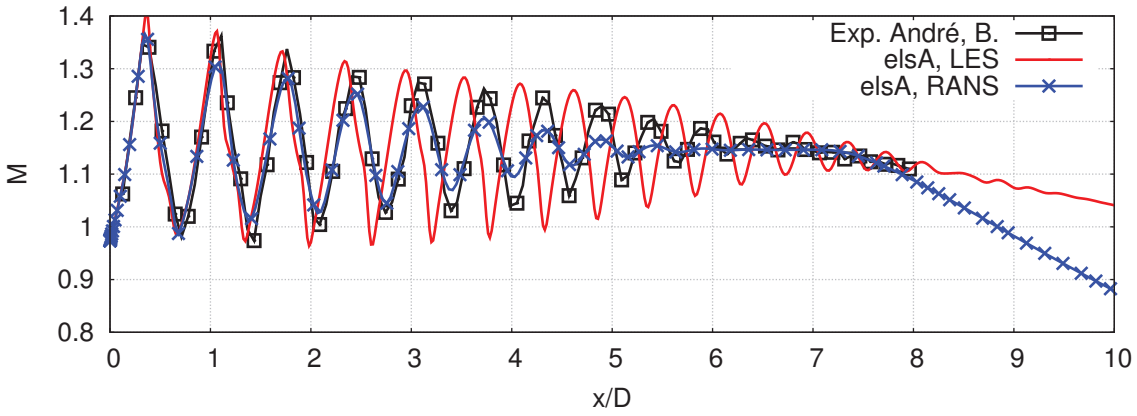

Figure 5.4: *Mach number profile at the axis.*

The averaged Mach number profile at the axis for the RANS, the LES and the experimental results, is shown in Fig. 5.4. As it is expected, the RANS simulations dissipate more the shock-cells loosing the amplitude with respect to the experimental profile. Moreover, the potential core obtained for the RANS decays at a different rate than the LES. The RANS models have been demonstrated not to correctly propagate the turbulence to the centerline [200, 201]. On the other hand, a good agreement is found for all the positions of the shock-cells. The LES has good agreement for the shock-cell spacing in the first three shock-cells. But further downstream, there is a shift between the experimental and the numerical Mach number profiles. The shock-cell spacing is reduced by about 5%. Even though the amplitudes are higher than in the experimental results, they follow the same decay and they have the end of the potential core at the same position. Figure 5.5 shows the shock-cell spacing for all shock-cells in (a)

and the computation of the main frequency peak associated to that shock-cell spacing using Eq. (5.2) in (b). Here, the convective velocity is considered as $U_c = 0.7U_j$, which is usually used as a reference.

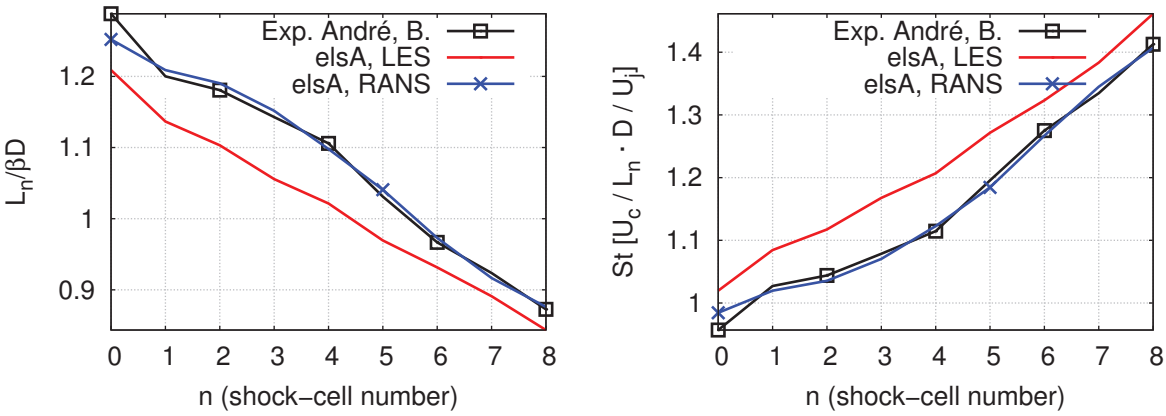

Figure 5.5: ***(a)*** *Shock-cell spacing $L_n/\beta D$ for each shock-cell where L_n is the shock-cell spacing of the $n-th$ shock-cell, β is the shock parameter and D the diameter.* ***(b)*** *Strouhal number of the frequency $f_{sh} = U_c/L_n$.*

The two-dimensional field at $z/D = 0$ of the numerical LES are compared against the RANS, the experimental PIV from VKI, and the experimental Schlieren from LMFA [17] in Fig. 5.6. Figure 5.6 (a) shows the comparison of the Mach number contours for the LES and the RANS. A good agreement is found in the first 4 shock-cells, however, farther downstream, the expansion of the shear-layer is greater for the RANS simulation which makes the shock-cells disappear sooner due to the collapse of the potential core. A different numerical scheme and a highly denser mesh could help solve this problem even though the price to pay may be too high for the purpose of the RANS.

Next, the LES is compared against the PIV from VKI in Fig. 5.6 (b). A good agreement is found for the first three shock-cells and the expansion of the shear-layer even though the conditions were not exactly the same and the shape of the internal nozzle is different. The PIV shows that the shock-cells are highly attenuated after the fourth shock-cell. One of the main differences between the experimental results and the LES is the appearance of screech. The screech has been known to affect drastically the structure of the shock-cells downstream of the source [43] which could explain the difference after $x/D = 4$.

On the other hand, if the numerical Schlieren is compared against the experimental one from LMFA (Fig. 5.6 (c)), an excellent agreement is found for the intensity (shades of gray) of the density variation. As it was presented in Fig. 5.4, the shock-cell size of the LES differs from the experimental results by a phase of exactly one shock-cell at $x/D = 7$. The difference in the shock-cell length has a direct effect on the positioning in frequency of the peak of the BBSAN as it is shown in the following.

The expansion rate of the shear-layer in the radial direction defines the length of the potential core and the length of the shock-cell structure. A higher expansion rate means a smaller potential core and thus a smaller shock-cell structure [202]. In addition, if the expansion is

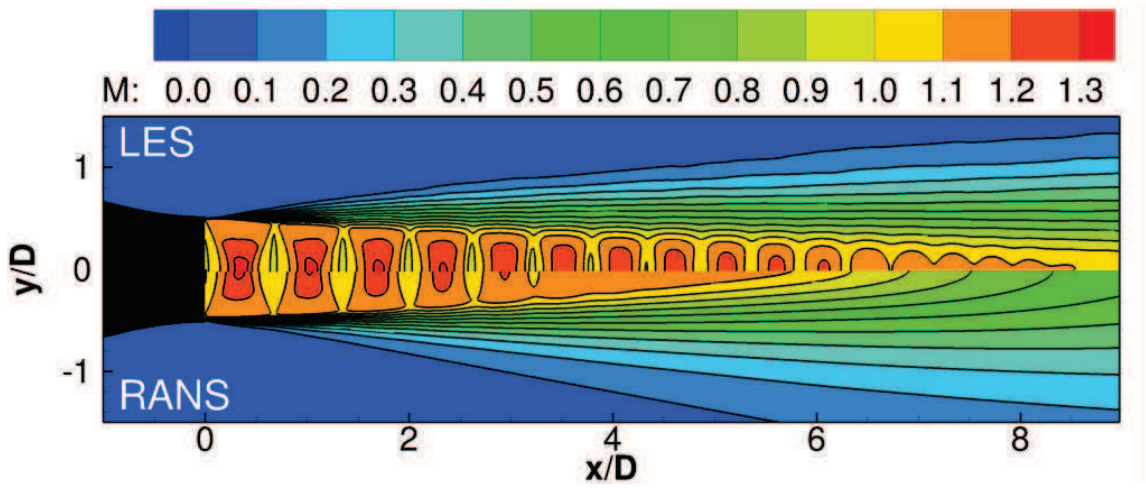

(a)

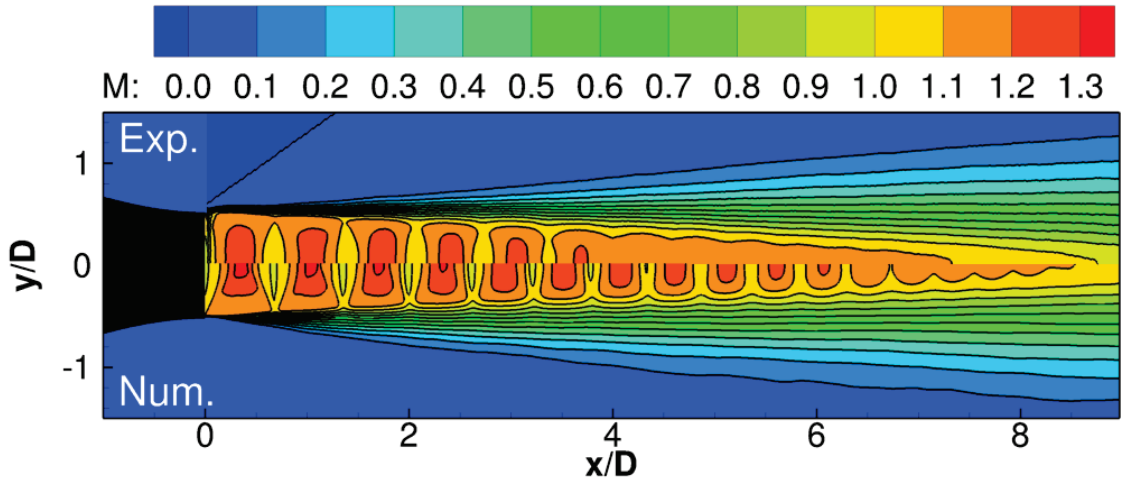

(b)

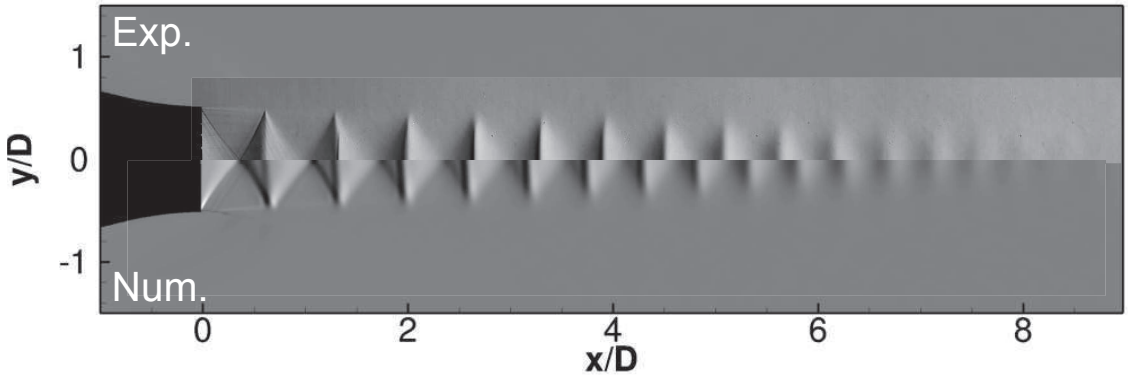

(c)

Figure 5.6: *Mach number contour plots comparisons between* ***(a)*** *LES and RANS,* ***(b)*** *PIV from VKI and LES and* ***(c)*** *Schileren from LMFA [17] and numerical Schieleren from the LES.*

too small, the shock-cell structure could be unrealistically extended farther downstream. The axial velocity profile along the radius at $x/D = 0.16$ and $x/D = 0.41$ are shown in Fig. 5.7 (a) and (b). Good agreement is obtained within the first 3 diameters. Further downstream, the shift in the shock-cells makes the comparison not viable.

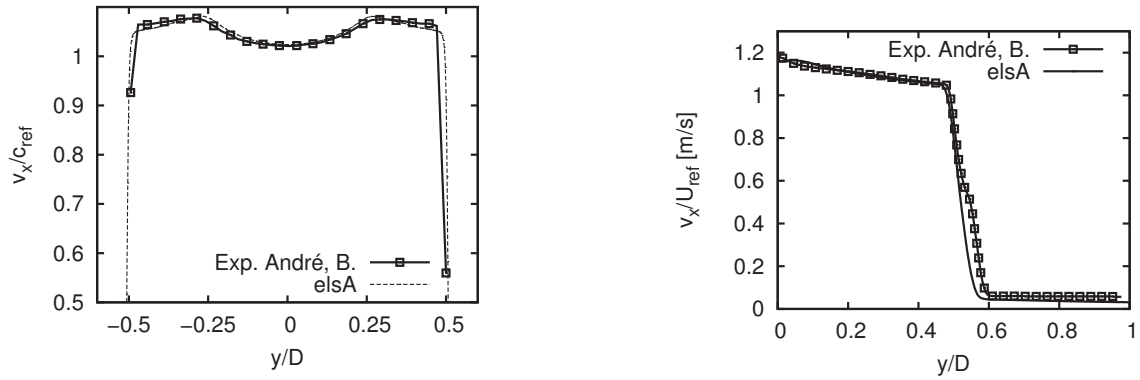

(a) (b)

Figure 5.7: *Axial velocity along the radius at* ***(a)*** $x/D = 0.16$ *and* ***(b)*** $x/D = 0.41$

The expansion of the shear-layer represented in Fig. 5.7 is in part influenced by the turbulence levels. Although no inflow forcing is applied, matching the jet exit profile against the experimental velocity profiles and a good discretization of the flow, seems to be sufficient for this supersonic jet to transition to a fully turbulent flow within the first radius from the exit nozzle plane. To support this statement, the turbulence levels of the velocity components at the lip-line are shown in Fig. 5.8. Although the shape of the imposed profile at the nozzle exit is turbulent, the fact that it is a steady profile from the RANS simulation implies that the actual turbulence is zero. However, after the first radius, it reached the same levels of *rms* as in the experiments even though an overshoot is found within the first 2 diameters and there is a decay of 25% at $x/D = 8$.

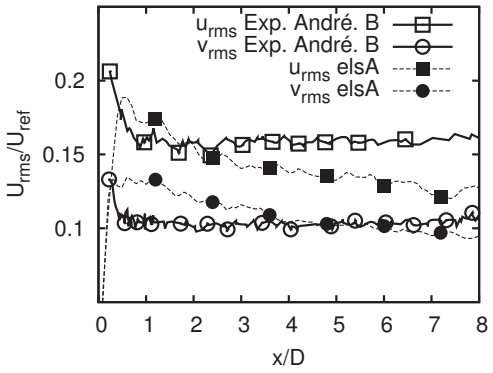

Figure 5.8: *Turbulence levels of the axial and radial component of velocity at* $r/D = 0.5$

The size of the turbulent structures generated along the lip-line ($r/D = 0.5$) is measured by means of a spatial auto-correlation following the same formulation as in [17]. The spatial

cross-correlation R_{uu} is computed as

$$R_{uu} = \frac{u'(\overline{x},t)u'(\overline{x}+\overline{\xi},t)}{u^{rms}(\overline{x},t)u^{rms}(\overline{x}+\overline{\xi},t)}, \tag{5.3}$$

where u' is the axial velocity perturbation, u^{rms} the axial velocity root mean square, $\overline{x}$ is the actual position, and $\overline{\xi}$ the spatial separation. The axial velocity auto-correlations R_{uu} are shown at the positions $x/D = 1.5$ and $x/D = 9.0$ in Fig. 5.9 (a) and (b) respectively. For this purpose, the computational flow field was probed every 0.1 D. The increase in the size of the turbulence structures in the mixing layer is clearly illustrated.

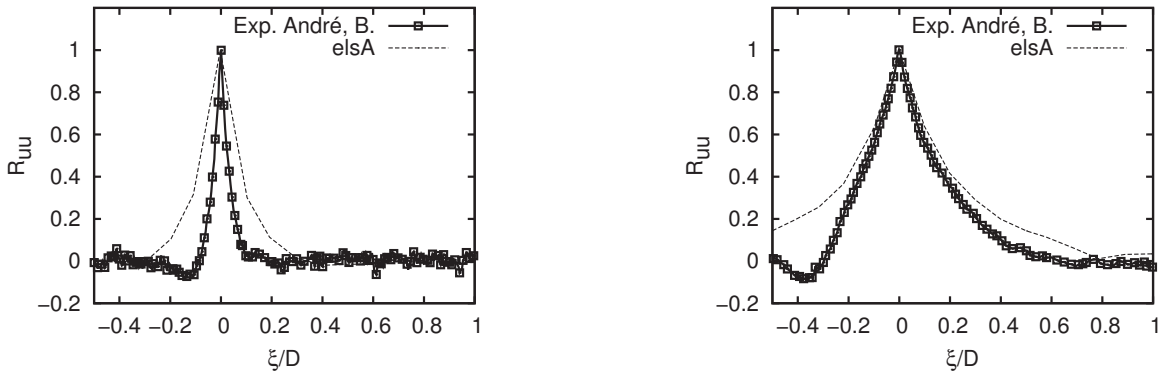

(a) (b)

Figure 5.9: *Axial velocity along the radius at* ***(a)*** $x/D = 0.16$ *and* ***(b)*** $x/D = 0.41$

The turbulence length-scale computed from the auto-correlations along the lip-line L_{uu} is shown in Fig. 5.10. The integration of R_{uu} is calculated up to the value 0.1. Despite the fact that Fig. 5.9 (a) and (b) display an increase in size of the turbulence structures with respect to the experimental results, Fig. 5.10 shows that it presents the same growth rate, but shifted 1.5 diameters in the axial direction. This displacement is probably due to the imposed steady profiles at the exit of the nozzle, where the transition occurs in a more abrupt fashion as seen in Fig. 5.8.

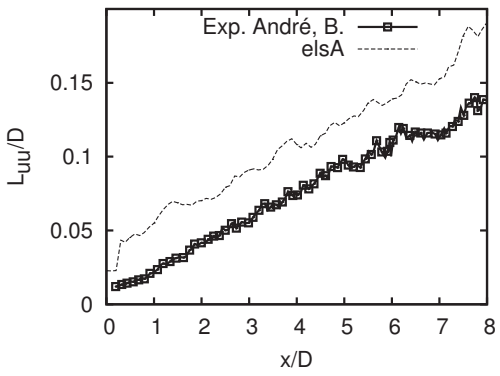

Figure 5.10: *Axial velocity length-scale at* $r/D = 0.5$

5.3.2 Acoustic-hydrodynamic filtering in the near-field

The near-field pressure field is compared to the one from A. Savarese (Pprime, Poitiers) [197]. The pressure signal is extracted from a linear array located at $r/D = 3$ and expanding with an angle of 5°. Unfortunately, the experimental microphones were located in a horizontal linear array at $r/D = 4$ and were obtained after the simulation. The comparison at the same position is not possible because the linear array would traverse the sponge zone at $r/D = 4$. The Power Spectral Density (PSD) from both arrays is shown in Fig. 5.11. Even though the differences in the positioning of the arrays and the fact that the experimental NPR is higher than the numerical one, similar patterns are found. The main peak has a "banana like" [197] shape in the axial direction. The secondary peak that appears at higher frequencies is also captured even though it is highly dissipated due to the coarsening of the mesh and its associated cut-off frequency. Following [197], the frequency axis is normalized by the parameter β defined as

$$\beta = \sqrt{M_j^2 - M_e^2}, \tag{5.4}$$

where M_j is the Mach number calculated at perfectly expanded conditions and M_e is the actual Mach number, which is equal to one for non-perfectly expanded jets. This parameter can be used to normalize the frequency from two jets that have different NPRs because the main peak positioning is based on the mean shock-cell length, which in fact depends on the perfectly expanded Mach number. In a similar fashion, the pressure amplitude can be normalized as

$$\Delta p' = \frac{\Delta p}{\beta^2}, \tag{5.5}$$

before converting it to dB. This normalization has been shown to be effective for a larger number of NPR in [197].

The PSD of the pressure field shown in Fig. 5.11 contains the hydrodynamic and the acoustic components. In order to study independently both the acoustic and the hydrodynamic components of a jet, the acoustic-hydrodynamic filtering [181] presented in Sec. 3.3.2 is applied to the near-field of the supersonic under-expanded single jet.

The filtering was applied over several linear arrays in order to obtain a two-dimensional field of the filtered pressure perturbation. Figure 5.12 displays the original pressure perturbations of a snapshot and the filtered hydrodynamic and acoustic components. The filtering allows the hydrodynamic component to be clearly visible and the acoustic component to gain in detail specially near the jet, where the hydrodynamic perturbations are more intense. The hydrodynamic component of a jet extends several diameters radially and even though it is in fact a pressure perturbation, it can not be considered as an acoustic wave because it is convected at a speed smaller than the ambient speed of sound a_∞. From Fig. 5.12 it can be seen how the filtering shows a noisy behavior closer to the jet, due to the fact that the Mach number is of order unity and thus, it contains a high level of non-linearities [182]. At the axial edges of the domain, some waves appear on the hydrodynamic component that should belong to the acoustic component even though a smoothing window was applied.

The spectrum obtained by the different components is depicted in Fig. 5.13 and can be compared to the original signal. The acoustic component (Fig. 5.13 (c)) mostly recovers the BBSAN peak that appeared at 3 D in Fig. 5.11. The hydrodynamic component is shown in Fig. 5.13 (b). Shock-cell noise is generated by the interaction between the vortical structures

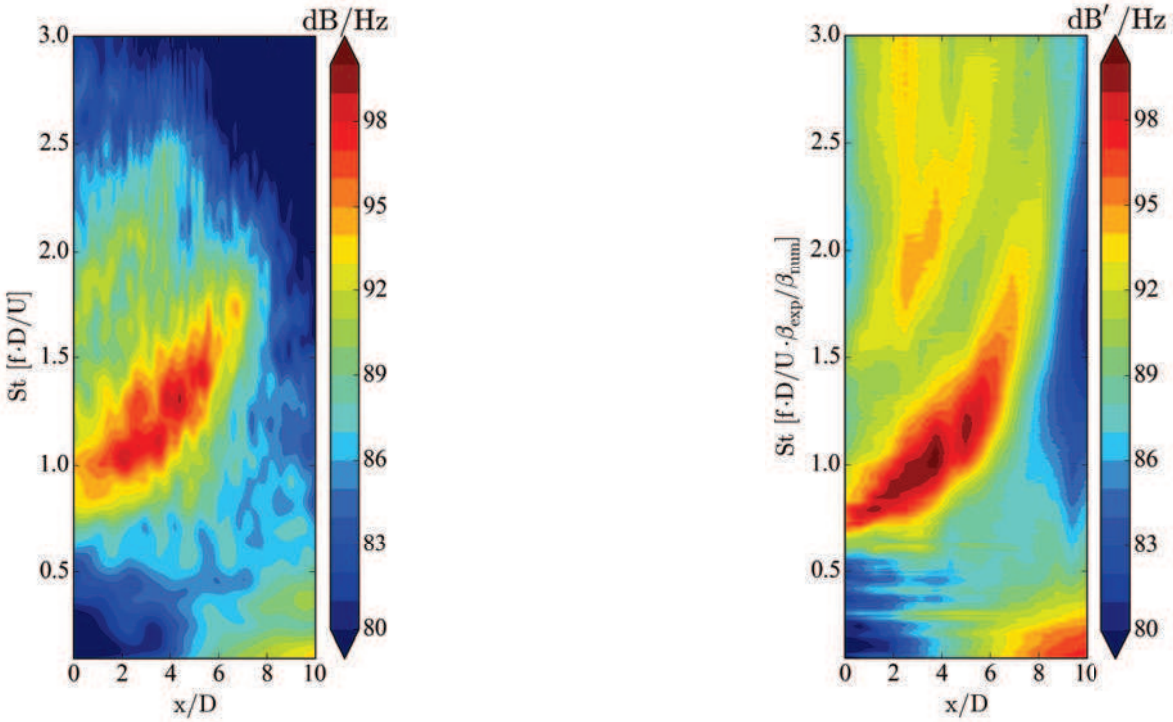

(a) (b)

Figure 5.11: *PSD of the pressure* ***(a)*** *for an array located in the near-field at* $r/D = 3$ D *and and expansion angle of* 5% *for the LES* ***(b)*** *and an experimental array of microphones at* $r/D = 4$ *from Pprime [197].*

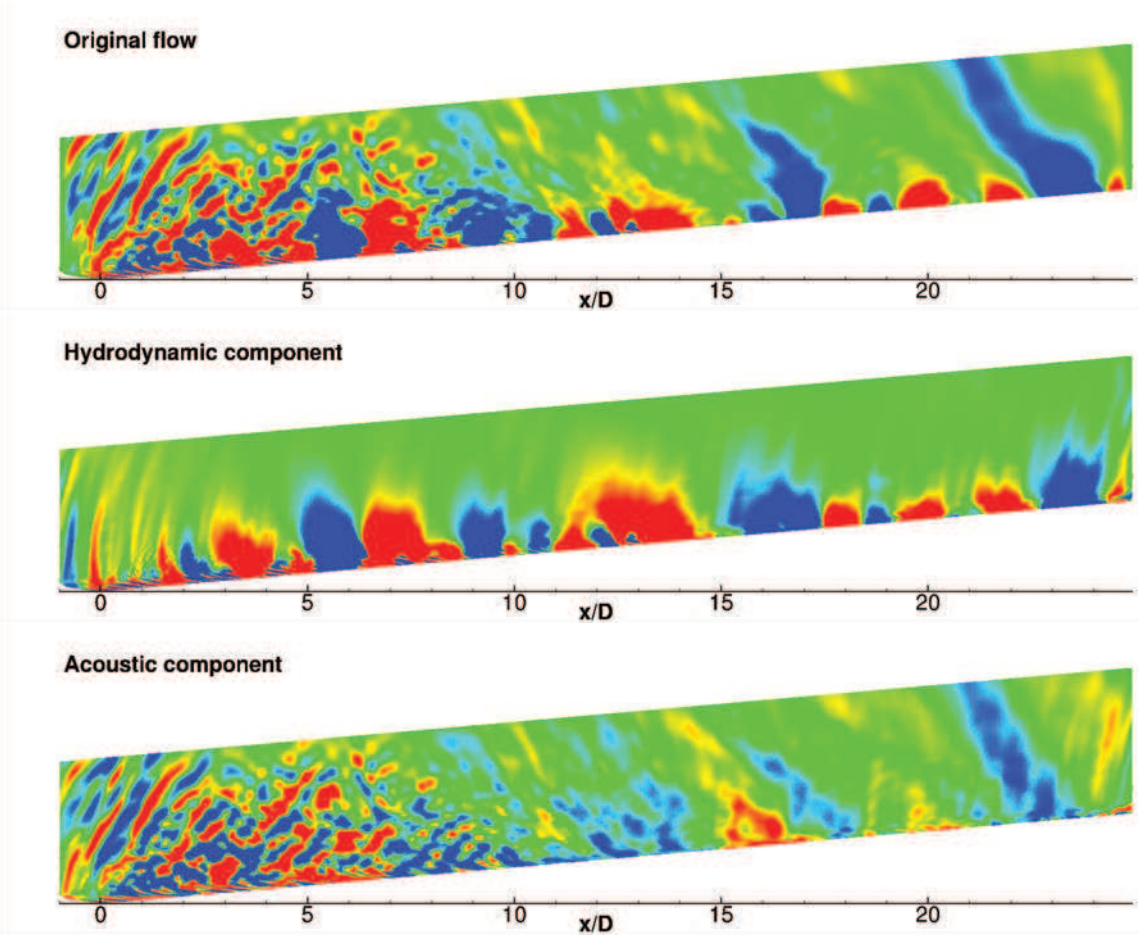

Figure 5.12: *Snapshot of the hydrodynamic-acoustic filtering in the near-field of a supersonic under-expanded single jet. Pressure perturbation contours in the range* $[-150, 150]$ *Pa.*

and the shock-cells. The later oscillates due to the passage of the vortices and, at the same time, shock-cell noise is radiated through the saddle point of the vortical structures [40]. These interactions are present in Fig. 5.13 (b) as a tonal behavior which in fact is also visible in the acoustic field. The axial pattern of this energetic event matches the shock-cell system. As it can be seen in Fig. 5.13 (c), some of the excited regions of the hydrodynamic component overlap with some regions of the acoustic component.

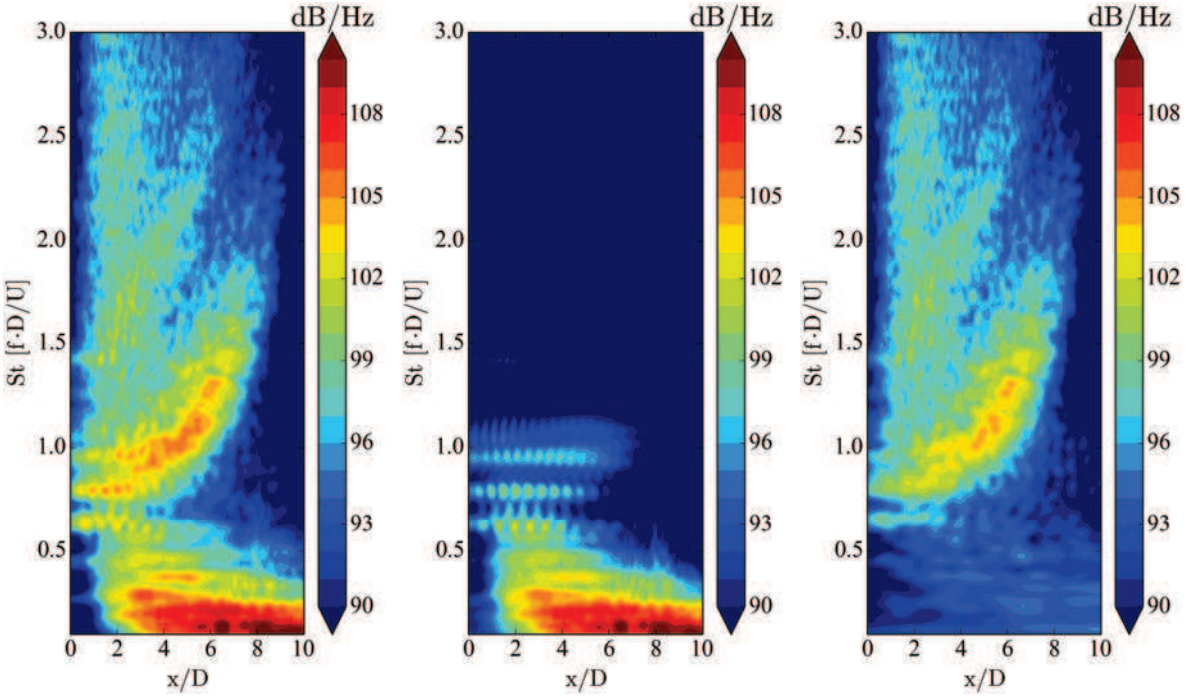

Figure 5.13: *Sound pressure level of an array of probes located at* 1 D *from the axis which extends up to* 10 D *in the axial direction with an expansion angle of* 5°. ***(a)*** *Full signal,* ***(b)*** *hydrodynamic component and* ***(c)*** *supersonic component.*

The importance of the acoustic-hydrodynamic filtering is further noticed when spatial-temporal cross-correlations of the filtered pressure are carried out in the near-field. Figures 5.14 (a), 5.14 (b) and 5.14 (c) show the pressure cross-correlation of the original - original signal, hydrodynamic - hydrodynamic component and the acoustic - acoustic component respectively. The cross-correlation is performed between one point located at $[x/D = 0, y/D = 3]$ and an array located at $y/D = 1$ with an inclination of 5°, following the expansion of the shear-layer. Figure 5.14 (a) displays the shock-cell noise about $x/D = 4$ with a maximum normalized cross-correlation of 0.38. When the filtering is applied, the cross-correlation peak increases up to 0.41 (5.14 (c)) and it becomes clearer downstream of the end of the potential core ($x/D > 9$) (Fig. 5.14 (a) focuses only on the shock-cell noise region). The filtering improves the cross-correlation specially downstream where the hydrodynamic components have the same general direction as the acoustic waves. The cross-correlation of the hydrodynamic component from Fig. 5.14 (b) some correlated areas most likely due to the entrainment caused by the jet.

Figures 5.14 (d), 5.14 (e) and 5.14 (f) now focus the cross-correlation on the point located

at $[x/D = 15, y/D = 3]$ and the above-mentioned array. At this position, the original cross-correlation from Fig. 5.14 (d) differs completely from the acoustic component from Fig. 5.14 (f). The original signal is clearly dominated by the hydrodynamic component from 5.14 (e) which adopts the same shape. The mixing noise of the large turbulent structures is mostly generated at the end of the potential core and radiated at 30° [23]. The cross-correlation of the acoustic component agrees with the theory, showing a high correlation up to this location, with a convective velocity of the speed of sound.

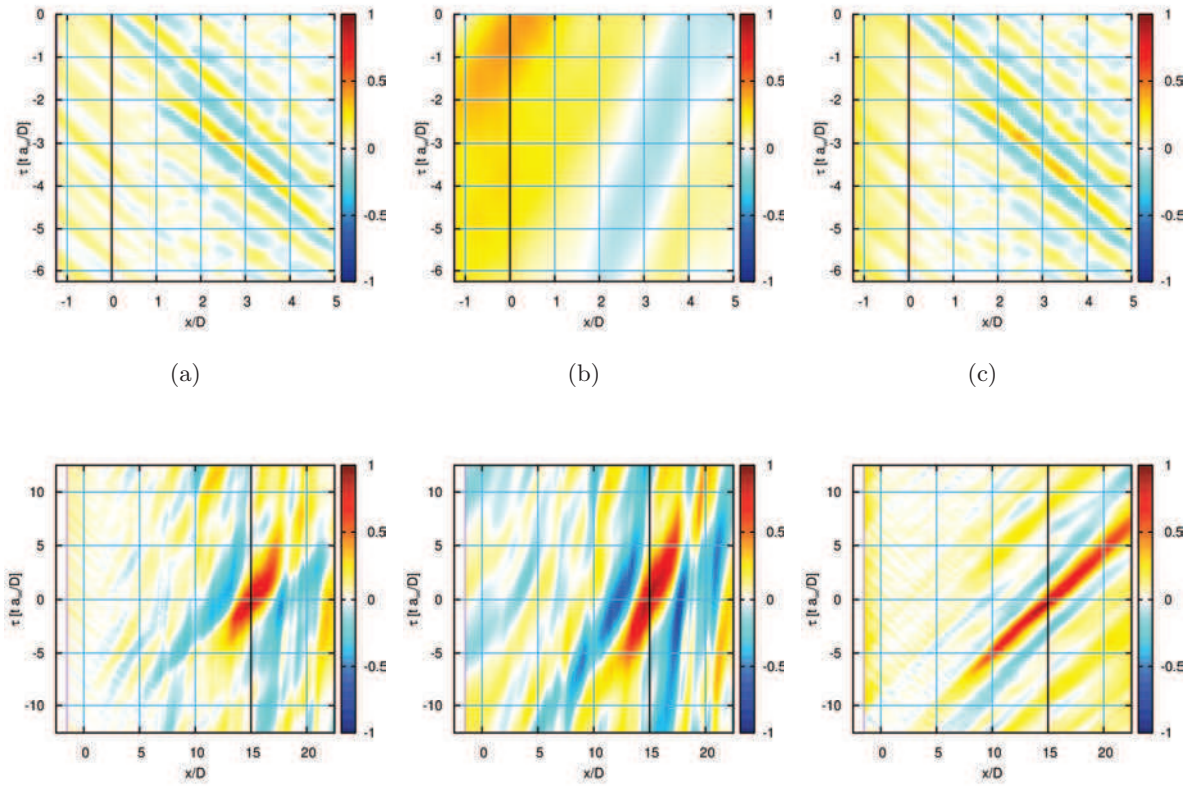

(a) (b) (c)

(d) (e) (f)

Figure 5.14: *Spatial-temporal pressure cross-correlation at* $x/D = 0.0$ *of the* ***(a)****, original component,* ***(b)*** *the hydrodynamic component, and* ***(c)*** *the acoustic component and at* $x/D = 15.0$ *for* ***(d)****,* ***(e)*** *and* ***(f)*** *respectively.*

The acoustic-hydrodynamic filtering, even if it is not exact nor fully accurate in the separated flow components, is shown to be a powerful tool to use in the near-field of a jet. The application to shock-cell noise does not greatly improve the correlations because the directivity is opposite to the one of the large turbulent structures. Nonetheless, it allows for a better interpretation of the results and future post-processing techniques as it is discussed in the following.

5.3.3 Far-field acoustic field

In this section, the SPL at the far-field at $r/D = 53$ from the nozzle exit plane is compared against numerical results from the University of Leicester (noted as $COSMIC$), experimental results from LMFA [17] (noted as $exp.André$) and experimental results from VKI (noted as $exp.VKI$).

The pressure perturbations from ***elsA*** were propagated to the far-field using the Ffowcs Williams-Hawkings analogy presented in Sec. 3.3.1 and averaged over 20 azimuthal probes in order to artificially increase the convective time of the signal. On the other hand, both experimental far-field pressure spectra were measured with a single array of microphones situated at different angles. The experimental results from the VKI are normalized to the actual distance based on the diameter. The amplitudes are also normalized by the Strouhal number to take into account the difference in diameter.

The comparisons are shown in Fig. 5.15 for different angles computed from the jet direction. The following analysis is focused at 30°, 60°, 90°, and 120°. The lower downstream angles are identified with the noise generated by the large structures that are convected downstream. At 30°, both experimental spectra have a similar decay and amplitude at Strouhal numbers higher than 2.5. On the other hand, they differ by a maximum of 5 dB at the lower frequencies which could be due to the differences in the inner geometries of the nozzles, different turbulence levels or installation effects. Similarly to the experimental results, the numerical spectra differ as well with the same trend, similar decays and amplitudes at high frequencies, and a discrepancy in amplitude for the lower frequencies. The decay shown about $St \approx 2.5$ for the simulations comes only from the frequency cut-off of the mesh, not able to resolve the higher frequencies.

At 60°, more differences are visible between both experiments. First, the results from VKI display the BBSAN peak about $St \approx 1.9$ whereas the LES pressure spectra from ***elsA*** are dissipated by the cut-off Strouhal number of the mesh. The higher frequencies cannot be compared between both simulations due to the different mesh cut-off Strouhal numbers, being about $St \approx 2$ for ***elsA*** and $St \approx 3$ for COSMIC. A similar difference in amplitude as for the lower angles is shown for the lower frequencies. The difference in the azimuthal discretization could explain why at this angle, the numerical sound pressure levels differ up to 10 dB at the lower frequencies. A coarser mesh in the azimuthal direction would generate larger and more energetic structures convected downstream. Preliminary investigations obtained by Leicester confirm a bigger size of the structures when comparing the axial velocity length-scales.

At 90°, the experimental results show similar amplitudes at the lower frequencies and the same position for the BBSAN peak. On the other hand, the peak is broader for the results from VKI which increases the amplitude in the surrounding Strouhal numbers about 4 dB. The DES from COSMIC is able to capture the BBSAN peak at this location, however, the amplitude at the lower frequencies is still shifted by 5 to 10 dB. The BBSAN peak from ***elsA*** has a lower amplitude and is shifted in frequency with respect to the experimental SPL due to the fact that the shock-cell length captured is smaller than the experimental one as it is shown by Eq. (5.2).

The effect of the shock-cell length is clearly visible at 120°. Here, the BBSAN is well captured by ***elsA***, but it is shifted to higher Strouhal numbers. Good agreement in amplitude is found for all the resolved Strouhal numbers (up to $St \approx 2$). At this angle, the difference in amplitude is smaller for the numerical results from COSMIC. The experimental results show

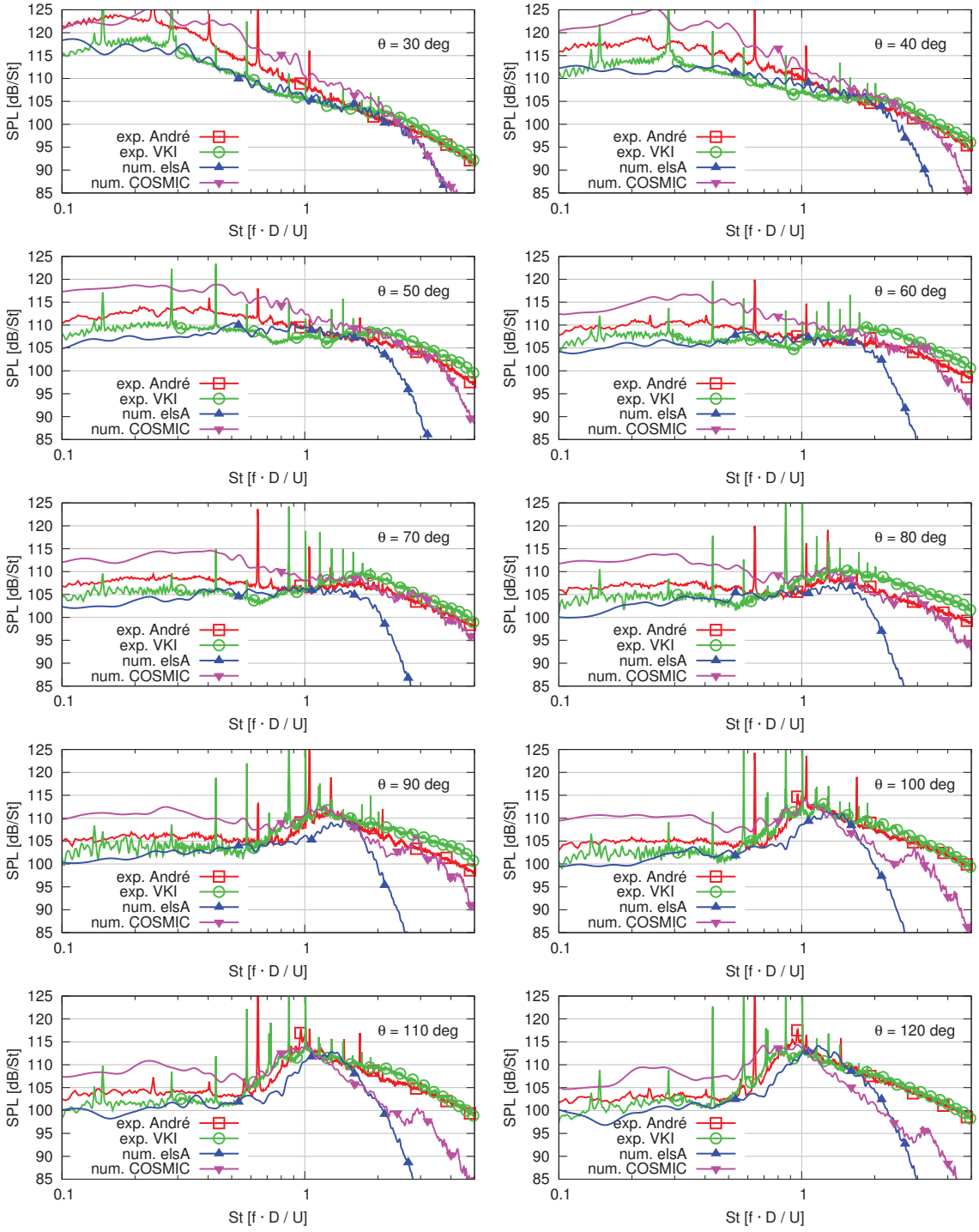

Figure 5.15: *Far-field sound pressure level at $r/D = 53$ from the nozzle exit for different angular positions with respect to the jet direction.*

a very good agreement for all frequencies. On the other hand, the screech is not captured at the same frequencies and more screech peaks appear in the facility at VKI than at LMFA. The screech is not captured in the numerical simulations. The initial conditions used for this LES, a poor discretization of the nozzle lip, and the fact that the interior of the nozzle is not modeled [81, 203, 80, 66] are the key points for not obtaining screech. Moreover, some other factors could have influenced the lack of screech. For example, not having enough simulation time in order to develop the feedback loop required for screech to appear, or an excessive dissipation caused by the sixth-order spatial filter.

In this section, two numerical and two experimental far-field noise spectra are compared. Geometrical differences in the nozzles, different experimental setups and slightly different working conditions as well as different dimensions and characteristics of the anechoic rooms can result in the differences observed in the comparison. If the impact of the different anechoic rooms is important, it could not be captured by CFD simulations because only a small part of the experimental setup is simulated. The numerical results are computed with two different solvers with different meshes and numerical schemes. The mesh cut-off frequency limit drastically impacts the higher frequencies and extra care should be taken when defining the mesh or positioning of the FWH surfaces in the domain to try to capture as much as possible of the physics of interest. The difference between the numerical results in amplitude for the lower frequencies is believed to come from the difference in the azimuthal discretization of the mesh. The azimuthal discretization of the mesh for COSMIC has only 64 points in comparison with 256 for ***elsA***. This implies that the vortical structures are larger and may radiate more sound at the lower end of the spectrum. The effect on the shock-cell noise is yet to be studied.

5.3.4 Azimuthal modal analysis

In this section, the azimuthal modal analysis discussed in Sec. 3.3.3 is applied to the pressure signal from the single jet. First, the focus is drawn to the near-field pressure at the nozzle exit plane, then the study is extended to the evolution in the axial direction of the different azimuthal modes.

Even though screech does not develop in the simulations, some phenomena related to screech is captured. The total power spectral density (PSD) contained at the plane $z = 0$, *i.e* the sum of the PSD at every location in space $[x, y]$ for each frequency is shown in Fig. 5.16. A peak is found at $St = 0.62$, close to the experimental screech main tone ($St = 0.65$) from LMFA [17] as illustrated in Fig. 5.15. This Strouhal number and its vicinity are the focus of this section. A supersonic under-expanded screeching jet would show a similar amplitude in the screech (and some of its harmonics) for a wide range of angular positions (as it can be seen in the experimental results from Fig. 5.15). However, in order for the screech to occur, the feedback loop must be initiated with a strong noise radiation at 180° that will impact the region where the instabilities develop. In the following, the positions at $x/D = 0$ are studied to focus mainly on the acoustic perturbations without entering in the BBSAN main lobe region shown in the upstream angles of Fig. 5.15.

The PSD of the pressure is displayed in Fig. 5.17 for several Strouhal numbers and different radius at the exit plane. The position closer to the jet ($r/D = 1$), shows clearly the tonal noise that occurs at $St = 0.62$ and a secondary peak at $St = 0.65$ (Fig. 5.17 (a)). The intensity of these two peaks is attenuated for the position $r/D = 2$ (Fig. 5.17 (b)) and non-relevant at

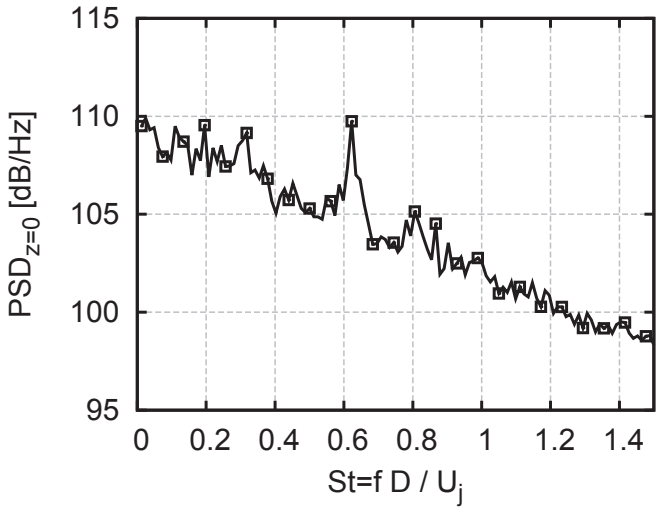

Figure 5.16: *Total PSD contained at the plane $z/D = 0$ for different frequencies*

$r/D = 3$ (Fig. 5.17 (c)) which is in agreement with a high upstream directivity ($\theta \approx 180°$) of the perturbations. This highlights the possibility to obtain screech by increasing the mesh resolution near the nozzle lip, and modeling the interior of the nozzle.

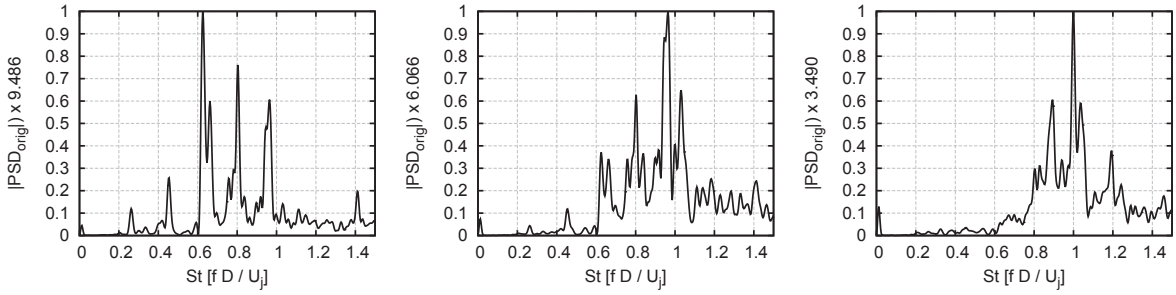

(a) (b) (c)

Figure 5.17: *PSD of the pressure at the positions $[x/D, r/D]$ **(a)** $[0, 1]$, **(b)** $[0, 2]$, **(c)** $[0, 3]$. The ordinate axis is scaled by the maximum value.*

The azimuthal modal decomposition of the pressure at the same positions is shown in Fig. 5.18. The perturbations reaching the nozzle exit are composed of different modes for a wide range of Strouhal numbers. Close to the axis (Fig. 5.18 (a),(d) and (g)), these modes alternate with the frequency. As explained for Fig. 5.17, although the modes are still distinguishable, an attenuation occurs at $x/D = 2$ (Fig. 5.18 (b),(e) and (h)). However, farther away from the axis at $x/D = 3$ (Fig. 5.18 (c),(f) and (i)), a position where the BBSAN starts to be important, the perturbations are composed of several superimposed modes for the frequency range of the shock-cell noise.

For the sake of clarity, the single values of the PSD are shown in Fig. 5.19 for the previous positions at the Strouhal numbers of interest 0.62 and 0.65. The dominant mode at $St = 0.62$ is fully axisymmetric (mode 0) whereas, at $St = 0.65$, there is a composition of axisymmetric

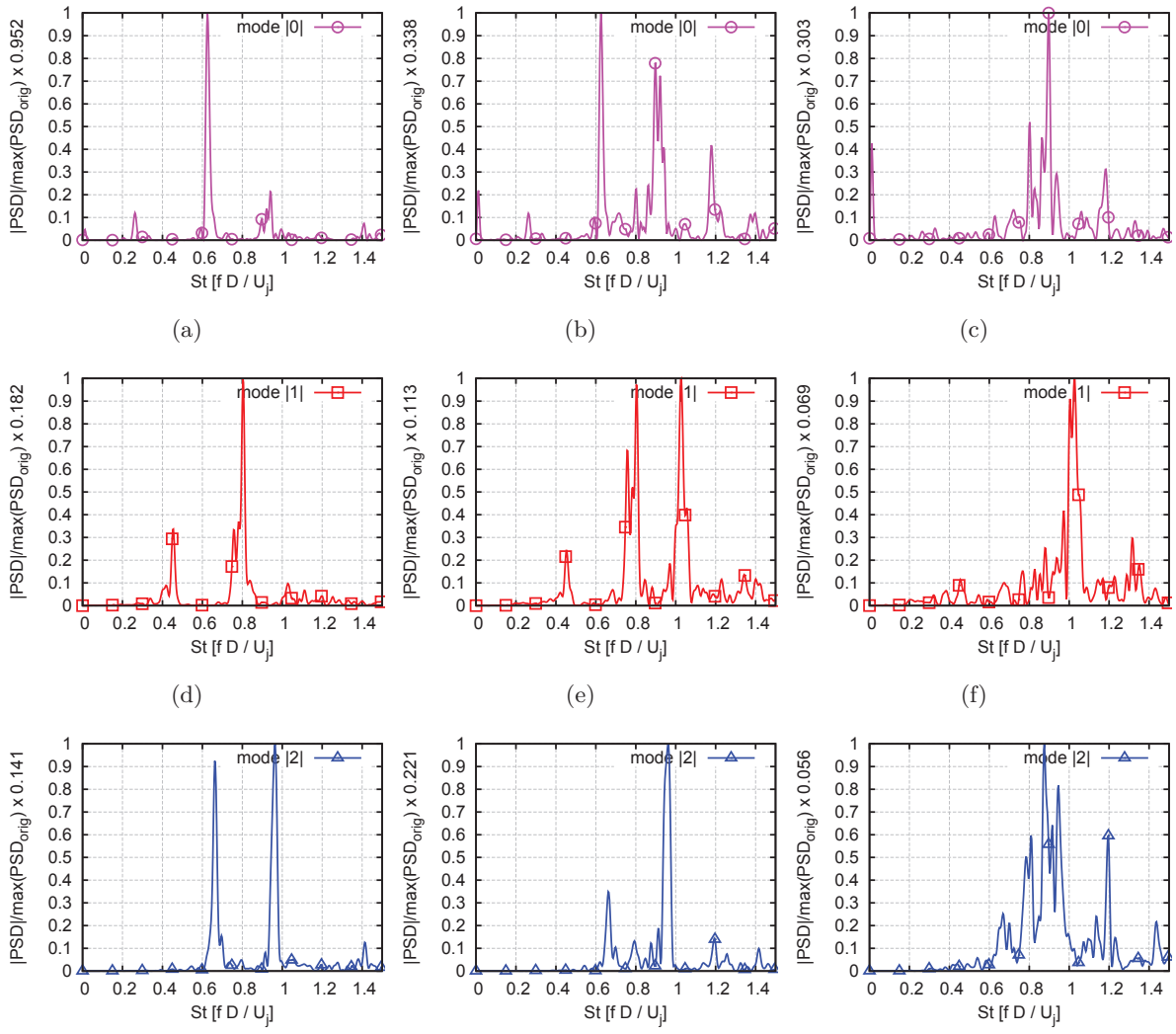

Figure 5.18: *PSD of pressure of the azimuthal modes at the positions* $(x/D, y/D) = (0, 1)$ *in* ***(a,d,g)****,* $(x/D, y/D) = (0, 2)$ *in* ***(b,e,h)*** *and* $(x/D, y/D) = (0, 3)$ *in* ***(c,f,i)****, where the PSD is averaged between positive and negative modes. The ordinate axis is scaled by the maximum value.*

and helical modes. At the first two positions (Fig. 5.19 (a) and (b)), the axisymmetric mode is dominant. However, at the farthest position (Fig. 5.19 (c)), the dominant mode changes to the second helical mode.

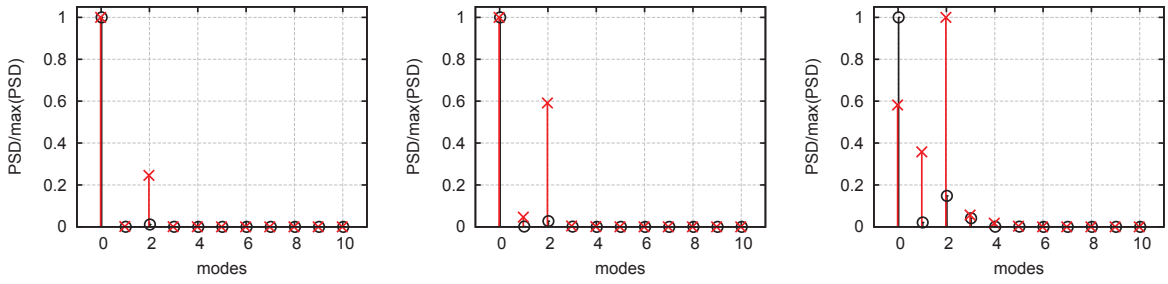

(a) (b) (c)

Figure 5.19: *PSD of pressure of the azimuthal modes at* $St = 0.62$ *and* $St = 0.65$ *in* ∘ *and* × *respectively at the positions* $(x/D, y/D) = (0, 1)$ *in* ***(a)***, $(x/D, y/D) = (0, 2)$ *in* ***(b)***, *and* $(x/D, y/D) = (0, 3)$ *in* ***(c)***, *where the PSD is averaged between positive and negative modes.*

Figures 5.17, 5.18 and 5.19 all show that the modes are distinct close to the jet axis and with the same order of magnitude otherwise. The PSD of the modes at the lip-line is displayed in Fig. 5.20 for both Strouhal numbers. At $St = 0.62$, the contribution of the axisymmetric mode 0 reaches the maximum at $x/D = 5$ and is dominant up to $x/D = 6$, farther downstream all the modes are mixed with the same order of magnitude. At $St = 0.65$, the dominance of the axisymmetric mode 0 is lost downstream of $x/D = 4$ in favor of the helical mode 2, reaching the maximum at $x/D = 6$, again, farther downstream all the modes are superimposed.

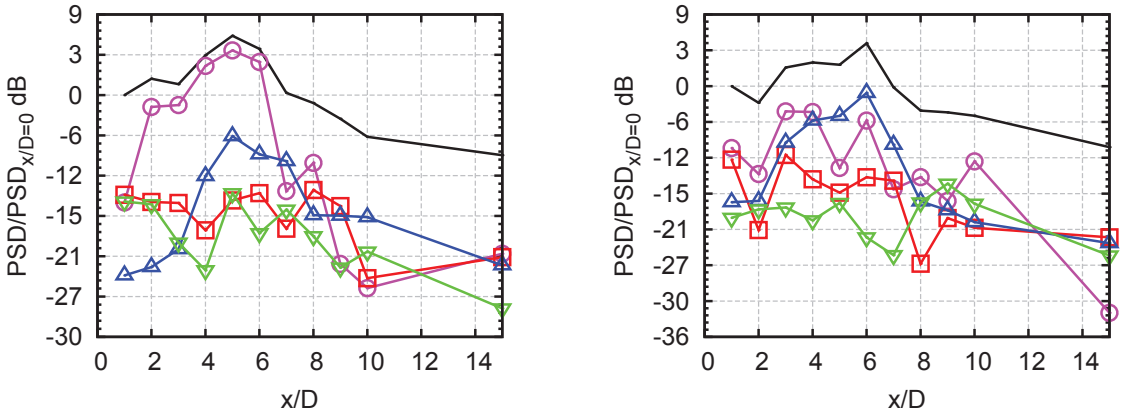

(a) (b)

Figure 5.20: *PSD of pressure of the azimuthal modes at* ***(a)*** $St = 0.62$ *and* ***(b)*** $St = 0.65$ *at* $y/D = 0.5$. *The complete signal is shown in solid black line. The modes 0, 1, 2 and 3 are shown as* ∘, □,△ *and* ▽ *respectively, where the PSD is averaged between positive and negative modes.*

The modal decomposition at the lip-line can be applied to the root-mean-square (*rms*) of the pressure in order to identify where these modes are contributing to the total spectra, or on this case, to the *rms* of the complete signal. Figure 5.21 (a) illustrates how the peak of the

mode 0 lays on $x/D = 5$ and the peaks of the higher modes lay on $x/D = 6$ in agreement with Fig. 5.20. Figure 5.21 (b) depicts that the behavior changes due to the BBSAN components that reach this region ($y/D = 3$). The peak of the mode 0 at $x/D = 4$, which corresponds to the peak shown in Fig. 5.21 (a) at $x/D = 5$ is almost dissipated, while the peaks of the other modes of the signal are clearly visible.

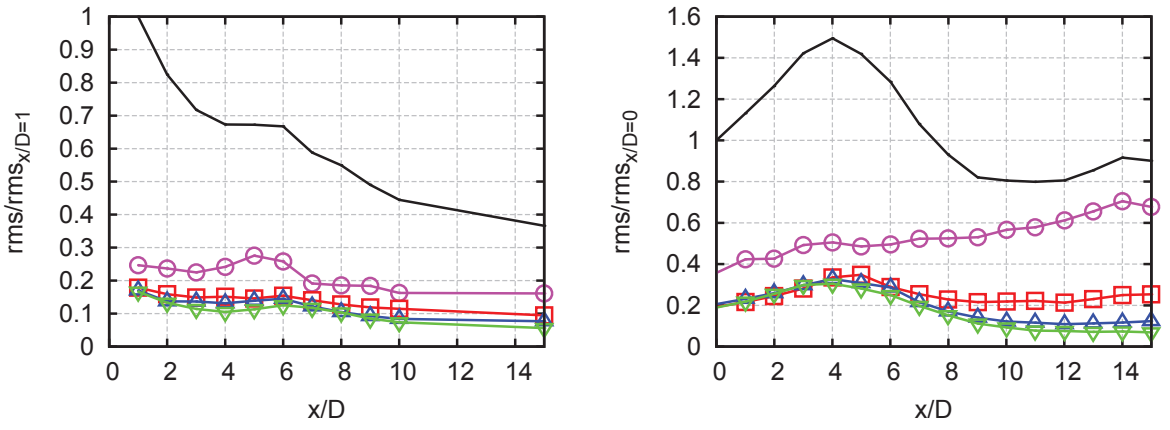

(a) (b)

Figure 5.21: *RMS of pressure of the azimuthal modes at* ***(a)*** $y/D = 0.5$ *and* ***(b)*** $y/D = 3$. *The complete signal is shown in solid black line. The modes 0, 1, 2 and 3 are shown as* ○, □,△ *and* ▽ *respectively, where the PSD is averaged between positive and negative modes.*

Finally, in order to visualize the axisymmetric and helical modes, the DFT modulus of the pressure at an axial plane at $x/D = 6$ is shown in Fig. 5.22 and 5.23 at the Strouhal numbers 0.62 and 0.65 respectively. Suda et al. [38] reported high oscillations of the shock-cells for a rectangular supersonic screeching jet. Figures 5.22 and 5.23 illustrate this mixed motion between axisymmetric and helical modes for a circular supersonic non-screeching jet. At $St = 0.62$ (Fig. 5.22) the central part of the jet and the tips of the shock-cells oscillate in time axisymmetrically with the same phase and an annular region near the position of $M = 1.0$ that is not excited at this frequency. The helical behavior at $St = 0.65$ (Fig. 5.23) is presented with a cloverleaf pattern that alternates from negative to positive phases on each lobe.

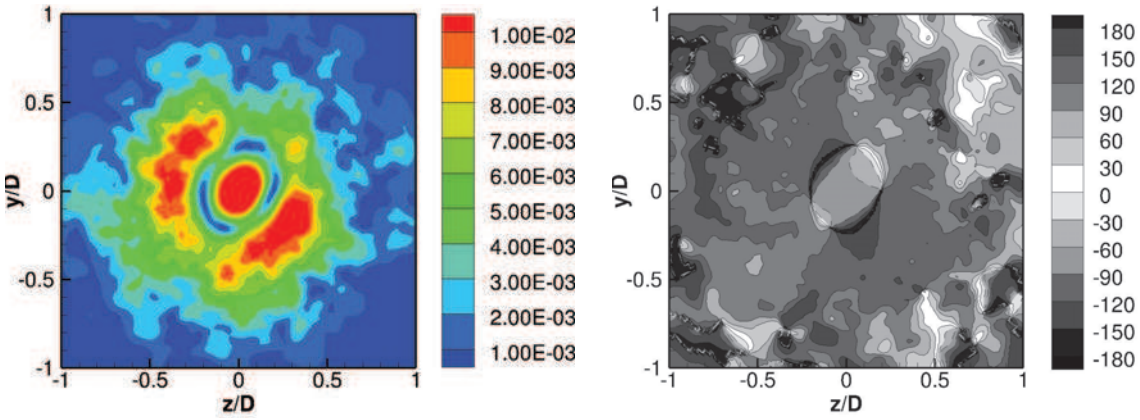

(a) (b)

Figure 5.22: ***(a)*** *DFT modulus of the non-dimensional pressure ($\hat{p} = p/p_{ref}/\gamma$) and* ***(b)*** *its phase at $St = 0.62$ at the plane $x/D = 6$. The negative values of the phase are represented with dashed isolines.*

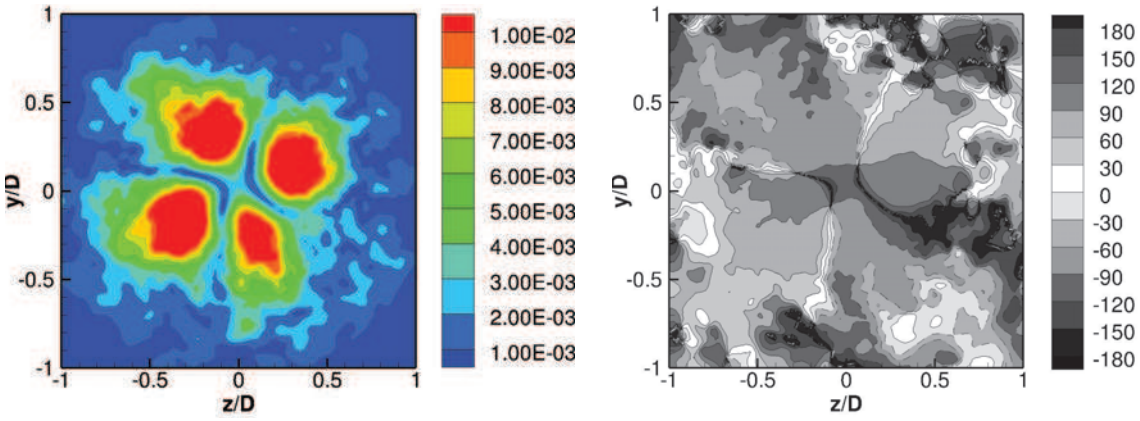

(a) (b)

Figure 5.23: ***(a)*** *DFT modulus of the non-dimensional pressure ($\hat{p} = p/p_{ref}/\gamma$) and* ***(b)*** *its phase at $St = 0.65$ at the plane $x/D = 6$. The negative values of the phase are represented with dashed isolines.*

5.3.5 Power spectral density axial distribution

The previous section showed how some regions of the shock-cell system are more excited at particular frequencies. This section studies in depth the different PSD energy distributions inside the jet.

The PSD of the pressure at the axis is displayed in Fig. 5.24 (a) and at $r/D = 1$ in Fig. 5.24 (b). The power spectral density at the axis illustrates the effect of the shock-cell system on the pressure. The vertical patterns correspond at each axial position where the maximum compression of the shock-cells is achieved. The horizontal patterns are detected at about $St \approx \{0.3, 0.6, 0.9\}$. The maximum of the energy spectrum is found about $x/D = 5$. At $r/D = 1$, there is a similar shape than the one of the near-field at $r/D = 3$ (see Fig. 5.11). Moreover, some traces of the frequencies with higher levels of PSD can be seen in the range $0 < x/D < 2$.

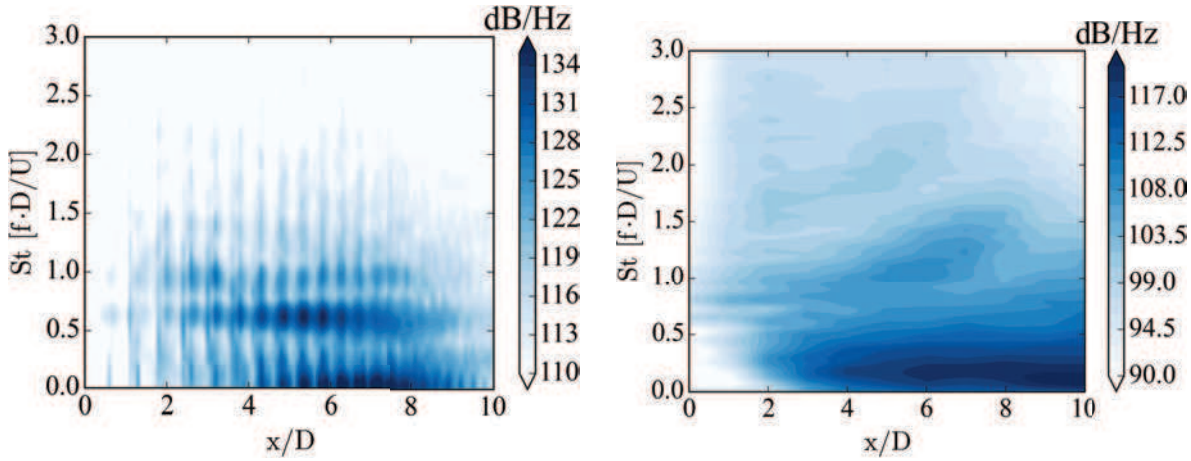

(a) (b)

Figure 5.24: *Frequency-space pressure energy distribution along the axial direction for the data set* ***(a)*** *at the axis and* ***(b)*** *at* $r/D = 1$.

If the azimuthal decomposition is performed on the array located at $r/D = 1$ the different excited frequencies can be separated in azimuthal modes. Similarly to what is shown in Sec. 5.3.4, characteristic frequencies are found for different azimuthal modes. Figure 5.25 displays the energy contribution of each azimuthal mode. In all of them, a distinguishable "banana-like" shape [197] is detected, that corresponds to the shock-cell noise as it was depicted in Fig. 5.11. For each mode, there are some frequencies that are more excited than others. Mode 0 has peaks for Strouhal numbers $St \approx \{0.57, 0.91, 1.16\}$, mode 1 at $St \approx \{0.74, 1.05\}$, mode 2 at $St \approx \{0.61, 0.91\}$ and mode 3 at $St \approx \{0.80, 1.09\}$. All modes present peaks at frequencies that are separated by a small $\Delta\ St$ ranging from 0.25 to 0.34.

In order to study in more detail the different peaks, the signal comprised in the region within the shock-cells is transformed into the frequency-wavenumber domain. The transformation at the axis is shown in Fig. 5.26 (a) and at the lip-line in Fig. 5.26 (b). Both locations illustrate that the excited tones previously found are in fact mainly in the negative part of the axial wavenumber and travel at a group velocity between $U_c - a$ and a_∞. This indicates that the axis and the lip-line are capturing a negative traveling pressure wave even when the flow is supersonic. This can be explained taking into account the upstream directivity of the

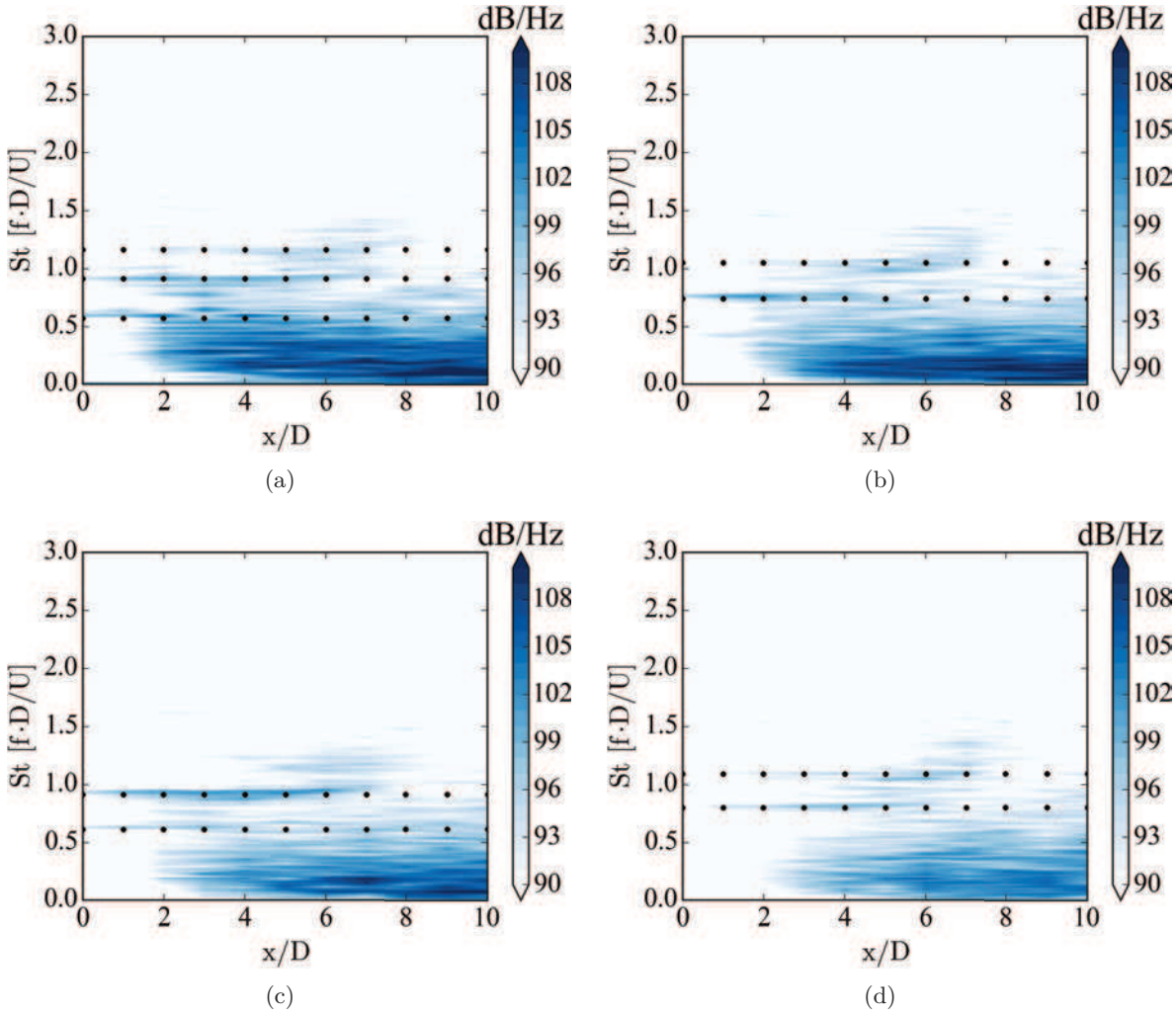

Figure 5.25: *Frequency-space pressure energy distribution along the axial direction for the data set at $r/D = 1$ for the azimuthal modes:* ***(a)*** *mode 0,* ***(b)*** *mode 1,* ***(c)*** *mode 2 and,* ***(d)*** *mode 3. The horizontal dotted line highlights the frequencies of interest.*

shock-cell noise.

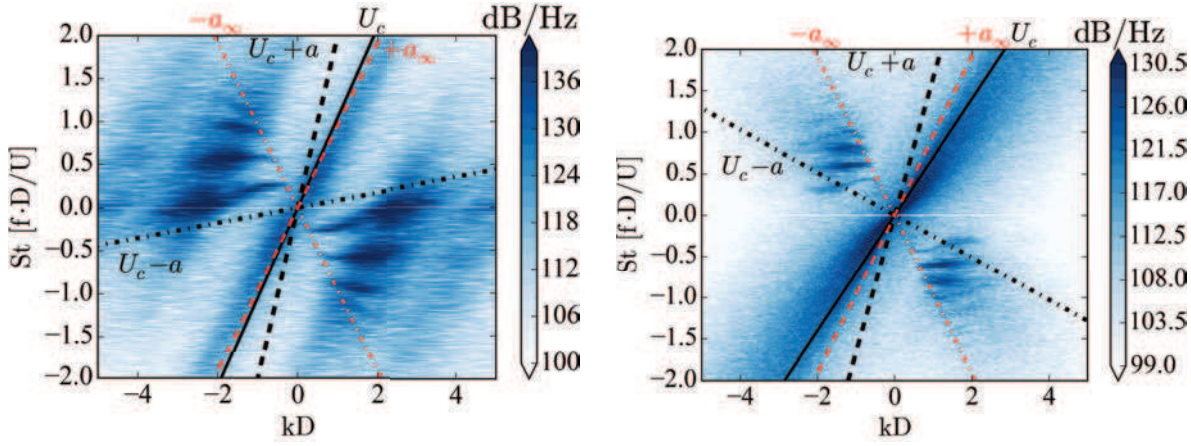

Figure 5.26: *Frequency-wavenumber energy distribution along the axial direction for the pressure* ***(a)*** *at the axis and* ***(b)*** *at the lip-line.*

Figure 5.27 shows a snapshot of a DNS from Daviller [204] of a two-dimensional interaction of a spatially developing mixing-layer with a compression wave separating a supersonic stream at $M = 1.2$. In Fig. 5.27, the shock-cell noise that is convected outside the jet at the ambient speed of sound is also convected inside at an axial velocity of $\overline{U_j} - \overline{a_\infty}$, the jet being supersonic, deforms the perturbation in the axial direction displacing it downstream locally. However, due to the fact that the origin of the perturbation in the shear-layer is moving upstream it creates an oblique front wave that is seen by an axial array of probes to travel upstream at a speed $\overline{a_\infty}\hat{\mathbf{e}}_\mathbf{x}$ as sketched in Fig. 5.28.

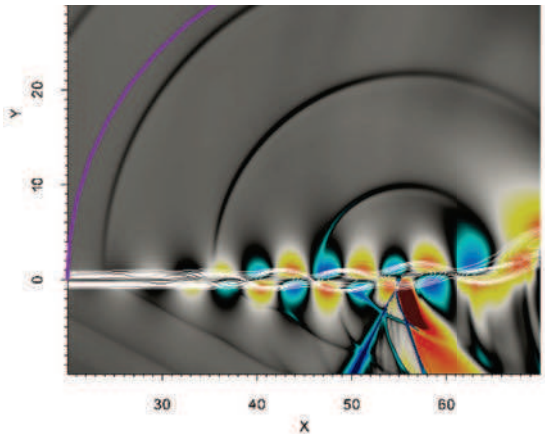

Figure 5.27: *Shock-leakage mechanism represented by an isosurface of the dilatation field (colors) and contours of vorticity (white lines) from [204]*

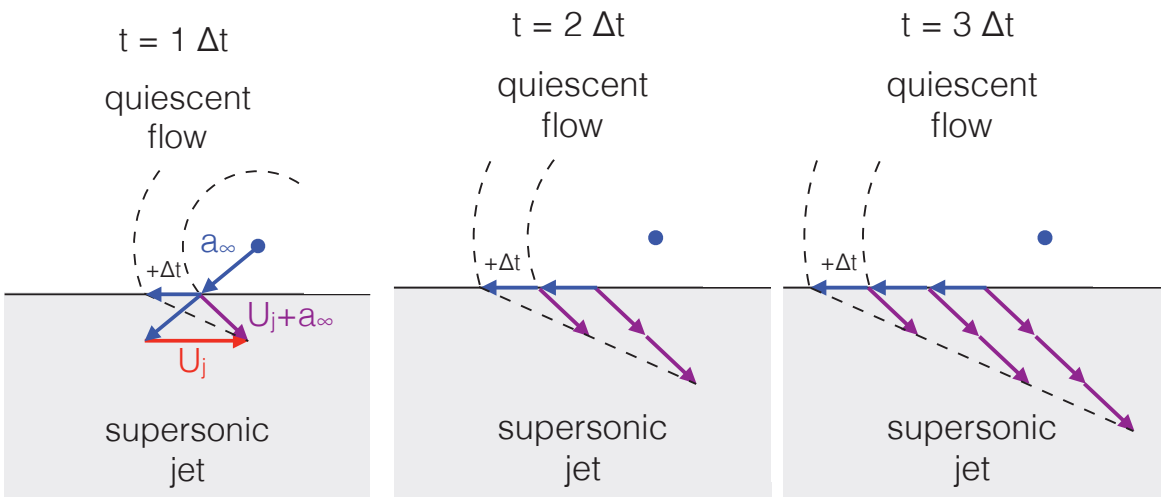

Figure 5.28: *Evolution of a negative traveling front wave inside a supersonic jet.*

5.3.6 Wavelet analysis

The wavelet based methodology described in Ch. 4 used to identify and extract the characteristic events of the flow is utilized here for the supersonic under-expanded single jet. In this section, the procedure is applied at different scales (or equivalent frequencies) and the events are located based on the energy criteria identified as SIG95 with a background red noise. The mother wavelet used in this case of study is the DOG mother wavelet as it presented the higher number of events necessary for a good convergence of the signatures. Unfortunately, this mother wavelet makes it difficult to identify different events that have similar scales and so, the events obtained probably are an average of different events captured at other scales. Here, the events are filtered over a temporal window that corresponds to $2.5D/U_j$ dimensionless time units.

In order to identify the events corresponding to the negative and positive traveling pressure waves shown in Sec. 5.3.5 separately, the signal was reconstructed using only the positive or negative regions of the spatial wavenumber kD from Fig. 5.26. The wavelet transform and the event identification procedure are then applied to the original axial velocity, the reconstructed negative traveling and positive traveling pressure waves of the data sets AXIS, LIP_LINE and NF1D. Moreover, a comparison is done against the results obtained with the acoustic filtered pressure and the negative traveling pressure for the data set NF1D.

As explained in Sec. 4, the cross-conditioning needs two different variables, the reference or conditioning variable and the plotting variable. The reference or conditioning variable is set in order to detect the events and the plotting variable is the one that is averaged. As an example, the axial velocity can be used as reference variable to detect the events, but the average is performed using the pressure. Here, the conditioning variables are the axial velocity, the negative traveling pressure and the positive traveling pressure, on the other hand, the plotting variables are the axial velocity and the original pressure signal. In this example, it means that the pressure plots are conditioned by the axial velocity. Even if the acoustic-hydrodynamic filtering or the separation of negative and positive traveling waves is inaccurate due to the linear

behavior of the procedure, the cross-conditioning averages the original variables, minimizing associated problems.

Axis probes analysis

First the results at the axis are analyzed as follows. Figure 5.29 shows the cross-conditioning in space (in the range $0 < x/D < 10$) of the above-mentioned variables of the events captured at $x/D = 5$, that is the position where the maximum energy is found according to Fig. 5.24 (a). The event localization at $x/D = 5$ gives as output a list with the positions in time where the peaks of the events are located. The cross-conditioning in space is done by averaging the values corresponding to the time list at all axial positions. The signature computed from the cross-conditioning is illustrated in solid line. Moreover, in Fig. 5.29, the envelope of the event is depicted by the dashed line. The envelope corresponds to the maxima and minima of the signatures, captured at all axial positions. The thin gray vertical lines represent the position of the expansion peak of the shock-cells. The scale used for the averaging corresponds to a $St(s) = 0.6$, that is the Strouhal number for which the higher energy content is identified at the axis. In addition, Fig. 5.30 depicts the cross-conditioning in space at different times. Here, in order to recover a different time with respect to the list of times obtained with the procedure, a positive or negative Δt is applied to the list before the averaging of the windows. The envelope shown in Fig. 5.30 corresponds to the envelope of the evolution in time of the signature seen at $x/D = 5$. The upside down red triangle line represent the signature at $-1000\ \Delta t$, the solid black line is the actual time of the event, whereas the blue triangle line corresponds to the average at $+1000\ \Delta t$.

Figures 5.29 (a) and 5.29 (b) display the signatures computed with the axial velocity events for the axial velocity and the pressure respectively. The signature of the event detected in Fig. 5.29 (a) grows axially and has most of the peaks of the envelope at the expansion regions of the shock-cells. At $x/D = 5$, there is the maximum peak of the signature. Some other peaks are found farther downstream due to a poor averaging because of a lower number of events detected. From Fig. 5.30 (a) it can be seen that the signature moves downstream. The average speed of the signature corresponds to U_j. Moreover, the signature obtained for the pressure (Fig. 5.29 (b)) shows that the pressure related to these events decays after $x/D = 6$ to a small value at $x/D = 10$ even when the envelope for the axial velocity is the maximum. As it can be seen from these figures, the axial velocity and the pressure are shifted in phase by π rad meaning that a positive amplitude in the velocity correlates with a negative amplitude for the pressure. The pressure signature seems to move upstream in Fig. 5.30 (b).

Similarly, the signatures obtained with the negative traveling pressure events are illustrated in Fig. 5.29 (c) and (d) plotting respectively, the axial velocity and the pressure. In this case, the axial velocity envelope shown in Fig. 5.29 (c) remains fairly constant after $x/D = 6$ compared to the growing envelope in Fig. 5.29 (a). The cross-conditioning with the original component of the pressure displayed in Fig. 5.29 (d) presents a maxima around $x/D = 5$ (as in Fig. 5.29 (b)). The amplitudes of the signatures exhibit a bias for the positive values. Here, due to the fact that the events were extracted using the negative traveling pressure variable, both signatures move upstream as it is shown in Fig. 5.30 (c) and Fig. 5.30 (d). This signature corresponds to the shock-cell noise that enters the jet as explained in Sec. 5.3.5 because it is the only signal that travels upstream.

Last, the signatures obtained with the positive traveling pressure events are displayed in Fig. 5.29 (e) and (f). The signatures for the axial velocity exhibit a similar envelope than the one calculated with the negative traveling pressure even though the signature itself has a different shape with less oscillations. For both the axial velocity and the pressure, the signatures have the peak slightly shifted from the position where the event was detected. Figure 5.30 (e) shows that the signature computed for the axial velocity moves downstream while from Fig. 5.30 (d) the direction of the pressure signature is not clear. The inaccuracy of these signature could mean that the number of events detected with the positive traveling pressure is not enough to have a converged signature or that the distinction between the positive and the negative events is not fully accurate.

Following the observations at the axis, the cross-conditioning can be applied over a two-dimensional or a three-dimensional field. Due to the storage cost of saving the three-dimensional field, here, only the two-dimensional cuts were used for the cross-conditioning. The average of the snapshots is done taking both the planes $z/D = 0$ ($y/D > 0$ and $y/D < 0$) and $y/D = 0$ ($z/D > 0$ and $z/D < 0$) increasing the convergence of the signature. A signature can be said to be converged if the normalized modulus by the standard deviation is greater than 1 and there are enough snapshots to average out the other turbulence scales, *i.e.* the normalized amplitudes are close to zero outside of the region of influence of the signature. Figures 5.31, 5.32, 5.33 show the signatures of the cross-conditioning obtained in a two-dimensional cut where the reference events are detected at the same position of the previous analysis ($r/D = 0$ and $x/D = 5$). The black solid line represents the sonic Mach number. Here, the results are non-dimensionalized by the local standard deviation in order to allow for a better discrimination of the effect of the event. The reader should take into account that the amplitude of the hydrodynamic pressure inside the jet differs by several orders of magnitude with respect to the acoustic component propagated outside. On the other hand, the previous results from Fig. 5.29 and Fig. 5.30 were in dimensional units to illustrate the decay of the signatures along the axial direction.

The two-dimensional signatures obtained with the axial velocity events are shown in Fig. 5.31 (a) and (b) plotting respectively, the axial velocity and the pressure. The signatures for the axial velocity (Fig. 5.31 (a)) illustrate the movement of the shock-cells inside the potential core. The shear-layer is well captured but no clear structures are visible from the cross-conditioning. The pressure signature (Fig. 5.31 (b)) exhibits a similar pattern inside the potential core with inverse colors as it was shown in Fig. 5.29 (b). Some structures are visible outside the potential core but they are not fully converged. On the upstream region, on top of the nozzle, some pressure waves can be discerned but they also present a lack of convergence.

The two-dimensional signatures obtained with the negative traveling pressure events are depicted in Fig. 5.32 (a) and (b) plotting respectively, the axial velocity and the pressure. From the axial velocity signature shown in Fig. 5.32 (a), it can be seen that the patterns inside the potential core are merged with the external velocity diagonally at $x/D = 5$ with a negative peak, and at $x/D = 4$ with a positive peak. The pressure signature presents a pattern inside the potential core and another outside the potential core with opposite amplitudes that extend up to $r/D = 1$. The pressure waves are being convected upstream inside the potential core (as in Fig. 5.28). Because they are being convected diagonally, the positive region of the external pressure wave lays on top of the negative pressure wave which gives this distinctive checkerboard pattern. The diagonal pattern can be clearly seen close to the nozzle, where the jet is

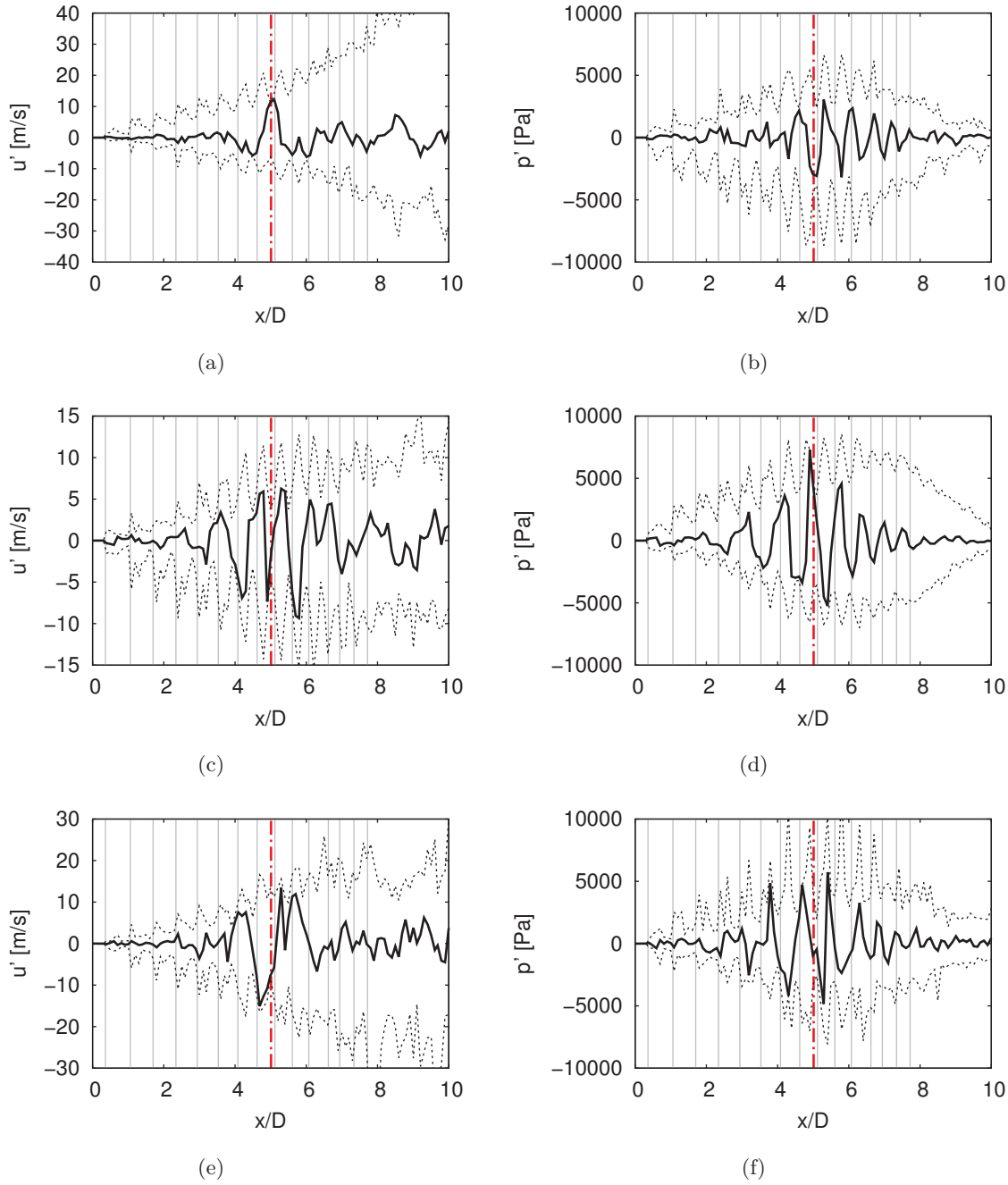

Figure 5.29: *Cross-conditioning of* ***(a)*** $u-u$, ***(b)*** $u-p$, ***(c)*** $p_{neg}-u$, ***(d)*** $p_{neg}-p$, ***(e)*** $p_{pos}-u$ *and* ***(f)*** $p_{pos}-p$ *from AXIS where the first variable is the one used to locate the events and the second variable is the one plotted. The dash black line represents the envelope of the signature for all axial positions. The vertical dashed line represents the axial position where the events are located and the vertical thin solid line represent the axial location of the shock-cells.*

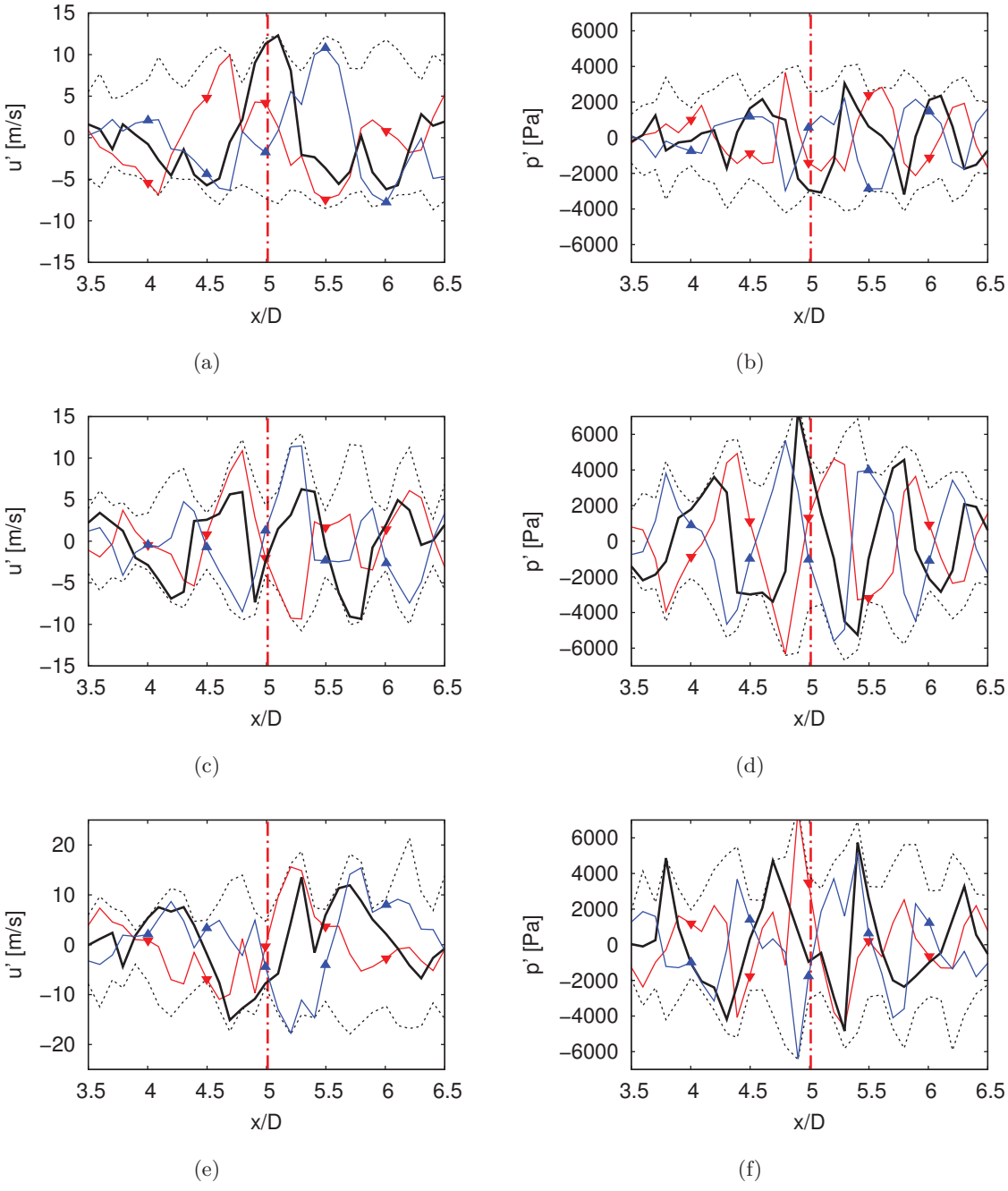

Figure 5.30: *Cross-conditioning of* ***(a)*** $u-u$, ***(b)*** $u-p$, ***(c)*** $p_{neg}-u$, ***(d)*** $p_{neg}-p$, ***(e)*** $p_{pos}-u$ *and* ***(f)*** $p_{pos}-p$ *from AXIS where the first variable is the one used to locate the events and the second variable is the one plotted. The upside down red triangles represent the signature at* $t = t_{ref} - 1000\ \Delta t$, *the black solid line at* $t = t_{ref}$ *and in blue triangles at* $t = t_{ref} + 1000\ \Delta t$. *The dash black line represents the envelope of the signature for all shifted times. The vertical dashed line represents the axial position where the events are located.*

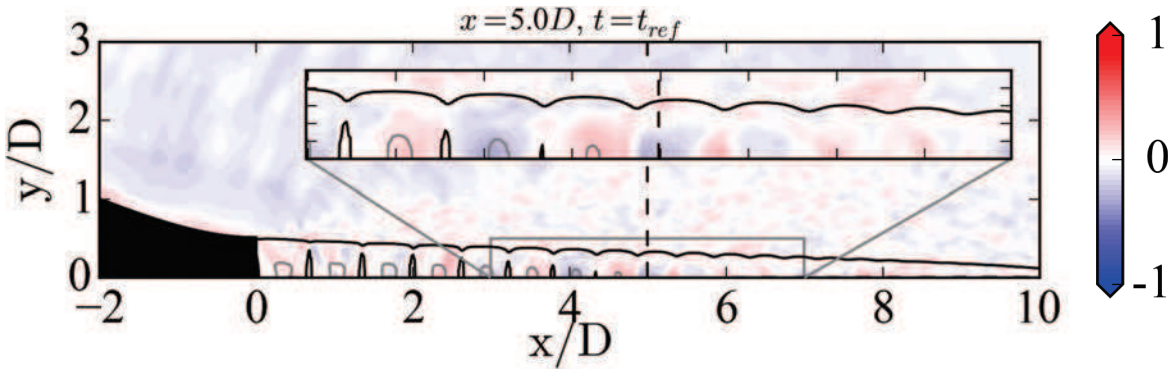

(a)

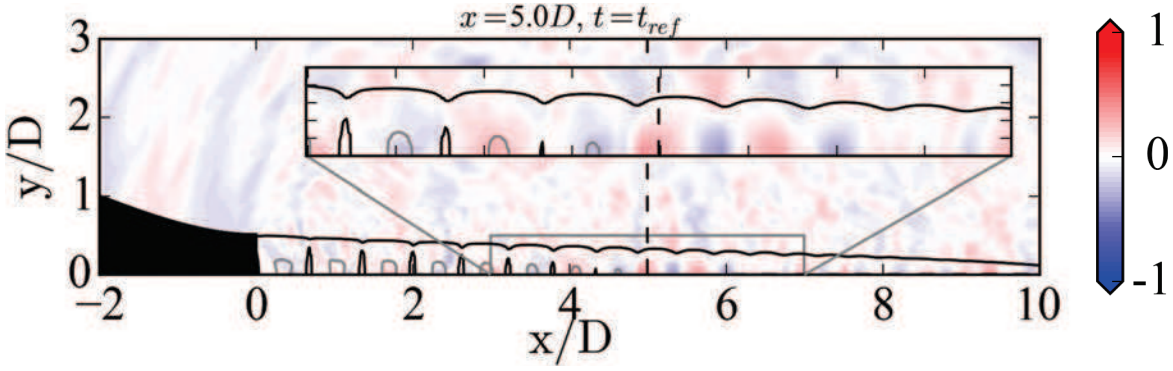

(b)

Figure 5.31: *Two-dimensional cross-conditioning of* ***(a)*** $u-u$ *and* ***(b)*** $u-p$*, from the axis where the first variable is the one used to locate the events and the second variable is the one plotted. The black solid lines represent the Mach number contours above 1. The vertical dashed line represents the location in space at the axis of the reference point.*

fully laminar. Outside the nozzle, the shock-cell noise peaks at $St = 0.6$ which corresponds to the one used to select the scale in the event detection procedure.

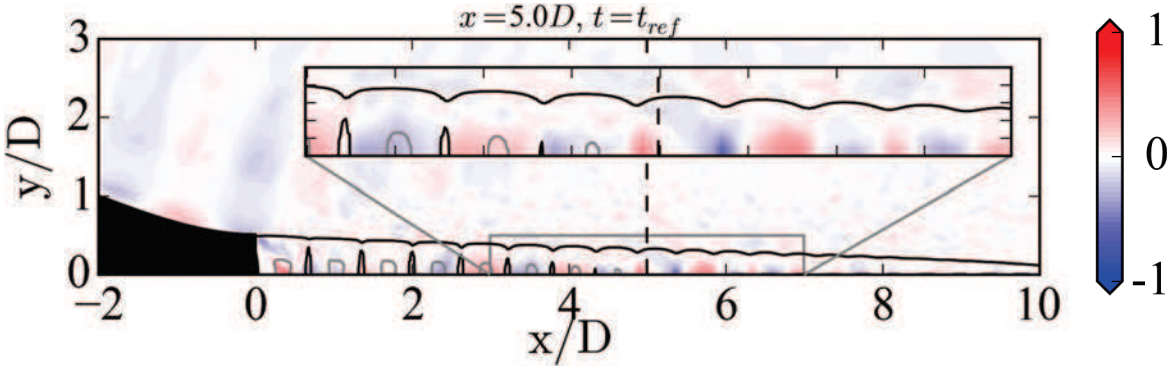

(a)

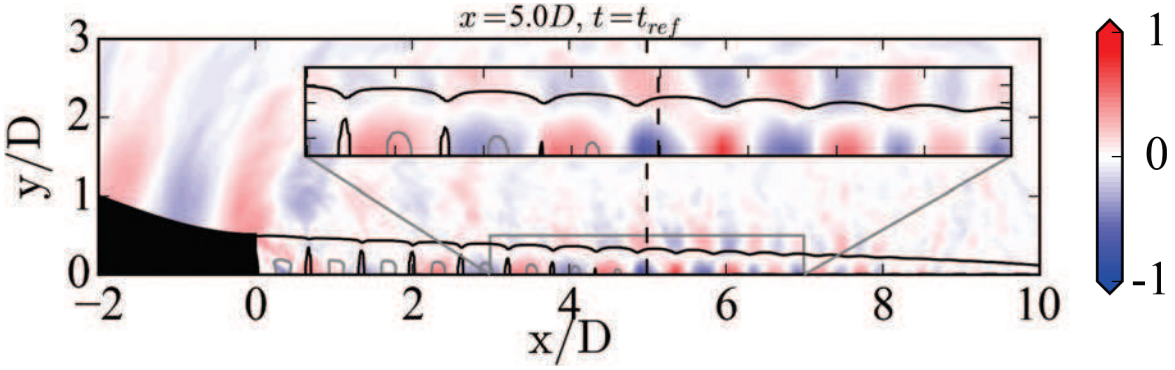

(b)

Figure 5.32: *Two-dimensional cross-conditioning of* ***(a)*** $p_{neg} - u$ *and* ***(b)*** $p_{neg} - p$*, from the axis where the first variable is the one used to locate the events and the second variable is the one plotted. The black solid lines represent the Mach number contours above 1. The vertical dashed line represents the location in space at the axis of the reference point.*

As it can be seen in Fig. 5.33 (a), the cross-conditioning between the positive traveling pressure waves and the velocity gives a similar noisy image in the two-dimensional cut than in the axis (Fig. 5.29 (e)). Some patterns are recognizable, however their normalized amplitude is close to zero which means that they are not too significant. On the other hand, the cross-conditioning between the positive traveling pressure waves and the pressure gives a similar pattern inside the potential core and over the nozzle as the one obtained for the negative traveling pressure waves. Moreover, outside the jet, a pattern of positive traveling waves is discerned. These pressure waves actually travel at the convective velocity of the vortices convected downstream.

Lip-line probes analysis

The same analysis that was carried out for the probes at the axis can be done for the probes located at the lip-line ($r/D = 0.5$). However, in order to ease the lecture of the manuscript, here only the two-dimensional cross-conditioning plots are shown in Fig. 5.34, Fig. 5.35 and Fig. 5.36. For this data set, the solution is averaged as well over the cuts in $z/D = 0$ and

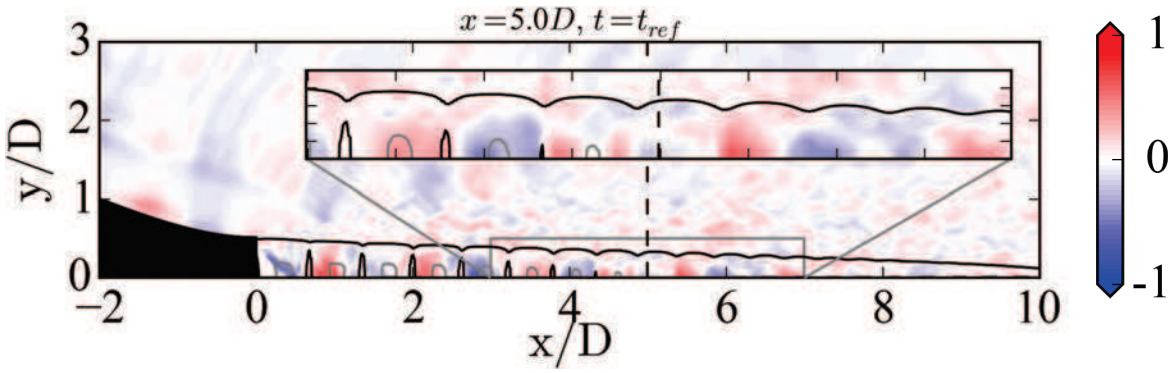

(a)

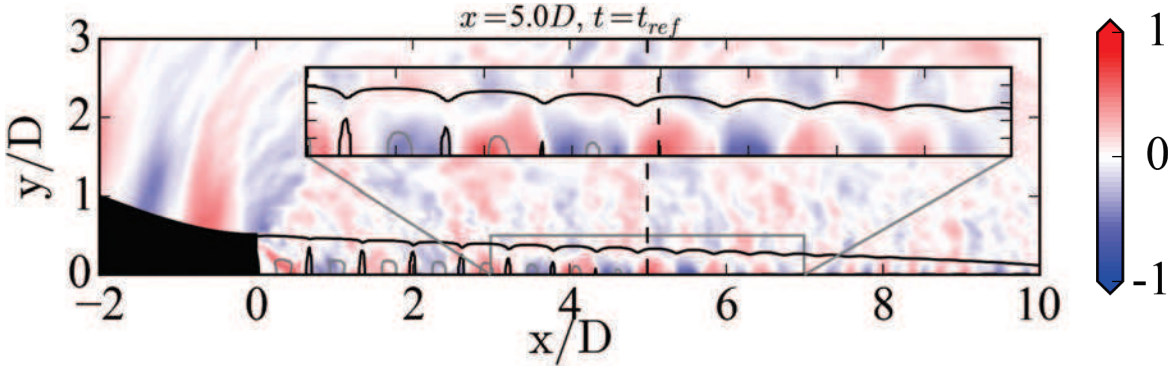

(b)

Figure 5.33: *Two-dimensional cross-conditioning of* ***(a)*** $p_{pos} - u$ *and* ***(b)*** $p_{pos} - p$ *from the axis where the first variable is the one used to locate the events and the second variable is the one plotted. The black solid lines represent the Mach number contours above 1. The vertical dashed line represents the location in space at the axis of the reference point.*

$y/D = 0$, however, due to the fact that the position $r/D = 0.5$ and $x/D = 5$ where the events are detected lays on four different azimuthal positions, each of them, is treated independently before doing the average. This means that the list of times obtained for the event identification differs for the 4 azimuthal positions. Nonetheless, using the same scale implies that the events identified correspond to the same characteristic Strouhal number. For events related to an axisymmetric mode, they should have similar detection times.

The two-dimensional signatures obtained with the axial velocity events are shown in Fig. 5.34 (a) and (b) plotting respectively, the axial velocity and the pressure. Contrary to the results at the axis illustrated in Fig. 5.31 (a), at this location a clear signature of the structures traveling downstream is visible. These structures are elongated by the differences in velocity in the shear-layer, having a higher convective velocity near the jet. Radially, these structures extend half a diameter whereas axially, they extend about 1.8 D for a full period. The signature obtained for the pressure shown in Fig. 5.34 (b) present structures that are extended radially over the shear-layer. The signature captures an interaction between the downstream shock-cells and its shear-layer with patterns that extend from the axis to $r/D = 1$.

The two-dimensional signatures computed with the negative traveling pressure events are displayed in Fig. 5.35 (a) and (b) plotting respectively, the axial velocity and the pressure. The signature obtained for the axial velocity (Fig. 5.35 (a)) exhibits the same pattern inside the potential core for $x/D < 4.5$. Farther downstream, the pattern stretches to the axis and a similar pattern with opposite amplitude is found that extends from $r/D = 0.2$, inside the shock-cells to $r/D = 0.7$. The same pattern can be seen with more detail when plotting the pressure as shown in Fig. 5.35 (b). The maximum of the pattern is located at the sonic line (noted with the black solid line) which suggests that the perturbation is generated at this location. Contrary to the signatures obtained with the events detected at the axis, the secondary pattern formed outside the potential core extends up to $r/D = 2$ and it is clearly propagated upstream.

Last, the results of the two-dimensional signatures computed with the positive traveling pressure events are shown in Fig. 5.36 (a) and (b) plotting respectively, the axial velocity and the pressure. The axial velocity displayed in Fig. 5.36 (a) presents a pattern in the lip-line that again seems to be stretched from the axis. Outside the shear-layer, the pattern is found but it is disconnected to the pattern in the lip-line by the shear-layer. On the other hand, the pressure displayed in Fig. 5.36 (b) exhibits the same pattern but connected through the shear-layer. This last signature identifies the influence of the pressure in the near-field of the vortical structures convected downstream through the shear-layer.

Near-field probes analysis

Finally, the two-dimensional cross-conditioning is shown in Fig. 5.37 and Fig. 5.38 for the results obtained in the near-field. The pressure data of the array of probes situated at $r/D = 1$, $x/D = 0$ with an expansion angle of 5° is filtered using the acoustic-hydrodynamic filtering from Sec. 3.3.2 and between negative and positive traveling pressure waves. At this location, due to the fact that the velocity is negligible as it is located outside the jet shear-layer, the signatures computed with the axial velocity events are omitted in the analysis.

Figure 5.37 (a) and (b) display the results obtained for the negative traveling pressure waves. A comparison between both filtered variables is shown in Fig. 5.39 and discussed in the fol-

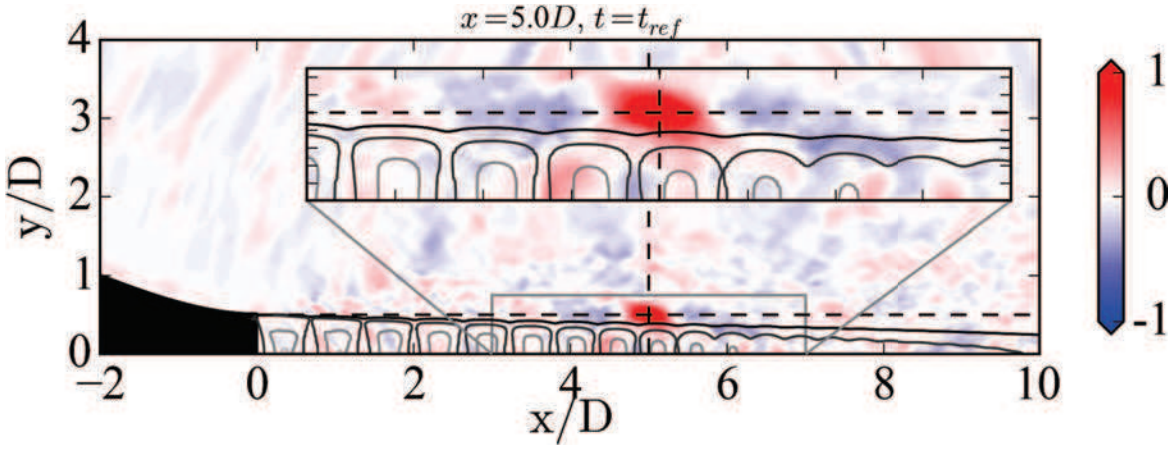

(a)

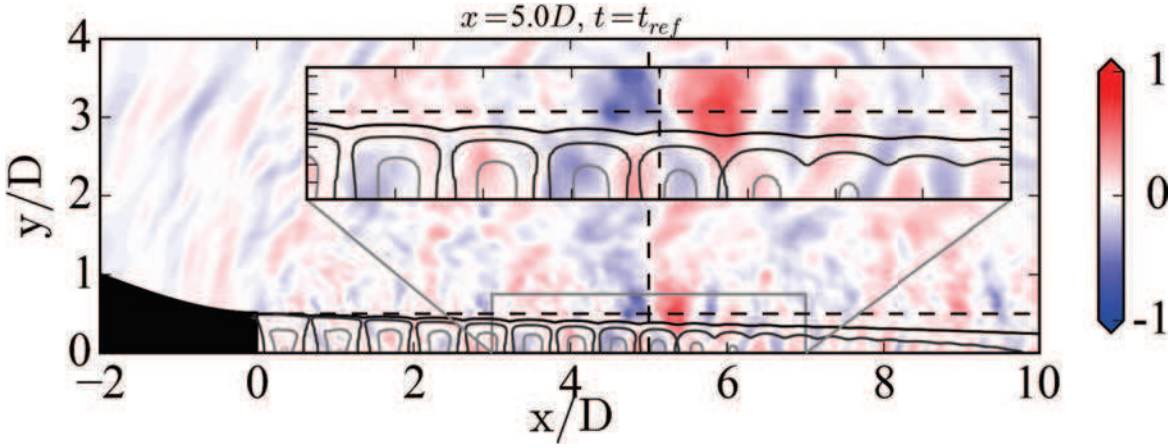

(b)

Figure 5.34: *Two-dimensional cross-conditioning of* ***(a)*** $u-u$ *and* ***(b)*** $u-p$*, from the lip-line where the first variable is the one used to locate the events and the second variable is the one plotted. The black solid lines represent the Mach number contours above 1. The intersection of the dashed lines represents the location in space of the reference point.*

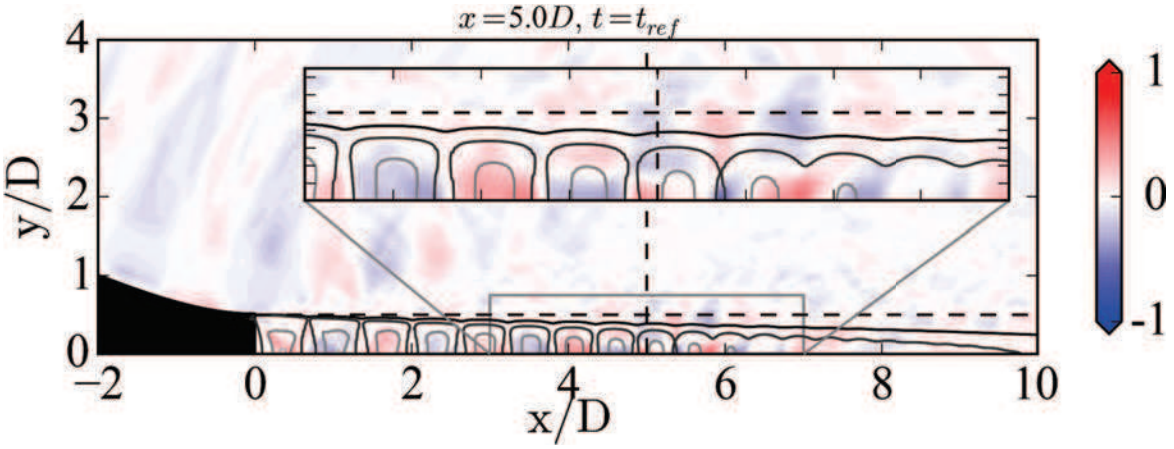

(a)

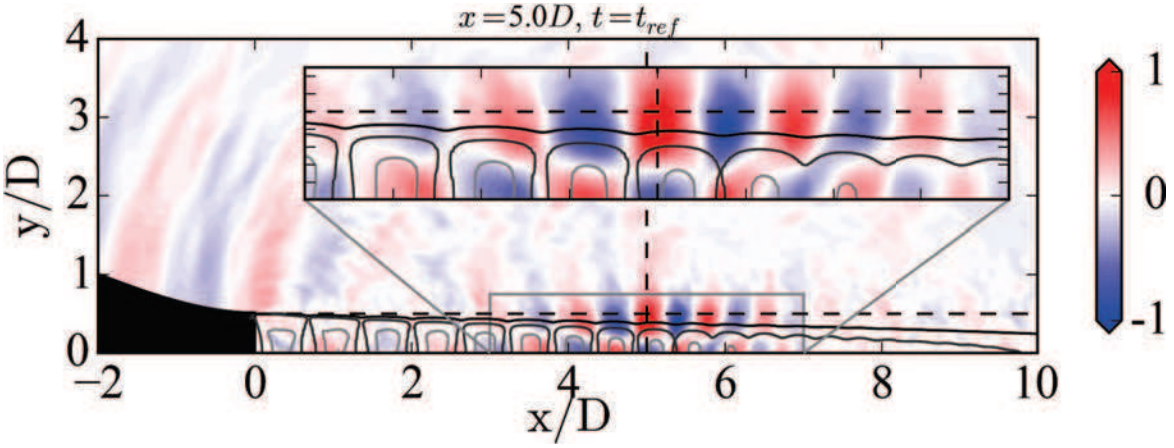

(b)

Figure 5.35: *Two-dimensional cross-conditioning of* ***(a)*** $p_{neg} - u$ *and* ***(b)*** $p_{neg} - p$*, from the lip-line where the first variable is the one used to locate the events and the second variable is the one plotted. The black solid lines represent the Mach number contours above 1. The intersection of the dashed lines represents the location in space of the reference point.*

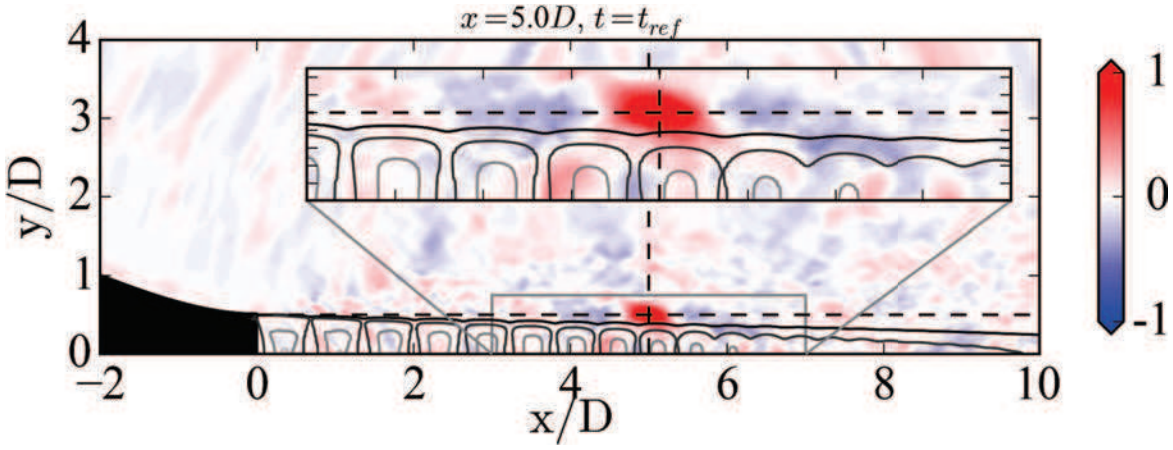

(a)

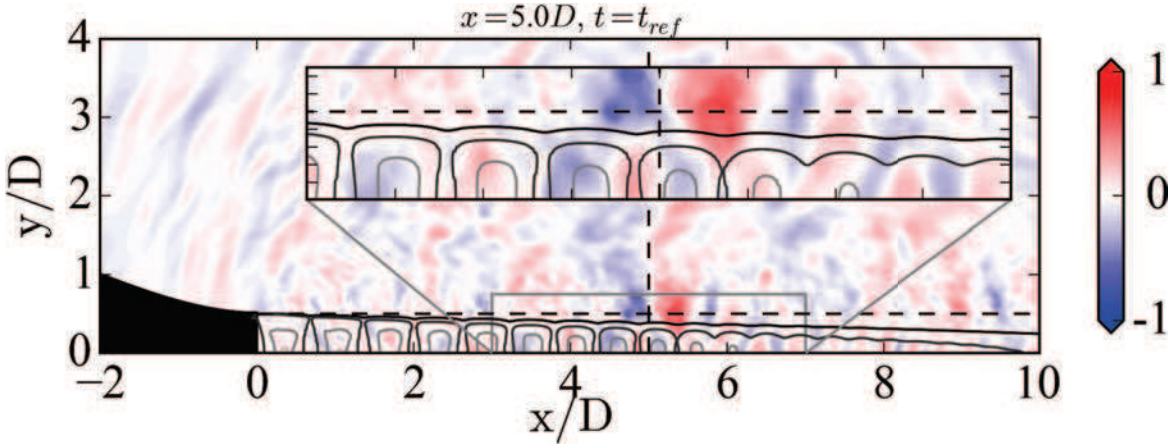

(b)

Figure 5.36: *Two-dimensional cross-conditioning of* **(e)** $p_{pos} - u$ *and* **(f)** $p_{pos} - p$ *from the lip-line where the first variable is the one used to locate the events and the second variable is the one plotted. The black solid lines represent the Mach number contours above 1. The intersection of the dashed lines represents the location in space of the reference point.*

lowing. The signatures in the near-field computed with the negative traveling pressure or the acoustic component were calculated with the averaging of the events detected at the scale that corresponds to a $St(s) = 1.1$ which lays on the center of the shock-cell noise peak displayed in Fig. 5.11 (a) at $x/D = 4.5$. The cross-conditioning obtained with the positive traveling pressure events and the hydrodynamic events gives qualitatively identical results. Therefore, only the signatures computed with the positive traveling waves are illustrated in Fig. 5.38 (a) and (b). The scale used to compute the signatures from the hydrodynamic or positive traveling pressure events is set to $St(s) = 0.21$ which corresponds to the main Strouhal number of the hydrodynamic perturbations.

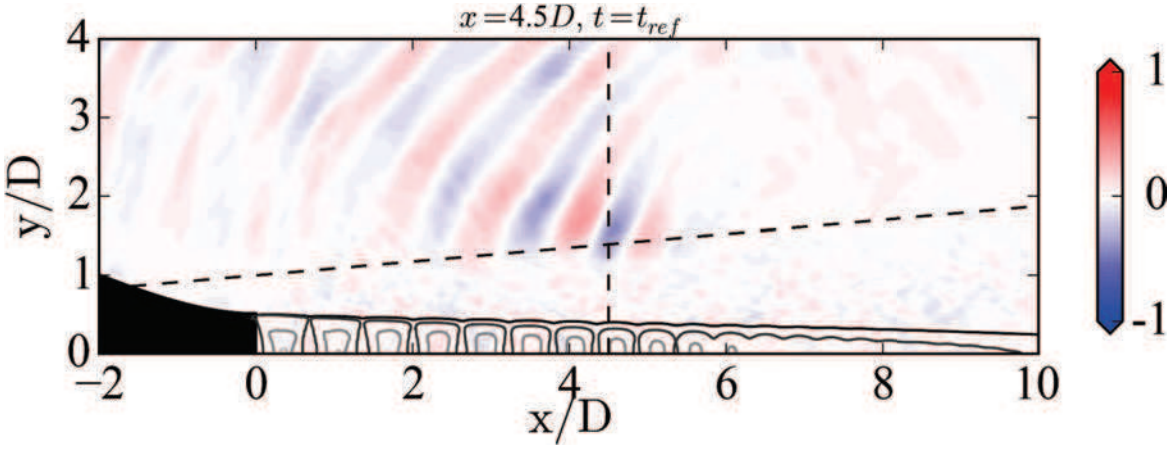

(a)

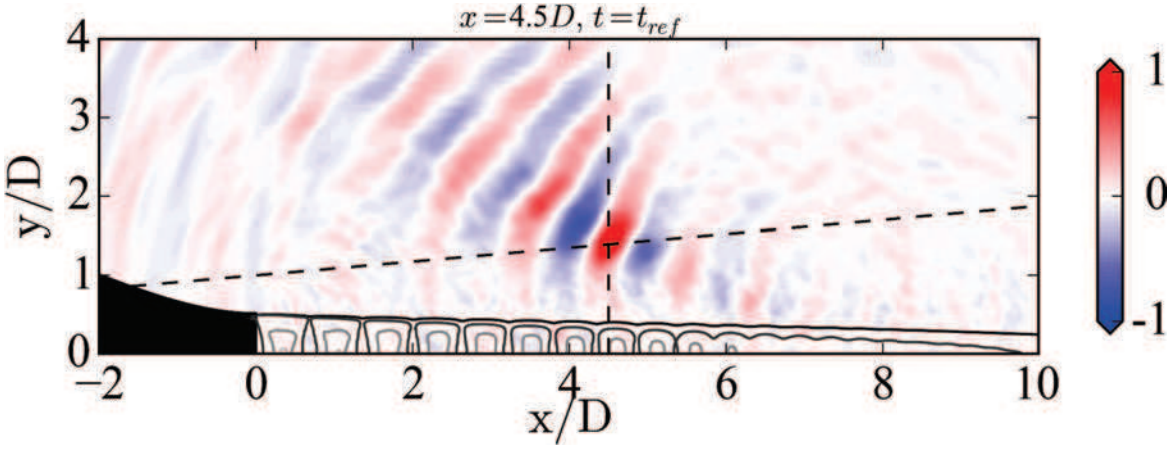

(b)

Figure 5.37: *Two-dimensional cross-conditioning of* ***(a)*** $p_{neg} - u$ *and* ***(b)*** $p_{neg} - p$*, from the near-field where the first variable is the one used to locate the events and the second variable is the one plotted. The black solid lines represent the Mach number contours above 1. The intersection of the dashed lines represents the location in space of the reference point.*

The two-dimensional cross-correlation obtained from the negative traveling pressure events is shown in Fig. 5.37 (a) and (b), for the axial velocity and the pressure respectively. The signatures calculated for the axial velocity and the pressure look similar with the exception that the signature for the axial velocity is not well defined inside the shear-layer (Fig. 5.37 (a)).

On the other hand, the signature of the pressure is well defined inside the shear-layer up to $x/D = 8$ with pressure perturbations coming from the shock-cell noise. The signature captured at this position travels upstream at an average angle of 140°.

In a similar fashion, the signatures obtained with the positive traveling pressure events shown in Fig. 5.38 exhibit a comparable pattern when the axial velocity or the pressure are plotted with the exception that in the shear-layer, the axial velocity is not well defined. The pressure presents a pattern that reaches the axis. This pattern, characteristic of the downstream propagating pressure waves, has a spatial length-scale greater than the one found in the lip-line. This is explained by the fact that the scale or equivalent frequency used to detect the events in the lip-line is a smaller one, which corresponds to a higher Strouhal number. The signature of the shock-cell noise is detected as well over the nozzle. This indicates that it is linked to the downstream traveling pressure waves characteristic from the convected vortical structures.

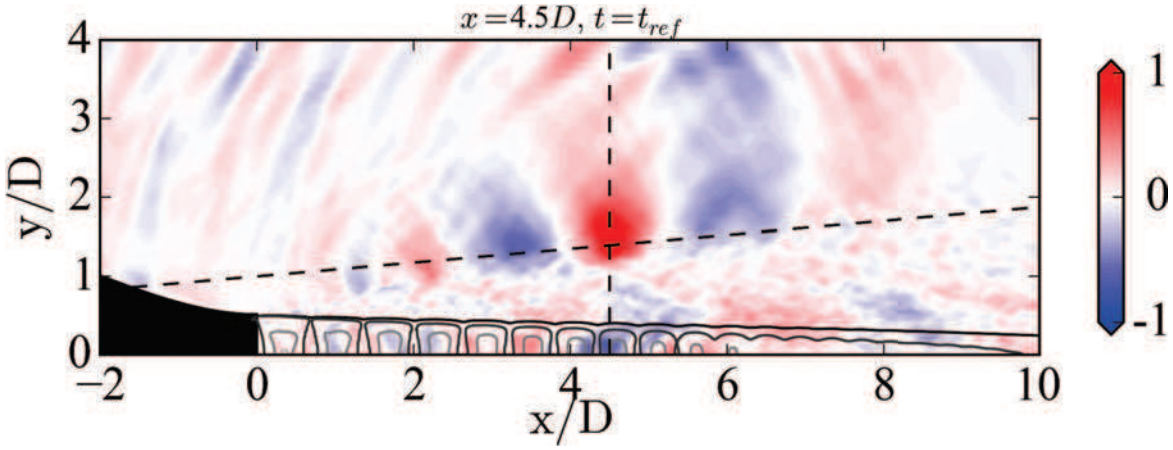

(a)

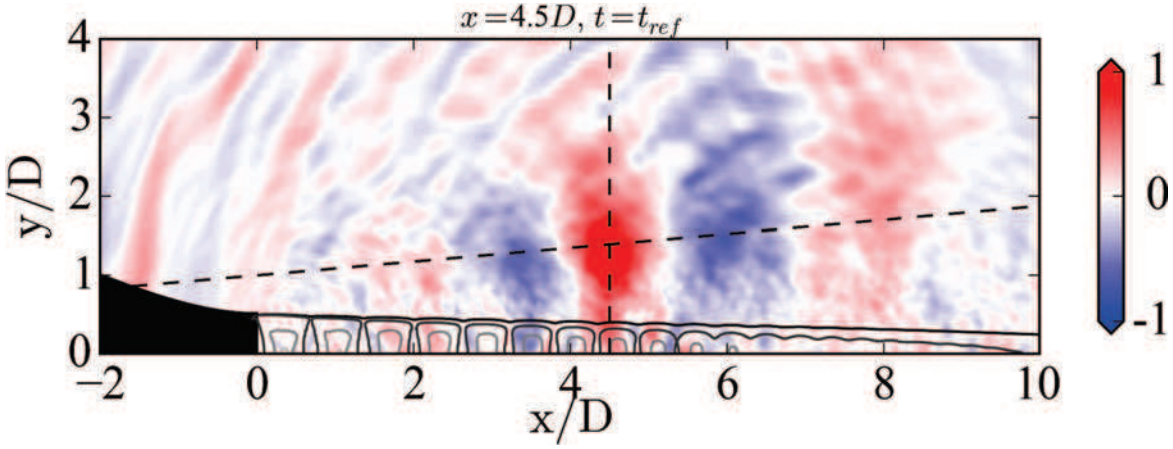

(b)

Figure 5.38: *Two-dimensional cross-conditioning of* ***(a)*** $p_{pos} - u$ *and* ***(b)*** $p_{pos} - p$*, from the near-field where the first variable is the one used to locate the events and the second variable is the one plotted. The black solid lines represent the Mach number contours above 1. The intersection of the dashed lines represents the location in space of the reference point.*

One of the limitations of this methodology is the fact that two different types of events that have the same or a similar scale cannot be easily differentiated. The event detection procedure of this study is based on the energy of the signal for different scales. If two independent events radiate noise at similar frequencies and with a similar energy content, the event detection procedure will not be able to discriminate between them. Having the knowledge of the physics and the case that is being studied can be used to your own advantage in order to pre-process the signal before applying the event detection procedure. In this case, Figure 5.39, shows the cross-conditioning with the pressure of the acoustic component of the pressure signal on the left column and of the negative traveling waves on the right column for different instants. Overall, the results are similar, however, taking a closer look at the advanced times, there is a pressure wave that can be seen traveling downstream for the cross-conditioning using the acoustic component. This high frequency acoustic pressure wave is suspected to be originated near the exit of the nozzle where the flow undergoes transition and several acoustic perturbations at a wide frequency range are emitted. On the other hand, if the pressure signal is filtered into negative traveling pressure waves, and the cross-conditioning is performed with this variable as a reference to detect the events, this perturbation disappears, due to the fact that it is traveling downstream. The remaining patterns are not highly affected by the selection of the reference variable. From the advance times shown in Fig. 5.39 (g) and (h), it can be seen that the event detected extends in space over the size of the potential core. This is expected because the shock-cell noise is generated over several shock-cells, and the events from the different shock-cells are taken into account as a whole.

5.4 Summary and perspectives

This chapter was devoted to the large eddy simulation of a supersonic under-expanded jet using high-order compact schemes. The computation was validated against different experimental results from different research facilities and against other numerical results obtained with a different solver.

The shock-cell pattern was compared with the Mach number profiles at the axis and PIV or Schlieren images showing good agreement for the first 4 shock-cells, farther downstream, there is a minimal displacement of the shock-cells. The shear-layer followed the same expansion rate and similar turbulence levels even though the internal part of the nozzle was not modeled and no turbulence forcing was applied. The acoustic spectra in the near-field and in the far-field were analyzed, obtaining good agreement with the experimental results. In the near-field, a ”banana-like” shape peak was found for the broadband shock-associated noise with an harmonic in the range $0 < x/D < 6$. The far-field acoustic pressure perturbations that were propagated with the FWH analogy presented an overall good agreement with the experimental results. Nonetheless, the peak of the BBSAN was shifted to higher frequencies due to the mismatch in the length of the shock-cells. Moreover, screech was not capture because the interior of the nozzle was not modeled. The near-field pressure perturbations were filtered into acoustic and hydrodynamic components in order to increase the accuracy of other post-treatments. The azimuthal modal decomposition was carried out at different radial positions and several modes were investigated. Moreover, different patterns were found on the pressure energy distribution for different arrays of probes with negative pressure traveling waves inside the supersonic potential core. This is possible due to the fact that the shock-cell noise that is

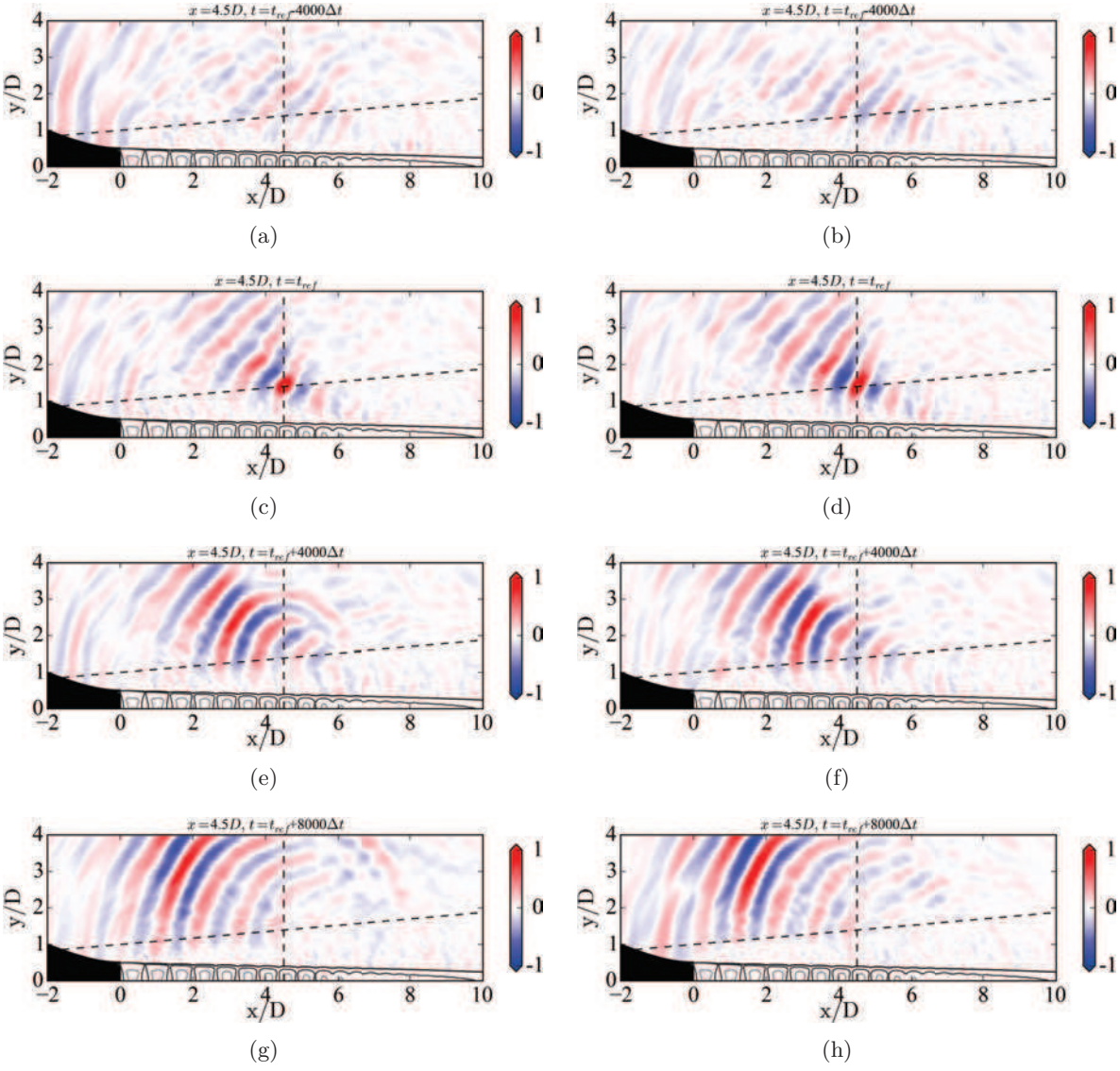

Figure 5.39: *Two-dimensional cross-conditioning of* $p_{acoustic} - p$ *on the left hand side and* $p_{neg} - p$ *on the right hand side at different shifted times where the first variable is the one used to locate the events and the second variable is the one plotted. The black solid lines represent the Mach number contours above 1. The intersection of the dashed lines represents the location in space of the reference point.*

propagated upstream outside the jet enters the potential core and generates an oblique front wave. Last, this characteristic front wave was studied with the wavelet-based methodology. A cross-conditioning was carried out between the events obtained using either the axial velocity, the negative traveling pressure waves or the positive traveling pressure waves and either the axial velocity or the pressure. The cross-conditioning illustrates how the signatures of the events are localized in space and their evolution in time. Notably, the shock-cell noise exhibited a checkerboard pattern between the shear-layer and the potential core due to the diagonal front wave that is convected inside the potential core. Moreover, the shock-cell noise was clearly visible for the upstream positions that showed a spatial length-scale of the order of the potential core.

In order to improve the results, different approaches are available. First, the interior of the nozzle could be modeled to better match the turbulence levels on the shear-layer and possibly capture screech tones, together with a new mesh able to capture up to a cut-off Strouhal number of at least three. This would increase the range of the resolvable frequencies and help capture the complete BBSAN peak. The post-processing techniques based on the wavelet could benefit from an extended simulation time. In particular, the mother wavelet Morlet could be used for achieving a better discretization in frequency and discern the cross-conditioning of different events that have different characteristic scales.

This case of study served the purpose of validation of an aeroacoustic simulation of a supersonic jet with the high-order compact numerical schemes implemented in ***elsA***, the methodology and the post-processing techniques. Following this chapter, a supersonic under-expanded dual-stream jet characteristic of nowadays commercial engines is studied.

Chapter 6

Supersonic under-expanded dual stream jet

The nowadays turbofan engines installed in commercial aircrafts have been designed for specific conditions in order to increase the efficiency at cruise taking into account take-off constraints. The secondary stream of a turbofan engine, in general, is either subsonic or fully expanded, and does not present a shock-cell system characteristic of shock-cell noise. However, due to traffic constraints, the flight level at which the pilot could have the ideal atmospheric conditions for the design point of the engine, cannot always be achieved. The atmospheric conditions and the thrust required at that point determines if a system of shock-cells appears. Due to the fact that the exhaust of the combustion chamber goes through the primary stream, its temperature is higher than the one encountered in the secondary stream. For this reason, it is most likely to find the shock-cell system in the secondary stream.

This chapter discusses the results obtained with LES of a dual stream configuration at conditions representative of real flight. This case of study has been tested experimentally at the von Karman Institute for Fluid Dynamics in the new Free jet AeroacouSTic laboratory (FAST). First, the definition of the case of study, the characteristics of the mesh and the simulation parameters are described in Sec. 6.1. Next, in Sec. 6.2 a few words are given to the experimental setup against which the numerical results are compared. Then, the analysis of the results are discussed in Sec. 6.3. Finally, a summary and some perspectives are introduced.

A part of the results discussed in this chapter were presented in the 2016 AIAA/CEAS conference [205]. Some of the data produced with this case of study was used by other partners of the project AeroTraNet2. More information about the collaborations can be found in Appx. C.

6.1 LES configuration

This section presents the main characteristics of the large eddy simulation of a dual stream jet. The characteristics of the code used for the LES are explained in Ch. 2. In addition, the LES procedure and mesh generation are extensively described in Ch. 3.

6.1.1 Case conditions

The case of study is a coaxial jet where the primary flow is cold and subsonic with an exit Mach number of $M_p = 0.89$ ($CNPR = 1.675$) and the secondary stream is operated at supersonic under-expanded conditions with a perfectly expanded exit Mach number of $M_s = 1.20$ ($FNPR = 2.45$). Here, $CNPR$ and $FNPR$ stand for Core and Fan Nozzle to Pressure Ratio respectively (see Ch. 1 for a wider explanation of the NPR). The jets are established from two concentric convergent nozzles with primary and secondary diameters of $D_p = 23.4$ mm and $D_s = 55.0$ mm respectively. The thicknesses of the nozzles at the exit are of 0.3 mm. The Reynolds numbers based on the exit diameters and the perfectly expanded conditions are

$$Re_{jp} = \left\{ \frac{\rho_j U_j D}{\mu_j} \right\}_p = 0.67 \times 10^6, \tag{6.1}$$

and

$$Re_{js} = \left\{ \frac{\rho_j U_j D}{\mu_j} \right\}_s = 2.64 \times 10^6, \tag{6.2}$$

where the subscript $\{\bullet\}_j$ refers to the perfectly expanded conditions, and the subscript $\{\bullet\}_p$ and $\{\bullet\}_s$ refer to the primary and secondary streams respectively. The ambient conditions used for this case of study are a pressure $p_\infty = 101,325$ Pa and a temperature $T_\infty = 283$ K. The generating pressure or total pressure is $p_{tp} = 1.6972 \times 10^5$ Pa for the primary stream and $p_{ts} = 2.4825 \times 10^5$ Pa for the secondary stream. The total temperature T_t is set equal to the ambient temperature T_∞ for both streams.

A supersonic under-expanded jet expands to the ambient pressure by means of the so-called shock-cell system. Its subsonic counterpart matches the nozzle exit pressure with the local static pressure found outside the nozzle without the need of an expansion fan. The three-dimensional effects of the secondary stream and the shape of the nozzle can modify the local pressure in its vicinity. When the local static pressure is modified with respect to the room static pressure the jet actually expands to the new static pressure, modifying the local nozzle to pressure ratio. In this study, the regular definition of NPR for the primary jet is kept, *i.e.* with respect to the room static pressure and not the local static pressure.

The main conditions are summarized in table 6.1.

	D [mm]	M_j	NPR	p_t [Pa]	T_t [K]	Re_j
Primary	23.4	0.89	1.675	1.6972×10^5	283	0.67×10^6
Secondary	55	1.20	2.45	2.4825×10^5	283	2.64×10^6

Table 6.1: *Conditions for the primary and secondary nozzles.*

6.1.2 Mesh definition

The structured multi-block mesh used for the LES is defined in this section. The mesh contains 200×10^6 cells. Figure 6.1 (a) displays a gridplane of the mesh at $z/D_s = 0$ where the interior of the pink region represents the physical domain. The region outside the pink region defines the sponge zone. As explained in Ch. 3, it consists in a butterfly type mesh in order to avoid

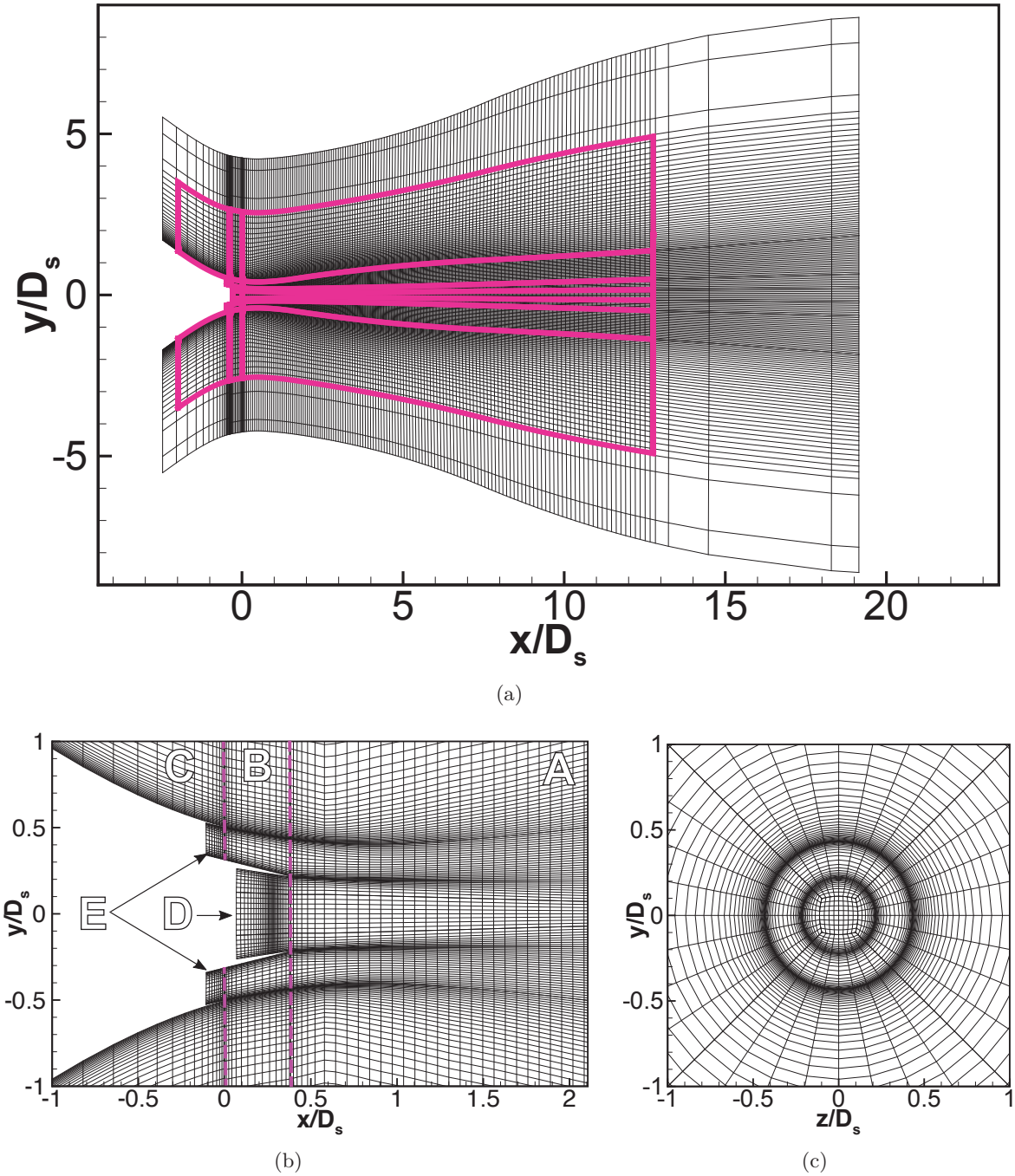

Figure 6.1: *Mesh grid planes representing every fourth nodes in the plane* $z/D_s = 0$ *for* ***(a)*** *a general view and* ***(b)*** *a closer look at the nozzle exit.* ***(c)*** *shows the exit plane of the nozzle. The capital letters* $[A, E]$ *illustrate different sections of the mesh.*

the singularity at the axis. The capital letters $[A, \ldots, E]$ depicted in Figure 6.1 (b) illustrate different sections of the mesh. Section A is situated forward to the primary nozzle exit plane. Section B considers the region between the exit of the primary and secondary nozzle. Section C is located over the secondary nozzle and sections D and E, define the interior of the primary (D) and secondary (E) nozzles respectively. The lips of both nozzles are discretized with 6 cells. The axial gridplane situated at the exit of the primary nozzle is shown in Fig. 6.1 (c). Table 6.2 summarizes the mesh distributions in each section.

	A	B	C	D	E
Axial	$1,132$	108	172	100	110
Radial	600	490	326	100	162
Azimuthal	256	256	256	256	256

Table 6.2: *Mesh distribution in each section for the axial, the radial and the azimuthal directions.*

The walls of the internal sections of the nozzles (section D and E) as well as the external section of the primary nozzle (section B) attain a resolution at the wall of $y^+ \approx 15$ with 20 points in the boundary layers. The maximum expansion ratio between adjacent cells achieved in the mesh is not greater than 4%. The radial discretization at different axial positions is shown in Fig. 6.2 (a).

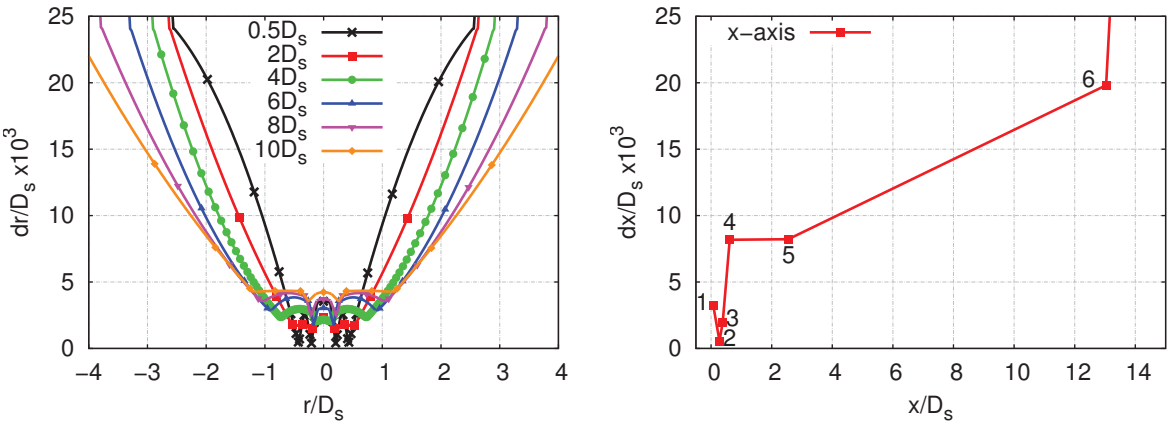

(a) (b)

Figure 6.2: *Discretization of the mesh along* ***(a)*** *the radial distribution for different x/D_s and* ***(b)*** *the axial distribution along the axis, where dr is the radial step and dx the streamwise one.*

The maximum Helmholtz number ($He_s = fD_s/a_\infty$) that the mesh is able to capture at the end of the physical domain is about 4. The radial domain size grows with the axial position in order to take into account the expansion of the jet (from $r/D_s = 2.5$ at the exit of the primary nozzle to $r/D_s = 5$ at $x/D_s = 13$), nonetheless, the maximum He_s number is kept constant at the boundary with the sponge layer. The axial discretization shown in Fig. 6.2 (b) is composed of 6 sections defined by the enumerated symbols. In the interior of the primary nozzle, segments $\overline{1\ 2}$ and $\overline{2\ 3}$, the mesh is refined where the vortex-ring is located (point 2). At this position, the mesh achieves an aspect ratio of 1 at the wall; this ensures an appropriate definition of a

vortex-ring used to transition to turbulence. At the exit of the primary nozzle (point 3), the aspect ratio of the cells at the wall attains a value of 4. In the third segment $\overline{3\ 4}$, the mesh elongates at a rate of 3%. This stretching allows for a drastic reduction of the total amount of cells in the axial direction. The segment $\overline{4\ 5}$ consists in a uniform discretization. Then, in segment $\overline{5\ 6}$, the mesh is slowly elongated up to a mesh size able to capture a Helmholtz number of 4. The last section, starting at point 6, is the one corresponding to the sponge layer where the mesh has a stretching ratio of 10%.

6.1.3 Simulation parameters

The numerical computation is initialized by a Reynolds-Averaged Navier-Stokes (RANS) simulation using the Spalart-Allmaras turbulence model [169] as explained in Sec. 3.2. The RANS solution is fully wall-resolved in the internal and external sections of the nozzles with a maximum wall unit (y^+) of unity with 30 points in the boundary layer. The nozzle is modeled in the interior up to 10 primary diameters and the RANS domain extends to 50 primary diameters in the radial and axial directions. The LES is then initialized from the RANS simulation keeping the inlet profiles. In order to accelerate the initialization from a steady state to a temporal resolved state, an intermediate coarse mesh of 25×10^6 cells is considered. The flow is initialized over 90 dimensionless convective times ($\hat{t}_p = ta_\infty/D_p$) and then the data are interpolated over the fine mesh explained in Sec. 6.1.2. Before the flow could be considered as initialized, 60 additional dimensionless convective times are computed with the fine mesh to evacuate interpolation errors and let the flow adapt to the fine mesh. The final computation is then run for 186 dimensionless convective times to obtain the statistics. The simulation time corresponds to 80 dimensionless convective times with respect to the secondary diameter D_s. As it is described in Sec. 6.3, the secondary stream presents an oblique shock at the axial position of the exit plane of the primary nozzle. After 186 $\hat{t}_p$ some instabilities occurred near the oblique shock which forced us to stop the LES. Due to the small computational time and in order to increase the convergence of the results, some of them are averaged in the azimuthal direction. A dimensionless time step of 0.00027 equivalent to a CFL about 0.9 was selected for the data extraction phase. In dimensional quantities, the time step is equivalent to 0.0187 μs.

The boundary conditions used in the simulation are sketched in Fig. 6.3 (a). Non-reflective boundary conditions of Tam and Dong [160] extended to three dimensions by Bogey and Bailly [161] are set at the inlets as well as at the lateral boundaries. The exit boundary condition is based on the characteristic formulation of Poinsot and Lele [158]. Additionally, sponge layers are employed around the domain to attenuate exiting vorticity waves. An inflow forcing based on the vortex-ring of Bogey and Bailly [73] is applied in the interior of the subsonic nozzle to help transition to turbulence as shown in Fig. 6.3 (b) but not in the interior of the secondary supersonic nozzle. In order to accurately define the vortex-ring and maintain the levels of turbulence throughout the convergent secondary nozzle, a much finer discretization and longer interior section would have been needed. This would have increased the cost of the computation, without assuring the correct (at the moment unknown) turbulent levels. Last, no-slip adiabatic wall conditions are set at all the wall boundaries of the nozzles. No wall turbulence models are used.

This simulation was run with the shock-limiting scheme explained in Sec. 2.3 due to the fact

that an oblique shock appears at the end of the primary nozzle in the secondary stream as it is later described in Sec. 6.3.1. Although the shock-limiting technique was active, the flow became unstable near the oblique shock. This computation was run with the spatial filter explained in Sec. 2.2.2 of order 6.

In terms of computing cost, the LES was run on 1024 processors using HPC resources from GENCI-OCCIGEN [CCRT/CINES/IDRIS] (Grant 2016-[x20162a6074]). The total computational time was about $1,750,000$ CPU h, which counts for the RANS used to initialize the LES, the computation on the coarse mesh, the adaptation phase from the coarse mesh to the fine mesh, and the actual LES of 80 convective times.

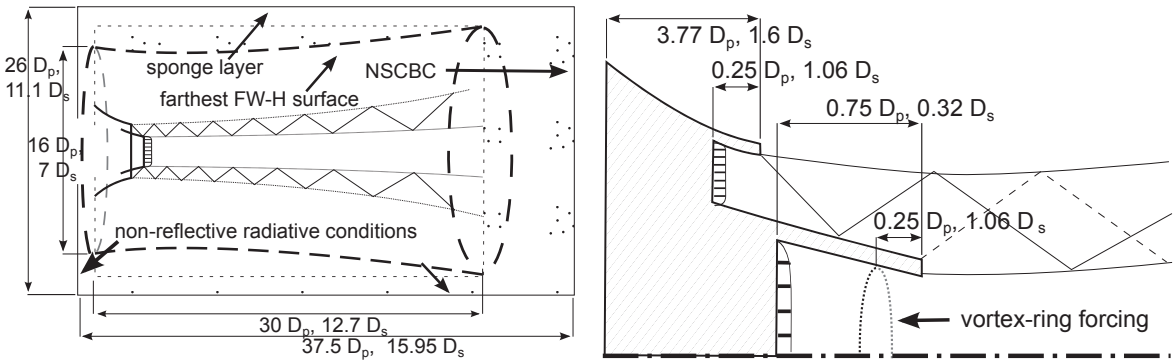

Figure 6.3: *Sketch of the numerical and physical domain in* ***(a)*** *a general view and* ***(b)*** *a detailed view.*

6.1.4 Data extraction

The data extracted are divided in mean, cuts, numerical probes and topological surfaces. The cuts and topological surfaces were saved every 400 iterations which is equivalent to a frequency of 133.45 kHz. On the other hand, the numerical probes were extracted every 100 iterations or 533.78 kHz.

The mean flow was averaged azimuthally to increase the convergence. Due to the reduced simulated physical time, the second order moments are not fully converged, notably in the downstream regions where the large structures are developed. Therefore, an interpolation into a polar mesh was performed in order to facilitate the azimuthal average. The average of second order moments was done following a prior change of variables at each azimuthal position as formulated in Appx. A.

Plane cuts were extracted at $z/D_p = 0$, and at the axial locations $x/D_p \in \{0, 5, 10\}$. Three sets of probes were extracted in this simulation sharing the same axial discretization. In the range $-0.9 < x/D_p < 15$ the data were extracted every 0.1 D_p. Farther downstream, in the range $15 < x/D_p < 25$ the data were extracted every 1 D_p. The different data sets are: a set of probes at the axis (referred to as AXIS), a set at the shear-layer between the primary and the secondary stream (referred to as LIP_P), a set at the secondary shear-layer (referred to as LIP_S), and three sets situated in the near-field with an expansion angle of 8 degrees from $x/D_p = 0$ and $r/D_p = \{1, 2, 3\}$ (referred to as NF1D, NF2D and NF3D respectively). All the

sets but the one located at the axis are composed of 16 azimuthally distributed probes.

The far-field sound is obtained by means of the Ffowcs-Williams and Hawkings analogy (FWH) [196]. The surfaces used to extrapolate the variables to the far-field are located in three concentric topological surfaces starting at $r/D_p = \{3, 4, 5\}$ from the axis and growing with the mesh. The surfaces are closed on the exterior of the secondary nozzle and open at the outlet. The cut-off mesh Strouhal number is $St_s = fD_s/U_{js} \approx 6.0$. The sampling frequency was set to 65 kHz which gives a sampling Strouhal number higher than the mesh cut-off limit. The noise is propagated up to a distance of 30 D_s which is far enough to be considered as proper far-field according to Viswanathan [57].

6.2 Experimental setup

In this chapter, the numerical results are compared to the experimental data obtained at the von Karman Institute for Fluid Dynamics (VKI) by its researchers and other partners of the same European project AeroTraNet2, framework of this thesis. The facility named FAST (Free jet AeroacouSTic laboratory) was built between 2013 and 2016 and it has been specially designed for coaxial jets [206, 198] even though it can also be run for single jets. The nominal testing conditions of the facility are for the core stream $1.35 < CNPR < 1.72$ and for the fan stream $2.00 < FNPR < 2.50$. Unfortunately, as a result of several delays in the manufacturing process of some parts of the experimental facility, the CFD was carried out before the experimental campaign. This has led to some geometrical differences that are summarized in the following.

The Computer Assisted Design (CAD) of the final coaxial nozzle installed at VKI is shown in Fig. 6.4 (a). The screws used to attach the nozzle to the ducts are not modeled in the current study as seen in Fig. 6.4 (b). After discussion with the experts at VKI, the effect of the screws was assumed to be negligible and thus, it was not modeled in the RANS simulation nor were considered for the LES domain as illustrated in Fig. 6.4 (b). Moreover, due to some pressure losses in the feeding pipeline of the experimental facility, the target conditions where not possible to reach with the original nozzle diameters presented in Table 6.1. Therefore, a new nozzle was machined with reduced dimensions by 20%. Since the numerical campaign started before the experimental one, the modeled nozzle in this work has the original dimensions. The different dimensions have an impact on the Re_j, the development of the internal boundary layers, and the acoustics. In addition, it was later found that when the air flow was active in the experiments, the secondary nozzle moved vertically about 2 mm (or 0.05 D_s) in the jet direction. The researchers at VKI believe that this could be due to the vertical strain of the external ducts when the pressurization is active.

Two sets of data are compared in this chapter, pressure probes situated in the far-field and the field obtained by Particle Image Velocimetry (PIV). The polar antenna was placed at a distance equal to 30 D_s set with a frequency sampling of 250 kHz, which corresponds to about 2^{24} samples (67 seconds). The PIV was captured with two cameras set in parallel with a small overlapped region. The images were captured with a resolution of $2,360 \times 1,766$ pixels^2 and a sampling frequency of 15 Hz. The experiments were run in five realizations of 40 seconds, generating 600 images per run. Two experiments were done with the same conditions but with a different location of the cameras in order to generate an extended view of the flow

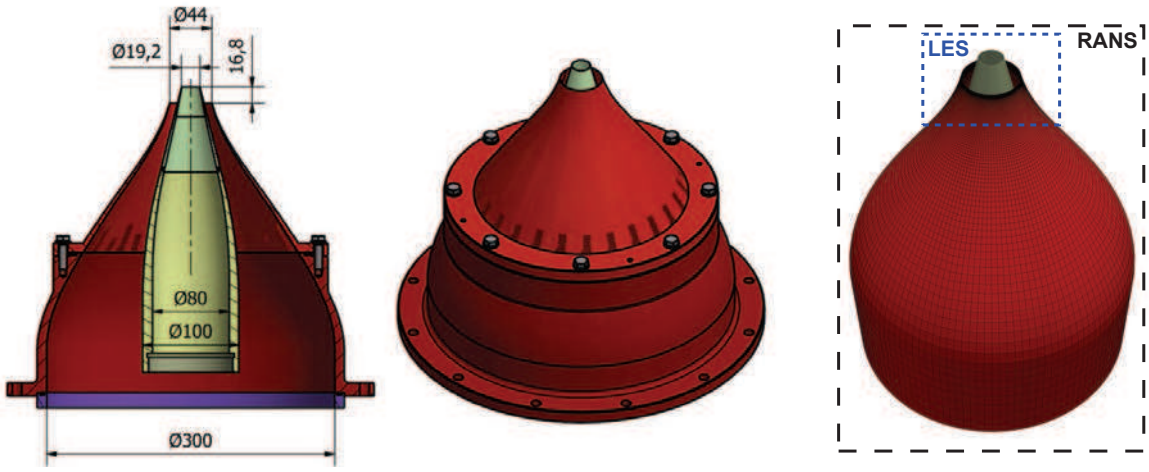

(a) (b)

Figure 6.4: ***(a)*** *CAD drawing of the manufactured coaxial nozzle.* ***(b)*** *Modeled nozzle for the RANS simulations and LES. Courtesy of D. Guariglia [198].*

downstream. With a 50% overlap of the windows a resolution of 393×294 vectors is imposed. The final image, with the 4 nested frames as shown in Fig. 6.5 is composed of 393×1085 vectors.

6.3 Analysis of results

6.3.1 Aerodynamic field

Comparisons with experimental PIV

In this section, the main aerodynamic flow features of the LES are compared with the experimental PIV fields from VKI. The contour plots investigated in this section, are divided in a top part where the experimental PIV results are displayed, and a bottom part with the numerical PIV. The sign of the vertical velocity is inverted on the numerical contours in order to have the same color scheme. The Mach number isolines with levels $M = \{0.9, 1.0, 1.1, 1.2, 1.3, 1.4\}$ are shown on all contours plots in solid black line. In addition, the data contained over some vertical lines are extracted at the starting and middle point of the last 7 recognizable shock-cells. The extracted profiles are depicted in a separate figure where the top represents the line crossing the starting point of a shock-cell and the bottom, the middle point. Due to differences in shock-cell size and location between the experimental and the numerical fields, the extracted lines are grouped by shock-cell number. The comparable average quantities of interest that were computed with the PIV are: Mach number, axial velocity $\overline{u}$, radial velocity $\overline{v_r}$, variance of the axial velocity $\overline{u'^2}$, variance of the radial velocity $\overline{v_r'^2}$ and the variance of the product of the axial and radial velocities $\overline{u'v_r'}$. The experimental Mach number is computed from the

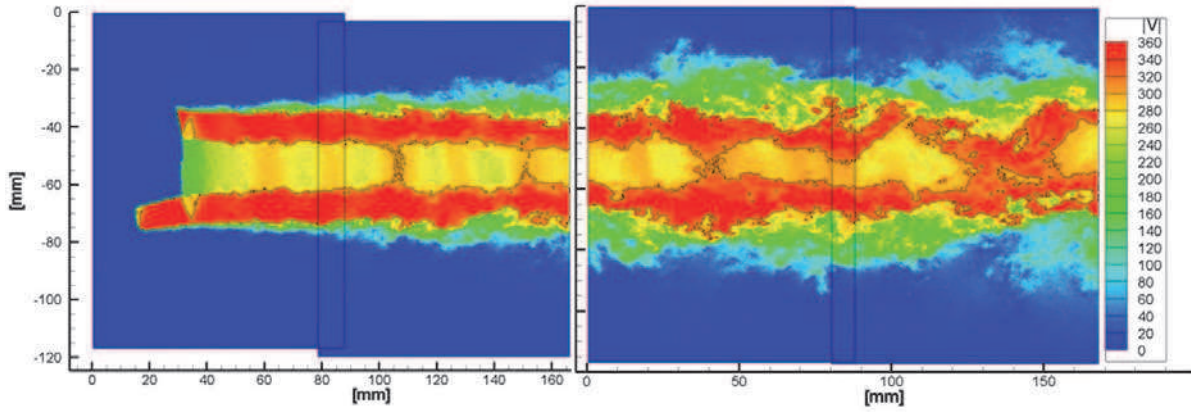

Figure 6.5: *Instantaneous PIV velocity flow field with Mach number* $M = 1$ *isolines for the conditions* $CNPR = 1.675$ *and* $FNPR = 2.500$*. Courtesy of D. Guariglia.*

absolute velocity (assuming $w = 0$) from the PIV, using the isentropic relation

$$M = \sqrt{\frac{u^2 + v^2}{\gamma R T_t - (u^2 + v^2)\dfrac{(\gamma - 1)}{2}}}, \tag{6.3}$$

where T_t is the total temperature taken as 283 K.

The Mach number contours are shown in Fig. 6.6. The primary subsonic jet is enclosed by a supersonic under-expanded annular jet. It creates the primary potential core surrounded by an annular potential core where the shock-cells live. These concentric potential cores merge further downstream. The supersonic under-expanded secondary flow undergoes the birth of an oblique shock at the exit of the primary nozzle due to the difference in slope between the internal section of the primary nozzle and the outer section of the nozzle. This oblique shock theoretically generates a secondary shock-cell system that coexists with the one generated by the under-expanded supersonic jet at the exit of the secondary nozzle even though is not clearly visible in Fig. 6.6. Due to the oblique shock, and the shock-cell system that appears in the secondary stream, the actual Mach number obtained at the exit of the primary nozzle achieves a value of 0.51 instead of the design value of 0.89. Nonetheless, the design value is reached after an axial distance of 1 D_p. Moreover, the shock-cells of the secondary stream modify the Mach number and the pressure in the primary stream.

The shock-cell lengths measured with the Mach number oscillations in the axis of the primary jet are shown in Table 6.3. Due to a different development of the jet, and the displacement of the experimental secondary nozzle, the last shock-cell differs in position about 0.62 D_s. The shock-cell lengths are smaller in the numerical simulation with a reduction between 10% in the first measured shock-cells to up to 20% in the last ones. This remarkably difference has an impact on the shock-cell noise main frequencies. Because the shock-cell distribution changes, the data from particular lines were extracted at the locations relative to each shock-cell as it is illustrated in Fig. 6.7 for the Mach number. Regardless of the differences in position, and shock-cell length, the extracted LES data of each line have good agreement with the experimental Mach number profiles at all relative positions. The peaks at the center of the secondary stream and the values at the axis of the primary stream have the same values. The

main discrepancy comes from the shape of the shear-layer, being about 40% wider in the LES. This difference in the shear-layer thickness is responsible for the difference in shock-cell length. The compression wave that is reflected in the shear-layer will occur closer to the axis if the shear-layer is wider. Due to the geometry of the shock-cells, the smaller the shock-cells are in the vertical direction, the smaller they are in the axial direction. The difference in the thickness of the shear-layer can be a matter of a bad discretization of the shear-layer which could increase the dissipation on that region or/and by a difference in the initial turbulence levels.

	L^2_{sh}/D_s	L^3_{sh}/D_s	NPR	$L^4_{sh}/D_s L^5_{sh}/D_s$	L^6_{sh}/D_s
PIV	0.476	0.473	0.486	0.455	0.420
LES	0.425	0.400	0.390	0.365	0.340
%decrease	10.78	15.40	19.67	19.69	19.04

Table 6.3: *Shock-cell length obtained with the PIV and LES measured at the axis of the primary stream.*

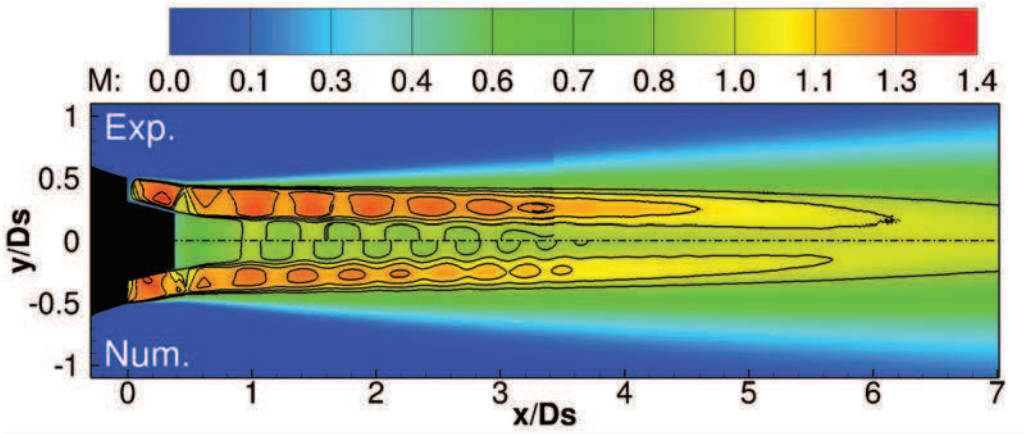

Figure 6.6: *Mach number contours of the mean field from PIV (top) and LES (bottom). The black solid lines represent the Mach number from 0.9 to 1.4 with an interval of 0.1.*

The radial velocity $\overline{v_r}$ contours are displayed in Fig. 6.8 and the extracted vertical lines in Fig. 6.9. The axial velocity exhibits a similar pattern than the Mach number and is not presented. On the other hand, the vertical velocity shows a very distinguished pattern in the boundaries of the shock-cells, classical of under-expanded jets. As it happens for an under-expanded single jet as explained in Ch. 5, the expansion fan generated at the lip of the nozzle bounces back to the jet as a compression wave. The jet expands radially in the expansion zones whereas it comes back to the center in the compression zones. Between each different region, compression-expansion or expansion-compression, there is a neutral zone where the jet changes the sign of the second axial derivative of the pressure. In other words, there is a maximum and a minimum in the pressure (and other variables such as Mach number and axial velocity). On the other hand, at these locations, the radial velocity changes the sign from positive to negative values when it goes from the expansion to the compression zone, and

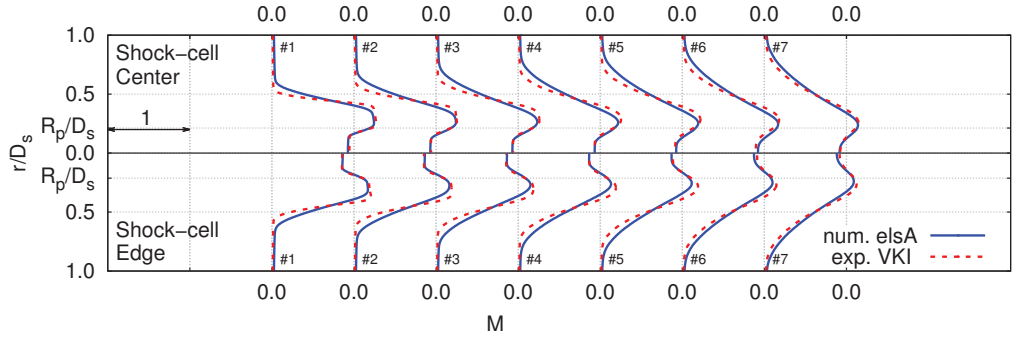

Figure 6.7: *Mach number profiles of the mean field from PIV (dashed) and LES (solid). The top part corresponds to axial positions at the center of a shock-cell and the bottom part to axial positions at the edge of a shock-cell.*

from negative to positive values otherwise. Differently to the single jet, here, the expansion occurs only from the lip of the secondary nozzle and it bounces back as a compression wave on the shear-layer of the primary jet instead of on the symmetry axis. Figure 6.8 displays the expansion fans and compression waves on the secondary stream with a triangular shape.

Figure 6.9 (a) shows the velocity profiles in the neutral zones of the jet. As it can be seen, the different profiles have the same shape independently from the axial location and independently of whether they are located after the expansion zone or after the compression zone. The experimental results exhibit less smooth profiles than the numerical ones due to the fact that only 3000 snapshots were averaged in the PIV against the average of $679,200$ iterations for the LES. As it can be seen, the position of the peaks are well captured even though they are smoother in the simulation. Regardless of the amplitude of the peaks, on one hand, the profiles have good agreement in the downstream positions. On the other hand, the negative radial velocity caused by the suction of the jet outside the shear-layer is higher in the LES. This might be because the modeled nozzle is bigger than the experimental one or by some installation effects. A peak of radial velocity is achieved in the shear-layer generated by the expansion of the jet. Moreover, a smaller negative peak is found in the shear-layer between the primary and the secondary jet. At this location, it is negative because the secondary stream expands on to the primary stream. At the axis, the mean radial velocity should be zero. This is confirmed by the LES, however, the experimental results present a slight positive value in the first shock-cells. At the time of writing of this manuscript, three possible hypothesis were shared by private communications with D. Guariglia at VKI: the laser sheet could be not perfectly centered at the axis, there is a misalignment of the axis direction of the primary nozzle, or last, the PIV is biased by the uncertainty of an average over only 3000 images. The profiles of some of the shock-cells in the compression and expansion zones are shown in Fig. 6.9 (b). The suction differs about 50% close to the nozzle exit but this difference is reduced further downstream. In the expansion zone, the flow expands and tends to go away from the axis which is represented by a positive radial velocity. The effect of the expansion can be seen as an extra peak which is overlapped with the peak of the expansion of the jet. The two peaks can be slightly recognized in the first shock cell as a change of curvature. In addition, in the compression zone, there is a positive peak that is developed from the expansion of the

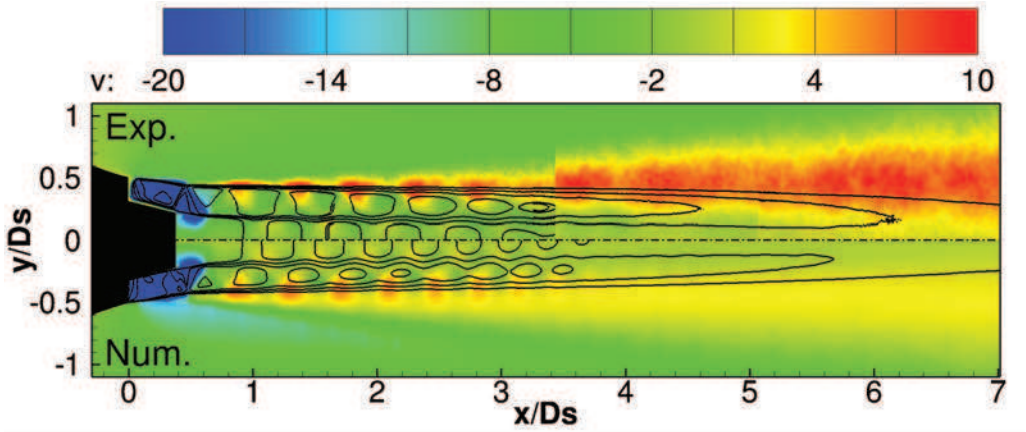

(a)

Figure 6.8: ***(a)*** *Radial velocity $\overline{v_r}$ contours of the mean field from PIV (top) and LES (bottom). The black solid lines represent the Mach number from 0.9 to 1.4 with an interval of 0.1.*

jet followed by the negative peak of the compression zone. The peak related to the expansion or compression has an opposite influence over the primary jet, as it is demonstrated by the peaks close to the axis. Overall, good agreement with the experiments is obtained.

The contours of the second order central moments of the axial $\overline{u'^2}$ and radial velocity $\overline{v_r'^2}$ are computed and shown in Fig. 6.10. As it was presented in Fig. 6.9, here, the higher expansion ratio of the jet is noticeably closer to the nozzle exit but it achieves the same width at the end of the potential core. Figure 6.11 illustrates quantitatively the difference on the extracted lines. At first glance, both the axial and the radial velocity variances present higher levels close to the nozzle exit for the numerical results. This can be expected from a bad resolution of the PIV [207, 208] in the thinner regions of the shear-layers. Moreover, further downstream, the axial velocity variance increases for the experiments in the secondary shear-layer. However, the simulation captures well the peak in the primary shear-layer in the first shock-cells and shows a slight reduction in the last ones for the axial velocity. The peaks are encountered at the same radial positions.

Next, the Reynolds stress expressed by the cross-term $\overline{u'v_r'}$ displayed in Fig. 6.12 is analyzed. Figure 6.12 (a) focuses on the secondary shear-layer whereas Fig. 6.12 (b) is saturated in order to focus on the primary shear-layer. Similarly to the variance of the axial and radial velocity, the cross-term presents a higher intensity closer to the nozzle for the LES whereas farther downstream it is dissipated. The primary shear-layer shows high-level spots at the edge of the shock-cells. As shown in Fig. 6.13, the cross-term $\overline{u'v_r'}$ computed for the LES is twice the amount of the experimental results. Further downstream the levels are similar.

Length-scales analysis

The length-scales and time-scales for the axial ($L_{11}^{(1)}$) and radial velocity ($L_{22}^{(1)}$) are shown in Fig. 6.14 and Fig. 6.15 respectively. They are computed along the axis, the primary lip-line and the secondary lip-line and compared to those of Laurence [209] and Davies *et al.* [210]. Both length-scales and time-scales were computed as the integral of the main peak of the

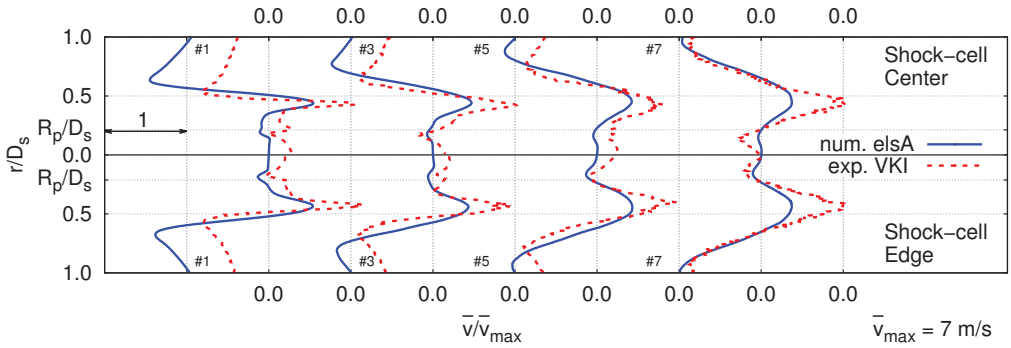

(a)

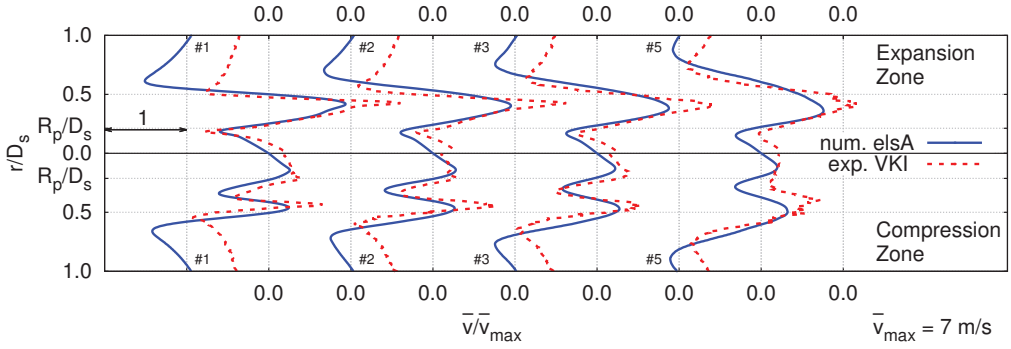

(b)

Figure 6.9: ***(a,b)*** *Radial velocity $\overline{v_r}$ profiles of the mean field from PIV (dashed) and LES (solid). For* ***(b)****, the top part corresponds to axial positions at the center of a shock-cell and the bottom part to axial positions at the edge of a shock-cell. For* ***(b)****, the top part corresponds to axial positions in the expansion zone of a shock-cell and the bottom part to axial positions in the compression zone of a shock-cell. In this figure, some of the shock-cells are omitted for clarity.*

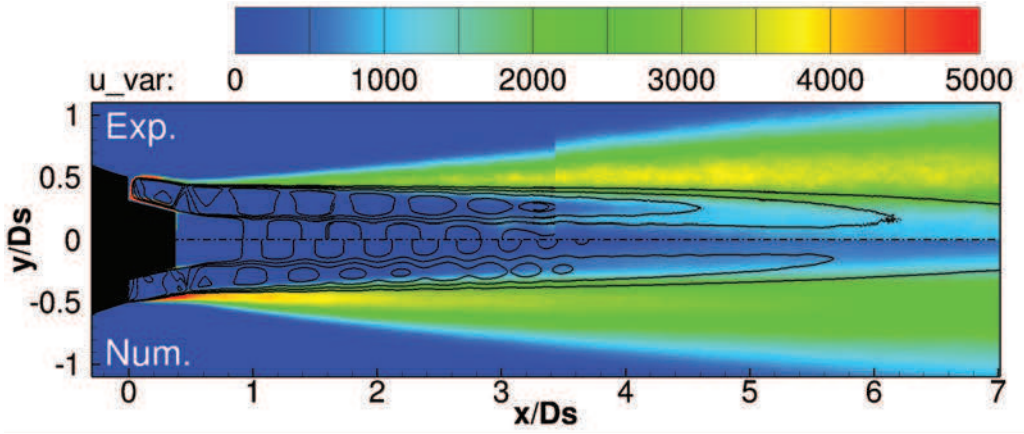

(a)

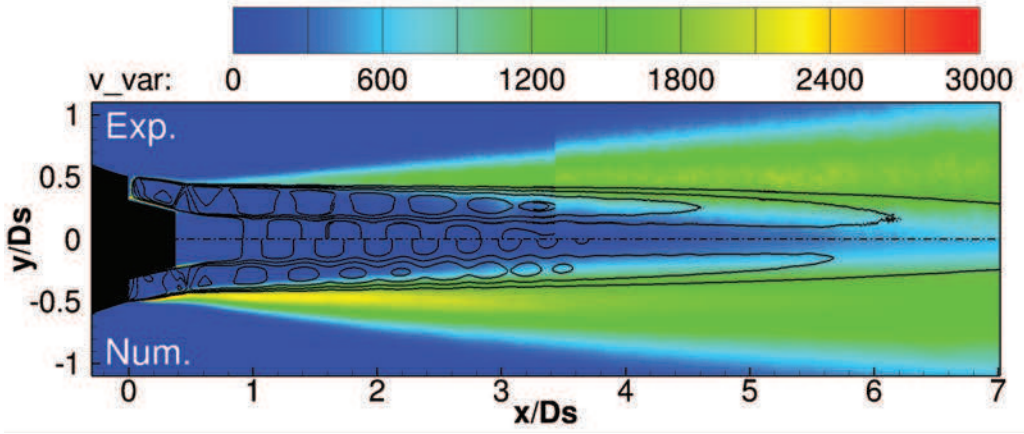

(b)

Figure 6.10: ***(a)*** *Variance of the axial velocity* $\overline{u'^2}$ *and* ***(b)*** *radial velocity* $\overline{v_r'^2}$ *contours of the mean field from PIV (top) and LES (bottom). The black solid lines represent the Mach number from 0.9 to 1.4 with an interval of 0.1.*

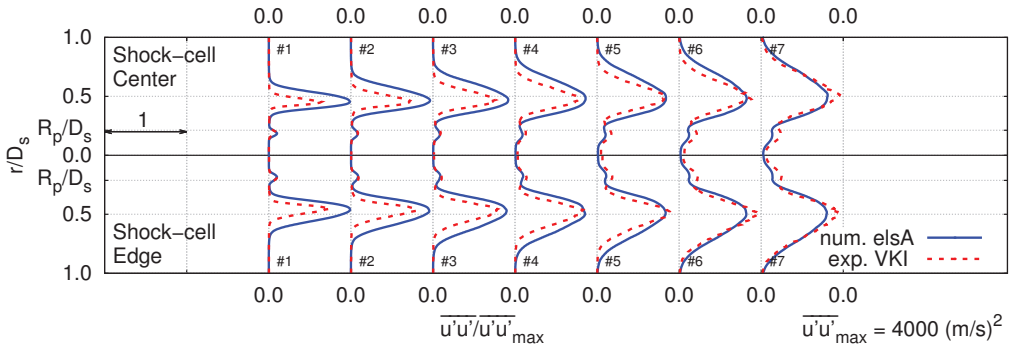

(a)

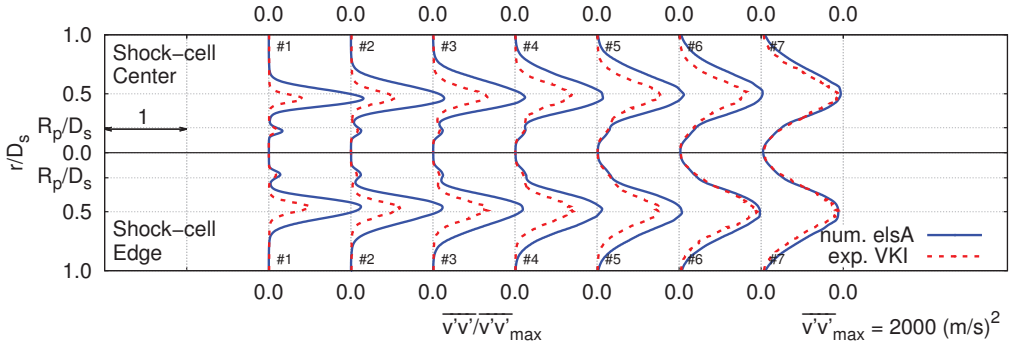

(b)

Figure 6.11: ***(a)*** *Variance of the axial velocity* $\overline{u'^2}$ *and* ***(b)*** *radial velocity* $\overline{v_r'^2}$ *profiles of the mean field from PIV (dashed) and LES (solid). The top part corresponds to axial positions at the center of a shock-cell and the bottom part to axial positions at the edge of a shock-cell.*

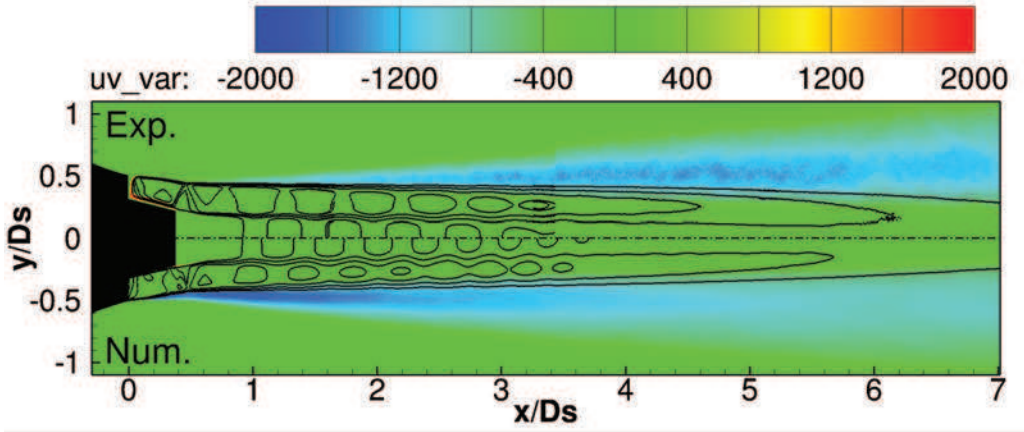

(a)

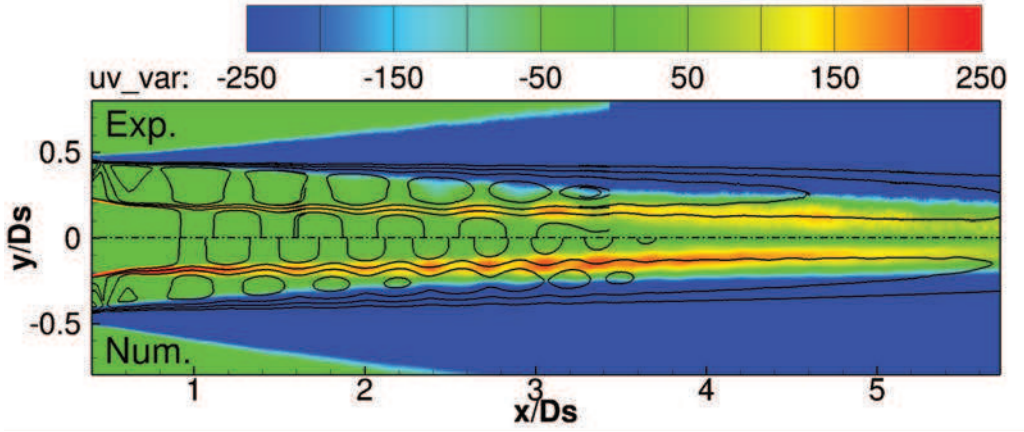

(b)

Figure 6.12: *Variance of the product of the axial and radial velocities $\overline{u'v'_r}$ contours of the mean field from PIV (top) and LES (bottom).* ***(a)*** *General view.* ***(b)*** *Zoomed view with saturated contours. The black solid lines represent the Mach number from 0.9 to 1.4 with an interval of 0.1.*

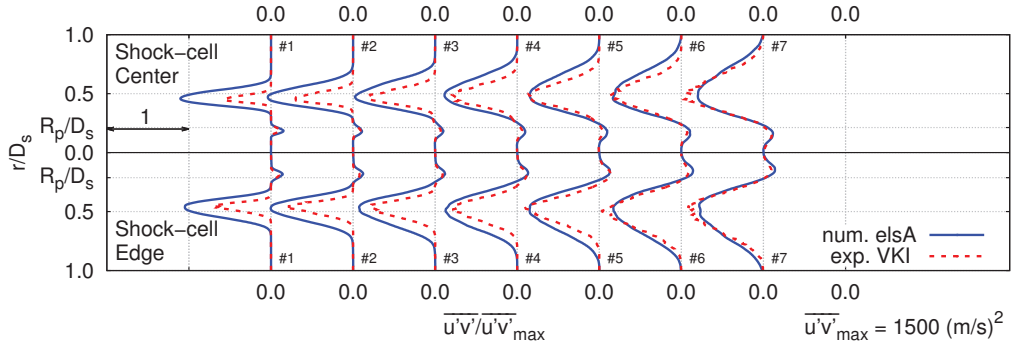

Figure 6.13: *Variance of the product of the axial and radial velocities $\overline{u'v'_r}$ profiles of the mean field from PIV (dashed) and LES (solid). The top part corresponds to axial positions at the center of a shock-cell and the bottom part to axial positions at the edge of a shock-cell.*

auto-correlation up to the first minima. The length-scales of the axial velocity have good agreement with the experimental fit for both the primary and secondary lip-lines as displayed in Fig. 6.14 (a). The length-scales at the axis overcome a maxima at the position of the shock-cells that oscillates with them. Then, it decreases due to the increase in axial velocity related to the mixing of the secondary supersonic jet. Finally it increases again and recovers the same length-scales as the other references. A similar effect can be encountered at the primary lip-line where two slopes are clearly differentiated before and after the merging with the secondary stream. As expected, the length-scales of the radial velocity shown in Fig. 6.14 (b) are lower to those computed for the axial velocity. The time-scales of the axial velocity presented in Fig. 6.15 (a) exhibit an increase at two different rates, one before the merging of the potential cores and one afterwards. The maxima observed at the axis (Fig. 6.14 (a)) is smoothed into a plateau for the timescale. On the other hand, the time-scales of the radial velocity converge into the same time-scales independently of the radial position as displayed in Fig. 6.15 (b).

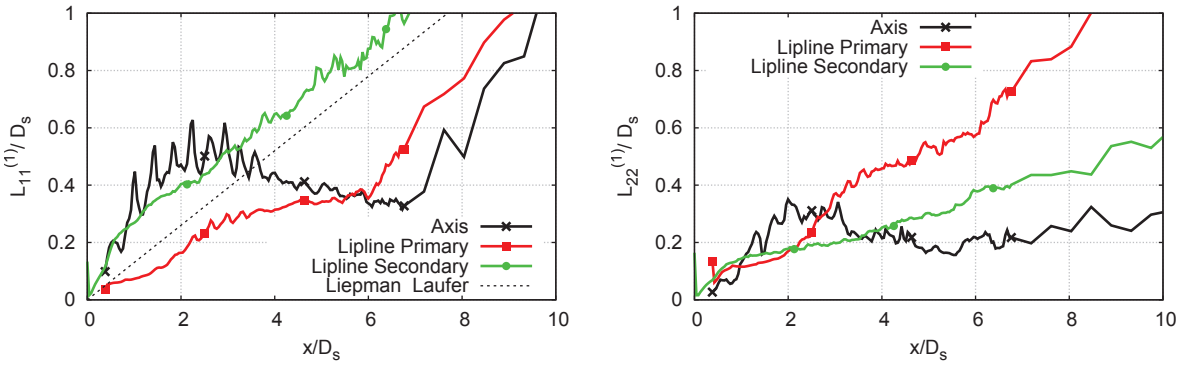

(a) (b)

Figure 6.14: *Lengthscale of* ***(a)*** *the axial velocity u and* ***(b)*** *the radial velocity v_r along the axis, the lip-line of the primary nozzle and the lip-line of the secondary nozzle.*

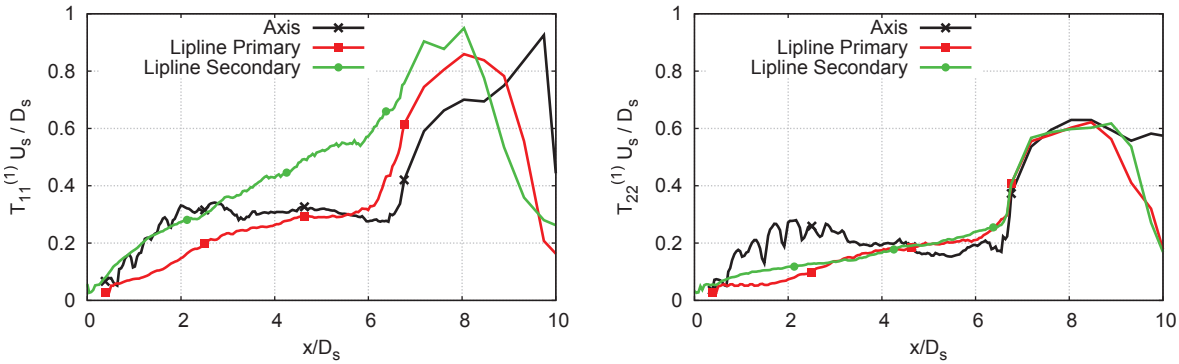

(a) (b)

Figure 6.15: *Timescale of* ***(a)*** *the axial velocity u and* ***(b)*** *the radial velocity v_r along the axis, the lip-line of the primary nozzle and the lip-line of the secondary nozzle.*

Impact of a shifted nozzle

As it was mentioned in Sec. 6.2, the experimental secondary nozzle suffered from a slight axial shift when the flow was active. Unfortunately, this effect was reported after the large eddy simulation was carried out. In this section, a RANS computation of the shifted nozzle is compared to the original one used to initialize the LES in order to quantitatively measure the impact on the shock-cell development. A positive axial shift of 0.05 D_s was considered.

Due to the shape of the primary nozzle, the shift of the secondary nozzle increases the effective area of the secondary stream by 5% from $A/D_s^2 = 47.63$ to $A/D_s^2 = 50.05$. This increase in area implies that the mass flow rate also increases 5% with respect to the original position of the nozzle (see Eq. (1.24)). On the other hand, the shift does not affect the FNPR because as shown in Eq. (1.25) it is determined by the total and the ambient pressure.

The Mach number contours are compared in Fig. 6.16. The Mach number at the primary axis and at the skewed secondary axis are displayed in Fig. 6.17 and 6.18 respectively. The general view of Fig. 6.16 (a) shows that the pattern of the shock-cells is similar but shifted to the right which is also visible as an extension of the Mach number lines in the potential core. A close-up look of the nozzle exit (Fig. 6.16 (b)) displays that the first shock-cell is intersected by the oblique shock that appears at the exit of the primary nozzle. Due to this intersection, the pressure is higher closer to the oblique shock in the shifted configuration which makes the Mach number jump increase astonishingly by 48%. The original nozzle has a Mach number jump from $M_l = 1.165$ to $M_r = 0.99$ (where the subscripts $\{\bullet\}_l$ and $\{\bullet\}_r$ stand for conditions at the left and right sides of the shock). The shifted nozzle has a Mach number jump from $M_l = 1.19$ to $M_r = 0.93$. This higher intensity is perceived by the subsonic primary jet as shown in Fig. 6.17. The amplitude of the Mach number variations in the primary jet increases and is also shifted. This effect is less prominent in the secondary stream as displayed in Fig. 6.18. The shock-cell length is measured in the primary axis in order to avoid topological differences between both nozzles. They are presented in Table 6.4. The variation in shock-cell length is of less than 4% and identical for some shock-cells.

	L_{sh}^1/D_s	L_{sh}^2/D_s	L_{sh}^3/D_s	L_{sh}^4/D_s	L_{sh}^5/D_s
Modeled	0.408	0.408	0.396	0.357	0.345
Shifted	0.421	0.408	0.408	0.370	0.345
%increase	3.12	0	3.22	3.57	0

Table 6.4: *RANS shock-cell length for the modeled and the shifted nozzle measured at the axis of the primary stream.*

In summary, the shift of the nozzle increases the mass flow rate of the secondary stream, it increases the intensity of the oblique shock and the Mach number variations in the primary stream and slightly increases the shock-cells length. All these changes could have an impact on the acoustics, for example: the reinforced oblique shock could modify the behavior of the tonal noise screech or the change in the Mach number in the primary stream could affect the development of the internal shear-layer. Nonetheless, the actual impact of this displacement on the acoustics remains uncertain and should be further studied experimentally and numerically in the future.

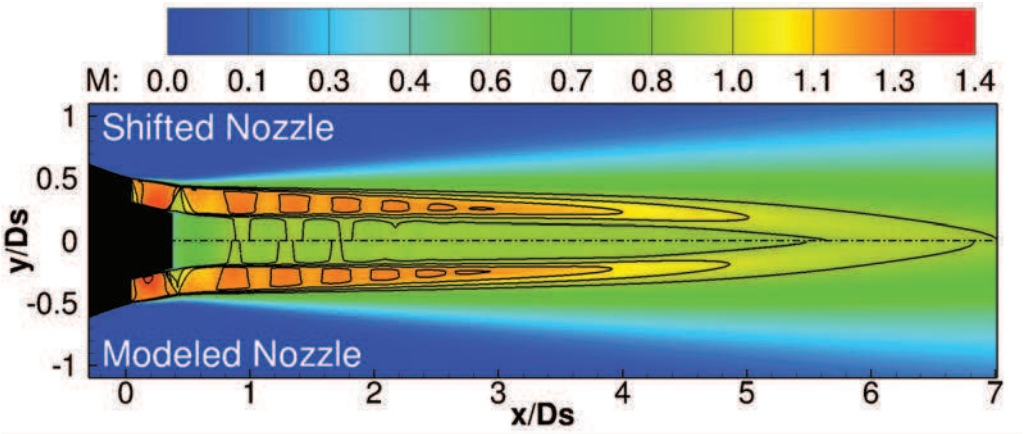

(a)

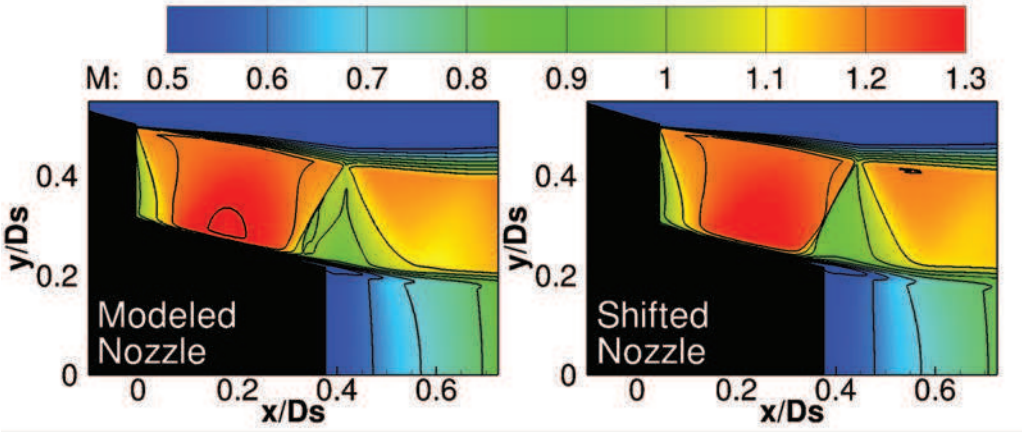

(b)

Figure 6.16: *Mach number contours for the* ***(a)*** *LES mean (top) and RANS (bottom) simulations.* ***(a)*** *General view.* ***(b)*** *Zoomed view.*

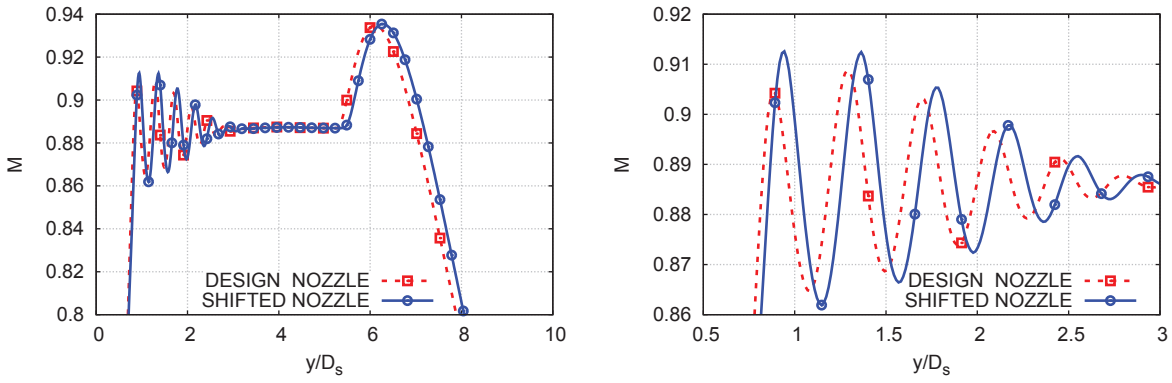

(a) (b)

Figure 6.17: *Comparison of the Mach number profiles along the axis of the primary nozzle between the modeled nozzle and the manufactured one.* ***(a)*** *General view.* ***(b)*** *Zoomed view.*

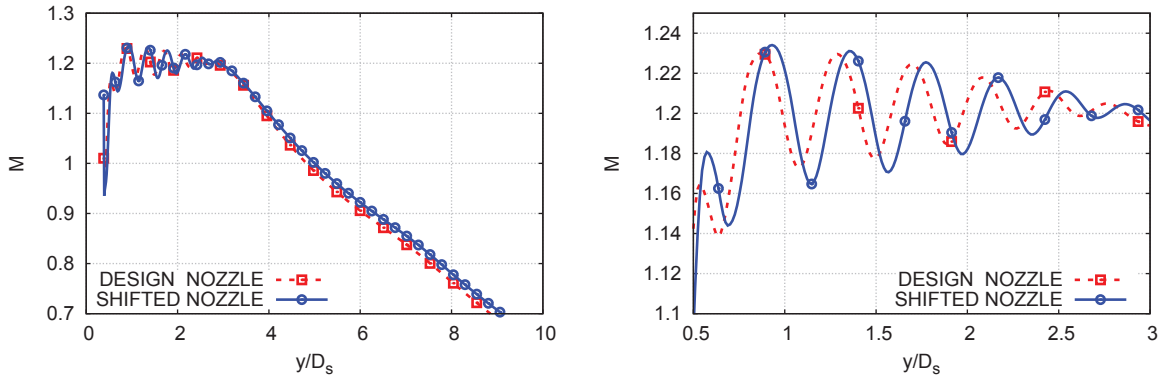

(a) (b)

Figure 6.18: *Comparison of the Mach number profiles along the skewed secondary potential core between the modeled nozzle and the manufactured one.* ***(a)*** *General view.* ***(b)*** *Zoomed view.*

6.3.2 Acoustic-hydrodynamic filtering in the near-field

The near-field flow is composed of hydrodynamic and acoustic perturbations. In order to focus the study in either one or the other, the acoustic-hydrodynamic filtering [181] is applied to the dual stream jet. This procedure was successfully applied to the supersonic under-expanded single jet in Sec. 5.3.2 and it is explained in detail in Sec. 3.3.2. The filtering is carried out on the probes located in the near-field at $r = \{0.85D_s, 1.7D_s\}$ at the secondary nozzle exit plane with an expansion angle of 8°.

Figure 6.19 shows the transformed signal in the $k-\omega$ domain (see Eq. (3.6)). The results are averaged azimuthally to increase their accuracy. The acoustic lines are illustrated with a solid line and a dashed line for the positive and negative ambient sound speed $\pm a_\infty$ respectively. The dotted line illustrates a convective velocity of $0.62U_s$. The region that lays within the acoustic lines represents the acoustic content of the signal. The region that lays outside corresponds to the hydrodynamic perturbations.

Some conclusions can be drawn from Fig. 6.19. Firstly, Fig. 6.19 (a) shows that the hydrodynamic lobe follows the convective velocity of the secondary jet, which exhibits an independence of the near-field with the primary flow. This could be expected, as the energy content of the secondary supersonic flow is much higher than that of the primary subsonic jet. The lobe corresponding to the primary jet convective velocity may lay underneath the one of the secondary jet. This is an expected different behavior with respect to a subsonic dual stream jet [181] where both lobes are clearly present. Secondly, as expected, the hydrodynamic lobe is reduced when the probe is farther away from the axis as it is found at $r/D_s = 1.7$ in Fig. 6.19 (b). The shape of the $k-\omega$ distribution gives information about the dispersion of the pressure fluctuations. In a non-dispersive media the energy of the convective eddies would lay aligned perfectly with the convective velocity instead of presenting a lobe. The amount of dispersion with respect to the convective line, gives an idea of how the perturbations can be seen as *frozen* [166]. Due to this dispersion, some hydrodynamics components would lie on the acoustic side of the $k-\omega$ distribution and *vice-versa*. The energy of the acoustic component is spread over a wide range of the wavenumber axis k because there are several acoustic sources

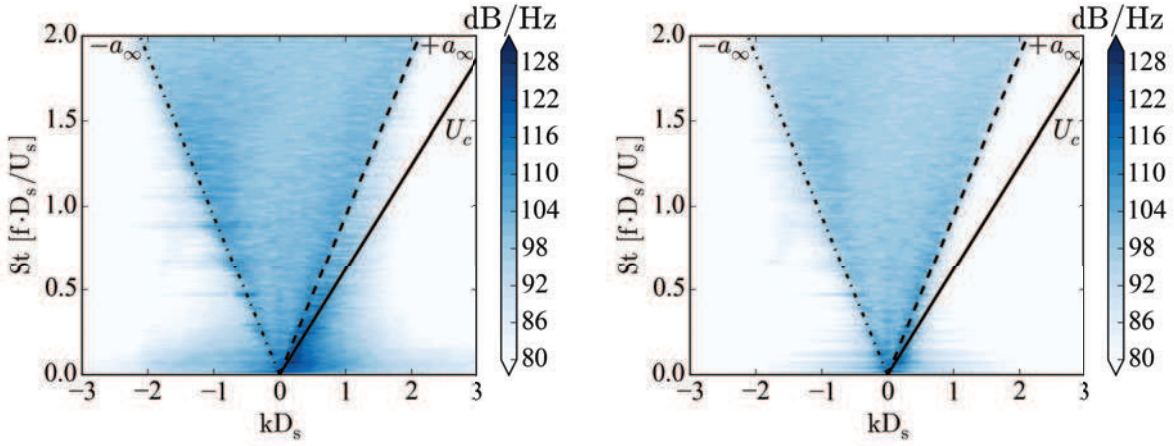

(a) (b)

Figure 6.19: *$k-\omega$ representation of the near-field flow at the probes located at* ***(a)*** 0.85 D_s *and* ***(b)*** 1.7 D_s *from the axis. The solid and dashed lines represent the speed of sound. The dotted line represents the convective velocity.*

inside the jet. The acoustic content is clearly higher with respect to the subsonic jet of Tinney and Jordan [181] due to the fact that here, the acoustic captured is mostly due to the shock-cell noise that is being propagated upstream with a higher intensity whereas in their subsonic jet, it is generated by the mixing noise of fine-scale turbulence.

After the signal is transformed into the $k-\omega$ space, it can be reconstructed into the acoustic and the hydrodynamic component separately. Figures 6.20 (a), (b) and (c), display the original signal, the hydrodynamic signal and the acoustic signal respectively as a function of time and the axial position. The hydrodynamic signal, that is clearly appreciated in Fig. 6.20 (b), shows that it is well aligned with the convective speed $U_c = 0.62U_s$ noted by the solid black line as on the hydrodynamic lobe in Fig. 6.19 (b). As expected, some acoustic components traveling upstream are still present due to the dispersion of the signal at different frequencies. The acoustic component travels upstream and downstream at velocities greater than the sound speed a_∞.

Once the flow is filtered in hydrodynamic and acoustic components, the spatial pressure cross-correlation can be studied for the original signal, and both filtered components. The spatial pressure cross-correlation gives not only information about the spatial size of the large turbulence structures, *i.e.* the wavelength of the wave-like pattern produced by the convected vortices but it also gives information about the characteristic acoustic wavelength being seen at each position of the array. This is done by computing the spatial cross-correlation on the hydrodynamic and the acoustic components separately. The spatial cross-correlation R_{pp} is computed using an analogous expression to Eq. (5.3) but using the pressure. Figure 6.21 depicts the cross-correlation carried out at 3 different reference points along the axial direction averaged with all the azimuthal probes. The first point presented in Fig. 6.21 (a) is located at $x/D_s = 0.85$ and it shows that the acoustic correlation gives the same result as the original signal. At this axial position, the signal is mostly acoustics-originated at the shock-cells due to the fact that the shear-layer has not expanded enough in the radial direction. Farther

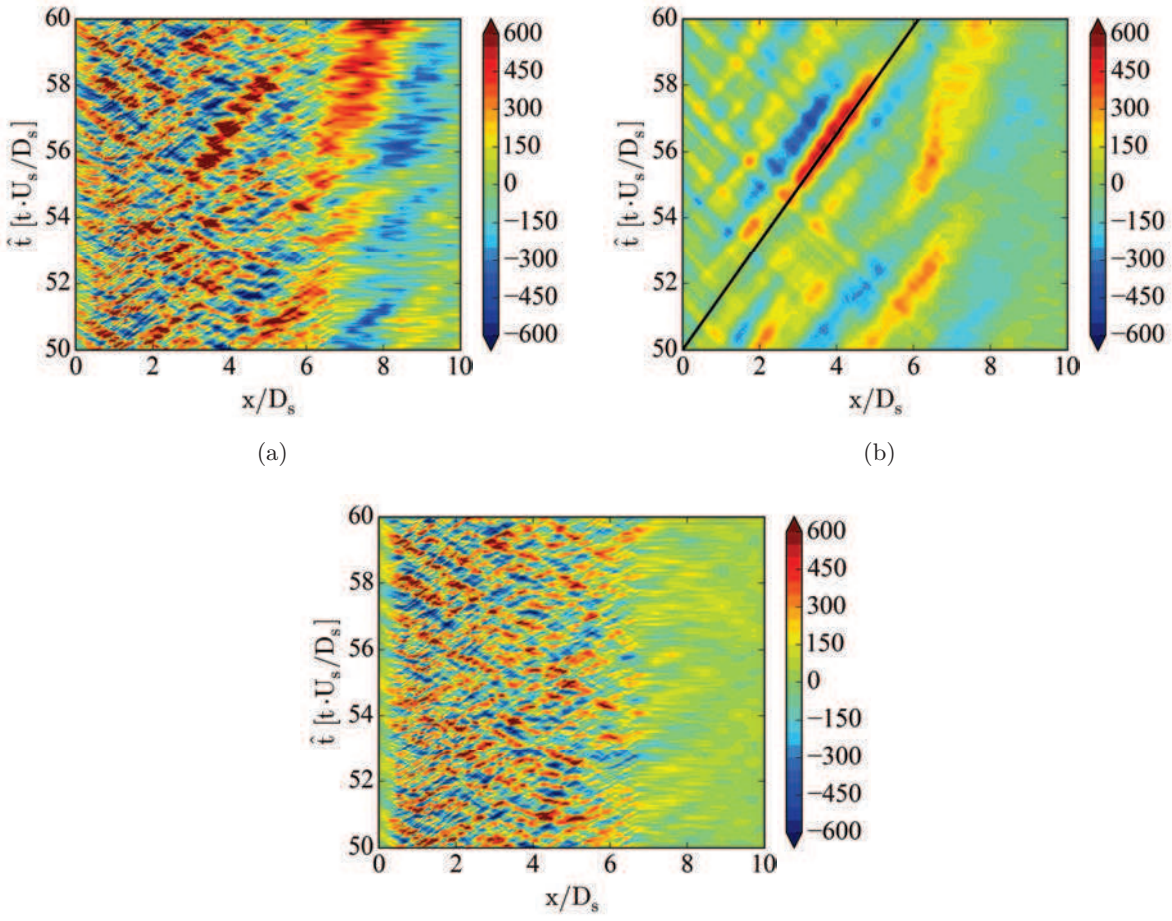

Figure 6.20: *Pressure on a single probe of an azimuthal array of* 16 *probes located at* 0.85 D_s *from the axis which extends up to* 10 D_s *in the axial direction with an expansion angle of* 8°. ***(a)*** *Full signal,* ***(b)*** *hydrodynamic component and* ***(c)*** *supersonic component.*

downstream of the jet, at $x/D_s = 2.6$ Fig. 6.21 (b) the acoustic correlation starts to deviate from the original signal. In particular, the negative side lobes around the maxima are closer together. At this location, the hydrodynamic perturbations are fully developed which can be seen from the larger negative lobes typical from a train of vortices. The last position displayed in Fig. 6.21 (c) is located at $x/D_s = 4.2$. At this position, the three correlations are fully different which emphasizes the importance of an acoustic-hydrodynamic separation of the flow when the measures are done close to the jet. Nonetheless, the three cross-correlations share a common crossing point which shows that the cross-correlation of the original signal keeps the main features of both the acoustics and the hydrodynamics of the flow.

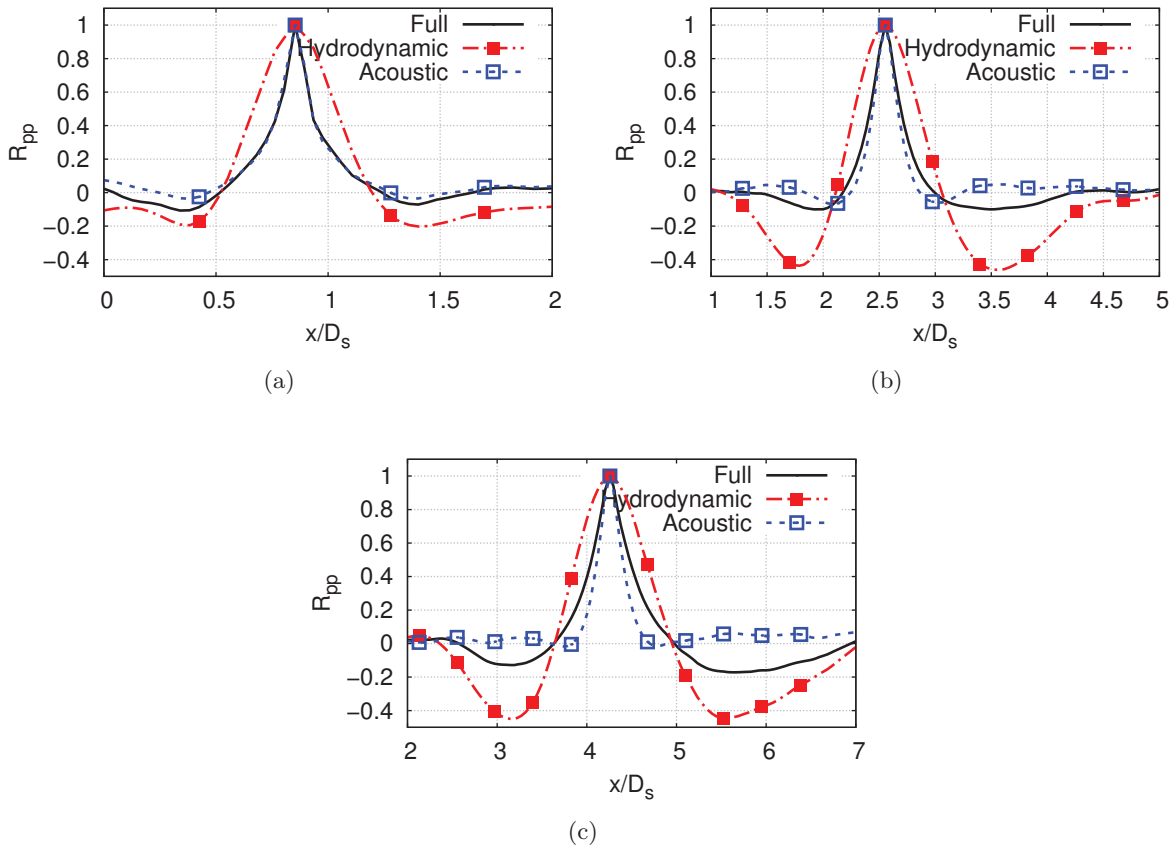

Figure 6.21: *Azimuthally averaged pressure cross-correlation of an azimuthal array of* 16 *probes located at* 0.85 D_s *from the axis which extends up to* 10 D_s *in the axial direction with an expansion angle of* 8°. *Cross-correlations centered at* ***(a)*** $x/D_s = 1$, ***(b)*** $x/D_s = 2$ *and* ***(c)*** $x/D_s = 3$.

The characteristic wavelength λ from Fig. 6.22 (a) can be computed by measuring the distance between the negative peaks around the maxima of the correlations. As expected the characteristic wavelength of the acoustic component clearly differs from the one of the hydrodynamic component. In addition, even though the cross-correlations shown in Fig. 6.21 are mostly different for the original signal and the two components, the characteristic wavelength of the original signal is similar to the one of the hydrodynamic component. The characteristic frequency can be computed from the characteristic wavelength by setting a characteristic

velocity as $f = U_{ref}/\lambda$. The velocity chosen for the hydrodynamic component is the convection velocity $U_c = 0.62\ U_s$. When dealing with the acoustic component, special care should be taken to the way the reference velocity is calculated. As it is illustrated by the sketch of Fig. 3.6, the characteristic pseudo-wavelength λ' along the axis x' is the one that is being computed when measuring the distance between the negative peaks. Moreover, as it is expressed by Eq. (3.8) the velocity a' on the same axis varies with the wavelength. The frequency is therefore computed as

$$f = \frac{\lambda' a_\infty}{\lambda' \left(\sqrt{r^2 + \lambda'^2} - r\right)} = \frac{a_\infty}{\sqrt{r^2 + \lambda'^2} - r}, \tag{6.4}$$

where λ' on the numerator is simplified with the λ' used to compute the frequency f. Here, r being the perpendicular distance from noise source to the array, grows with x as the array has an expansion angle of 8 degrees. The resulting frequencies illustrated in Fig. 6.22 (b) give information about the peak frequencies of the convected vortices and the broadband shock-associated noise. The frequency of the hydrodynamic component starts at $St = 0.65$ but it decays up to a value of $St = 0.17$. On the other hand, the acoustic component shows good agreement with the frequency estimated by the mean shock-cell frequency $\overline{f}_{sh} \approx 1.82$. The reader needs to keep in mind that Eq. (6.4) is an approximation due to the fact that it only takes into account the Doppler effect of the shock-cell noise in the measured λ' but not the fact that the noise comes from several noise sources distributed along the shock-cells.

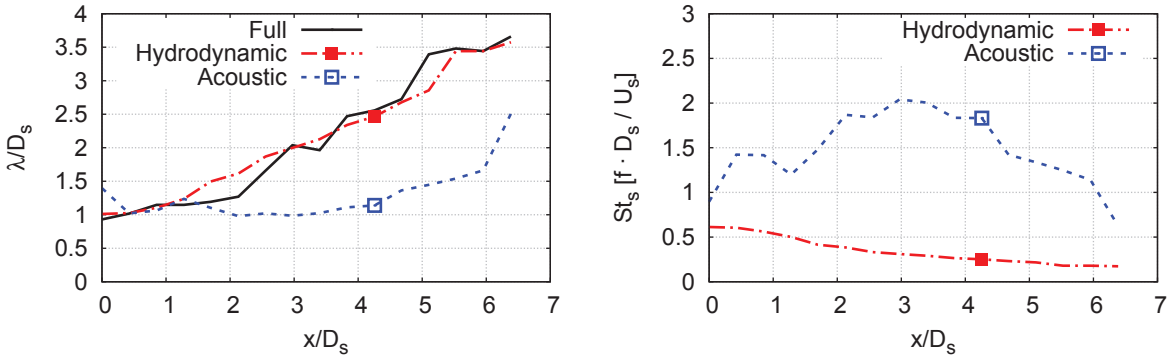

(a) (b)

Figure 6.22: ***(a)*** *Characteristic wavelength computed with the spatial cross-correlation of an azimuthal array of* 16 *probes located at* 0.85 D_s *and* ***(b)*** *the associated frequency with a reference phase velocity.*

Figure 6.23 displays the SPL in dB/Hz computed for the original signal (a), the hydrodynamic component in (b) and the acoustic component in (c). The estimated frequencies computed with Eq. (3.8) and shown in 6.22 (b) are compared to the actual Sound Pressure Level (SPL) computed for each component. Good agreement is found for both the acoustic and the hydrodynamic frequencies which confirms the validity of this approach. Here, the standard reference pressure of $2 \cdot 10^{-5}$ Pa is used.

The SPL is computed as well for the acoustic component in the near-field at the arrays located at $r/D_s = \{0.85D_s, 1.3D_s, 1.7D_s\}$ The shock-cell noise is depicted in Fig. 6.24 centered around

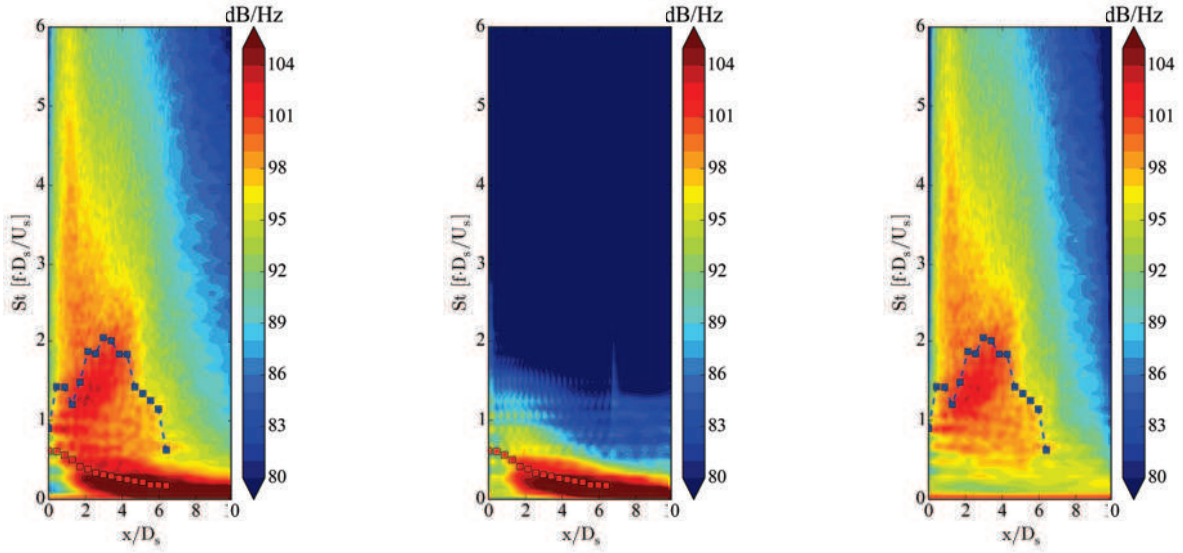

Figure 6.23: *Sound pressure level of an array of probes located at* 0.85 D_s *from the axis which extends up to* 10 D_s *in the axial direction with an expansion angle of* 8°. ***(a)*** *Full signal,* ***(b)*** *hydrodynamic component and* ***(c)*** *supersonic component. The blue symbols represent the characteristic frequencies of acoustic component computed with Eq.* (3.8). *The red symbols correspond to characteristic frequencies of the hydrodynamic component.*

$St_s = 2$, $x/D_s = 2$ highlighted with the dashed circle. This "banana-like" shaped signature that was already encountered for the supersonic under-expanded jet in Sec. 5.3.2 is characteristic of the Doppler effect of shock-cell noise. At the closest position to the axis, there are some higher frequency components that overlap with the shock-cell noise. This high frequency noise is generated at the region where the secondary shear-layer overcomes transition to turbulent regime.

6.3.3 Far-field acoustic field

In the previous section, the acoustics in the near-field were investigated. Here, the noise at the far-field at $r/D_s = 30$ from the inner nozzle exit plane is compared against the experimental measurements from VKI. The pressure perturbations from ***elsA*** were propagated to the far-field using the Ffowcs-Williams and Hawkings analogy presented in Sec. 3.3.1 and the SPL was averaged over 16 azimuthal probes in order to increase the smoothness of the spectra. On the other hand, the experimental measurements were obtained with a single array of microphones.

The comparisons are shown in Fig. 6.25 for different angles computed from the jet direction. Overall, a good agreement is found in the positioning in frequency of the main peak of the broadband shock-associated noise at the angles where it is clearly present, that is, in the upstream angles in the range of $90° - 120°$. On the other hand, the amplitudes are off by 10 dB. The far-field pressure spectra from the single jet matched well the numerical results and other experimental results as displayed in Fig. 5.15. Without fully discarding the possibility of an error in the measurements, some of the differences observed in the aerodynamics could

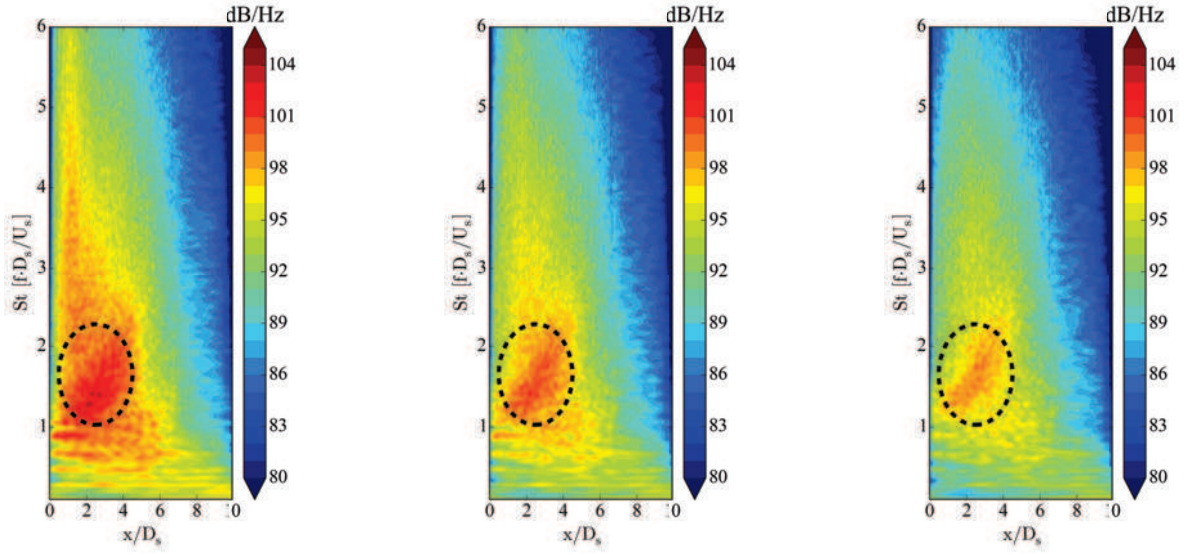

Figure 6.24: *Acoustic component of the near-field in dB/Hz along different axial positions for a line array with an angle of* 7.3° *at* ***(a)*** $r/D_s = 0.85$, ***(b)*** $r/D_s = 1.3$ *and* ***(c)*** $r/D_s = 1.7$.

explain a difference in the far-field noise. An increase in the noise levels of the LES could be related to the higher *rms* values obtained in the secondary shear-layer as shown in Fig. 6.10. Also, the appearance of screech in experiments tends to lower by 1 to 2 dB the amplitude of the main peak of the BBSAN for supersonic under-expanded single jets [43]. Moreover, the fact that the first shock-cell presents a different pattern due to the axial shift of the experimental secondary nozzle (see Sec. 6.3.1) may change the stability of the jet and its associated noise.

For comparison purposes, the spectra are shifted 10 dB in Fig. 6.26 (a). Due to the fact that the shock-cell lengths are smaller in the simulation, a shift is expected in the main peak of the BBSAN as it is inversely proportional to this parameter as stated by Eq. (5.2). The frequency axis is multiplied by a factor proportional to the mean variation of the shock-cell length shown in Table 6.3 as

$$f_{mod} = \frac{\overline{L_{sh}^{exp.}}}{\overline{L_{sh}^{num.}}} f_{orig}, \tag{6.5}$$

where f_{orig} is the original frequency vector, $\overline{L_{sh}^{exp.}}$ is the average experimental shock-cell length and $\overline{L_{sh}^{num.}}$ is the average numerical shock-cell length. The modified frequency vector is then used for the experimental results as it is shown in Fig. 6.26 (b). The peak of the BBSAN agrees well with the experimental spectra when the new modified frequency vector is defined.

6.3.4 Power spectral density axial distribution

The data extracted in the axis (AXIS) can be analyzed in terms of power spectral density in the axial range $0 < x/D_s < 10$. When the pressure energy distribution is transformed into the frequency-wavenumber domain (Fig. 6.27 (a)), different tones are found in the negative part of the wavenumber, which suggests that they are waves being convected upstream. The same

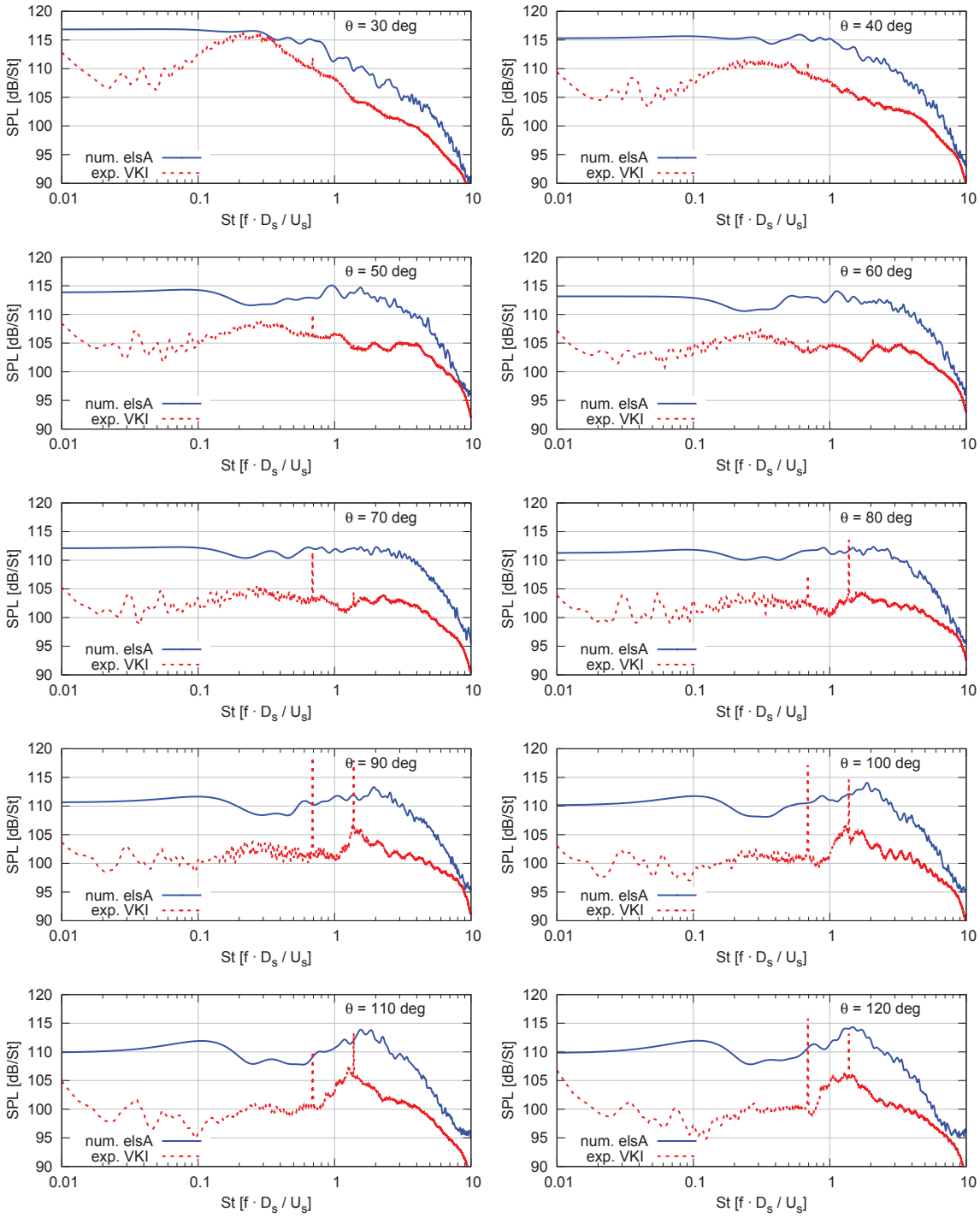

Figure 6.25: *Far-field sound pressure level at $r/D_s = 30$ from the primary nozzle exit for different angular positions with respect to the jet direction.*

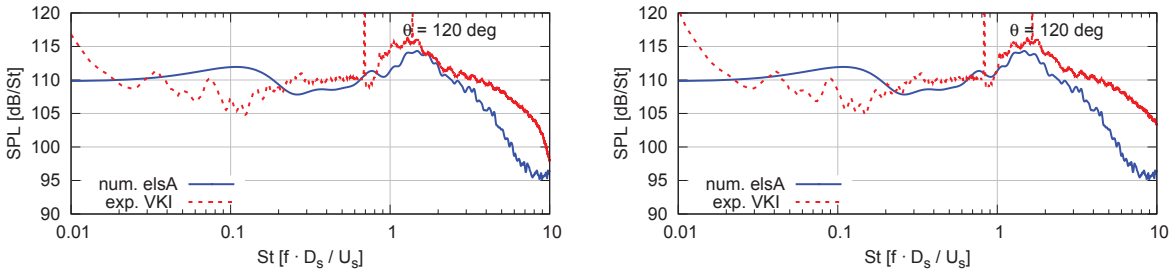

Figure 6.26: *Far-field acoustics at* $r/D_s = 30$ *from the primary nozzle exit at* 120° *with* ***(a)*** *a shift of 10 dB applied and* ***(b)*** *a shift in frequency is also applied.*

decomposition is carried out for the data sets at the primary (LIP_P) and secondary (LIP_S) lip-lines shown in Fig. 6.27 (b) and Fig. 6.27 (c) respectively. As it can be seen in Fig. 6.27, the patterns are mainly contained between the line that represents the acoustic ambient velocity a_∞ and the mean negative acoustic velocity of the corresponding data set. The convective velocity as well as the local sound speed change with the axial position. For all data sets displayed in Fig. 6.27, the convective velocity $U_c = 0.62U_s$ lays on the lobe of the downstream convective velocity.

Theoretically, in a dual stream jet whose primary jet is subsonic, four sets of negative traveling waves could be detected in the flow. First, a wave that is generated by the shock-cell noise of the secondary shear-layer could enter the supersonic secondary stream in the same way as it happens for a supersonic single jet (see Fig. 5.28). Moreover, these waves would travel up to the shear-layer of the primary inner subsonic stream which then would be convected as a regular wave inside. This wave could be again convected outside if it has not been dissipated already. Second, the shock-cell noise generated in the primary inner shear-layer could be directly convected upstream throughout the inner subsonic jet. Third, a set of trapped acoustic waves generated at the end of the inner potential core could be formed and travel through the subsonic jet as it was demonstrated by Towne *et al.* [211] for subsonic single jets at Mach numbers about $M = 0.9$. At certain frequencies, these trapped waves resonate due to the end conditions provided by the nozzle and the streamwise contraction of the potential core. Last, upstream traveling parasitic waves generated at the exit boundary of the domain could also appear but are not contemplated in this study as the simulation was carried out with non-reflective boundary conditions and a sponge layer that would attenuate them.

The positive and negative traveling waves can be analyzed independently by reverting the transformation of the data sets from the frequency-wavenumber domain to the time-space domain by only using the positive or the negative wavenumbers. Figure 6.28 shows the positive and negative pressure waves for the AXIS and Fig. 6.29 for the data sets LIP_P and LIP_S which are averaged among the 16 azimuthally distributed probes at each axial location. The negative traveling waves are now clearly visible, especially for the data sets in both shear-layers that are superimposed with the downstream traveling vortices. A problem that arises with this separation is the fact that the axial discretization of the probes changes after $x/D_s = 7$ from 0.1 D_p to 1 D_p. Even though the probes were interpolated into a uniform mesh size before the transformation, the change in axial discretization is evident in some of the separations

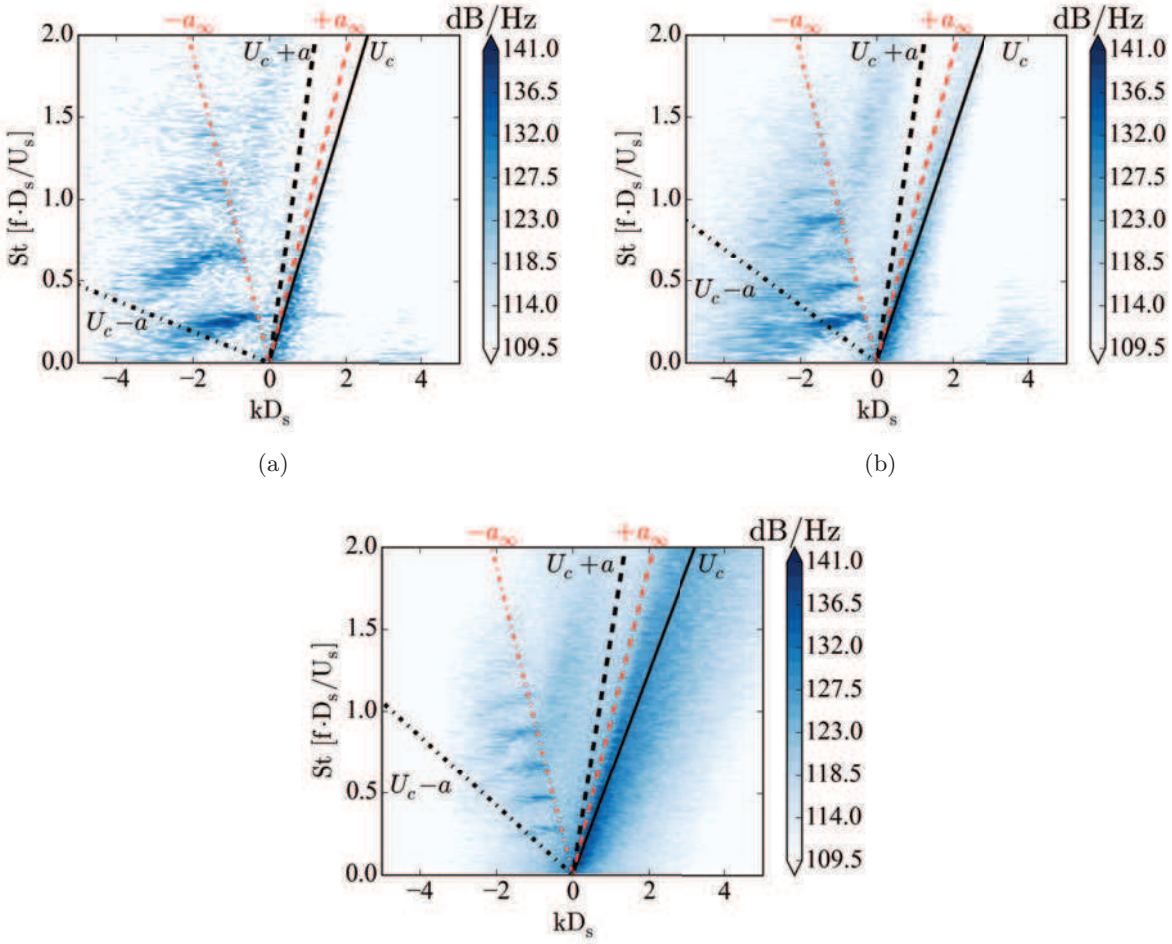

(a) (b)

(c)

Figure 6.27: *Frequency-wavenumber energy distribution of the pressure for the data set* ***(a)*** *AXIS,* ***(b)*** *LIP_P and* ***(c)*** *LIP_S*

investigated in this work. The different main distinguishable tones for all three pressure data sets are summarized in Table 6.5.

Data Set	St_1	St_2	St_3	St_4	St_5	St_6
AXIS	0.27	0.53	0.64	1.07	1.39	
LIP_P	0.27	0.46	0.64	0.86	1.03	1.22
LIP_S	0.27	0.46	0.64	0.86	1.03	1.22

Table 6.5: *Frequency tones observed for the pressure energy distribution at the AXIS, LIP_P and LIP_S data sets. The Stouhal number is defined based on the secondary diameter and the secondary perfectly expanded jet exit velocity.*

In order to understand better the excited frequencies and its axial localization, four different axial positions have to be evoked. First, the shock-cells are mainly located between $0 < x/D_s < 4$, second, the mean flow of the secondary stream, even if it does not clearly show a shock-cell pattern, it is still supersonic up to $x/D \approx 5.75$, which could be taken as the end of the secondary potential core. Third, the secondary stream merges with the primary between $6.25 < x/D < 8$. And last, the end of the primary potential core could be considered to be about $x/D \approx 9$, which is elongated due to the merging with the secondary stream.

The PSD on AXIS presented in Fig. 6.28 demonstrates that the identified tones belong indeed to the negative traveling waves reaching up to $St_s = 2$ (Fig. 6.28 (a)). The first tone St_1 has an extreme at the position where both concentric jets fully merge (about $x/D_s = 8$) and it is being excited up to an upstream distance of $x/D_s = 2$. The remaining tones exhibit a higher intensity in the range $2 < x/D_s < 6$. On the other hand, the positive traveling waves shown in Fig. 6.28 (b) are accumulated below $St = 0.5$ which are characteristic lower frequencies for the hydrodynamic perturbations that are convected downstream. The energy distribution for the original axial velocity displayed in Fig. 6.28 (b) presents a peak at $St = 0.5$ and $x/D_s = 6$, farther downstream, the energy distribution levels grow due to the mixing of the jet after the end of the potential cores.

A similar energy content of the pressure energy distribution is found for the LIP_P and LIP_S data sets shown in Fig. 6.29. At this last location it is clear that the separation in negative and positive traveling waves is limited and a discontinuity is distinguishable where the discretization changes. Some of the peaks appear to be harmonics of a fundamental frequency. The peaks are not clearly defined in the frequency domain which suggests that the group velocity is not singular but broadband. The impact of the shock-cells is seen in the pressure energy distribution with a higher level in the compression zone. The results found at LIP_P and LIP_S present two sets of patterns. The first one at the lower frequencies is situated between the end of the shock-cell region and the start of the merging region around $4 < x/D_s < 7$, which shares a portion of the supersonic (non-shocked) region of the secondary stream. The higher frequencies clearly are in the region of the shock-cells between $2 < x/D_s < 4$. Additionally, LIP_P (Fig. 6.29 (c)) presents a similar distribution for the positive traveling waves than in AXIS. The positive traveling waves at LIP_S shown in Fig. 6.29 (d) exhibit a logarithmic shape, with higher frequencies excited close to the nozzle lip, and lower frequencies excited when the shear-layer is developed.

In the present work, the primary subsonic jet has a Mach number close to the one proposed by

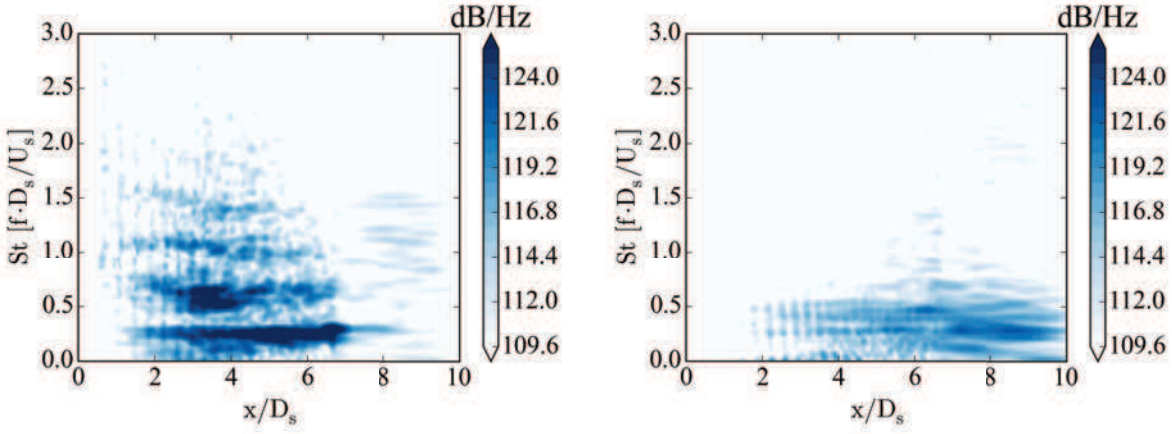

Figure 6.28: *Frequency-space energy distribution along the axial direction for the data set AXIS of* ***(a)*** *the negative traveling pressure waves and* ***(b)*** *the positive traveling pressure waves.*

Towne *et al.* [211] which has a high receptivity to establish trapped acoustic waves, however, here the case of consideration is the one of a dual-stream with a supersonic under-expanded secondary stream. Moreover, the PSD shows a great resemblance with the patterns obtained for the supersonic under-expanded single jet. The patterns present at the AXIS extend up to the merging point of both streams for the lower frequencies, and then they reduce their axial extension for higher frequencies. On the other hand, the PSD computed at LIP_P and LIP_S are composed of two sets of patterns. The first one for the lower frequencies is situated between the end of the shock-cell region and the start of the merging region, which shares a portion of the supersonic (non-shocked) region of the secondary stream.

The data sets located in the primary and secondary lip-lines are composed of 16 azimuthal probes and they can be further decomposed into the azimuthal modes as explained in Sec. 3.3.3. Here, only the decomposition of the negative traveling waves is investigated as they are the only ones that present a noticeable pattern. Only the first 3 modes and the mean value are used as they are the ones with the highest energy content and they are the less polluted by the aliasing as discussed in Appx. B. The results are shown in Fig. 6.30 and 6.31 for the LIP_P and LIP_S respectively and the associated frequencies presented in Table 6.5 at each mode are summarized in Table 6.6.

	mode 0	mode 1	mode 2	mode 3
LIP_P and LIP_S	St_1, St_3	St_2, St_4	St_3, St_5	St_4, St_6

Table 6.6: *Frequency tones observed for the pressure energy distribution at the LIP_P and LIP_S data sets according to the azimuthal mode.*

As it can be seen from Table 6.6, the different azimuthal modes share some of the frequencies. This could imply that the generation of the modes are linked and corresponds to the same phenomena encountered for the single jet, the shock-cell noise. Moreover, two main regions where the patterns are found share common azimuthal modes.

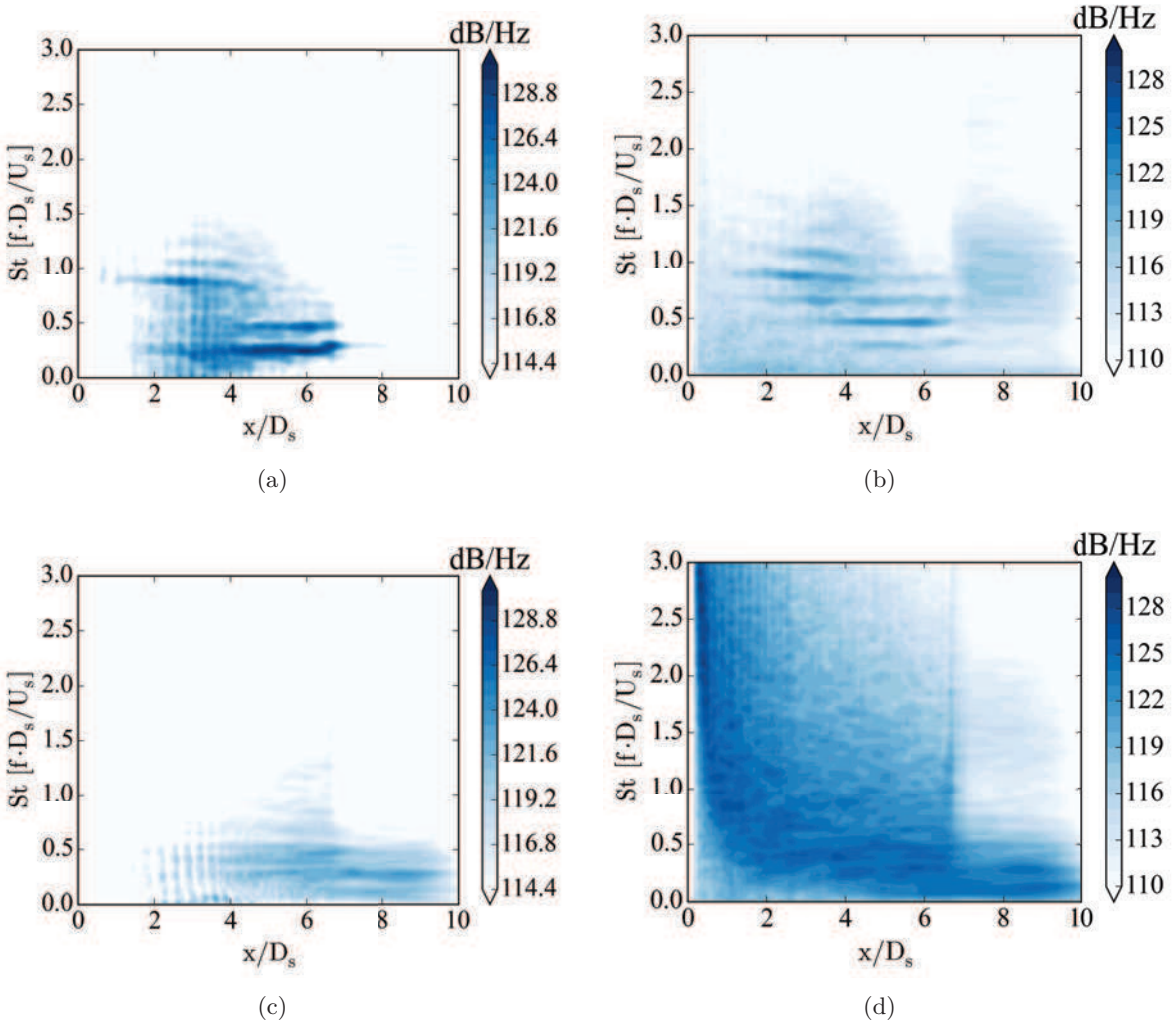

Figure 6.29: *Frequency-space energy distribution along the axial direction for the data set LIP_P on the left column and LIP_S on the right column of* ***(a)***,***(b)*** *the negative traveling pressure waves and* ***(c)***,***(d)*** *the positive traveling pressure waves.*

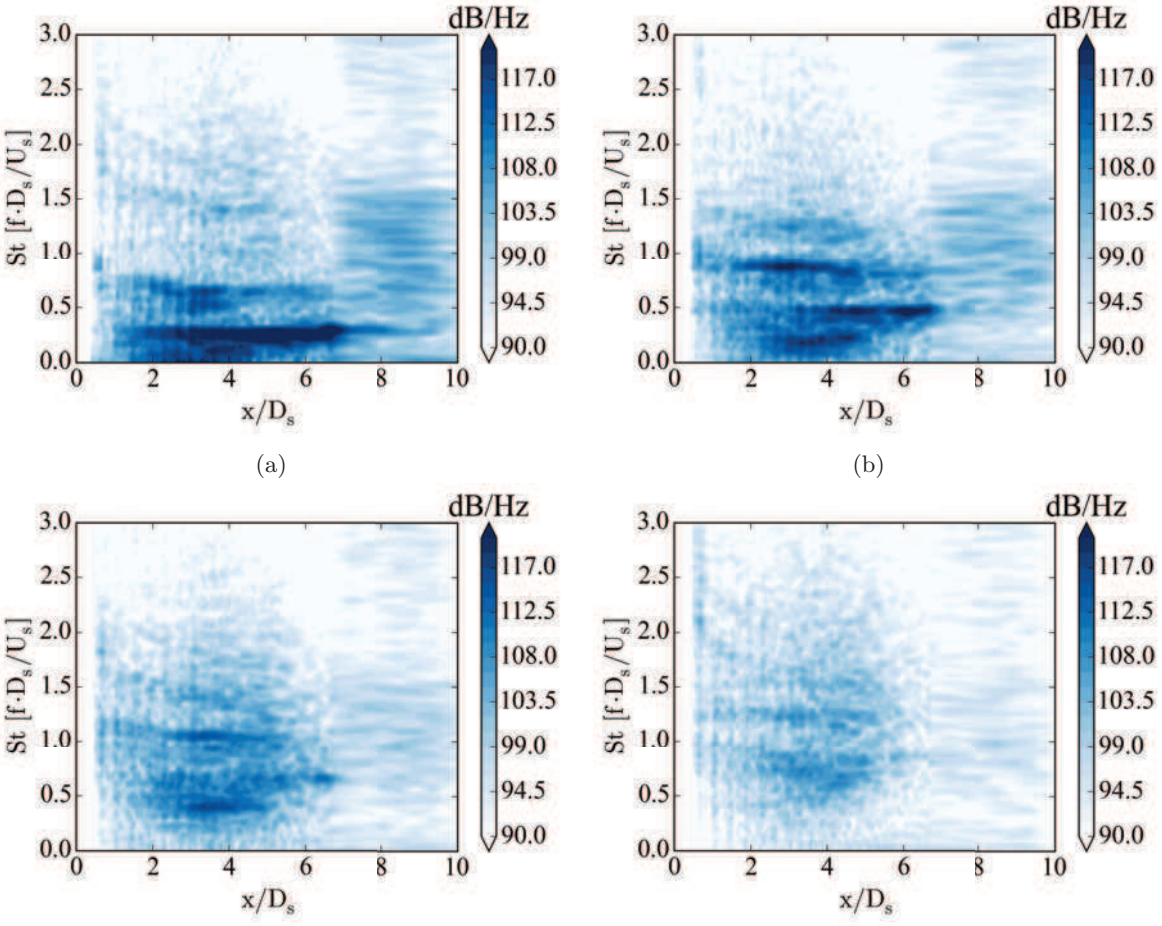

Figure 6.30: *Frequency-space energy distribution along the axial direction for the data set LIP_P of the negative pressure traveling waves for the azimuthal modes:* ***(a)*** *mode 0,* ***(b)*** *mode 1,* ***(c)*** *mode 2 and,* ***(d)*** *mode 3.*

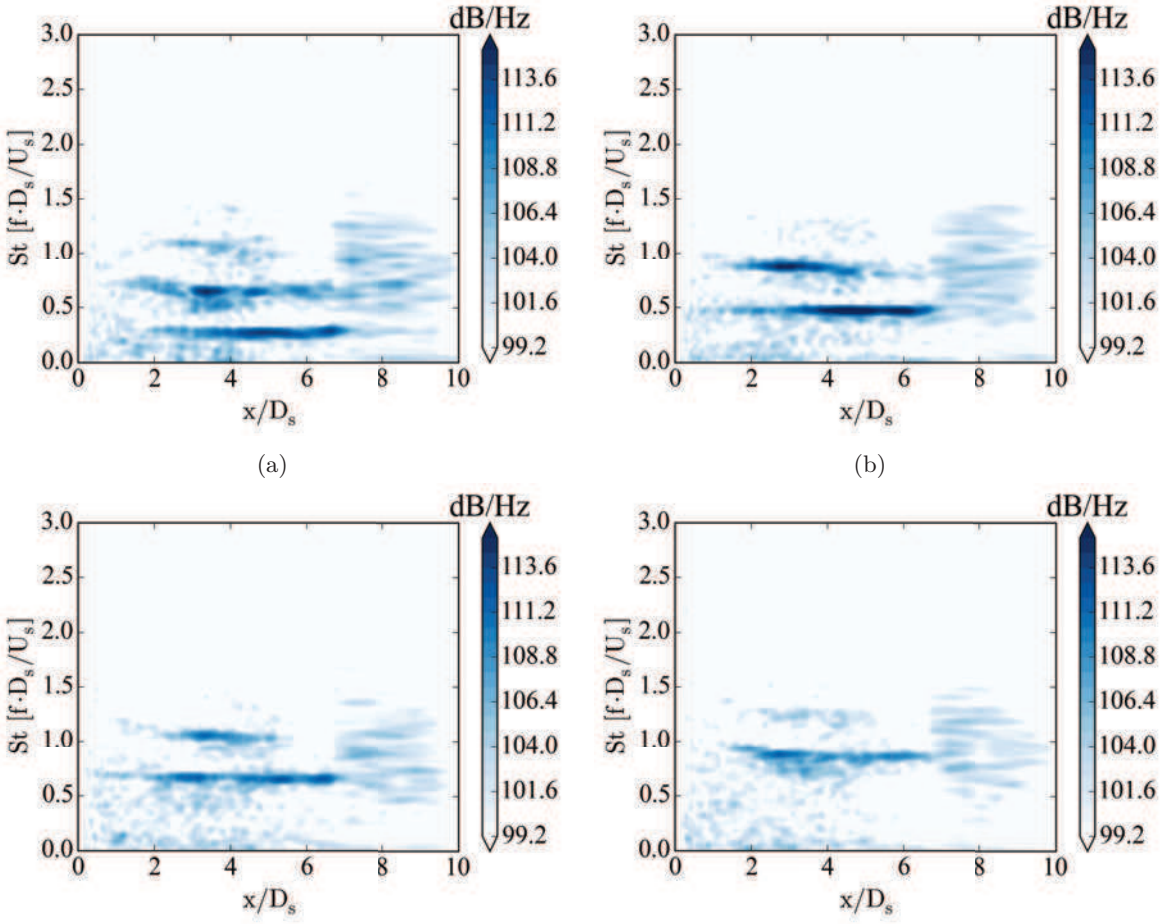

Figure 6.31: *Frequency-space energy distribution along the axial direction for the data set LIP_S of the negative pressure traveling waves for the azimuthal modes:* ***(a)*** *mode 0,* ***(b)*** *mode 2 and,* ***(b)*** *mode 3.*

6.3.5 Wavelet analysis

The wavelet-based methodology described in Ch. 4 implemented to identify and extract the characteristic events of the single jet (Sec. 5.3.6) is applied in this section to the data sets AXIS, LIP_P, LIP_S and NF1D. The wavelet parameters set for the single jet are kept constant for this case of study. Moreover, a similar representation of the results is discussed (see Sec. 5.3.6). The two-dimensional cross-conditioning is performed by the average of only the positive $y/D_s > 0$ and negative $y/D_s < 0$ regions of the cut at $z/D_s = 0$. Moreover, the azimuthal decomposition is used as well in order to identify the shape of the events of each mode with a two-dimensional cross-conditioning averaged over an axial cut. The equivalent frequencies and axial positions of the reference point used to detect the events are presented in the following for each variable and data set.

Axis probes analysis

The cross-conditioning applied to the AXIS is displayed in Fig. 6.32. The axial velocity events were computed at an equivalent frequency of $St_s(s) = 0.5$, that is the frequency where the energy distribution at the axial position $x/D_s = 5$ exhibits a higher energy distribution. The auto-conditioning of the axial velocity (*i.e.* the plot of the axial velocity using as a reference the events obtained with the same variable) is shown in Fig. 6.32 (a). Down traveling waves that grow with the axial direction are originated achieving a local maximum about $x/D_s = 5$, that is the position where the u_{rms} is maximum. The cross-conditioning with the pressure displayed in Fig. 6.32 (b) presents two different waves. The first wave is found in the range $2 < x/D_s < 4$ where the shock-cells are concentrated and it is demonstrated later that they are waves traveling upstream. The impact of the shock-cells on the amplitude of the signature is clearly illustrated by all the peaks in this region. The second wave, traveling downstream is the corresponding signature of the velocity displayed in Fig. 6.32 (a), phased π *rad* (negative amplitude). The two-dimensional auto-conditioning shown in Fig. 6.33 (a) presents events that are extended in the radial direction up to 0.5 D_s and shifted with the higher velocity of the secondary stream. The two-dimensional cross-conditioning depicted in Fig. 6.33 (b) shows that the impact on the pressure is extended radially more than 1 D_s. In the detailed region, the negative traveling waves are present in the subsonic primary jet only.

Next, the cross-conditioning using the negative traveling pressure waves on the AXIS is discussed using as reference frequency $St_s(s) = 0.64$. This equivalent frequency is used as it is one of the frequencies that presents a higher number of events at $x/D_s = 3$. Figure 6.32 (c) shows the cross-conditioning between p_{neg} and the axial velocity u. A wave with constant amplitude traveling downstream is captured at a downstream position, where the event is located. This could mean that the downstream traveling waves are coupled to the events detected at $x/D_s = 3$. The amplitude of the down-traveling waves grows in the region of the shock-cells and then it keeps a constant mean value. Figure 6.34 (a) exhibits a similar pattern as the one obtained with the axial velocity events shown in Fig. 6.33 (a). The auto-conditioning of the negative traveling pressure waves is displayed in Fig. 6.32 (d). Taking a look at the envelope of the signature, it seems that different events are captured as well. The positive envelope grows with the shock-cells and then it is constant up to $x/D_s = 6$, where it decays. On the other hand, the negative envelope presents two minima at $x/D_s = 3$ and $x/D_s = 6$. As it is discussed later, the second peak could correspond to an azimuthal mode 0, while the first peak

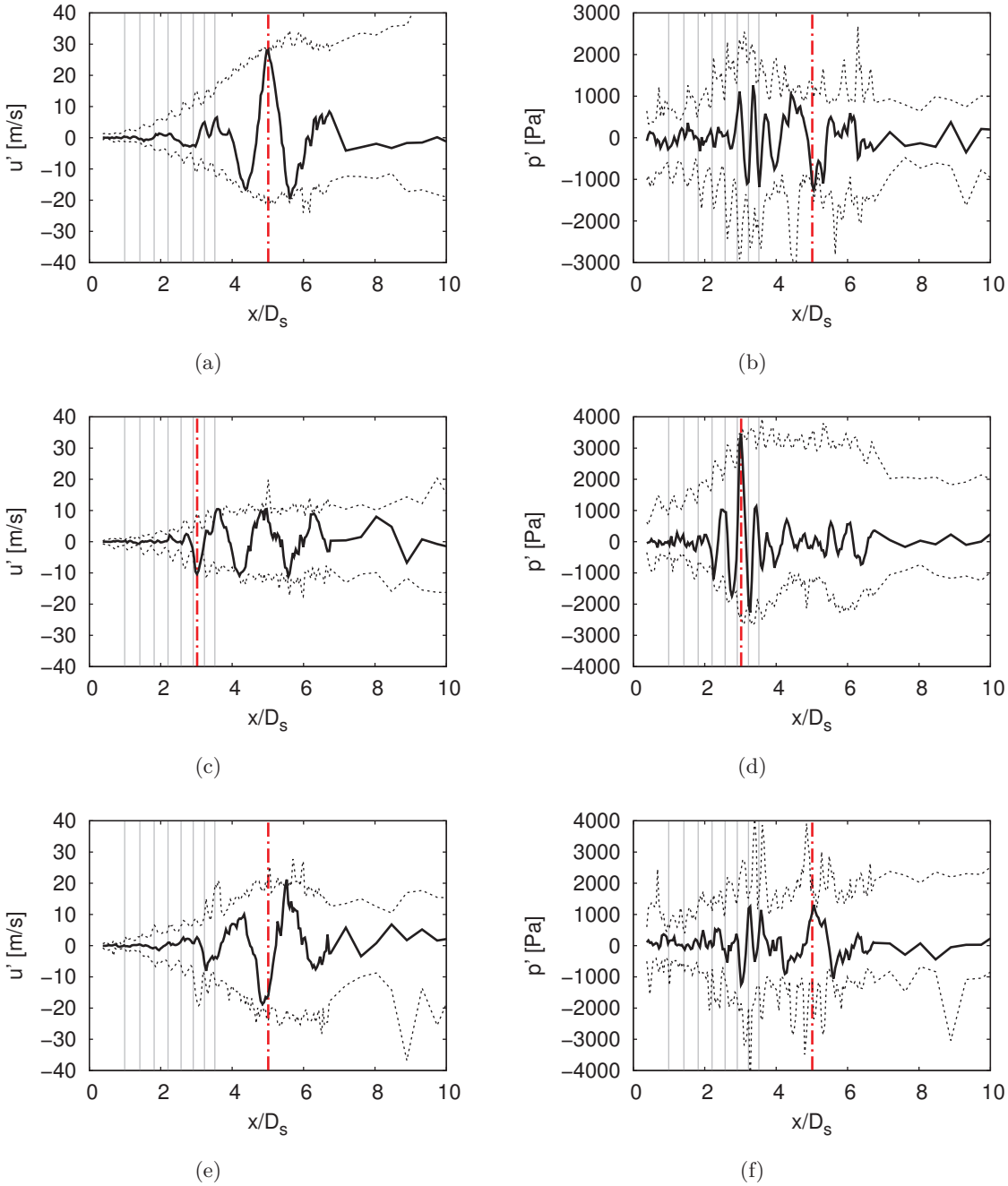

Figure 6.32: *Cross-conditioning of* ***(a)*** $u-u$, ***(b)*** $u-p$, ***(c)*** $p_{neg}-u$, ***(d)*** $p_{neg}-p$, ***(e)*** $p_{pos}-u$ *and* ***(f)*** $p_{pos}-p$ *from AXIS where the first variable is the one used to locate the events and the second variable is the one plotted. The dash black line represents the envelope of the signature for all axial positions. The vertical dashed line represents the axial position where the events are located.*

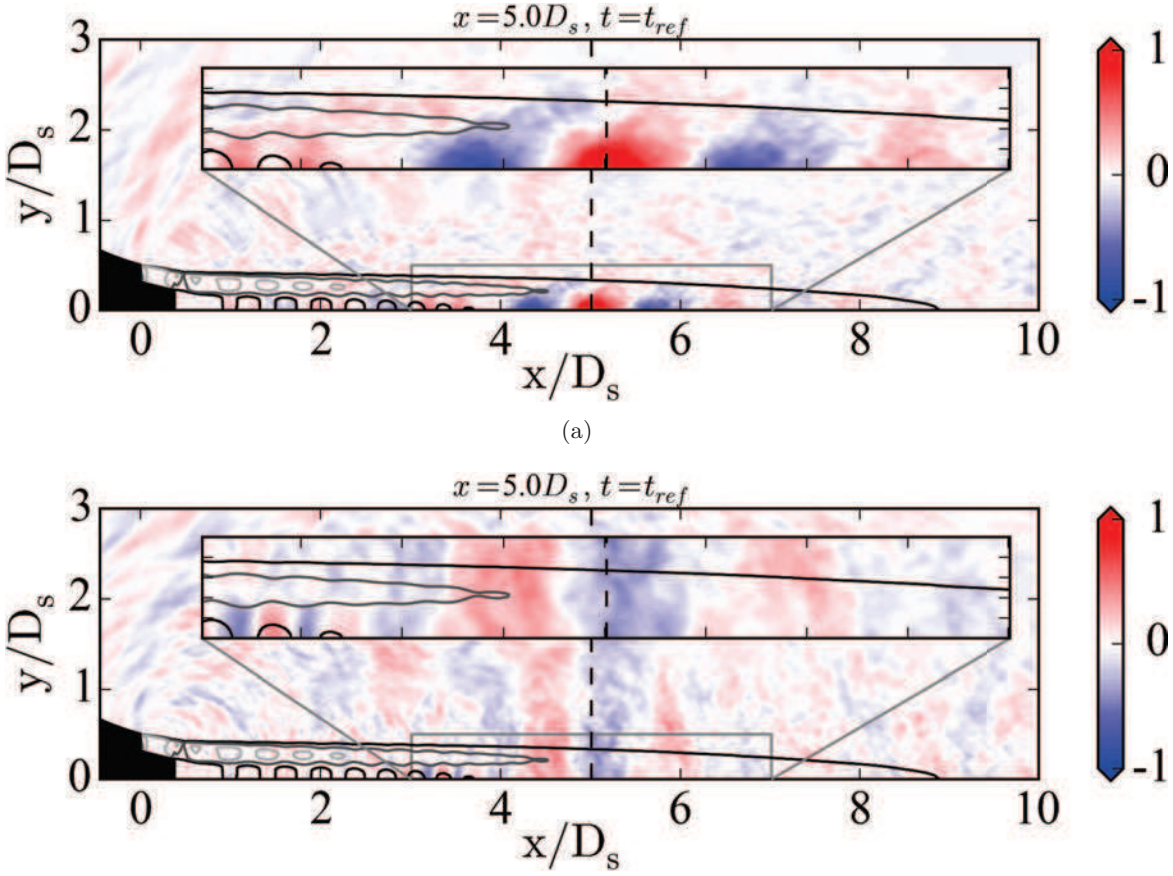

Figure 6.33: *Cross-conditioning of* ***(a)*** $u - u$ *and* ***(b)*** $u - p$ *from AXIS for the event localized at the axial position* $x/D_s = 5$ *where the first variable is the one used to locate the events and the second variable is the one plotted which is non-dimensionalized by the standard deviation. The vertical dashed line represents the location in space at the axis of the reference point.*

could correspond to the azimuthal mode 1. Contrary to the signature computed with u, here both signatures travel upstream with different spatial scales. As it is displayed in Fig. 6.32 (d), the negative traveling waves presented in the two-dimensional cross-conditioning are trapped in the subsonic jet.

The signatures calculated with the cross-conditioning of the positive traveling pressure waves on the AXIS is shown in Fig. 6.32 (e) for an equivalent frequency $St_s(s) = 0.64$. Contrary to the signature obtained with u, the signature of u using as the reference events the p_{pos} are skewed in shape, having the maxima downstream of the event position. The maxima of the envelope lays in the same general position but on this case, the amplitude decays farther downstream. The auto-conditioning of the pressure displayed in Fig. 6.32 (f) presents a similar behavior than the one of the axial velocity. A wave traveling upstream is found between $x/D_s = 2$ and $x/D_s = 4$ and the actual event captured travels downstream. The contours of the two-dimensional cross-conditioning using p_{pos} exhibit the same features as the ones shown in Fig. 6.32 and are thus omitted.

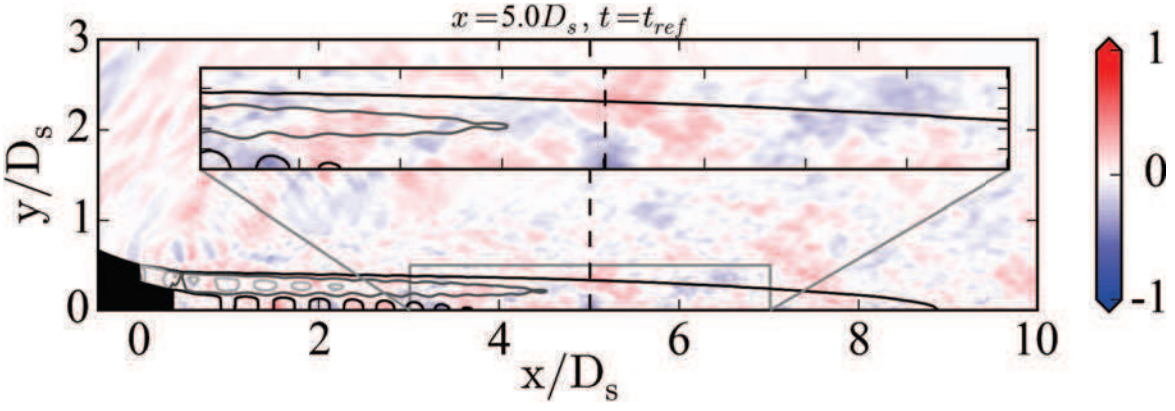

(a)

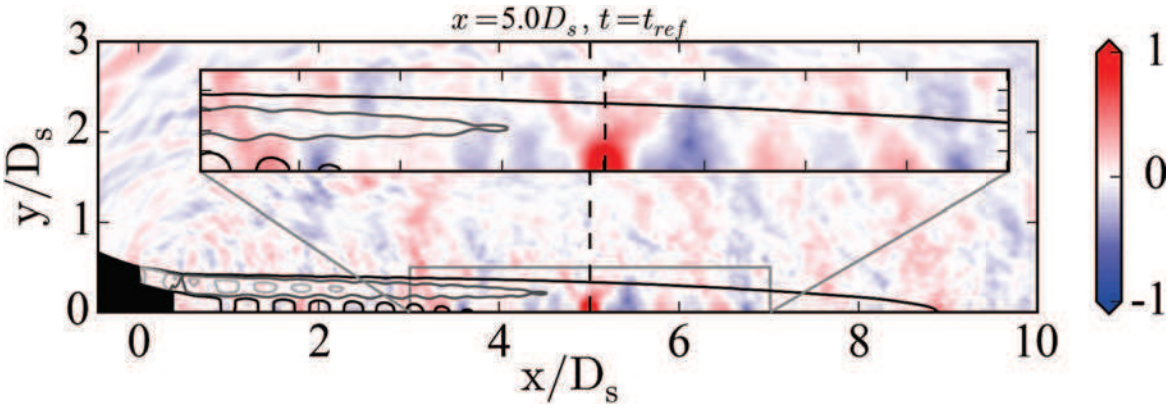

(b)

Figure 6.34: *Cross-conditioning of* ***(a)*** $p_{neg} - u$ *and* ***(b)*** $p_{neg} - p$ *from AXIS for the event localized at the axial position* $x/D_s = 5$ *where the first variable is the one used to locate the events and the second variable is the one plotted which is non-dimensionalized by the standard deviation. The vertical dashed line represents the location in space at the axis of the reference point.*

Primary lip-line probes analysis

Next, the signatures of the events computed with the data set LIP_P shown in Fig. 6.35 are discussed. For this data set, a constant equivalent frequency of $St_s(s) = 0.86$ was used for all variables and axial positions. The auto-conditioning calculated with the axial velocity displayed in Fig. 6.35 (a) presents a constant growth from $x/D_s = 1$. The higher levels appearing in the first diameter are due mostly to a bad averaging because of a lower number of events detected at this equivalent frequency. The constant growth of the signature amplitude agrees with the u_{rms} that also follows a constant growth. Contrary to the AXIS, no clear peaks are found on this signature. Figure 6.36 (a) illustrates the signature of the large structures that are convected downstream in the interior of the jet which are being distorted by the secondary jet. On the other hand, the envelope of the signature obtained for the pressure presented in Fig. 6.35 (b) exhibits a maximum around $x/D_s \approx 4$, at the end of the shock-cells where the axial velocity is maximum. Similarly to the signatures at the AXIS, two different waves can be distinguished. The first one is a negative traveling wave located at $x/D_s = 3$ and the second one, which is the one captured by the event, is traveling upstream at the convective velocity of this axial location. The traveling directions are verified by examining the evolution of the signatures in time as it was investigated in Sec. 5.3.6 for the single jet, but those figures are omitted in order to ease the lecture of this section. For the data sets LIP_P and LIP_S, the envelopes and the signatures are depicted after averaging of each azimuthal position. The envelope is obtained checking the maximum and minimum values for the events at all axial positions. For this reason, the difference between the signature (computed at one axial position) and the envelope is higher. Figure 6.36 (b) shows how the pressure is extended through the shear-layers up to the near-field of the jet.

The cross-conditioning of $p_{neg} - u$ at the LIP_P is displayed in Fig. 6.35 (c) to present similar results than those obtained at the AXIS. However, the two-dimensional cross-conditioning shown in Fig. 6.37 (a) does not highlight any patterns with the same intensity than AXIS because the amplitude of the mean wave is half the one captured at the AXIS and the rms values are higher. A wave traveling downstream is captured for the axial velocity while Fig. 6.35 (d) displays the negative traveling pressure wave which decays in amplitude when it encounters the first shock-cells. Compared to the signature computed at the AXIS, it presents less oscillations in the axial direction. This could be due to the fact that the signature is shifted to the axis as shown in Fig. 6.37 (b). From this figure, it can be seen that the signal in the secondary shear-layer is in opposite phase to the one encountered in the primary shear-layer and inside the subsonic jet. On the other hand, the event in the secondary shear-layer moves downstream instead of upstream, indicating a link between the down-traveling waves and the upstream traveling waves.

Last, the events obtained using the positive traveling pressure waves are depicted in Fig. 6.35. The cross-conditioning of the axial velocity shown in Fig. 6.35 (e) displays a negative peak with a similar shape than the one corresponding to AXIS. However, in this case, the envelope does not present a clear peak along the axial direction. When checking the two-dimensional cross-conditioning displayed in Fig. 6.38 (a), it is clear that the event that is being captured is the same one that was found in the AXIS as the main patterns extend to the axis instead of being centered on the actual LIP_P. Regarding the auto-conditioning at this location, the pressure profile shown in Fig. 6.35 (f) presents only a wave traveling downstream. If a closer look is taken to the two-dimensional cross-conditioning illustrated in Fig. 6.38 (b), it can be

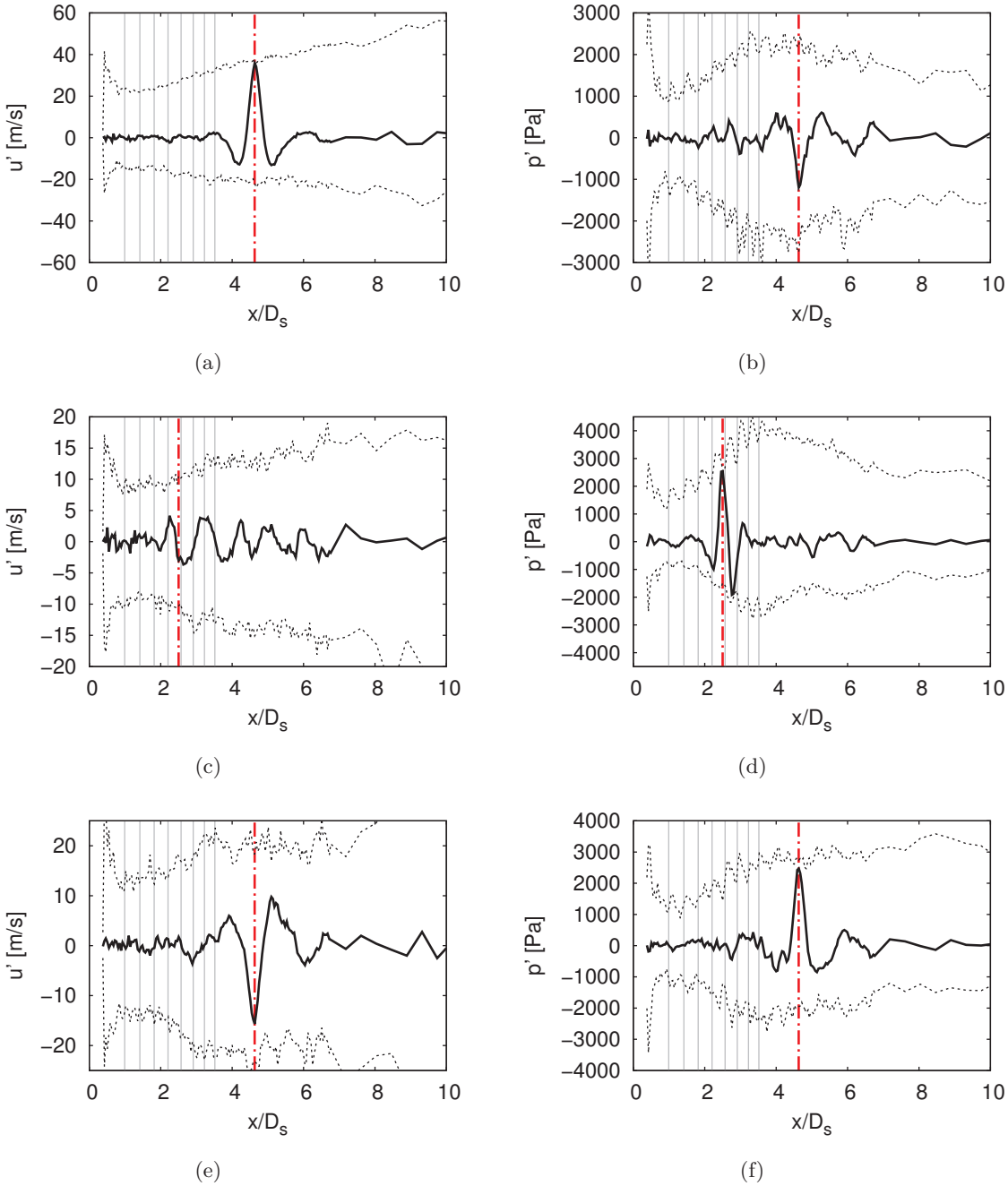

Figure 6.35: *Cross-conditioning of* ***(a)*** $u-u$, ***(b)*** $u-p$, ***(c)*** $p_{neg}-u$, ***(d)*** $p_{neg}-p$, ***(e)*** $p_{pos}-u$ *and* ***(f)*** $p_{pos}-p$ *from LIP_P where the first variable is the one used to locate the events and the second variable is the one plotted. The dash black line represents the envelope of the signature for all axial positions. The vertical dashed line represents the axial position where the events are located.*

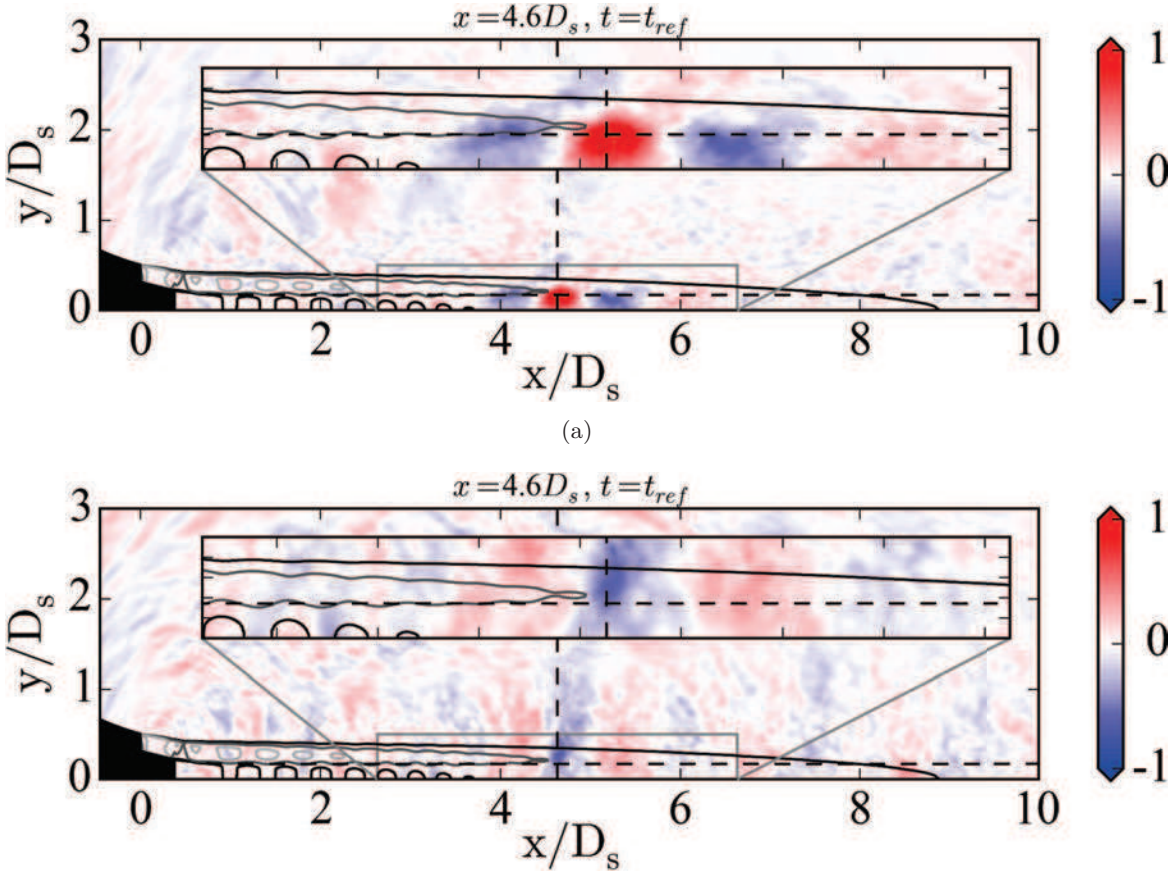

Figure 6.36: *Cross-conditioning of* ***(a)*** $u - u$ *and* ***(b)*** $u - p$ *from LIP_P for the event localized at the axial position* $x/D_s = 5$ *where the first variable is the one used to locate the events and the second variable is the one plotted which is non-dimensionalized by the standard deviation. The intersection of the dashed lines represents the location in space of the reference point.*

seen that the negative traveling waves are still there but barely intersect the data set LIP_P.

The different tonal behaviors shown with the energy distributions for all the azimuthal modes of the negative traveling pressure waves displayed in Fig. 6.30 can be further studied. The signatures of each azimuthal mode can also be computed using as a reference the events obtained with each mode of the negative waves and representing the pressure of the azimuthal modes of the complete signal. This procedure was applied to the data set LIP_P and LIP_S. The signatures of the azimuthal modes of LIP_P are illustrated in Fig. 6.39 where mode 0 is shown in (a), mode 1 in (b), mode 2 in (c) and mode 3 in (d). In the same way, Fig. 6.40 displays the signatures in the corresponding axial cut. The equivalent frequencies used to detect the events were the St_3, St_4, St_5 and St_6 for the modes 0, 1, 2 and 3 respectively from Table 6.5. These frequencies were selected because they showed a higher number of events with respect to the other frequencies present for each azimuthal mode. In terms of amplitude, mode 0 shows the highest levels, on the other hand, the higher modes present a decay in amplitude. Mode 0 displays a peak in the envelope around $x/D_s = 6$ at the same location as the signature at AXIS. Taking a look at the x-cut in Fig. 6.40 (a), mode 0 completely

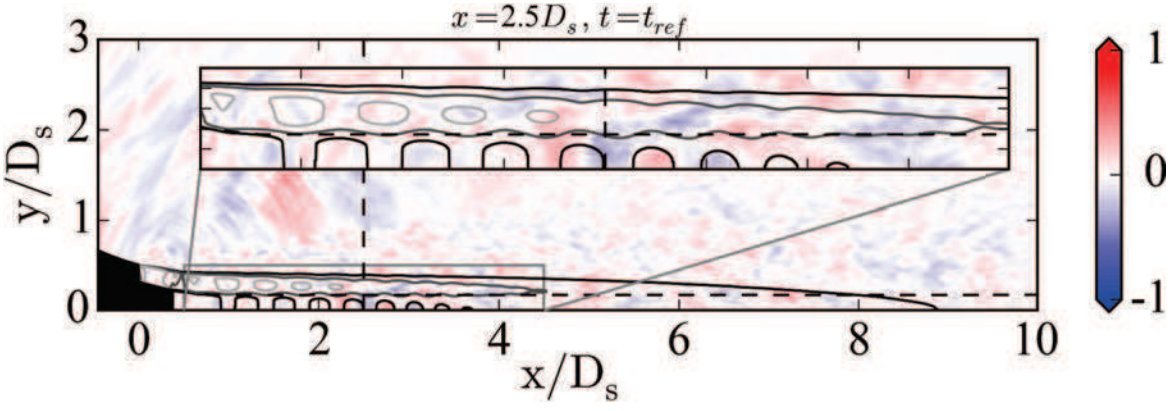

(a)

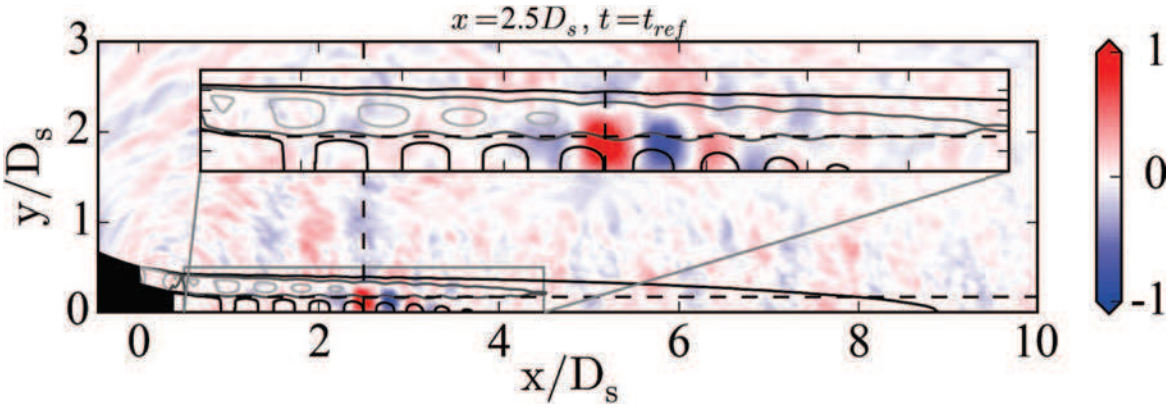

(b)

Figure 6.37: *Cross-conditioning of* ***(a)*** $p_{neg} - u$ *and* ***(b)*** $p_{neg} - p$ *from LIP_P for the event localized at the axial position* $x/D_s = 5$ *where the first variable is the one used to locate the events and the second variable is the one plotted which is non-dimensionalized by the standard deviation. The intersection of the dashed lines represents the location in space of the reference point.*

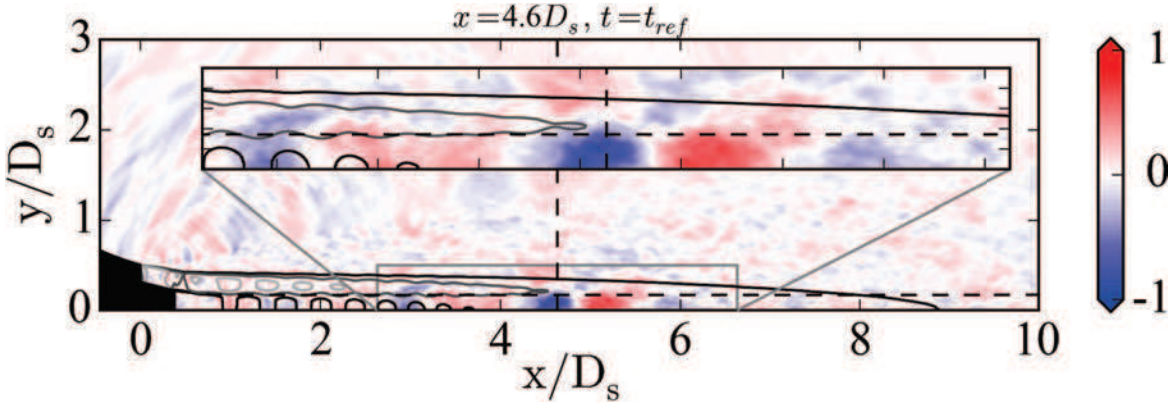

(a)

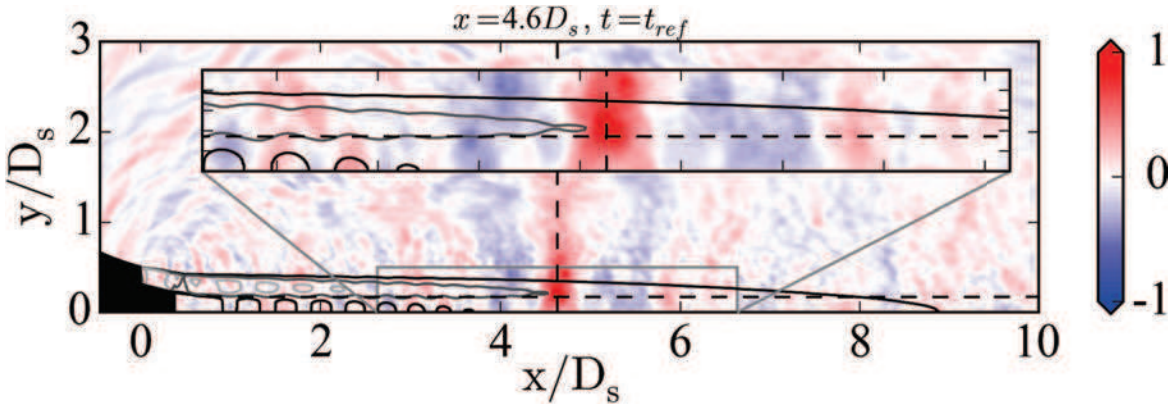

(b)

Figure 6.38: *Cross-conditioning of* ***(a)*** $p_{pos} - u$ *and* ***(b)*** $p_{pos} - p$ *from LIP_P for the event localized at the axial position* $x/D_s = 5$ *where the first variable is the one used to locate the events and the second variable is the one plotted which is non-dimensionalized by the standard deviation. The intersection of the dashed lines represents the location in space of the reference point.*

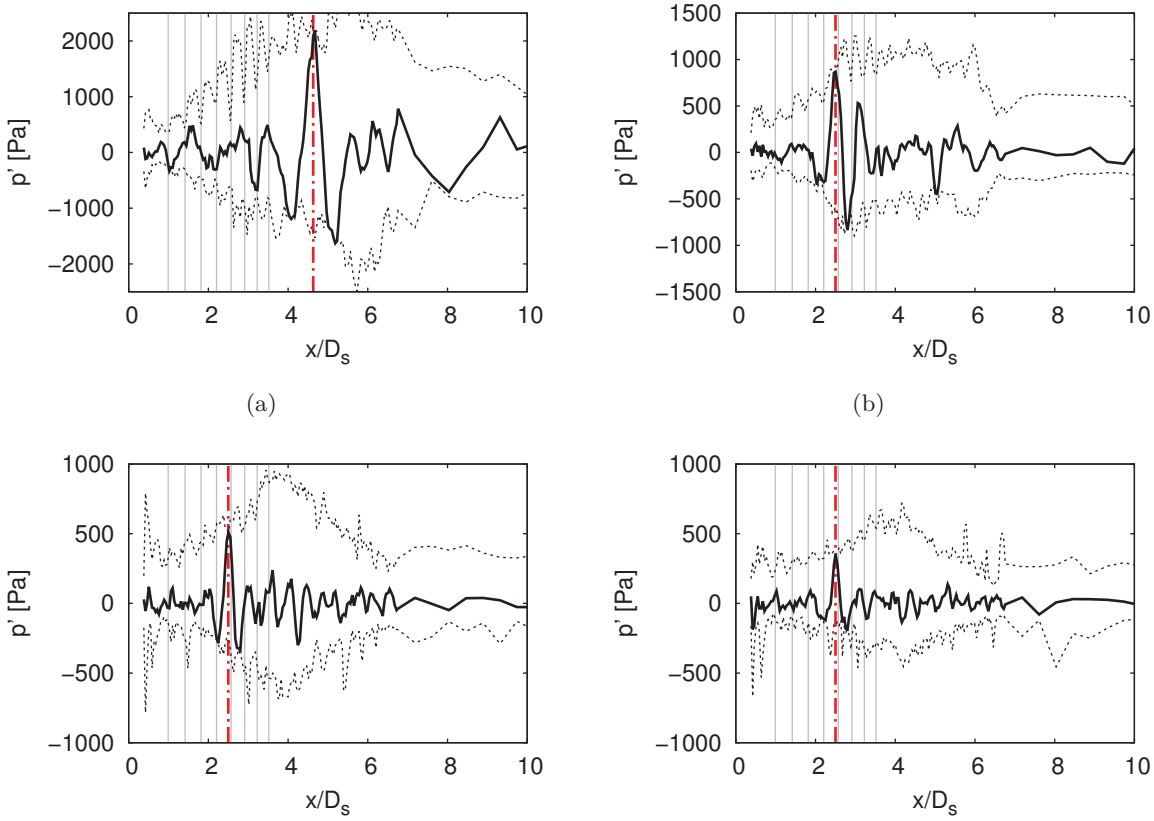

Figure 6.39: *Cross-conditioning of $p_{neg} - p$ at LIP_P for* ***(a)*** *the mode 0,* ***(b)*** *mode 1,* ***(c)*** *mode 2 and* ***(d)*** *mode 3, where the first variable is the one used to locate the events and the second variable is the one plotted. The dash black line represents the envelope of the signature for all axial positions. The vertical dashed line represents the axial position where the events are located.*

covers the inner subsonic jet, thus a footprint of the mode 0 is expected to be recovered at the axis. The signature of mode 1 shows a similar shape than the signature at the axis in terms of the envelope even though the amplitude is smaller as it is only taking into account one mode. The first negative peak of the envelope is at a similar axial position and the upper limit achieves a plateau in the range of $3 < x/D_s < 6$. Mode 1 is clearly defined in the axial cut in Fig. 6.40 (b). The pattern of this mode extends to the interior of the secondary jet and is in opposite phase with the pressure in the secondary shear-layer. Mode 2 and mode 3 display a peak in the envelope at $x/D_s = 4$ but they are not clearly defined in the axial cut and the associated figures are thus omitted.

Secondary lip-line probes analysis

The next data set studied is LIP_S where the obtained signatures are shown in Fig. 6.41. The auto-conditioning of the axial velocity displayed in Fig. 6.41 (a) presents a singular event as for the case of LIP_P, moreover, the envelope also follows the u_{rms} trend. Figure 6.42 (a) shows

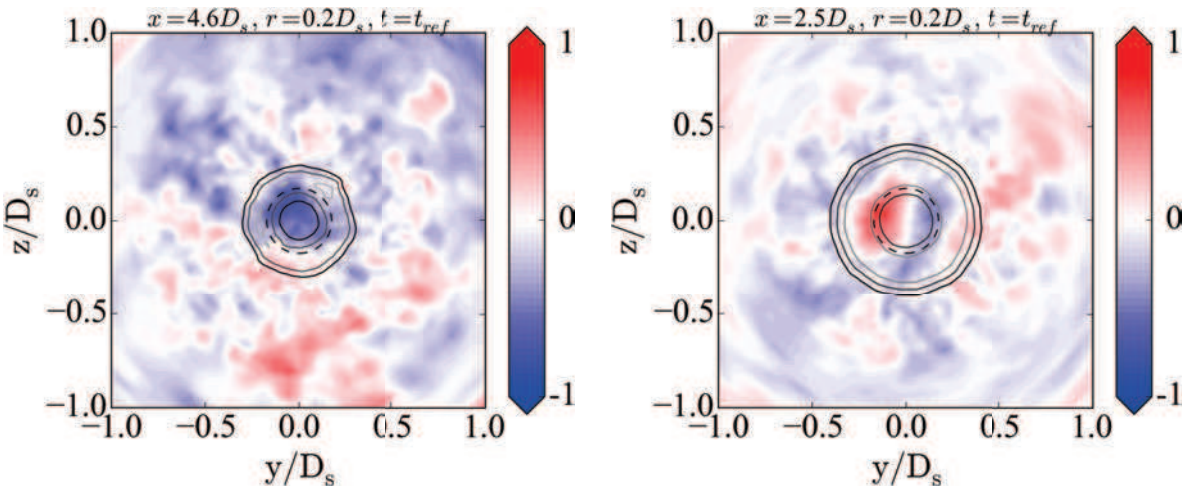

(a) (b)

Figure 6.40: *Cross-conditioning of $p_{neg} - p$ for LIP_P at for* ***(a)*** *mode 0 at $x/D_s = 4.6$ and* ***(b)*** *mode 1 at $x/D_s = 2.5$, where the first variable is the one used to locate the events and the second variable is the one plotted which is non-dimensionalized by the standard deviation.*

that the event is mainly local and does not extend radially into the secondary shear-layer. The cross-conditioning performed with the pressure illustrated in Fig. 6.41 (b) presents an event that is phased only $\pi/2$ rad with respect to the axial velocity in contrast to the regular phase of π rad between the velocity and the pressure. This is clear in Fig. 6.42 (b) where the event falls in between the positive and negative pressure peak.

The events obtained with the negative traveling pressure waves shown in Fig. 6.41 (c) for the axial velocity do not exhibit any characteristic feature when the cross-conditioning is applied. The same conclusion can be drawn from the two-dimensional cross-conditioning displayed in Fig. 6.43 (a). When the pressure is plotted, even though an event is captured, it is unclear whether it actually moves upstream or downstream. On the other hand, the pressure perturbations captured in the near-field that are shown in Fig. 6.43 (b), are moving upstream which could be generated from the interaction between the down traveling vortices and the shock-cells.

The axial velocity signature computed with the positive traveling pressure waves events is displayed in Fig. 6.41 (e). Similarly to when the pressure is plotted from the events obtained with the axial velocity, a phase of $\pi/2$ rad is found between the event and the axial velocity. The amplitude of the envelope follows the same trend as the rest, reducing with the positive axial position. The two-dimensional cross-conditioning shown in Fig. 6.44 (a) shows that the axial velocity has a phase shift with the pressure of π rad which could be simply caused by the difference in velocity at the different radial positions. The auto-conditioning of the positive traveling pressure events is displayed in Fig. 6.41 (f). Similarly to the AXIS, and LIP_P data sets, the positive pressure and the axial velocity present the same signatures and patterns in the two-dimensional cross-conditioning (Fig. 6.44 (b)).

The signatures of each azimuthal mode for LIP_S do not show any clear pattern (figures omitted). This could be due to the fact that a higher number of events are needed in order to

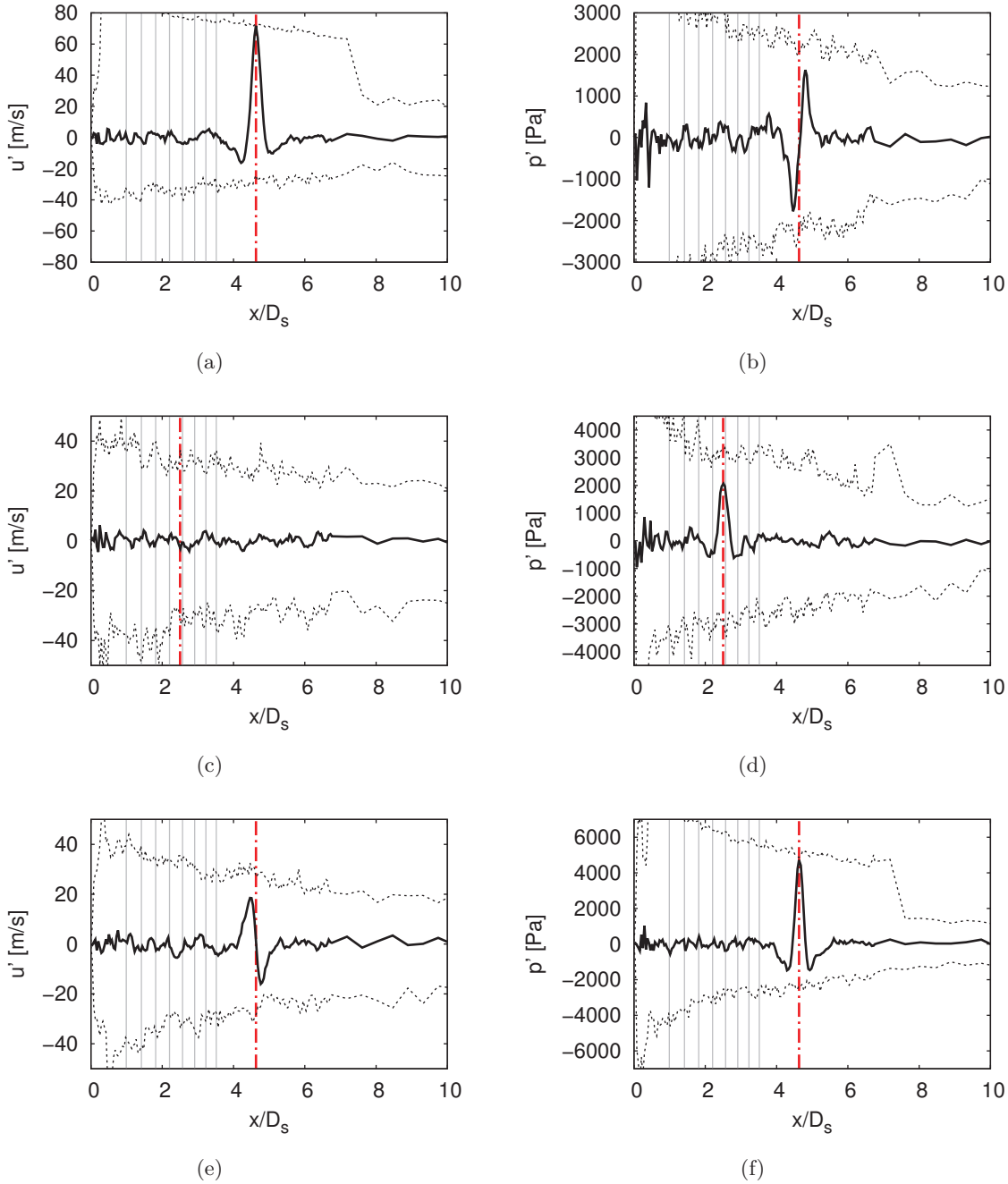

Figure 6.41: *Cross-conditioning of* ***(a)*** $u-u$, ***(b)*** $u-p$, ***(c)*** $p_{neg}-u$, ***(d)*** $p_{neg}-p$, ***(e)*** $p_{pos}-u$ *and* ***(f)*** $p_{pos}-p$ *from LIP_S where the first variable is the one used to locate the events and the second variable is the one plotted. The intersection of the dashed lines represents the location in space of the reference point. The vertical dashed line represents the axial position where the events are located.*

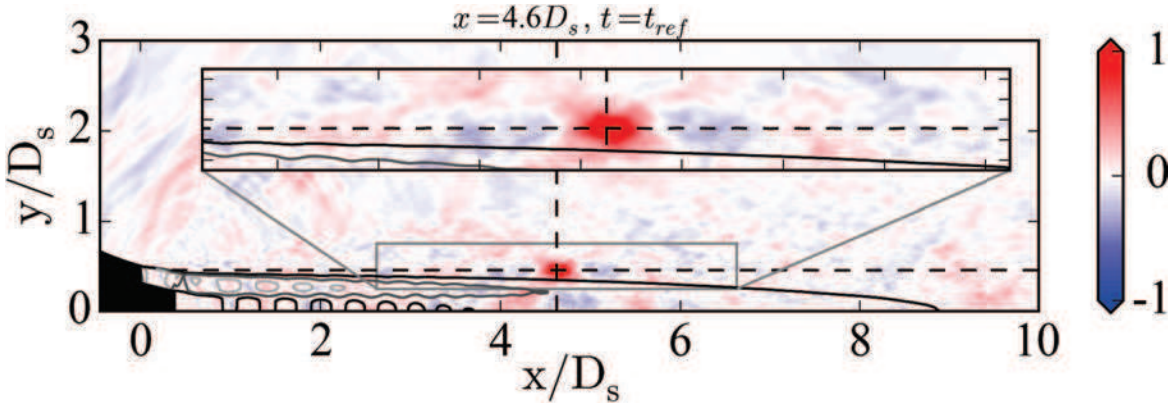

(a)

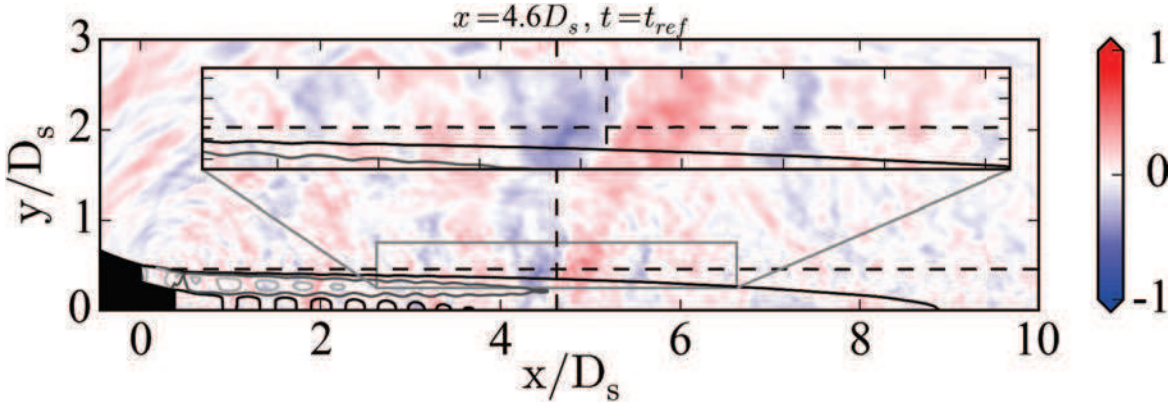

(b)

Figure 6.42: *Cross-conditioning of* ***(a)*** $u - u$ *and* ***(b)*** $u - p$ *from LIP_S for the event localized at the axial position* $x/D_s = 5$ *where the first variable is the one used to locate the events and the second variable is the one plotted which is non-dimensionalized by the standard deviation. The intersection of the dashed lines represents the location in space of the reference point.*

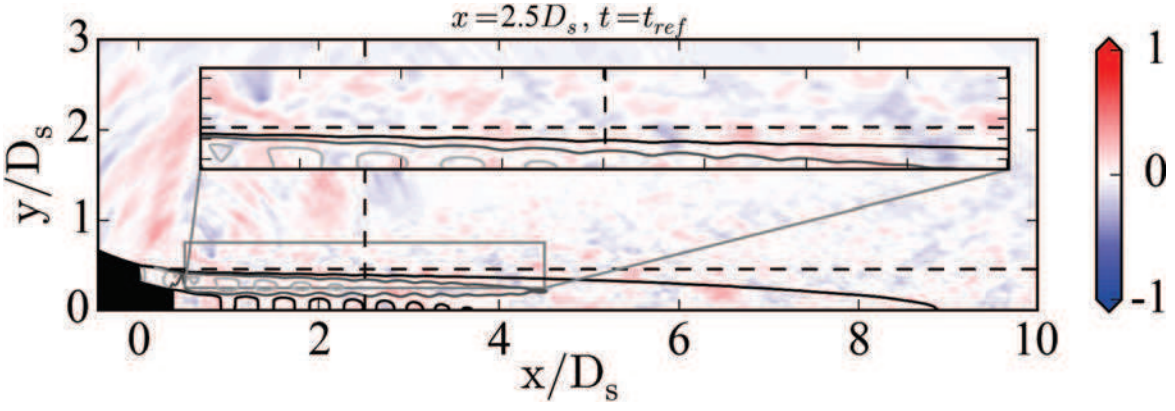

(a)

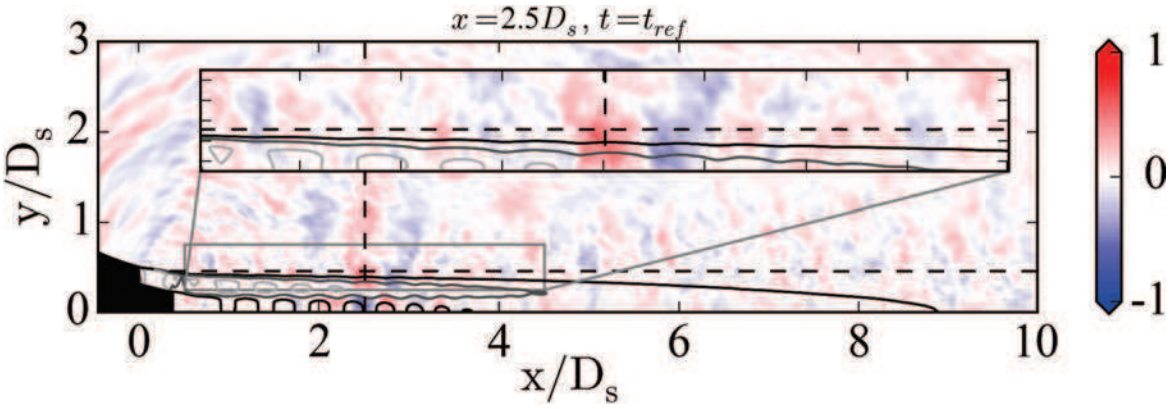

(b)

Figure 6.43: *Cross-conditioning of* ***(a)*** $p_{neg} - u$ *and* ***(b)*** $p_{neg} - p$ *from LIP_S for the event localized at the axial position* $x/D_s = 5$ *where the first variable is the one used to locate the events and the second variable is the one plotted which is non-dimensionalized by the standard deviation. The intersection of the dashed lines represents the location in space of the reference point.*

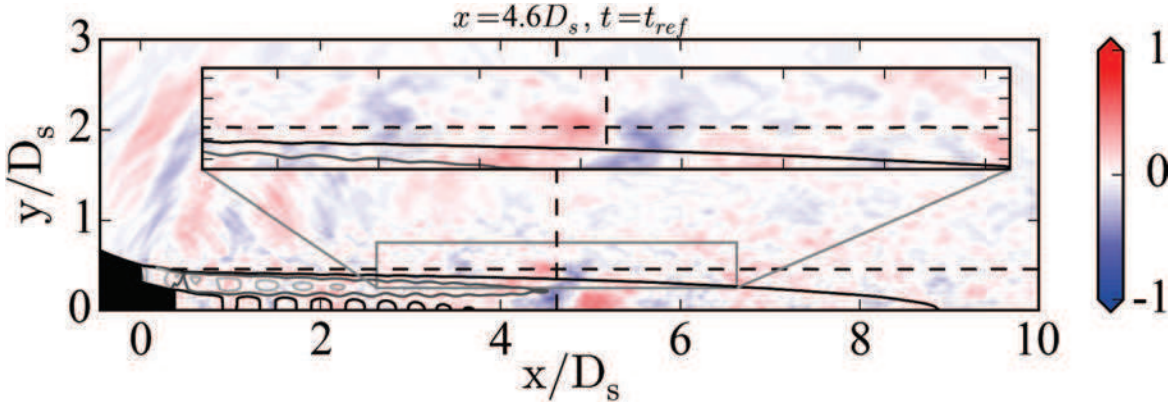

(a)

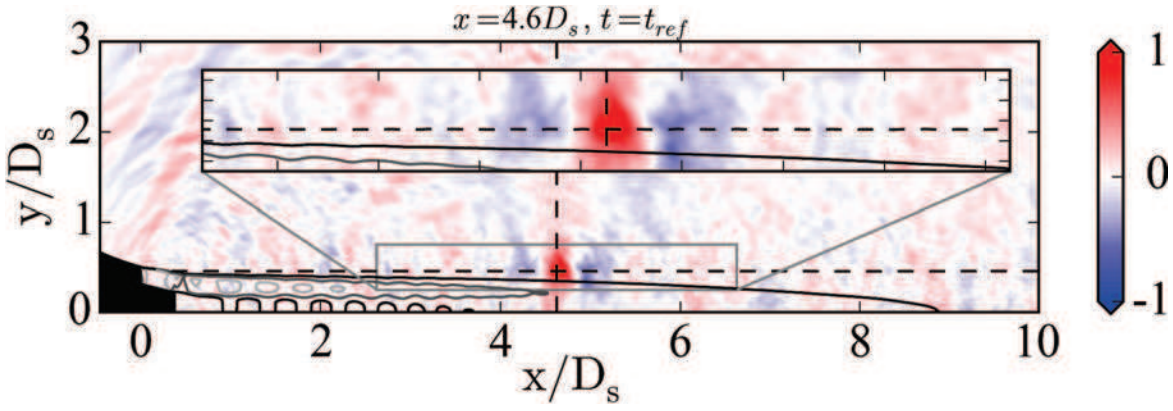

(b)

Figure 6.44: *Cross-conditioning of* ***(a)*** $p_{pos} - u$ *and* ***(b)*** $p_{pos} - p$ *from LIP_S for the event localized at the axial position* $x/D_s = 5$ *where the first variable is the one used to locate the events and the second variable is the one plotted which is non-dimensionalized by the standard deviation. The intersection of the dashed lines represents the location in space of the reference point.*

average out all the perturbations that are not related to the event in the shear-layer.

Near-field probes analysis

Last, the two-dimensional cross-conditioning at the near-field is shown in Fig. 6.45 at different times following the procedure used for the single jet in Sec. 5.3.6. The events are detected at $x/D_s = 2.5$ and a equivalent $St_s(s) = 1.38$ which corresponds to the axial position where the shock-cell noise is maximum as displayed in Fig. 6.20. The array of probes situated axially at 1 D_p from the secondary nozzle exit and with an expansion angle of 8° was previously filtered between negative and positive pressure waves and using the acoustic-hydrodynamic filtering from Sec. 3.3.2. The signature computed from the acoustic pressure is shown in the left column of Fig. 6.45 and the signature obtained from the negative traveling pressure in the right column. The results at $-8000\ \Delta t$ displayed in Fig. 6.45 (a) and (b) do not present any well defined signature although some patterns can be deduced around $x/D_s = 3$. The signature at the reference time depicted in Fig. 6.45 (c) and (d), exhibits more evident differences between the acoustic and the negative traveling signatures. The acoustic signature shows a peak at the location where the event was detected for the positive amplitude surrounded by the negative peaks that resemble an acoustic wave originated somewhere around $x/D_s \approx 4$. On the other hand, the signature calculated with the negative traveling events present a clearer acoustic wave shape. At the time $+8000\ \Delta t$ illustrated in Fig. 6.45 (e) and (f), the signature computed with the acoustic event shows that in fact two different acoustic waves were detected, one traveling upstream and another traveling downstream. The peak that is displayed in Fig. 6.45 (c) appears due to the fact that both acoustic waves interact with each other when doing the average of the cross-conditioning. For that reason, the shape of the signature does not look like a wave with a singular origin. At this axial position and frequency, a down-traveling acoustic wave is encountered which was originated next to the nozzle, in the transition to turbulent regime. On the other hand, the signature that is obtained using the negative traveling pressure events (Fig. 6.45 (d)) presents only an upstream traveling signature which in this case, is characteristic of the shock-cell noise. The signatures are further convected at time $16000\ \Delta t$ depicted in Fig. 6.45 (e) and (f) and last, at time $24000\ \Delta t$, they reach the external wall of the nozzle in Fig. 6.45 (i) and (g). It can be seen that at this time, the pressure wave perfectly reaches the nozzle lip which could induce the tonal noise screech. At this region, the quality of the cross-conditioning is increased because there are only acoustic waves. Most of the signatures shown in this section could be greatly improved by having extended duration in time of the signal which would increase the number of events used in the cross-conditioning.

The signatures obtained for the dual stream jet in the near-field have similar shapes to those computed for the single jet in Sec. 5.3.6. However, a clear difference can be noticed in terms of the spatial influence of the signature. For the dual stream case, the signature linked to shock-cell noise are extended about two secondary diameters, which is the size of the shock-cell region. On the other hand, the single jet presented a signature of the order of the potential core. This could indicate that the origin of the shock-cell noise is more localized in space with respect to the single jet or equivalently, there are less shock-cells radiating noise. Another important point to take into account is the fact that the dual stream case was run for only 80 dimensionless convective times with respect to the secondary stream parameters and that the average of the cross-conditioning was only done with one plane ($z/D_s = 0$), instead of with two. Both issues impact the number of events used in the average of the cross-conditioning

and its accuracy.

6.4 Summary and perspectives

In this chapter the large eddy simulation of a supersonic under-expanded dual stream jet and the analysis of the results were discussed. The LES was compared against experimental results from the von Karman Institute for Fluid Dynamics. The methodology and the post-processing techniques that were applied to the supersonic under-expanded single jet were also applied to the dual-stream supersonic jet. First, the conditions of the jet, the mesh characteristics and the simulation parameters were described. Second, the experimental data base against which the LES was compared was explained in detail. Finally, the results were analyzed.

Due to time constraints, the simulation of this case of study was carried out before the setup of the experimental facility was even finished. For this reason, many hypotheses were assumed for the definition of the case of study. First, the nozzle shape and dimensions were defined by the experimental partner and modeled assuming a negligible effect on the acoustic spectra of the connecting region between the nozzle and the support. Second, no reflections coming from the walls of the anechoic room or the instrumentation were considered. Last, the operating conditions defined in the design phase of the experimental facility were set in the computation. Once the experimental facility was fully set up and tested, some concerns were raised which obliged for some modifications of the initial experimental design. Due to a problem in the supply line detected after the design of the facility, the design conditions were only attainable if the nozzles were scaled down by 20%. Moreover, an axial shift in the secondary nozzle was noticed when the flow was pressurized. The impact of the spatial shift of the nozzle was quantified with RANS simulations as a direct displacement on the shock-cells positions. The oblique shock that appeared as a result of the change in direction of the flow between both streams suffered from an increase in the pressure jump when the shift was modeled.

Regarding the aerodynamics, a maximum difference of 20% was found for the shock-cell lengths between the experimental results and the LES. A very good agreement was obtained between the LES and the experiments for the Mach number and the axial and radial velocities at each relative shock-cell position. The velocity rms components showed a higher value for the first shock-cells but then they achieved the same levels for the last shock-cells. The computed time-scales and length-scales presented a different behavior for the regions where both concentric jets are independent and the region after they are merged.

In terms of acoustics, the near-field was filtered to recover only the acoustic component. The wavelength of the different components computed with an auto-correlation of the pressure on an axial array were used in order to estimate the shock-cell noise main frequencies. A similar shape than the one found for the single jet was displayed in the near-field, however, the spectra was slightly polluted by some acoustic waves generated at the exit of the nozzle, in the transition from laminar to turbulent regime. The far-field acoustics presented only the BBSAN peak corresponding to the secondary shear-layer. They were compared against the experimental spectra obtaining some agreement. First, several screech tones were recovered in the experimental measurements that did not appear in the simulation. Moreover, a shift in frequency was found which was expected due to the difference in shock-cell lengths and its inversely proportional law. On the other hand, the amplitude differed about 10 dB. The

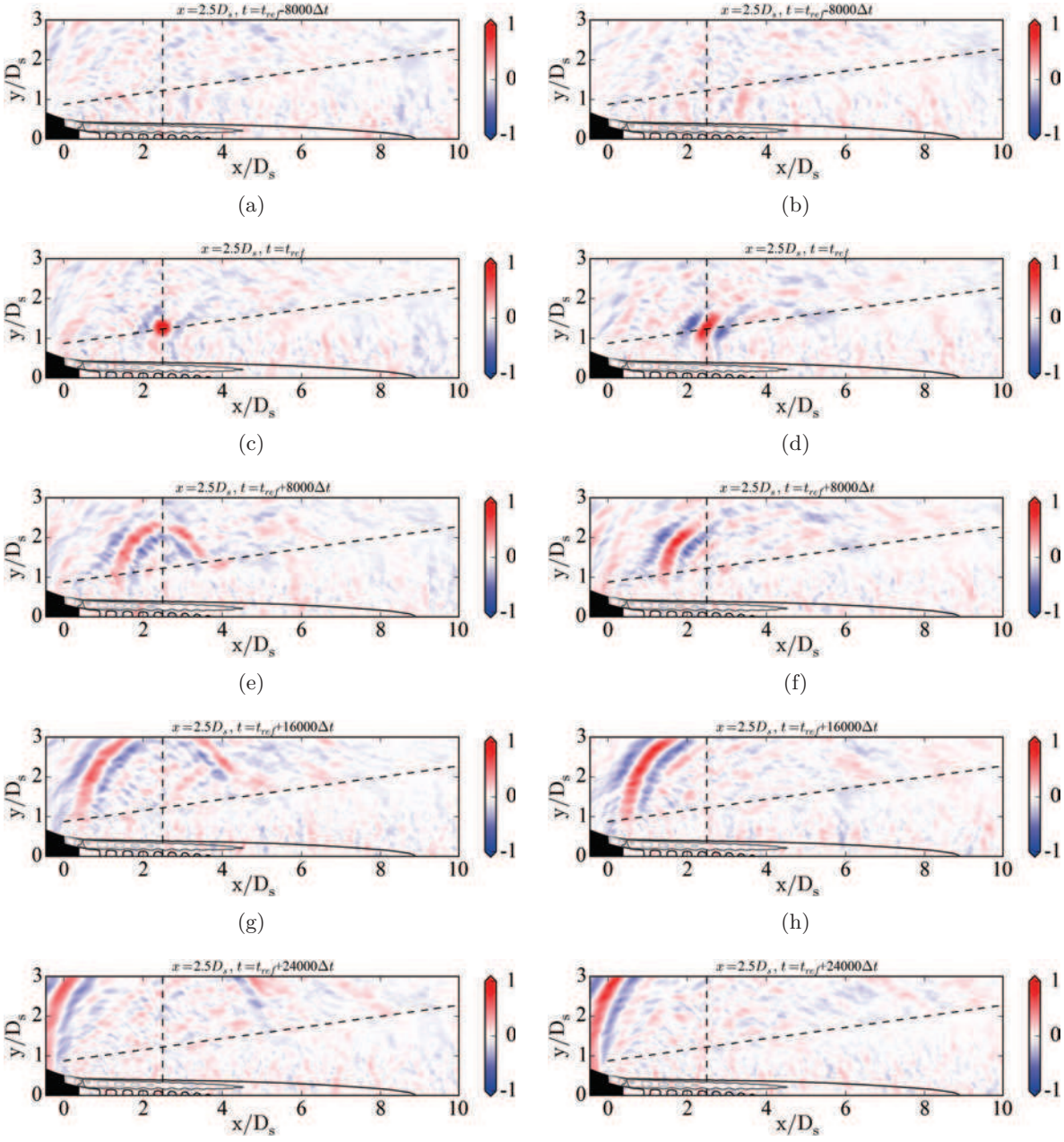

Figure 6.45: *Two-dimensional cross-conditioning of $p_{acoustic} - p$ on the left hand side and $p_{neg} - p$ on the right hand side at different shifted times where the first variable is the one used to locate the events and the second variable is the one plotted. The black solid lines represent the Mach number contours above 0.9. The intersection of the dashed lines represents the location in space of the reference point.*

above-mentioned differences on the geometry, the difference in turbulence levels for the first shock-cells, or some still unaccounted errors in the numerical or experimental procedure could be responsible for the difference in amplitude.

From spectral analysis it was shown that a set of negative traveling waves were found in the region where the supersonic secondary stream merges with the primary stream. Another set of negative traveling waves that is related to the first one could be distinguished in the shock-cell region. Using wavelet analysis it was demonstrated that the negative traveling waves that are propagated inside are originated by the merging of both jets and by the shock-cell noise. The maxima of the signatures were found systematically in the region where the shock-cells were located for the negative traveling pressure waves. A two-dimensional cross-conditioning, showed that the signatures computed with the axial velocity were contained radially over 1 D_s whereas for the pressure of the hydrodynamic component, they extended several diameters into the near-field. The signatures were obtained as well for the azimuthal modes independently. Shock-cell noise was captured in the near-field with a spatial length-scale of the order of the secondary diameter and the shock-cell region.

The large eddy simulation of a supersonic under-expanded dual-stream jet is a step forward in increasing difficulty with respect to the supersonic under-expanded single jet of the previous chapter. The addition of the secondary stream increases the complexity of the physics that need to be accurately resolved by the numerical schemes. The jet conditions and the nozzle geometries gave birth to an oblique shock in the secondary stream, stretching the limits of the former shock-limiting schemes. Moreover, a special care has to be taken to the mesh generation near the internal and external walls of the nozzles, which increases the cost, and could potentially increase the computational time. Moreover, in order to achieve the correct levels of turbulence at the exit of the secondary nozzle, the interior should be extended more diameters to be able to add an efficient forcing source term. The impact of the shifted nozzle in the acoustics could be studied with a new geometry of the nozzle, although it may be cheaper to redo the experiments assuring that the nozzle is in a fixed position.

Overall, the results discussed in this chapter have good agreement with the experiments and some physical insights were given with the advanced post-processing techniques. An extended simulation time could help in increasing the accuracy of the results. However, the actual shock-limiting schemes applied to this case of study were not accurate enough and the LES had to be stopped. To this end, new shock-capturing schemes were developed and are discussed in the following chapter.

Chapter 7

Towards a new shock-capturing technique for aeroacoustics

Contrary to the simulation of the supersonic under-expanded single jet from Ch. 5, the dual stream jet presented in Ch. 6 required the activation of an in-house shock-limiting technique (see Sec. 2.3). In the present dual stream configuration, an oblique shock is established in the secondary stream due to an abrupt change of direction of the flow. However, the numerical schemes and former shock-limiting technique were able to withstand the discontinuity of the shock for only eighty convective times. After this simulation time, some flow instabilities were developed which increased the jump across the oblique shock. The computation became numerically unstable and had to be stopped. As a consequence, a new shock-limiting technique was mandatory for supersonic simulations with high Mach numbers. S. Bidadi is a postdoctoral researcher recruited in the framework of the AeroTraNet2 project to develop and validate a new shock-capturing technique for aeroacoustic simulations.

This chapter details the implementation and validation of an extension of the high-order compact schemes for finite volume presented in Sec. 2.2 to handle simultaneously the aeroacoustics aspects of the flow in smooth turbulent regions as well as sharp discontinuities. The chapter is organized as follows. In Sec. 7.2, the adaptive shock-filtering methodology is detailed. Results of numerical canonical test-cases are presented in Sec. 7.3 and the application to supersonic jets in Sec. 7.4 Finally, the conclusions are summarized in Sec. 7.5. A detailed explanation of the governing equations, their finite volume discretization and the spatial filtering employed can be found in Ch. 2

This work is the result of a joint effort between several researchers at CERFACS which was submitted to the Journal of Computational Physics. The developments of the new numerical schemes were carried out by S. Bidadi under the supervision of G. Puigt and J-F. Boussuge. The test-cases of this chapter were validated by the author of this PhD thesis.

7.1 Review of shock-capturing techniques

The standard approach to resolving jump discontinuities in the flow-field is to utilize shock-capturing schemes. Although the schemes correctly capture shocks and contact discontinuities

in the flow field, they are known to be excessively dissipative for turbulent flows. Garnier *et al.* [212] studied the dissipative characteristics of a number of high-order shock-capturing schemes in the simulation of decaying isotropic turbulence of various levels of compressibility. The excessive dissipation of the schemes was reflected in their inability to capture the $-5/3$ slope of the inertial subrange. Thornber and co-workers [213] performed a quantitative investigation to analyze the behavior of such schemes. The analysis showed the dissipation rate to scale as square of the velocity jump. This scaling is larger than the dissipation rate of velocity-jump-cubed from theory. More recently, Bidadi and Rani [214] quantified the numerical viscosity and dissipation rate of Roe-MUSCL scheme in both physical and spectral space. The normalized spectral profiles showed unacceptably high level of dissipation in the energy containing and inertial subrange regions. In order to examine the dispersive and dissipative nature of nonlinear schemes, Pirozzoli [215] proposed the modified wavenumber analysis referred to as Approximate Dispersion Relation (ADR). The analysis showed that shock-capturing schemes damp not only the amplitude of high-frequency waves but also the intermediate and low-wavenumber modes. Moreover, the schemes were comparatively more dispersive than central differenced compact schemes of the same order. Hence, to address the conflicting requirements of high-speed flows, two classes of numerical methods have been developed that combine the spectral-like resolution of compact schemes with the shock-capturing capability of Godunov-type schemes.

The first technique is referred to as the hybrid method. It consists of two key steps: (i) cells containing discontinuities are detected by a shock sensor; and (ii) the discontinuities are resolved by replacing the compact scheme with a shock-capturing scheme. The shock zone is padded with additional cells on either side to allow for the decoupling of the compact scheme and to allocate proper stencil width for the shock-capturing scheme. Adams and Shariff [216] proposed the first adaptive hybrid scheme for shock-turbulence interaction problems. The formulation involves blending an upwinding compact scheme with a fifth-order Essentially Non-Oscillatory (ENO) scheme. Upwinding is achieved with non-symmetric coefficients on a centered stencil. Pirozzoli [7] extended the work of Adams and Shariff to develop the first truly conservative finite-difference hybrid scheme consisting of a fifth-order upwind compact scheme and seventh-order (Weighted ENO) WENO scheme. Shocks are detected based on the absolute value of difference in the density on either side of the interface of interest. When the difference exceeds a user defined threshold value, fluxes at the current and neighboring faces are computed using the WENO algorithm. Compared to the previous method [216], the fully conservative upwind compact algorithm made it easier to combine with the WENO scheme. Furthermore, the overall stability was enhanced by lowering the level of numerical oscillations. A more sophisticated fully conservative hybrid formulation involving a weighted averaged compact-WENO scheme was proposed by Ren *et al.* [217]. Hybrid methods while being largely successful in activating dissipation on the basis of sensing discontinuities in the flow-field are susceptible to generating oscillations and reduced accuracy near discontinuities [218]. In order to maintain high accuracy and robustness, Shen and Zha [219] developed a sensor-free hybridized scheme. Here, shock regions are identified based on WENO smoothness indicators of Jiang and Shu [220] and Borges *et al.* [221]. In the case of central differenced compact schemes, Visbal and Gaitonde also introduced in [148] a (second) technique analogous to the method of Adams and Shariff [216]. The method consisted of replacing a sixth-order compact scheme [147] with a third-order MUSCL scheme in the vicinity of high-gradient regions, and successively reducing the order of the spatial filter to zero inside the shock zone. The shock

region consisted of two additional buffer points on either side of the cells occupied by the shock. This was necessary in order to exclude the shock from the stencil of the first grid point outside the shock zone.

An alternate approach to the hybrid methodology was suggested by Yee *et al.* [222]. Here, local replacement of the high-order compact scheme with shock-capturing method is avoided. Instead, the baseline compact scheme is activated throughout the domain. Near jumps, the nonlinear dissipative portion of shock-capturing methods are turned on by means of a flow sensor. This technique is therefore referred to as 'nonlinear filtering'. Unlike the standard hybrid approach, the diffusive terms are added at the end of the multi-stage time-stepping algorithm, resulting in substantial savings in computational cost. The algorithm of Yee *et al.* [222] consists of a Split High-Order Entropy Conserving (SHOEC) scheme for evaluating the spatial derivatives. Near jumps, dissipative portion of a total variation diminishing (TVD) scheme is activated using Harten's sensor [172]. To improve accuracy, a problem dependent parameter κ is incorporated into the shock filtering step. The diffusive flux is sometimes referred as the characteristic-based filter since the nonlinear terms are applied to each wave or characteristic. Garnier *et al.* [223] replaced the Harten's sensor and TVD filter with the Ducros' sensor [224] and ENO/WENO filter, respectively. The study demonstrated superior accuracy of Ducros switch in distinguishing turbulent fluctuations from shocks compared to the Harten's sensor. Lo *et al.* [152] incorporated the second technique of Visbal and Gaitonde [148] to minimize the dissipation of the characteristic-based filter. To detect shocks, a WENO-type smoothness criterion for one dimensional flows and Ducros switch for multidimensional simulations were examined. Yee and Sjögreen [225] proposed to control the magnitude of the shock sensor by setting the shock filtering parameter κ to be constant for all test cases. However, Johnsen *et al.* [226] showed reduced accuracy for certain problems. In order to achieve better control of the nonlinear dissipation, Kotov *et al.* [227] proposed a κ parameter that depended on the local flow conditions. Moreover, different combination of flow sensors were used depending on the locally computed flow data.

The nonlinear filtering method discussed in all of the above mentioned studies employ the finite difference formalism for the base scheme. In the present study, however, the baseline scheme is an adaptation of the compact method of Lele [147] to the finite volume framework. Such an extension leads to the sixth-order compact method of Fosso *et al.* [146]. The compact finite volume scheme is stabilized using an eighth-order accurate filter of Visbal and Gaitonde [150]. The goal of the chapter is to introduce an extension of this finite volume methodology to handle simultaneously the aeroacoustics aspects of the flow in smooth turbulent regions as well as sharp discontinuities. Both the base scheme and nonlinear filtering method are implemented in a manner that reduces the computational cost. To improve accuracy, the order of the base scheme and spatial filter are kept constant throughout the domain. Moreover, a spectrally optimized filter dependent κ-factor is incorporated inside the adaptive nonlinear filter formulation to control the dissipation near shocks.

7.2 Adaptive shock-filtering methodology

The numerical diffusion of the compact filter (2.17) is insufficient to satisfy the entropy condition across discontinuities. As a result, spurious oscillations commonly referred to as the Gibbs' phenomena are generated. Such unphysical solutions adversely affect the propagation of not

just the high frequency waves but also to a large extent the intermediate and low wavenumber modes as well. This reduces stability and convergence rate at high Mach numbers [228]. To prevent instabilities of this nature from contaminating the solution, Yee and co-workers [222] proposed the adaptive filtering methodology. Broadly, the procedure involves activating the dissipative fluxes of a nonlinear shock-capturing scheme near discontinuities. The two key steps associated with this method are: 1. Harten's shock sensor [229] detects genuine discontinuities in the flowfield, and 2. in the vicinity of these high-gradients, the nonlinear dissipative fluxes of a high-resolution shock-capturing scheme are turned on. The technique is commonly referred to as the Artificial Compression Method (ACM) since it is loosely based on the hybrid scheme of Harten where the sensor switches between a high-order scheme and first-order Artificial Compression Method (ACM) scheme. In Yee *et al.* [222] filtering method, the application of nonlinear dissipative terms is similar to activating second- or third-order ACM-like scheme. To minimize the computational cost, the filter is applied at the end of a Runge-Kutta time algorithm. Following the notation of Yee and co-workers, the high-pass filter fluxes are of the form:

$$\mathbf{F}^*_{i+1/2} = \frac{1}{2}\mathbf{R}_{i+1/2}\Phi^*_{i+1/2}, \tag{7.1}$$

where $\mathbf{R}_{i+1/2}$ is the right eigenvector of Roe's Jacobian [155], and Φ^* is the nonlinear dissipative vector whose elements $\phi^{l*}_{i+1/2}$, $l = 1, .., 5$ are

$$\phi^{l*}_{i+1/2} = \kappa\theta^l_{i+1/2}\phi^l_{i+1/2}. \tag{7.2}$$

Here κ is a problem dependent parameter between 0.03 and 2. The flow sensor $\theta^l_{i+1/2}$ is the Harten's switch and $\phi^l_{i+1/2}$ is the dissipative portion of a nonlinear shock-capturing scheme. Lo *et al.* [152] chose κ to be 1 for all test problems in their paper. To improve the accuracy of DNS and LES simulations, Touber and Sandham [230] proposed to automatize the control of κ by setting it equal to Ducros *et al.* [224] sensor. In the study of Kotov *et al.* [227], a Mach number based κ was utilized for low-speed flows. Furthermore, the authors performed a comparative study between flow dependent and constant κ values in conjunction with Ducros *et al.*, Harten, and wavelet sensor of Sjögreen and Yee [231].

In this section, the formulation of a spectrally optimized adaptive filtering methodology is presented. The procedure involves applying the baseline scheme (2.16) and the eighth-order spatial filter (2.17) throughout the domain, including those regions occupied by shocks and contact discontinuities. To remove spurious oscillations in the vicinity of high gradients, the dissipative portion of a high-order extrapolation of Roe's flux [155] is activated. The net intercell flux is then expressed as

$$\mathbf{F}_{i+1/2} = \mathbf{F}^{FL}_{i+1/2} - \kappa^{opt}\sigma^{sc}_{i+1/2}\mathbf{F}^{sc}_{i+1/2}, \tag{7.3}$$

where κ^{opt} and σ^{sc} are the spectrally optimized scheme-dependent-parameter and filter strength between 0 and 1, respectively; and $\mathbf{F}^{sc}_{i+1/2}$ is the nonlinear dissipative flux vector of a high-order shock-capturing scheme. In Sec. 7.2.1, the procedure for estimating the filter strength σ^{sc} is outlined. The discussion on the computation of $\mathbf{F}^{sc}_{i+1/2}$ as well as the methodology for constructing two shock-capturing schemes are presented in Sec. 7.2.2. Specifically, the reconstruction methods of second-order minmod and fifth-order monotonicity preserving approach

(MPA) [232] are illustrated in Sec. 7.2.2 and Sec. 7.2.2, respectively. In Sec. 7.2.3, the optimized parameters κ^{opt} for the minmod and MPA filters are determined by performing an Approximate Dispersion Relation (ADR) analysis [215]. As in Yee *et al.* [222] study, the filtering step (7.3) is applied at the end of the sixth stage Runge-Kutta algorithm of Bogey and Bailly (2.15).

7.2.1 Estimation of the filter strength

The filter strength $\sigma^{sc}_{i+1/2}$ is evaluated using the adaptive spatial filtering algorithm of Bogey *et al.* [233]. In order to detect genuine shocks, the filtering procedure involves evaluating the magnitude of the shock detector r_i at each cell-center i. Based on dilatation $\theta = \nabla \cdot \mathbf{u}$,

$$r_i = \frac{D\theta_i^{mag}}{a_i^2/\Delta^2} + \epsilon_1, \tag{7.4}$$

where $a = \sqrt{\gamma p/\rho}$ and Δ are the sound speed and cell size, respectively, $D\theta_i^{mag}$ is the magnitude of the high-pass filtered dilatation θ and the constant $\epsilon_1 = 10^{-16}$ to avoid division by zero in Eq. (7.8). $D\theta_i^{mag}$ is computed as

$$D\theta_i^{mag} = \frac{1}{2}\left[(D\theta_i - D\theta_{i+1})^2 + (D\theta_i - D\theta_{i-1})^2\right], \tag{7.5}$$

where

$$D\theta_i = \left(-\theta_{i+1} + 2\theta_i - \theta_{i-1}\right)/4. \tag{7.6}$$

Shock detection can also be performed using a pressure-based shock sensor. However, to better distinguish turbulent fluctuations from shocks, sensor based on the above local compressibility (7.4) formula has been suggested by Bogey *et al.* [233]. An alternate version [234] to estimate r_i is also examined in this study. In this formulation, shocks are distinguished from turbulent regions using Ducros *et al.* [224] based shock sensor

$$r_i = \frac{|p_{i+1} - 2p_j + p_{i-1}|}{|p_{i+1} + 2p_i + p_{i-1}|}\frac{\theta^2}{\theta^2 + \boldsymbol{\omega}^2 + \epsilon_1} + \epsilon_2. \tag{7.7}$$

Here $\boldsymbol{\omega} = \nabla \times \mathbf{u}$ is the local vorticity, and $\epsilon_1 = 10^{-30}$ and $\epsilon_2 = 10^{-16}$ to prevent division by zero in Eq. 7.8. Once r_i is determined using either Eq. (7.4) or Eq. (7.7), the filter strength σ^{sc} is estimated with the following expression:

$$\sigma_i^{sc} = \frac{1}{2}\left(1 - \frac{r_{th}}{r_i} + \left|1 - \frac{r_{th}}{r_i}\right|\right), \tag{7.8}$$

where the threshold parameter r_{th} is between 10^{-6} and 10^{-4}. The shock filter is activated only when r_i exceeds r_{th}; i.e., σ^{sc} is non-zero when $r_i > r_{th}$. Moreover, lowering the threshold value increases the width of the shock zone resulting in greater smearing of the solutions. Once the cell-centered filter strengths are evaluated, the interface quantities are obtained by performing a simple average of the neighboring cell-centered values

$$\sigma^{sc}_{i+1/2} = \frac{1}{2}\left(\sigma^{sc}_{i+1} + \sigma^{sc}_i\right). \tag{7.9}$$

7.2.2 On the nonlinear dissipative flux

The nonlinear dissipation zone is defined as the region where σ^{sc} is greater than zero. Within this region, dissipative portion of the Roe's flux-difference scheme [155] is activated. Roe's intercell flux at the $i+1/2$ interface is defined as:

$$\mathbf{F}^{\text{Roe}}_{i+1/2} = \frac{1}{2}\left[\mathbf{F}^{L}_{i+1/2} + \mathbf{F}^{R}_{i+1/2}\right] - \frac{1}{2}|\tilde{\mathbf{A}}_{i+1/2}|\left(\mathbf{U}^{R}_{i+1/2} - \mathbf{U}^{L}_{i+1/2}\right), \tag{7.10}$$

where $\mathbf{U}^L$ and $\mathbf{U}^R$ are the conservative states immediately to the left and right side of the interface. The matrix $|\tilde{\mathbf{A}}_{i+1/2}|$ is the Roe-averaged constant Jacobian satisfying the conservation property $\Delta\mathbf{F} = \tilde{A}\ \Delta\mathbf{U}$ for an ideal gas. It is diagonalized as

$$|\tilde{\mathbf{A}}| = \tilde{\mathbf{R}}\tilde{\mathbf{\Lambda}}\tilde{\mathbf{L}}. \tag{7.11}$$

Here, $\tilde{\mathbf{R}}$ and $\tilde{\mathbf{L}}$ are the right and left eigenvector matrices, and $\tilde{\mathbf{\Lambda}}$ is a diagonal matrix containing real eigenvalues. The Roe-averaged quantities comprising the matrices are

$$\tilde{\mathbf{u}} = \frac{\sqrt{\rho_L}\mathbf{u}_L + \sqrt{\rho_R}\mathbf{u}_R}{\sqrt{\rho_L} + \sqrt{\rho_R}}, \tag{7.12}$$

$$\tilde{H} = \frac{\sqrt{\rho_L}H_L + \sqrt{\rho_R}H_R}{\sqrt{\rho_L} + \sqrt{\rho_R}}, \tag{7.13}$$

$$\tilde{a} = \sqrt{(\gamma-1)\left[\tilde{H} - \frac{1}{2}(\tilde{u}^2 + \tilde{v}^2 + \tilde{w}^2)\right]}, \tag{7.14}$$

where $\tilde{\mathbf{u}} = (\tilde{u}, \tilde{v}, \tilde{w})^{\mathrm{T}}$ and $H = e_t + \frac{p}{\rho}$ is the total enthalpy. In practice, constructing $|\tilde{\mathbf{A}}_{i+1/2}|$ is inherently expensive [235]. Hence, to reduce cost, we utilize the Roe-Pike [236] method instead. The approach consists of decomposing the dissipative fluxes in Eq. (7.10) into three flux components [237], each corresponding to the three distinct eigenvalues:

$$\mathbf{F}^{sc}_{i+1/2} = |\tilde{\mathbf{A}}_{i+1/2}|\left(\mathbf{U}^{R}_{i+1/2} - \mathbf{U}^{L}_{i+1/2}\right) = |\Delta\tilde{\mathbf{F}}_{\tilde{u}}| + |\Delta\tilde{\mathbf{F}}_{\tilde{u}+\tilde{a}}| + |\Delta\tilde{\mathbf{F}}_{\tilde{u}-\tilde{a}}|, \tag{7.15}$$

with

$$|\Delta\tilde{\mathbf{F}}_{\tilde{u}}| = |\tilde{u}|\left\{\left(\Delta\rho - \frac{\Delta p}{\tilde{a}^2}\right)\begin{bmatrix}1\\ \tilde{u}\\ \tilde{v}\\ \tilde{w}\\ \frac{\tilde{u}^2+\tilde{v}^2+\tilde{w}^2}{2}\end{bmatrix} + \tilde{\rho}\begin{bmatrix}0\\ 0\\ \Delta v\\ \Delta w\\ \tilde{v}\Delta v + \tilde{w}\Delta w\end{bmatrix}\right\}, \tag{7.16}$$

and

$$|\Delta\tilde{\mathbf{F}}_{\tilde{u}\pm\tilde{a}}| = |\tilde{u}\pm\tilde{a}|\left\{\left(\frac{\Delta p \pm \tilde{\rho}\tilde{a}\Delta u}{2\tilde{a}^2}\right)\begin{bmatrix}1\\ \tilde{u}\pm\tilde{a}\\ \tilde{v}\\ \tilde{w}\\ \tilde{H}\pm\tilde{u}\tilde{a}\end{bmatrix}\right\}. \tag{7.17}$$

Remark 2: In the earlier works [222, 152] on shock-filtering, the Riemann problem at a cell interface is resolved using Roe's flux-difference splitting technique [155]. However, in the

current framework, the method of Roe and Pike [236] is employed to reduce computational cost.

However, preliminary tests showed the numerical viscosity supplied by the eigenvalues $\tilde{u}$ and $\tilde{u} \pm \tilde{a}$ in Eqs. (7.16) and (7.17) to be insufficient in damping the spurious oscillations due to the compact scheme-spatial filter combination. Hence, to smoothen the solution near jumps, Harten's entropy correction [172] is employed. The original purpose of the correction is to prevent entropy-violating solutions in the neighborhood of sonic points. This is achieved by artificially increasing the numerical viscosity in a quadratic manner in the vicinity of such regions [238]. The correction takes the form

$$\psi(\tilde{\lambda}) = \begin{cases} \frac{\tilde{\lambda}^2+\delta^2}{2\delta}, & |\tilde{\lambda}| < \delta \\ |\tilde{\lambda}|, & |\tilde{\lambda}| \geq \delta \end{cases} \tag{7.18}$$

where ψ and $\tilde{\lambda}$ are the Harten's entropy correction and Roe-averaged eigenvalue, respectively and δ is a small user-defined positive parameter. For high-Mach number flows, Yee *et al.* [228] identified δ as one of the parameters affecting the stability and convergence rate of the solution. The parameter is typically set to zero for problems involving simple unsteady shocks [222, 228]. Following Yee and co-workers [228], unphysical oscillations in the shock region is damped by setting δ to be proportional to the interface velocity and sound speed

$$\delta = \tilde{\delta}\left(\tilde{u}_{i+1/2} + \tilde{a}_{i+1/2}\right), \tag{7.19}$$

where $\tilde{\delta}$ is referred to as the entropy correction parameter. Numerical experiments for shock-turbulence interaction problems showed good results for $\tilde{\delta}$ in the range of 0.1 and 1.0. The upper limit resulted in sharper profiles with minimal dissipation. Hence, unless stated otherwise, $\tilde{\delta}$ is chosen to be 1.0 for all test problems in this study. The correction parameter ψ is then computed with the Harten's expression:

$$\psi(\tilde{\lambda}) = \frac{\tilde{\lambda}^2 + \delta^2}{2\delta}, \quad \sigma^{sc} > 0. \tag{7.20}$$

In the following subsections, the second-order minmod and fifth-order monotonicity preserving approach (MPA) methods are discussed for evaluating the jumps in primitive variables in Eqs. (7.16) and (7.17).

Minmod filter

This section discusses the second-order minmod filter for reconstructing the conserved variables $\mathbf{U}$ at the $i + 1/2$ interface. Once the left and right reconstructed quantities are known, the corresponding primitive variables are recovered. Here, only the reconstruction steps for the left state $U^L_{i+1/2}$ is presented. The formulas for the right state can be obtained by symmetry. A three-point stencil is used to compute three slopes upstream of the interface. The original interface value obtained with the compact formulation (2.16) is used to evaluate one of the three slopes. The slopes are

$$
\begin{aligned}
s_1 &= U^{FL}_{i+1/2} - U_i, && (7.21)\\
s_2 &= U_i - U_{i-1}, && (7.22)\\
s_3 &= U_{i-1} - U_{i-2} && (7.23)
\end{aligned}
$$

where s_1, s_2 and s_3 are computed using the conserved variable U at $i+1/2$, and at cell-centers i, $i-1$ and $i-2$. This is followed by the computation of their minmod which is defined as:

$$
minmod(s_1, s_2, s_3) = \frac{sgn(s_1) + sgn(s_2)}{2} \left| \frac{sgn(s_1) + sgn(s_3)}{2} \right| min(|s_1|, |s_2|, |s_3|), \tag{7.24}
$$

where the signum (sgn) function is used to determine the sign of the slopes. It is defined as $s_i/|s_i|$, where the subscript i denotes the slope number. The left reconstructed state is then

$$
U^L_{i+1/2} = U_i + minmod(s_1, s_2, s_3). \tag{7.25}
$$

The use of this new dissipation technique leads to an interface net flux of the form:

$$
\mathbf{F}_{i+1/2} = \mathbf{F}^{\mathrm{FL}}_{i+1/2} - \mathbf{F}^{\mathrm{MM^{opt}}}_{i+1/2}, \tag{7.26}
$$

MPA filter

The second filter examined is the monotonicity preserving approach (MPA) of Balsara and Shu [232]. It is an extension of the Suresh and Huynh [239] scheme. The method employs a five point stencil to prevent clipping of the local extrema. Moreover, the value $U^L_{j+1/2}$ is successfully bounded within the monotonicity preserving region. The first step in the filtering procedure is to define a local curvature d_i

$$
d_i = U_{i+1} - 2U_i + U_{i-1}. \tag{7.27}
$$

An interface measure of curvature $d_{i+1/2}$ is then computed to restrict the spacing for local extrema to develop. Suresh and Huynh propose the following expression

$$
d_{i+1/2} = minmod(4d_i - d_{i+1}, 4d_{i+1} - d_i, d_i, d_{i+1}). \tag{7.28}
$$

For certain hyperbolic equations, Balsara and Shu observed that solution profiles with the above expression contaminate the solution when spread over four cells or less. To prevent unphysical oscillations from developing, the following measure of curvature with a larger domain was proposed

$$
d_{i+1/2} = minmod(4d_i - d_{i+1}, 4d_{i+1} - d_i, d_i, d_{i+1}, d_{i-1}, d_{i+2}). \tag{7.29}
$$

The expressions for the minimum and maximum values within which the solution must lie are then

$$
\begin{aligned}
U^{L,min}_{j+1/2} &= max[min(U_j, U_{j+1}, U^{MD}_{j+1/2}), min(U_j, U^{UL}_{j+1/2}, U^{LC}_{j+1/2})], && (7.30)\\
U^{L,max}_{j+1/2} &= min[max(U_j, U_{j+1}, U^{MD}_{j+1/2}), max(U_j, U^{UL}_{j+1/2}, U^{LC}_{j+1/2})], && (7.31)
\end{aligned}
$$

where the left sided upper limit $U^{UL}_{j+1/2}$, median $U^{MD}_{j+1/2}$, and allowance for large curvature $U^{LC}_{j+1/2}$ are defined as:

$$U^{UL}_{j+1/2} = U_j + \alpha(U_j - U_{j-1}), \tag{7.32}$$

$$U^{MD}_{j+1/2} = \frac{1}{2}(U_j + U_{j+1}) - \frac{1}{2}d_{j+1/2}, \tag{7.33}$$

$$U^{LC}_{j+1/2} = U_j + \frac{1}{2}(U_j + U_{j-1}) - \frac{2}{3}d_{j+1/2}. \tag{7.34}$$

The parameter α in $U^{UL}_{j+1/2}$ limits the maximum value of the CFL number. Here, $\alpha = 2$ for all test problems. Finally, the left-state monotonicity preserving value is

$$U^{L}_{j+1/2} = median(U^{L}_{j+1/2}, U^{L,min}_{j+1/2}, U^{L,max}_{j+1/2}), \tag{7.35}$$

$$= U^{L}_{j+1/2} + minmod(U^{L,min}_{j+1/2} - U^{L}_{j+1/2}, U^{L,max}_{j+1/2} - U^{L}_{j+1/2}). \tag{7.36}$$

By symmetry, the right state can be obtained in a similar manner.

7.2.3 Optimization of the shock filter

In computational aeroacoustics (CAA), it is necessary to optimize the numerical schemes so that the weak acoustic disturbances at the far-field are neither damped by excess diffusion nor contaminated by numerical waves due to high dispersion errors. Both the dispersion and dissipation properties for the current methodology are quantified by examining the evolution of the Fourier modes [240]. The spectral analysis, commonly referred to as the modified wavenumber analysis begins by performing the Fourier decomposition of a periodic function [147]:

$$f(x) = \sum_{k=0}^{N-1} \hat{f}_k exp\left(2\pi ikx/L\right),$$

where N is the number of grid points in the domain of size L, k is the wavenumber and $i = \sqrt{-1}$. The derivative of f with respect to a scaled coordinate, $s = x/\Delta x$ is

$$f'(s) = \sum_{k=0}^{N-1} iw\hat{f}_k \; exp(i\omega \; s). \tag{7.37}$$

Here the scaled wavenumber $\omega = 2\pi k\Delta x/L = 2\pi k/N$. Considering a single mode $\hat{f}_k$, the exact first derivative is $\hat{f}'_k = i\omega \; \hat{f}_k$. In the case of a linear finite difference scheme, the derivative is

$$\hat{f}'_k = i\omega^* \; \hat{f}_k, \tag{7.38}$$

where ω^* is the modified or effective wavenumber. Exact analytical expressions for ω^* is obtained by solving Eq. (7.38). The difference between ω and ω^* characterizes the dispersion and dissipative errors of a numerical scheme [145]. The coefficients of the high-order central differencing schemes for CAA are typically optimized by minimizing the integral error of this difference for certain range of wavenumbers. Notable works are those of Tam and Webb [159],

and Bogey and Bailly [145]. Sun *et al.* [240] developed the minimized dispersion and controllable dissipation (MDCD) technique to construct an optimal sixth-order finite difference scheme. The dispersion properties were optimized based on an integrated error function. Fosso *et al.* [146] performed spectral analysis of the sixth-order centered compact scheme (2.16). The study showed the scheme to be less dispersive than standard centered schemes of the same order. On a uniform grid, its dispersive property is identical to the compact finite difference scheme of Lele [147]. Therefore, the coefficients of the formulation require no further optimization.

The modified wavenumber analysis was developed to obtain optimal values for the coefficients of high-order linear centered schemes. However, there is no straightforward method to analyze the wave propagation characteristics of nonlinear shock-capturing schemes. Pirozzoli [215] proposed an Approximate Dispersion Relation (ADR) to study the spectral behavior of shock-capturing schemes. Unlike their linear counterparts, the study showed that nonlinear terms affect not only the current mode k but also the neighboring modes as well. Nevertheless, the linear portion of scheme dominates and is considered to be the main source of dissipation [241]. The ADR method is used here to quantify the dissipative properties of the minmod and MPA filters, and to obtain optimal values for the parameter κ.

To optimize the nonlinear schemes, Hu *et al.* [242] developed the following dispersion-dissipation relation. The expression indicates the minimum numerical dissipation necessary to damp the high wavenumber modes. It is of the form:

$$r(\omega) = \frac{|\mathcal{R}e'(\omega^*) - 1|}{|Im(\omega^*)|} \sim 1, \tag{7.39}$$

where r is the dispersion-dissipation ratio, $Re'(\omega^*)$ is the derivative of the real part ω^*, and $\mathcal{I}m(\omega^*)$ refers to the imaginary part of ω^*. Ideally, the value of r must be close to 1 to ensure the solution is free of spurious waves.

Following the ADR analysis, dispersion and dissipation spectra of the fully finite volume scheme with the minmod filter are shown in Fig. 7.1. The profiles for $\kappa = 0.0$, 0.25, 0.5 and 1.0 are compared with the minmod and fifth-order WENO shock-capturing schemes. For all cases, the filtering strength σ^{sc} is set to 1. The dispersion distribution in Fig. 7.1(a) is the same for all κ since the parameter only controls the dissipative term. Compared to the minmod and WENO5 schemes, the base scheme is less dispersive. The dissipation plot in Fig. 7.1(b) shows the effect of varying κ. For the upper limit of $\kappa = 1.0$, the dissipation supplied is equal to that of the minmod scheme. As κ is decreased, dissipation is reduced for all wavenumbers. However, for the lowest non-zero choice of κ, finite amount of dissipation is still activated at low and intermediate wavenumbers. By contrast, the fifth-order WENO scheme supplies no dissipation until $\omega \approx 1$. But for $\omega > 2$, the damping of the high wavenumber Fourier modes is larger than that of the $\kappa = 0.25$ minmod filter.

The dispersion-dissipation ratio r (7.39) quantifies the magnitude of dissipation supplied relative to dispersion. For a given wavenumber ω, a high value of r signifies excess dispersion. Hu *et al.* [242] suggest maintaining r below 10 to sufficiently damp the unresolved waves. Fig. 7.2 shows the dispersion-dissipation ratio profiles for all four values of κ. For the choice of $\kappa = 0$, the profile crosses $r = 10$ threshold level at $\omega \approx 1$. Conversely, the upper limit of $\kappa = 1.0$ supplies sufficient dissipation to maintain r below 10 at all wavenumbers. However, at the low wavenumber modes, the scheme is highly dissipative with a minimum at $\omega \approx 0.65$. The choice

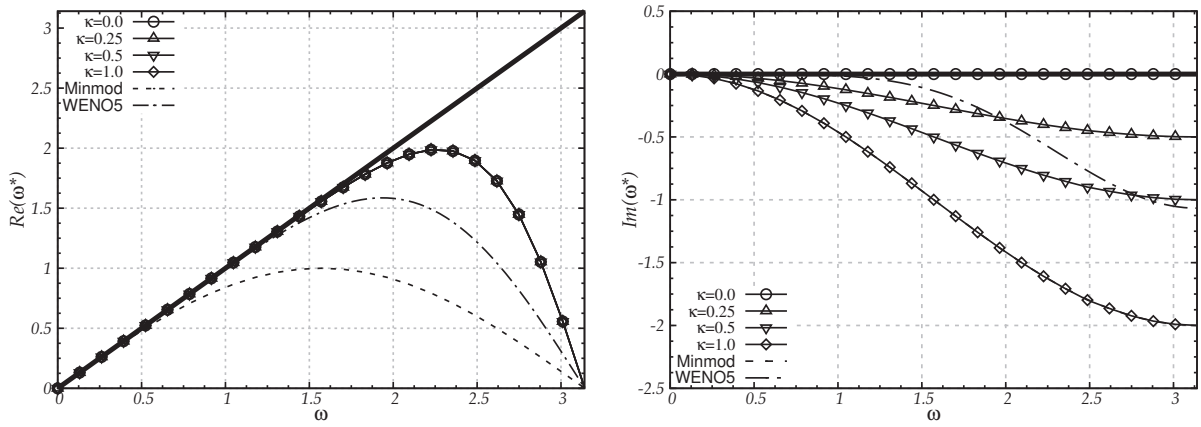

Figure 7.1: Comparison of **(a)** dispersion and **(b)** dissipation properties for various κ parameters of the minmod filter. The profiles are compared with the second-order minmod and fifth-order WENO schemes.

of $\kappa = 0.25$ reduces the dissipation by a factor of ~ 10 and ~ 4 compared to $\kappa = 1.0$ and 0.5, respectively. Moreover, the condition $r \leq 10$ is always satisfied. Hence, $\kappa^{opt} = 0.25$ is chosen as the optimal value for the minmod filter.

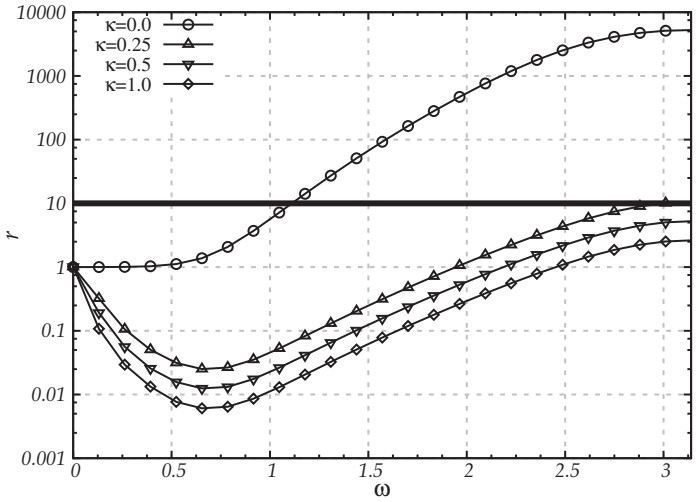

Figure 7.2: Comparison of dispersion-dissipation ratio (r) for various κ parameters of the minmod filter.

The dissipation profiles for the same set of κ-parameters with the MPA filter are shown in Fig. 7.3. The dispersion profiles are exactly the same as for the minmod filter, and are not shown. Compared to the minmod profiles in Fig. 7.1(b) and WENO5 scheme, the MPA filter in Fig. 7.3(a) is considerably less diffusive. Moreover, the profiles are almost indistinguishable from each other. Fig. 7.3(b) is a close-up view near the zero dispersion level. To examine whether κ-controlled dissipation of the MPA filter is adequate for capturing shocks, profiles of r for all four κ-parameters are plotted in Fig. 7.4. As before, $\kappa = 0$ scheme is highly dispersive

at the intermediate and high wavenumbers, whereas the upper limit of $\kappa = 1$ is the most diffusive choice with a minimum at $\omega \approx 0.75$. As κ is increased, the high wavenumber modes responsible for the high-frequency oscillations are damped. But for ω in the range of 0 and 0.5, r increases albeit slightly.

Comparing the profiles of $\kappa = 0.5$ and 1.0, we observe that the former is more dispersive in the intermediate and high wavenumber regions. However, in the low wavenumber region, it is closer (on average) to the ideal limit of $r = 1$. Furthermore, since the dissipation of the spatial filter (2.17) damps the high-frequency artificial waves, the high wavenumber dispersion of $\kappa = 0.5$ may be deemed acceptable. Hence, $\kappa^{opt} = 0.5$ is chosen as the optimal parameter with the MPA filter.

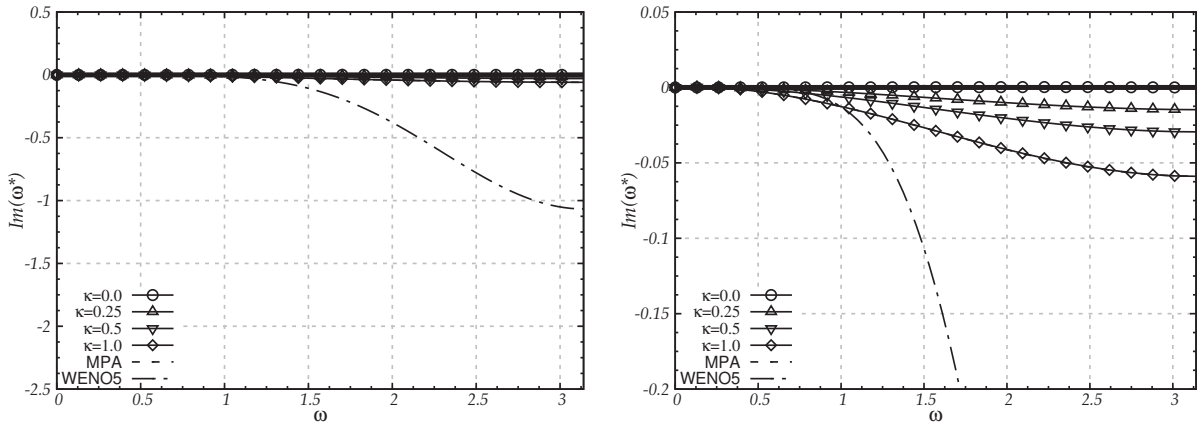

Figure 7.3: Comparison of the dissipation properties for various κ parameters of the MPA filter. **(a)** General view and **(b)** close-up at high wavenumbers. The profiles are compared with the fifth-order MPA and WENO schemes.

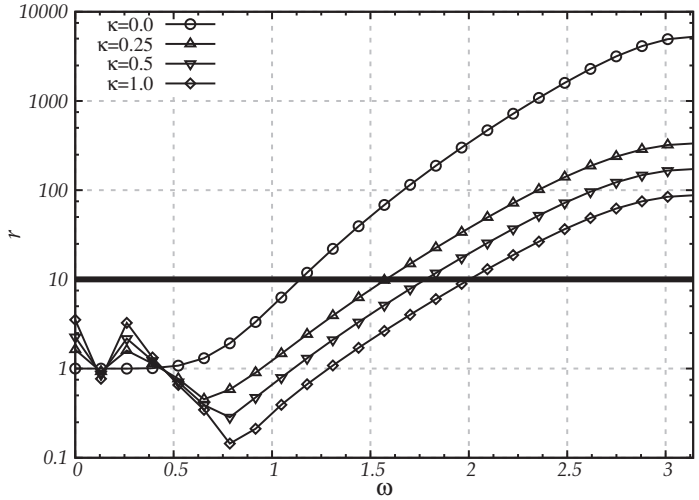

Figure 7.4: Comparison of dispersion-dissipation ratio (r) for various κ parameters of the MPA filter.

7.3 Canonical test-cases

The fully finite volume methodology is examined for four canonical problems: (1) 1-D shock-tube, (2) 1-D shock-entropy, (3) 2-D shock-vortex, and (4) 2-D shock-shear layer interaction. The Bogey *et al.* [233] sensor based on dilatation is investigated for all four cases. For the 1-D tests, the influence of varying the entropy correction parameter $\tilde{\delta}$ and the spectral parameter κ on the solution are examined. For the 2-D cases, $\tilde{\delta}$ and κ are fixed, and the performance of Ducros sensor is investigated and compared with the solutions obtained using the Bogey *et al.* [233] sensor. The two shock sensors will henceforth be referred to as Bogey and Ducros. Additionally, the effect of the filtering magnitude σ^{sc} and optimized parameter κ^{opt} controlling the numerical viscosities of the minmod and MPA filters are discussed. For convenience, the spectrally optimized minmod and MPA filters are denoted as MM^{opt} and MPA^{opt}, respectively. Unless stated otherwise, the threshold parameter $r_{th} = 10^{-4}$ for all cases.

7.3.1 Shock tube problem

The 1-D Sod's shock-tube problem [243] is a special case of the Riemann's initial value problem. Here, the 1-D Euler equations are solved in conservative form. The initial states of the perfect gas on either side of a diaphragm located at $x = 0.5$ are:

$$(\rho, u, p) = \begin{cases} (1.0, 0.0, 1.0), & x \leq 0.5 \\ (0.125, 0.0, 0.1), & x \geq 0.5 \end{cases} \tag{7.40}$$

The computational domain of size $x \in [0, 1]$ is discretized into 100 cells. Simulations were conducted with CFL number of 0.1 until $t = 0.2$.

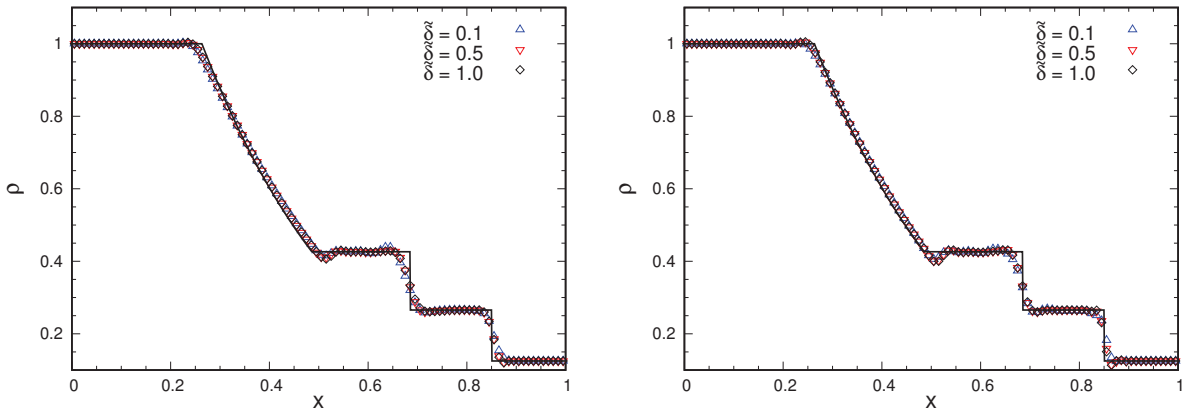

Figure 7.5: Profiles of density with **(a)** minmod, and **(b)** MPA filters are compared for $\tilde{\delta} = 0.1$, 0.5 and 1.0 (see Eq. (7.19)). Parameters κ and r_{th} are 1.0 and 10^{-4}, respectively for all three scenarios. Solid line represents the exact profile.

The large pressure difference between the left and right states causes the diaphragm to break. As a result, a shock wave and a contact discontinuity develop and travel to the right. In addition, a left moving expansion fan is also generated. In this test-case, the performance

of the viscosity controlled shock filters to capture the three waves are examined. Fig. 7.5 shows the density profiles using the minmod and MPA filters in Eq. 7.3 for $\tilde{\delta} = 0.1$, 0.5 and 1.0. The spectral parameter $\kappa = 1.0$ for all three cases. This value represents the maximum possible dissipation which can be supplied by the nonlinear filters (see Figs. 7.1 and 7.3). Numerical experiments performed with lower values of κ generated high level of instabilities. As the figure shows, $\delta = 1$ profile for both cases exhibits small undershoot downstream of the shock front. This unphysical result is prominent for MPA due to its less dissipative nature compared to minmod. As $\tilde{\delta}$ is progressively decreased, the magnitude of viscosity supplied by the Harten's correction increases. This leads to monotonicity preservation for both filters across the discontinuity. In the region between the expansion fan and contact discontinuity, all three profiles display low-amplitude grid-to-grid oscillations. The reason for this unphysical behavior is due to the evaluation of the shock sensor r_i using dilatation. Specifically, since the dilatation is zero across the contact discontinuity, the shock-capturing filter is switched-off in this region. In addition, a prominent undershoot appears in the vicinity of $x = 0.5$. At this location, the flow becomes sonic (i.e., $u = a$) and the numerical viscosity supplied by the Harten's correction fails to overcome the dispersion of the baseline compact scheme. The size of the extremum is larger for the MPA filter compared to minmod. For the lower limit of the correction parameter (i.e., $\tilde{\delta} = 0.1$), there is little improvement compared to the less dissipative higher values of $\tilde{\delta}$. Fig. 7.6 shows the density, velocity and pressure profiles for the minmod and MPA filters. All profiles are for $\tilde{\delta} = 0.1$. The entropy violation at the sonic point ($x = 0.5$) is magnified by the large hump in the velocity profiles for MPA. Overall, these results indicate that the shock-tube problem is a difficult test-case for non-characteristic based schemes of the order of three or more [219, 220].

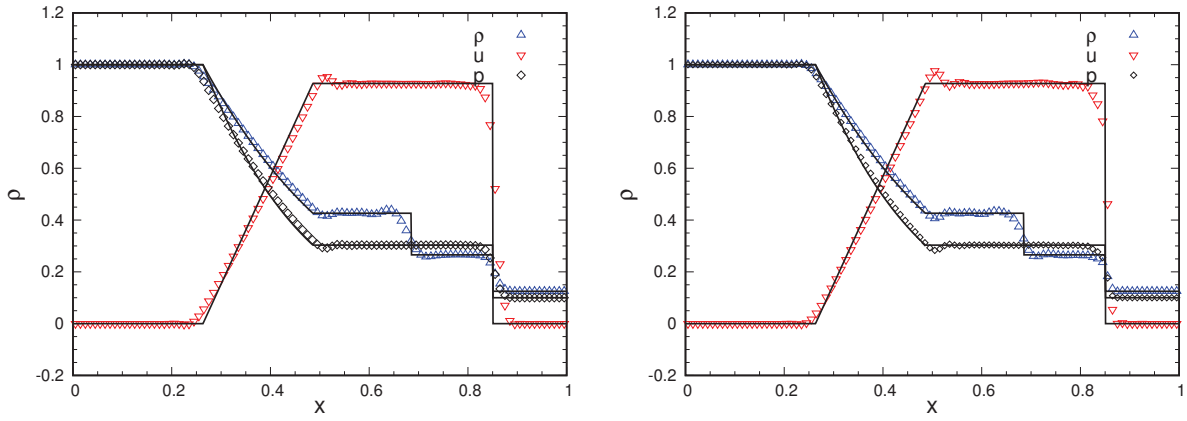

Figure 7.6: Profiles of density, velocity and pressure for **(a)** minmod, and **(b)** MPA filters. Parameters $\tilde{\delta}$, κ and r_{th} are 0.1, 1.0 and 10^{-4}, respectively for all three scenarios.

The influence of the threshold parameter (r_{th}) on the evolution of the density profiles is illustrated in Figs. 7.7(a) and 7.7(b). As expected, reducing r_{th} from 10^{-4} to 10^{-5} results in smoother solutions for both filters. To further investigate the role of r_{th}, profiles of the corresponding filtering magnitude σ^{sc} are plotted in Figs. 7.8(a) and 7.8(b). These plots provide greater insights into the performance of the sensor. As the figures show, the choice of $r_{th} = 10^{-5}$ supplies dissipation over a wider region around the shock compared to $r_{th} = 10^{-4}$.

Focusing on the minmod case, it can be seen that the filter strength σ^{sc} is maximum (i.e., unity), whereas the choice of $r_{th} = 10^{-4}$ reduces the magnitude by approximately 20%. On the contrary, the viscosity supplied by the MPA filter is maximum for both cases. Moreover, $r_{th} = 10^{-5}$ also activates viscosity in the vicinity of the sonic point. This behavior is indicative of the fact that the strength of the filtering magnitude depends strongly on the solution. It is seen to be inversely proportional to the magnitude of the dissipation supplied by the shock filter. Since MPA filter supplies less dissipation than minmod, the corresponding strength of the filter magnitude is higher. This observation is in agreement with the analysis of Bogey *et al.* [233]. Although $r_{th} = 10^{-5}$ supplies viscosity at the sonic points, it is insufficient to damp the unphysical behavior of the solution. Based on the above analysis, minmod filter with $\tilde{\delta} = 0.1$, $\kappa = 1.0$ and $r_{th} = 10^{-5}$ combination provides the best results for the shock-tube problem.

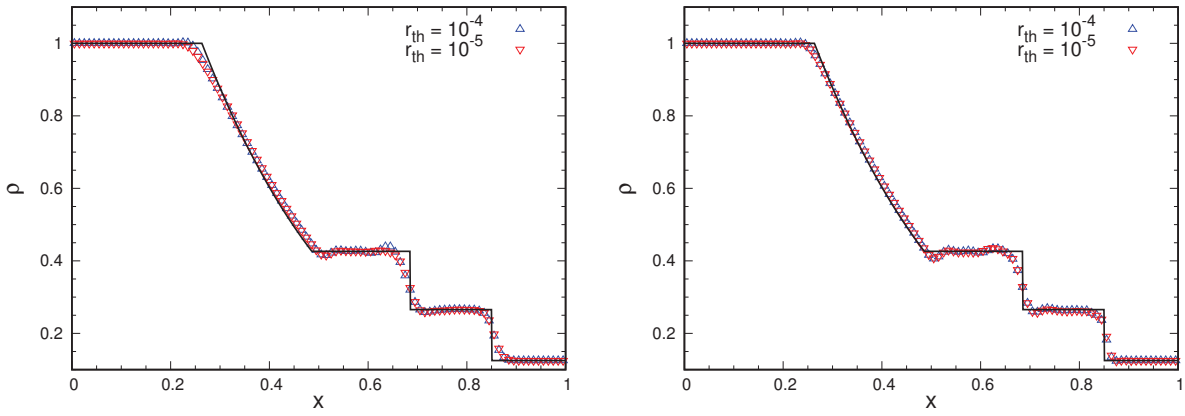

(a) Minmod filter

(b) MPA filter

Figure 7.7: Comparison of the density profiles for **(a)** minmod filter and **(b)** MPA filter for threshold parameter $r_{th} = 10^{-4}$ and 10^{-5}. For both minmod and MPA, $\tilde{\delta} = 0.1$ and $\kappa = 1$.

7.3.2 Shu-Osher problem

In this problem, a moving Mach 3 shock wave interacts with a low amplitude sinusoidal entropy/density wave [244]. It is considered as the simplest shock-turbulence interaction test-case. The solution is governed by the 1-D Euler equations. The initial conditions are:

$$(\rho, u, p) = \begin{cases} (3.857143, 2.62, 10.3333), & x < -4 \\ (1 + \epsilon\ sin(5x), 0.0, 1.0), & x \geq -4 \end{cases} \tag{7.41}$$

where $\epsilon = 0.2$, and the 1-D computational domain spans $x = [-5, 5]$. A uniform mesh of 400 cells is used to study the performance of MM^{opt} and MPA^{opt} filters. Their profiles are compared with a reference WENO5 solution obtained using 1600 cells. Simulations were performed until $t = 1.8$ with CFL = 0.5. The results shown are for this time. The entropy correction parameter $\tilde{\delta}$ was chosen to be 1. The density profiles for MM^{opt} and MPA^{opt} filters along with the reference solution are shown in Fig. 7.9. Both shock filters successfully capture

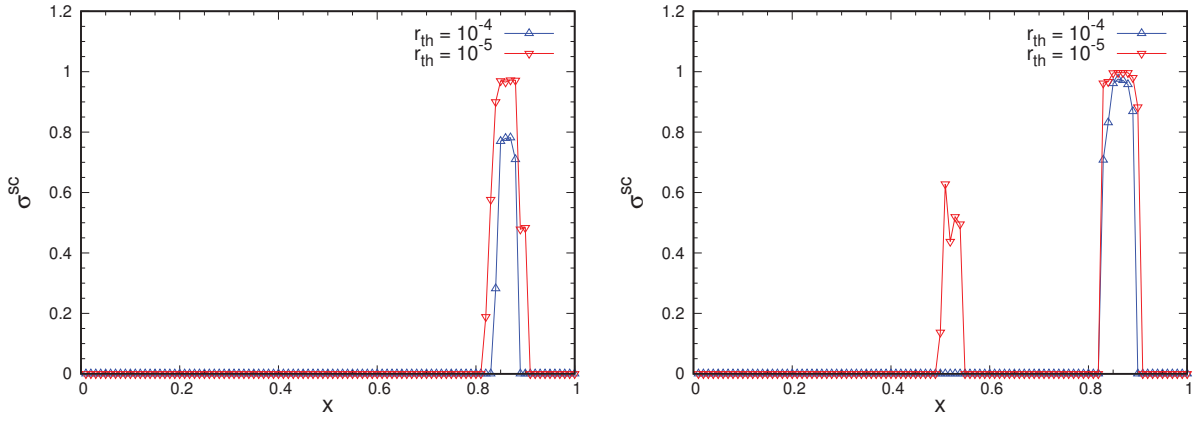

Figure 7.8: Comparison of the magnitudes of the shock-capturing filter σ^{sc} for **(a)** minmod filter and **(b)** MPA filter for threshold parameter $r_{th} = 10^{-4}$ and 10^{-5}. For both minmod and MPA, $\tilde{\delta} = 0.1$ and $\kappa = 1$.

the normal shock as well as the compressed and amplified density oscillations immediately behind the shock in the range of $x = [0.6, 2.2]$ (see Fig. 7.9(b)). At the shock front, the nonlinear filters activate the right amount of dissipation to prevent the formation of Gibbs' oscillations due to the centered base scheme. Furthermore, the amplified profiles downstream of the shock show good agreement with the reference solution. The high accuracy is due to: (i) correct choice of the threshold parameter r_{th}, (ii) flow (scheme)-dependency of the filter magnitude σ^{sc}, and (iii) optimal value for the κ-factor.

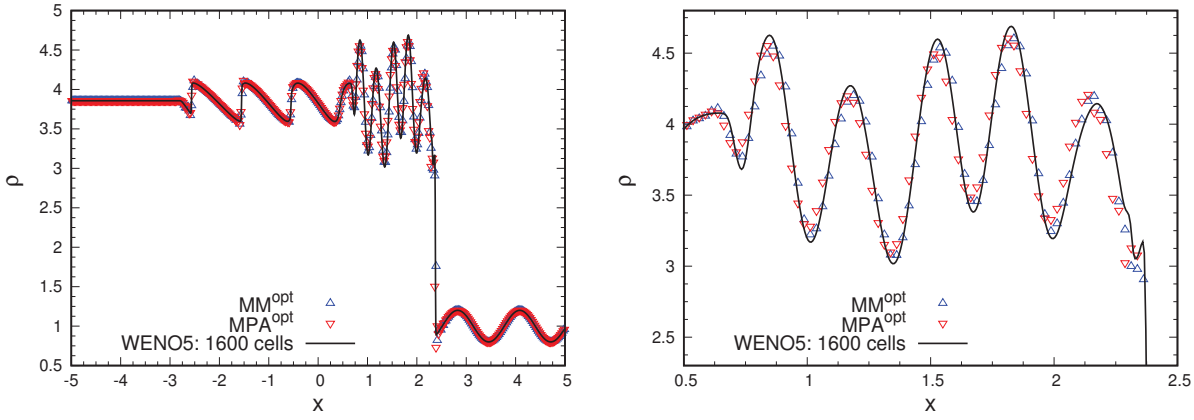

Figure 7.9: Comparison of density profiles of MM^{opt} and MPA^{opt} filters with WENO5 scheme at $t = 1.8$. **(a)** General view and **(b)** detailed plots of the profiles between $0.5 < x < 2.3$. For all cases, $\tilde{\delta} = 1$.

The threshold value r_{th} plays a critical role in managing the viscosity of both shock filters. As seen in the shock tube case, increasing r_{th} from 10^{-5} to 10^{-4} reduced the width of the dissipation window. Here, the higher threshold value improved the accuracy of the solution for

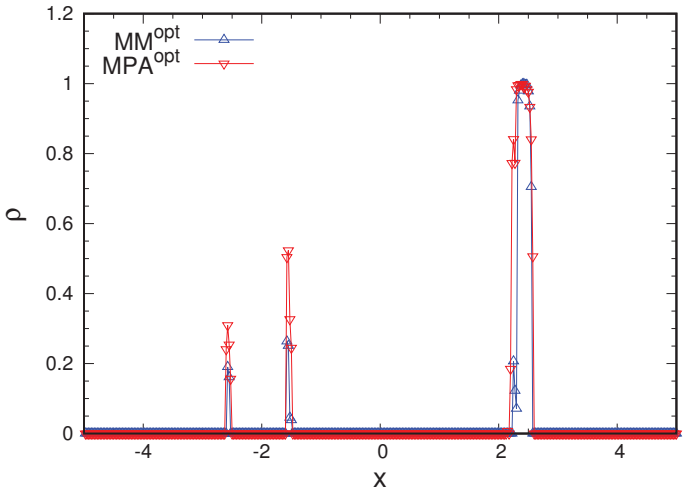

Figure 7.10: Distribution of the shock-capturing filter magnitude σ^{sc} for MM^{opt} and MPA^{opt} at $t = 1.8$.

both filters. It is interesting that MM^{opt} performs as well as MPA^{opt} even though it is more dissipative and has the undesirable property of clipping the local extrema [239]. To investigate why, corresponding σ^{sc} profiles are plotted in Fig. 7.10. For both cases, the width of the dissipation window surrounding the moving shock is roughly 0.3 (i.e., 12 points), whereas the wavelength of the entropy wave is, $\Delta x = 1.25$ (i.e., 50 points per wavelength); approximately four times the size of the dissipation region. This difference indicates that to preserve extrema with second-order TVD-based schemes, the width of the shock region must be approximately less than or equal to 1/4 the wavelength of the oncoming density fluctuations. However, a smaller dissipation window increases the likelihood of generating Gibbs' oscillations.

The low dissipative nature of the MM^{opt} filter is also partly due to the smaller magnitude of σ^{sc} compared to MPA^{opt} filter. The low optimization factor (κ^{opt}) of 0.25 contributes to increased accuracy as well. It is interesting to note that downstream of the amplified density oscillations, the entropy wave resembles a saw-tooth structure. In order to capture these sharp gradients, numerical dissipation of the shock filters is turned on by the shock sensor. However, the amplitudes of the shock-filtering magnitude at these locations are much lower than near the shock. This is due to the relatively low strength of the discontinuity in the density oscillations. As in the shock-tube case, MPA^{opt} produces higher peaks for σ^{sc} compared to MM^{opt}.

Fig. 7.11 shows the density profiles of the scheme with $\tilde{\delta} = 0.1$, 0.5 and 1.0 for both MM^{opt} and MPA^{opt} filters in the region of compressed entropy waves. In general, varying the entropy parameter $\tilde{\delta}$ seems to have negligible effect on the solution for minmod. In the case of MPA^{opt}, both $\tilde{\delta} = 0.5$ and 1.0 preserve the extrema whereas $\tilde{\delta} = 0.1$ damps the peaks. Moreover, there is noticeable phase error with the latter as well. This behavior indicates that MPA filter is more sensitive to $\tilde{\delta}$ than minmod. Fig. 7.12 compares the profiles of κ^{opt} and $\kappa = 1$. For minmod, increasing the parameter dampens the peaks and to a lesser extent the troughs. But in the case of MPA, the troughs are fully preserved while the peaks are damped.

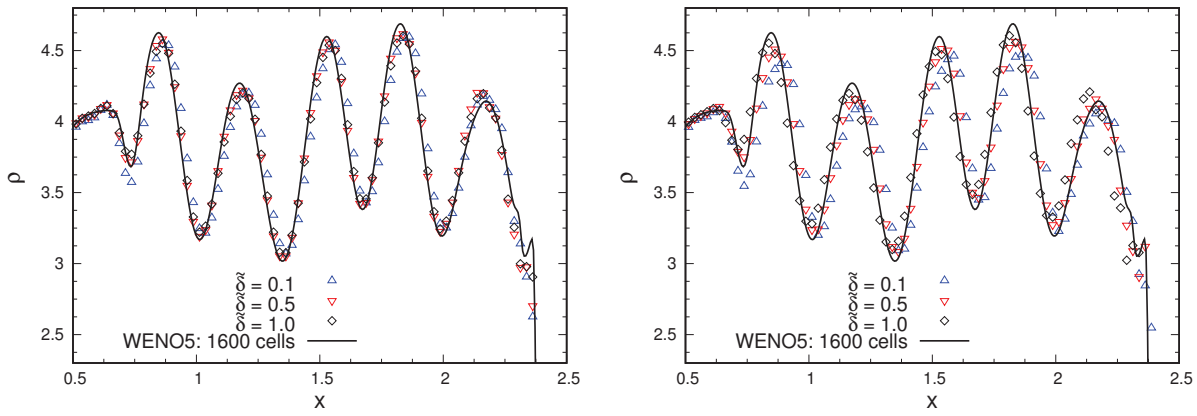

Figure 7.11: Comparison of density profiles of $\tilde{\delta} = 0.1$, 0.5 and 1.0 for **(a)** MM^{opt} and **(b)** MPA^{opt} filters with the reference WENO5 solution at $t = 1.8$.

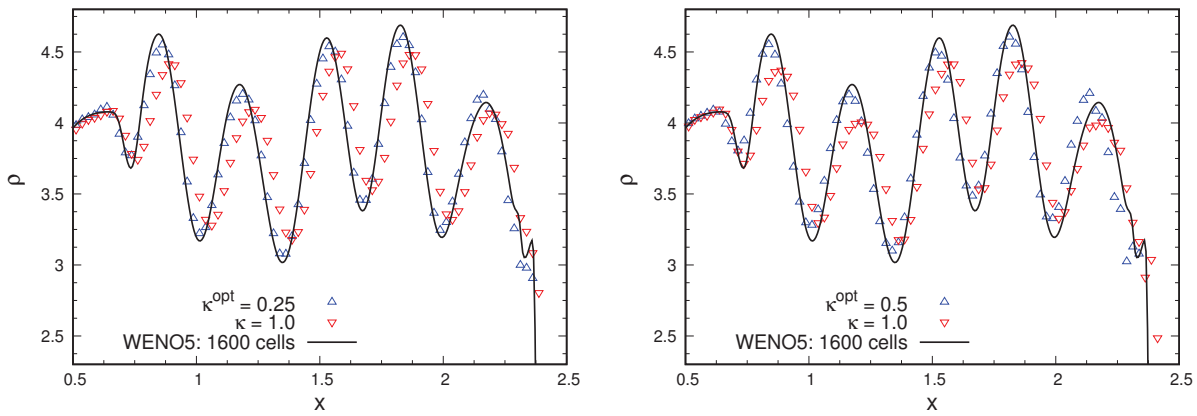

Figure 7.12: Comparison of density profiles of κ^{opt} and $\kappa = 1.0$ for **(a)** minmod and **(b)** MPA filters with the reference WENO5 scheme at $t = 1.8$. Parameter $\tilde{\delta} = 1.0$ for both cases.

7.3.3 Shock vortex interaction problem

This problem is governed by the 2-D Euler equations. Here a stationary normal shock interacts with a moving vortex [220]. The Mach 1.1 shock is positioned at $x = 0.5$ and the state variables upstream of the shock are $(\rho, u, v, p) = (1, 1.1\sqrt{\gamma}, 0, 1)$. At $t = 0$, a small vortex superimposed on the inflow is centered at $(x_c, y_c) = (0.25, 0.5)$. The following perturbations (denoted by tilde) to the velocity (u, v), temperature $(T = p/\rho)$, and entropy $S = ln(p/\rho^{\gamma})$ of the mean flow define the vortex:

$$\begin{cases} \tilde{u} = \epsilon\tau e^{a\left(1-\tau^2\right)} sin\ \theta \\ \tilde{v} = -\epsilon\tau e^{a\left(1-\tau^2\right)} cos\ \theta \\ \tilde{T} = -\frac{(\gamma-1)\epsilon^2 e^{2a\left(1-\gamma^2\right)}}{4a\gamma} \\ \tilde{S} = 0 \end{cases} \tag{7.42}$$

where $\tau = r/r_c$ and $r = \sqrt{(x - x_c)^2 + (y - y_c)^2}$. The parameter r_c is defined as the critical radius for which the vortex has the maximum strength. In the expressions, ϵ and α describe the strength and decay rate of the vortex, respectively. From Jiang and Shu [220], $r_c = 0.05$, $\epsilon = 0.3$ and $\alpha = 0.204$. The simulations were conducted on a computational domain of size $[0, 2] \times [0, 1]$ with a mesh resolution of 251×101. The CFL number, $\tilde{\delta}$ and r_{th} are 0.5, 1.0 and 10^{-4}, respectively.

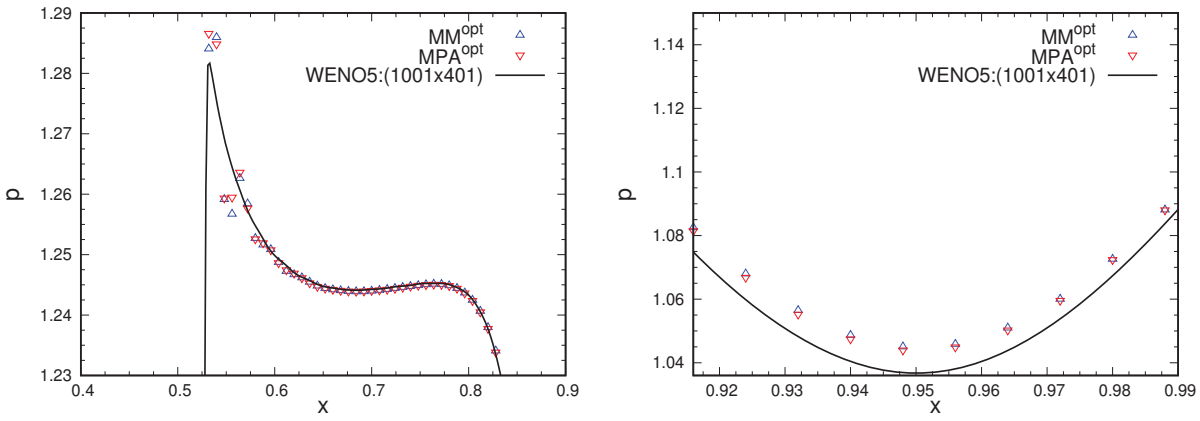

(a) (b)

Figure 7.13: Comparison of pressure profiles for MM^{opt} and MPA^{opt} filters with reference WENO5 scheme **(a)** downstream of the shock, and **(b)** center of the vortex core at $y = 0.5$ cross-section and $t = 0.6$. Filtering magnitude σ_i is evaluated using Bogey sensor (see Eq. 7.4).

Fig. 7.13 shows the pressure distribution along the vortex centerline ($y = 0.5$) for the MM^{opt} and MPA^{opt} filters in conjunction with the Bogey sensor at $t = 0.6$. At this time instance, the vortex has fully interacted with the normal shock and is located downstream. In order to examine the performance of the schemes, the profiles are compared with the reference WENO5 solution obtained on a highly refined mesh of 1001×401 cells. Fig. 7.13(a) shows the pressure profiles in the region immediately downstream of the broken shock. As in the shock-entropy

interaction case, the optimized filters display similar behavior. The methods also generate higher peaks compared to the reference WENO5 solution. However, the downside to the high accuracy is the unphysical jump observed downstream of the peak at $t = 0.6$. Near the vortex core (see Fig. 7.13(b)), both schemes perform almost as well as the refined WENO5 solution in capturing the low-pressure parabolic profile. In addition, a closer observation shows the MPA$^{\text{opt}}$ filter performing slightly better in capturing the minimum compared to the MM$^{\text{opt}}$ filter. In order to better understand the performance of the two filters, corresponding σ^{sc} profiles are plotted in Fig. 7.14 at $t \approx 0.11$ when the vortex is located upstream of the stationary shock. As in the Shu-Osher case, MPA$^{\text{opt}}$ filter produces higher values of σ^{sc} compared to the MM$^{\text{opt}}$ filter. However, the values of σ^{sc} are not high enough to prevent the formation of unphysical jump downstream of the peak.

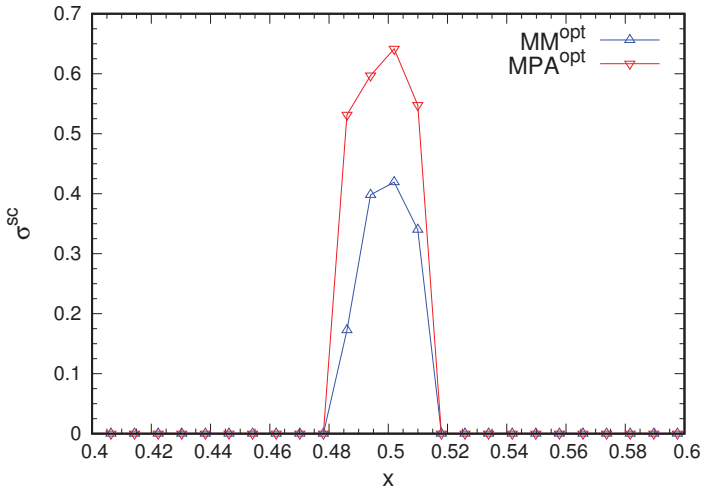

Figure 7.14: Distribution of the filtering strength σ^{sc} using Bogey sensor for MM$^{\text{opt}}$ and MPA$^{\text{opt}}$ filters at $t \approx 0.11$.

The pressure distributions of the two filtering methodologies with the Ducros sensor are displayed in Fig. 7.15. As before, the performance of the schemes are evaluated by comparing with the reference WENO5 solution. Overall, the profiles show good agreement with the reference solution. However, in the vicinity of the broken shock region the schemes exhibit greater smearing compared to those with the Bogey sensor shown in Fig. 7.13. The additional dissipation is due to the relatively larger magnitude of σ^{sc} (see Fig. 7.16) which prevents the formation of spurious oscillations downstream of the peak. Furthermore, MM$^{\text{opt}}$ profile experiences greater damping compared to MPA$^{\text{opt}}$. There are two reasons for the dissipative behavior of the minmod filter. Firstly, the magnitude of σ^{sc} in the shock zone is nearly one. Secondly, this large value in conjunction with the low-order dissipation of the minmod filter is responsible for the higher damping compared to MPA$^{\text{opt}}$ in. In the vicinity of the vortex, both filters capture the low pressure minimum and their accuracy is comparable to those with the Bogey sensor.

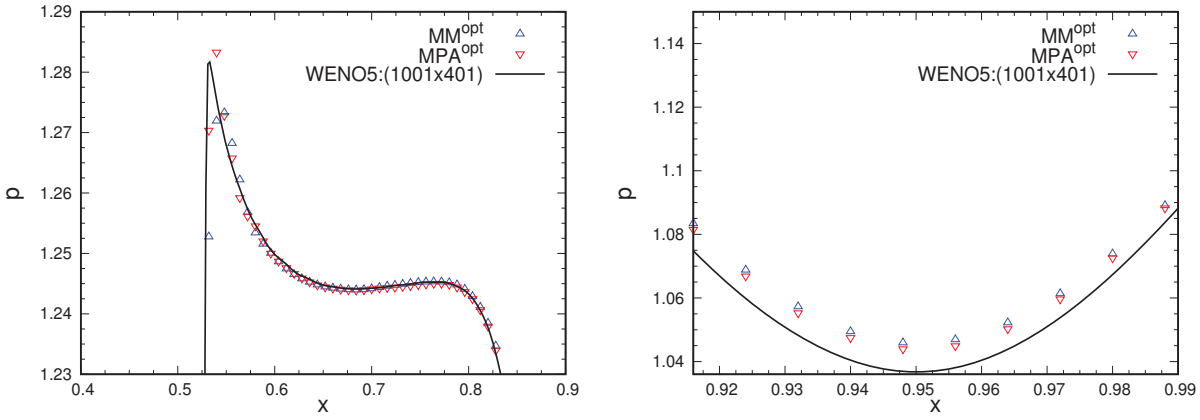

(a) (b)

Figure 7.15: Comparison of pressure profiles for MM^{opt} and MPA^{opt} filters with reference WENO5 scheme (a) downstream of the shock, and (b) center of the vortex core at $y = 0.5$ cross-section and $t = 0.6$. Filtering magnitude σ^{sc} is evaluated using Ducros sensor (see Eq. 7.7).

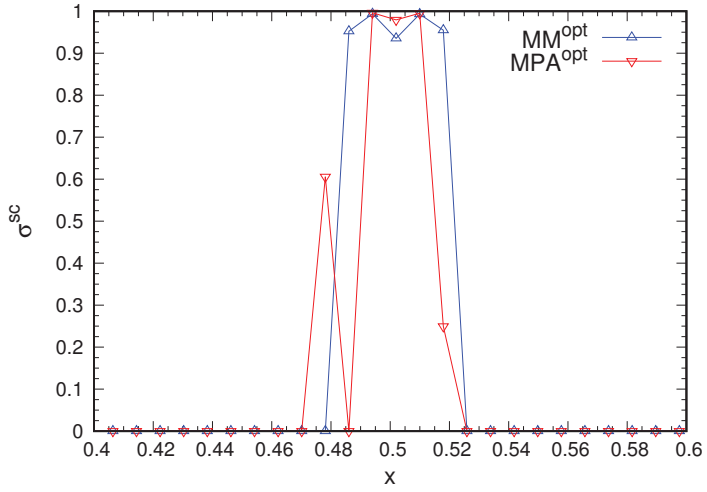

Figure 7.16: Distribution of the filter strength σ^{sc} using Ducros sensor for MM^{opt} and MPA^{opt} at $t \approx 0.11$.

7.3.4 Shock/shear layer interaction

The performance of MM$^{\text{opt}}$ and MPA$^{\text{opt}}$ shock filters with the 6^{th} order base scheme (2.16) and 8^{th} order spatial filter (2.17) are investigated for an oblique shock wave interacting with a spatially evolving mixing layer. The flow conditions for this 2-D problem are taken from Yee *et al.* [222]. The computational domain is of size $[x, y] = [0, 200] \times [-20, 20]$. The following velocity profile is imposed at the left inflow boundary:

$$u = 2.5 + 0.5\ tanh(2y), \tag{7.43}$$

where velocities of the upper u_1 and lower u_2 inflow streams are 3 and 2, and the initial convective Mach number is 0.6. The velocities were chosen such that the flow remains supersonic throughout the domain. The density and pressure inflow conditions of the upper stream are $\rho_1 = 1.6374$ and $p_1 = 0.3626$, and that of the lower stream are $\rho_2 = 0.3626$ and $p_2 = 0.3327$. A 12° oblique shock wave originates at the top-left corner of the domain and impinges on a stream of vortices generated from a perturbed shear layer. The perturbations are introduced by adding the following fluctuations to the v-component of velocity at the inflow boundary

$$v' = \sum_{k=1}^{2} a_k\ cos(2\pi kt/T + \phi_k)\ exp(-y^2/b), \tag{7.44}$$

where the period $T = \lambda/u_c$, wavelength $\lambda = 30$, and convective velocity $u_c = 2.68$. Other constants in the expressions are: $b = 10$, $a_1 = a_2 = 0.05$, $\phi_1 = 0$ and $\phi_2 = \pi/2$. The Prandtl and Reynolds numbers are chosen to be 0.72 and 500, respectively. The interaction between the oblique shock and the shear layer deflects the latter by a small amount. At the location of the intersection, a shock wave originates below the shear layer and an expansion fan above it. The refracted shock below bounces of the slip wall at the bottom and crosses the deflected shear layer. Further downstream, a series of successive eddy shocks are generated around the vortices.

The two-dimensional Navier-Stokes equations (2.1)-(2.11) are solved on a grid of size 321×81. The mesh is uniform in the x-direction and is stretched mildly in the y-direction as in [222, 152]. The viscous terms are treated using a standard five point central scheme. The simulations are performed with $\Delta t = 0.12$ for $t = 120$. Just as in the shock-vortex test-case, the entropy correction parameter $\tilde{\delta} = 1$ for both filter formulations. However, the threshold parameter r_{th} is set to 0.02 since preliminary numerical experiments conducted using lower threshold values including with $r_{th} = 10^{-4}$ wrongly activated the filtering strength σ^{sc} in the high pressure stagnation regions between the vortices downstream of the reflected shock. Uzun and coworkers [234] also determined $r_{th} = 0.02$ to be the best choice in their analysis of tonal noise generation by supersonic impinging jets.

Fig. 7.17 shows the density contours for the MM$^{\text{opt}}$ filter together with Bogey (Figs. 7.17(a) and 7.17(b)) and Ducros (Figs. 7.17(c) and 7.17(d)) sensors. In general, the contours for both cases are similar and display good resolution of the counter-rotating vortices downstream of the reflected shock. However, a closer observation of the Bogey sensor plots reveal the formation of weak artificial oscillatory structures downstream of the oblique shock. The reason for the appearence of these unphysical structures is due to the inability of the method to activate the sensor in this region. In the context of CAA, these artificial waves may incorrectly predict

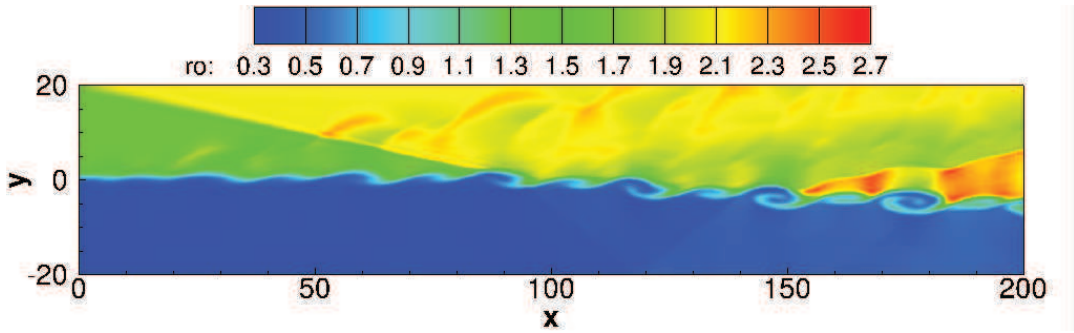

(a)

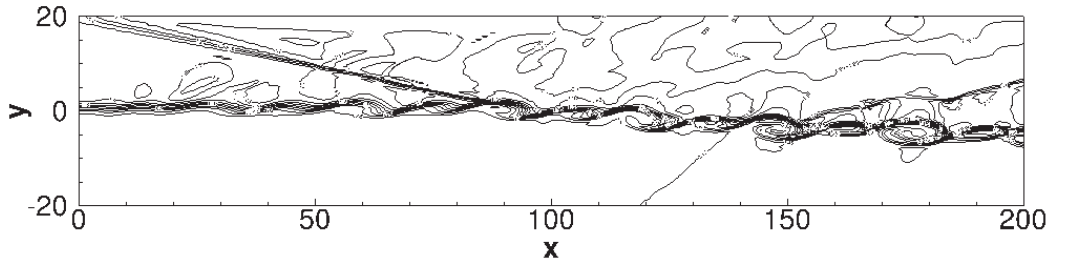

(b)

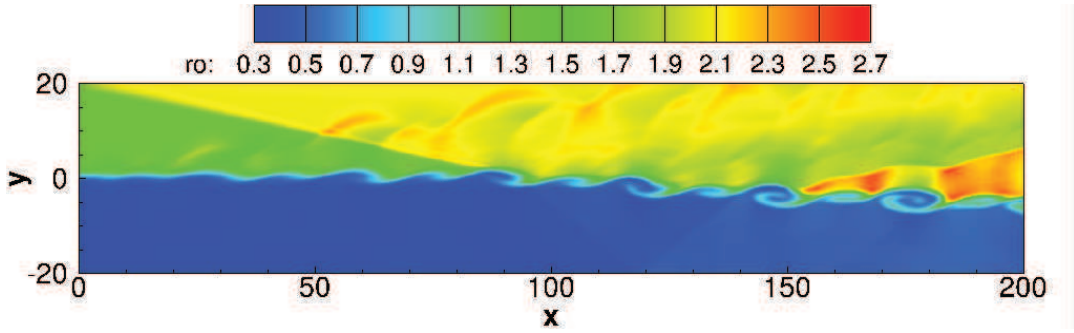

(c)

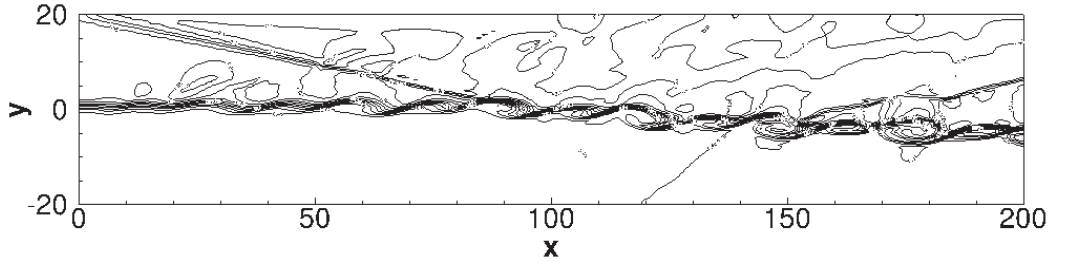

(d)

Figure 7.17: Density contours using **(a)**,**(b)** Bogey sensor, and **(c)**,**(d)** Ducros sensor with MM^{opt} filter.

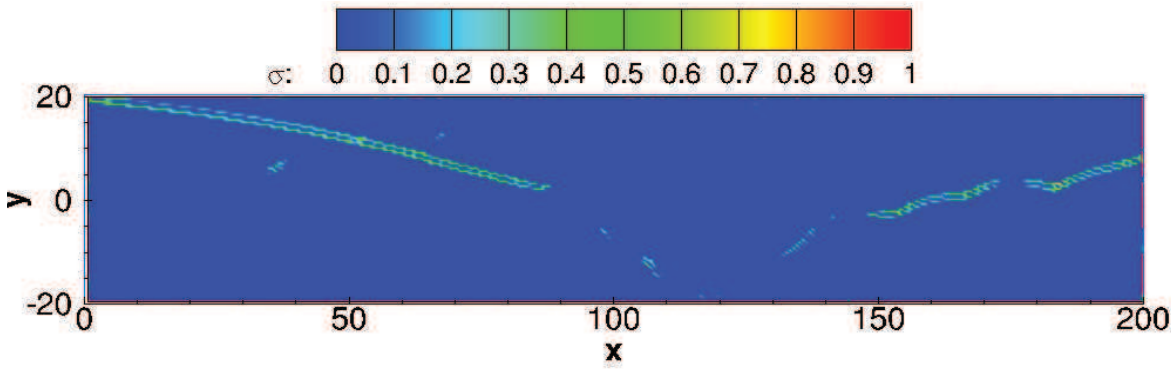

Figure 7.18: Distribution of filter strength σ^{sc} using Ducros sensor for MM^{opt} filter.

the sound pressure level (SPL) at the far field. On the contrary, the contours with the Ducros sensor are relatively cleaner due to the activation of the sensor near the shock as shown in Fig. 7.18. Furthermore, the size of the dissipation window around the shocks is wide enough to prevent unphysical oscillations while preserving high shock resolution. The figure also shows the dissipation being supplied at the refracted, reflected and eddy shock regions.

The density contours of both sensors with the MPA^{opt} filter are shown in Fig. 7.19. As with MM^{opt} scheme, the filter strength σ^{sc} with Bogey sensor is zero throughout the domain. For the Ducros sensor, the plots of density contours are shown in Figs. 7.19(c) and 7.19(d), while Fig. 7.20 shows the corresponding σ^{sc} distribution. As before, the sensor is activated primarily at the shock front with the purpose of damping the unphysical fluctuations downstream of the shock. Compared to the sensor distribution with MM^{opt}, the magnitude with MPA^{opt} is on average larger. This observation is in agreement with the results obtained in the previous test-cases.

The minimum and maximum contour levels for all four scheme combinations are presented in Table 3. Both shock-capturing methods with the minmod sensor generate the same range. This is not surprising since the dissipation due to these schemes are not activated. In the case of Ducros, MPA^{opt} produces a larger contour range than MM^{opt}. Moreover, the scheme generates the maximum contour range. Hence, MPA^{opt} filter together with the Ducros sensor provides the best results for this test-case. The results are consistent with the highly accurate profiles obtained for the shock-entropy and shock-vortex interaction test-cases. It is interesting to note that for the simulation with $\kappa = 1$ a contour range of $(0.332, 2.87)$ was obtained. This range is larger compared to $\kappa^{opt} = 0.5$ due to lower amount of dissipation being supplied. This can be seen in the dispersion-dissipation ratio profile of Fig. 7.4 where the average dispersion-dissipation ratio r for low wavenumbers is slightly higher with $\kappa = 1$ compared to $\kappa = 0.5$.

Table 7.1: **Min and max contour values for MM^{opt} and MPA^{opt} filters with Bogey and Ducros sensors**

	Bogey		**Ducros**	
	min	max	min	max
MM^{opt}	0.331	2.696	0.331	2.624
MPA^{opt}	0.331	2.696	0.331	2.788

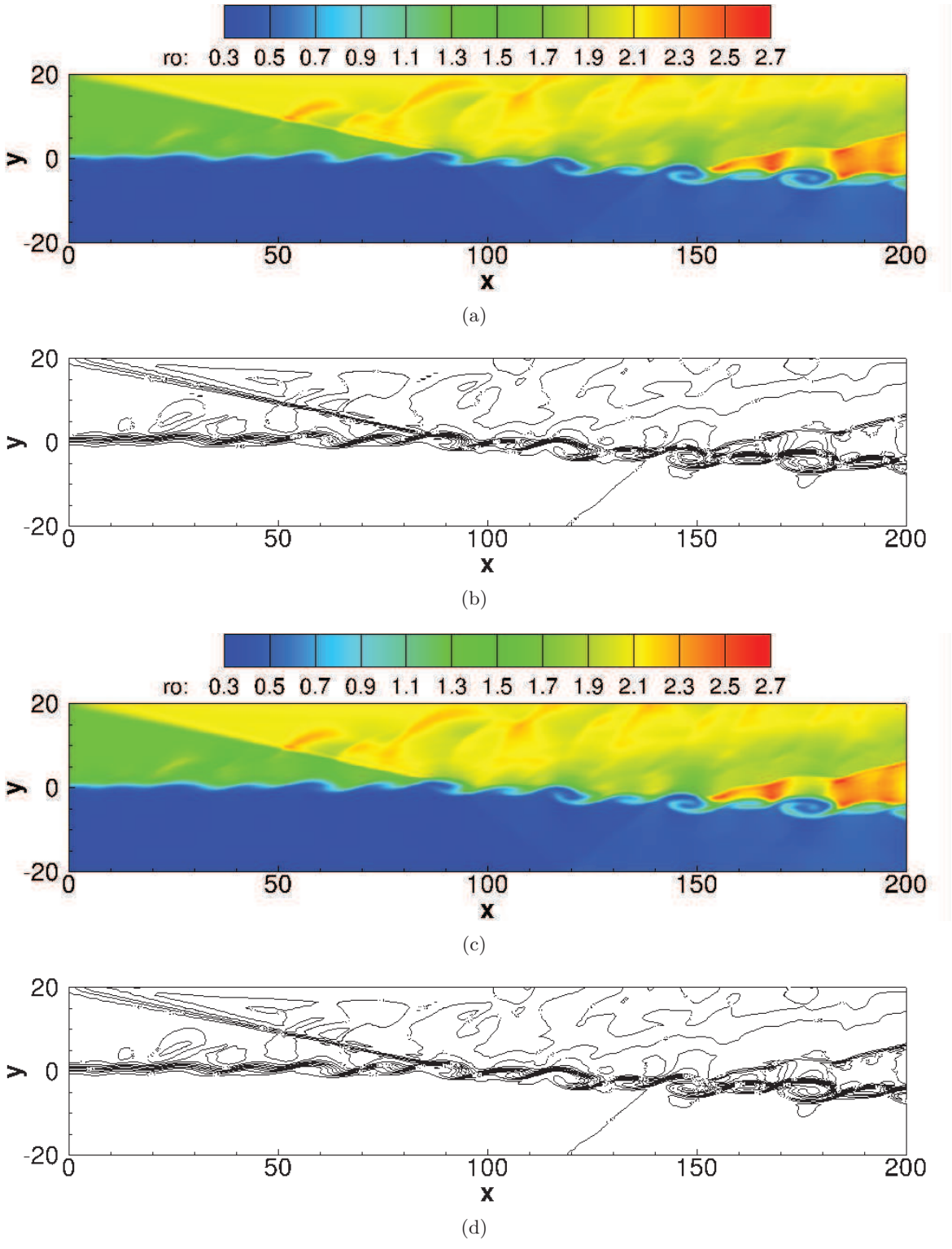

Figure 7.19: Density contours using **(a)**,**(b)** Bogey, and **(c)**,**(d)** Ducros sensors with MPA$^{\text{opt}}$ filter.

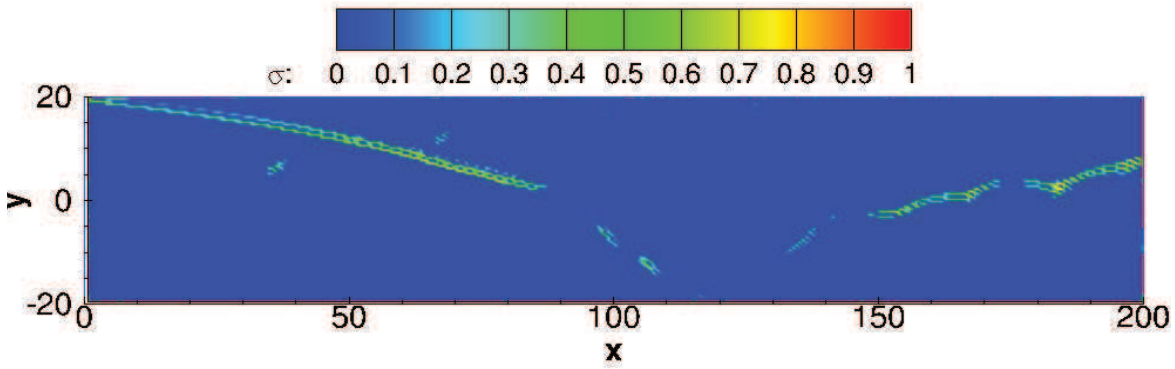

Figure 7.20: Distribution of filter strength σ^{sc} using Ducros sensor for MPA$^{\text{opt}}$ filter.

Table 7.2: **Comparison of percentage increase in computational cost**

	Bogey	**Ducros**
MM$^{\text{opt}}$	13	15
MPA$^{\text{opt}}$	23	25

Table 4 presents the percentage increases in computational cost for the two filters compared to the simulation conducted using just the compact scheme and spatial filter on the same grid. The results for both sensors are shown in the table. MPA$^{\text{opt}}$ filter is 10 percent more expensive than MM$^{\text{opt}}$ due to the larger stencil employed. Comparing the computational cost of Bogey and Ducros sensors, it can be seen that the latter is more expensive. While the MPA$^{\text{opt}}$ filter with the Ducros sensor is the best performing scheme, it also takes the most amount of computational time. Overall, the percentage increases shown are lower compared to the ACM filtering methodology of Lo and co-workers [152]. Specifically, the local ACM approach with HYTVD, MUSCL and WENO schemes resulted in percentages increases of 56, 50 and 160, respectively. The higher computational cost compared to the current methodology may be attributed to two factors: (i) utilizing Roe scheme [155] in evaluating the Riemann problem, and (ii) reducing the order of the spatial filter to zero and allocating buffer points near shocks. By utilizing the Roe and Pike method [236] and keeping the accuracy of the eighth-order spatial filter fixed throughout the domain resulted in lower computational cost with the current finite volume approach.

7.4 Application to supersonic jets

In this section, the shock-filtering techniques MM$^{\text{opt}}$ and MPA$^{\text{opt}}$ are applied to the supersonic under-expanded single jet conditions from Ch. 5 and compared to the base scheme. The parameter $\tilde{\delta}$ is fixed to 1 and the Ducros sensor is used for both cases. The optimized parameter κ^{opt} is set to 0.25 and 0.5 for MM$^{\text{opt}}$ and MPA$^{\text{opt}}$, respectively.

A new mesh was generated with a higher cut-off Strouhal of 3 which increased in 30% the total number of cells. On the other hand, the interior of the nozzle is still not modeled for this case of study. In the course of this Phd, the spatial filter of order 6 used in the computations shown in Ch. 5 and Ch. 6, was remarked to over dissipate pressure perturbations for subsonic

jets. As part of best practices, the order of the spatial filter was increased to 8. The simulation was directly initialized from an interpolated solution from Ch. 5 and let run for 60 convective times with the base scheme [147]. Three computations are then started: one with the base scheme (*i.e.* no shock-filtering), one with minmod and one with MPA. At the present time, only 12.8 convective non-dimensional times ($\hat{t} = ta_\infty/D$) were achieved for all the cases.

Preliminary results of the pressure perturbations in the near-field and the Mach number contours are shown in Fig. 7.21. Similar large turbulence structures can be seen around $x/D = 15$ for all three computations. These structures were convected outside the shear-layer and thus are not directly modified by the shock-filtering techniques. On the other hand, the supersonic region at the center presents a different behavior. Despite the small computational time, different patterns are already present in the near-field pressure perturbation field for both hydrodynamic and acoustic components. The pressure footprint of a large structure at $x/D = 8$ is clearly visible in Fig. 7.21(a) with the base scheme is modified by pressure waves propagating upstream in Fig. 7.21(b) and Fig. 7.21(c). Moreover, the pressure perturbations of the shock-cell associated noise are strongly marked for MM^{opt} and one with MPA^{opt}.

The preliminary results are encouraging for the application of the shock-filtering techniques to supersonic under-expanded jets. A complete study of the aerodynamics and the acoustics will determine the influence of minmod and MPA. In addition, following this study, a computation of a dual stream jet configuration will be carried out.

7.5 Summary and perspectives

Numerical methods for CAA must exhibit low dispersion and dissipation characteristics to accurately capture weak acoustic disturbances at the far-field. Accordingly, compact schemes were devised with minimal dispersion and zero dissipation. Such schemes have been highly successful in resolving the far-field pressure fluctuations as well as ensuring proper scale-separation between energy containing and dissipative eddies in smooth turbulent flow regimes.

For flows containing sharp discontinuities, an adaptive shock-filtering step was activated to provide sufficient dissipation at the end of the sixth-stage Runge-Kutta algorithm of Bogey and Bailly [145]. The filter term is composed of three components: (i) nonlinear dissipative flux $\mathbf{F}^{sc}$ of a high-order shock-capturing scheme, (ii) filter strength σ^{sc}, and (iii) spectrally optimized scheme-dependent-parameter κ^{opt}. The shock zone was identified as a region of non-zero σ^{sc} whose strength was estimated using the adaptive spatial filtering algorithm of Bogey *et al.* [233]. In this study, the performances of dilatation-based Bogey *et al.* [233] and Ducros *et al.* [224] sensors were examined. The sensor magnitude depends on a threshold parameter r_{th} which controls the width of the shock zone. Inside this zone, the accuracy of the second-order minmod and fifth-order Monotonicity Preserving (MP) approach [232] shock filters were analyzed. The local Riemann problems resulting from the reconstruction of the primitive variables were resolved using the dissipative portion of Roe's scheme [155]. To further minimize the computational cost, the algorithm of Roe and Pike [236] was used to construct $\mathbf{F}^{sc}$. Preliminary numerical experiments showed the numerical viscosity of the Roe's scheme to be insufficient in damping the Gibbs' oscillations at the edges of the shock zone. In order to suppress this unphysical behavior, Harten's entropy correction formula was employed to artificially increase the numerical viscosity. The correction term consisted of an entropy

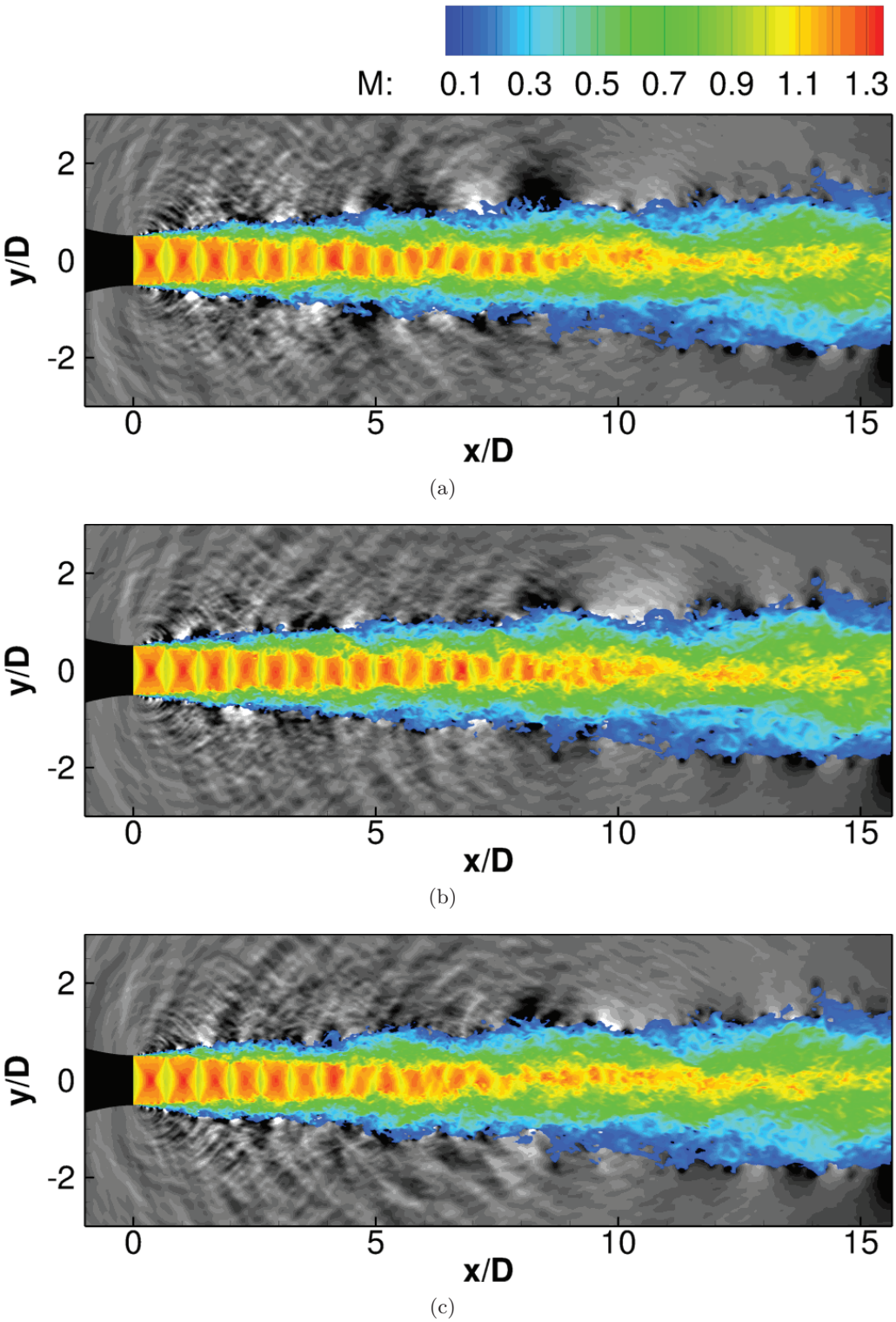

Figure 7.21: *Snapshot of a supersonic under-expanded single jet with* ***(a)*** *base scheme,* ***(b)*** *MPA and* ***(c)*** *Minmod. The black and white contours represent the pressure perturbations with respect to* P_∞ *in the range* $[-30, +30]$ *Pa.*

parameter $\tilde{\delta}$ whose value was set to 1.0. For improving the spectral accuracy, a spectrally optimized parameter κ^{opt} obtained using the dispersion-dissipation ratio condition of Hu *et al.* [242] was incorporated into the filter formulation. The parameter minimized the diffusivity of the nonlinear filter without introducing artificial waves in the solution.

The new adaptive finite volume methodology was applied to four standard test-cases of increasing complexity. For the 1-D shock-tube case, it was shown that the strength of σ^{sc} is inversely proportional to the magnitude of the dissipation supplied by the shock filter. Secondly, increasing r_{th} from 10^{-4} to 10^{-5} widened the dissipation region. This particular test-case was found to be the most challenging for the present finite volume method. Hence, to suppress instabilities near the discontinuities and sonic point, high numerical dissipation was necessary. Therefore, MM^{opt} filter with $\tilde{\delta} = 0.1$, $\kappa = 1.0$ and $r_{th} = 10^{-5}$ provided the best results for this test-case. The second test-case concerning the 1-D shock-entropy interaction problem provided valuable information on the capability of the present scheme to distinguish turbulent fluctuations from shocks. Both MM^{opt} and MPA^{opt} together with the parameters $\tilde{\delta} = 1.0$, κ^{opt} and $r_{th} = 10^{-4}$ showed excellent agreement with the reference WENO5 solution. The results also demonstrated the benefit of choosing the optimal values of $\kappa = 0.25$ and $\kappa = 0.5$ for minmod and MPA schemes, respectively. The choice of these optimal parameters played an important role in correctly capturing the speed of the normal shock and amplitudes of the entropy waves. The third test-case involved the interaction of a stationary normal shock with an oncoming vorticity perturbation. For this 2-D problem, the profiles of MM^{opt} and MPA^{opt} filters correctly captured the peak near the broken shock region as well as the pressure miminum at the vortex core. However, both schemes displayed unphysical jump in the immediate vicinity downstream of the shock. The reason for this unphysical behavior was attributed to the low magnitude of the shock sensor σ^{sc}. The tests with Ducros sensor showed excellent resolution of the flow structure throughout the domain. The jump observed with the Bogey sensor was absent in this scenario due to the larger values of σ^{sc}. However, MM^{opt} scheme clips the peak due to its lower accuracy compared to MPA^{opt}. The final test-case consisted of an oblique shock interacting with a spatially evolving mixing layer. As in the shock-vortex interaction case, the density contours of both methods with the Bogey sensor showed spurious wiggles downstream of the oblique shock. This behavior was attributed to the inactivity of the sensor near the shock. However, with the Ducros sensor, the shock-capturing methods were properly activated. Comparing the contour levels for the four combinations, MPA^{opt} scheme with Ducros sensor provided maximum contour range. While it is the most expensive of the schemes considered in this study, its computational cost is approximately two times lower than the least computationally expensive method of Lo *et al.* [152].

Even if the results presented in this chapter are encouraging for aerodynamic analysis, the validation for aeroacoustics of supersonic configurations is still ongoing. The first results are promising. Nevertheless, the initiated study needs to be finished for the supersonic under-expanded single and dual stream jets.

General conclusions and perspectives

The aircraft industry has developed since the first commercial flights in the beginning of the last century. Since then, reduction in flight time and fuel consumption has been the primary objective of commercial aviation research. Airports were initially located far away from urban areas, however, especially in Europe, they have been victims of the constant growth of the cities and now, they are often found in the vicinity of residential areas. Noise generated by aviation is a hazard that not only affects the quality of life of those who reside next to the airports but also of cabin personnel and passengers inside the planes. In 2015, several commercial airlines connected cities separated by more than $13,000$ km with flights that took over sixteen hours. Over the last decades, many studies were conducted with the aim of increasing comfort and reducing noise propagated to the ground and transmitted into the cabin. The increase in efficiency of new technologies needs to be supported by new standards in perceived noise and studies of the physical phenomena behind noise generation. This argument emphasizes the relevance of the investigations carried out throughout this thesis.

The development of the turbofan engine with higher by-pass ratios has brought an unexpected noise source: shock-cell noise. The bypass stream of a turbofan can reach supersonic under-expanded conditions at the exhaust and generate shock-cell noise. The physics behind supersonic jet noise are not fully understood, which limits progress in the development of advanced noise suppression techniques. To this end, new multi-disciplinary investigations are being carried out globally to increase our knowledge on shock-cell noise. These include: stability studies using reduced-order modeling, computational fluid dynamics and experimental campaigns among others. The general objective of this thesis was to study numerically the physics of shock-cell noise with Large Eddy Simulations (LES).

General conclusions

The numerical approach carried out in this investigation was complemented by several collaborations with other partners from the AeroTraNet2 project, framework of this thesis. Nowadays, a numerical simulation is able to compute the aerodynamic and acoustic fields of a jet with a great level of detail, yet the validity of the simulation will be usually determined if it can reproduce experimental measurements. In addition, the study of noise generation can be accomplished not only with the standard analysis techniques, but also by applying different post-processing procedures that have been widely used in other fields of research. A collabo-

rative work encompassing different areas of expertise has the potential to increase the quality of an investigation as demonstrated by this dissertation. Nevertheless, computational fluid dynamics has become one of the preferred means of action for researchers and industry. The increase in the number and complexity of the configurations of study has made experimental investigations more costly over the years compared to numerical simulations. Computing power has been following Moore's law and new efficient and accurate numerical schemes have been developed to study new physics. In the case of supersonic jets, numerical schemes must be capable of resolving the unsteady flow features and strong non-linearities. In the present work, a high-order family of compact schemes was validated for aeroacoustic simulations of supersonic jets. The validation was carried out with the LES of a supersonic under-expanded single jet at a perfectly expanded Mach number of 1.15. In the following, the main conclusions from this computation are presented.

Supersonic under-expanded single jet

The simulation was able to match the shock-cell lengths to the experimental ones with an error no greater than 5%. The modeling of the internal part of the nozzle was not necessary to obtain the correct turbulence levels and expansion rate of the shear-layer when the appropriate profiles were used as inlet boundary conditions. In addition, the cost of the simulation was reduced by a factor of five by modeling only the external part of the nozzle and not using a fully resolved mesh. In terms of acoustics, shock-cell noise was correctly propagated through the near-field and the simulation was able to capture, with the correct amplitude, the main broadband peak and harmonic. The pressure perturbations were correctly propagated to the far-field with the Ffowcs-Williams and Hawkings analogy. The difference in shock-cell length was manifested as a shift in frequency of the broadband shock-associated noise. Despite the fact that strong noise components associated to different azimuthal modes were propagated to the nozzle exit plane, no screech was captured. The lack of the internal part of the nozzle meant that the feedback loop fundamental for screech to appear was not completed. In addition, a hydrodynamic-acoustic filtering was successfully applied to the pressure near-field of the jet. The filtered components showed a higher cross-correlation for the pressure perturbations related to mixing noise, but did not qualitatively improve the correlations for the shock-cell noise. It was concluded that the acoustic component associated to shock-cell noise was not directly correlated to the hydrodynamic components that are traveling in the opposite direction. Moreover, a spectral analysis was used to identify pressure perturbations that were propagated inside the supersonic region of the jet as an oblique front wave. These waves appeared inside the jet when the shock-cell noise (convected upstream) entered the jet. A wavelet-based post-processing technique was applied in order to study this phenomena in detail. The oblique front wave presented a checkerboard pattern inside the jet and the shock-cell length-scale was of the same order of magnitude as the potential core. The simulation of this supersonic under-expanded jet was not only performed to validate the numerical schemes for supersonic flows but also to establish the correct methodology and post-processing techniques. The spatial filter used to dissipate the high-frequency oscillations inherent to compact schemes is not enough to capture strong discontinuities. Fortunately, the first study case presented a shock-cell system that exhibited low variations in Mach number and allowed for a correct discretization of the fields with the actual schemes. Once the validation step was finished, the complexity of the study was increased in order to better approximate an industrial turbofan.

In the following, the main outcomes from the aeroacoustic LES of a dual stream jet with subsonic primary stream and supersonic under-expanded secondary stream are summarized.

Supersonic under-expanded dual stream jet

The shock-cell length was obtained with a 20% reduction with respect to the experimental results. On the other hand, the radial profiles of the mean velocities and Mach number showed a very good agreement at the relative positions of each shock-cell with less than 5% difference. Moreover, the velocity root-mean-square displayed a higher value in the first shock-cells and similar values at the downstream shock-cells with respect to the experimental profiles. The length-scales and time-scales exhibited distinctive behaviors in the region where both jets were independent, but similar trends after they merged. A pseudo-wavelength was defined using the hydrodynamic-acoustic filtering in order to successfully calculate the central frequency of the main broadband shock-associated peak. The shock-cell noise component resulting from the interaction of the vortical structures with the shear-layer developed surrounding the primary jet was not detected. As a consequence, the acoustic fields presented similar shapes to the ones encountered in the single jet. As expected, no screech was found. The shape of the spectra was in good agreement with the experimental measurements, however, the sound pressure levels exhibited a non-negligible difference of 10 dB. The responsible for this separation, be it physical, numerical, or human, remains uncertain. Similarly to the single jet, pressure waves traveling upstream were found inside the subsonic primary jet and the supersonic secondary jet. They were originated in the shock-cell region and in the merging zone of both jets. The signatures obtained for the shock-cell noise with the wavelet-based methodology corresponded in length-scale to the size of the shock-cell region. Contrary to the validation case, a strong discontinuity appeared in the flow. For this reason, this simulation was performed with an in-house shock-limiting technique, unfortunately, it became unstable and had to be prematurely stopped. To this end, new shock-capturing schemes were developed and tested for four academic test-cases of increasing complexity whose conclusions are reviewed next.

Canonical test-cases for the new adaptive shock-capturing schemes

The one-dimensional shock-tube case was found to be the most challenging for the new numerical schemes. In order to suppress instabilities near the discontinuities and sonic point, high numerical dissipation was necessary. The second test-case concerned the one-dimensional shock-entropy interaction problem. The capability of the new scheme to discern turbulent fluctuations from shocks was tested. The choice of optimal shock-capturing parameters was decisive for correctly capturing the speed of the normal shock and amplitudes of the entropy waves. The third test-case involved the interaction of a steady normal shock with an oncoming two-dimensional vorticity perturbation. The implemented schemes displayed unphysical jumps in the immediate vicinity downstream of the shock. Finally, a shock interacting with a spatially evolving mixing layer was tested. Even if the results obtained for the four canonical test-cases were encouraging for aerodynamic analysis, the new shock-capturing schemes need to be validated for aeroacoustic computations of supersonic jets.

Perspectives

The increase in complexity of aeronautical investigations and other areas of research has transformed one-dimensional and two-dimensional test-cases to parallel computations of realistic three-dimensional industrial models employing meshes with more than $1,000$ million nodes. At the present time, these massive simulations can not be carried out by modest research facilities due to their cost and complexity. These massive computations have been possible not only as a result of the increase in computing power, but also because the numerical schemes and resolution algorithms have been improved. Nowadays, Reynolds-Average Navier-Stokes simulations are fully accessible to Uncertainty Quantification (UQ) studies that require many computations. Furthermore, the developments on computational fluid dynamics are opening the door to UQ studies with large eddy simulations. In the following, perspectives associated to the mesh generation, the numerical schemes, the physical approximation of the flows and the post-processing techniques are reviewed.

Mesh generation

In this work, the generation of the mesh was shown to be a laborious task for the modeling of supersonic single and dual stream jets with conformal structured meshes. In a conformal mesh, the grid lines are continuous at the block interfaces. Further investigations must be continued with the modeling of the internal part of the nozzle of the single jet to verify that it is actually possible to obtain screech. The dual stream jet could benefit from an extended geometry of the internal ducts as well as the addition of a synthetic turbulence forcing to better match the experimental turbulence levels. The inclusion of a plug to the inner nozzle, a co-flow or a pylon, could add a more realistic modeling of the problem. In order to facilitate this work, the numerical schemes must be adapted to non-conformal meshes, keeping its interesting properties. The blocks of non-conformal meshes can have a different number of cells in the connected faces, which leaves the block interface with hanging nodes. At the interface, the high-order compact schemes must keep the same order of accuracy and not generate spurious noise. Moreover, even if the mesh is non-conformal, flux conservation should be assured between the blocks. In addition to non-conformal meshes, hybrid meshes could help reduce the cost of aeroacoustic computations. Indeed, a hybrid mesh is an unstructured grid composed of several basic elements (tetrahedron, prism, pyramid and hexahedron). These meshes should be used if they allow for the generation of a manageable mesh that is in accordance with the numerical scheme constraints for LES. Nonetheless, the generation of standard meshes, can take from weeks to months with the actual numerical schemes used to represent the Navier-Stokes equations. In the problem encountered in this PhD thesis the complexity of the mesh can escalate quickly if the nozzle includes chevrons, fluidic injection, vortex generators or the wing itself. The present work is a step forward in achieving the goals of PUMA challenge at CERFACS, which aims to compute the instantaneous flow around a complete aircraft at realistic conditions.

Numerical schemes

Focusing specifically on hybrid grids, the definition of high-order schemes in finite volume follows direct extensions from the Godunov's method. Today, Essentially Non-Oscillatory (ENO)

and Weighted-ENO schemes are standard high-order shock-capturing upwind schemes. They are all based on a polynomial representation of data built from the cell-centered values; two values are built using an upwind scheme and a Riemann solver accounts for the discontinuity of the interpolated values at the interface. In an unstructured mesh, the polynomial reconstruction needs the definition of a local stencil around the interface, something which can be difficult to perform in a massively parallel environment. But, it should be of great interest to implement and test such a procedure in the near future.

It seems that the new spectral discontinuous methods (such as Discontinuous Galerkin or Spectral Difference) are a great alternative to ENO schemes for unstructured grids. Indeed, the main interest is the definition of many degrees of freedom inside the element, which leads to a compact stencil suitable for High Performance Computing. Nowadays, CERFACS is involved in the development of the solver JAGUAR. But the validation of these methods for aeroacoustics is still open and many questions need to be answered (validation and best practices).

Solving another set of equations

In this context, Lattice Boltzmann Methods (LBM) arise as an advantageous solution. Lattice Boltzmann equations are obtained from the Boltzmann equation by a discretization of the microscopic particle speed. The latest is derived from kinetic theory and represent the flow with particle distribution functions. These functions describe the behavior of a distribution of particles at a given position and a given time. Nonetheless, the well-known Navier-Stokes equations can be recovered with the Chapman-Enskog approximation and a collision model. Computations based on LBM are optimized to run on massive parallel architectures and the mesh can be automated and produced in a couple of minutes, even for complex geometries. At the present time, the majority of LBM implementations are restricted to subsonic and isothermal flows.

Including thermo-chemistry effects

Aside from the geometry and its associated mesh, the study of jet noise could be improved by adding realistic perturbations that are propagated from the combustion chamber to the exhaust of the jet. With this in mind, a coupling of different computations carried out with the same or a different solver would be a powerful and valuable inclusion. In addition, a multi-species reactive solver (as AVBP) could be applied considering that the exhaust gas of a real engine is composed of several species able to react due to temperature effects. Given this background, CERFACS is addressing the computation of a complete aircraft engine, from the compressor to the turbine as part of COUGAR challenge.

Post-processing techniques

Carrying out computations with better and more realistic physics implies that the numerical results will increase in complexity and innovative post-processing techniques will be required to understand and analyze the phenomena of interest. In this PhD thesis, it was demonstrated that wavelet-based post-processing techniques are a powerful tool for the analysis of aeroa-

coustic simulations. This technique uses a conditional criterion in order to investigate the signatures in the flow. Another conditional technique such as Linear-Stochastic Estimation could be used in order to better describe the coherent structures and motions of the turbulent flow. Furthermore, a technique that is not based on a conditional criterion such as Proper Orthogonal Decomposition could be performed on jet flows to extract the large-scale structures responsible for shock-cell noise.

Concluding remarks

In this thesis work, shock-cell noise was successfully investigated with large eddy simulations. In the framework of a collaborative environment, the study raised some concerns on the numerical schemes but was able to find solutions. Moreover, different phenomena generated by shock-cell noise were analyzed in detail with advanced post-processing techniques. Technology is reaching a plateau in terms of efficiency, reduction of the emission of pollutants and reduction of aircraft noise. New numerical schemes and mesh generation procedures, a faithful representation of the flow and more accurate post-processing techniques are key factors in achieving the new goals for society.

Appendix A

Second order moment azimuthal mean

The second order moment between the axial velocity u and the radial velocity v_r can be obtained as

$$\overline{u'v'_r} = \overline{(u_i - \overline{u})(v_{ri} - \overline{v_r})}, \tag{A.1}$$

where the subscript $\{\bullet\}_i$ stands for the instantaneous value, and the over-line for the temporal mean. The components v_{ri} and $\overline{v_r}$ are defined with the Cartesian components of the velocity shown in Fig. A.1 as

$$v_{ri} = v_i cos(\theta) - w_i sin(\theta) \tag{A.2}$$

$$\overline{v_r} = \overline{v} cos(\theta) - \overline{w} sin(\theta). \tag{A.3}$$

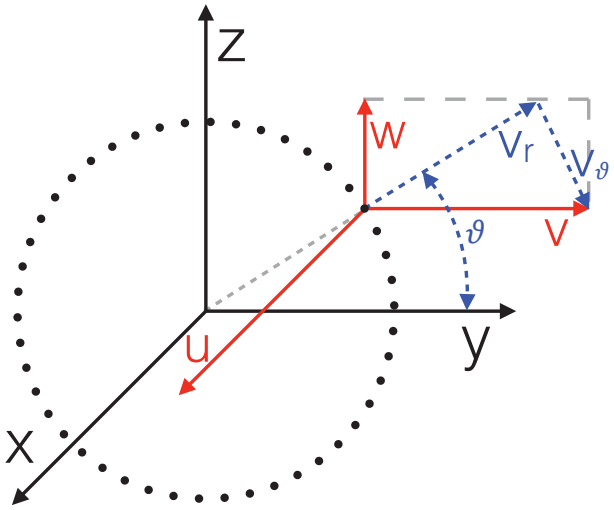

Figure A.1: *Diagram of the velocity components in Cartesian and Cylindrical coordinates.*

Inserting the values of v_{ri} and $\overline{v_r}$ into Eq. (A.1) gives

$$\overline{u'v'_r} = \overline{(u_i - \overline{u})(v_i cos(\theta) - w_i sin(\theta) - \overline{v} cos(\theta) + \overline{w} sin(\theta))}, \tag{A.4}$$

$$\overline{u'v'_r} = \overline{(u_i - \overline{u})((v_i - \overline{v}) cos(\theta) - (w_i - \overline{w}) sin(\theta))}, \tag{A.5}$$

$$\overline{u'v'_r} = \overline{u'(v' cos(\theta) - w' sin(\theta))}, \tag{A.6}$$

$$\overline{u'v'_r} = \overline{u'v'} cos(\theta) - \overline{u'w'} sin(\theta). \tag{A.7}$$

Appendix B

Azimuthal signal aliasing

In signal processing, the Nyquist Theorem states that one needs two samples per cycle of the input signal to define it. Therefore, one can accurately measure the frequency of a signal f as long as the number of samples per second is greater than two-f. If the user tries to measure a frequency higher than half the frequency sampling, the measured signal will be aliased. When the signal is aliased, the unresolved frequencies according to the Nyquist Theorem will fold back on the resolved part of the spectrum, aliasing the signal. This phenomena appears as well for the azimuthal decomposition. Therefore, if M probes are set to decompose the signal, but the energy content of the signal is distributed above $M/2$ modes, the energy content of the unresolved modes will fold back on the resolved modes. If the energy content of the higher modes is small compared to the resolved modes, the results of the resolved modes will not loose accuracy. On the other hand, if the energy content of the unresolved modes is of the same order, the results might be completely aliased.

This section shows the impact of the azimuthal aliasing on the case of the dual stream jet of Ch. 6. The results are analyzed with 16 and 256 azimuthally distributed probes referred to as A16 and A256 respectively. The second set of probes is chosen as the maximum value of resolution due to the fact that the mesh has actually an azimuthal discretization of 256 cells. A set of three different axial locations are studied $x/D_s = 2.5, 4.5, 6.75$. For each axial location, the results are analyzed at 4 radial positions, one in the near-field (referred to as NF3D), one outside the shear-layer of the secondary jet (referred to as NF1D), one inside the shear-layer of the secondary jet (referred to as LIP_S), and one inside the primary jet (referred to as LIP_P). The different axial and radial positions are summarized in Table B.1.

Reference	$x/D_s = 2.5$ r/D_s	$x/D_s = 4.5$ r/D_s	$x/D_s = 6.75$ r/D_s
NF3D	2.07	2.37	2.67
NF1D	1.22	1.52	1.82
LIP_S	0.45	0.45	0.45
LIP_P	0.20	0.20	0.20

Table B.1: *Study locations*

The results are analyzed as follows. First, the total energy contained in the resolved spectrum is considered by integrating the Power Spectral Density (PSD). The integration of the spectrum is approximated by a piece-wise constant method. A third order polynomial integration presented the same results and is therefore not studied in this work. The integration of the PSD is applied to each resolved mode. Clearly, A16 has less resolved modes than A256. As explained above, the number of resolved modes for A16 is $M/2 = 8$. Here the energy contained in the higher resolved modes, *i.e.* up to 128 for A256 is added together and it is noted in the figures as $m > 8$. This remaining energy aliases the lower modes A16 giving an idea of how accurate is to use only 16 probes when dealing with azimuthal decompositions of a supersonic under-expanded jet. An example of these results is shown in the first column of Fig. B.1. Second, the energy of the modes is stacked and divided by the total energy of the full signal. Here, the energy of the full signal is the azimuthally average energy of the probes. This type of plot displays the amount of energy resolved with respect to the total energy of the signal for a finite number of modes. However, due to the aliasing, the total energy ratio resolved is always of 100%. This is where the comparison with respect to the results with 256 probes is important. A clear difference between both of them would indicate that the energy is not well resolved with only 16 probes. An example of these results is shown in the second column of Fig. B.1. The previous two analysis give information about the total energy that is aliased from the higher unresolved azimuthal modes. However, even if one mode does not capture the total energy of the actual mode, it may happen that the aliasing occurs only for frequencies that do not lay on a frequency range of interest. For this reason, the accumulated error growing with the frequency is computed. The actual percentage error for a frequency range of interest should be computed by multiplying the percentage error of the mode by the accumulated error of the frequency range of interest. An example of these results is shown in the left column of Fig. B.2. Moreover, the accumulated energy of each mode with growing Strouhal number gives more information with respect to the error committed. If an error of 50% is reached, but only 10% of the energy of the whole mode is achieved for the frequency range of interest, the actual error will be much smaller. An example of these results is shown in the right column of Fig. B.2. Finally, the power spectral density of each mode can be accounted for as a ratio with respect to the total energy or by itself. Even though this type of plot gives an idea of the distribution per mode and frequency, it only allows for a qualitative comparison between both sets of arrays. An example of these results is shown in Fig. B.3 and B.4.

B.1 Analysis of results

B.1.1 NF3D probes analysis

In this section, the analysis of the NF3D array is explained. The different positions of the array are characteristic positions of a supersonic under-expanded jet. The first position located at $x/D_s = 2.5$, $r/D_s = 2.07$ falls in the center of the shock-cell noise spectrum. The second position located at $x/D_s = 4.5$, $r/D_s = 2.37$ is at the edge of the shock-cell noise main lobe. Last, the third position located at $x/D_s = 6.75$, $r/D_s = 2.67$ is completely outside of the shock-cell noise spectrum and it shows only the effect of the mixing noise.

The left column of Fig. B.1 displays the energy distribution between each mode for each axial position. Clearly, the energy content of the full signal is distributed over more modes for

the first axial position. At $x/D_s = 6.75$ the first two modes have over twice the energy of the third mode. The energy of the unresolved modes for A16 aliases the resolved modes as shown in the last bar of the left column of Figure B.1. This remaining energy is distributed over the other modes increasing their energy. When the energy is better scattered among more modes as it happens at the first axial position due to the shock-cell noise, it presents a higher remaining energy of the unresolved modes. On the other hand, at the farthest axial position, the remaining energy is greatly reduced. The folding back of the unresolved modes is illustrated in the right column of Fig. B.1 which compares the accumulated energy between A16 and A256. As it can be seen in Fig. B.1 (b), only the first 12 modes are needed to recover 95% of the total energy and the first three modes to recover 50% of the total energy. As the probes are farther away from the shock-cell noise lobe, the number of modes needed to achieve 95% of the total energy are reduced to 11 at $x/D_s = 4.5$ and 10 at $x/D_s = 6.75$ as shown in Fig. B.1 (d) and (f) respectively. A greater reduction is observed in order to resolve 50% of the total energy with only 3, 2 and 1 modes at the same positions without taking into account the mean or mode zero. This emphasizes how the acoustics of the flow at the downstream positions are basically driven by the mixing noise of large turbulence structures. Overall, A16 assures that an error in energy of no more than 15% is generated for the first three modes.

The reader needs to keep in mind that even if the total energy of the mode differs between the A16 and A256, it may occur that the frequency of interest does not contribute to that disparity. In other words, the aliased energy may be encountered at higher frequencies than the frequency range of interest. The left column of Fig. B.2 shows the accumulated percentage error growing with the frequency whereas the right column shows the accumulated energy of each mode. At the first two axial positions displayed in Fig. B.2 (a) and (b), the accumulated error of all the modes with the exception of the mean is less than 20% up to $St_s = 2$ with the exception of the last mode that grows up to 40%. The accumulated error of the mean or mode 0 grows about 25% for $St_s < 1$ but then it only increases another 5% up to $St_s = 3$. At the last axial position, where the acoustics are mainly due to the turbulence of the large structures, the error spikes even more at the lower frequencies and then grows at a similar rate of $5\%/St_s$ for the modes 0 and 1. A steeper trend of $10\%/St_s$ accumulated error exhibits at all locations for the higher modes above $St_s = 2$. Overall, if the frequency of interest for shock-cell noise is below $St_s = 2$, the total error in energy that would be committed for the first three modes is less than 3%.

In a similar fashion, the power spectral density can be plotted in a stacked plot in relation to the total power spectral density or by its own. The first type of plot, gives a qualitative measure of how far is the mode being represented by A16 with respect to the ideally discretized A256. Figure B.3 shows a comparison between the stacked PSD for A256 on the left, and A16 on the right. Clearly, as it was stated above, the weight of each mode starts to deviate from the fully discretized array above $St_s = 2$. This effect is most perceived by the higher modes than by the first three modes. On the other hand, if the non-stacked version of the plot is studied, as it is shown in Fig. B.4, it can be seen than the total PSD of the stacked higher modes is lower in amplitude than the lower modes. This is specially true for the last axial position, where as it was presented in Fig. B.1 (d), the first three modes are the dominant modes.

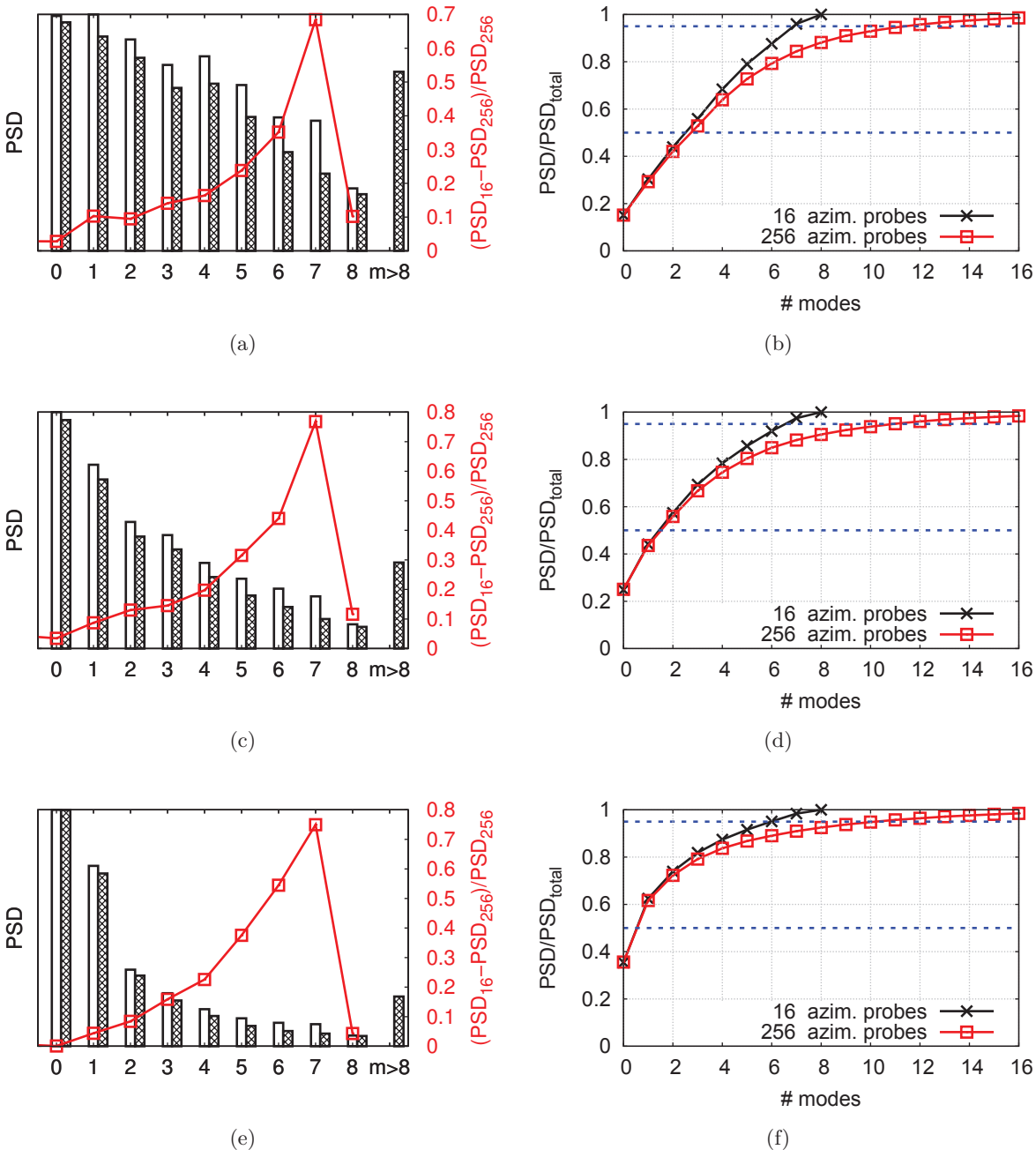

Figure B.1: *On the left column, the total energy density is represented for the A16 and A256 in blank and hatched bars respectively. Moreover, the line plot shows the relative deviation of the A16 with respect to the A256. On the right column, the accumulated energy by number of modes is represented for both arrays. The horizontal dashed lines represent the* 50% *and* 95% *thresholds. The radial position considered is NF3D. The axial positions are* ***(a)****,* ***(b)*** $x/D_s = 2.5$*,* ***(b)****,* ***(c)*** $x/D_s = 4.5$ *and* ***(d)****,* ***(e)*** $x/D_s = 6.75$*.*

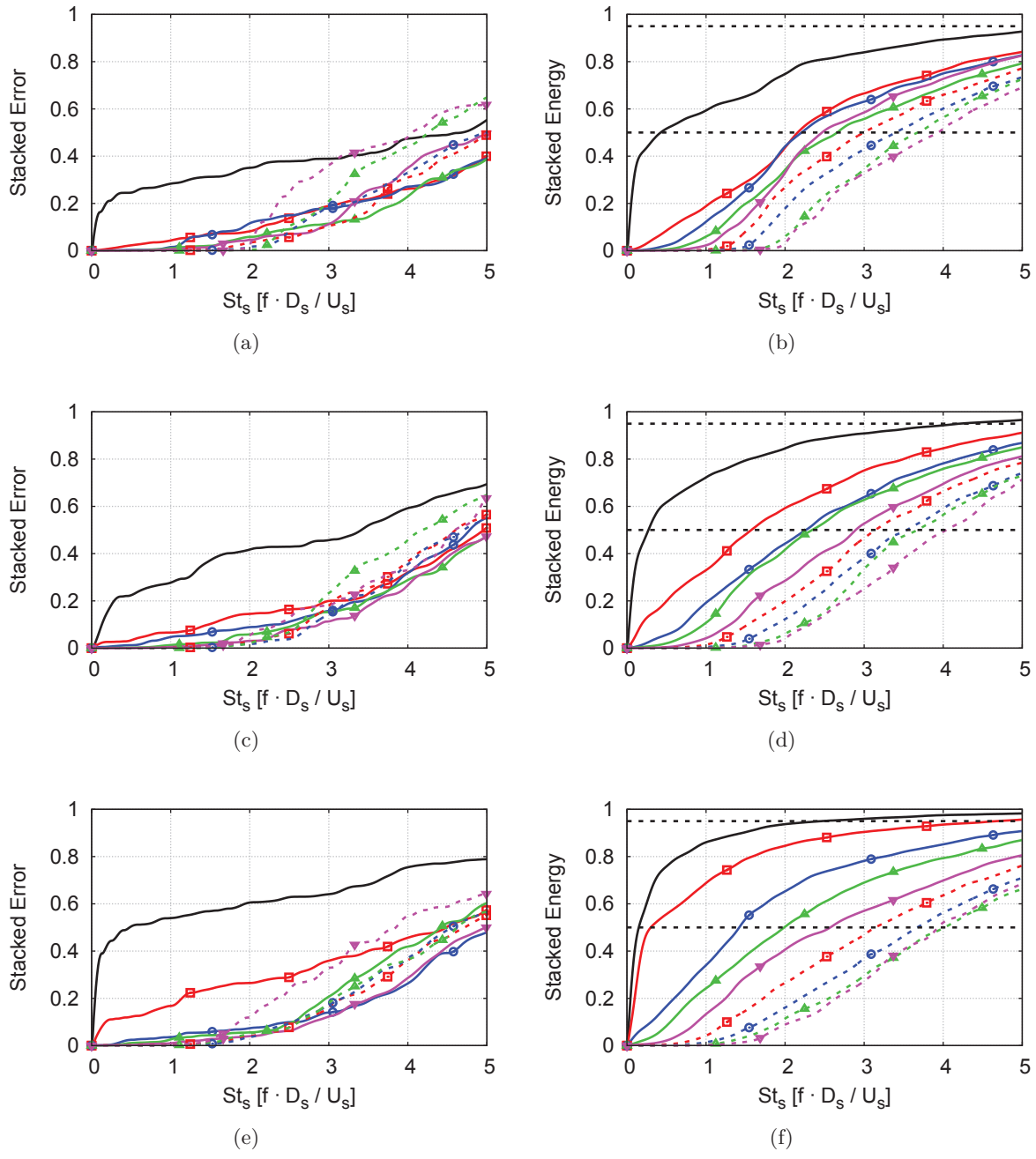

Figure B.2: *On the left column, the stacked error growing with the frequency is represented for A16 with respect to A256. On the right column, the stacked energy growing with the frequency is represented for A16. In solid line: mode 0 in black without symbol, mode 1 in red □, mode 2 in blue ○, mode 3 in green △ and mode 4 in magenta ▽. In dashed line: mode 5 in red □, mode 6 in blue ○, mode 7 in green △ and mode 8 in magenta ▽. The radial position considered is NF3D. The axial positions are* ***(a)****,* ***(b)*** $x/D_s = 2.5$*,* ***(b)****,* ***(c)*** $x/D_s = 4.5$ *and* ***(d)****,* ***(e)*** $x/D_s = 6.75$*.*

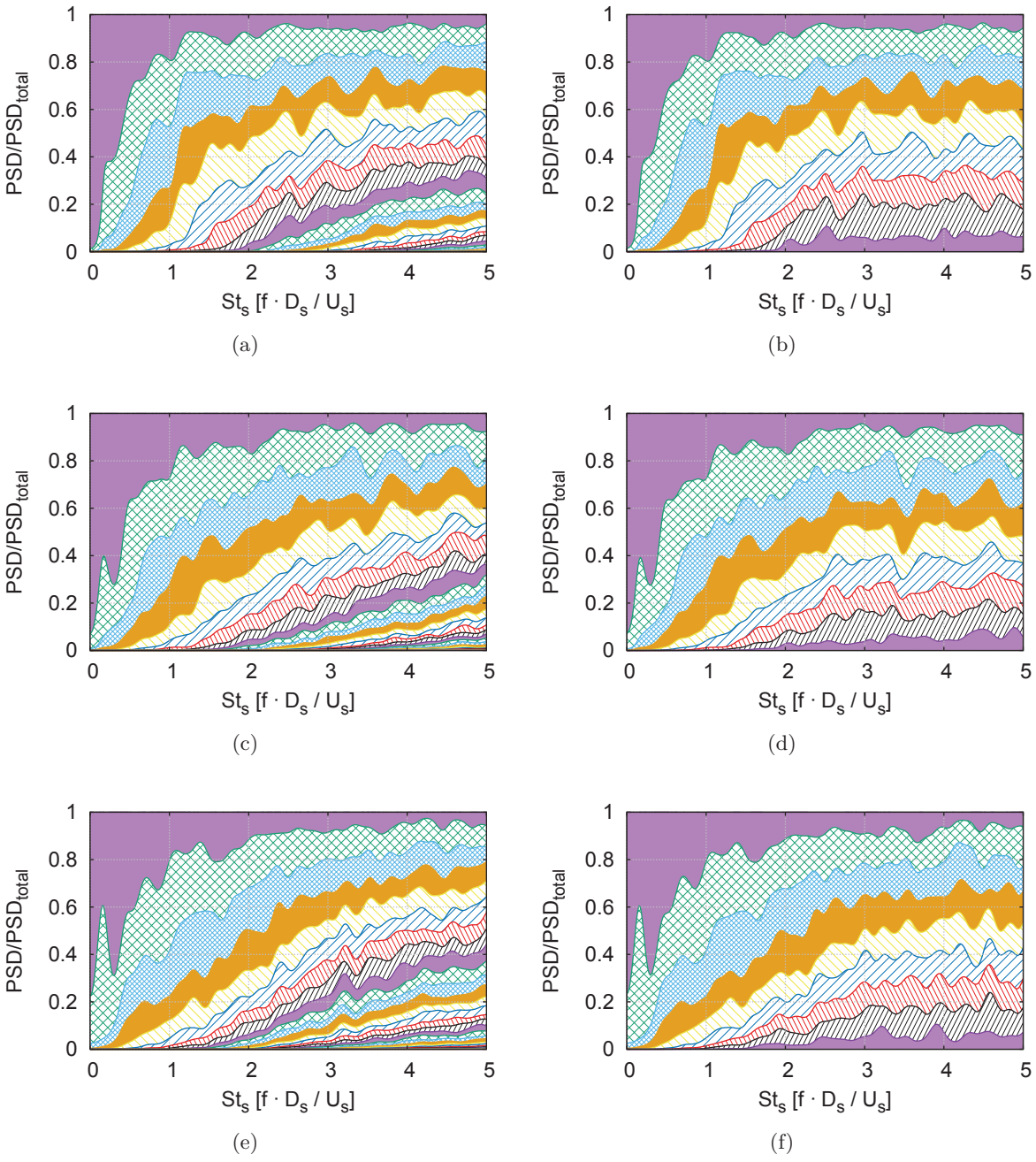

Figure B.3: *Pressure PSD Ratio of each mode with respect to the total PSD. A256 is shown in the left column* ***(a)****,* ***(c)*** *and* ***(e)*** *and A16 in the right column* ***(b)****,* ***(d)*** *and* ***(f)****. The radial position considered is NF3D. The axial positions are* ***(a)****,* ***(b)*** $x/D_s = 2.5$*,* ***(b)****,* ***(c)*** $x/D_s = 4.5$ *and* ***(d)****,* ***(e)*** $x/D_s = 6.75$*.*

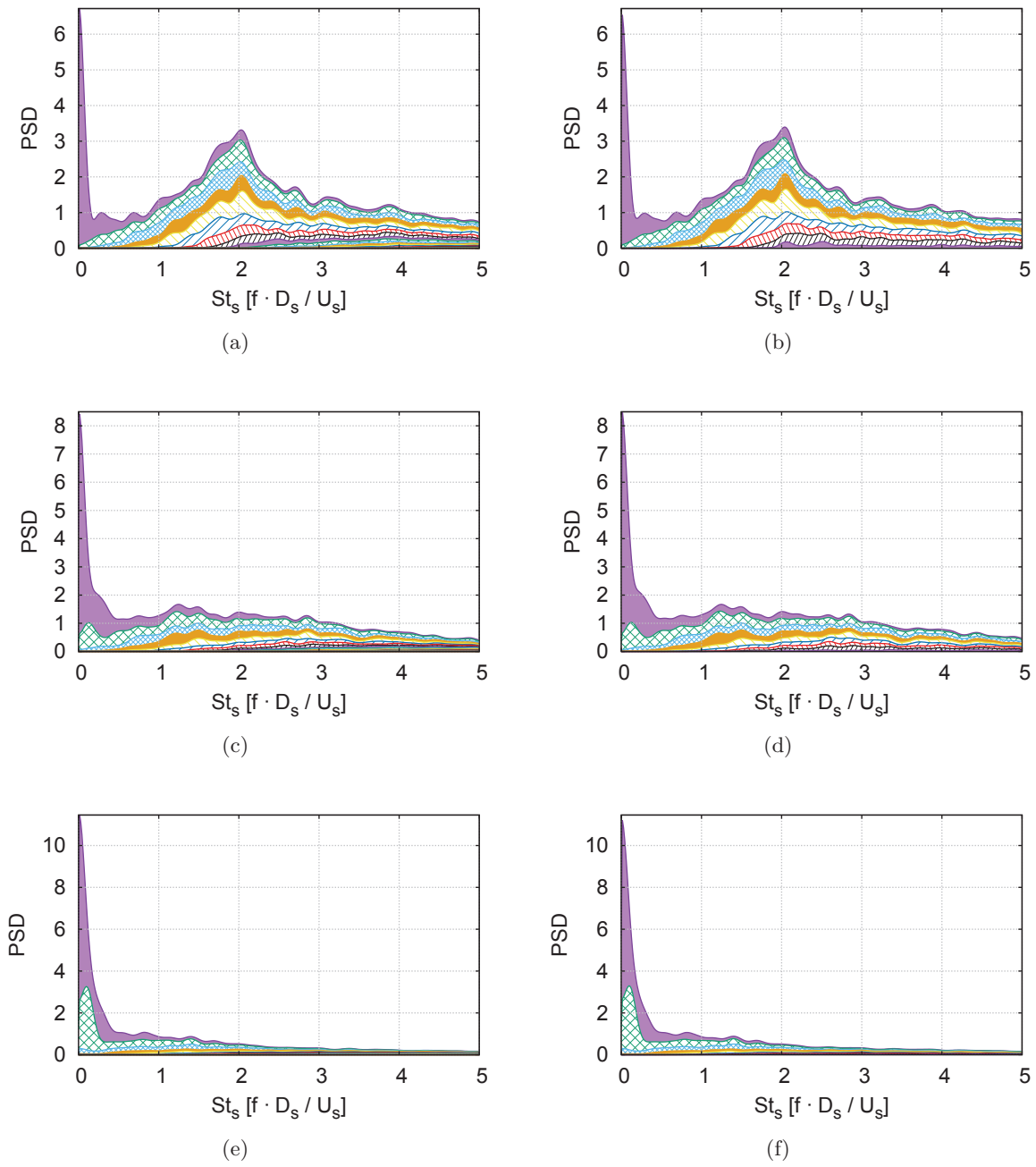

Figure B.4: *Stacked pressure PSD of each mode with respect to the total PSD. A256 is shown in the left column* ***(a)****,* ***(c)*** *and* ***(e)*** *and A16 in the right column* ***(b)****,* ***(d)*** *and* ***(f)****. The radial position considered is NF3D. The axial positions are* ***(a)****,* ***(b)*** $x/D_s = 2.5$*,* ***(b)****,* ***(c)*** $x/D_s = 4.5$ *and* ***(d)****,* ***(e)*** $x/D_s = 6.75$*.*

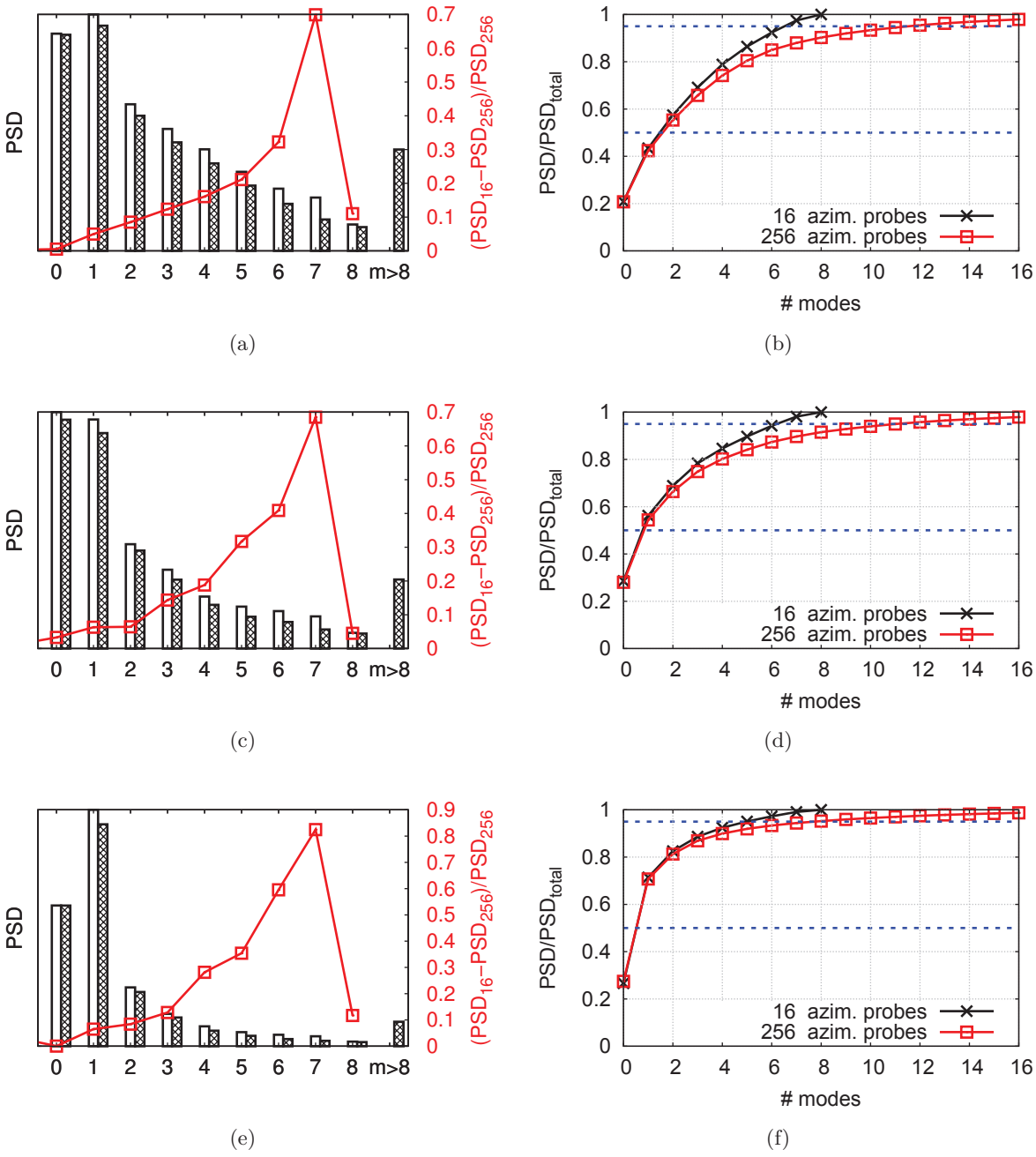

Figure B.5: *On the left column, the total energy density is represented for A16 and A256 in blank and hatched bars respectively. Moreover, the line plot shows the relative deviation of A16 with respect to A256. On the right column, the accumulated energy by number of modes is represented for both arrays. The horizontal dashed lines represent the* 50% *and* 95% *thresholds. The radial position considered is NF1D. The axial positions are* ***(a)****,* ***(b)*** $x/D_s = 2.5$*,* ***(b)****,* ***(c)*** $x/D_s = 4.5$ *and* ***(d)****,* ***(e)*** $x/D_s = 6.75$*.*

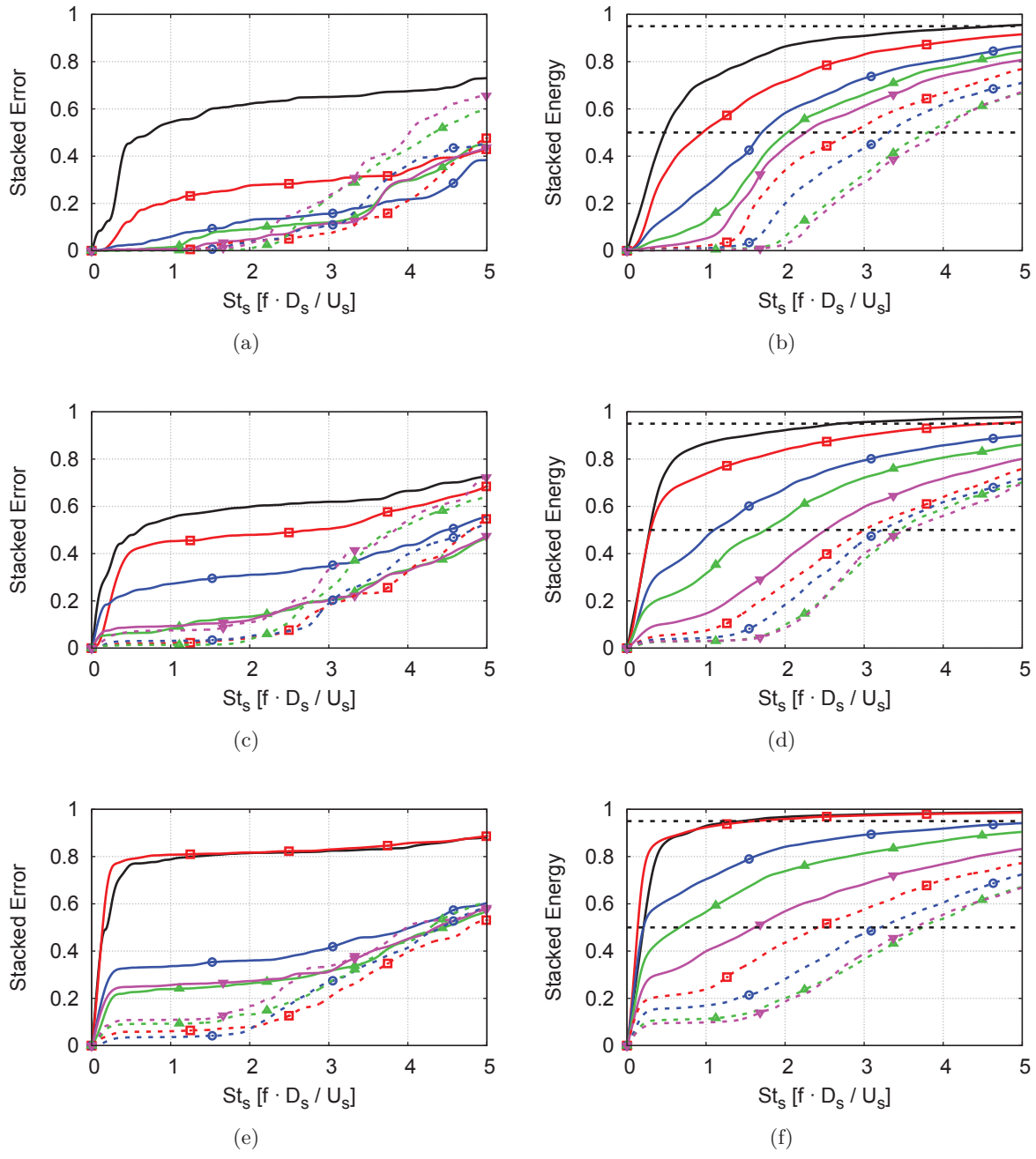

Figure B.6: *On the left column, the stacked error growing with the frequency is represented for A16 with respect to A256. On the right column, the stacked energy growing with the frequency is represented for A16. In solid line: mode 0 in black without symbol, mode 1 in red □, mode 2 in blue ○, mode 3 in green △ and mode 4 in magenta ▽. In dashed line: mode 5 in red □, mode 6 in blue ○, mode 7 in green △ and mode 8 in magenta ▽. The radial position considered is NF1D. The axial positions are* ***(a)****,* ***(b)*** $x/D_s = 2.5$*,* ***(b)****,* ***(c)*** $x/D_s = 4.5$ *and* ***(d)****,* ***(e)*** $x/D_s = 6.75$*.*

B.1.2 NF1D probes analysis

In this section, the analysis of the NF1D array is explained. The first position located at $x/D_s = 2.5$, $r/D_s = 1.22$ falls in the center of the shock-cell noise spectrum. The second position located at $x/D_s = 4.5$, $r/D_s = 1.52$ is at the edge of the shock-cell noise main lobe. Last, the third position located at $x/D_s = 6.75$, $r/D_s = 1.82$ is completely outside of the main shock-cell noise radiation, illustrating the effect of the mixing noise. Contrary to the NF3D array, this array is fully immersed in the hydrodynamic part of the jet and thus, the contribution of the hydrodynamic component should be expected to be higher. A decomposition into hydrodynamic and acoustic components was not possible because the poor axial discretization of the axial cuts used in this study.

The energy distribution between each mode for each axial position presented in Fig. B.5 shows a different behavior that the one encountered in NF3D. At this radial position, for the first axial position Fig. B.5 (a), the energy of the mode zero and mode one are about 50% higher than the following modes. This is expected, as the probes are inside the hydrodynamic region, usually driven by the lower azimuthal modes. The same increment occurs for mode one at the second axial position (Fig. B.5 (c)). The third axial position displayed in Fig. B.5 (e) reveals a higher amplitude in energy for mode one with respect to mode zero. At this radial position, the remaining energy is smaller than the one left at NF3D, nonetheless, due to the fact that the first two modes are much greater in amplitude, the value of the remaining energy has a similar amplitude as the second-to-fourth modes in NF1D and NF3D. Even though the energy contained in the first modes is greater than in NF3D, the right column of Fig. B.5 shows that the number of modes needed to accurately capture 95% of the total energy is about 12, 11 and 8, for each axial position. In NF3D 12, 11 and 10 modes were needed. The number of modes needed to capture half the energy is even more reduced than for NF3D, thus needing in this case only 2 modes at the first axial position and 1 at the others. The total error assumed by using only 16 probes remains about 15% for the first three modes.

The accumulated percentage error of NF1D is displayed in Fig. B.6 for all the axial positions. Similarly to NF3D, the higher modes start to accumulate error above $St_s = 2$. At the first axial position, 50% of the total error of mode 0 is accumulated below $St_s = 0.5$, then, another 10% is accumulated up to $St_s = 2$. In a similar fashion, the error grows up to 10% below $St_s = 0.5$ and then up to 30%. This higher growth of the accumulated error with respect to NF3D for the lower modes at lower frequencies is linked to the fact that the probes are well inside the hydrodynamic region. At the second axial position, the accumulated error of mode 2 grows as well, and mode 1 reaches a value of 40% of accumulated error at $St_s = 0.5$. At the farthest axial position, an accumulated error for mode 0 and 1 of 80% is reached below $St_s = 0.5$ but is kept constant above 0.5. Modes 2, 3 and 4 follow a similar trend but with a smaller accumulated error. Nonetheless, even if the accumulated error is high, the actual error in the frequency range of interest is smaller.

The error is accumulated for $St_s < 0.5$ because it is the region of the spectrum where most of the energy lays. Figure B.7 shows how the energy in this region is basically composed of the first 4 modes which are then contributing to the accumulated error. Moreover, Fig. B.8 illustrates how the energy is greater for $St_s < 0.5$ than for higher Strouhal numbers. Shock-cell noise is still visible at this radial position for the first axial position and it is spread over higher frequencies for the second axial position as is shown in Fig. B.8 (a) (b) and (c) (d) respectively.

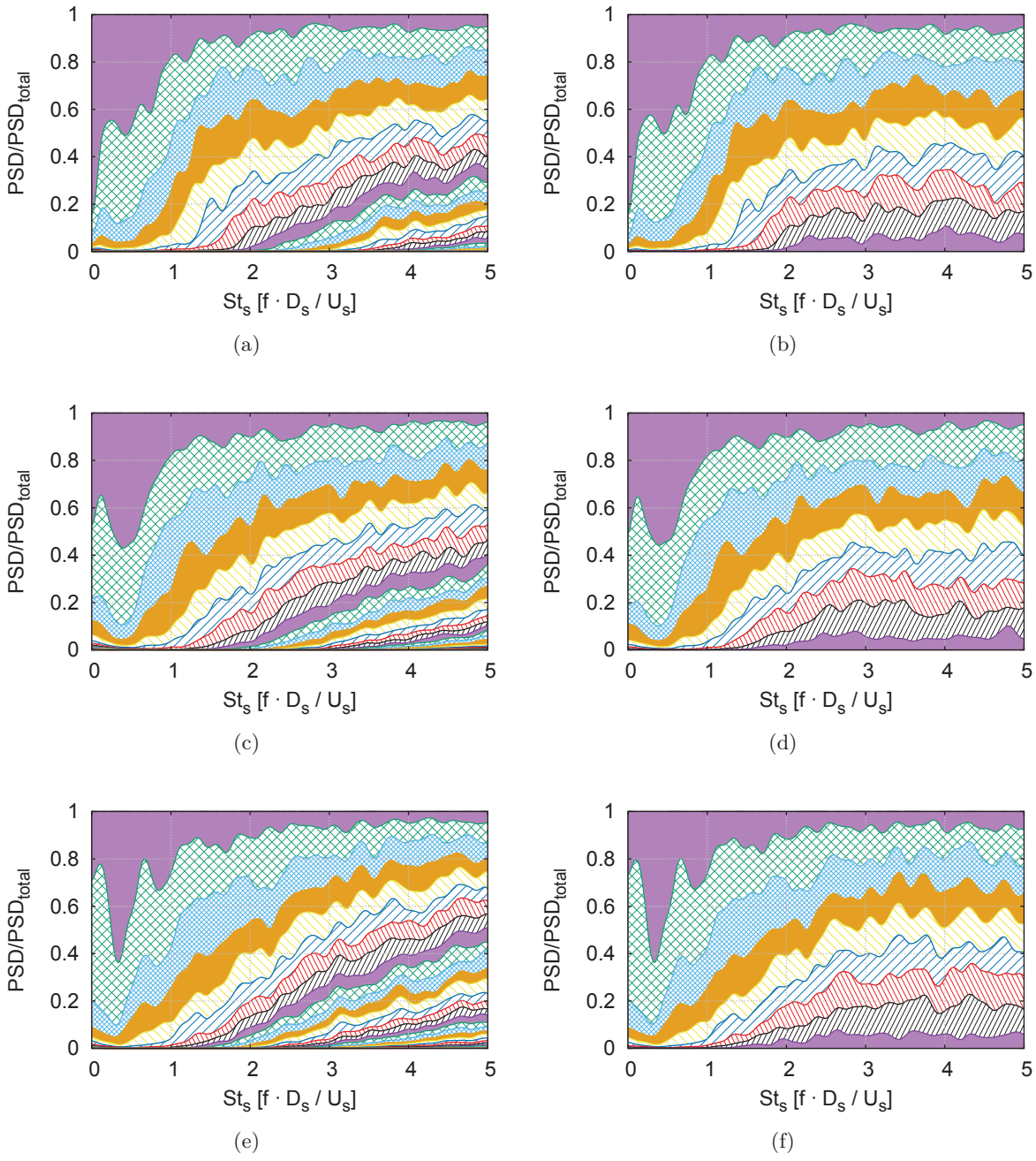

Figure B.7: *Pressure PSD Ratio of each mode with respect to the total PSD. A256 is shown in the left column* ***(a)****,* ***(c)*** *and* ***(e)*** *and A16 in the right column* ***(b)****,* ***(d)*** *and* ***(f)****. The radial position considered is NF1D. The axial positions are* ***(a)****,* ***(b)*** $x/D_s = 2.5$*,* ***(b)****,* ***(c)*** $x/D_s = 4.5$ *and* ***(d)****,* ***(e)*** $x/D_s = 6.75$*.*

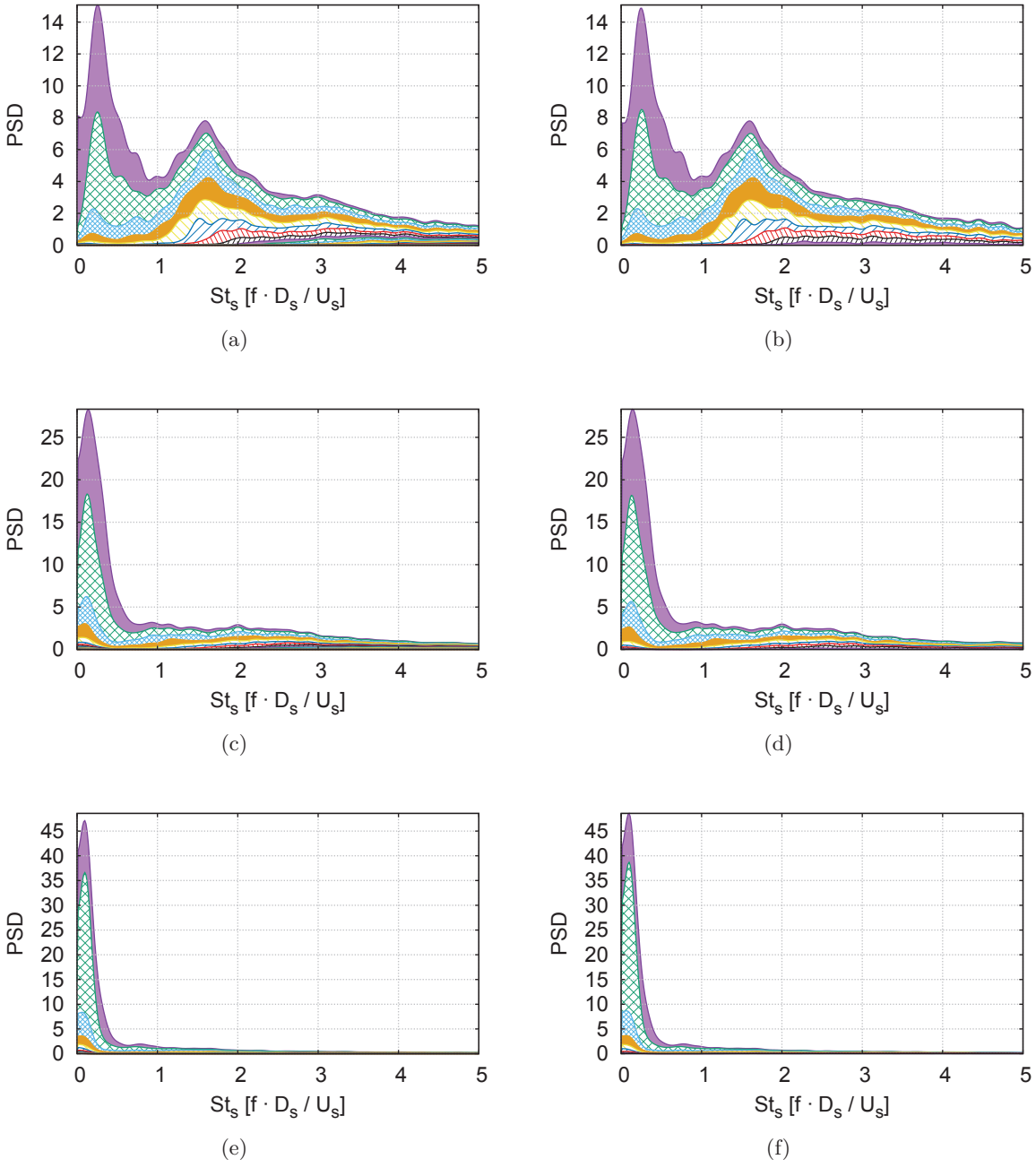

Figure B.8: *Stacked pressure PSD of each mode with respect to the total PSD. A256 is shown in the left column* ***(a)***, ***(c)*** *and* ***(e)*** *and A16 in the right column* ***(b)***, ***(d)*** *and* ***(f)***. *The radial position considered is NF1D. The axial positions are* ***(a)***, ***(b)*** $x/D_s = 2.5$, ***(b)***, ***(c)*** $x/D_s = 4.5$ *and* ***(d)***, ***(e)*** $x/D_s = 6.75$.

B.1.3 LIP_S probes analysis

In this section, the analysis of the LIP_S array is explained. The first position located at $x/D_s = 2.5$, $r/D_s = 0.45$ falls between the fifth and the sixth shock-cells. These shock-cells are the first ones to generate shock-cell noise. The second position located at $x/D_s = 4.5$, $r/D_s = 0.45$ is at the end of the shock-cell system. Last, the third position located at $x/D_s = 6.75$, $r/D_s = 0.45$ is at the end of the potential core. This radial position falls inside the non-linear part of the flow, therefore, a higher uncertainty is expected in the results, even for A256.

At this radial position, a higher number of modes is excited. This is due to the fact that when the flow is represented by a linear superposition of functions, in this case, based on the Fourier series, the interactions between different modes, and singular phenomena are discretized by higher modes. As it can be seen in the left column of Fig. B.9, the energy is distributed fairly equally among all the discretized modes in A16. At the second and third axial positions, the vortices are more developed and rearranged in the first mode, obtaining a higher amplitude for this mode. The remaining energy that is aliased into the discretized modes is about 3 to 4 times the total energy of the discretized modes. The higher the remaining energy is, the higher the error in amplitude is captured. At this radial position, the error is well above 20% for almost all the modes. Mode 0 and mode 1 are below this value at the second and third axial position. The right column of Fig. B.9 shows that the energy of the flow is distributed among more modes than for NF3D and NF1D. In particular, at the first axial position, closer to the shock-cells, 27 linear modes are needed to recover 95% of the energy. At the second and third axial locations, the number of required modes is reduced, but it still achieves 21 and 18 modes respectively. It is clear that the 16 probes is not enough to well represent the flow by a linear superposition of modes. In order to recover 50% of the energy, five and three modes are needed for the second and third axial positions respectively. This value is twice the number of modes needed at NF3D and NF1D. The higher energy remaining is clearly seen in these plots and is illustrated by the area between the lines of A16 and A256 for the first 8 modes. This area, is the same as the one found between A16 and A256 for the modes superior to 8, which is in fact, the remaining energy shown in the plots of the left column of Fig. B.9.

The accumulated error with growing frequency can be seen in Fig. B.10. Contrarily to the radial positions where the flow is still in the linear region, here, all the modes accumulate error following the same logarithmic trend. The error accumulated up to $St_s = 2$ is about 40% for the first axial position, 50% for the second axial position and about 60% for the third axial position with a higher dispersion between different modes. In a similar way, the non-linearities distribute the error among a higher range of frequencies than for NF3D and NF1D where the error was mostly accumulated for discrete frequencies linked to regular events.

The aliased energy of the higher modes is qualitatively depicted in Fig. B.11 where a comparison between the left column (A256) and the right column (A16) shows the difference in percentage amplitude of each mode, being easily discerned when growing with the frequency.

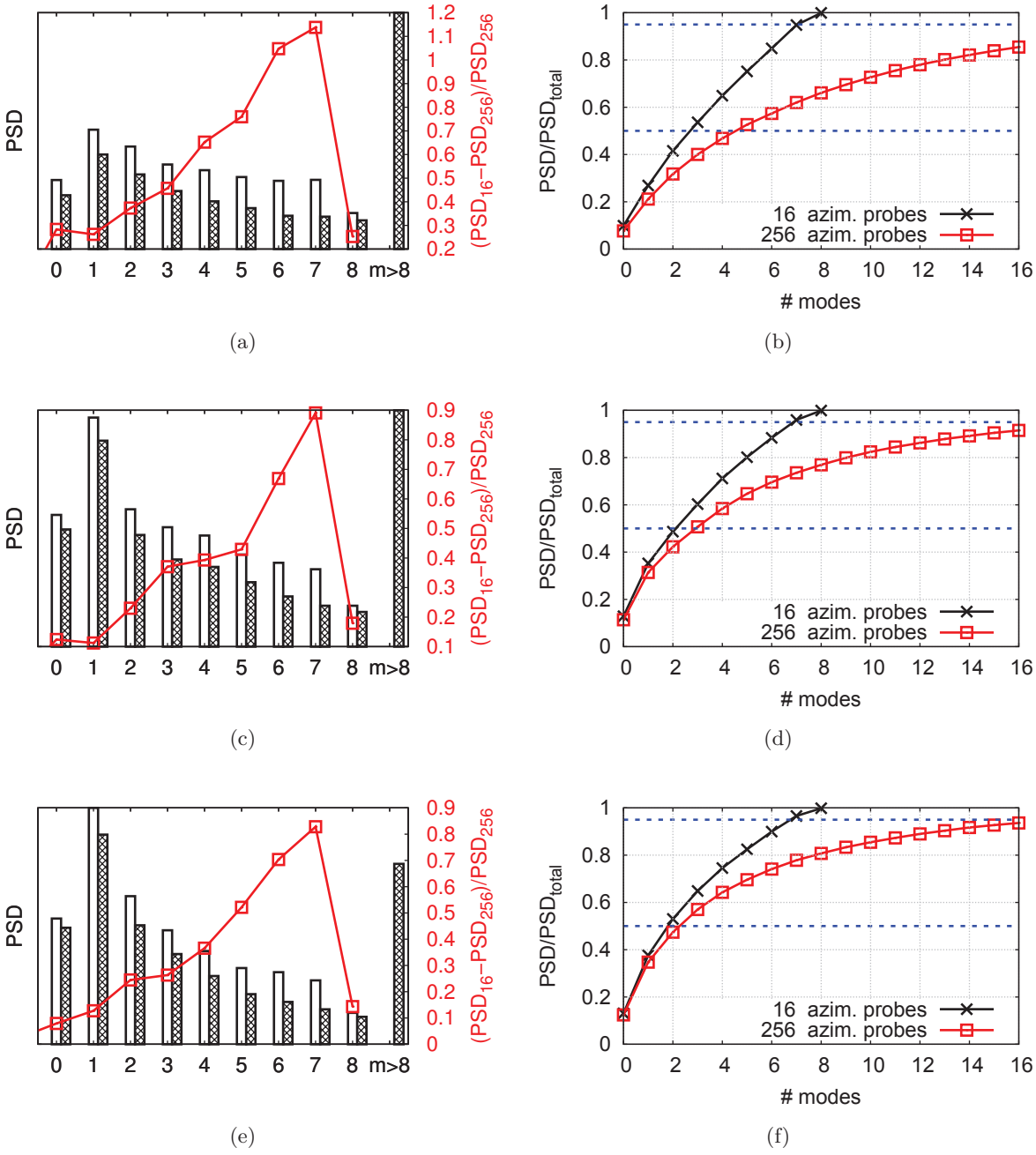

Figure B.9: *On the left column, the total energy density is represented for A16 and A256 in blank and hatched bars respectively. Moreover, the line plot shows the relative deviation of A16 with respect to A256. On the right column, the accumulated energy by number of modes is represented for both arrays. The horizontal dashed lines represent the* 50% *and* 95% *thresholds. The radial position considered is LIP_S. The axial positions are* ***(a)****,* ***(b)*** $x/D_s = 2.5$*,* ***(b)****,* ***(c)*** $x/D_s = 4.5$ *and* ***(d)****,* ***(e)*** $x/D_s = 6.75$*.*

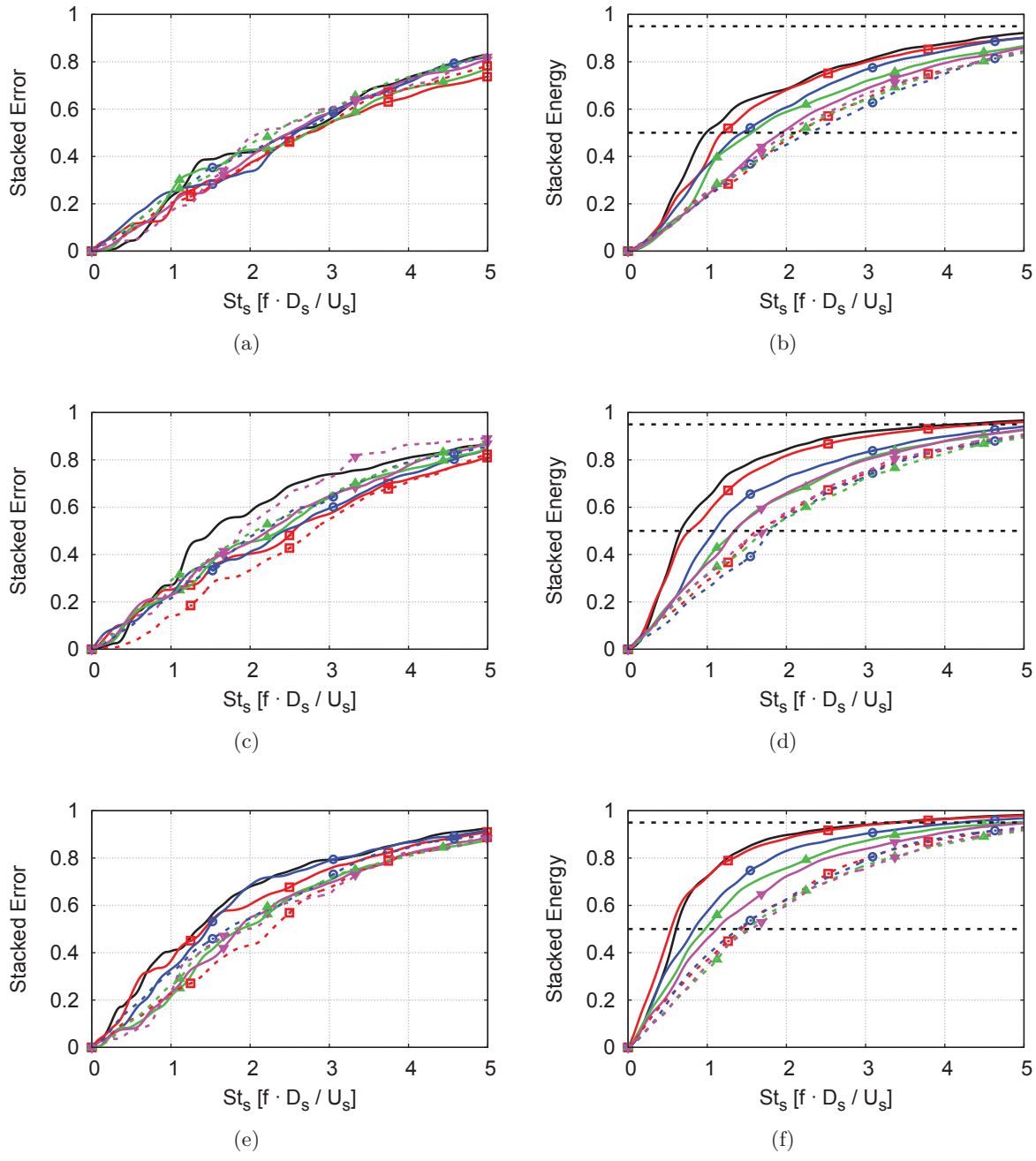

Figure B.10: *On the left column, the stacked error growing with the frequency is represented for A16 with respect to A256. On the right column, the stacked energy growing with the frequency is represented for A16. In solid line: mode 0 in black without symbol, mode 1 in red □, mode 2 in blue ○, mode 3 in green △ and mode 4 in magenta ▽. In dashed line: mode 5 in red □, mode 6 in blue ○, mode 7 in green △ and mode 8 in magenta ▽. The radial position considered is LIP_S. The axial positions are* ***(a)****,* ***(b)*** $x/D_s = 2.5$*,* ***(b)****,* ***(c)*** $x/D_s = 4.5$ *and* ***(d)****,* ***(e)*** $x/D_s = 6.75$*.*

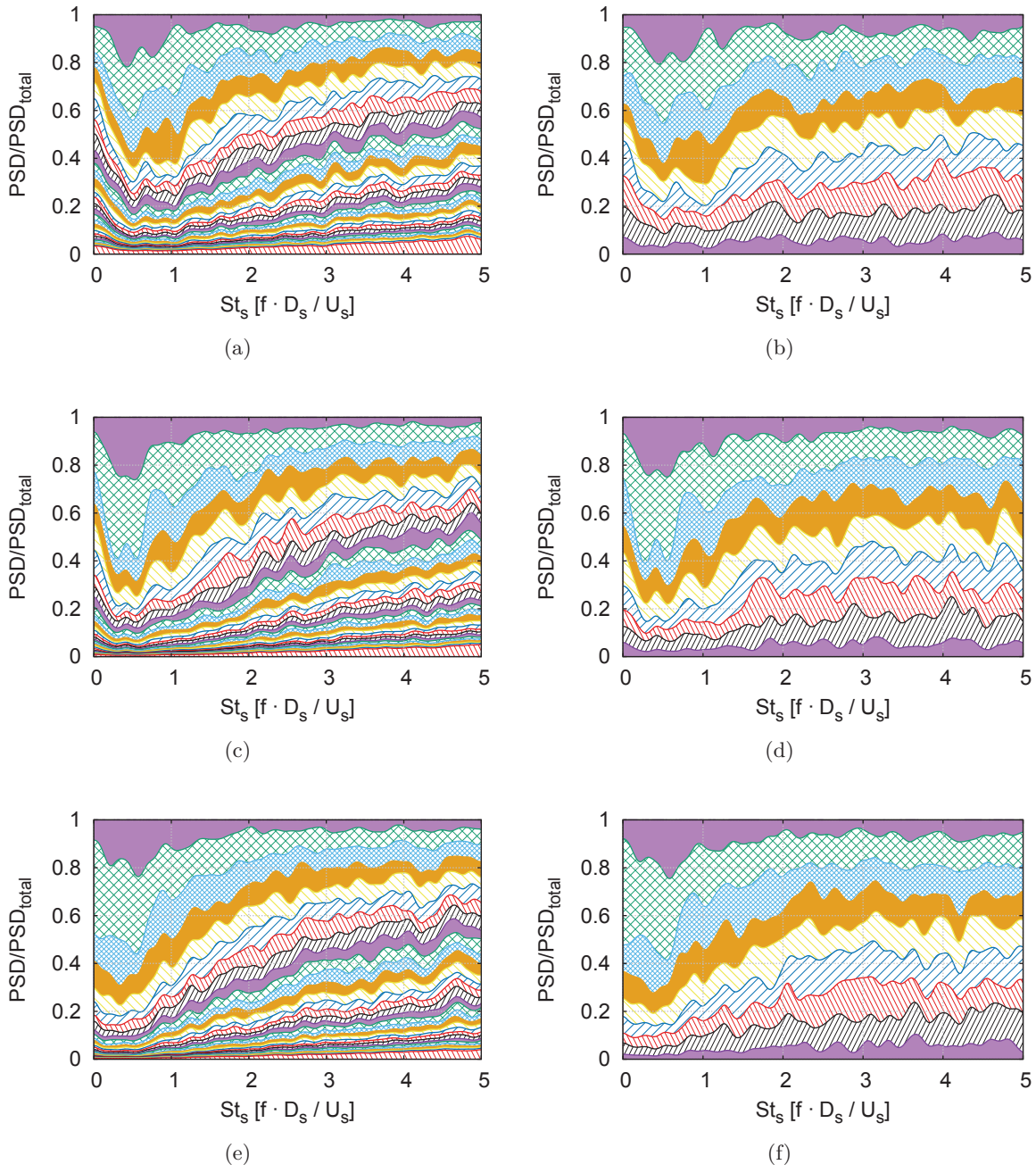

Figure B.11: *Pressure PSD Ratio of each mode with respect to the total PSD. A256 is shown in the left column* ***(a)****,* ***(c)*** *and* ***(e)*** *and A16 in the right column* ***(b)****,* ***(d)*** *and* ***(f)****. The radial position considered is LIP_S. The axial positions are* ***(a)****,* ***(b)*** $x/D_s = 2.5$*,* ***(b)****,* ***(c)*** $x/D_s = 4.5$ *and* ***(d)****,* ***(e)*** $x/D_s = 6.75$*.*

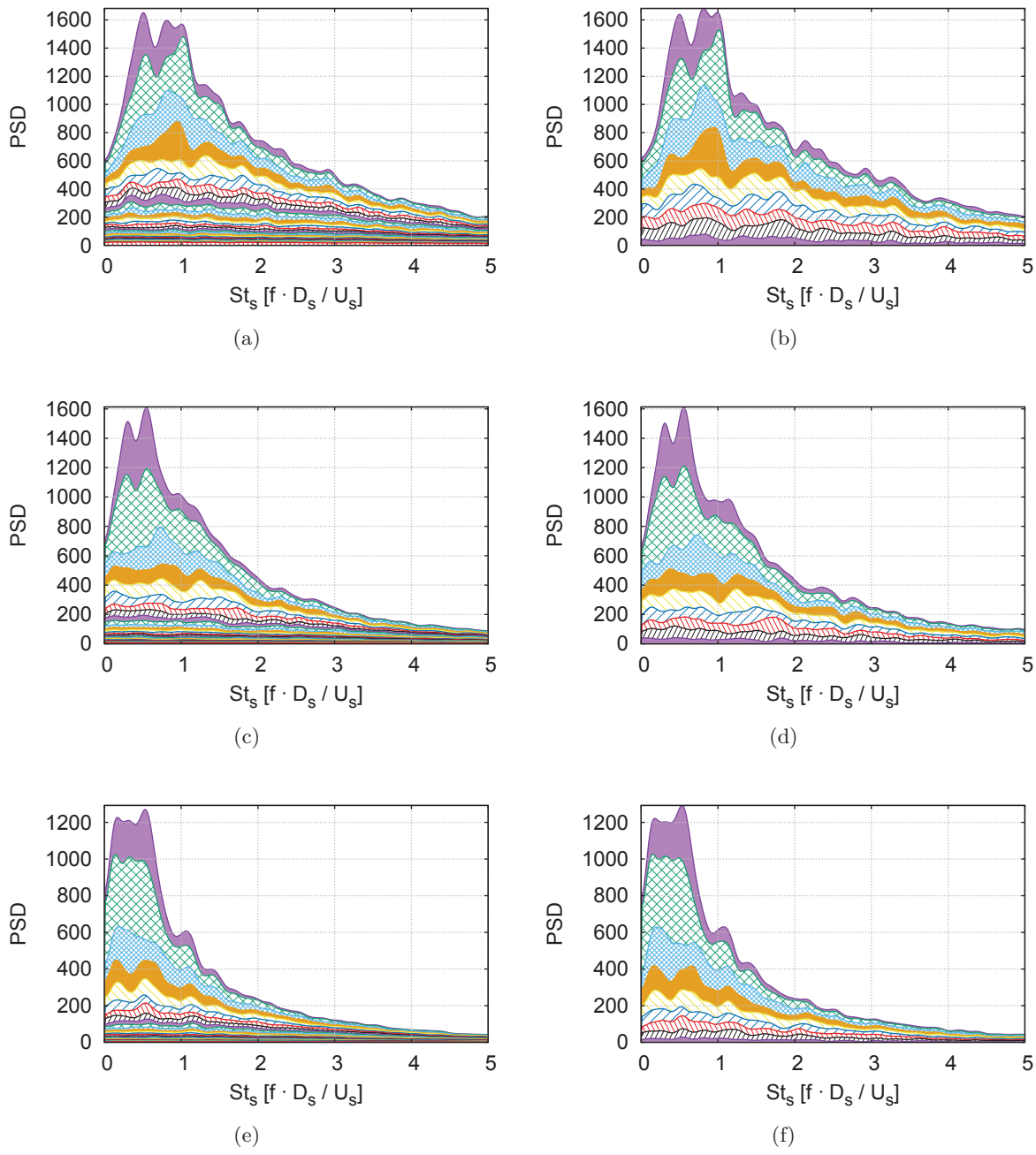

Figure B.12: *Stacked pressure PSD of each mode with respect to the total PSD. A256 is shown in the left column* ***(a)****,* ***(c)*** *and* ***(e)*** *and A16 in the right column* ***(b)****,* ***(d)*** *and* ***(f)****. The radial position considered is LIP_S. The axial positions are* ***(a)****,* ***(b)*** $x/D_s = 2.5$*,* ***(b)****,* ***(c)*** $x/D_s = 4.5$ *and* ***(d)****,* ***(e)*** $x/D_s = 6.75$*.*

B.1.4 LIP_P probes analysis

In this section, the analysis of the LIP_P array is explained. The different positions of the array are characteristic positions of a supersonic under-expanded jet. The first position located at $x/D_s = 2.5$, $r/D_s = 0.20$ falls between the fifth and the sixth shock-cells as for LIP_S, however, in this case, the probes are inside the potential core of the primary jet. The second position located at $x/D_s = 4.5$, $r/D_s = 0.20$ is at end of the shock-cell system but as before, it is located in the primary jet. Last, the third position located at $x/D_s = 6.75$, $r/D_s = 0.20$ is at the end of the potential core as with the LIP_S array, but closer to the axis. At this radial position, the axial velocity is higher than in LIP_S but the mixing is smaller due to the fact that the difference in velocity between the primary jet and the secondary jet is smaller than the difference between the secondary jet and the flow at rest. Inside the primary jet, the azimuthal non-linearities are expected to be smaller than in the shear-layer of the secondary jet. Moreover, the probes being closer together and having a similar order of magnitude of the vortices should lead to a reduction in the number of excited modes.

The energy distribution between each mode is shown in the left column of Fig. B.13. At all axial positions, mode 0 and mode 1 have about two to three times the energy of the second mode depending on the axial position. The higher modes have an amplitude that is reduced about 50% per mode. The remaining energy of the unresolved modes has the same order of magnitude as the higher modes. Therefore, the impact of the aliasing to the first modes will be minimal. The error committed by using A16 is below 15% for the first 4 to 5 modes. The right column of B.13 ascertains the fact that the energy is comprised in the first modes. The number of modes required to achieve 95% of the energy is about 6 for each axial position. Only the mode 0 and the mode 1 are sufficient in order to recover 50% of the total energy. It can be seen that the A16 line slightly deviates from the one with A256 which assures a good azimuthal discretization with only 16 probes.

Even if the total error is small, the accumulated error with growing frequency can still give information about where it is occurring. From Fig. B.14, similarly to NF1D, it is found that the error is accumulated mostly for $St_s < 1$, depending on the mode. The higher and of low amplitude modes (above 4), accumulate the error in a linear manner throughout the whole spectra.

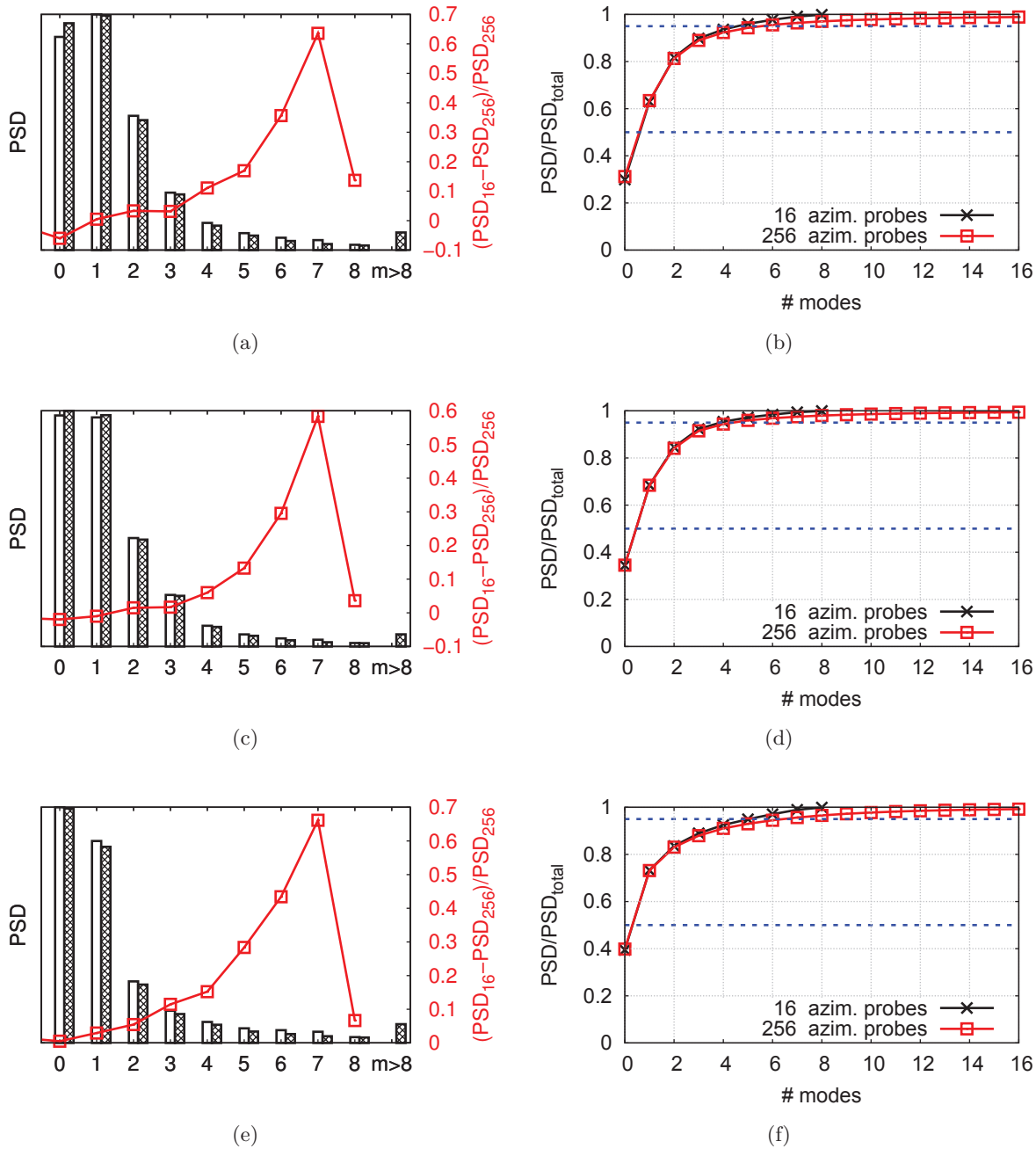

Figure B.13: *On the left column, the total energy density is represented for the A16 and A256 in blank and hatched bars respectively. Moreover, the line plot shows the relative deviation of A16 with respect to A256. On the right column, the accumulated energy by number of modes is represented for both arrays. The horizontal dashed lines represent the* 50% *and* 95% *thresholds. The radial position considered is LIP_P. The axial positions are* ***(a)****,* ***(b)*** $x/D_s = 2.5$*,* ***(b)****,* ***(c)*** $x/D_s = 4.5$ *and* ***(d)****,* ***(e)*** $x/D_s = 6.75$*.*

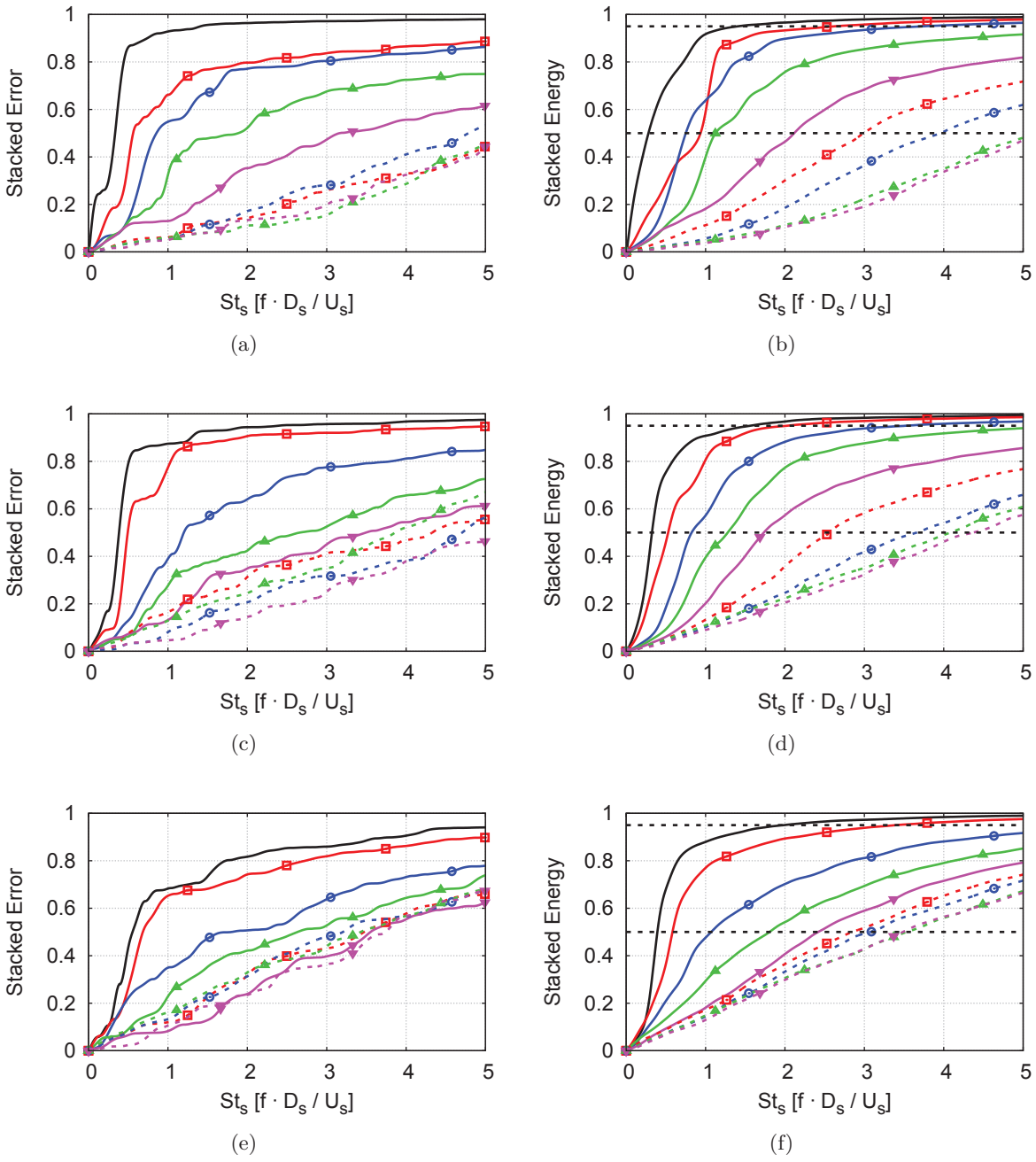

Figure B.14: *On the left column, the stacked error growing with the frequency is represented for A16 with respect to A256. On the right column, the stacked energy growing with the frequency is represented for A16. In solid line: mode 0 in black without symbol, mode 1 in red □, mode 2 in blue ○, mode 3 in green △ and mode 4 in magenta ▽. In dashed line: mode 5 in red □, mode 6 in blue ○, mode 7 in green △ and mode 8 in magenta ▽. The radial position considered is LIP_P. The axial positions are* ***(a)****,* ***(b)*** $x/D_s = 2.5$*,* ***(b)****,* ***(c)*** $x/D_s = 4.5$ *and* ***(d)****,* ***(e)*** $x/D_s = 6.75$.

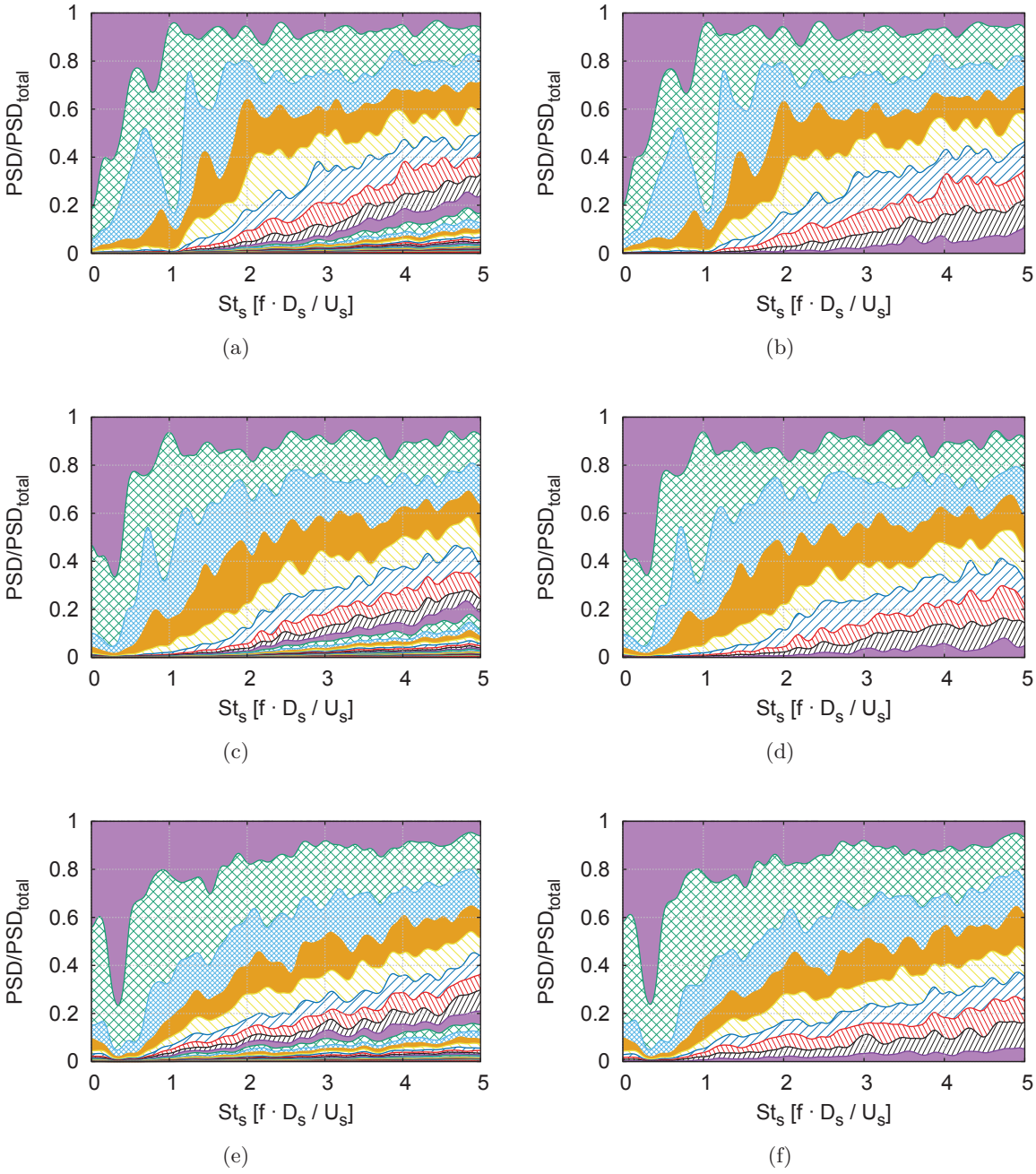

Figure B.15: *Pressure PSD Ratio of each mode with respect to the total PSD. A256 is shown in the left column* ***(a)****,* ***(c)*** *and* ***(e)*** *and A16 in the right column* ***(b)****,* ***(d)*** *and* ***(f)****. The radial position considered is LIP_P. The axial positions are* ***(a)****,* ***(b)*** $x/D_s = 2.5$*,* ***(b)****,* ***(c)*** $x/D_s = 4.5$ *and* ***(d)****,* ***(e)*** $x/D_s = 6.75$*.*

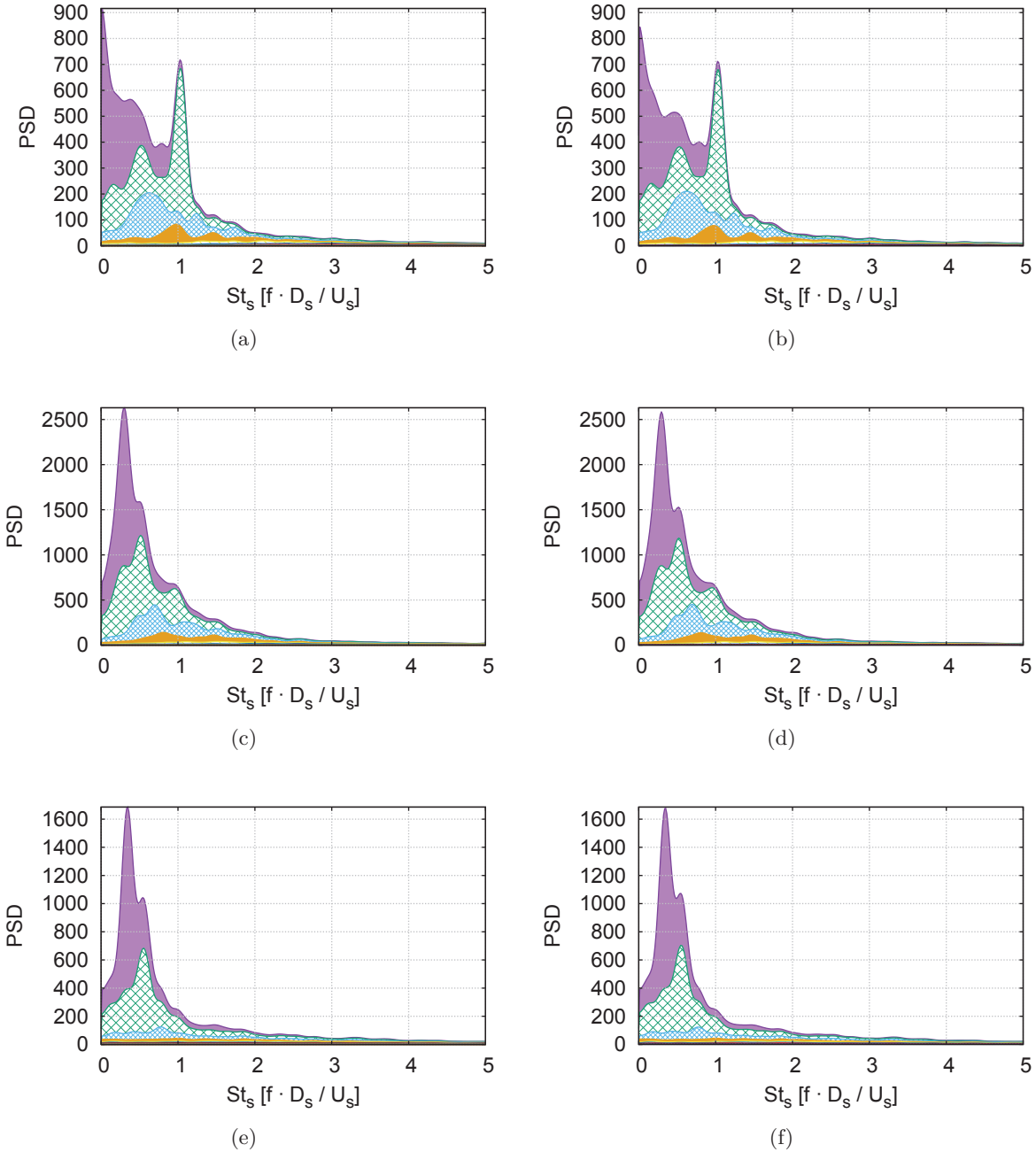

Figure B.16: *Stacked pressure PSD of each mode with respect to the total PSD. A256 is shown in the left column* ***(a)***, ***(c)*** *and* ***(e)*** *and A16 in the right column* ***(b)***, ***(d)*** *and* ***(f)***. *The radial position considered is LIP_P. The axial positions are* ***(a)***, ***(b)*** $x/D_s = 2.5$, ***(b)***, ***(c)*** $x/D_s = 4.5$ *and* ***(d)***, ***(e)*** $x/D_s = 6.75$.

B.2 Summary and conclusions

In this appendix, the methodology used to extract the azimuthal modes in a flow was presented. The azimuthal decomposition of the flow was carried out by approximating the solution with a linear superposition of terms obtained with the Fourier series. In the present study, the azimuthal decomposition was carried out using the python library *numpy*. As it happens with the time domain when the signal is decomposed in Fourier modes, the azimuthal decomposition suffers from aliasing when the number of azimuthal modes is not high enough. In this appendix, the focus was drawn to the aliasing phenomena, investigated with an array of 16 probes and 256 probes. According to the Nyquist theorem, the number of modes that are resolved is half the number of probes, thus resulting in 8 and 128 modes plus the mean. However, if the energy of the higher modes is not zero, it will fold back on the resolved modes aliasing the signal. The flow was analyzed at three different axial locations and at 4 different radial locations recovering distinct results.

The first data analyzed, referenced as NF3D, were located in the near-field, far from the hydrodynamic disturbances. In this region, the shock-cell noise is well defined. The 95% of the energy of the shock-cell noise is mainly distributed among the first 12 modes. Using a 16 probe array allowed to compute the first three modes with less than 15% error in the total energy. Nonetheless, less than a 15% of this error was accumulated in the frequency region of interest that for supersonic jets could be considered up to $St_s = 3$. Therefore, a 16 probes array allowed the shock-cell noise to be resolved within a 2.25% error from a fully discretized array. The results in the near-field where the hydrodynamic disturbances are important, referenced as NF1D showed how the flow was mainly dominated by the first mode and the mean. A similar number of modes were needed in order to capture 95% of the energy as in NF3D. However, at the downstream axial position the error was mainly committed below $St_s = 0.5$ because it is there where most of the energy was concentrated. Contrary to the results in the near-field, the energy was equally distributed among all the discretized modes for 16 probes. At the first axial position which is closer to the shock-cells, 27 modes were required to recover 95% of the energy. Farther downstream, it is reduced to 18 modes. The accumulated error up to $St_s = 2$ reached between 40% and 60%. Inside the jet (LIP_P), the energy is contained mainly the first 6 modes with a higher accumulated error for $St_s < 1$.

This study illustrated how depending on the physics of interest, the number of probes of an azimuthal array can determine whether or not a good accuracy of the results is obtained. Moreover, different positions inside the flow show different responses to the azimuthal discretization.

Appendix C

Collaborations and related publications

Within the framework of the project AeroTraNet2, several joint efforts were carried out between the partners. In this chapter, the main collaborations with the author of the thesis are reviewed. These contributions were published in conferences or were submitted to a journal for review.

In addition, the collaboration with the postdoctoral researcher S. Bidadi (CERFACS) is detailed in Ch. 7.

PSE-based sensitivity analysis of turbulent and supersonic single stream jet

The mean flow of the LES of the supersonic under-expanded jet from Sec. 5 and the supersonic under-expanded dual jet from Sec. 5 were used by Ansaldi *et al.* [245] from the IMFT in order to carry out a sensitivity analysis of the jet instability to any local forcing. The sensitivity analysis is carried out using the Parabolized Stability Equations (PSE) and their adjoint counter-part. The validation of the methodology was carried out on a simple semi-analytical supersonic jet. Then sensitivity functions to a source of momentum, mass or energy forcing were given for the above-mentioned supersonic jets. Highest sensitivities were found inside the shear-layer close to the external boundary of the potential core and close to the jet inlet, similar to previous results found for incompressible single stream jets [246]. This work was presented in the 22nd AIAA/CEAS Aeroacoustics Conference.

Broadband shock-cell noise signature identification using a wavelet-based method

The study of shock-cell noise from supersonic under-expanded single of a wavelet-based methodology was done in collaboration with Gefen *et al.* [247]. The event detection technique LIM shown in Ch. 4 was applied to a pressure near-field line array obtained from the LES in order to extract the signatures related to shock-cell noise. Each signature is characterized by its shape and time-scale. The signatures found in the near-field are in good agreement with the far-field signatures. This work was presented in the 22nd AIAA/CEAS Aeroacoustics Conference.

Uncertainty quantification and sensitivity analysis applied to an under-expanded single jet

The aim of CFD simulations is to model and compute the ideal performance of a flow under some particular conditions. A standard approach is to perform simulations with fixed parameters and boundary conditions. However, this is not accurate enough due to the fact that under realistic conditions, some parameters may be uncertain. Non-intrusive Uncertainty Quantification (UQ) was applied to a matrix of 64 three-dimensional RANS simulations in collaboration with Granados *et al.* [248], in order to understand the impact of input uncertainties. The case of consideration is the supersonic under-expanded single jet from Ch. 5. Results show that some regions of the jet plume are very sensitive to a combination of both physical and turbulence model variance. These regions are in fact corresponding to the parts of the jet where screech and shock-cell noise is generated, so this can be an indicator of a relevant impact of uncertainties in jet noise emission, what can guide to future research and more robust developments in aircraft industry. This work was presented in the AIAA/AVIATION Conference in Washington (2016) [248] and it was submitted for publication to the AIAA Journal.

Other collaborations

In addition, it can be highlighted the generation of the meshes used for the same cases shown in Ch. 5 and Ch. 6 but adapted to the second-order scheme solver COSMIC (Leicester University) and the data and knowledge transfer between all the partners. As an example, the PhD candidate Di Stefano [249, 250] (Leicester University), whose work is related to acoustic analogies for noise propagation to the far-field, benefited from the data saved from the dual stream jet of Ch. 6.

References

[1] S. A. Stansfeld and M. P. Matheson, "Noise pollution: non-auditory effects on health," *British medical bulletin*, vol. 68, no. 1, pp. 243–257, 2003.

[2] C. D. Francis, C. P. Ortega, and A. Cruz, "Noise pollution changes avian communities and species interactions," *Current biology*, vol. 19, no. 16, pp. 1415–1419, 2009.

[3] P. Arguelles, M. Bischoff, P. Busquin, B. A. C. Droste, R. Evans, W. Kroll, J. L. Lagardere, A. Lina, J. Lumsden, and D. Ranque, "European aeronautics: A vision for 2020," vol. 12, pp. –, 2001.

[4] E. Commission *et al.*, "Flightpath 2050. Europe's vision for aviation," vol. –, pp. –, 2012.

[5] H. H. Hubbard, "Aeroacoustics of flight vehicles: Theory and practice. Volume 1. Noise sources," Tech. Rep. 90-3052, NASA, 1991.

[6] A. Fosso-Pouangué, M. Sanjosé, S. Moreau, G. Daviller, and H. Deniau, "Subsonic jet noise simulations using both structured and unstructured grids," *AIAA J.*, 2014.

[7] S. Pirozzoli, "Conservative hybrid compact-WENO schemes for shock-turbulence interaction," *J. Comput. Phys.*, vol. 178, no. 1, pp. 81 – 117, 2002.

[8] B. J. W. S. Rayleigh, *The theory of sound, Vol. I.* MacMillan and Company Ltd., London, 1894.

[9] B. J. W. S. Rayleigh, *The theory of sound, Vol. II.* MacMillan and Company Ltd., London, 1896.

[10] M. J. Lighthill, "On sound generated aerodynamically. I. general theory," *Philos. T.R. Soc. Lond.*, vol. 211, no. 1107, pp. 564–587, 1952.

[11] M. J. Lighthill, "On sound generated aerodynamically. II. turbulence as a source of sound," *Philos. T.R. Soc. Lond.*, vol. 222, no. 1148, pp. 1–32, 1954.

[12] M. J. Lighthill, "The Bakerian lecture, 1961. Sound generated aerodynamically," *Philos. T.R. Soc. Lond.*, vol. 267, no. 1329, pp. 147–182, 1962.

[13] C. K. W. Tam, "Jet noise: since 1952," *Theor. Comp. Fluid Dyn.*, vol. 10, no. 1-4, pp. 393–405, 1998.

[14] J. E. F. Williams, "The noise from turbulence convected at high speed," *Philos. T.R. Soc. Lond.*, pp. 469–503, 1963.

[15] G. M. Lilley, "On the noise from jets," in *Agard 131*, 1974.

[16] J. D. Anderson Jr, *Fundamentals of aerodynamics*. McGraw-Hill Education, 1985.

[17] B. André, *Etude expérimentale de l'effet du vol sur le bruit de choc de jets supersoniques sous-détendus*. PhD thesis, L'École Centrale de Lyon, 2012.

[18] J. M. Seiner, J. C. Manning, and M. K. Ponton, "The preferred spatial mode of instability for a Mach 2 jet," in *10th AIAA Aeroacoustics Conference, July 9–11, Seattle, Washington, AIAA Paper 1986–1942*, 1986.

[19] S. C. Crow and F. H. Champagne, "Orderly structure in jet turbulence," *J. Fluid Mech.*, vol. 48, no. 03, pp. 547–591, 1971.

[20] G. L. Brown and A. Roshko, "On density effects and large structure in turbulent mixing layers," *J. Fluid Mech.*, vol. 64, no. 04, pp. 775–816, 1974.

[21] C. D. Winant and F. K. Browand, "Vortex pairing: the mechanism of turbulent mixing-layer growth at moderate Reynolds number," *J. Fluid Mech.*, vol. 63, no. 02, pp. 237–255, 1974.

[22] C. K. W. Tam and K. C. Chen, "A statistical model of turbulence in two-dimensional mixing layers," *J. Fluid Mech.*, vol. 92, no. 02, pp. 303–326, 1979.

[23] C. K. W. Tam, "Supersonic jet noise," *Annu. Rev. of Fluid Mech.*, vol. 27, no. 1, pp. 17–43, 1995.

[24] C. K. W. Tam and D. E. Burton, "Sound generated by instability waves of supersonic flows. Part 1. Two-dimensional mixing layers," *J. Fluid Mech.*, vol. 138, pp. 249–271, 1 1984.

[25] C. K. W. Tam and D. E. Burton, "Sound generated by instability waves of supersonic flows. Part 2. Axisymmetric jets," *J. Fluid Mech.*, vol. 138, pp. 273–295, 1 1984.

[26] C. K. W. Tam, M. Golebiowski, and J. M. Seiner, "On the two components of turbulent mixing noise from supersonic jets," in *2nd AIAA/CEAS Aeroacoustics Conference, 6–8 May, State College, Pennsylvania, AIAA Paper 1996–1716*, 1996.

[27] C. K. W. Tam, K. Viswanathan, K. K. Ahuja, and J. Panda, "The sources of jet noise: experimental evidence," *J. Fluid Mech.*, vol. 615, no. 1, pp. 253–292, 2008.

[28] C. K. W. Tam, "Stochastic model theory of broadband shock associated noise from supersonic jets," *J. Sound Vib.*, vol. 116, no. 2, pp. 265–302, 1987.

[29] L. Prandtl, "Stationary waves in a gaseous jet," *Physikalische Zeitschrift*, vol. 5, pp. 599–601, 1904.

[30] D. C. Pack, "A note on Prandtl's formula for the wave-length of a supersonic gas jet," *Q. J. Mech. Appl. Math.*, vol. 3, no. 2, pp. 173–181, 1950.

[31] A. Powell, "On the mechanism of choked jet noise," *Proceed. of the Phys.l Soc.*, vol. 66, no. 12, p. 1039, 1953.

[32] C. K. W. Tam, J. M. Seiner, and J. C. Yu, "Proposed relationship between broadband shock associated noise and screech tones," *J. Sound Vib.*, vol. 110, no. 2, pp. 309–321, 1986.

[33] J. Panda, "An experimental investigation of screech noise generation," *J. Fluid Mech.*, vol. 378, pp. 71–96, 1999.

[34] G. Raman, "Supersonic jet screech: Half-century from Powell to the present," *J. Sound Vib.*, vol. 225, no. 3, pp. 543–571, 1999.

[35] C. K. W. Tam, J. A. Jackson, and J. M. Seiner, "A multiple-scales model of the shock-cell structure of imperfectly expanded supersonic jets," *J. Fluid Mech.*, vol. 153, pp. 123–149, 1985.

[36] C. K. W. Tam, "The shock-cell structures and screech tone frequencies of rectangular and non-axisymmetric supersonic jets," *J. Sound Vib.*, vol. 121, no. 1, pp. 135–147, 1988.

[37] J. Panda, "Shock oscillation in underexpanded screeching jets," *J. Fluid Mech.*, vol. 363, pp. 173–198, 1998.

[38] H. Suda, T. A. Manning, and S. Kaji, "Transition of oscillation modes of rectangular supersonic jet in screech," in *15th AIAA Aeroacoustics Conference, 25–27 October, Long Beach, California, AIAA Paper 1993–4323*, 1993.

[39] T. Suzuki and S. K. Lele, "Shock leakage through an unsteady vortex-laden mixing layer: application to jet screech," *J. Fluid Mech.*, vol. 490, pp. 139–167, 2003.

[40] C. Lui and S. K. Lele, "Sound generation mechanism of shock-associated noise," in *9th AIAA/CEAS Aeroacoustics Conference and Exhibit, 12-14 May, Hilton Head, South Carolina, AIAA Paper 2003–3315*, 2003.

[41] T. D. Norum, "Screech suppression in supersonic jets," *AIAA J.*, vol. 21, no. 2, pp. 235–240, 1983.

[42] J. Panda, G. Raman, and K. B. M. Q. Zaman, "Underexpanded screeching jets from circular, rectangular, and elliptic nozzles," Tech. Memo. 2004-212481, NASA, 2003.

[43] B. André, T. Castelain, and C. Bailly, "Broadband shock-associated noise in screeching and non-screeching underexpanded supersonic jets," *AIAA J.*, vol. 51, no. 3, pp. 665–673, 2013.

[44] H. K. Tanna, B. J. Tester, and J. C. Lau, "The noise and flow characteristics of inverted-profile coannular jets," Ctr. Rep. 158995, NASA, 1979.

[45] H. K. Tanna and W. H. Brown, "Shock associated noise reduction from inverted-velocity-profile coannular jets," Ctr. Rep. 3454, NASA, 1981.

[46] H. K. Tanna, W. H. Brown, and C. K. W. Tam, "Shock associated noise of inverted-profile coannular jets, Part I: Experiments," *J. Sound Vib.*, vol. 98, no. 1, pp. 95–113, 1985.

[47] C. K. W. Tam, "Shock associated noise of inverted-profile coannular jets, part III: Shock structure and noise characteristics," *J. Sound Vib.*, vol. 98, no. 1, pp. 127–145, 1985.

[48] C. K. W. Tam and H. K. Tanna, "Shock associated noise of inverted-profile coannular jets, part II: Condition for minimum noise," *J. Sound Vib.*, vol. 98, no. 1, pp. 115–125, 1985.

[49] M. D. Dahl and P. J. Morris, "Noise from supersonic coaxial jets, part 1: Mean flow predictions," *J. Sound Vib.*, vol. 200, no. 5, pp. 643–663, 1997.

[50] M. D. Dahl and P. J. Morris, "Noise from supersonic coaxial jets, part 2: normal velocity profile," *J. Sound Vib.*, vol. 200, no. 5, pp. 665–699, 1997.

[51] T. V. R. Rao, R. R. Kumar, and J. Kurian, "Near field shock structure of dual co-axial jets," *Shock Waves*, vol. 6, no. 6, pp. 361–366, 1996.

[52] P. H. Bent, A. M. Blackner, S. A. Newsum, and E. H. Nesbitt, "Shock associated noise of dual flow nozzles," *AIAA J.*, vol. 2323, 1998.

[53] E. Murakami and D. Papamoschou, "Mean flow development in dual-stream compressible jets," *AIAA J.*, vol. 40, no. 6, pp. 1131–1138, 2002.

[54] E. Murakami and D. Papamoschou, "Mixing layer characteristics of coaxial supersonic jets," *AIAA J.*, vol. 2060, pp. 1–16, 2000.

[55] M. D. Dahl, D. Papamoschou, and R. Hixon, "Supersonic coaxial jets: Noise predictions and measurements," Tech. Memo. 1998-207422, NASA, 1998.

[56] K. Viswanathan, "Parametric study of noise from dual-stream nozzles," *J. Fluid Mech.*, vol. 521, pp. 35–68, 2004.

[57] K. Viswanathan, "True farfield for dual-stream jet noise measurements," *AIAA J.*, vol. 49, no. 2, pp. 443–447, 2011.

[58] K. Viswanathan, M. J. Czech, and I. C. Lee, "Towards prediction of dual-stream jet noise: Database generation," *AIAA J.*, vol. 49, no. 12, pp. 2695–2712, 2011.

[59] T. R. S. Bhat, U. W. Ganz, and A. Guthrie, "Acoustic and flow field characteristics of shock-cell noise from dual flow nozzles," in *11th AIAA/CEAS Aeroacoustics Conference, 23–25 May, Monterey, California AIAA Paper 2005–2929*, 2005.

[60] Y. A. Abdelhamid and U. W. Ganz, "Prediction of shock-cell structure and noise in dual flow nozzles," in *13th AIAA/CEAS Aeroacoustics Conference (28th AIAA Aeroacoustics Conference), 21–23 May, Rome, Italy, AIAA Paper 2007–3721*, 2007.

[61] C. K. W. Tam, N. N. Pastouchenko, and K. Viswanathan, "Broadband shock-cell noise from dual stream jets," *J. Sound Vib.*, vol. 324, no. 3, pp. 861–891, 2009.

[62] C. K. W. Tam, N. N. Pastouchenko, and K. Viswanathan, "Computation of shock cell structure of dual-stream jets for noise prediction," *AIAA J.*, vol. 46, no. 11, pp. 2857–2867, 2008.

[63] M. L. Shur, P. R. Spalart, M. K. Strelets, and A. V. Garbaruk, "Further steps in LES-based noise prediction for complex jets," in *44th AIAA Aerospace Sciences Meeting and Exhibit, 9–12 January, Reno, Nevada, AIAA Paper 2006–485*, 2006.

[64] S. J. Eastwood and P. G. Tucker, "Hybrid LES-RANS of complex geometry jets," *International Journal of Aeroacoustics*, vol. 10, no. 5-6, pp. 659–684, 2011.

[65] F. Vuillot, N. Lupoglazoff, and M. Huet, "Effect of chevrons on double stream jet noise from hybrid CAA computations," *49th AIAA Aerospace Sciences Meeting including the New Horizons Forum and Aerospace Exposition, 4 – 7 January, Orlando, Florida, AIAA Paper 2011–1154*, 2011.

[66] M. L. Shur, P. R. Spalart, and M. K. Strelets, "Noise prediction for underexpanded jets in static and flight conditions," *AIAA J.*, vol. 49, no. 9, pp. 2000–2017, 2011.

[67] K. Viswanathan, P. R. Spalart, M. J. Czech, A. Garbaruk, and M. Shur, "Tailored nozzles for jet plume control and noise reduction," *AIAA J.*, vol. 50, no. 10, pp. 2115–2134, 2012.

[68] M. Sanjosé, A. Fosso Pouangué, S. Moreau, G. Wang, and T. Padois, "Unstructured LES of the baseline EXEJET dual-stream jet," in *20th AIAA/CEAS Aeroacoustics Conference, 16–20 June, Atlanta, Georgia, AIAA Paper 2014–1155*, 2014.

[69] T. Colonius and S. K. Lele, "Computational aeroacoustics: progress on nonlinear problems of sound generation," *Prog. Aerosp. Sci.*, vol. 40, no. 6, pp. 345–416, 2004.

[70] J. Smagorinsky, "General circulation experiments with the primitive equations: I. the basic experiment," *Mon. Weather Rev.*, vol. 91, no. 3, pp. 99–164, 1963.

[71] C. Bogey, C. Bailly, and D. Juvé, "Noise investigation of a high subsonic, moderate Reynolds number jet using a compressible large eddy simulation," *Theor. Comp. Fluid Dyn.*, vol. 16, no. 4, pp. 273–297, 2003.

[72] D. J. Bodony and S. K. Lele, "Jet noise prediction of cold and hot subsonic jets using large–eddy simulation," in *10th AIAA/CEAS Aeroacoustics Conference, 10–12 May 2004, Manchester, U.K., AIAA Paper 2004–3022*, 2004.

[73] C. Bogey and C. Bailly, "Effects of inflow conditions and forcing on subsonic jet flows and noise.," *AIAA J.*, vol. 43, no. 5, pp. 1000–1007, 2005.

[74] C. Bogey and C. Bailly, "Computation of a high Reynolds number jet and its radiated noise using large eddy simulation based on explicit filtering," *Comput. Fluids*, vol. 35, no. 10, pp. 1344–1358, 2006.

[75] C. Bogey and C. Bailly, "Large eddy simulations of round free jets using explicit filtering with/without dynamic Smagorinsky model," *Int. J. Heat Fluid Fl.*, vol. 27, no. 4, pp. 603–610, 2006.

[76] C. Bogey and C. Bailly, "Large eddy simulations of transitional round jets: Influence of the Reynolds number on flow development and energy dissipation," *Phys. Fluids*, vol. 18, pp. 1–14, 2006.

[77] C. Bogey and C. Bailly, "Investigation of downstream and sideline subsonic jet noise using large eddy simulation," *Theor. Comp. Fluid Dyn.*, vol. 20, no. 1, pp. 23–40, 2006.

[78] S. Bühler, L. Kleiser, and C. Bogey, "Simulation of subsonic turbulent nozzle jet flow and its near-field sound," *AIAA J.*, pp. 1–17, 2014.

[79] J. Schulze and J. Sesterhenn, "Numerical simulation of supersonic jet-noise," *Proceed. Ap. Math Mech.*, vol. 8, no. 1, pp. 10703–10704, 2008.

[80] J. Schulze, J. Sesterhenn, P. Schmid, C. Bogey, N. de Cacqueray, J. Berland, and C. Bailly, "Numerical simulation of supersonic jet noise," in *Num. Sim. of Turbulent Flows & Noise Generation, NNFM*, pp. 29–46, Springer, 2009. Numerical Simulation of Turbulent Flows and Noise Generation.

[81] J. Berland, C. Bogey, and C. Bailly, "Large eddy simulation of screech tone generation in a planar underexpanded jet," in *12th AIAA/CEAS Aeroacoustics Conference (27th AIAA Aeroacoustics Conference), 8–10 May, Cambridge, Massachusetts, AIAA Paper 2006–2496*, 2006.

[82] S. Mendez, M. Shoeybi, A. Sharma, F. E. Ham, S. K. Lele, and P. Moin, "Large-eddy simulations of perfectly-expanded supersonic jets: Quality assessment and validation," in *48th AIAA Aerospace Sciences Meeting Including the New horizons Forum and Aerospace Exposition, 4–7 January 2010, Orlando, Florida, AIAA Paper 2010–271*, 2010.

[83] D. J. Bodony, J. Ryu, and S. K. Lele, "Investigating broadband shock-associated noise of axisymmetric jets using large-eddy simulation," in *12th AIAA/CEAS Aeroacoustics Conference, 8–10 May, Cambridge, Massachusetts, AIAA Paper 2006–2495*, 2006.

[84] S.-C. Lo, K. Aikens, G. Blaisdell, and A. Lyrintzis, "Numerical investigation of 3-D supersonic jet flows using large-eddy simulation," *Int. J. Aeroacoustics*, vol. 11, no. 7-8, pp. 783–812, 2012.

[85] J. W. Nichols, F. E. Ham, S. K. Lele, and P. Moin, "Prediction of supersonic jet noise from complex nozzles," in *Annual Research Briefs 2011*, pp. 3–14, Center for Turbulence Research, 2011.

[86] J. Nichols, F. Ham, S. Lele, and J. Bridges, "Aeroacoustics of a supersonic rectangular jet: Experiments and LES predictions," in *50th AIAA Aerospace Sciences Meeting including the New Horizons Forum and Aerospace Exposition, 09–12 January, Nashville, Tennessee, AIAA Paper 2012–0678*, 2012.

[87] N. Andersson, L.-E. Eriksson, and L. Davidson, "A study of Mach 0.75 jets and their radiated sound using large–eddy simulation," in *10th AIAA/CEAS Aeroacoustics Conference, May 10–12, Manchester, United Kingdom, AIAA Paper 2004–3024*, 2004.

[88] C. Bogey, S. Barré, D. Juvé, and C. Bailly, "Simulation of a hot coaxial jet: Direct noise prediction and flow-acoustics correlations," *Phys. Fluids*, vol. 21, pp. 1–14, 2009.

[89] J. B. Freund, "Noise sources in a low-Reynolds-number turbulent jet at Mach 0.9," *Journal of Fluid Mechanics*, vol. 438, pp. 277–305, 2001.

[90] J. B. Freund, S. K. Lele, and P. Moin, "Numerical simulation of a Mach 1.92 turbulent jet and its sound field," *AIAA J.*, vol. 38, no. 11, pp. 2023–2031, 2000.

[91] C. K. W. Tam and H. K. Tanna, "Shock associated noise of supersonic jets from convergent-divergent nozzles," *J. Sound Vib.*, vol. 81, no. 3, pp. 337–358, 1982.

[92] C. Bailly, P. Lafon, Sé, and b. Candel, "Subsonic and supersonic jet noise predictions from statistical source models," *AIAA J.*, vol. 35, no. 11, pp. 1688–1696, 1997.

[93] T. Colonius, S. K. Lele, and P. Moin, "Sound generation in a mixing layer," *J. Fluid Mech.*, vol. 330, pp. 375–409, 1997.

[94] C. Schram, J. Anthoine, and A. Hirschberg, "Calculation of sound scattering using curle's analogy for non-compact bodies," in *11th AIAA/CEAS Aeroacoustics Conference (26th AIAA Aeroacoustics Conference), 23 - 25 May, Monterey, California, AIAA Paper 2005–2836*, no. 2005-2836, 2005.

[95] P. J. Morris, L. N. Long, T. E. Scheidegger, Q. Wang, and A. R. Pilon, "High speed jet noise simulations," *AIAA J.*, no. 98-2290, 1998.

[96] C. Henry, C. Bailly, and G. Bodard, "Stochastic prediction of broadband shock-associated noise including propagation effects," in *Acoustics 2012*, 2012.

[97] P. J. Morris and S. A. E. Miller, "The prediction of broadband shock-associated noise using RANS CFD," in *15th AIAA/CEAS Aeroacoustics Conference (30th AIAA Aeroacoustics Conference), 11–13 May, Miami, Florida, AIAA Paper 2009–3315*, 2009.

[98] S. A. E. Miller and P. J. Morris, "The prediction of broadband shock-associated noise including propagation effects," *Int. J. Aeroacoustics*, vol. 11, no. 7, pp. 755–782, 2012.

[99] A. Kalyan and S. Karabasov, "Towards a suitable turbulence length and temporal scale model for broadband shock associated noise," in *22nd AIAA/CEAS Aeroacoustics Conference, 30 May – 1 June, Lyon, France, AIAA Paper 2016–2802*, 2016.

[100] B. Henderson, "Fifty years of fluidic injection for jet noise reduction," *Int. J. Aeroacoustics*, vol. 9, no. 1-2, pp. 91–122, 2010.

[101] B. S. Henderson and M. P. Wernet, "A PIV study of slotted air injection for jet noise reduction," Tech. Memo. 2012-217251, NASA, 2012.

[102] P. J. Morris, D. K. McLaughlin, and C.-W. Kuo, "Noise reduction in supersonic jets by nozzle fluidic inserts," *J. Sound Vib.*, vol. 332, no. 17, pp. 3992–4003, 2013.

[103] K. B. M. Q. Zaman, "Jet noise reduction by microjets: A parametric study," Tech. Memo. 2010-215846, NASA, 2010.

[104] M. Huet, B. Fayard, G. Rahier, and F. Vuillot, "Numerical investigation of the micro-jets efficiency for jet noise reduction," in *15th AIAA/CEAS Aeroacoustics Conference (30th AIAA Aeroacoustics Conference), 11–13 May, Miami, Florida, AIAA Paper 2009–3127*, 2009.

[105] S. Enomoto, K. Yamamoto, K. Yamashita, N. Tanaka, Y. Oba, and T. Oishi, "Large-eddy simulation of high-subsonic jet flow with microjet injection," *17th AIAA/CEAS Aeroacoustics Conference(32nd AIAA Aeroacoustics Conference), 05 – 08 June, Portland, Oregon, AIAA Paper 2011–2883*, vol. 2883, p. 2011, 2011.

[106] M. L. Shur, P. R. Spalart, and M. K. Strelets, "LES-based evaluation of a microjet noise reduction concept in static and flight conditions," *J. Sound Vib.*, vol. 330, no. 17, pp. 4083–4097, 2011.

[107] P.-T. Lew, A. Najafi-Yazdi, and L. Mongeau, "Unsteady numerical simulation of a round jet with impinging microjets for noise suppression," *J. Acoust. Soc. Am.*, vol. 134, no. 3, pp. 1982–1989, 2013.

[108] R. Westley and G. M. Lilley, "An investigation of the noise field from a small jet and methods for its reduction.," Rep. 53, The College of Aeronautics, Cranfield, 1952.

[109] D. Alec, M. Geoffrey, R. Westley, W. End, and W. Lane, "Jet noise suppression means," Oct. 20 1964. US Patent 3,153,319.

[110] A. Adrian and H. Wilfred, "Jet noise suppressor nozzle," 1962. US Patent 3,065,818.

[111] D. C. Mathews and J. K. C. Low, "Tabbed nozzle for jet noise suppression," Nov. 13 2001. US Patent 6,314,721.

[112] S. Martens, "Shelf truncated chevron exhaust nozzle for reduction of exhaust noise and infrared (IR) signature," 2003. US Patent 6,532,729.

[113] W. M. Presz Jr and G. Reynolds, "Contoured thrust reverser and lobed nozzle noise suppressor for gas turbine engines," May 2001.

[114] M. Samimy, K. B. M. Q. Zaman, and M. F. Reeder, "Effect of tabs on the flow and noise field of an axisymmetric jet," *AIAA J.*, vol. 31, no. 4, pp. 609–619, 1993.

[115] D. Papamoschou, "Engine cycle and exhaust configuration for quiet supersonic propulsion," in *38th AIAA/ASME/SAE/ASEE Joint Propulsion Conference & Exhibit, 7–10 July, Indianapolis, Indiana, AIAA Paper 2002–3917*, 2002.

[116] D. Papamoschou and M. Debiasi, "Conceptual development of quiet turbofan engines for supersonic aircraft," *J. Propul Power*, vol. 19, no. 2, pp. 161–169, 2003.

[117] D. Papamoschou, "Engine cycle and exhaust configuration for quiet supersonic propulsion," *J. Propul Power*, vol. 20, no. 2, pp. 255–262, 2004.

[118] D. Papamoschou, "Pylon-based jet noise suppressors," in *46th AIAA Aerospace Sciences Meeting and Exhibit, 7 – 10 January, Reno, Nevada, AIAA Paper 2008–40*, 2008.

[119] K. B. M. Q. Zaman, F. Y. Wang, and N. J. Georgiadis, "Noise, turbulence, and thrust of subsonic freejets from lobed nozzles," *AIAA J.*, vol. 41, no. 3, pp. 398–407, 2003.

[120] J. M. Seiner and M. M. Gilinsky, "Undulated nozzle for enhanced exit area mixing," 2000.

[121] J. Bridges and C. A. Brown, "Parametric testing of chevrons on single flow hot jets," Tech. Memo. 2004-213107, NASA, 2004.

[122] O. H. Rask, E. J. Gutmark, and S. Martens, "Shock cell modification due to chevrons," in *45th AIAA Aerospace Sciences Meeting and Exhibit, Reno, Nevada, AIAA Paper 2007–0831*, pp. 2007–0831, 2007.

[123] E. J. Gutmark, O. H. Rask, and U. Michel, "How chevrons decrease broadband jet noise in cruise," in *13th AIAA/CEAS Aeroacoustics Conference, Roma Italy, AIAA Paper 2007–3611*, 2007.

[124] R. H. Schlinker, J. C. Simonich, D. W. Sharon, R. A. Reba, T. Colonius, K. Gudemendsson, and F. Ladeincla, "Supersonic jet noise from round and chevron nozzles: experimental studies," in *15th AIAA/CEAS Aeroacoustics Conference (30th AIAA Aeroacoustics Conference), 11–13 May 2009, Miami, Florida, AIAA Paper 2009–3257*, 2009.

[125] V. G. Mengle, U. Ganz, E. Nesbitt, E. J. Bultemeier, and R. Thomas, "Flight test results for uniquely tailored propulsion-airframe aeroacoustic chevrons: shockcell noise," *12th AIAA/CEAS Aeroacoustics Conference (27th AIAA Aeroacoustics Conference), 8–10 May, Cambridge, Massachusetts, AIAA Paper 2006–2439*, vol. 2439, p. 2006, 2006.

[126] V. G. Mengle, U. Ganz, E. J. Bultemeier, and F. T. Calkins, "Clocking effect of chevrons with azimuthally-varying immersions on shockcell/cabin noise," in *14th AIAA/CEAS Aeroacoustics Conference (29th AIAA Aeroacoustics Conference), 5–7 May, Vancouver, British Columbia Canada, AIAA Paper 2008–3000*, 2008.

[127] E. Bultemeier, U. Ganz, J. Premo, and E. Nesbitt, "Effect of uniform chevrons on cruise shockcell noise," in *12th AIAA/CEAS Aeroacoustics Conference (27th AIAA Aeroacoustics Conference), 8–10 May, Cambridge, Massachusetts, 2006–2440*, 2006.

[128] J. Huber, A. A. Sylla, V. Fleury, J. Bulté, K. Britchford, E. Laurendeau, and D. Long, "Understanding and reduction of cruise jet noise at model and full scale," in *15th AIAA/CEAS Aeroacoustics Conference (30th AIAA Aeroacoustics Conference), 11–13 May, Miami, Florida, AIAA Paper 2009–3382*, 2009.

[129] M. L. Shur, P. R. Spalart, and M. K. Strelets, "Noise prediction for increasingly complex jets. Part I: Methods and tests," *Int. J. Aeroacoustics*, vol. 4, no. 3 & 4, pp. 213–246, 2005.

[130] A. Uzun and M. Y. Hussaini, "Simulation of noise generation in the near-nozzle region of a chevron nozzle jet," *AIAA J.*, 2009.

[131] H. Xia, P. G. Tucker, and S. Eastwood, "Large-eddy simulations of chevron jet flows with noise predictions," *Int. J. Heat Fluid Fl.*, vol. 30, no. 6, pp. 1067–1079, 2009.

[132] H. Xia, S. Karabasov, O. Graham, P. Tucker, A. Dowling, K. Depuru, and T. Hynes, "Hybrid RANS-LES modeling of chevron nozzles with prediction of far field sound," in *49th AIAA Aerospace Sciences Meeting Including the New horizons Forum and Aerospace Exposition, 4–7 January 2010, Orlando, Florida, AIAA Paper 2011–21*, vol. 21, p. 2011, 2011.

[133] H. Xia and P. G. Tucker, "Numerical simulation of single-stream jets from a serrated nozzle," *Flow, turbulence and combustion*, vol. 88, no. 1-2, pp. 3–18, 2012.

[134] N. K. Depuru Mohan, A. P. Dowling, S. Karabasov, H. Xia, O. Graham, T. P. Hynes, and P. G. Tucker, "Acoustic sources and far-field noise of chevron and round jets," *AIAA J.*, vol. 53, no. 9, pp. 2421–2436, 2015.

[135] M. B. Alkislar, "Flow characteristics of a jet controlled with chevron-microjet combination for noise reduction," in *47th AIAA Aerospace Sciences Meeting Including The New Horizons Forum and Aerospace Exposition, 5 – 8 January, Orlando, Florida, AIAA Paper 2009–851*, vol. 851, 2009.

[136] K. Viswanathan, "Apparatus and method for reduction of jet noise from turbofan engines having separate bypass and core flaws," 2010. US Patent 7,836,700.

[137] K. Viswanathan, M. Shur, M. Strelets, and P. R. Spalart, "Numerical prediction of noise from round and beveled nozzles," in *Turbulent Flow and Noise Generation, EUROMECH Colloquium 467, Marseille, France*, 2005.

[138] K. Viswanathan, M. Shur, P. R. Spalart, and M. Strelets, "Flow and noise predictions for single and dual-stream beveled nozzles," *AIAA J.*, vol. 46, no. 3, pp. 601–626, 2008.

[139] K. Viswanathan and M. J. Czech, "Adaptation of the beveled nozzle for high-speed jet noise reduction," *AIAA J.*, vol. 49, no. 5, pp. 932–944, 2011.

[140] B. Henderson, "Aeroacoustics of three-stream jets," in *18th AIAA/CEAS Aeroacoustics Conference (33rd AIAA Aeroacoustics Conference), 04–06 June, Colorado Springs, Colorado, AIAA Paper 2012–2159*, 2012.

[141] B. S. Henderson, S. J. Leib, and M. Wernet, "Measurements and predictions of the noise from three-stream jets," in *21st AIAA/CEAS Aeroacoustics Conference, 22–26 June, Dallas, Texas, AIAA Paper 2015âĂŞ3120*, 2015.

[142] D. Papamoschou, V. Phong, J. Xiong, and F. Liu, "Quiet nozzle concepts for three-stream jets," in *54th AIAA Aerospace Sciences Meeting, AIAA SciTech, San Diego, California, AIAA Paper 2016–0523*, 2016.

[143] L. Cambier, S. Heib, and S. Plot, "The Onera elsA CFD software: input from research and feedback from industry," *Mech. & Ind.*, vol. 14, no. 03, pp. 159–174, 2013.

[144] H. Schlichting, K. Gersten, and K. Gersten, *Boundary-layer theory*. Springer Science & Business Media, 1979.

[145] C. Bogey and C. Bailly, "A family of low dispersive and low dissipative explicit schemes for flow and noise computations," *J. Comput. Phys.*, vol. 194, no. 1, pp. 194–214, 2004.

[146] A. Fosso-Pouangué, H. Deniau, F. Sicot, and P. Sagaut, "Curvilinear finite volume schemes using high order compact interpolation," *J. Comput. Phys.*, vol. 229, no. 13, pp. 5090–5122, 2010.

[147] S. K. Lele, "Compact finite difference schemes with spectral-like resolution," *J. Comput. Phys.*, vol. 103, pp. 16–42, 1992.

[148] M. R. Visbal and D. V. Gaitonde, "Shock capturing using compact-differencing-based methods," in *43rd AIAA Aerospace Sciences Meeting and Exhibit, 10-13 January, Reno, Nevada, AIAAP 2005–1265*, 2005.

[149] S. Pirozzoli, "Numerical methods for high-speed flows," *Annu. Rev. of Fluid Mech.*, vol. 43, pp. 163–194, 2011.

[150] M. R. Visbal and D. V. Gaitonde, "On the use of higher-order finite-difference schemes on curvilinear and deforming meshes," *J. Comput. Phys.*, vol. 181, pp. 155–185, 2002.

[151] A. Fosso-Pouangué, *Schémas Volumes Finis précis: application à l'aéroacoustique de jets subsoniques*. PhD thesis, Université Pierre et Marie Curie, Paris, 2011.

[152] S.-C. Lo, G. A. Blaisdell, and A. S. Lyrintzis, "High-order shock capturing schemes for turbulence calculations," *Int. J. Numer. Method Fluids*, vol. 62, no. 5, pp. 473–498, 2010.

[153] G. Puigt, J.-F. Boussuge, and H. Deniau, "Projet JECOP2 - aéroacoustique des jets supersoniques - rapport final," Ctr. Rep. 13-23494, Cerfacs, 7 2013.

[154] P. Colella and P. R. Woodward, "The piecewise parabolic method (PPM) for gas-dynamical simulations," *J. Comput. Phys.*, vol. 54, no. 1, pp. 174–201, 1984.

[155] P. L. Roe, "Approximate Riemann solvers, parameter vectors and difference schemes," *J. Comput. Phys.*, vol. 43, no. 2, pp. 357–372, 1981.

[156] A. Fosso Pouangué, H. Deniau, and N. Lamarque, "A sixth-order compact finite-volume scheme for aeroacoustics : application to a large eddy simulation of a jet," in *V European Conference on Computational Fluid Dynamics ECCOMAS CFD, 14–17 June, Lisbon, Portugal*, 2010.

[157] K. W. Thompson, "Time dependent boundary conditions for hyperbolic systems," *J. Comput. Phys.*, vol. 68, no. 1, pp. 1–24, 1987.

[158] T. J. Poinsot and S. K. Lele, "Boundary conditions for direct simulations of compressible viscous flows," *J. Comput. Phys.*, vol. 101, pp. 104–129, 1992.

[159] C. K. W. Tam and J. C. Webb, "Dispersion-relation-preserving finite difference schemes for computational acoustics," *J. Comput. Phys.*, vol. 107, no. 2, pp. 262–281, 1993.

[160] C. K. W. Tam and Z. Dong, "Radiation and outflow boundary conditions for direct computation of acoustic and flow disturbances in a nonuniform mean flow," *J. Comput. Phys.*, vol. 4, no. 02, pp. 175–201, 1996.

[161] C. Bogey and C. Bailly, "Three-dimensional non-reflective boundary conditions for acoustic simulations: far field formulation and validation test cases," *Acta Acust.*, vol. 88, no. 4, pp. 463–471, 2002.

[162] A. Fosso-Pouangué, H. Deniau, N. Lamarque, and T. J. Poinsot, "Comparison of outflow boundary conditions for subsonic aeroacoustic simulations," *Int. J. Numer. Method Fluids*, vol. 68, no. 10, pp. 1207–1233, 2012.

[163] R. Hixon, S.-H. Shih, and R. R. Mankabadi, "Evaluation of boundary conditions for computational aeroacoustics," *AIAA J.*, vol. 33, no. 11, pp. 2006–2012, 1995.

[164] S. Le Bras, H. Deniau, C. Bogey, and G. Daviller, "Development of compressible large–eddy simulations combining high–order schemes and wall modeling," in *21st AIAA/CEAS Aeroacoustics Conference, 22–26 June, Dallas, Texas, AIAA Paper2015–3135*, 2015.

[165] H. Choi and P. Moin, "Grid-point requirements for large eddy simulation: Chapman's estimates revisited," *Phys. Fluids*, vol. 24, no. 1, p. 011702, 2012.

[166] H. Tennekes and J. L. Lumley, *A first course in turbulence*. The MIT press, 1972.

[167] H. Ribner, "The generation of sound by turbulent jets," *Adv. Appl. Mech.*, vol. 8, pp. 103–182, 1964.

[168] J. Edmonds, "Matroids and the greedy algorithm," *Math. Program.*, vol. 1, no. 1, pp. 127–136, 1971.

[169] P. R. Spalart and S. Allmaras, "A one-equation turbulence model for aerodynamic flows," in *30th Aerospace Sciences Meeting and Exhibit, 6–9 January, Reno, Nevada (1992), AIAA Paper 1992–0439*, 1992.

[170] B. van Leer, "Towards the ultimate conservative difference scheme. V. A second-order sequel to Godunov's method," *J. Comput. Phys.*, vol. 32, no. 1, pp. 101–136, 1979.

[171] S. Chakravarthy, "High resolution upwind formulations for the Navier-Stokes equations," in *Computational Fluid Dynamics, VKI Lecture Series 1988-05, 7-11 March*, 1988.

[172] A. Harten, "High resolution schemes for hyperbolic conservation laws," *J. Comput. Phys.*, vol. 49, no. 3, pp. 357 – 393, 1983.

[173] B. Larrouturou, "How to preserve the mass fractions positivity when computing compressible multi-component flows," *J. Comput. Phys.*, vol. 95, pp. 59–84, 1991.

[174] C. Weber, *Développement de méthodes implicites pour les équations de Navier-Stokes moyennes et la simulation des grandes échelles : Application à l'aérodynamique externe*. PhD thesis, Institut National Polytechnique de Toulouse, France, 1998.

[175] Adrien Gomar, Thomas Léonard and others, "Antares: Python post-processing library," 2012–.

[176] W. Schroeder, K. Martin, and B. Lorensen, "The visualization toolkit (4th ed.)," 2006. ISBN 978-1-930934-19-1.

[177] N. Curle, "The influence of solid boundaries upon aerodynamic sound," in *P. Roy. Soc. Lond. A. Mat.*, vol. 231, pp. 505–514, The Royal Society, 1955.

[178] A. Powell, "Theory of vortex sound," *J. Acoust. Soc. Am.*, vol. 36, no. 1, pp. 177–195, 1964.

[179] J. E. F. Williams and D. L. Hawkings, "Sound generation by turbulence and surfaces in arbitrary motion," *Philos. T.R. Soc. Lond.*, vol. 264, no. 1151, pp. 321–342, 1969.

[180] F. Farassat, "Derivation of Formulations 1 and 1A of Farassat," Tech. Memo. 2007-214853, NASA, 2007.

[181] C. E. Tinney and P. Jordan, "The near pressure field of co-axial subsonic jets," *J. Fluid Mech.*, vol. 611, pp. 175–204, 2008.

[182] B.-T. Chu and L. S. Kovásznay, "Non-linear interactions in a viscous heat-conducting compressible gas," *J. Fluid Mech.*, vol. 3, no. 5, pp. 494–514, 1958.

[183] J. Lau, M. Fisher, and H. Fuchs, "The intrinsic structure of turbulent jets," *J. Sound Vib.*, vol. 22, no. 4, pp. 379–406, 1972.

[184] F. Coiffet, P. Jordan, J. Delville, Y. Gervais, and F. Ricaud, "Coherent structures in subsonic jets: a quasi-irrotational source mechanism?," *Int. J. Aeroacoustics*, vol. 5, no. 1, pp. 67–89, 2006.

[185] K. C. Massey and K. K. Ahuja, "Screech frequency prediction in light of mode detection and convection speed measurements for heated jets," in *3rd AIAA/CEAS Aeroacoustics Conference, Atlanta, Georgia, AIAA Paper 1997–1625*, 1997.

[186] V. F. Kopiev and G. A. Faranosov, "Generalization of the method of azimuthal decomposition of an acoustic field of a compact source for measurements in the vicinity of a rigid surface," *Acoust. Phys.*, vol. 61, no. 1, pp. 60–63, 2015.

[187] J. Morlet, "Sampling theory and wave-propagation," in *Geophysics*, 1982.

[188] M. Farge, "Wavelet transforms and their applications to turbulence," *Annu. Rev. of Fluid Mech.*, vol. 24, no. 1, pp. 395–458, 1992.

[189] C. Torrence and G. P. Compo, "A practical guide to wavelet analysis," *B. Am. Meteorol. Soc.*, vol. 79, no. 1, pp. 61–78, 1998.

[190] G. Kaiser, *A friendly guide to wavelets*. Springer Science & Business Media, 2010.

[191] C. Pérez Arroyo, G. Daviller, G. Puigt, and C. Airiau, "Shock-cell noise of supersonic under expanded jets," in *50th 3AF International Conference on Applied Aerodynamics, 29–30 March âĂŞ 01 April, Toulouse - France*, 2015.

[192] C. Pérez Arroyo, G. Daviller, G. Puigt, and C. Airiau, "Hydrodynamic - acoustic filtering of a supersonic under-expanded jet," in *ERCOFTAC WORKSHOP Direct and Large-Eddy Simulation 10, 27–29 May*, 2015.

[193] C. Pérez Arroyo, G. Daviller, G. Puigt, and C. Airiau, "Modal structure of a supersonic under–expanded jet," in *22éme Congrès Français de Mécanique, 24 – 28 August, Lyon, France*, 2015.

[194] M. Grottadaurea and A. Rona, "The radiating pressure field of a turbulent cylindrical cavity flow," in *14th AIAA/CEAS Aeroacoustics Conference (29th AIAA Aeroacoustics Conference), 5 - 7 May 2008*, 2008.

[195] D. Di Pasquale and A. Rona, "Data assessment of two Ercoftac transition test cases for CFD validation," in *7th International Conference on Heat Transfer, Fluid Mechanics and Thermodynamics, 19-21 July 2010, Antalya, Turkey*, 2010.

[196] F. Farassat and G. P. Succi, "The prediction of helicopter rotor discrete frequency noise," in *38th Am. Hel. Soc., Annual Forum, Anaheim, CA, 4–7 May*, 1982.

[197] A. Savarese, P. Jordan, S. Girard, A. Royer, C. Fourment, E. Collin, Y. Gervais, and M. Porta, "Experimental study of shock-cell noise in underexpanded supersonic jets," in *19th AIAA/CEAS Aeroacoustics Conference, Aeroacoustics Conferences, 27–29 May, Berlin, Germany, AIAA Paper 2013-2080*, 2013.

[198] D. Guariglia, A. R. Carpio, and C. Schram, "Design of a facility for shock-cells noise experimental investigation on a subsonic/supersonic coaxial jet," in *22nd AIAA/CEAS Aeroacoustics Conference, May 30 – June 1, Lyon, France, AIAA Paper*, 2016.

[199] J. M. Seiner, "Advances in high speed jet aeroacoustics," in *AIAA/NASA 9th Aeroacoustics Conference, 15–17 October, Williamsburg, Virginia, AIAA Paper 1984–2275*, 1984.

[200] L. D. Koch, J. Bridges, and A. Khavaran, "Flow field comparisons from three navier-stokes solvers for an axisymmetric separate flow jet," *AIAA J.*, vol. 672, p. 2002, 2002.

[201] W. A. Engblom, N. J. Georgiadis, and A. Khavaran, "Investigation of variable-diffusion turbulence model correction for round jets," in *11th AIAA/CEAS Aeroacoustics Conference (26th AIAA Aeroacoustics Conference), 23–25 May, Monterey, California, AIAA Paper 2005–3085*, 2005.

[202] T. B. Gatski and J.-P. Bonnet, *Compressibility, turbulence and high speed flow*. Academic Press, 2013.

[203] A. Singh and A. Chatterjee, "Numerical prediction of supersonic jet screech frequency," *Shock Waves*, vol. 17, no. 4, pp. 263–272, 2007.

[204] G. Daviller, G. Lehnasch, and P. Jordan, "Numerical investigation of the influence of upstream conditions on properties of shock noise in shock/mixing layer interaction," in *International Symposium of Turbulence and Shear Flow Phenomena*, vol. 1, 2013.

[205] C. Pérez Arroyo, G. Puigt, and C. Airiau, "Large eddy simulation of shock-cell noise from a dual stream jet," in *22nd AIAA/CEAS Aeroacoustics Conference, 30 May – 1 June, Lyon, France, AIAA Paper 2016–2798*, 2016.

[206] D. Guariglia, C. Schram, and F. Stella, "Design of a facility for shock-cell noise investigation on a subsonic/supersonic coaxial jet," in *PhD VKI Symposium*, 2015.

[207] F. Scarano, "Iterative image deformation methods in PIV," *Meas. Sci. Technol.*, vol. 13, no. 1, p. R1, 2001.

[208] J. Westerweel, "On velocity gradients in PIV interrogation," *Exp. Fluids*, vol. 44, no. 5, pp. 831–842, 2008.

[209] J. C. Laurence, "Intensity, scale, and spectra of turbulence in mixing region of free subsonic jet," Tech. Note 3561, NACA, 1956.

[210] P. O. A. L. Davies, M. J. Fisher, and M. J. Barratt, "The characteristics of the turbulence in the mixing region of a round jet," *J. Fluid Mech.*, vol. 15, no. 03, pp. 337–367, 1963.

[211] A. Towne, A. V. G. Cavalieri, P. Jordan, T. Colonius, V. Jaunet, O. T. Schmidt, and G. A. Brès, "Trapped acoustic waves in the potential core of subsonic jets," in *22nd AIAA/CEAS Aeroacoustics Conference, 30 May – 1 June, Lyon, France, AIAA Paper 2016–2809*, 2016.

[212] E. Garnier, M. Mossi, P. Sagaut, P. Comte, and M. Deville, "On the use of shock-capturing schemes for large-eddy simulation," *J. Comput. Phys.*, vol. 153, no. 2, pp. 273 – 311, 1999.

[213] B. Thornber, D. Drikakis, R. Williams, and D. Youngs, "On entropy generation and dissipation of kinetic energy in high-resolution shock-capturing schemes," *J. Comput. Phys.*, vol. 227, no. 10, pp. 4853 – 4872, 2008.

[214] S. Bidadi and S. L. Rani, "Investigation of numerical viscosities and dissipation rates of second-order TVD-MUSCL schemes for implicit large-eddy simulation," *J. Comput. Phys.*, vol. 281, pp. 1003 – 1031, 2015.

[215] S. Pirozzoli, "On the spectral properties of shock-capturing schemes," *J. Comput. Phys.*, vol. 219, no. 2, pp. 489–497, 2006.

[216] N. Adams and K. Shariff, "A high-resolution hybrid compact-ENO scheme for shock-turbulence interaction problems," *J. Comput. Phys.*, vol. 127, no. 1, pp. 27 – 51, 1996.

[217] Y.-X. Ren, M. Liu, and H. Zhang, "A characteristic-wise hybrid compact-WENO scheme for solving hyperbolic conservation laws," *J. Comput. Phys.*, vol. 192, no. 2, pp. 365 – 386, 2003.

[218] S. Zhang, S. Jiang, and C.-W. Shu, "Development of nonlinear weighted compact schemes with increasingly higher order accuracy," *J. Comput. Phys.*, vol. 227, no. 15, pp. 7294 – 7321, 2008.

[219] Y. Shen and G. Zha, "Generalized finite compact difference scheme for shock/complex flowfield interaction," *J. Comput. Phys.*, vol. 230, no. 12, pp. 4419–4436, 2011.

[220] G.-S. Jiang and C.-W. Shu, "Efficient implementation of weighted ENO schemes," *J. Comput. Phys.*, vol. 126, pp. 202–228, 1996.

[221] R. Borges, M. Carmona, B. Costa, and W. S. Don, "An improved weighted essentially non-oscillatory scheme for hyperbolic conservation laws," *J. Comput. Phys.*, vol. 227, no. 6, pp. 3191–3211, 2008.

[222] H. C. Yee, N. D. Sandham, and M. J. Djomehri, "Low-dissipative high-order shock-capturing methods using characteristic-based filters," *J. Comput. Phys.*, vol. 150, no. 1, pp. 199–238, 1999.

[223] E. Garnier, P. Sagaut, and M. Deville, "A class of explicit ENO filters with application to unsteady flows," *J. Comput. Phys.*, vol. 170, no. 1, pp. 184 – 204, 2001.

[224] F. Ducros, V. Ferrand, F. Nicoud, C. Weber, D. Darracq, C. Gacherieu, and T. J. Poinsot, "Large-eddy simulation of the shock/turbulence interaction," *J. Comput. Phys.*, vol. 152, no. 2, pp. 517–549, 1999.

[225] H. Yee and B. SjÃűgreen, "Development of low dissipative high order filter schemes for multiscale NavierâĂŞStokes/MHD systems," *J. Comput. Phys.*, vol. 225, no. 1, pp. 910 – 934, 2007.

[226] E. Johnsen, J. Larsson, A. V. Bhagatwala, W. H. Cabot, P. Moin, B. J. Olson, P. S. Rawat, S. K. Shankar, B. Sjögreen, and H. C. Yee, "Assessment of high-resolution methods for numerical simulations of compressible turbulence with shock waves," *J. Comput. Phys.*, vol. 229, no. 4, pp. 1213–1237, 2010.

[227] D. Kotov, H. Yee, A. Wray, B. SjÃűgreen, and A. Kritsuk, "Numerical dissipation control in high order shock-capturing schemes for LES of low speed flows," *J. Comput. Phys.*, vol. 307, pp. 189 – 202, 2016.

[228] H. Yee, G. Klopfer, and J.-L. Montagne, "High-resolution shock-capturing schemes for inviscid and viscous hypersonic flows," *J. Comput. Phys.*, vol. 88, pp. 31 – 61, 1990.

[229] A. Harten, "The artificial compression method for computation of shocks and contact discontinuities. III. self-adjusting hybrid schemes," *Mathematics of Computation*, vol. 32, no. 142, pp. 363 – 389, 1978.

[230] E. Touber and N. D. Sandham, "Comparison of three large-eddy simulations of shock-induced turbulent separation bubbles," *Shock Waves*, vol. 19, no. 6, pp. 469 – 478, 2009.

[231] B. Sjogreen and H. C. Yee, "Multiresolution wavelet based adaptive numerical dissipation control for shock-turbulence computations," *Res. Inst. for Adv. Comput. Sci.*, vol. 1, pp. 1–43, 2001.

[232] D. S. Balsara and C.-W. Shu, "Monotonicity preserving weighted essentially non-oscillatory schemes with increasingly high order of accuracy," *J. Comput. Phys.*, vol. 160, no. 2, pp. 405 – 452, 2000.

[233] C. Bogey, N. De Cacqueray, and C. Bailly, "A shock-capturing methodology based on adaptative spatial filtering for high-order non-linear computations," *J. Comput. Phys.*, vol. 228, no. 5, pp. 1447–1465, 2009.

[234] A. Uzun, R. Kumar, M. Y. Hussaini, and F. S. Alvi, "Simulation of tonal noise generation by supersonic impinging jets," *AIAA J.*, vol. 51, no. 7, pp. 1593 – 1611, 2013.

[235] C. Laney, *Computational Gas Dynamics*. Cambridge: Cambridge University Press, 1998.

[236] P. L. Roe and J. Pike, "Efficient construction and utilisation of approximate Riemann solutions," in *Proceedings of the Sixth International Symposium on Computing Methods in Applied Sciences and Engineering, VI*, pp. 499–518, 1985.

[237] N. T. Frink, "Upwind scheme for solving the Euler equations on unstructured tetrahedral meshes," *AIAA J.*, vol. 30, no. 1, pp. 70 – 77, 1992.

[238] E. Toro, *Riemann solvers and numerical methods for fluid dynamics*. New York: Springer, 3rd ed. ed., 2009.

[239] A. Suresh and H. T. Huynh, "Accurate monotonicity-preserving schemes with Runge–Kutta time stepping," *J. Comput. Phys.*, vol. 136, no. 1, pp. 83–99, 1997.

[240] Z.-S. Sun, L. Luo, Y.-X. Ren, and S.-Y. Zhang, "A sixth order hybrid finite difference scheme based on the minimized dispersion and controllable dissipation technique," *J. Comput. Phys.*, vol. 270, pp. 238 – 254, 2014.

[241] L. Fu, X. Y. Hu, and N. A. Adams, "A family of high-order targeted ENO schemes for compressible-fluid simulations," *J. Comput. Phys.*, vol. 305, pp. 333 – 359, 2016.

[242] X. Y. Hu, V. K. Tritschler, S. Pirozzoli, and N. A. Adams, "Dispersion-dissipation condition for finite difference schemes," *arXiv:1204.5088 [physics.flu-dyn]*, 2012.

[243] G. Sod, "A survey of several finite difference methods for systems of nonlinear hyperbolic conservation laws," *J. Comput. Phys.*, vol. 27, pp. 1 – 31, 1978.

[244] C.-W. Shu and S. Osher, "Efficient implementation of essentially non-oscillatory shock-capturing schemes, II," *J. Comput. Phys.*, vol. 83, no. 1, pp. 32–78, 1989.

[245] T. Ansaldi, C. Airiau, C. Pérez Arroyo, and G. Puigt, "PSE-based sensitivity analysis of turbulent and supersonic single stream jet," in *22nd AIAA/CEAS Aeroacoustics Conference, 30 May – 1 June, Lyon, France, AIAA Paper 2016–3052*, 2016.

[246] T. Ansaldi and C. Airiau, "Sensitivity analysis for subsonic jet using adjoint of non local stability equations," in *21st AIAA/CEAS Aeroacoustics Conference, 22–26 June, Dallas, Texas, AIAA Paper 2015-2219*, 2015.

[247] L. Gefen, C. Pérez Arroyo, R. Camussi, G. Puigt, and C. Airiau, "Broadband shock-cell noise signature identification using a wavelet-based method," in *22nd AIAA/CEAS Aeroacoustics Conference, 30 May – 1 June, Lyon, France, AIAA Paper 2016–2732*, 2016.

[248] F.-J. Granados-Ortiz, C. Pérez Arroyo, C.-H. L. G. Puigt, and C. Airiau, "Uncertainty quantification and sensitivity analysis applied to an under-expanded single jet," in *AIAA/AVIATION Conference, 13–17 June, Washington, Washington D.C, AIAA Paper 2016–4091*, 2016.

[249] D. Di Stefano, A. Rona, E. Hall, C. Morfey, and G. Puigt, "Validating the Ffowcs Williams and Hawkings acoustic analogy implementation in antares," in *22nd AIAA/CEAS Aeroacoustics Conference, 30 May – 1 June, Lyon, France, AIAA Paper 2016–3059*, (Lyon, France), pp. AIAA 2016–3059, AIAA, 2016.

[250] D. Di Stefano, A. Rona, E. Hall, and G. Puigt, "Modelling directional sound radiation in Antares by the Ffowcs Williams and Hawkings analogy," in *23rd International Congress on Sound & Vibration - ICSV23*, vol. 23, (Athens, Greece), 7 2016.

Abstract

This thesis deals with the shock-cell noise generated by under-expanded supersonic jets in single- and dual-stream configurations. Shock-cell noise is generated by the interaction between the turbulent structures of the shear-layer and the shock-cell system developed in the potential core of the jet. In order to study shock-cell noise, large eddy simulations adapted to aeroacoustics are carried out using high-order compact schemes that allow for a non-dissipative non-dispersive approach. The results are analyzed and compared to experimental results. In particular, an acoustic-hydrodynamic filtering is carried out in the near field in order to analyze the acoustic and hydrodynamic azimuthal modes. Moreover, a wavelet-based analysis is implemented in order to identify the relevant acoustic and hydrodynamic features of the supersonic jets.

Résumé

Cette thèse fait référence au bruit de choc généré par des jets sous-détendus simple ou en configuration co-axial. Le bruit de choc est généré par l'interaction entre les structures turbulentes de la couche de cisaillement et le réseaux de cellules de choc développé dans le cÃťne potentiel du jet. Afin d'étudier le bruit choc, simulations Ãă grandes échelles adaptés pour l'aéro-acoustique sont effectué avec des schémas d'ordre élevé qui permet une approche non-dissipative et non-dispersive. Les résultats sont analysés et comparés avec des résultats expérimentaux. Notamment, une filtrage hydrodynamique et acoustique est réalisé dans le champ proche pour analyser les modes azimutaux acoustiques et hydrodynamiques. En outre, un analyse basé sur la transformé en ondelettes est mis en œuvre pour identifier les caractéristiques acoustiques et hydrodynamiques importants des jets supersoniques.